The cover features a vertical strip of six microscopic images showing various material microstructures, including grain boundaries, precipitates, and cellular structures. The background of the cover is a dark, textured surface, possibly a metal or composite material, with a vertical crease or seam running down the right side.

THERMOMECHANICAL FATIGUE BEHAVIOR OF MATERIALS: 4TH VOLUME

Technical Editors:
Michael A. McGaw, Sreeramesh Kalluri,
Johan Bressers, Stathis D. Peteves

STP 1428

The logo for ASTM International, featuring the letters 'ASTM' in a stylized, bold font with a circular swoosh around them, and the word 'INTERNATIONAL' below it.

ASTM
INTERNATIONAL
Standards Worldwide

STP 1428

Thermomechanical Fatigue Behavior of Materials: 4th Volume

*Michael A. McGaw, Sreeramesh Kalluri, Johan Bressers,
and Stathis D. Peteves, Editors*

ASTM Stock Number: STP1428



ASTM International
100 Barr Harbor Drive
PO Box C700
West Conshohocken, PA 19428-2959

Printed in the U.S.A.

Library of Congress Cataloging-in-Publication Data
ISBN:

Thermomechanical fatigue behavior of materials. Fourth volume / Michael A. McGaw . . .
[et al.].

p. cm. — (STP ; 1428)

“ASTM Stock Number: STP1428.”

Includes bibliographical references and index.

ISBN 0-8031-3467-3

1. Alloys—Thermomechanical properties—Congresses. 2. Composite materials—Thermomechanical properties—Congresses. 3. Fracture mechanics—Congresses. I. McGaw, Michael A., 1959- II. Symposium on “Thermomechanical Fatigue Behavior of Materials (4th : 2001 : Dallas, Tex.) III. ASTM special technical publication ; 1428.

TA483.T48 2003

620.1'126—dc22

2003058256

Copyright © 2003 ASTM International, West Conshohocken, PA. All rights reserved. This material may not be reproduced or copied, in whole or in part, in any printed, mechanical, electronic, film, or other distribution and storage media, without the written consent of the publisher.

Photocopy Rights

Authorization to photocopy items for internal, personal, or educational classroom use, or the internal, personal, or educational classroom use of specific clients, is granted by ASTM International (ASTM) provided that the appropriate fee is paid to the Copyright Clearance Center, 222 Rosewood Drive, Danvers, MA 01923; Tel: 978-750-8400; online: <http://www.copyright.com/>.

Peer Review Policy

Each paper published in this volume was evaluated by two peer reviewers and at least one editor. The authors addressed all of the reviewers' comments to the satisfaction of both the technical editor(s) and the ASTM International Committee on Publications.

The quality of the papers in this publication reflects not only the obvious efforts of the authors and the technical editor(s), but also the work of the peer reviewers. In keeping with long-standing publication practices, ASTM International maintains the anonymity of the peer reviewers. The ASTM International Committee on Publications acknowledges with appreciation their dedication and contribution of time and effort on behalf of ASTM International.

Foreword

This publication, *Thermomechanical Fatigue Behavior of Materials: 4th Volume*, contains papers presented at the Fourth Symposium on Thermomechanical Fatigue Behavior of Materials, held in Dallas, Texas on November 7–8, 2001. The Symposium was sponsored by ASTM Committee E08 on Fatigue and Fracture and its Subcommittee E08.05 on Cyclic Deformation and Fatigue Crack Formation. Symposium co-chairmen and publication editors were Michael A. McGaw, McGaw Technology, Inc.; Sreeramesh Kalluri, Ohio Aerospace Institute, NASA Glenn Research Center at Lewis Field; Johan Bressers (Retired), Institute for Energy, European Commission - Joint Research Center; and Stathis D. Peteves, Institute for Energy, European Commission - Joint Research Center.

Contents

Overview	vii
SECTION I: THERMOMECHANICAL DEFORMATION BEHAVIOR AND MODELING	
Modeling Thermomechanical Cyclic Deformation by Evolution of its Activation Energy —X. J. WU, S. YANDT, P. AU, AND J.-P. IMMARIGEON	3
Modeling of Deformation during TMF-Loading —E. E. AFFELDT, J. HAMMER, AND L. CERDÁN DE LA CRUZ	15
Modelling of Hysteresis Loops During Thermomechanical Fatigue —R. SANDSTRÖM AND H. C. M. ANDERSSON	31
Cyclic Behavior of Al319-T7B Under Isothermal and Non-Isothermal Conditions —C. C. ENGLER-PINTO, JR., H. SEHITOGLU, AND H. J. MAIER (Received the Best Presented Paper Award at the Symposium)	45
Cyclic Deformation Behavior of Haynes 188 Superalloy Under Axial-Torsional, Thermomechanical Loading —P. J. BONACUSE AND S. KALLURI	65
SECTION II: DAMAGE MECHANISMS UNDER THERMOMECHANICAL FATIGUE	
Damage and Failure Mechanisms of Thermal Barrier Coatings Under Thermomechanical Fatigue Loadings —E. TZIMAS, P. HÄHNER, P. MORETTO, S. D. PETEVES, AND J. BRESSERS	83
Thermo-mechanical Creep-Fatigue of Coated Systems —L. RÉMY, A. M. ALAM, AND A. BICKARD	98
Enhancement of Thermo-Mechanical Fatigue Resistance of a Monocrystalline Nickel-Base Superalloy by Pre-Rafting —F. C. NEUNER, U. TETZLAFF, AND H. MUGHRABI	112
Environmental Effects on the Isothermal and Thermomechanical Fatigue Behavior of a Near-γ Titanium Aluminide —H. J. MAIER, F. O. R. FISCHER, AND H.-J. CHRIST	127

SECTION III: THERMOMECHANICAL FATIGUE BEHAVIOR AND CYCLIC LIFE PREDICTION

Using Fracture Mechanics Concepts for a Mechanism-Based Prediction of Thermomechanical Fatigue Life —H.-J. CHRIST, R. TETERUK, A. JUNG, AND H. J. MAIER	145
Thermomechanical Fatigue Behavior of an Aluminide-Coated Monocrystalline Ni-Base Superalloy —F. GRUBE, E. E. AFFELDT, AND H. MUGHRABI	164
Collaborative Research on Thermo-Mechanical and Isothermal Low-Cycle Fatigue Strength of Ni-Base Superalloys and Protective Coatings at Elevated Temperatures in The Society of Materials Science, Japan (JSMS) —M. OKAZAKI, K. TAKE, K. KAKEHI, Y. YAMAZAKI, M. SAKANE, M. ARAI, S. SAKURAI, H. KANEKO, Y. HARADA, Y. SUGITA, T. OKUDA, I. NONAKA, K. FUJIYAMA, AND K. NANBA	180
The Fatigue Behavior of NiCr22Co12Mo9 Under Low-Frequency Thermal-Mechanical Loading and Superimposed Higher-Frequency Mechanical Loading —M. MOALLA, K.-H. LANG, AND D. LÖHE	195
Thermomechanical Response of Single Crystal Nickel-Base Superalloy CM186SX —C. N. KONG, C. K. BULLOUGH, AND D. J. SMITH	210
Thermomechanical Fatigue Behavior of Stainless Steel Grades for Automotive Exhaust Manifold Applications —P.-O. SANTACREU, C. SIMON, AND A. COLEMAN	227
Thermomechanical Fatigue Analysis of Cast Aluminum Engine Components —X. SU, M. ZUBECK, J. LASECKI, H. SEHITOGLU, C. C. ENGLER-PINTO, JR., C.-Y. TANG, AND J. E. ALLISON	240
SECTION IV: EXPERIMENTAL TECHNIQUES FOR THERMOMECHANICAL TESTING	
Acoustic Emission Analysis of Damage Accumulation During Thermal and Mechanical Loading of Coated Ni-Base Superalloys —Y. VOUGIOUKLAKIS, P. HÄHNER, F. DE HAAN, V. STAMOS, AND S. D. PETEVES	255
Miniature Thermomechanical Ramping Tests for Accelerated Material Discrimination —B. ROEBUCK, M. G. GEE, A. GANT, AND M. S. LOVEDAY	270
Improving the Reproducibility and Control Accuracy of TMF Experiments with High Temperature Transients —T. BRENDEL, M. NADERHIRN, L. DEL RE, AND C. SCHWAMINGER	282
Two Specimen Complex Thermal-Mechanical Fatigue Tests on the Austenitic Stainless Steel AISI 316 L —K. RAU, T. BECK, AND D. LÖHE	297
Analysis of Thermal Gradients during Cyclic Thermal Loading under High Heating Rates —E. E. AFFELDT, J. HAMMER, U. HUBER, AND H. LUNDBLAD	312

Overview

Thermal fatigue and thermomechanical fatigue (TMF) of structural materials have been topics of intense research interest among materials scientists and engineers for over fifty years, and are subjects that continue to receive considerable attention. Several symposia have been sponsored by ASTM on these two topics over the previous thirty years, and have resulted in Special Technical Publications (STPs) 612, 1186, 1263, and 1371. The Fourth Symposium on Thermomechanical Fatigue Behavior of Materials was held at a time when significant efforts have been underway both in the U.S., under the auspices of ASTM, and internationally, under the auspices of ISO, to develop standards for thermomechanical fatigue testing of materials. This STP represents a continuation of the effort to disseminate all aspects of thermomechanical fatigue behavior of materials from a wide variety of disciplines. The materials scientist, for example, seeks a deeper understanding of the mechanisms by which deformation and damage develop, how they are influenced by microstructure, and how this microstructure may be tailored to a specific application. The analyst wishes to develop engineering relationships and mathematical models that describe constitutive and damage evolution behaviors of materials. Ultimately, the designer seeks engineering tools and test methods to reliably and economically create load-bearing structures subjected to cyclic, thermally-induced loads.

The present STP continues the trend of past symposia of strong international participation. The twenty-one contributed papers in this STP have been organized into four sections. The first section is on Thermomechanical Deformation Behavior and Modeling. Continuation of rapid advances in computational technology has provided greater opportunity than ever before to enable the identification and characterization of the complex viscoplastic deformation of materials under thermomechanical conditions, and this section's collection of five papers is a consequence of these endeavors. Notable among these is the paper, "Cyclic Behavior of Al319-T7B Under Isothermal and Non-Isothermal Conditions," by C. C. Engler-Pinto, Jr., H. Sehitoglu, and H. J. Maier, as it received the Best Presented Paper Award at the Symposium. The second section, Damage Mechanisms under Thermomechanical Fatigue, contains four contributions addressing coated alloys, single crystal nickel-base superalloys, and titanium aluminide materials. The third section, Thermomechanical Fatigue Behavior and Cyclic Life Prediction, contains the following seven contributions: an approach utilizing fracture mechanics for TMF life prediction, a contribution on coated TMF behavior of a monocrystalline superalloy, a collaborative, round-robin style effort to characterize behaviors of uncoated and coated superalloys under TMF conditions, a work on complex loading effects, and two contributions dealing, significantly, with applications in the automotive arena. The fourth and final section addresses Experimental Techniques for Thermomechanical Testing. Too often, especially in thermomechanical fatigue, experimental details are given secondary importance in the literature, when in reality the conduct of thermomechanical fatigue tests requires unusually fine attention to detail and practice. Here again, the tremendous advances in computer technology have enabled the development and implementation of sophisticated testing techniques. The five papers in this section are reflective of these advances, and can be read with profit by the experimentalist interested in establishing or improving thermomechanical fatigue testing capability.

Finally, we would like to express our sincere gratitude to the authors, the reviewers, and ASTM staff (Ms. Dorothy Fitzpatrick, Ms. Crystal Kemp, Ms. Maria Langiewicz, Ms. Christina Painton, Ms.

Holly Stupak, Ms. Qiu Ping Gong, Mr. Scott Emery, and Ms. Annette Adams) for their contributions to the publication of this STP.

Michael A. McGaw
McGaw Technology, Inc.
Fairview Park, Ohio
Symposium Co-Chairman and Editor

Sreeramesh Kalluri
Ohio Aerospace Institute
NASA Glenn Research Center at Lewis Field
Brook Park, Ohio
Symposium Co-Chairman and Editor

Johan Bressers
Institute for Energy, JRC-EC (Retired)
Petten, The Netherlands
Symposium Co-Chairman and Editor

Stathis D. Peteves
Institute for Energy, JRC-EC
Petten, The Netherlands
Symposium Co-Chairman and Editor

Thermomechanical Deformation Behavior and Modeling

Modeling Thermomechanical Cyclic Deformation by Evolution of Its Activation Energy

REFERENCE: Wu, X. J., Yandt, S., Au, P., and Immarigeon, J.-P., “Modeling Thermomechanical Cyclic Deformation by Evolution of its Activation Energy,” *Thermomechanical Fatigue Behavior of Materials: 4th Volume, ASTM STP 1428*, M. A. McGaw, S. Kalluri, J. Bressers, and S. D. Peteves, Eds., ASTM International, West Conshohocken, PA, 2002, Online, Available: www.astm.org/STP/1428/1428_10577, 24 June 2002.

ABSTRACT: This paper presents a new approach for modeling the deformation response of metallic materials under thermomechanical fatigue loading conditions, based on the evolution of thermal activation energy. In its physical essence, inelastic deformation at high temperatures is a thermally activated process. The thermal activation energy, which controls the time and temperature dependent deformation behavior of the material, generally evolves with the deformation state (γ_p) of the material, in response to the applied stress τ . In the present approach, the inelastic flow equation is integrated for a deformation range where strain hardening is predominant. The simplified integration version of the model only needs to be characterized/validated by isothermal tensile and fatigue testing, and it offers an explicit description of the TMF behavior in terms of physically defined variables. By identifying the dependence of these variables on the cyclic microstructure, the model may also offer a mechanistic approach for fatigue life prediction.

KEYWORDS: thermomechanical fatigue, stress-strain curves, hysteresis loop, thermal activation, modeling

Introduction

Thermomechanical fatigue (TMF) refers to the damage induced by simultaneously alternating temperature and mechanical loads. TMF loading occurs in hot section components of gas turbines such as turbine blades. The stress-strain responses of materials under TMF conditions are complex and depend on phasing between thermal and mechanical loads. Therefore, modeling TMF behavior is a challenge for life prediction of turbine blades.

From the early 1980s to the late 1990s, some frameworks of “unified constitutive laws of plasticity and creep” have been developed, which were also applicable to thermomechanical fatigue [1–3]. In these constitutive models, the inelastic strain rate is described by a flow equation, which depends on two state variables, *back stress* and *drag stress*, responsible for kinematic hardening and isotropic hardening, respectively. The specific forms of those hardening rules, i.e., governing equations for back/drag stresses, however, differ from model to model, and depend on several parameters, which are difficult to verify experimentally.

¹ Institute for Aerospace Research, National Research Council of Canada, Ottawa, ON K1A 0R6.

² Department of Mechanical and Aerospace Engineering, Carleton University, Ottawa, ON K1S 5B6.

³ Institute for Aerospace Research, National Research Council of Canada, Ottawa, ON K1A 0R6.

⁴ Institute for Aerospace Research, National Research Council of Canada, Ottawa, ON K1A 0R6

4 THERMOMECHANICAL FATIGUE BEHAVIOR OF MATERIALS

In this paper, a new approach of modeling TMF deformation response is developed. It is based on the evolution of thermal activation energy. In its physical essence, inelastic deformation at high temperatures is a thermally activated process [4], and therefore the deformation process is determined by the thermal activation energy:

$$\Delta G^\ddagger = \Delta G^\ddagger(\tau, \gamma_p, T) \quad (1a)$$

where τ is the stress, γ_p is the inelastic strain of the material, and T is the absolute temperature.

In keeping with the same principle as discussed by Kocks on thermodynamics of slip [5], the activation energy for inelastic deformation can be expanded, to the first order, as

$$\Delta G^\ddagger = \Delta G_0^\ddagger + \frac{\partial \Delta G^\ddagger}{\partial \tau} \tau + \frac{\partial \Delta G^\ddagger}{\partial \gamma_p} \gamma_p = \Delta G_0^\ddagger - V\tau + VH\gamma_p \quad (1b)$$

where $V = -\left(\frac{\partial \Delta G^\ddagger}{\partial \tau}\right)$ is the activation volume and $H = \frac{1}{V}\left(\frac{\partial \Delta G^\ddagger}{\partial \gamma_p}\right)$ is the work hardening coefficient.

A differential equation, governing the evolution of this activation energy, is derived from deformation kinetics. Then, the equation is integrated to obtain the constitutive equations for isothermal and thermomechanical fatigue over the range where strain hardening is predominant. By demonstrating the application of the model for a Ni-base superalloy, IN738LC, under these conditions, the physical meanings of the parameters of the model are illustrated, and the results are discussed. This simplified model is shown to be effective in characterization of the stress-strain behavior of materials under monotonic and cyclic loads.

The Constitutive Model

Based on deformation kinetics theory, inelastic strain rate can be expressed as [6]:

$$\dot{\gamma}_p = 2A \sinh \Psi \quad (2a)$$

$$\dot{\Psi} = \frac{V}{kT}(\dot{\tau} - H\dot{\gamma}_p) \quad (2b)$$

where A is a temperature dependent activation rate constant, Ψ is the mechanical energy of the activation system normalized by its thermal energy, V is the activation volume, H is the work hardening coefficient.

For loading at a constant mechanical strain rate,

$$\dot{\gamma} = \frac{\dot{\tau}}{\mu} + \dot{\gamma}_p = \text{constant} \quad (3)$$

where μ is the elastic shear modulus.

We assume that the evolution of the energy term, Ψ , undergoes a series of infinitesimal isothermal steps, for each i -th step, the energy state evolves from Ψ_{i-1} to Ψ_i over the time interval $\Delta t_i = t_i - t_{i-1}$ at a constant temperature T_i . Then, Eq 2 can be integrated into the form (see Appendix for detail):

$$\ln \left(\frac{e^{-\Psi} - a}{\chi e^{-\Psi} + b} \right) \Bigg|_{\Psi_{i-1}}^{\Psi_i} = - \frac{V\mu\dot{\gamma}\sqrt{1+\chi^2}}{kT_i} \Delta t_i \quad (i = 1, 2, \dots) \quad (4)$$

where

$$\chi = \frac{2A}{\dot{\gamma}} \left(1 + \frac{H}{\mu} \right), \quad a = \frac{\sqrt{1+\chi^2} - 1}{\chi}, \quad b = \sqrt{1+\chi^2} + 1$$

Summing up all these infinitesimal steps, we have:

$$\sum_{i=1}^N \ln \left(\frac{e^{-\Psi} - a}{\chi e^{-\Psi} + b} \right) \Bigg|_{\Psi_{i-1}}^{\Psi_i} = - \sum_{i=1}^N \frac{V\mu\dot{\gamma}\sqrt{1+\chi^2}}{kT_i} \Delta t_i \quad (5)$$

Let $N \rightarrow \infty$, the left-hand side of Eq 5 will be equal to the logarithmic difference between the final state and the initial state, and the right-hand side is an integration of the temperature-dependent terms over the loading period. After mathematical rearrangement, we have:

$$\left(\frac{e^{-\Psi} - a}{\chi e^{-\Psi} + b} \right) = \left(\frac{1-a}{\chi+b} \right) \exp \left\{ - \int_{t_0}^t \frac{V\mu\dot{\gamma}\sqrt{1+\chi^2}}{kT} dt \right\} \quad (6)$$

where t_0 is the time to reach the elastic limit, or in other words, for plastic flow to commence.

Let

$$\omega(t) = \left(\frac{1-a}{\chi+b} \right) \exp \left\{ - \int_{t_0}^t \frac{V\mu\dot{\gamma}\sqrt{1+\chi^2}}{kT} dt \right\} \quad (7)$$

we can rewrite Eq 6 as a function of stress vs. strain under constant strain rate conditions:

$$\tau - H\gamma_p - \tau_0 = - \frac{kT}{V} \ln \left(\frac{a + \omega b}{1 - \omega\chi} \right) \quad (8)$$

where τ_0 is the back stress from the material's initial microstructure.

Equation 8 is derived as the relationship between the equivalent shear stress and the equivalent shear strain, for 3D generalization. For uniaxial cases, as seen for examples in the following section, conversion to uniaxial stress/strain can be obtained by multiplying the Taylor's factor, as

$$\begin{aligned} \sigma &= \sqrt{3}\tau \\ \varepsilon &= \gamma / \sqrt{3} \end{aligned}$$

Application of the Constitutive Model

As an example of the application of the above constitutive model, deformation responses of nickel-base superalloy IN738LC were investigated in the practical temperature range of 750–950°C. The model was used to describe isothermal tensile behavior of the material loaded at constant strain rates of 2×10^{-3} to $2 \times 10^{-5} \text{ sec}^{-1}$, as well as isothermal low-cycle fatigue (at 950°C) and TMF (750–950°C) at a constant strain rate of $2 \times 10^{-5} \text{ sec}^{-1}$. The parameter values for the model were obtained from isothermal tension tests

conducted under axial true-strain control at temperatures of 750–950°C using cast-to-size tensile specimens. The isothermal-LCF and TMF data was obtained from previous experimental work, the details for which are described elsewhere [7]. Two grain-sized IN738LC materials, one with a grain size of ~1 mm, and the other 1–5 mm, were used for testing. Both materials were in the standard heat-treated state (solution treated at 1120°C for 2 h and aged at 843°C for 24 h), which contain a bimodal distribution of gamma prime precipitates (primary: 0.4–1.0 μm; secondary: ~0.05 μm) of 45% in volume fraction.

The application of the constitutive model has been limited to the low strain range in which deformation behavior is dominated by strain hardening effects. In the following, we shall apply Eqs 6–8 to various isothermal and thermomechanical deformation processes.

Isothermal Tensile Loading

Under isothermal loading conditions, Eq 7 simply becomes:

$$\omega(t) = \left(\frac{1-a}{\chi+b} \right) \exp \left\{ - \frac{V\mu\dot{\gamma}(t-t_0)\sqrt{1+\chi^2}}{kT} \right\} \tag{9}$$

Since the strain rate is constant, $\dot{\gamma}(t-t_0) = \gamma - \gamma_0$ where $\gamma_0 = \tau_0/\mu$ is the strain at the elastic limit. Then, Eq 8 describes the stress-strain response during such a process. A schematic of stress-strain curve is shown in Fig. 1 (all shear stress/strain are substituted by the principal axial stress/strain). As illustrated, three components contribute to the flow stress: i) the material’s initial hardening, σ_0 or τ_0 ; ii) deformation hardening (also referred as *strain hardening* or *work hardening*), $H\epsilon_p$ (or $H\gamma_p$); and iii) the rate-dependent term. Stress-strain curves of the fine-grained IN738LC at three temperatures are shown in Fig. 2. The model, Eq 8, provides satisfactory descriptions for all the three cases. Figs. 3a and 3b illustrate the strain rate dependence of the stress-strain response in the fine-grained IN738LC during tensile loading at 750°C and 950°C, respectively.

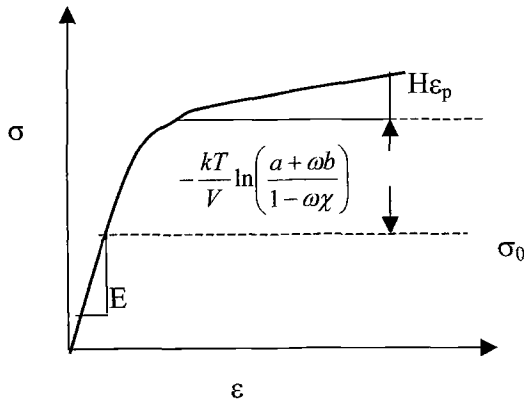


FIG. 1 —A schematic of stress-strain curve.

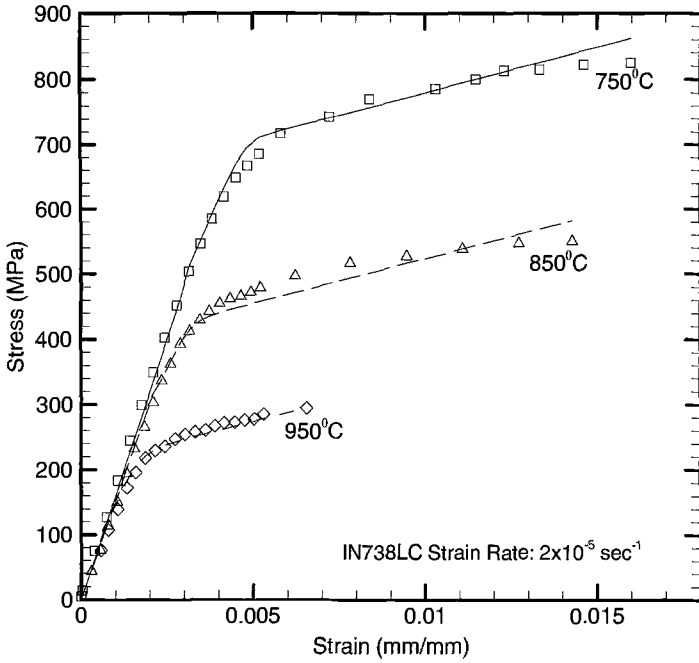


FIG. 2—Stress-strain curves for the IN738LC (fine-grain) at three different temperatures. The solid lines represent Eq 8 and the symbols represent the observed behavior.

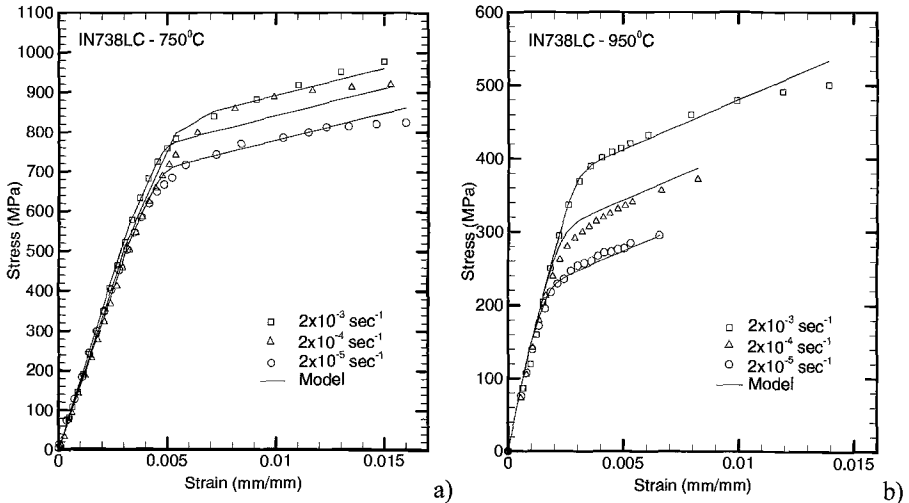


FIG. 3—Stress-strain response of IN738LC (fine-grain) loaded at three strain rates at a) 750°C and b) 950°C. The solid lines represent Eqs 8 and 9 and the symbols represent the observed behavior.

Values of the parameters in the model are given in Table 1. Several basic material properties are seen to change with temperature. The strain rate constant, A , follows the Arrhenius relationship. The decrease of the structural back stress with temperature could be associated with changing of deformation mechanism from γ' cutting (at low temperature) to dislocation climb at higher temperatures, whereas the decrease of elastic modulus and the work-hardening coefficient with temperature are common material behaviour.

TABLE 1— *Values of the parameters of the model derived for isothermal tension.*

Temperature (°C)	750	850	950
Temperature-Dependent Material Constants			
Initial Back Stress, σ_0 (MPa)	540	285	110
Work Hardening Coefficient, H (MPa/mm/mm)	15000	13736	12478
Modulus of Elasticity, E (GPa)	175.5	151.4	137.0
Strain-Rate Constant, $A = A_0 \exp[-Q/RT]$ (sec^{-1})	3.5×10^{-8}	1.56×10^{-7}	5.5×10^{-7}
Activation Constants			
Activation Volume, V (m^3)	3.977×10^{-22}
Pre-exponential, A_0 (sec^{-1})	0.7
Activation Energy, Q (J/mol)	143,276

Isothermal Fatigue

Equation 8 can also be applied to cyclic deformation behavior as in isothermal fatigue. An isothermal fatigue test was conducted on the coarse-grained IN738LC at a strain rate of 2×10^{-5} . Figure 4 shows the description of the model for the first stress-strain hysteresis loop of the material, based on the monotonic parameters (except that a lower value of $\sigma_0 = 40$ MPa is used corresponding to the coarse-grained material), in comparison with the experimental data. It is noted that upon the first reversal, a portion of the accumulated plastic work ($H\epsilon_p = 45$ MPa) contributed to kinematic hardening, which shifts the center of loop, about 10 MPa, towards the positive stress axis. The rest of the accumulated plastic work, together with σ_0 , contributed to isotropic hardening. In the light of this discussion, it appears that the energy, $\Psi = V(\sigma - H\epsilon_p - \sigma_0)/kT = 0$, defines an absolute yield surface (as opposed to the yield surface constructed based on the stress at 0.2% offset strain, which depends on the loading rate). This formulation resembles Chaboche's model as in reference [2]. There is, however, a discrepancy between the model description, using parameters based on the static tests, and the experimental behavior in the transition region between the elastic and work-hardened plastic regimes. This is understandable since it is known that the material's dislocation structure would change during cyclic deformation and it would affect the hysteresis loop shape [8]. Hence, in modeling, the strain rate constant, A , should be modified to reflect this change, because it depends on dislocation density, but a detailed description of the evolution of the dislocation structure is lacking.

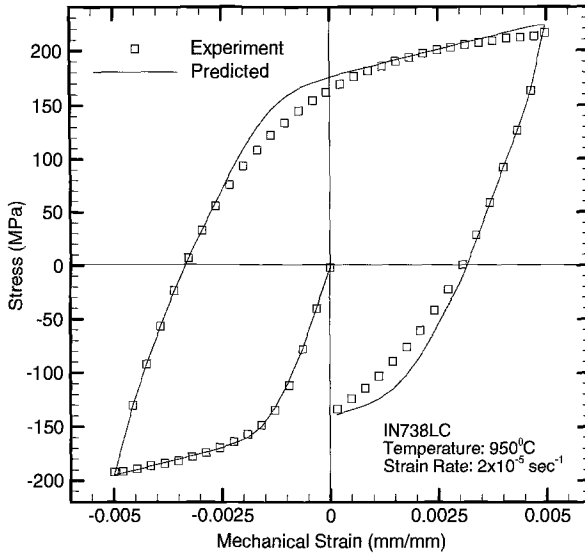


FIG. 4—Cyclic stress-strain curves of IN738LC (coarse-grain).

Thermomechanical Fatigue

In the simplest form of thermomechanical fatigue, temperature varies simultaneously with the mechanical strain at the same frequency. Since the temperature dependence in μ , V and $\sqrt{1 + \chi^2}$ are not strong, because χ is usually small compared to 1, we can assume these terms take their average values in Eq 6 for first approximation. For in-phase (IP) and out-of-phase (OP) TMF where strain is synchronized with temperature at the maximum/minimum in each cycle, Eq 7 can be easily integrated into the form for triangular waveforms:

$$\omega = \left(\frac{1-a}{\chi+b} \right) \exp \left\{ \mp \frac{V\mu\Delta\gamma\sqrt{1+\chi^2}}{k\Delta T} \ln \frac{T}{T_0} \right\} \quad (10)$$

where T_0 denotes the temperature point at which the strain reaches the elastic limit, $\Delta T = T_{\max} - T_{\min}$ is the temperature range, $\Delta\gamma$ is the total strain range, the \mp sign is used for the temperature rising or declining halves of the cycle, respectively. For more complex thermomechanical cycles, the integration can be performed step-wisely.

TMF tests were also conducted on IN738LC (coarse-grain) and the experimental details were described elsewhere [7]. The stress-strain response of IN738LC under an out-of-phase thermomechanical fatigue condition was predicted using Eq 8 with the parameters given in Table 1 where the structural back stresses have been lowered to the corresponding values for the coarse-grained material, as shown in Fig. 5, which shows that the model using parameters derived from isothermal tensile testing produced good agreement with the TMF hysteresis loop obtained experimentally.

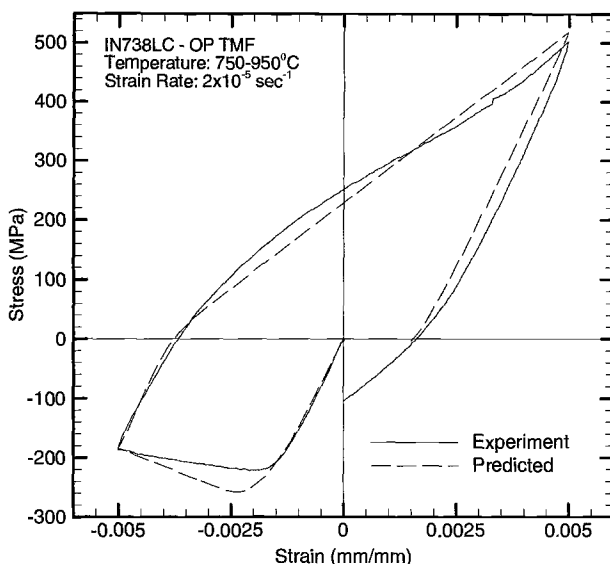


FIG. 5—Stress-strain response of IN738LC (coarse-grain) during out-of-phase thermomechanical fatigue. The solid line represents the observed behavior and the dashed line represents Eqs 8 and 10.

Discussion

In this paper, constitutive equations for monotonic tensile/compressive loading and isothermal/thermomechanical fatigue conditions have been derived based on the evolution of the activation energy of the plastic deformation process. As simple illustrations, evaluation of the model was deduced exclusively from the results of isothermal constant-true-strain-rate tensile tests, and good agreement with the experimental data was observed, however, there are several issues worthy of further characterisation and they are briefly discussed below.

The Strain Rate Constant, A

The strain rate constant, A , from its physical origin, is related to dislocation density. It has been hypothesized by Jiao et al. that the cyclic response of IN738LC during isothermal fatigue at 950°C stabilises after 10 cycles, due to saturation in the dislocation density [9]. This implies that the strain rate constant, A , may change from the value for the first loading of the material to a value for the state of cyclic stability. The sensitivity of the model to variations in the strain rate constant has not been addressed in this study. The present model predicts rather well the cyclic peak stresses and the inelastic strain range, which may be acceptable for practical applications.

It has also been shown that there is a dependence on the deformation path and the dislocation substructure that evolves during thermomechanical deformation. For example, Marchand et al. [10] have observed increasing dislocation density in cast B-1900+Hf in the following order: isothermal fatigue (T_{\min} and T_{\max}), out-of-phase, and in-phase TMF cycling. The dislocation substructures and their dependence on loading

profile have not been evaluated in this work. In cases where there are wide variations in dislocation density between loading conditions, potentially the strain rate constant, as defined in the context of the present model, may also vary with the loading condition. Even though the dependence of A on dislocation substructures was not addressed specifically, the validity of the model was tested for thermomechanical fatigue conditions, and the comparison with the experimental TMF data on IN738LC is reasonably good. Frenz et al. [11] used a unified viscoplastic model with two state variables (viz. back stress, drag stress) and parameters evaluated from isothermal fatigue data to describe the response of TMF for IN738LC. They observed a deviation between the predicted and experimental material response for the cooling portion of the TMF cycles. They attributed this deviation to the large inelastic strain that arises at high temperature, which increases the resistance of the material to inelastic flow at low temperatures.

Effect of Microstructure

The strength and hardening behaviours of IN738LC have been observed to vary considerably with the size, distribution and morphology of gamma prime precipitates in the material during isothermal tensile deformation [12]. The model, in its present form, can be extended to describe the evolution of hysteresis loops of the material under fatigue loading conditions, if the dependence of some parameters, e.g., σ_0 and H , on the cyclic microstructure is properly described. Micrographs representative of the gamma prime morphology of IN738LC (a) before and (b) after the out-of-phase TMF test are shown in Fig. 6. The original microstructure consisted of a bimodal gamma prime distribution, however it is clear from these figures that the fine secondary gamma prime has dissolved and the primary precipitates have rounded and coarsened. The effect of fully reversed uniaxial cyclic loading on the gamma prime morphology in nickel-base superalloys has been widely documented in the literature, for example references [13–15]. Antolovich [13] has reported dissolution of secondary precipitates, and coarsening of primary precipitates in Rene 80 during isothermal fatigue, which resulted in a gradual softening of the material. It has also been demonstrated that the coarsening kinetics in plastically deformed materials is considerably higher than a material in its undeformed state [16]. Similar behaviour was observed in this investigation. The effect of gamma prime morphological changes on the cumulative glide behaviour at 950°C is exemplified in Fig. 7, which suggests that the structural back stress progressively decrease as fatigue cycling proceeds. This may necessitate an evolution equation governing the change in the structural back stress as a function of temperature, cycle and deformation path (e.g., in-phase or out-of-phase). However, insufficient information is available at present to determine the relationship between the structural back stress and gamma prime morphological changes.

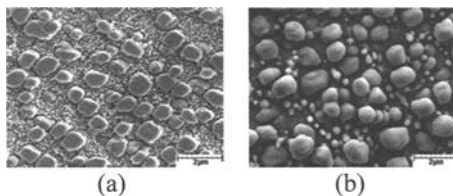


FIG. 6—Gamma prime morphology a) before and b) after OP-TMF 750–950°C testing.

12 THERMOMECHANICAL FATIGUE BEHAVIOR OF MATERIALS

At this point, the present model only serves as a framework for modelling the entire TMF history. Assuming that the parameters are constant for each fatigue cycle, the model needs to be further supplemented with evolutionary equations for those parameters in a general form such as

$$\frac{\partial X_i}{\partial N} = f_i(\Delta\gamma_p, \sigma_{\max} \text{ or } \Delta\sigma, T, X_i) \quad (11)$$

where X_i represent any parameter that is likely to be in dependence upon the evolution of the cyclic microstructure.

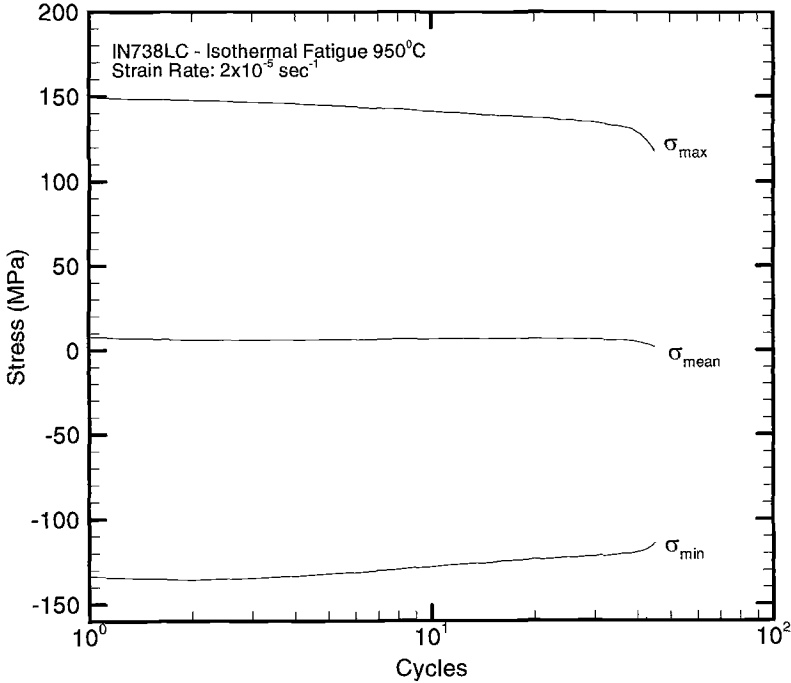


FIG. 7—Evolution of cyclic peak, valley and mean stresses in IN738LC (coarse-grain) under isothermal fatigue at 950°C.

Conclusions

1. A single constitutive equation has been derived, based on deformation kinetics, for inelastic deformation during i) monotonic tension/compression, ii) isothermal and iii) thermomechanical fatigue loading, which is expressed in the form of

$$\left(\frac{e^{-\Psi} - a}{\chi e^{-\Psi} + b} \right) = \left(\frac{1 - a}{\chi + b} \right) \exp \left\{ - \int_{t_0}^t \frac{V\mu\dot{\gamma} \sqrt{1 + \chi^2}}{kT} dt \right\}$$

$$\Psi = \frac{V}{kT} (\tau - H\gamma_p - \tau_0)$$

with the parameters defined in the context of Eq 6.

2. As a first approximation, the model with parameters evaluated from isothermal tensile tests provides adequate description of the material's behaviour under thermo-mechanical conditions. Especially, predictions for the peak stresses and inelastic strain ranges are quite satisfactory.
3. For description of the entire cyclic deformation process, however, evolution of the parameters with the cyclic deformation microstructure has to be considered. Hypothetically, this can be accomplished by, firstly modeling the monotonic stress-strain curve to get the fundamental constants of V and E , and initial values of A , H and σ_0 , and secondly evaluating A , H and σ_0 , as a function of cycle number, assuming that they are constant for each cycle. Evolutionary equations for these parameters need to be derived based on the underlying physics (dislocation multiplication, γ' coarsening, etc.).

Acknowledgments

Financial supports from the Air Vehicles Research Section, Department of National Defence of Canada, and Natural Sciences and Engineering Research Council of Canada are acknowledged.

References

- [1] *Unified Constitutive Equations for Creep and Plasticity*, A. K. Miller, Ed., Elsevier Applied Science, NY, 1987.
- [2] *Unified Constitutive Laws of Plastic Deformation*, A. S. Krausz, and K. Krausz, Eds., Academic Press, 1996.
- [3] Schitoglu, H., "Thermomechanical Deformation of Engineering Alloys and Components—Experiments and Modeling," *Mechanical Behavior of Materials at High Temperature*, NATO ASI Series, Vol. 15, 1996, pp. 349–380.
- [4] Krausz, A. S. and Eyring, H., *Deformation Kinetics*, Wiley Interscience, NY, 1975.
- [5] Kocks, U. F., Argon, A. S. and Ashby, M. F., "Thermodynamics and Kinetics of Slip," *Prog. Material Science*, Vol. 19, 1975.
- [6] Wu, X. J. and Krausz, A. K., *Journal of Materials Engineering and Performance*, Vol. 3, 1994, pp. 169–177.
- [7] Yandt, S., "Development of a Thermal-Mechanical Fatigue Testing Facility," Master Thesis, Carleton University, Ottawa, ON, 2000.
- [8] Feltner, C. E. and Laird, C., "Cyclic Stress-Strain Responses of F.C.C. Metals and Alloys," *Acta Metaterialia*, Vol. 15, 1967, pp. 1621–1653.
- [9] Jiao, F., Chen, W., Mukherji, D., Zhu, J., and Chen, W., "Deformation Behavior and Microstructural Evolution in IN738LC Under LCF Loading," in *Mechanical Behavior of Materials-VI: Proceedings of the Sixth International Conference*, Kyoto, Japan, 29 July–2 August 1991, pp. 385–390.
- [10] Marchand, N., L'Espérance, G. L., and Pelloux, R. M., "Thermal-Mechanical Cyclic Stress-Strain Responses of Cast B-1900+Hf," *Low Cycle Fatigue, ASTM STP 942*, ASTM International, West Conshohocken, PA, 1988, pp. 638–656.
- [11] Frenz, H., Meersmann, J., Ziebs, J., Kuhn, H.-J., Sievert, R., and Olschewski,

- J., "High-Temperature Behavior of IN738LC Under Isothermal and Thermo-mechanical Cyclic Loading," *Materials Science and Engineering A*, Vol. A230, 1997, pp. 49–57.
- [12] Balikci, E., Mirshams, R. A., and Raman, A., "Tensile Strengthening in the Nickel-Base Superalloy IN738LC," *Journal of Materials Engineering and Performance*, ASM, Vol. 9, No. 3, June 2000, pp. 324–329.
- [13] Antolovich, S. D., Baur, R., and Liu, S., "A Mechanistically Based Model for High Temperature LCF of Ni Base Superalloys," *Superalloys 1980*, J. K. Tien et al., American Society for Metals, Metals Park, OH, Eds., 1980, pp. 605–613.
- [14] Antolovich, S. D., Rosa, E., and Pineau, A., "Low Cycle Fatigue of René 77 at Elevated Temperatures," *Materials Science and Engineering*, Vol. 47, 1981, pp. 47–57.
- [15] Antolovich, S. D., Liu, S., and Baur, R., "Low Cycle Fatigue Behavior of Rene 80 at Elevated Temperature," *Metallurgical Transactions A*, Vol. 12A, 1981, pp. 473–481.
- [16] Milligan, W. W., Huron, E. S., and Antolovich, S. D., "Deformation, Fatigue and Fracture of Two Cast Anisotropic Superalloys," *Fatigue '87*, Vol. 3, 28 June–3 July 1987, Charlottesville, VA, pp. 1561–1591.

APPENDIX A

As stated in Section 2, inelastic deformation under constant strain rate loading condition is described by the following set of equations:

$$\dot{\gamma}_p = 2A \sinh \Psi \quad (\text{A.1})$$

$$\dot{\Psi} = \frac{V}{kT} (\dot{\tau} - H\dot{\gamma}_p) \quad (\text{A.2})$$

and

$$\dot{\gamma} = \frac{\dot{\tau}}{\mu} + \dot{\gamma}_p = \text{constant} \quad (\text{A.3})$$

Substituting Eqs A.1 and A.3 into Eq A.2, we have

$$\dot{\Psi} = \frac{V\mu}{kT} \left[\dot{\gamma} - 2A \left(1 + \frac{H}{\mu} \right) \sinh \Psi \right] \quad (\text{A.4})$$

Let $u = e^{-\Psi}$, Eq A.4 can be integrated into the form

$$\ln \left(\frac{u - a}{\chi u + b} \right) \Bigg|_{u_1}^{u_2} = - \frac{V\mu\dot{\gamma}\sqrt{1 + \chi^2}}{kT_i} \Delta t \quad (\text{A.5})$$

where u_1 and u_2 correspond to arbitrary energy states Ψ_1 and Ψ_2 respectively. The energy state Ψ assumes an initial value of zero, corresponding to the absolute yield surface.

Ernst E. Affeldt,¹ Joachim Hammer,² and Lorena Cerdán de la Cruz³

Modeling of Deformation During TMF-Loading

REFERENCE: Affeldt, E. E., Hammer, J., and Cerdán de la Cruz, L., “**Modeling of Deformation During TMF-Loading,**” *Thermomechanical Fatigue Behavior of Materials: 4th Volume, ASTM STP 1428*, M. A. McGraw, S. Kalluri, J. Bressers, and S. D. Peteves, Eds., ASTM International, West Conshohocken, PA, Online, Available: www.astm.org/STP/1428/1428_10578_19 May 2003.

ABSTRACT: The deformation behavior of two extremely different nickel base alloys under cyclic loading is reported and discussed with respect to the underlying micro-structural mechanisms. One is a high strength cast single crystal alloy and the other is a wrought carbide strengthened alloy with comparably low yield strength showing pronounced plasticity during cyclic deformation. A procedure for modeling of the deformation behavior is described that take this mechanism into account. It implies elastic deformation, yielding, and relaxation. For the low strength alloy, cyclic hardening is additionally accounted for. The modeling procedure, the evaluation of the necessary parameters from isothermal tests, and the predicted results for isothermal and anisothermal loading are compared with experimental results.

KEYWORDS: thermal mechanical fatigue, TMF, low-cycle fatigue, LCF, nickel base alloy, deformation behavior, cyclic hardening, relaxation, modeling, simulation, hysteresis loop

Introduction

Design of components for aeroengines, e.g., turbine blades, is based on the prediction of the temperatures and stresses developed during service. An essential tool in that procedure is the modeling of the deformation behavior. Modeling of deformation is reported often in literature [1–10]. Constitutive models, like [1], formulate a mathematical framework, which must be filled with adapted experimental results. Other models are phenomenological descriptions, which concentrate and handle only the special topics necessary for the specific task (e.g., [2]). Typically this modeling is done on the basis of standard test results, which means it is mainly or totally based on isothermal data. The procedure of prediction should be not too complex and time-consuming, and it is of some advantage if the procedure has a physical basis, which helps to understand the mechanisms involved. An excellent proof for the procedure applied in this work is a comparison with test results that were evaluated under conditions that consider all important boundary conditions endured under service. Additionally, a possibility to measure the material’s response (e.g., temperatures and stresses) is quite important. For the above-mentioned example design of turbine blades, it is important to know the materials’ response to strain controlled anisothermal loading with heating and cooling rates comparable to that under service. Strain controlled testing reflects the origin of the main contribution to stress, which is the existence of thermal gradients, and which

¹ Dr. rer. nat. MTU Aero Engines GmbH, Dachauer Straße 665, D-80995 Munich, Germany.

² Professor Dr. Ing. Fachhochschule Regensburg, University of Applied Sciences, Regensburg, Germany.

³ Dip. Ing. Material Engineering, MTU Aero Engines GmbH, Dachauer Straße 665, D-80995 Munich, Germany.

cause the consequent thermal strains. Anisothermal testing also enables the interaction of low temperature mechanisms (e.g., brittle cracking of intermetallic coating at temperatures below DBTT) and high temperature mechanisms (e.g., high crack growth rates at high temperature or relaxation). Such measurements are possible with the TMF test. The aim of the work presented was to concentrate mainly on the prediction of TMF loops from isothermal standard data with the intention of modeling the behavior with a physical background. One reason is that a physical basis is helpful in handling unexpected situations, e.g., how it will influence the TMF life if the microstructure is not as expected. Additionally, it defines a broad base of common knowledge that correlates with experience from other fields, e.g., if a calculation explicitly implies particle strengthening, it is possible to estimate the influence of temperature on the strength by correlation to the temperature-dependence of the size and density of particles.

Modeling of the behavior measured is not only a proof for the procedure, but also for the standard isothermal data set if it is established under the right conditions, (e.g., one will fail to predict the relaxation if the data set is based on the minimum creep rate because primary creep is also an important contribution to relaxation). Such data sets typically imply information of elastic deformation, yield strength, and UTS as well as data for creep deformation. Additional information for cyclic deformation will be found only for some percentage of blade materials.

The work presented describes a model to predict the deformation behavior of two different nickel base alloys tested and modeled under loading conditions in which the behaviors are mainly controlled by different deformation mechanisms. One is used in moderate temperature regimes and shows pronounced cyclic hardening, and the other is used at very high temperatures where relaxation is very important.

Experimental Details

The materials under investigation were two nickel base alloys. One is the first generation single crystal alloy SRR99, and the other is the wrought alloy Haynes 230.

The chemical compositions are given in Table 1. The single crystal alloy has a small amount of carbon and small widely dispersed carbides in the interdendritic zones. The relatively high strength is caused by a high volume fraction of cuboidal γ' -precipitates of an approximate size of 0.5 μm . In contrast, the nickel base alloy Haynes 230 has a high carbon content and a small Al + Ti content, which results in a higher amount of carbides without any of the γ' -precipitates in the matrix.

TABLE 1—Nominal chemical composition of SRR99 and HAYNES 230 alloys in weight%.

Alloy	Cr	Co	Ta	Al	Ti	W	C	Mo	Fe
SRR99	8	5	3	5.5	2.2
Haynes230	22	5	...	0.3	...	14	0.1	2	3

The thermo-mechanical fatigue tests of the Haynes alloy were performed with a specimen as shown in Fig.1, which has threaded ends and a rectangular cross section in the gauge length, but with semicircular corners to avoid temperature and stress concentrations. The flat cross section enables a high ratio of surface to volume, with small dimensions normal to the surface. Due to this short distance in the direction of heat

flow, the temperature gradients during induction heating and enforced air cooling can be minimized. To prove that the remaining gradients are insignificant, the thermal strain versus temperature is measured before starting the test and compared to the standard data for thermal strain evaluated by dilatometric measurements.

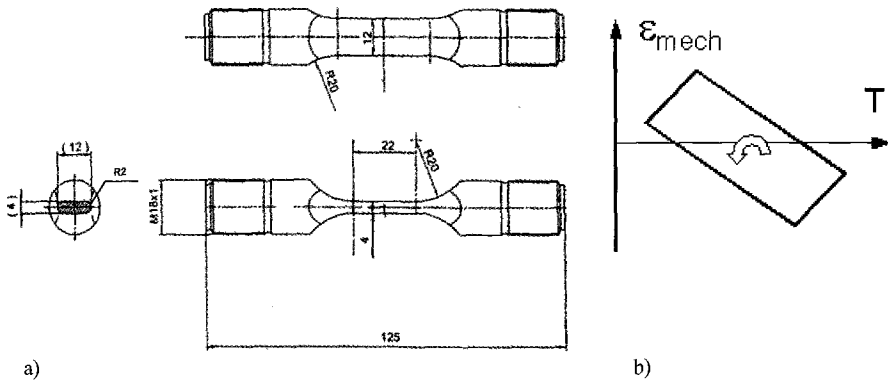


FIG. 1—*a) Thermo-mechanical fatigue specimen (dimensions in mm); b) Thermo-mechanical fatigue cycle.*

Testing was performed in a servo-hydraulic rig under total strain control with an extensometer of about 13 mm gauge length, which has ceramic rods and was attached to the semicircular edges. To evaluate the thermal strain of the specimen, a pretest was performed under load control to ensure that the stress equals zero with the same temperature signal as applied during the subsequent test. The resulting strains were measured as a function of the temperature. Two separate polynomial fits for the heating and cooling branch of the strain were used as a representative for the thermal strain. To calculate the control signal for the total strain, both signals (mechanical strain and thermal strain) were added. Pt-PtRh-thermocouple wires were spot-welded separately to the center of the gauge length to enable temperature control.

The applied cycle for mechanical strain versus temperature is shown in Fig. 1*b*.

All testing of the SRR99 material and part of the Haynes 230 material was done at the Institute for Advanced Materials at the JRC in Petten in different collaborative programs. The testing rig is similar to the one described above. More details can be found in [11].

Deformation Modeling

In this model a superposition of three different physical deformation mechanisms is acting during TMF loading. This is described as follows:

Elastic and Plastic Deformation

To calculate the material deformation behavior, both the temperature and mechanical strain signals were defined as a function of time in increments. First the stress was calculated from the mechanical strain with a Ramberg-Osgood formulation of the elasto-plastic deformation behavior with respect to temperature (see Eq 1), which essentially describes the mechanical strain as the sum of the elastic and the plastic part, with the

latter being correlated to stress by a power law. Temperature dependence is described by an Arrhenius relation for both the hardening exponent n and the inverse of the factor k times E (Young's modulus), where k is the divisor of the stress contribution to the plastic strain.

$$\varepsilon = \frac{\sigma}{E} + \left(\frac{\sigma}{k} \right)^{1/n} \quad (1)$$

where:

$$\frac{k}{E} = (D_1 \cdot \exp(Q_1 / R \cdot T) + D_2 \cdot \exp(Q_2 / R \cdot T)) \quad (2)$$

$$n = (A_1 \cdot \exp(Q_{n1} / R \cdot T) + A_2 \cdot \exp(Q_{n2} / R \cdot T)) \quad (3)$$

k = Ramberg-Osgood parameter [MPa]

n = Ramberg-Osgood parameter [m/m]

D_1, D_2 = material constants

A_1, A_2 = material constants [m/m]

Q_1, Q_2 = activation energy for self-diffusion [J/mol]

R = universal gas constant, 8.31 [J/molK]

T = absolute Temperature [K]

Relaxation

Relaxation is described based on a threshold stress concept for the stress dependence, which takes into account that plastic deformation during creep is confined to the matrix and dislocations mostly circumvent the γ '-precipitates. The strain rate is therefore correlated to a reduced effective stress, which is the external stress σ minus σ_p , where σ_p summarizes all strengthening contribution, which reduces the external stress to that inner effective stress forcing dislocation movement. The creep rate is thus given by [12,13].

$$\frac{d\varepsilon}{dt} = A \cdot (\sigma - \sigma_p)^{n_m} \cdot \exp\left(\frac{-Q_{SD}}{RT}\right) \quad (4)$$

where:

$d\varepsilon/dt$ = strain rate [s^{-1}]

A = material constant [$MPa^{-1} s^{-1}$]

σ = externally applied stress [MPa]

σ_p = internal stress caused by particles and solution hardening [MPa]

n_m = material constant

Q_{SD} = activation energy for self-diffusion, here, Ni into the nickel based alloy [J/mol]

R = universal gas constant, 8.31 [J/molK]

T = absolute temperature [K]

Hardening

The experimental result for the single crystalline material SRR99 during TMF loading does not show any hardening; therefore it was not necessary to take hardening

into account. On the contrary, the Haynes 230 material exhibits strong hardening effects generating stresses at least as high as the yield strength. To describe this hardening behavior it seems useful to refer it to the underlying physical mechanism. Hardening is the result of increasing dislocation density. At the yield point the material has a basic strength, which is a superposition of solid solution hardening, particle strengthening, initial dislocation density and the influence of grain boundaries with minor contributions (e.g., Peierl's force and friction forces). During plastic deformation, interaction of dislocations with obstacles increases the dislocation density, resulting in increased strength, which could be expressed via Eq 5:

$$\sigma_p = \alpha M G b \sqrt{\rho} \quad (5)$$

where:

σ_p = internal increased stress caused by dislocation hardening [MPa]

α = interaction constant for dislocation hardening, 0.3

M = Taylor factor

G = Shear modulus [MPa]

ρ = dislocation density [m^{-2}]

b = Burger's vector

Stress variations are thereby correlated to the square root of the variations in dislocation density. Any variation in stress is based on dislocation interaction and thus requires plastic deformation, assuming no changes in the other contributions. This implies that an increase in stress should correlate to an accumulation of a corresponding plastic strain. This leads to the following equation for hardening,

$$\sigma_p = a_p + b_p * \ln(\sum abs(\Delta \epsilon_{pl})) \quad (6)$$

where:

σ_p = internal increased stress caused by dislocation hardening [MPa]

$\Delta \epsilon_{pl}$ = plastic strain range

a_p, b_p = material constants [MPa]

where the parameters a_p and b_p are functions of the plastic strain amplitude and the temperature. As shown in Fig. 2 the constant a_p is linearly correlated to the plastic strain amplitude. More details can be found in the *Evaluation of Model Parameters* section of this paper.

Superposition

The calculation sequence can be described as follows: Each hysteresis loop is subdivided into several time increments (about 200) and for each single time increment the following sequence is calculated:

For the first increment in the first loop the parameters of the Ramberg-Osgood equation Eq 1 are evaluated from isothermal data.

1. In a first step strain, temperature and Young's modulus are evaluated. Then, based on Eq 1, the initial stress σ_p is calculated.

2. The strain is checked if it is reversed. If so, a new Ramberg-Osgood parameter k is calculated based on the correlation between plastic strain range achieved since the last reversal and the stress.
3. In a second step the amount of hardening is evaluated from the difference in accumulated plastic strain based on Eq 6, resulting in a stress difference due to hardening $\Delta\sigma_h$.
4. In a third step, the amount of relaxation corresponding to this stress $\sigma_p + \Delta\sigma_h$ is calculated based on Eq 4, leading to a stress decrease $\Delta\sigma_{cr}$.
5. In the fourth step the resultant stress is calculated from σ_p and the contribution from hardening and relaxation.
6. The amount of plastic strain at the end of the time increment is calculated from total (mechanical) strain and Young's modulus.

The Ramberg-Osgood parameter n was calculated from the Arrhenius relation at the beginning of the loop, but then is kept constant throughout the whole prediction.

Evaluation of the Model Parameters

The elastic constants E and G are given as a fourth order polynomial. The Ramberg-Osgood parameters are fitted to a set of tensile test data for different temperatures. Temperature dependence of both parameters is described by an Arrhenius relation for both, the hardening exponent n and the inverse of the factor k times E (Young modulus), where k is the divisor of the stress.

The creep data and the procedure of parameter evaluation for the single crystal alloy SRR99 were taken from [13], which describes the experimental results and evaluation of parameters of Eq 4. With Eq 4 it is possible to describe the minimum creep rate for a set of different single crystal alloys as exemplified in [12].

For the material Haynes 230, the creep rate was evaluated by fitting the Eq 4 to a set of constant strain rate tensile tests. The result conforms to different other creep data evaluated in the program, but not used for the determination of the model parameters.

The description of the cyclic hardening was based on the results of the stress evolution in isothermal LCF tests. Figure 2a shows the stress increase at the end of the loop as a function of the accumulated plastic strain for different applied strain ranges in strain controlled experiments.

In addition to the data points, a linear approximation as given by Eq 6 is shown. The parameters a_p and b_p (axis intercept and slope) of the fit are both functions of temperature and plastic strain range. The correlation to the plastic range is again linear, whereas the temperature dependence shows comparable values at 300°C and 900°C, but a pronounced maximum at 600°C, as exemplified in Fig. 2b for b_p ; a_p shows the same behavior.

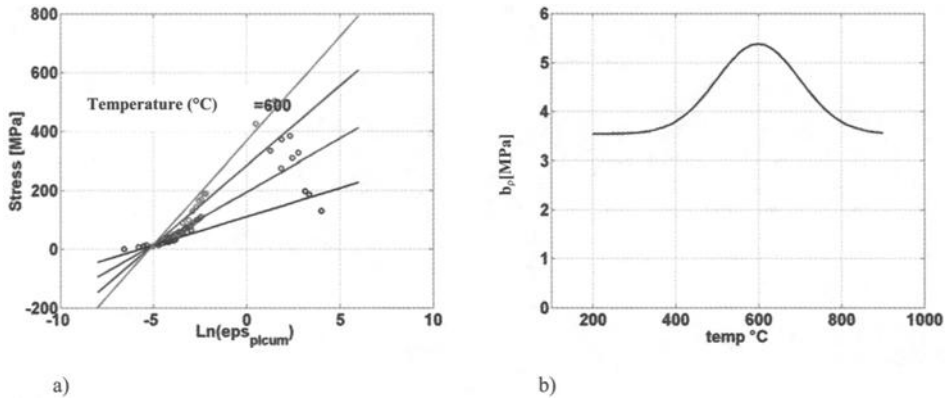
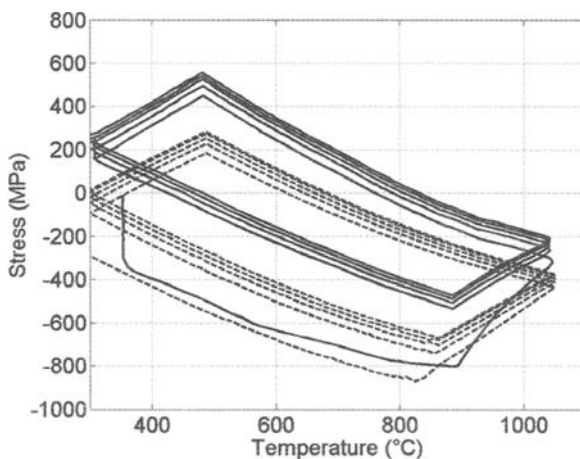


FIG. 2—*a) Relationship between stress increase and accumulated plastic strain; b) Relationship between b_p and temperature.*

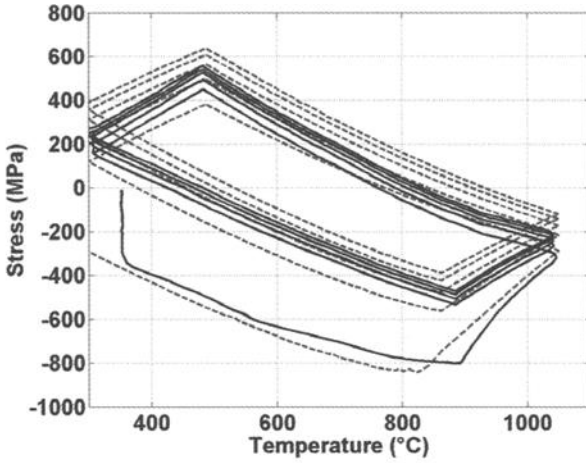
Results

Single Crystal Results

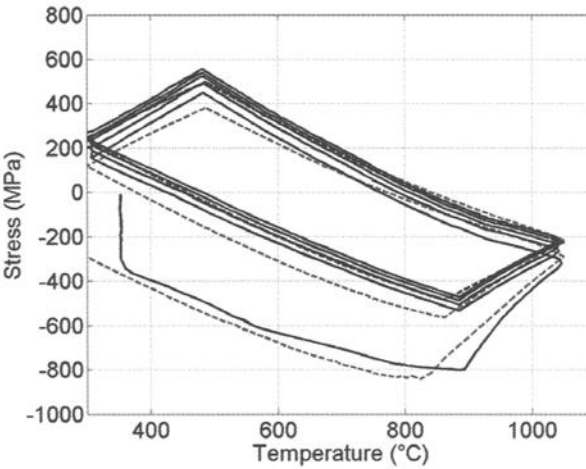
Figure 3 shows the experimental results for the single crystal alloy SRR99 under TMF loading tested with an upper strain of zero and a lower strain of -1.0% (full lines). In order to proof the model, one of the experiments with a high strain range was selected from a couple of experimental results, as it was expected that all relevant micro-structural mechanisms would be acting. For details of the strain / temperature path refer to Fig. 1b. In addition to the experimental data (full lines), three different results of calculations according to the above-mentioned model are shown (dashed lines).



a)



b)



c)

FIG. 3—Comparison between the experimental data and the modeling result of stress-temperature loops, during TMF for SRR99, with different parameter sets for modeling relaxation: (full lines: experimental data, dashes/dotted lines: modeling results). a) Model with minimum creep rate (dashed line); b) Model with primary creep (dashed line); c) Model with primary creep (for two cycles) and minimum creep rate (dashed line for three cycles).

The cycling starts at zero stress and at a temperature of about 350°C (slightly higher than the aimed for 300°C). The control unit first decreases the strain under constant temperature to the intended starting point of the loop, which is at a compressive strain of -0.25% (corresponding to a stress of about -350 MPa). Then anisothermal cycling starts

corresponding to Fig. 1*b*. Whereas the mechanical strain and the temperature now de/increase linearly with time, the stress versus temperature as shown in Fig. 3*b* deviates slightly from linearity according to the decrease of the Young's modulus with temperature and reaches a minimum of approximately -800 MPa at about 900°C , which occurs at a slightly higher temperature than the intended peak value of the compressive strain ($\text{eps} = -1.0\%$). After reversal of the strain with further increasing temperature, a strong increase in stress is observed until about 1050°C , when a stress of about -320 MPa is measured and the temperature control changes from heating to cooling. Continuation causes rising stress with slight non-linearity to the point of maximum stress (about 400 MPa) and maximum strain ($\text{eps} = 0\%$) at about 480°C . Reversed straining and further cooling until the end of the first loop, which is at 310°C and a stress of about 180 MPa indicating a difference in stress of about 450 MPa as compared to the starting point of the first cycle. This difference remains fairly constant while the strain decreases and stress reaches its minimum of approximately -530 MPa. Whereas the stress was rising after reversal of the strain from -800 MPa to -320 MPa, which is about 500 MPa in the first cycle, in the second cycle the increase is from -530 MPa to -260 MPa, which differs by 270 MPa and is approximately half of the first cycle increase. Subsequent cycling exhibits quite comparable behavior for the first, the second, and all following cycles. The small remaining difference in stress between the cycles decreases with increasing cycle number resulting in rising mean stress of each loop.

The main difference of the subsequent cycles as compared to the first cycle is the stress increase concentrated in the temperature range between 900°C and 1050°C . The strong temperature dependence indicates this pronounced stress change could be due to relaxation at the peak temperature of the cycle. This behavior is typical for TMF testing with -135° lag, as reported in several papers [11,14].

The modeling results as shown in Fig. 3*a-c* are all calculated with the same Ramberg-Osgood parameters for elastic and "immediate" plastic deformation. Additionally, relaxation but no hardening is taken into account, as it was not observed in the test result. The difference of Fig. 3*a-c* is only the data set used for calculating relaxation.

Figure 3*a* shows the described stress response of a single crystalline sample as compared to the model results based on data for the minimum creep rate [13]. The decreasing strain from zero to the starting point of the loop as shown in the experimental results was not modeled. After reaching the strain and temperature of the real loop the results from modeling and from the experiment are close to each other until a minimum of -850 MPa in the stress is reached. During heating from 900°C to 1050°C the stress increases but is less distinct than in the experiment, resulting in about 100 MPa lower stress for the model. This difference remains fairly constant during further cycling. Obviously, the measured relaxation in the first cycle is much more pronounced than the calculated, indicating that the minimum creep rate which is often used as basis for life prediction is unsatisfactorily low.

Figure 3*b* shows the same comparison, but takes (only) primary creep into account. In this case the calculated data for the first and for the second cycle correspond satisfactorily to the measured data up to 1050°C , but the modeling results show higher stress relaxation for the following cycles as compared to the experimental data. Thus the difference increases with increasing cycle number. This is not unexpected as primary creep causes hardening leading to secondary creep (minimum creep rate). To account for this, the data

set used was changed from primary creep to secondary creep in the model after two cycles. As shown in Fig. 3c, the result from the calculations corresponds to the experimental in the first two cycles and overlaps for the third through fifth cycle.

Haynes 230

The results presented for the polycrystalline nickel base alloy Haynes 230 are of a strain controlled LCF-test at 600°C and the an in-phase TMF-test conducted under loading conditions at appreciable lower temperatures ($T_{\min} = 300^{\circ}\text{C}$, $T_{\max} = 850^{\circ}\text{C}$). The isothermal LCF test was done at Turbomeca Bordes Cedex, and the TMF test was done at the Institute of Advanced Materials of the Joint Research Center in Petten, in the framework of a collaborative program.

Isothermal LCF

Experimental Results—Figure 4 shows the experimental results (full lines) for stress versus strain in the first five cycles and in the loop where half of the cycles to failure were achieved, respectively, for a strain-controlled LCF test at 600°C. The test was performed under a high strain range of 1.26% under symmetric conditions. The test starts at zero strain and after about 0.1% strain a pronounced yield point is observed with subsequent serrated yielding at a stress of about 230 MPa with some hardening. After the reversal of the strain, the material shows hardening after a smooth transition from elastic to plastic deformation and again with less distinct serrated yielding. The deformation in the following cycles is comparable, but with increasing stress at the strain limits clearly indicating cyclic hardening. Reference to the second diagram that shows the deformation behavior at half-life (538 cycles) exhibits stresses of about 600 MPa at the strain limits, thus the contribution that is due to hardening is higher than the yield stress, which emphasizes the importance of hardening to the deformation of that material.

Modeling Results—In Fig. 4a the results of the modeling are shown together with the experimental data. The first cycle starts at zero but exhibits an earlier comparable smooth transition to plastic deformation with subsequent higher hardening rate than the experiment, thus ending with a maximum stress of 300 MPa, which is about 50 MPa higher than in the experiment. After reversal of strain the measured stress path now exhibits a smoother yielding and hardening resulting in a stress, which is close to but a small percentage lower than, the modeling result. For the following cycles the path and achieved stress of the modeling result correspond well to the experimental result. Comparison of the results for the half-life cycle (Fig. 4b) exhibits a 20% lower prediction of the stress level at the strain limits than measured, which is confirmed by a comparison of the maximum and the minimum stresses of all cycles available from the experiment with the modeling result not shown here.

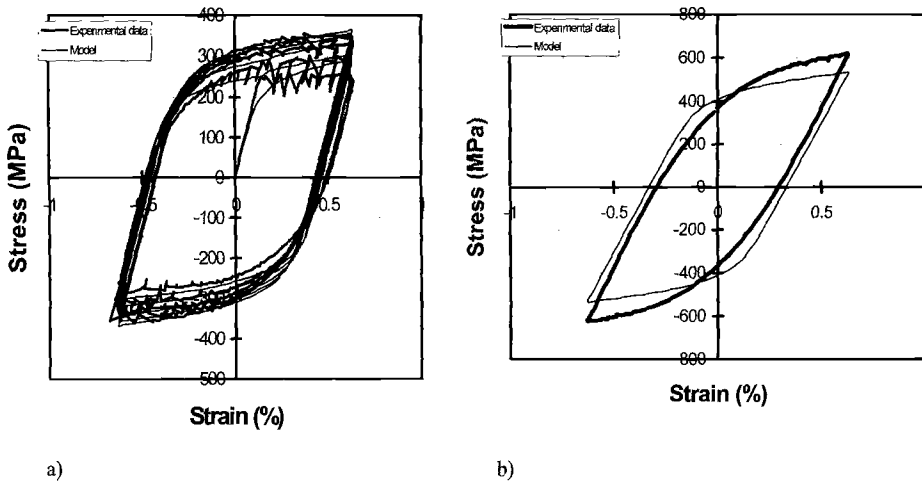


FIG. 4—Comparison between experimental data and modeling result of stress-strain loops, during isothermal strain controlled LCF tests of Haynes 230 for a) the first five cycles; b) cycle at half-life (538 cycles).

TMF

Experimental Results—Figure 5 shows the experimental results for stress versus strain in the first cycle and in the loop where half of the cycles to failure were achieved ($N = 88$), of an in-phase loaded TMF-sample with the strain limits between 0.0 and 0.8%. The stress starts at zero and increases up to 250 MPa, which is about the yield stress, and then remains constant until the temperature reaches 850°C. After reversal of strain and temperature, the stress decreases almost linearly to the compressive yield, (approximately 200 MPa), and reaches a compressive stress of about 330 MPa at the end of the first loop due to hardening.

The loop at half-life starts at a compressive stress of -550 MPa, increases up to the tensile yield, and reaches a pronounced maximum in stress of 420 MPa at a temperature of about 770°C, again due to hardening. Then, softening can be observed, acquiring the stress value of 330 MPa at maximum temperature. After reversal of strain and temperature, the drop in the stress exhibits yielding under compression with a subsequent hardening as in cycle number one but with a much steeper hardening rate reaching a stress of 550 MPa at the end of the loop.

Modeling Results—Figure 5 shows additionally the model results in the first and in the 80th loop under the same loading conditions as in the experiment. The deformation behavior is as described above. The stress starts at zero and increases up to 220 MPa, which is close to the yield stress. As a consequence of hardening and softening, maximum and minimum stresses of 320 and 270 MPa, respectively, are reached at maximum temperature. After reversal of strain and temperature, the stress decreases, showing yielding and hardening up to a maximum compressive stress of 300 MPa at the end of the first loop. In the following cycles (not shown in Fig. 5) the behavior is comparable, but with an increasing hardening rate. Under tension, a pronounced maximum stress is built up at a temperature of approximately 750°C, (which increases

with ongoing cycling up to 450 MPa after 80 cycles) followed by a softening down to a stress close to 300 MPa for the 80th cycle, whereas under compression, hardening decreases the stress until the end of the loop, corresponding to a stress value of 600 MPa for the 80th cycle.

A comparison of the loop shape between both modeling and experimental results shows a clear similarity, whereas the predicted stresses are about 10% higher at the maximum (tension) and fit satisfactorily at the minimum stress (compression).

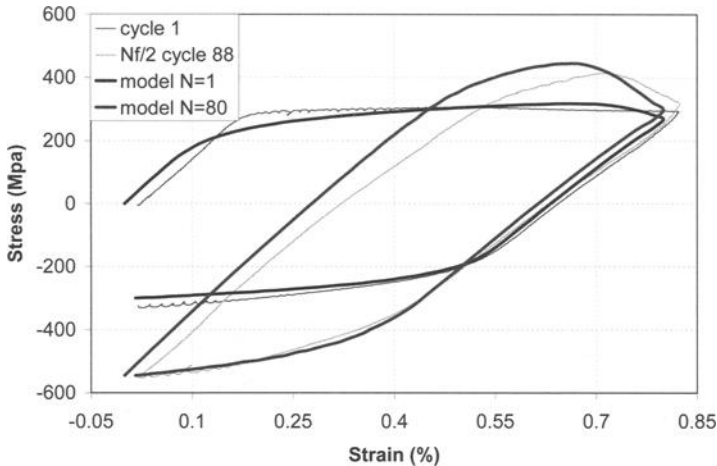


FIG. 5—Comparison between experimental data and modeling result of stress-strain loops, during TMF of Haynes 230 for a) the first cycle; b) half lifetime.

Discussion

With respect to the model described above, formulations for both creep and hardening are based on the effective stress concept, which takes the existence and evolution of internal stresses into account and refers to the correlation of this stress with dislocation density. Comparable descriptions are found in [3–5,8,10].

SRR 99

The comparison of the experimental results with the modeling results for the single crystal alloy shows clearly that it is sufficient to model the elastic and plastic deformation together with creep. Comparable conclusions can be found in [2]. But it emphasizes the importance of the primary creep range. The best prediction was achieved with a rough procedure by application of primary creep data for two cycles and then changing over to minimum creep rate data. This was done to simulate the reality, which continuously decreases the rate from the primary to secondary. It was successfully applied for strain ranges between 0.8 and 1.2%, and it shows that it is necessary to describe the transition from primary to secondary creep as a function of strain and temperature before application to other strain ranges and materials.

Since primary creep for nickel base single crystal alloys causes hardening, it led to the lower minimum creep rate. This behavior indicates that the dislocation density is increased during plastic deformation from the beginning, reaching a maximum in density at the minimum creep rate. This in principle is the same mechanism as for the Haynes material.

Haynes 230

The prediction of the polycrystalline alloy clearly shows the necessity to describe cyclic hardening for the isothermal as well as for the anisothermal deformation behavior. This was achieved by the assumption that it is caused by dislocation interaction increasing the dislocation density and was thus correlated to the amount of plastic deformation, which is the accumulated plastic strain in case of cyclic deformation. This correlation is confirmed by the isothermal LCF results as documented in Fig. 4 and results in good predictions of hysteresis loop evolution with a tendency to underestimate the stress extremes by about 20% for longer life. The loop shapes predicted are quite comparable to the measured shapes with the exception of bad similarity for the first loop. The reason for this is based in the modeling procedure where the influence of hardening or relaxation is calculated as a difference in stress with respect to the Ramberg-Osgood description. The parameters k and n of each loop remain constant until the strain is reversed, then k is updated to meet the last predicted stress at the corresponding strain. As n , which controls the basic shape (without additional contributions of hardening and relaxation), is constant throughout the test all predicted isothermal loop shapes are similar, whereas the first cycle of the LCF experiment exhibits a shape which deviates from all subsequent loops.

The hysteresis loops of the TMF test exhibit a distinct maximum at 700°C, which is enhanced with increasing cycle numbers in agreement with the simulation. This can be explained as an interaction of the cycle dependent hardening and the temperature dependent relaxation. So far, the model prediction is satisfactory. But a detailed comparison of the extreme stresses as a function of the cycle number shows relatively high hardening rates at the beginning of the tests and saturation or quite small hardening at mid-life for the isothermal tests, the anisothermal tests, and the isothermal simulation, whereas the predicted anisothermal simulation shows nearly constant hardening rates (not shown here). This causes increasing deviation from the measurement with increasing cycle numbers, which becomes important for the tests with lower strain ranges where the number of cycles to failure is higher. As this is observed only by the simulation of the TMF test, the difference is likely caused by the modeling procedure and not by a specific influence of the anisothermal loading, e.g., the interaction of low and high temperature mechanisms. One possible explanation might be that the description of hardening with a logarithmic term (which can in principle reach infinity) is not sufficient and a more elaborate description incorporating also strain and temperature controlled reduction of dislocation density (softening) is necessary. Another argument is that the experimental data used for evaluation of the parameters of hardening and for relaxation incorporate both and are therefore an inappropriate basis for the evaluation of the modeling parameters. A third hypothesis is that the assumption of hardening being solely controlled by the evolution of dislocation density is insufficient. In some references [15,16] the hardening of an alloy (IN 617), which shows comparable hardening and has also a high carbon content, was mainly attributed to the changes in carbide size and distribution. The

influence of temperature on the carbide distribution is expected to be thermally activated, causing different distributions at different temperatures. This would influence the contribution to particle strengthening and the hardening rate. The hardening rate is reflected in the simulation by the constant n of the Ramberg-Osgood equation and is changed during cyclic deformation controlled by the temperature dependent factor b_p , as shown in Fig. 2. The value of b_p is about the same for temperatures higher than 800°C and less than 400°C but raised by about 50% at 600°C. This might indicate more favorable—at least for H230—some interaction of carbon with the dislocations during movement, thus causing higher hardening rate, than some change in particle distribution which would influence mainly the yield strength and not the hardening rate.

It is not obvious which of the above-mentioned arguments is most important for the unrealistic hardening of the simulation. The logarithmic hardening rules were successfully applied for hardening, but the principal ability to harden up to infinity clearly shows that it needs a limitation. It is thus intended to incorporate softening in the evolution of dislocation density. Blum et al. [8,10] developed a more sophisticated modeling of plastic deformation correlating plastic deformation with dislocation structures and their evolution. It takes saturation into account, but the hardening rule used was minorly suitable for the description of the measured LCF behavior. Nevertheless, it exemplifies how to model saturation. When softening or saturation are embedded in the modeling procedure, the necessity of further modification with respect to the above mentioned hypotheses should be discussed.

Conclusions

Modeling of deformation under anisothermal loading has to account for elastic deformation, plastic deformation, relaxation, and cyclic hardening.

Relaxation has to comprise primary, secondary, and the transition from primary to secondary creep.

An interaction of consecutive incremental steps of hardening and relaxation and the summation of the corresponding stresses (increases and decreases) was modeled. A more sophisticated modeling should take into account the dislocation density reached after hardening as a basis to define the starting point of the following relaxation step and vice versa.

The presented model works well for isothermal and anisothermal loading up to a limited number of cycles. For the Haynes 230 alloy with strong cyclic hardening, the deviation between prediction and experiment becomes more and more important at a number of cycles higher than some thousand, and a more refined modeling would be recommended. No large deviations—even at high cycle numbers—were observed for the single crystalline alloy, SRR99, which shows no strong cyclic hardening.

Acknowledgment

Thanks are given to the Institute of Advanced Materials at the Joint Research Center of the European Community in Petten for TMF testing and also to Turbomeca SA Bordes Cedex for LCF testing in the framework of the BRITE-Euram programs under contract No. BREU-CT90-0338 (SRR99) and BRPR-CT97-0498 (Haynes 230). Thanks are also given to the European community for funding part of the testing and modeling work.

References

- [1] Chaboche, J.-L., "Bulletin de L'Academie des Sciences," Serie des Sciences Techniques XXV, No. 1, 1977.
- [2] Heine, J. E., Ruano, E., and DeLaneville, R. E., "TMF Life Prediction Approach for Turbine Blades," Agard Conference Proceedings 569, Banff, Canada, 2-4 October 1995, No. 20, pp. 1-6.
- [3] Boire-Lavigne, S., Gendron, S., Marchand, N. J., and Immarigeon, J. P., "Modelling of Thermomechanical Fatigue including Phase Transformations," Agard Conference Proceedings 569, Banff, Canada, 2-4 October 1995, No. 17, pp. 1-9.
- [4] Meersmann, J., Frenz, H., Ziebs, J., Kühn, H.-J., and Forest, S., "Thermo-mechanical Behaviour of IN 738 LC and SC 16," Agard Conference Proceedings 569, Banff, Canada, 2-4 October 1995, No. 19, pp. 1-11.
- [5] Schubert, F., Penkalla, H. J., and Frank, D., "Thermal Mechanical Fatigue of Model Blades Made from CC and DS Superalloys," Agard Conference Proceedings 569, Banff, Canada, 2-4 October 1995, No. 22, pp. 1-9.
- [6] Bhattachar, V. S. and Stouffer, D. C., "Constitutive Equations for the Thermomechanical Response of René 80: Part 1 - Development from Isothermal Data," *Journal of Engineering Materials and Technology*, Vol. 115, October 1993, pp. 351-357.
- [7] Sievert, R., Werner, Ö., Olschewski, J., and Ziebs, J., "Physical Interpretation of a Viscoplastic Model Applied to High Temperature Performance of a Nickel-base Superalloy," *Z. Metallkunde*, Munich, 1997, pp. 416-424.
- [8] An, S. U., Wolf, H., Vogler, S., and Blum, W., "Verification of the Effective Stress Model for Creep of NiCr22Co12Mo at 800°C," Fourth International Conference on Creep and Fracture of Engineering Materials and Structures, Swansea, April 1990, pp. 17-23.
- [9] Skelton, R. P., Webster, G. A., de Mestral, B., and Wang, C.-Y., "Modelling Thermo-mechanical Fatigue Hysteresis Loops from Isothermal Cyclic Data," *Third Symposium on Thermo-mechanical Fatigue Behaviour of Metals, ASTM STP 1371*, H. Sehitoglu and H. Maier, Eds., ASTM International, West Conshohocken, PA, 1999, pp. 227-232.
- [10] Meier, M., Qiang, Z., and Blum, W., "Demonstration of the Quantitative Differences Between Class M and Class A Deformation Behaviours Within the Composite Model," *Z. Metallkd.*, Munich, 1993, pp. 263-267.
- [11] Bressers, J., Timm, J., Williams, S. J., Bennett, A., and Affeldt, E. E., "Effects of Cycle Type and Coating on the TMF Lives of a Single Crystal Nickel Based Gas Turbine Blade Alloy," *Thermomechanical Fatigue Behaviour of Materials, ASTM STP 1263*, Michael J. Verrilli and Michael G. Castelli, Eds., ASTM International, Vol. 2, 1996, pp. 56-67.
- [12] Schneider, W. and Mughrabi, H., "Investigation of the Creep and Rupture Behaviour of the Single-Crystal Nickel-Base Superalloy CMSX-4 between 800°C and 1100°C," *Creep and Fracture of Engineering Materials and Structures*, Swansea, UK, 28 March-1 April 1993, pp. 209-221.

- [13] Hammer, J., "Kriech- und Zeitstandverhalten der Einkristallinen Nickelbasis-Superlegierung SRR99 unter besonderer Berücksichtigung der Mikrostrukturellen Vorgänge und der Materialfehler," Dissertation, Erlangen, Germany, 1990.
- [14] Bressers, J., Timm, J., Williams, S. J., Bennett, A., and Affeldt, E. E., "Effects of Cycle Type and Coating on the TMF Lives of CMSX6," Agard Conference Proceedings 569, Banff, Canada, 2-4 October 1995, No. 9, pp. 1-10.
- [15] Kleinpaß, B., Lang, K.-H., and Macherauch, E., "Zum thermisch-mechanischen Ermüdungsverhalten von NiCr22Co12Mo9," *Mat.-wiss. u. Werkstofftech.*, Vol. 25, 1994, pp. 389-398.
- [16] Moalla, M., Lang, K.-H., Löhe, D., and Macherauch, E., "Isothermal High Temperature Fatigue Behaviour of NiCr22Co12Mo9 under Superimposed LCF and HCF Loading," *Low Cycle Fatigue and Elasto-Plastic Behaviour of Materials*, 1998, pp. 27-32.

Modelling of Hysteresis Loops During Thermomechanical Fatigue

REFERENCE: Sandström, R. and Andersson, H. C. M., “**Modelling of Hysteresis Loops During Thermomechanical Fatigue,**” *Thermomechanical Fatigue Behavior of Materials: 4th Volume, ASTM STP 1428*, M. A. McGaw, S. Kalluri, J. Bressers, and S. D. Peteves, Eds., ASTM International, West Conshohocken, PA, Online, Available: www.astm.org/STP/1428/1428_10579, 3 Feb. 2003.

ABSTRACT: The hysteresis loops obtained during thermomechanical fatigue testing of the stainless steel 253 MA and the ODS alloy PM2000 have been analysed using a model taking elastic, plastic, and creep deformation into account. Data from previously performed creep and tensile tests were used to determine the constants in the model. Hysteresis loops both from in-phase and out-of-phase cycling were successfully reproduced. By integrating the fatigue and creep damage along the hysteresis loops, the cyclic lifetimes of 253 MA were predicted.

KEYWORDS: thermomechanical fatigue, TMF, hysteresis loops, modelling, computer simulations

During operation of high temperature plants such as gas turbines, temperature variations expose the material to thermal strains. In particular, the strains appearing during start-ups and shutdowns are frequently severe. After a sufficient number of cycles thermal fatigue cracking can take place. The ideal way to study thermal fatigue is to perform thermomechanical fatigue (TMF) tests, where both mechanical strain and temperature are cycled. The specimens should be exposed to temperature and strain cycles similar to those occurring in practice. This is unfortunately not always practical because of the difference in time scale. The transfer of the results of TMF testing to the more complex cycles that occur in service must be performed with the help of models.

Life prediction of TMF is challenging, since many damage mechanisms such as cyclic plastic strain, creep and oxidation, and combinations of the two are involved. The modelling in the literature has primarily been focused on low cycle fatigue (LCF), i.e. strain cycling at constant temperature. Empirical LCF life prediction models have been available for many years. Examples of such models are frequency modified damage, strain-range-partitioning, strain-energy-partitioning, and frequency separation. Overviews can be found in [1] and [2]. Each of these models involves the fitting of a number of constants to the experimental data. The limitations of the empirical models are particularly evident when they are applied to TMF with simultaneous temperature and strain cycles. For example, the differences between LCF and in-phase and out-of-phase TMF have been generally impossible to describe.

¹ Swedish Institute for Metals Research, Drottning Kristinas v. 48, S-114 28 Stockholm, Sweden.

² Prof. Materials Technology, Royal Institute of Technology, S-100 44 Stockholm, Sweden.

An alternative approach is to model the stress-strain loops and then to integrate the creep and fatigue damage that appears during the cycles. Creep and fatigue damage has in this study been treated as superimposed effects. This approach has previously been applied to LCF of soldered joints [3]. The purpose of the present paper is to apply such a model to results obtained from LCF and TMF testing of the austenitic stainless steel 253 MA and also to some results for the oxide dispersion strengthened alloy PM2000.

Modelling

Cyclic Deformation

In a TMF or LCF test, the total mechanical strain rate can be described as a superposition of strain rates obtained from elastic, plastic and creep strain as well as the Bauschinger effect, Eq 1. The model does not consider thermal strain, since the test controller compensates for it. The Bauschinger effect shows up as plastic deformation in the unloading part of the loop, and hence as a strain component of the total strain.

$$\frac{d\varepsilon_{el}}{dt} + \frac{d\varepsilon_{pl}}{dt} + \frac{d\varepsilon_{cr}}{dt} + \frac{d\varepsilon_B}{dt} = \frac{d\varepsilon_{tot}}{dt} \quad (1)$$

The elastic strain can be expressed as

$$\frac{d\varepsilon_{el}}{dt} = \frac{1}{E} \frac{d\sigma}{dt} \quad (2)$$

The plastic strain is obtained using the Kocks-Mecking [4] flow stress – strain model as a basis. It takes the form

$$\frac{d\sigma}{d\varepsilon_{pl}} = \frac{\omega}{2} (\sigma_m - \sigma) \quad (3)$$

where σ_m is the maximum stress and ω a constant. Eq 3 can be rewritten as

$$\frac{d\varepsilon_{pl}}{dt} = \frac{2H(\sigma)}{\omega(\sigma_m - \sigma)} \frac{d\sigma}{dt} \quad (4)$$

where $H(\sigma)$ is the Heaviside step function, which vanishes for $\sigma < 0$ and is unity for $\sigma > 0$. When the deformation direction is reversed (which happens twice each cycle), plastic deformation starts at a lower stress level than in the virgin material. This is referred to as the Bauschinger effect. The Kocks-Mecking model is used also for the Bauschinger effect, but with a different start stress σ_B .

$$\frac{d\varepsilon_B}{dt} = \frac{2H(\sigma - \sigma_B)}{\omega_B(\sigma_{mB} - (\sigma - \sigma_B))} \frac{d\sigma}{dt} \quad (5)$$

ω_B is given the same value as ω in Eq 4. σ_{mB} is twice the value of σ_m . The latter choice is made to take into account the reduced role of the Bauschinger effect in relation to that of the “ordinary” plastic strain.

The creep strain rate $\dot{\varepsilon}_{cr}$ is represented by the Norton equation

$$\dot{\varepsilon}_{cr} = A_N \sigma^n e^{\frac{T}{T_0}} \quad (6)$$

where A_N , n and T_0 are constants, and T is the temperature in Kelvin. The creep during the cycling has a transient component, since the stress is continuously changing. This can be interpreted as primary creep taking place in each cycle. To model the transient in the creep rate an inverted omega model is used [5]. This implies that the creep rate decreases exponentially with increasing strain. This approach has successfully been applied to low alloy and 9 and 12 % Cr-steels [5]. Although the conventional omega model for tertiary creep [6,7] works quite satisfactory for stainless steels [8], the inverted model does not seem to have been used for this type of steel. The inverted omega model is introduced by replacing the constant A_N in Eq 6 by the following expression at small creep strains. ε_{pr} defines the end of the primary creep range.

$$A_{Npr} = A_N e^{a_{pr} \left(1 - \frac{|\varepsilon_{cr}|}{\varepsilon_{pr}}\right)} \quad |\varepsilon_{cr}| < \varepsilon_{pr} \quad (7a)$$

$$A_{Npr} = A_N \quad |\varepsilon_{cr}| \geq \varepsilon_{pr} \quad (7b)$$

As will be seen later the transient creep plays an insignificant role for PM2000 and the exact values of the constants in Eq 7 are not critical. Inserting Eqs 3–6 and 7a into Eq 1 gives

$$\frac{1}{E} \frac{d\sigma}{dt} + \frac{2H(\sigma)}{\omega(\sigma_m - \sigma)} \frac{d\sigma}{dt} + \frac{2H(\sigma - \sigma_B)}{\omega_B(\sigma_{mB} - (\sigma - \sigma_B))} \frac{d\sigma}{dt} + A_{Npr} \text{sign}(\sigma) \text{abs}(\sigma)^n e^{\frac{T}{T_0}} = \frac{d\varepsilon_{tot}}{dt} \quad (8a)$$

Equation 6 for the creep strain rate has been modified to make it applicable also to negative stresses. Equation 8a is valid in the tension going cycle. The corresponding expression for the compression going part is

$$\frac{1}{E} \frac{d\sigma}{dt} + \frac{2H(-\sigma)}{\omega(\sigma_m + \sigma)} \frac{d\sigma}{dt} + \frac{2H(\sigma + \sigma_B)}{\omega_B(\sigma_{mB} + (\sigma + \sigma_B))} \frac{d\sigma}{dt} + A_{Npr} \text{sign}(\sigma) \text{abs}(\sigma)^n e^{\frac{T}{T_0}} = \frac{d\varepsilon_{tot}}{dt} \quad (8b)$$

The Bauschinger start stress σ_B is assumed to be negative in Eqs 8a and 8b.

Fatigue Damage

According to the Coffin-Manson relation, the number of cycles to failure initiation during LCF can be expressed as

$$N_{90} = \left(\frac{\Delta \varepsilon_{pl}}{A(T)} \right)^{-\alpha} \quad (9)$$

where A is a function of temperature and α is a constant. If a TMF test is evaluated, the fatigue damage must be integrated during the whole stress–strain loop to include effects from the varying temperature. If the principle of cumulative damage is assumed to apply, the fatigue damage D_{fat} can be expressed as

$$D_{fat} = \eta \int \frac{1}{N_{90}(T, \varepsilon_{pl})} dT \quad (10)$$

where η is the ratio between the strain generated by plastic deformation in each cycle and twice the strain range. This parameter has been introduced because both fatigue and creep damage occurs simultaneously, and only the part of the cycle where plastic deformation is controlling the damage process should be taken into account.

Creep Damage

During LCF and TMF of stainless steels using cycles containing significant creep portions the dominating creep damage mechanism is the formation of cavities and cracks [9]. Cavities form at the grain boundaries. Those that are located perpendicular to the stress direction have a strong tendency to grow. The creep damage D_{cr} can be defined in terms of initiation and growth of creep cavities [10]

$$D_{cr} = 8 N R^2 \quad (11)$$

where N is the number of cavities and R the cavity radius. This damage formulation is, for example, consistent with the mechanical damage model according to Cocks and Ashby [11]. N and R can be expressed as a function of strain as [10,12]

$$N = C_N \varepsilon_{cr}^{\nu} \quad (12)$$

$$R = C_R \varepsilon_{cr}^{\rho} \quad (13)$$

where C_N , C_R , ν , and ρ are constants. ν and ρ take values in the range 0.3–1 and 0.35–0.75 for a number of materials. Combining Eqs 11–13 gives the following expression [10]:

$$D_{cr} = C_D \varepsilon_{cr}^{\delta} \quad (14)$$

with the constant δ in the range 1–1.5. δ is not well known for stainless steels but the creep damage is assumed to be proportional to the creep strain ε_{cr} . The damage for in-phase TMF takes the form

$$D_{cr} = (1 - \chi) \int_{tension} \frac{\dot{\epsilon}_{cr}}{\epsilon_R} dt \quad (15a)$$

and for out-of-phase TMF the corresponding expression is

$$D_{cr} = -(1 - \chi) \int_{compr} \frac{\dot{\epsilon}_{cr}}{\epsilon_R} dt \quad (15b)$$

where ϵ_R is the creep ductility (creep strain at rupture). The factor $(1 - \chi)$ is introduced to take the opening and closure of cavities into account [13,14]. If LCF is considered, a factor φ has to be introduced to reflect the amount of closure of cavities during the compressive part of the LCF cycle. Equation 15a then takes the general form

$$D_{cr} = (1 - \chi) \int_{tension} \frac{\dot{\epsilon}_{cr}}{\epsilon_R} dt + \varphi \int_{compr} \frac{\dot{\epsilon}_{cr}}{\epsilon_R} dt \quad (16)$$

where $\varphi = 0$ for TMF testing and $\chi = 0$ for LCF testing. The first integral in Eq 16 is evaluated over the tension part of the loop and the second integral over the compression part.

Experimental

The testing that forms the basis for the modelling in this paper has been performed on two materials, namely the austenitic stainless steel 253 MA and the mechanically alloyed oxide dispersion strengthened alloy PM2000. Reports on the testing can be found in Refs. 15 and 16 and only a short description is included in the present paper. Chemical composition of the materials can be found in Table 1.

TABLE 1—*Chemical composition of the tested materials (wt%).*

Material	C	N	Cr	Ni	Si	Ce	Al	Ti	O	Y ₂ O ₃
PM2000	0.0065	0.0081	19.7	5.28	0.41	0.23	0.49
253 MA	0.086	0.152	20.97	10.98	1.70	0.038	0.013	0.007

In-phase TMF testing (TMF-IP), out-of-phase TMF testing (TMF-OP), and LCF tests were performed for both materials. All tests were conducted under symmetrical ($R = -1$) total (mechanical + thermal) strain control. The strain rates used for PM 2000 were $5 \cdot 10^{-5} \text{ s}^{-1}$ for TMF and both $5 \cdot 10^{-5} \text{ s}^{-1}$ and $7 \cdot 10^{-4} \text{ s}^{-1}$ for LCF. For 253 MA $1 \cdot 10^{-4} \text{ s}^{-1}$ (TMF) and $2 \cdot 10^{-3} \text{ s}^{-1}$ (LCF) were used. The temperature was cycled between 800 and 1200°C for PM2000 and between 500 and 1000°C for 253 MA. The specimens were allowed to run to final failure and the number of cycles to 10 % load drop of linear maximum tensile load, N_{90} , was determined.

Prior to each TMF test the thermal strain versus temperature within the investigated range was measured under a no-load condition. The temperature dependence of the elastic modulus was also evaluated. For 253 MA, a first-degree equation was sufficient and for PM2000 a second degree equation was used.

$$E = -87T + 198000 \quad (253 \text{ MA}) \quad (17)$$

$$E = -0.0033T^2 - 100.7T + 192100 \quad (\text{PM2000}) \quad (18)$$

The temperature T is given in $^{\circ}\text{C}$ and the elastic modulus E in MPa. This information was then used to separate the plastic, thermal, and elastic parts of the total strain after testing.

Modelling Hysteresis Loops

To allow for modelling of the hysteresis loops using Eqs 8a and 8b, the included constants have to be determined. For 253 MA the constants in Eq 4 were fitted to LCF data obtained at 750°C [17]. The values chosen are $\sigma_0 = 273 \text{ MPa}$, $\sigma_m = 274 \text{ MPa}$, and $\omega = 1934$. σ_0 and σ_m are assumed to vary with temperature in the same way as the elastic constant (as observed in tensile tests), whereas ω is kept independent of temperature. The coefficient in the Baushinger equation is chosen as $\sigma_{mB} = 2 \times 274 \text{ MPa}$. σ_B has been chosen to make the Bauschinger effect start immediately on the reversal of the stress.

The creep contribution to the strain has been estimated by evaluating the creep rates in uniaxial creep tests. For 253 MA the constants have been chosen as $A_N = 1.16 \cdot 10^{-35} \text{ 1/s}$, $n = 4.9$, and $T_0 = 24.8 \text{ K}$. The primary creep constants were chosen as $a_{pr} = 1.61$ and $\varepsilon_{pr} = 0.01$, which corresponds to a maximum increase in creep rate by a factor of 5. Since creep tests were not available for PM2000 at all the relevant temperatures, the stationary creep stress level for LCF tests conducted at 1200°C was used to determine the constants.

Applying the models in Eqs 8a and 8b with the constants given above, hysteresis loops for LCF, TMF-IP, and TMF-OP have been generated. Examples of analysis of 253 MA test loops are given in Figs. 1 and 2. As can be seen from the figures the model follows the experimental data closely. If the in-phase loop in Fig. 1 is considered, the various damage processes active in different parts of the loop can be identified. Starting from the compression corner going clock-wise around the loop the first part is elastic loading combined with a slight curvature due to the Bauschinger effect and the temperature dependence of the elastic modulus. After the zero stress point has been passed, ordinary plastic deformation sets in, followed by a gradual progression to creep deformation as the temperature and stress rise towards the maximum.

However, while elastic and plastic deformation only changes slowly with temperature, the creep saturation stress rapidly decreases at higher temperatures. At the high end of the temperature curve the creep saturation stress becomes the dominant factor and the stress decreases. This effect seems to be somewhat too pronounced for the model when compared to the experiments, but the difference can be explained by the presence of substructure in the material. During the plastic deformation a dislocation substructure is formed in the material. The dislocations then give rise to a back-stress in the material that reduces the creep rate until a sufficiently high temperature is reached and the dislocations are recovered gradually. A time lag does, however, exist between this recovery process and the prediction by Eq 8a, explaining the difference between the model and the experimental results.

After the maximum in tension has been reached there is an elastic unloading, but since the stress at this point is low, it is relatively short. After the zero load level has been passed the process is controlled by plastic deformation. The last part of the loop close to the minimum temperature has the shape of an elevated temperature slow tensile test.

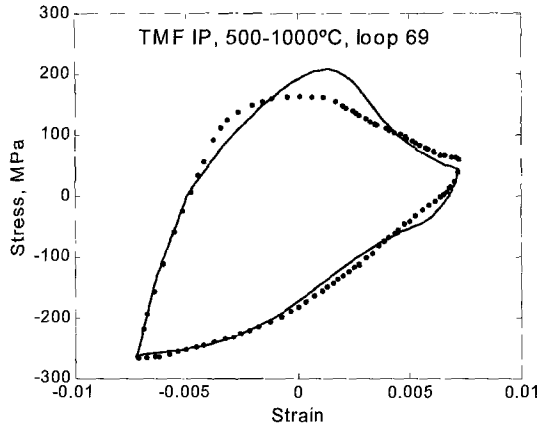


FIG. 1—Stress versus strain during in-phase thermomechanical fatigue of 253 MA. The temperature range is 500–1000°C. The experimental data is shown as dots and the model results as a line.

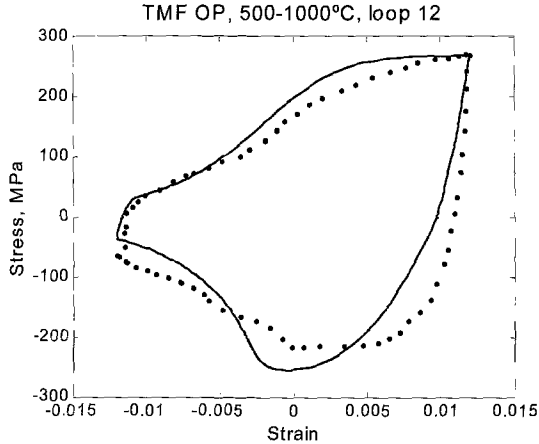


FIG. 2—Stress versus strain during out-of-phase thermo-mechanical fatigue of 253 MA. The temperature range is 500–1000°C. The experimental data is shown as dots and the model results as a line.

The shape of an out-of-phase loop is shown in Fig. 2. It can be explained in a similar manner as the in-phase loop and is essentially a mirror image of the former. Note that the model follows the experimental data as closely in this case as in the case of the in-phase loop, demonstrating that the model can describe the mechanisms involved.

PM2000 behaves very differently from 253 MA under LCF, TMF-IP as well as TMF-OP. In Fig. 3, a low cycle fatigue loop at 1200°C is illustrated. The loop has a pronounced elastic loading/unloading followed by a totally creep dominated stationary stress. The loop shows almost no plastic deformation or Bauschinger effect. The observations and the model are fully consistent in this respect.

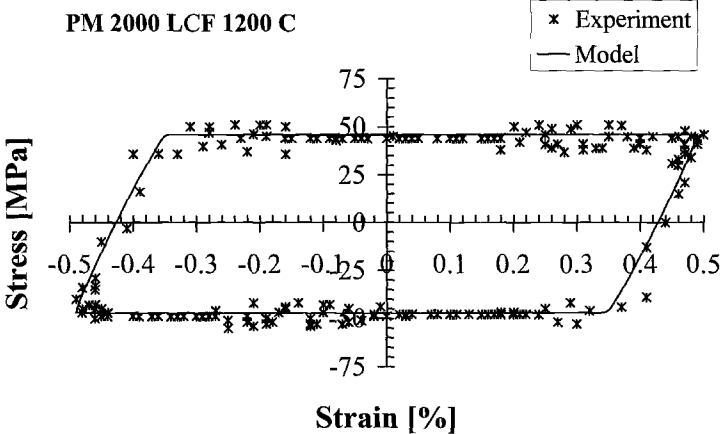


FIG. 3—Stress versus strain during low cycle fatigue of PM2000 at 1200°C. The experimental data is shown as crosses and the model results as a line.

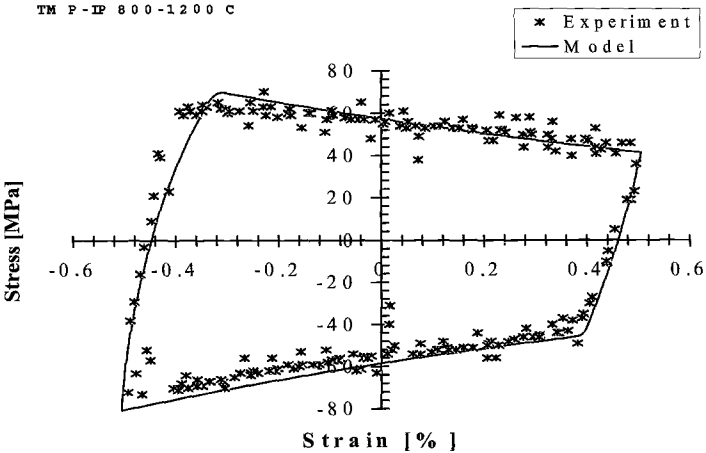


FIG. 4—Stress versus strain during in-phase thermo-mechanical fatigue of PM2000. The temperature range is 800–1200°C. The experimental data is shown as crosses and the model results as a line.

Examples of TMF-loops for PM2000 are given in Figs. 4 and 5. In the in-phase loop the stationary stress in the tensile part of the loop decreases with increasing strain. In the out-of-phase loop the stationary stress in compressive part increases in the same way with decreasing strain. This just illustrates how the stationary creep stress decreases

with increasing temperature. Both the in-phase and the out-of-phase cycles can be described almost completely by the model. As for 253 MA the same constants have been used in the LCF, TMF-in-phase, and TMF-out-of-phase. The small deviation in the stationary part of the cycles is likely to be due to the presence of substructure in the same way as for 253 MA, which provides a memory effect from low to high temperatures.

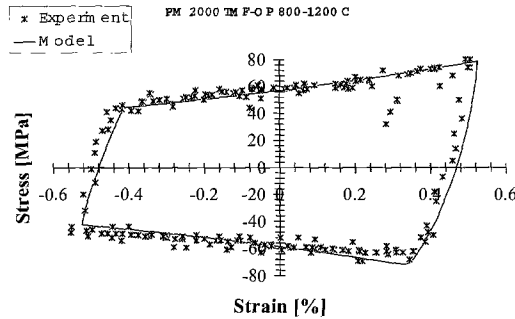


FIG. 5—Stress versus strain during out-of-phase thermo-mechanical fatigue of PM2000. The temperature range is 800–1200°C. The experimental data is shown as crosses and the model results as a line.

As can be seen from the figures, the dependence on temperature of the elastic modulus gives curved vertical parts of both the in-phase and the out-of-phase loops, see Figs. 4 and 5. This curved behaviour is fully consistent with the model results.

Observed and Predicted Lifetimes

The results from the LCF and TMF testing of 253 MA are shown in Fig. 6. The slope of the LCF curves is about the same at 25, 600, 750, and 1000°C. Hence α in Eq 9 can to a first approximation be given a temperature independent value ($\alpha = 1.64$). Since only data for a few temperatures are available, $\log(A)$ in Eq 9 is assumed to vary linearly with temperature between the data points. The minimum in life around 750°C is attributed to a reduction in the ductility due to the precipitation of carbides and nitrides at this temperature [18]. Both TMF in-phase and out-of-phase cycling give shorter lives than LCF.

For TMF the fatigue damage must be integrated around the stress–strain loops to take into account the varying temperature. Assuming the principle of cumulative damage, the fatigue damage D_{fat} is given by Eq 10. The integration is performed with a cyclic temperature. The number of cycles to failure initiation N_{90} is given when the fatigue damage has reached unity. The predicted lives corresponding to the in-phase TMF tests taking only fatigue damage into account are included in Fig. 6. Evidently the LCF tests from temperatures with a shorter life have a stronger influence on the TMF prediction than those with a longer life.

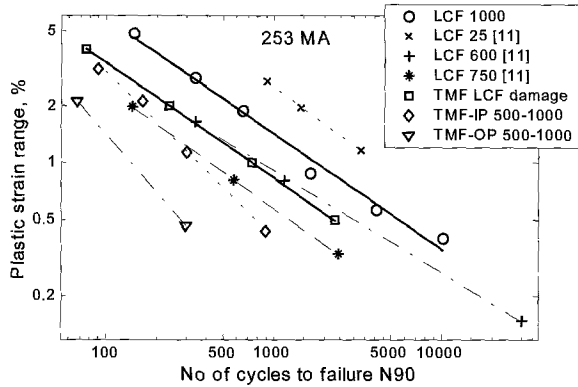


FIG. 6—Number of cycles to failure initiation for LCF results at 25, 600, 750, and 1000°C and for TMF OP and IP cycled between 500 and 1000°C at different levels of plastic strain range. TMF lives predicted from pure LCF damage are included in the figure.

During cycling, fatigue and creep damage is formed. Stress range versus number of cycles is shown in Fig. 7. After an initial transient there is an almost linear load drop as a function of the number of cycles. This load drop is interpreted as the effect of growing damage in the form of cavities and microcracks. For comparison, the expected effect of the computed fatigue and creep damage in Eqs 10 and 16 are included in the figures. Evidently, the model can represent the observed damage quite well. After about 9000 cycles in Fig. 7, the stress versus cycle curve starts to drop steeply. This suggests that rapid crack propagation, crack linkage, and eventually collapse take place. Metallographical observations support this hypothesis [16]. Unfortunately no stress versus cycle curves are available for the TMF tests, so it is not possible to analyse these tests in this respect.

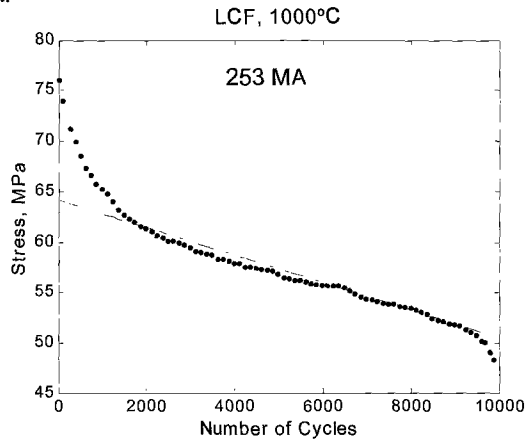


FIG. 7—Maximum stress versus number of cycles at 1000°C. Total strain range 0.0052. Number of cycles to 10 % load drop $N_{90} = 10120$. The dash-dotted line is the model results.

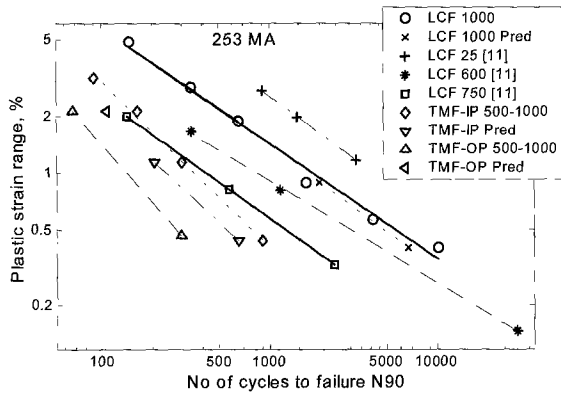


FIG. 8—Number of cycles to failure for LCF results at 25, 600, 750, and 1000°C and for TMF-OP and IP cycled between 500 and 1000°C at different levels of plastic strain range. LCF and TMF lives predicted by taking both fatigue damage and creep damage into account are shown.

With the help of Eqs 10 and 15, the number of cycles to the end of life can be predicted. Some results are illustrated in Fig. 8. Predicted and observed number of cycles to failures expressed as N_{90} are compared. The contributions to the total damage from creep and fatigue damage are linearly added. For all the tests the creep damage gives the largest contribution. It is two to three times larger than the fatigue damage. The predicted LCF values are close to the experimental ones. The computed TMF lives lie in between the in-phase and out-of-phase cycled specimens.

In deriving the predicted lives and the stress versus cycle curves, only two constants have been fitted to the data. These two constants χ and ϕ , cf. Eqs 15 and 16, describe the degree of cavity and crack closure during LCF and TMF testing respectively. During LCF testing, the creep damage is reduced during the compressive part of the cycles, where the deformation is mainly controlled by creep. For TMF, on the other hand, the creep damage is generated at the high temperature end, and there is little chance that there is sufficient creep in the reverse cycle to reduce the damage significantly. However, instead it is assumed that the reverse plastic deformation gives cavity and crack closure. This reduction is smaller than when the damage is reduced due to creep straining. Very limited data exist in the literature on the degree of closure [9,13].

LCF and TMF results for PM2000 are presented in Fig. 9. For the specimens machined along the main rolling direction, TMF-OP tests displayed only marginally lower cyclic lifetimes than the LCF tests. TMF-IP had a similar behavior as a function of strain as TMF-OP but with one order of magnitude shorter lifetime. A reduction of the strain rate of the LCF test (LCF-slow, $5 \cdot 10^{-5} \text{ s}^{-1}$) dramatically decreased the lifetime of PM 2000. Furthermore, the resulting lifetime reduction increased with increasing strain range. Thus, the tests that contained the most creep during the tensile part of the cycle (TMF-IP and LCF-slow) resulted in shorter lifetimes than for TMF-OP and normal LCF.

In Fig. 9, the results for some specimens taken from the plate along the secondary rolling direction are displayed. The order between the different tests regarding the lifetime is kept, that is in increasing life order LCF-slow, TMF-IP, and LCF. However, the overall lifetimes of all these specimens are around one order of magnitude or more shorter than for the specimens taken from the main rolling direction.

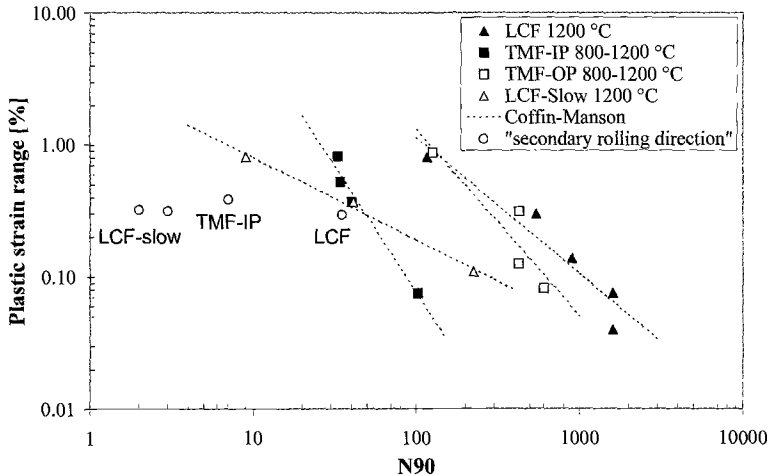


FIG. 9—Plastic strain range versus number of cycles to 10 % load reduction for PM 2000.

Conclusions

Low cycle fatigue and thermomechanical fatigue tests for an austenitic stainless steel 253 MA and a ferritic oxide dispersion strengthened alloy PM2000 have been used to enable comparison with model results for the deformation and failure life.

Hysteresis loops from low cycle fatigue, thermomechanical fatigue both in-phase and out-of-phase, have successfully been modelled. The model includes contributions from elastic deformation, plastic deformation, creep deformation from both transient (primary) and stationary creep, as well as contributions from the Bauschinger effect. All of these five processes were needed to make a successful model for the 253 MA loops, while plastic and Bauschinger contributions were insignificant while modelling the PM2000 loops.

By integrating the fatigue and creep damage around the hysteresis loops, cyclic lives of 253 MA as well as maximum load-time curves were derived.

Acknowledgments

This work was financed by Consortium for Materials Science in Thermal Energy Processes (KME) and the member companies; Alstom Power Sweden, AvestaPolarit, CSM Materialteknik, Birka Service, Sycon, Vattenfall and Volvo Aero Corporation. Their support is gratefully acknowledged.

References

- [1] Lundberg, L. and Sandström, R., "Application of Low-Cycle Fatigue Data to Thermal Fatigue Cracking," *Scandinavian Journal of Metallurgy*, Vol. 11, No. 2, 1982, pp. 85–104.
- [2] Halford, G. R., "Evolution of Creep–Fatigue Life Prediction Models," *Creep-Fatigue Interaction at High Temperature*, ASME AD-Vol. 21, ASME, NY, 1991, pp. 43–57.
- [3] Sandström, R., Österberg, J.-O., and Nylén, M., "Deformation Behaviour During Low Cycle Fatigue testing of 60 Sn – 40 Pb Solder," *Materials Science and Technology*, Vol. 9, 1993, pp. 811–819.
- [4] Mecking, H. and Kocks, U. F., "Kinetics of Flow and Strain Hardening," *Acta Metallurgica*. Vol. 29, No. 11, 1981, pp. 1865–1875.
- [5] Wu, R., Sandström, R., and Storesund, J., "Creep Strain Behaviour in a 12% CrMoV Steel," *Materials at High Temperatures*, UK, Vol. 12, 1994, pp. 277–283.
- [6] Sandström, R. and Kondyr, A., "A Model for Tertiary Creep in Mo- and CrMo-steels," *3rd International Conference on Mechanical Behaviour of Materials*, Cambridge, 1979.
- [7] Sandström, R. and Kondyr, A., "Creep Deformation, Creep Damage And Prediction of Residual Life for Three Mo- and Crmo-Steels," *VGB Kraftwerkstechnik*, Vol. 62, 1982, pp. 802–813 (in German).
- [8] Prager, M., "Development of the MPC Omega Method for Life Assessment in the Creep Range," *Journal of Pressure Vessel Technology, Transactions of the ASME*, Vol. 117, No. 2, 1995, pp. 95–103.
- [9] Sandström, R., Engström, J., Nilsson, J.-O., and Nordgren, A., "Elevated Temperature Low Cycle Fatigue of the Austenitic Stainless Steels Type 316 and 253 MA—Influence of Microstructure and Damage Mechanisms," *Swedish Institute for Metals Research Technical Report*, IM-2093, Drottning Kristinas v 48, S-114 23 Stockholm, Sweden, 1986.
- [10] Sandström, R., "Modelling of Creep Damage Development in Ferritic Steels," *Baltica IV, Int. conf. on plant maintenance for managing life & performance*, VTT, Helsinki, 1998, pp. 587–597.
- [11] Cocks, A. C. F. and Ashby, M. F., "Intergranular Fracture During Power-law Creep under Multiaxial Stresses," *Metals Science*, Vol. 14, 1980, pp. 395–402.
- [12] Wu, R. and Sandström, R., "Strain Dependence of Creep Cavity Nucleation in Low Alloy and 12% Cr Steels," *Materials Science and Technology*, Vol. 12, 1996, pp. 405–415.
- [13] McLean, D. and Pineau, A., "Grain-boundary Sliding as a Correlating Concept for Fatigue Hold-times," *Metals Science*, Vol. 12, No. 7, 1978, pp. 313–316.
- [14] Baudry, G., McLean, D., and Pineau, A., "Estimating the Reversibility of Plastic Strain During Fatigue with the Martensitic Transformation," *Scripta Metallurgica*, Vol. 11, No. 11, 1977, pp. 987–989.
- [15] Debord, D., Lofri, A., Lindé, L., and Sandström, R., "Low Cycle Fatigue and Thermo-mechanical Fatigue of the Ferritic ODS Fe-Cr-Al Alloy PM2000," *Swedish Institute for Metals Technical Report* IM-2000-027, Drottning Kristinas v 48, S-114 23 Stockholm, Sweden, 2000.

44 THERMOMECHANICAL FATIGUE BEHAVIOR OF MATERIALS

- [16] Lindé, L. and Sandström, R., "Thermal Fatigue of a Heat Resistant Austenitic Stainless Steel," *Parsons 2000, International Conference on Turbines*, Cambridge, 2000.
- [17] Jin, L.-Z. and Sandström, R., "Influence of Ageing on Low Cycle Fatigue of an Austenitic Stainless 21cr-11ni-2si Steel," to be published.
- [18] Sandström, R. and Maode, Y., "Influence of Carbon and Nitrogen Content on the Creep Properties of the Austenitic Stainless Steel 253 MA," *Scandinavian Journal of Metallurgy*, Vol. 17, 1988, pp. 156–167.

Cyclic Behavior of Al319-T7B Under Isothermal and Non-Isothermal Conditions

REFERENCE: Engler-Pinto, C. C., Jr., Sehitoglu, H., and Maier, H. J., "Cyclic Behavior of Al319-T7B Under Isothermal and Non-Isothermal Conditions," *Thermomechanical Fatigue Behavior of Materials: 4th Volume, ASTM STP 1428*, M. A. McGaw, S. Kalluri, J. Bressers, and S. D. Peteves, Eds., ASTM International, West Conshohocken, PA, Online, Available: www.astm.org/STP/1428/1428_10583, 31 March 2003.

ABSTRACT: The use of cast aluminum alloys for automotive components has greatly increased in the past two decades due mainly to the lower density and increased thermal conductivity of aluminum alloys as compared with cast iron. A unified constitutive model is developed for the aluminum alloy Al319 under T7B thermal treatment. The model is based on two state variables: the drag stress and the back stress. The constants for the model were determined systematically from isothermal experiments and the capabilities of the constitutive model were checked by comparing the simulations with isothermal and thermo-mechanical experiments. The results show that the model provides successful simulations for the material response over a broad range of temperatures and strain rates, including cyclic softening and thermal recovery.

KEYWORDS: cast aluminum alloy, thermo-mechanical fatigue, high temperature, constitutive modeling, cyclic behavior, stress-strain response

Introduction

The pursuit for higher efficiency in the automotive industry has caused an increase in the operation temperature of several engine components. The temperature of automotive cylinder heads in recent engines can reach peaks well above 200°C [1]. The use of cast aluminum alloys to replace cast iron for these components has become a reality and it is necessary to understand the behavior of these aluminum alloys under high temperature loading conditions. Although some studies have been performed on the physical metallurgy and processing of cast aluminum alloys [2–10], the description of the mechanical behavior of these materials at high temperatures is not well established.

A correct description of the stress-strain response at high temperatures is a prerequisite for any durability modeling at high temperatures. The stress-strain descriptions adopted for room temperature studies are obviously not capable of handling the creep-plasticity interactions and time or temperature dependent material changes at high temperatures.

The objective of this study is to develop a model to predict the stress-strain behavior over a broad range of temperatures. The availability of such a model is very important to reduce product development time and cost, especially during the design

¹ Technical Specialist, Materials Science Department, Ford Research Laboratory, Dearborn, MI 48121.

² Professor, Department of Industrial & Mechanical Engineering, University of Illinois, Urbana, IL 61801.

³ Professor, Lehrstuhl für Werkstoffkunde, Universität Paderborn, D-33095 Paderborn, Germany.

stage, because of the complexity of the thermo-mechanical loading that is present in engine blocks and heads.

The developed model predicts the stress response as a function of the applied strain, temperature, and strain rate (frequency). It can predict stress relaxation, creep, ratcheting under mean stress, and recovery effects at high temperatures. A systematic non-iterative method for determining the material constants from isothermal constant strain rate tests has been established and is described in details in this paper.

Material and Experimental Procedures

The alloy investigated presents an Al-Si-Cu microstructure and the nominal chemical composition is given in Table 1. It consists of a precipitate hardenable alloy, where the primary strengthening phase is Al_2Cu . The alloy is submitted to the T7B heat treatment (solutionizing at 495°C for 8 h followed by precipitating at 260°C for 4 h) before testing. This treatment produces an overaged microstructure that aims to confer thermal stability to the component. The tensile properties obtained at room temperature after the T7B treatment are given in Table 2.

TABLE 1—*Nominal composition of Al319-T7B in weight percent.*

Al	Si	Cu	Mg	Fe	Mn	Sr	Ti
Bal.	7.35	3.32	0.22	0.78	0.24	0.03	0.13

TABLE 2—*Room temperature properties of Al319-T7B.*

Yield Strength (at 0.2%)	Ultimate Strength	Elongation
198 MPa	284 MPa	2.5%

This alloy is a secondary alloy (obtained by the re-melting of aluminum alloys), which presents a higher iron (Fe) content as compared to a previously investigated alloy [1]. Iron is an undesirable impurity, which decreases the feeding ability of the metal during casting and can reduce the ductility and toughness through the formation of brittle intermetallics.

The samples were prepared from a sand-cast wedge with a copper chill positioned at the apex of the wedge. The wedge geometry results in different solidification rates, based upon a similar principle of the varied-cooling rate castings used in an earlier work [11]. This solidification control permits the machining of samples with controlled secondary dendrite arm spacing (SDAS) sizes. All samples used in the present investigation were taken from the region where the SDAS is between 15–30 μm . The samples were machined with a diameter of 7.6 mm and a gage length of 25.4 mm. All samples were polished longitudinally up to a 1200 sand paper prior to testing.

The tests were performed at the High Temperature Materials Laboratory at the University of Illinois using a computer-controlled servo hydraulic testing machine in conjunction with a 15 kW induction heater. An optical pyrometer focused on the gage

length of the specimen provided input to the temperature controller, which received a command signal from the computer. The temperature gradient over the gage length was minimized by the use of optimized induction coil geometry. The total strain was measured over the gage length with a high temperature axial extensometer utilizing quartz rods. Strain, force, and temperature were continuously acquired and stored by the computer.

All isothermal and thermo-mechanical fatigue (TMF) experiments were conducted in total strain control with a constant total strain rate. For the TMF tests, the strain and temperature waveforms followed a triangular wave shape.

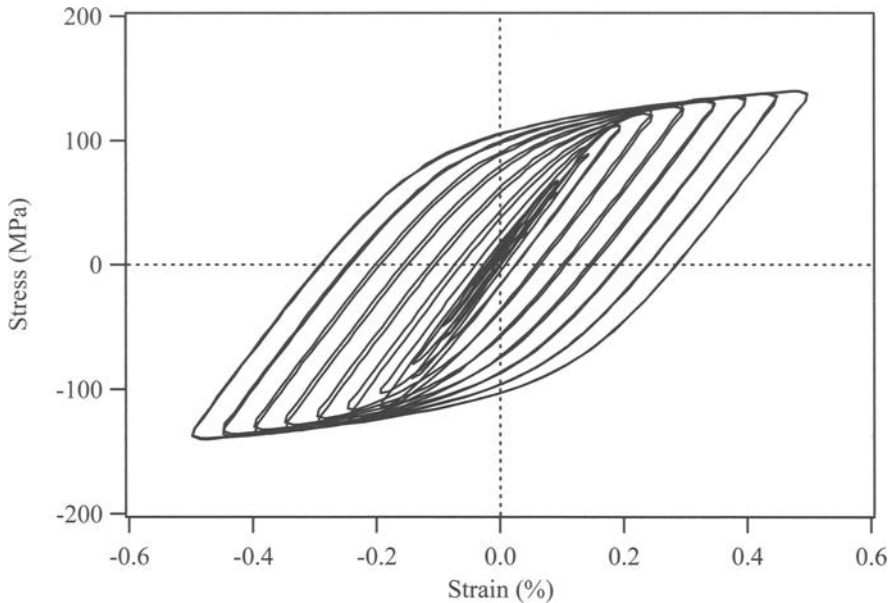


FIG. 1—Incremental hysteresis loops obtained at 250°C for $\dot{\epsilon} = 5 \times 10^{-3} \text{ s}^{-1}$.

Isothermal fatigue experiments at the following temperatures were performed: 20°C, 130°C, 250°C, and 300°C. All high temperature tests were performed under four different strain rates: $5 \times 10^{-3} \text{ s}^{-1}$, $5 \times 10^{-4} \text{ s}^{-1}$, $5 \times 10^{-5} \text{ s}^{-1}$, and $5 \times 10^{-6} \text{ s}^{-1}$. These tests were performed in an incremental manner, where the strain range increased gradually until it reached 1.0%. This experimental technique allows the determination of the stress-strain behavior for different strain ranges with a single specimen per temperature level, as showed in Fig. 1.

Some selected tests were performed on samples previously exposed to 300°C for 1, 10, and 100 h. These tests were used to determine evolution of the material strength with time and temperature. Some other tests were performed up to the fracture of the specimens. These tests were used for the determination of modification on the materials properties under cyclic loading. All these tests and results are described in more details later in this paper.

Out-of-phase and in-phase thermo-mechanical fatigue experiments were conducted to verify the validity of the constitutive model. It is important to emphasize that these TMF tests were not used for the determination of the constants of the model. These TMF experiments were performed between 100–300°C under fully reversed mechanical strain ranges.

The Unified Constitutive Model

A unified model originally proposed by Slavik and Sehitoglu [12–14] has been modified to describe the stress-strain behavior of the Al319-T7B alloy. In the unified theory, the creep and plastic strains are combined as inelastic strain and the concept of yield surface is replaced by a stress surface. Inelastic flow can occur either inside (creep regime) or outside (plasticity regime) the stress surface. This model utilizes two state variables to describe the stress surface: the *back stress* and the *drag stress*. The back stress describes the directional pile-up at precipitates, grain boundaries, and other obstacles, while the drag stress characterizes the material strength due to the number of blocked dislocations and depends on the dislocations arrangement. In other words, the back stress, a tensorial value, indicates the position of the center of the stress surface, while the drag stress, a scalar value, represents the size (radius) of the stress surface.

The basic assumption of the model is that the inelastic strain rate is determined by the current internal stress state and by the values of the two state variables. The expression below, known as the *flow rule*, describes this relation:

$$\dot{\varepsilon}_{ij}^{in} = \frac{3}{2} A f \left(\frac{\bar{\sigma}}{K} \right) \frac{S_{ij} - S_{ij}^C}{\bar{\sigma}} \quad (1)$$

where $\dot{\varepsilon}_{ij}^{in}$ represents the inelastic strain rate, K is the drag stress, S_{ij}^C is the deviatoric back stress, S_{ij} is the deviatoric stress, and $\bar{\sigma}$ is the effective stress defined as $\bar{\sigma} = \left[\frac{3}{2} (S_{ij} - S_{ij}^C)(S_{ij} - S_{ij}^C) \right]^{1/2}$. The term $S_{ij} - S_{ij}^C$ describes the direction of inelastic strain rate. The term A is a function of temperature and can be expressed as follows:

$$A = A_c \exp \left[-\frac{\Delta H}{R(T + 273)} \right] \quad (2)$$

where ΔH is the thermal activation energy, R is the universal gas constant, and the coefficient A_c is a material constant.

The term $f \left(\frac{\bar{\sigma}}{K} \right)$ from Eq 1 is a scalar function described by a different expression depending on the predominant deformation mechanism operative at a given stress state and temperature. If the stress state is located inside the stress surface ($\bar{\sigma}/K < 1$), the inelastic strain rates are smaller and the deformation is mainly time dependent, as typically observed in creep deformation. On the other hand, outside the stress surface ($\bar{\sigma}/K \geq 1$), the material behavior is essentially rate insensitive and plasticity deformation

mechanisms are predominant. These assumptions are introduced into the flow rule by the expressions below:

$$f\left(\frac{\bar{\sigma}}{K}\right) = \begin{cases} \left(\frac{\bar{\sigma}}{K}\right)^{n_1} & \text{for } \left(\frac{\bar{\sigma}}{K}\right) < 1 \\ \exp\left[\left(\frac{\bar{\sigma}}{K}\right)^{n_2} - 1\right] & \text{for } \left(\frac{\bar{\sigma}}{K}\right) \geq 1 \end{cases} \quad (3)$$

Equations 1–3 establish the flow rule completely. It is now necessary to determine how the two state variables utilized in this model, the back stress and the drag stress, evolve with time, temperature and number of cycles. The model assumes that both state variables evolve throughout the deformation history in a recovery-hardening format as:

$$\dot{S}_{ij}^C = \frac{2}{3} h_\alpha(\bar{\alpha}, T) \dot{\varepsilon}_{ij}^{in} - \left[r_\alpha^D(\bar{\alpha}, \dot{\varepsilon}_{ij}^{in}, T) + r_\alpha^S(\bar{\alpha}, T) \right] S_{ij}^C \quad (4)$$

$$\dot{K} = h_K(K, T) - r_K(K, T) + \theta(K, T) \dot{T} \quad (5)$$

where \dot{S}_{ij}^C is the deviatoric back stress rate, \dot{K} is the drag stress rate, the term $\bar{\alpha}$ is the effective back stress defined as $\bar{\alpha} = \sqrt{\frac{3}{2} S_{ij}^C S_{ij}^C}$, the term θ represents the variation of K_0 (initial value of drag stress) with temperature T as $\theta = \frac{\partial K_0}{\partial T}$, \dot{T} is the temperature variation rate, h_α and h_K are the hardening functions, r_α^D and r_α^S are the dynamic and static recovery functions, respectively, for the back stress, and r_K is the recovery function for the drag stress. The expressions for each of these functions must be appropriately chosen to fit the observed mechanical behavior for each particular alloy system.

Determination of the Constants for the Model

The Flow Rule

As stated before, the flow rule describes the inelastic strain rate as a function of the material internal stress state and temperature. It reflects different deformation mechanisms that lead to different strain rate sensitivity regimes. Therefore, to determine the flow rule, isothermal fatigue experiments at different temperatures and strain rates are needed. The uniaxial incremental fatigue tests results were used for this purpose. From these experiments, the initial yield strength (σ_y) at a very small strain offset (0.005%) was determined. This offset was intentionally chosen as very small to neglect the variation of the back stress ($S_{ij}^C \approx 0$), thus reducing the flow rule at that point to:

$$\frac{\dot{\varepsilon}^{in}}{A} = \begin{cases} \left(\frac{\sigma_y}{K_0}\right)^{n_1} & \text{for } \left(\frac{\sigma}{K}\right) < 1 \\ \exp\left[\left(\frac{\sigma_y}{K_0}\right)^{n_2} - 1\right] & \text{for } \left(\frac{\sigma}{K}\right) \geq 1 \end{cases} \quad (6)$$

The inelastic strain can be calculated from the expression below:

$$\varepsilon^{in} = \varepsilon^{mech} - \frac{\sigma}{E(T)} \quad (7)$$

where $E(T)$ is the modulus of elasticity as a function of temperature, σ is the current uniaxial stress, and ε^{mech} is the mechanical strain. The inelastic strain rate, $\dot{\varepsilon}^{in}$, is then determined by the numerically derivative of the inelastic strain versus time at $\varepsilon^{in} = 0.005\%$. The experimental yield strength versus inelastic strain rate for all test conditions is shown in Fig. 2.

To fit the flow rule to those experimental points, we first need to establish the equation for the variation of the modulus of elasticity as a function of temperature, which for this material is given by:

$$E = 78500 - 50 T \quad (8)$$

where the units for E and T are MPa and $^{\circ}\text{C}$, respectively.

The initial drag stress as a function of temperature, $K_0(T)$, can then be determined assuming that $K_0/E(T) = \text{constant}$ [13,14]. Therefore, knowing that the drag stress defines the transition from the creep deformation regime to the plasticity regime, we now need to find this transition point for a given temperature. Based on the graph showed on Fig. 2, the transition point could be determined at 250°C as $K_0 = \sigma_y = 65$ MPa and $\dot{\varepsilon}^{in} = 1 \times 10^{-5} \text{ s}^{-1}$. The expression for $K_0(T)$ is therefore given by:

$$K_0(T) = \frac{K_0^{250}}{E^{250}} \cdot E(T) = 77.31 - 0.0492 T \quad (9)$$

Furthermore, when $\sigma_y = K_0$, it comes from Eq 6 that $\dot{\varepsilon}^{in}/A = 1 \Rightarrow A^{250} = 1 \times 10^{-5} \text{ s}^{-1}$, which allows us to determine the constant A_c from Eq 2 as being:

$$A_c = \frac{A^{250}}{\exp\left(\frac{\Delta H_c}{R(250 + 273)}\right)} = 1.87 \times 10^{18} \text{ s}^{-1} \quad (10)$$

where $\Delta H_c = 2.33 \times 10^5 \text{ J/mol}$ and $R = 8.3143 \text{ J/mol}\cdot^{\circ}\text{C}$. Finally, the coefficients $n_1 = 8.5$ and $n_2 = 26$ could be determined by curve fitting Eq 6 for both creep and plasticity regimes, resulting in the final flow rule, shown in its normalized form on Fig. 3.

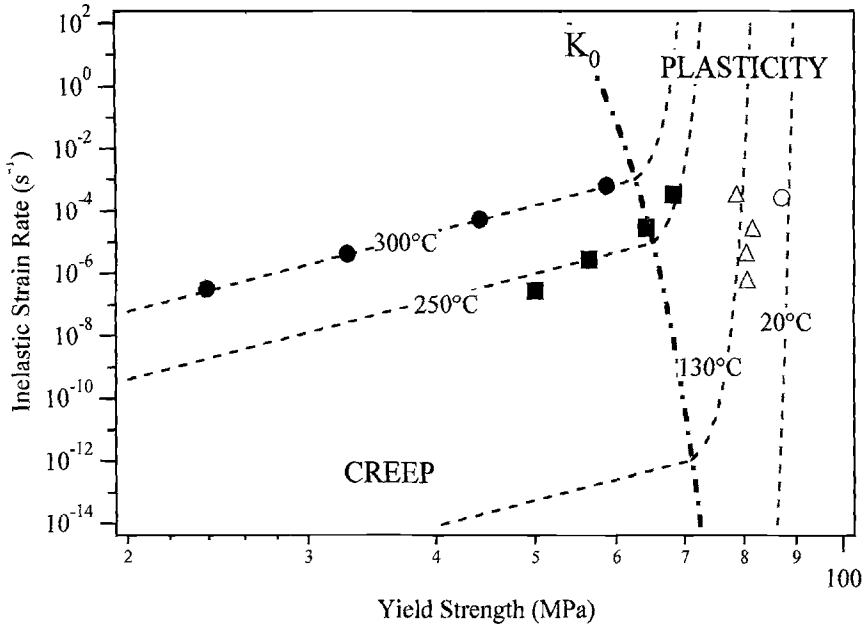


FIG. 2—Determination of the flow rule for the Al319-T7B alloy with small SDAS.

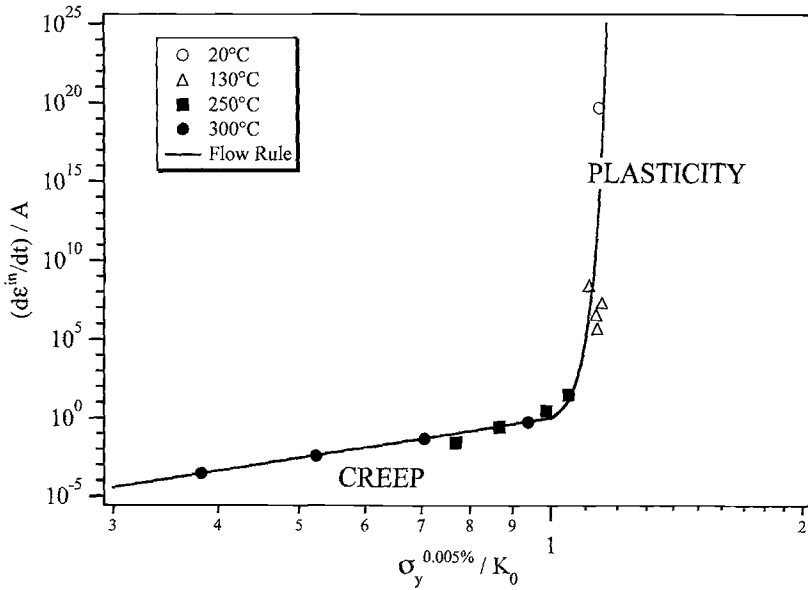


FIG. 3—The normalized flow rule for the Al319-T7B alloy with small SDAS.

The Evolution of the Back Stress

From unidirectional loading, the effective back stress, $\bar{\alpha}$, can be measured approximately as the current stress minus the material yield stress, $\sigma - \sigma_y$. The determination of the back stress hardening term, h_α , can be achieved using the tests performed with the highest strain rate used, $5 \times 10^{-3} \text{ s}^{-1}$, assuming that the recovery is negligible at this condition. In this case, Eq 4 is reduced to the following expression for uniaxial loading under constant temperature:

$$\dot{\alpha} = h_\alpha(\bar{\alpha})\dot{\varepsilon}_{ij}^{in} \quad (11)$$

The expression above can be rearranged to show that $h_\alpha = \frac{\partial \alpha}{\partial \varepsilon^{in}}$. The loading part of the first stress-inelastic strain loop at $\Delta \varepsilon^{mech} = 1.0\%$ was used to determine the back stress hardening coefficients. Figure 4 plots the numerical derivative $\frac{\partial \alpha}{\partial \varepsilon^{in}}$ versus α for the room temperature test. It can be noted that the exponential equation below fits very well the observed behavior:

$$h_\alpha(\bar{\alpha}) = \begin{cases} a_1 \exp\{-[a_2(\alpha_0 + \bar{\alpha})]^{a_3}\} & \text{if } \varepsilon^{in} \cdot \alpha \geq 0 \\ a_1 \exp\{-[a_2(\alpha_0 - \bar{\alpha})]^{a_3}\} & \text{if } \varepsilon^{in} \cdot \alpha \leq 0 \\ a_1 & \text{if } \varepsilon^{in} \cdot \alpha \leq 0 \text{ and } \bar{\alpha} \geq \alpha_0 \end{cases} \quad (12)$$

where the coefficients a_1 , a_2 , and a_3 are functions of temperature while the constant α_0 represents the maximum expected value for the back stress at the lowest operating temperature. The value adopted for α_0 is 180 MPa and the following set of equations could represent well the variation of the coefficients a_1 , a_2 , and a_3 with temperature:

$$\begin{aligned} a_1 &= 5.45 \times 10^5 \exp[3.074 \times 10^{-13} (T + 273)^{4.65}] \\ a_2 &= 0.010 \\ a_3 &= 0.9741 \exp[1.466 \times 10^{-11} (T + 273)^{3.928}] \end{aligned} \quad (13)$$

The back stress recovery terms can be determined at high temperature from experiments performed with slower strain rates. Based on experimental evidence, it is assumed that the static recovery term of the back stress is small, $r_\alpha^S(\bar{\alpha}, T) \approx 0$, and dynamic recovery from r_α^D to be dominant. For the uniaxial case, Eq 4 can be written as follows:

$$\dot{\alpha} = h_\alpha(\bar{\alpha}, T)\dot{\varepsilon}^{in} - r_\alpha^D(\bar{\alpha}, \dot{\varepsilon}^{in}, T)\alpha\dot{\varepsilon}^{in} \quad (14)$$

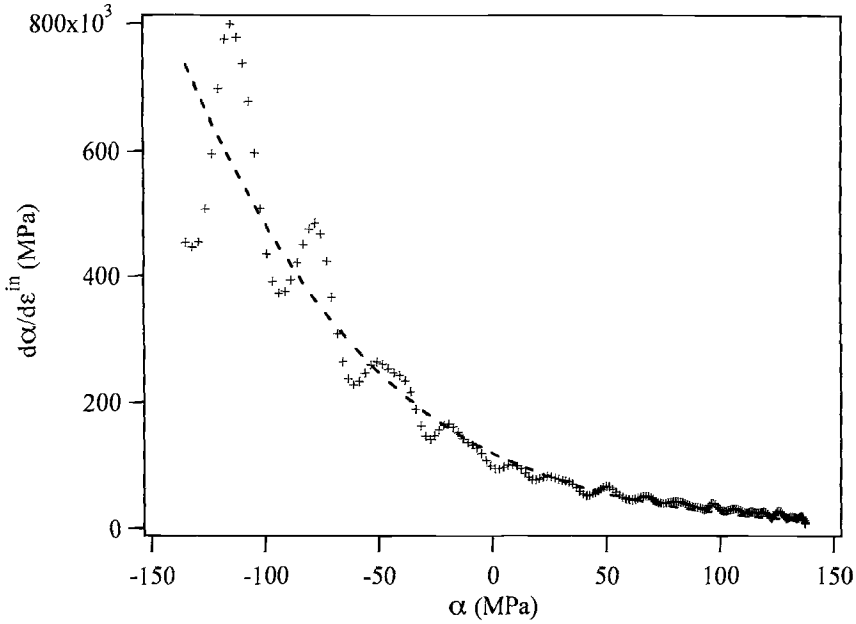


FIG. 4—Determination of the back stress hardening function at room temperature.

Then, for $\dot{\epsilon}^{in} \geq 0$:

$$r_{\alpha}^D(\bar{\alpha}, \dot{\epsilon}^{in}, T) = \frac{\left[h_{\alpha}(\bar{\alpha}, T) - \frac{d\alpha}{d\epsilon^{in}} \right]}{\alpha} \quad (15)$$

where $h_{\alpha}(\bar{\alpha}, T)$ is obtained from Eq 12 and $\frac{d\alpha}{d\epsilon^{in}}$ is the slope of the back stress versus inelastic strain curve for the tests where recovery exist. Figure 5 shows the effect of the strain rate on the $\frac{d\alpha}{d\epsilon^{in}}$ versus α curve for the tests performed at 250°C. The analysis of the results reveals that the back stress recovery term r_{α}^D can be expressed as a function of the effective back stress $\bar{\alpha}$ and the inelastic strain rate $\dot{\epsilon}^{in}$ as:

$$r_{\alpha}^D = C(\bar{\alpha})^d (\dot{\epsilon}^{in})^e \quad (16)$$

where the coefficients d and e were determined from the 250°C tests as being -0.5 and -0.24 , respectively. The influence of temperature is accounted for by the coefficient C , which follows an exponential expression given by:

$$C = 180.8 \exp[-1.546 \times 10^{-51} (T + 273)^{18.49}] \quad (17)$$

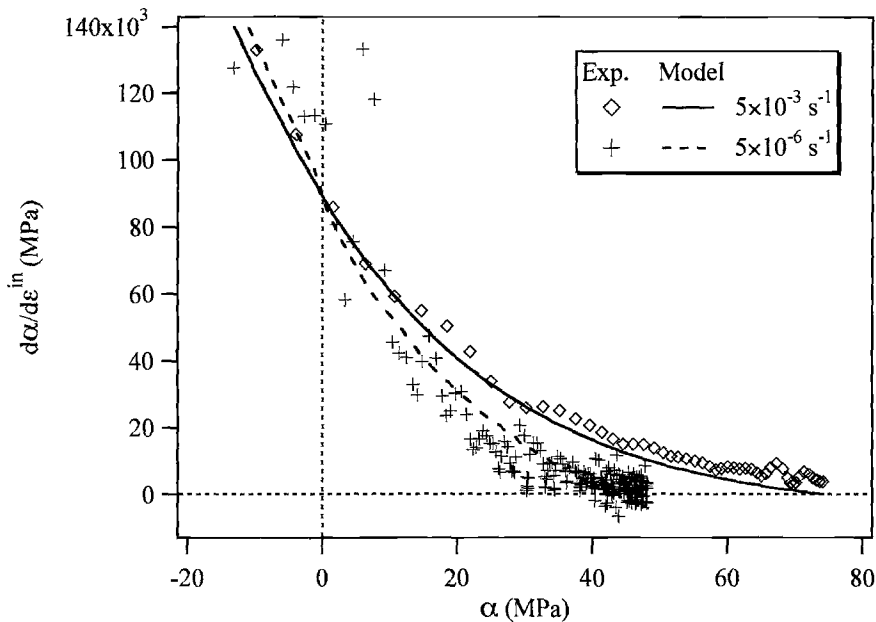


FIG. 5—Determination of the back stress recovery function at 250°C.

The Evolution of the Drag Stress

The initial drag stress, K_0 , was determined as described earlier. The evolution of the drag stress within the fatigue cycles is a consequence of the modifications on the microstructure due to alternating inelastic deformation (cyclic hardening or softening) and to high temperature exposure (thermal recovery).

The last item in Eq 5 accounts for the effect of changing temperature on the initial drag stress, $\theta = \frac{\partial K_0}{\partial T}$. The value for θ is obtained directly by derivating Eq 9, which gives $\theta = -0.0492 \text{ MPa}/^\circ\text{C}$.

The hardening function of drag stress, h_K , is determined by examining the cyclic material response, which can produce cyclic hardening or softening to the stable state. It can be expressed as:

$$h_K(K, T) = B_H (K_{sat} - K) \dot{\epsilon}^{in} \tag{18}$$

where B_H is the drag stress hardening rate coefficient, K_{sat} is the drag stress at the saturated state, and $\dot{\epsilon}^{in}$ is the effective inelastic strain rate.

To determine the constants above, a test at high temperature and high strain rate is needed, assuming that there is no thermal recovery for this test ($r_K = 0$). The test performed at 250°C/0.5 Hz with 0.5% strain range was chosen. The yield stress range

($2\sigma_y$, defined for an inelastic strain offset of 0.010%) was determined for every cycle up to the saturated cycle. The value of K for every cycle can be calculated by inverting Eq 1.

The saturated drag stress for this temperature is then obtained from the saturated hysteresis loop, $K_{sat} = 47$ MPa. The value of K_{sat} for all other temperatures is determined by assuming a linear variation of K_{sat} with temperature and no hardening at room temperature ($K_{sat} = K_0$):

$$K_{sat} = 78.88 - 0.128 T \quad (19)$$

The hardening rate B_H can be obtained from the slope of the plot of $\ln|K_{sat} - K|$ versus the cumulative inelastic strain. As shown in Fig. 6, $B_H = 0.3428$ MPa/s. Previous investigation on a similar alloy indicates that B_H is approximately independent of temperature [1].

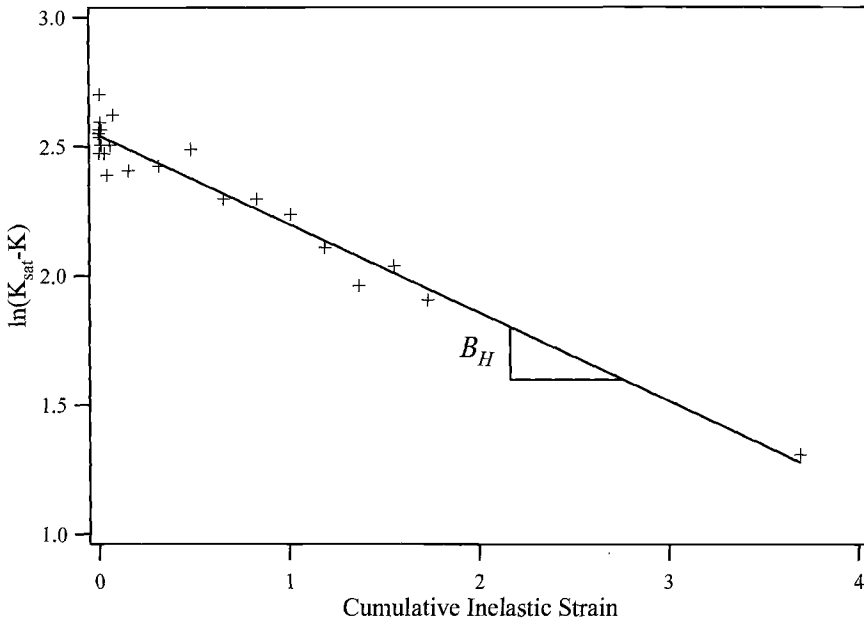


FIG. 6—Determination of the drag stress hardening coefficient.

The recovery term r_K is given by:

$$r_K(K, T) = B_R (K - K_{rec}) \quad (20)$$

where B_R is the drag stress recovery rate coefficient and K_{rec} is the fully recovered value of drag stress for a given temperature.

In order to determine B_R and $K_{rec}(T)$, three specimens were pre-exposed to 300°C for 1 h, 10 h, and 100 h, respectively. These specimens were then tested at room temperature and the results compared with the hysteresis obtained from the virgin (as

heat-treated) material. It was observed that exposing the material to high temperature greatly decreases its yield strength. Using the same procedure described before for the evaluation of the drag stress-hardening rate, the value of the drag stress for each of those recovered samples could be determined. The drag stress recovery is plotted as a function of the exposure time at 300°C on Fig. 7, together with the predicted recovery by the developed constitutive model.

Assuming that the value of the drag stress after 100 h at 300°C corresponds approximately to the fully recovered value and adopting a linear variation of K_{rec} with temperature, the expression for $K_{rec}(T)$ could be determined, which is given below (assuming that $K_{rec} = K_0$ at room temperature):

$$K_{rec} = 81.00 - 0.234 T \quad (21)$$

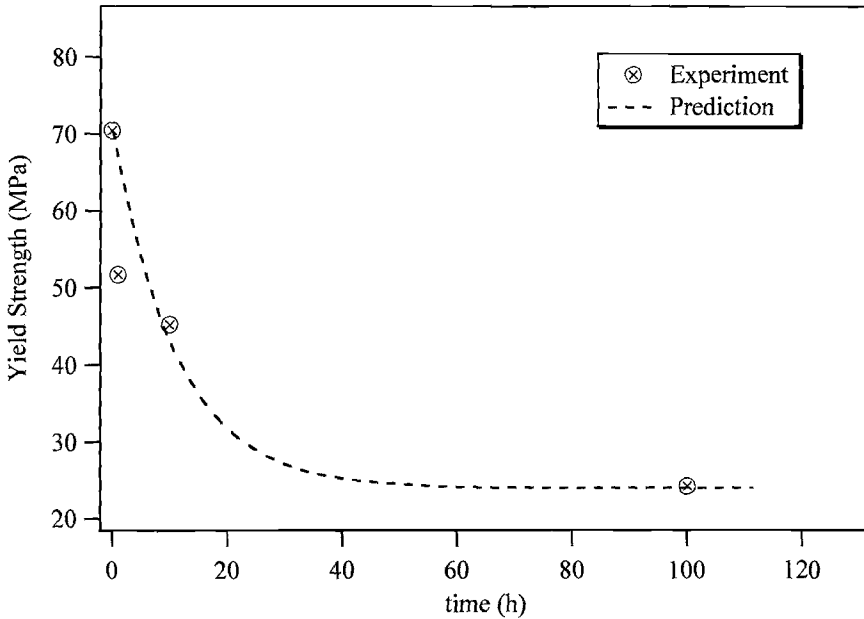


FIG. 7—Drag stress recovery due to thermal exposure at 300°C.

The drag stress recovery coefficient can then be determined from the plot of $(K - K_{rec})$ vs. thermal exposure time, as shown on Fig. 8 ($B_R = 3.0 \times 10^{-5}$ MPa/s).

The temperature dependence of the different components of the drag stress is summarized on Fig. 9, which clearly shows a pronounced decrease on the drag stress due to either cyclic deformation or to thermal exposure. The same behavior was observed on a similar alloy due to the coarsening of the precipitates [1,15].

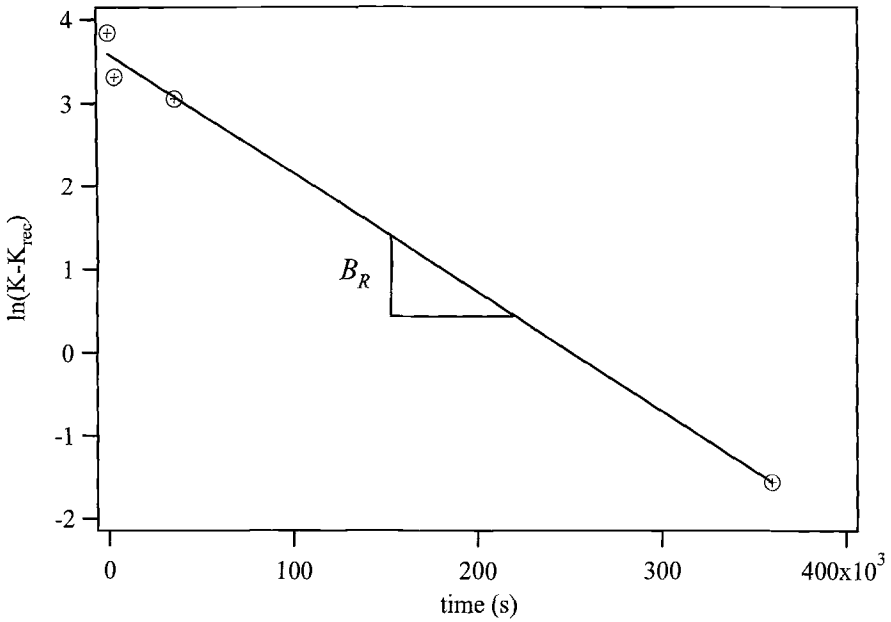


FIG. 8—Determination of the drag stress recovery coefficient.

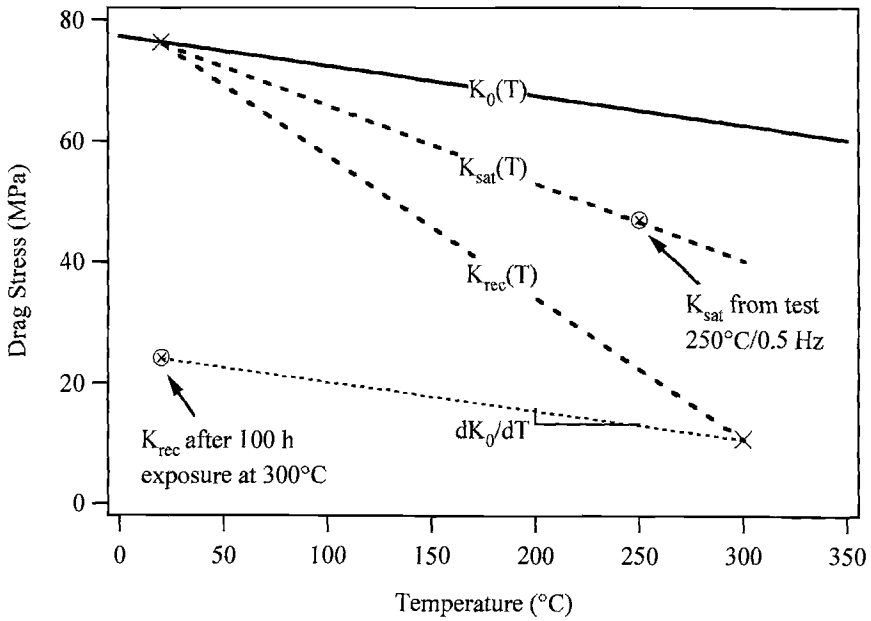


FIG. 9—Different components of drag stress as a function of temperature.

Stress-Strain Simulations

Isothermal Low-Cycle Fatigue

The capabilities of the constitutive model were first checked against critical isothermal experiments. Simulations of stress-strain response for the Al 319-T7B alloy during isothermal cycling at different temperature and high strain rate ($5 \times 10^{-3} \text{ s}^{-1}$) are shown in Fig. 10. It can be noted that the model can account for the different temperatures, predicting accurately the behavior of the alloy in the 20–300°C range. These results confirm the validity of the flow rule as well as the back stress hardening formulations used by the model. Another isothermal verification of the model is presented in Fig. 11, which shows simulations of stress-strain response for the first cycles at 250°C with different strain rate. It is observed that the model is also capable of predicting the influence of the strain rate on the behavior of this alloy. In this case, the flow rule and back stress recovery formulations are successfully validated.

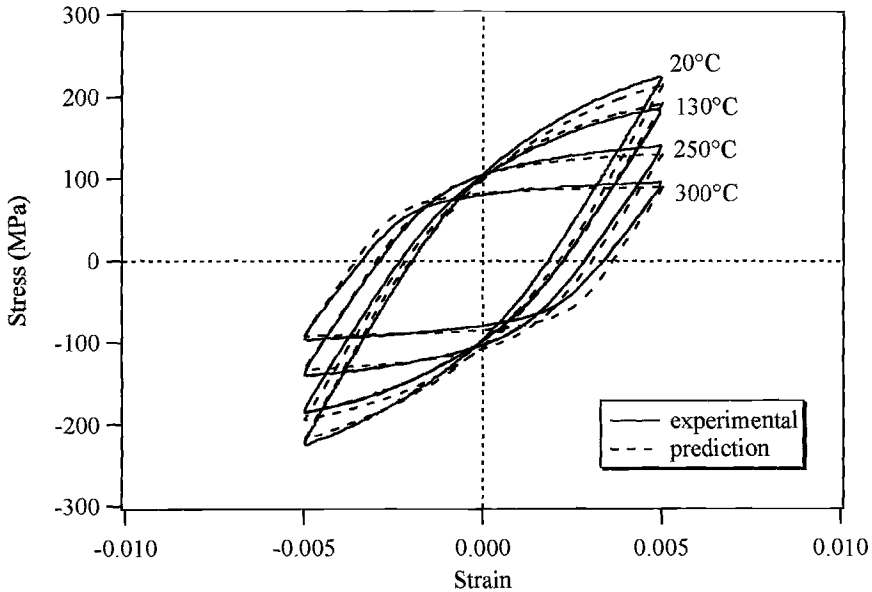


FIG. 10—*Experimental and predicted hysteresis for the tests performed at $5 \times 10^{-3} \text{ s}^{-1}$.*

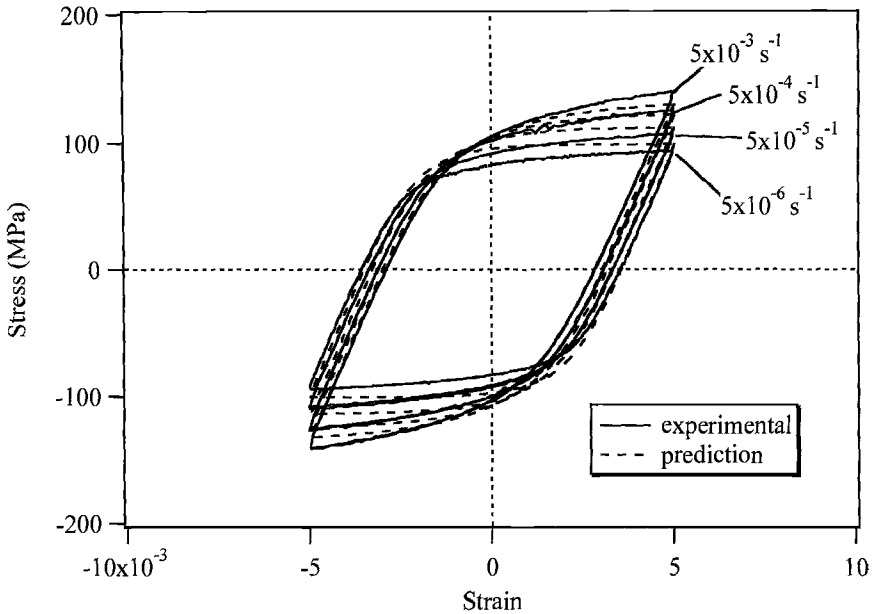


FIG. 11—Experimental and predicted hysteresis loops for the tests performed at 250°C.

Thermo-mechanical Fatigue

Out-of-phase and in-phase thermo-mechanical fatigue tests were performed until fracture for several strain ranges. The temperature variation for these tests was between 100–300°C with a constant temperature rate of 1.33°C/s, starting at the mean temperature, 200°C. In the out-of-phase testing, the specimen is first heated to 300°C while going into compression. It is then cooled to 100°C while loaded in tension. The mechanical strain rate is dependent on the applied mechanical strain range, but it varied between $1.33 \times 10^{-5} \text{ s}^{-1}$ and $5 \times 10^{-5} \text{ s}^{-1}$. The in-phase test procedure is similar, but the specimen is loaded into tension while heating and into compression while cooling.

The behavior of Al 319-T7B under thermo-mechanical fatigue can be observed in Fig. 12 for all strain ranges investigated. It can be noted that out-of-phase develops a tensile mean stress because the specimen is submitted to higher temperatures while in compression. The shape of the hysteresis is also different in the tensile and compressive part. This can be explained by the differences on the flow rule and on the back stress evolution at different temperatures. In fact, as the temperature increases, both initial drag stress and back stress hardening coefficient decrease, allowing the material to flow much easier in compression than in tension, when the temperatures are lower.

The opposite trend can be observed for in-phase testing, when a compressive mean stress is developed. It is noted, however, that this alloy behaves in a very similar manner under tension and compression at high temperature. This can be seen by inverting the hysteresis loop for the in-phase test and comparing it with the out-of-phase loop, as shown in Fig. 12a. Figure 12b compares the stress-inelastic strain hysteresis for the out-

of-phase and the inverted in-phase tests, confirming that the response of the material is practically identical in both cases.

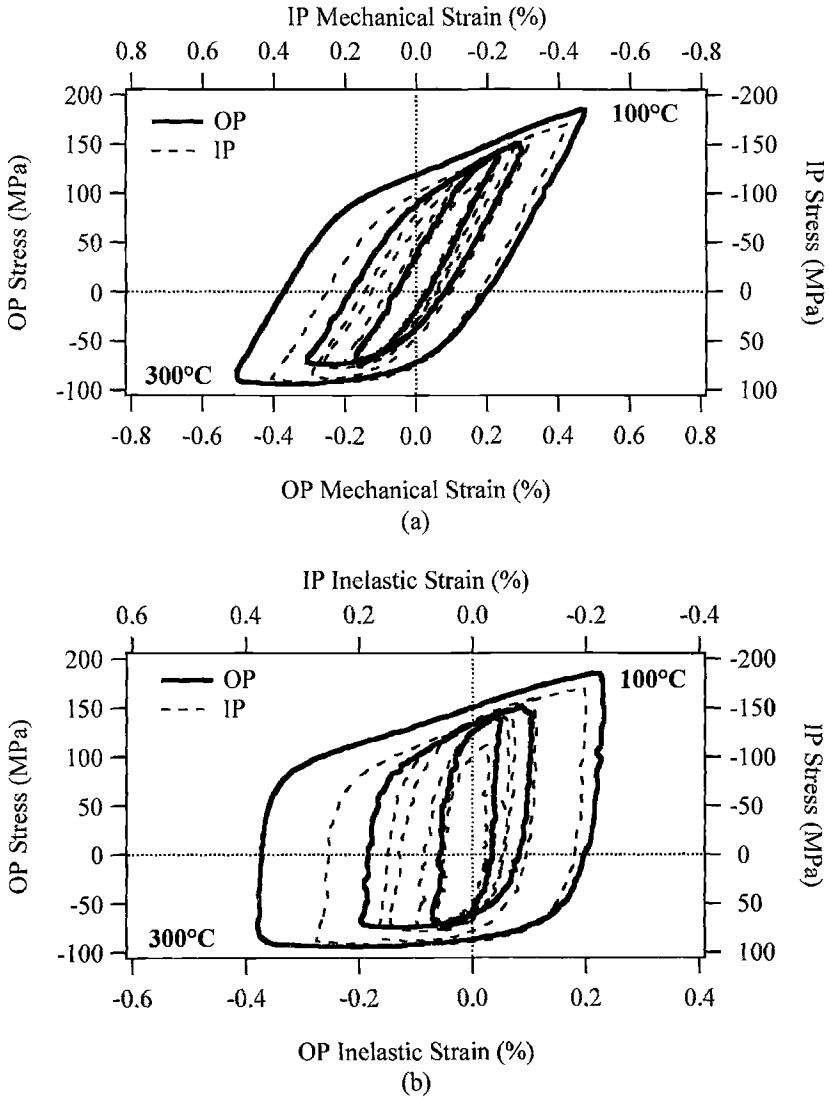


FIG. 12—Hysteresis loops obtained from out-of-phase and in-phase TMF.

A simulation of cyclic stress-strain behavior under out-of-phase TMF loading is presented in Fig. 13 for a strain range of 1.0%. It is noted that the model predicts very well not only the shape of the hysteresis, but also the evolution of the material's behavior after 300 cycles (which corresponds to 50% of the total fatigue life for this testing condition). This indicates that the constitutive model, developed exclusively from isothermal tests, is able to handle the interaction effects of simultaneously varying temperature and strain. In addition, the model also predicted successfully the evolution of the drag stress during the test, which is due to both cyclic softening and thermal recovery. This confirms the validity of the drag stress hardening and recovery formulations used by the model.

The model was also checked against a different thermo-mechanical fatigue test, which was performed at Ford Research Laboratory [16] with the same alloy. This test was performed between 50–250°C with a negative mean strain. The mechanical strain range was 1.26% and the temperature rate was 1.11°C/s. The comparison between experimental and predicted hysteresis loops for cycles 1 and 289 is presented in Fig. 14. In this case, because of the lower temperatures, the recovery of the material's properties within cycling is much less pronounced than for the 100–300°C temperature range. However, it is observed that the model can predict accurately the behavior of the alloy under these conditions as well.

Finally, to summarize all results obtained from the 100–300°C TMF tests, the stress range is plotted against the mechanical strain range on Fig. 15. The results of the isothermal tests performed at 300°C and 0.5 Hz are also plotted.

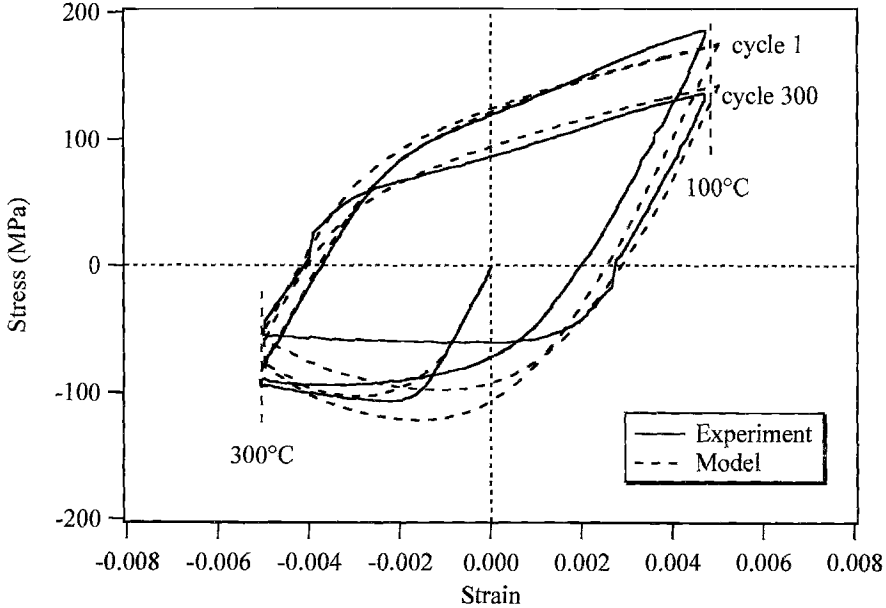


FIG. 13—Experimental and predicted hysteresis loops for the out-of-phase TMF test performed between 100–300°C with a 1.0% mechanical strain range.

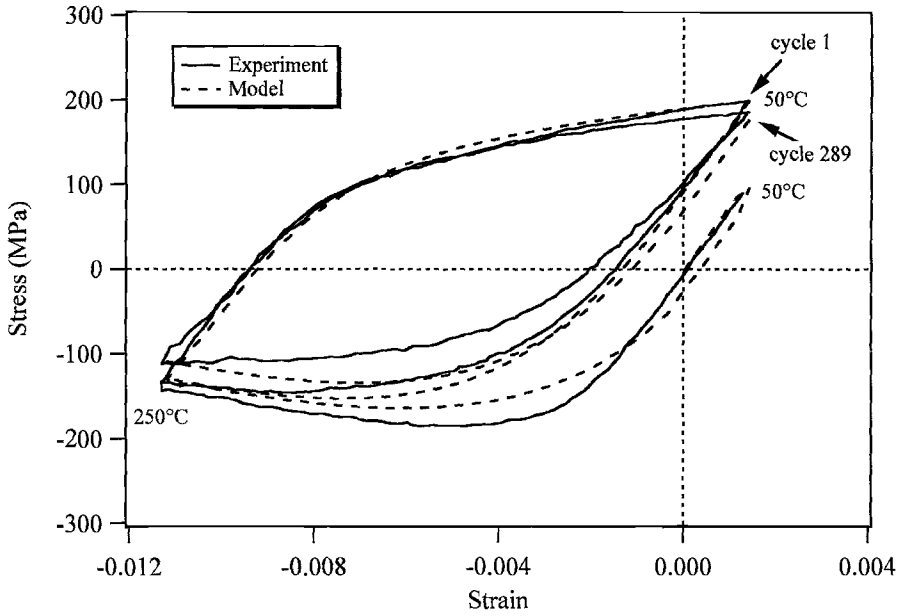


FIG. 14—Hysteresis loops for a 50–250°C out-of-phase TMF test.

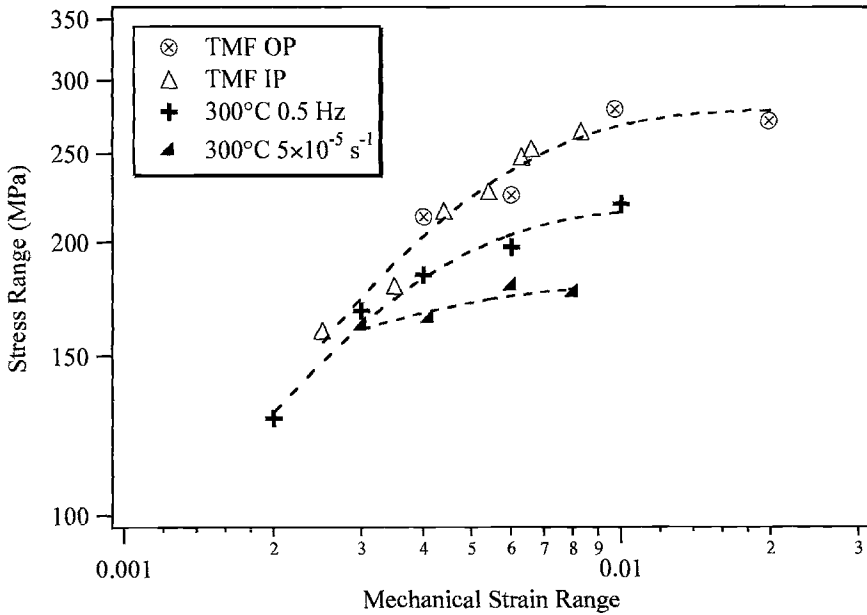


FIG. 15—Stress range of different TMF and isothermal tests as a function of $\Delta\epsilon^{mech}$

Discussion

The unified model presented in this paper is a modification of a model previously developed for other alloys [1,12–15]. It can be applied for both isothermal and thermo-mechanical loading and is able to handle creep-plasticity interactions, including strain rate effect, thermal recovery, and cyclic hardening or softening. All constants used in the model were determined exclusively from isothermal experiments performed at different temperatures and strain rates in a systematic non-iterative method, as described previously in this paper.

The temperature range investigated was between room temperature and 300°C. The material responses to both out-of-phase and in-phase loading are practically identical, demonstrating that the strain-temperature phasing does not affect the mechanical behavior of the alloy investigated.

The simulation of the 100–300°C thermo-mechanical stress-strain response for Al 319 T7B predicts accurately the behavior of the material at the lower temperature part of the cycle, while the stress response at high temperature is slightly overpredicted, as observed on Fig. 13. On the other hand, the 50–250°C simulation, presented in Fig. 14, shows a much better correlation for both high temperature (compressive) and low temperature (tensile) parts of the cycle. The inelastic strain range, however, is correctly predicted in all cases, which is very important for fatigue life modeling, as the low-cycle fatigue damage is usually associated with a high inelastic strain range.

Most of the constants used in the model are assumed to vary linearly with temperature for the complete temperature range investigated. While this assumption seems reasonable for temperatures up to 250°C, which corresponds to the maximum expected service temperature for the engine cylinder heads, this might not be true for higher temperatures. Therefore, further investigation of the material behavior above 250°C would be useful to clarify this issue and to refine the model for higher temperature applications.

Summary

A two state variables unified constitutive model is applied to describe the stress-strain response of Al 319-T7B alloy under thermo-mechanical loading. All material constants used in the model were established from isothermal experiments. The constitutive model can successfully handle different strain rates and thermo-mechanical loadings.

Acknowledgments

This work has been funded by the Ford Motor Company, which has also provided the cast alloy for the specimen preparation. The authors would like to thank Dr. John Allison, Leader of the Cast Metals Science and Technology Group at Ford Research Laboratory. Dr. Carlos Engler-Pinto was partially supported by grant 99/01540-0 from the Brazilian Institution FAPESP — Fundação de Amparo à Pesquisa do Estado de São Paulo.

References

- [1] Smith, T. J., Maier, H. J., Sehitoglu, S., Fleury, E., and Allison, J., "Modeling High-Temperature Stress-Strain Behavior of Cast Aluminum Alloys," *Metallurgical and Materials Transactions A*, Vol. 30A, January 1999, pp. 133–146.
- [2] Vorren, O., Evensen, J. E., and Pedersen, T. B., "Microstructure and Mechanical Properties of AlSi(Mg) Casting Alloys," *AFS Transactions*, Vol. 92, 1984, pp. 459–466.
- [3] Wickberg, A., Gustafson, G., and Larson, L. E., "Microstructural Effects on the Fatigue Properties of a Cast AlSiMg Alloy," *SAE Transactions*, Vol. 93, 1984, pp. 728–735.
- [4] Eady, J. A. and Smith, D. M., "Properties and Applications of a New Aluminum Foundry Alloy," *SAE Transactions*, Vol. 93, 1984, pp. 747–755.
- [5] Beumler, H., Hammerstad, A., Wieting, B., and DasGupta, R., "Analysis of Modified 319 Aluminum Alloy," *AFS Transactions*, Vol. 96, 1988, pp. 1–12.
- [6] Shercliff, H. R. and Ashby, M. F., "A Process for Age Hardening of Aluminum Alloys – I. The Model," *Acta Metallurgica et Materialia*, Vol. 38, 1990, pp. 1789–1802.
- [7] Shercliff, H. R. and Ashby, M. F., "A Process for Age Hardening of Aluminum Alloys – II. Applications of the Model," *Acta Metallurgica et Materialia*, Vol. 38, 1990, pp. 1803–1812.
- [8] Gundlach, R. B., Ross, B., Hetke, A., Valtierra, S., and Mojica, J. F., "Thermal Fatigue Resistance of Hypoeutectic Aluminum-Silicon Casting Alloys," *AFS Transactions*, Vol. 102, 1994, pp. 205–223.
- [9] Boileau, J. M. and Allison J. E., *Fatigue '96, Proceedings of the 6th International Fatigue Congress*, Berlin, Germany, 1996, pp. 941–946.
- [10] Vijayaraghavan, R., Palle, N., Boileau, J., Zindel, J., Beals, R., and Bradley, F., *Scripta Materiala*, Vol. 35, 1996, pp. 861–867.
- [11] Boileau, J., "The Effect of Solidification Time and Heat Treatment on the Tensile and Fatigue Properties of a Cast 319 Aluminum Alloy," *Proceedings of the 5th International AFS Conference on Molten Aluminum Processing*, AFS Inc., Des Plaines, IL, pp. 157–172.
- [12] Slavik, D. C. and Sehitoglu, H., "Constitutive Models Suitable for Thermal Loading," *Journal of Engineering Materials and Technology*, Vol. 108, 1986, pp. 303–312.
- [13] Slavik, D. C. and Sehitoglu, H., "A Constitutive Model for High Temperature Loading, Part I - Experimentally Based Forms of the Equations," *Thermal Stress, Material Deformation, and Thermo-mechanical Fatigue*, ASME PVP 123, H. Sehitoglu and S. Y. Zamrik, Eds. American Society of Mechanical Engineering, 1987, pp. 65–74.
- [14] Slavik, D. C. and Sehitoglu, H., "A Constitutive Model for High Temperature Loading, Part II- Comparison of Simulations with Experiments," *Thermal Stress, Material Deformation, and Thermo-mechanical Fatigue*, ASME PVP 123, H. Sehitoglu and S. Y. Zamrik, Eds., American Society of Mechanical Engineering, 1987, pp. 75–82.
- [15] Sehitoglu, S., Qing, X., Smith, T. J., Maier, H. J., and Allison, J., "Stress-Strain Response of a Cast 319-T6 Aluminum under Thermomechanical Loading," *Metallurgical and Materials Transactions A*, Vol. 31A, January 2000, pp. 139–151.
- [16] Lasecki, J. V., Allison, J., and Sehitoglu, H., "Thermo-Mechanical Fatigue of Cast 319 Aluminum," *Spring 2000 TMS Conference*, March 14, 2000.

Peter J. Bonacuse¹ and Sreeramesh Kalluri¹

Cyclic Deformation Behavior of Haynes 188 Superalloy Under Axial-Torsional, Thermomechanical Loading

REFERENCE: Bonacuse, P. J. and Kalluri, S., "Cyclic Deformation Behavior of Haynes 188 Superalloy Under Axial-Torsional, Thermomechanical Loading," *Thermomechanical Fatigue Behavior of Materials: 4th Volume, ASTM STP 1428*, M. A. McGaw, S. Kalluri, J. Bressers, and S. D. Peteves, Eds., ASTM International, West Conshohocken, PA, 2002, Online, Available: www.astm.org/STP/1428/1428_10595, 23 Dec. 2002.

ABSTRACT: Four types of axial-torsional, thermomechanical fatigue experiments have been performed on Haynes 188 superalloy: mechanically in-phase and thermally in-phase, mechanically in-phase and thermally out-of-phase, mechanically out-of-phase and thermally in-phase, and mechanically out-of-phase and thermally out-of-phase. In this study, representative cyclic deformation behavior of the axial-torsional, thermomechanical experiments is presented and compared with isothermal experiments performed at the two temperature extremes (316°C and 760°C) of the thermal cycle. The evolution of cyclic hardening under axial-torsional, thermomechanical conditions is also presented and compared with the corresponding isothermal data.

KEYWORDS: thermomechanical, cyclic deformation, multiaxial, axial-torsional, and cobalt-base superalloy

Introduction

As complex solid solution and precipitation hardened alloys are required to endure higher temperatures and larger stress excursions in the latest generation gas turbine engines, unanticipated interactions between the material chemistry and the environment may occur that may not be revealed by conventional, isothermal, uniaxial test methods. Stress state and thermal history can have a significant influence on the deformation behavior and damage accumulation in these materials. Experimental methods that more closely emulate the temperature and strain history encountered by gas turbine components are necessary to determine if, and under what conditions, these interactions are likely to occur.

Castelli and Rao [1], using solid cylindrical gage-section specimens, investigated the cyclic deformation behavior of Haynes 188, a wrought cobalt-base superalloy, under uniaxial, isothermal, and thermomechanical loading conditions. Thin-walled tubular specimens were used by the authors to perform isothermal uniaxial, torsional, and combined in- and out-of-phase axial-torsional fatigue studies on Haynes 188 at 316°C and 760°C [2–4]. After these isothermal experiments were performed on the thin-walled specimens, combined axial-torsional thermomechanical fatigue experiments were undertaken [5,6].

¹ Materials Research Engineer, US Army Research Laboratory and Senior Research Engineer, Ohio Aerospace Institute, respectively, NASA Glenn Research Center, 21000 Brookpark Rd., MS 49-7, Brook Park, OH 44135.

In the process of performing these strain-controlled fatigue studies on Haynes 188 under combined axial-torsional isothermal and thermomechanical loading, a significant amount of deformation data was collected. This paper details the stress-strain behavior and the cyclic stress evolution of Haynes 188 under a variety of axial-torsional, thermomechanical loading conditions. The data presented here is in no way meant to represent a comprehensive characterization of the multiaxial-thermomechanical deformation behavior of Haynes 188. The test matrix would have been designed differently if this were the primary goal. However, the data presented outline the complex interactions among the various thermal and load driven deformation mechanisms in a solid solution strengthened superalloy. Isothermal, cyclic axial-torsional deformation behavior of Haynes 188 at 760°C was previously reported [7].

Material, Specimens, and Test Equipment

Wrought, solution-annealed bars (50.8 mm) of Haynes 188 were acquired from a commercial vendor. The chemical composition of the superalloy in weight percent was as follows: S < 0.002; B : 0.002; P : 0.012; C : 0.10; Si : 0.40; La : 0.034; Mn : 0.75; Fe : 1.24; W : 13.95; Cr : 21.84; Ni : 22.43; and Co : Balance. Thin-walled tubular specimens with inner and outer diameters of 22 and 26 mm in the uniform cylindrical gage section (25 mm in length) were machined from the bar stock. The specimens were tested in an axial-torsional servohydraulic test rig. Specimen heating was accomplished with a three-coil induction heating fixture [8]. Additional details on the material, specimen fabrication, and testing equipment are available in Ref. 3.

Experimental Details

Four types of combined axial-torsional, thermomechanical fatigue (AT-TMF) experiments were performed with constant strain rate (triangular) waveforms. In Fig. 1, the three control inputs for each of the four AT-TMF experiments are displayed schematically. Mechanically in-phase (MIP) experiments were defined as those where axial strain and shear strain maxima and minima occurred simultaneously, i.e., no phase shift. Thermally in-phase (TIP) experiments were defined as those where the temperature extrema coincided with the axial strain extrema. Mechanically out-of-phase (MOP) experiments had the axial strain waveform leading the shear strain by 90° (shear strain passed through zero when the axial strain reached an extrema). In contrast, thermally out-of-phase (TOP) experiments were defined as those where the temperature minimum coincided with the axial strain maximum; shifted 180° from the thermally in-phase condition. Computer controlled induction heating was used to thermally cycle between 316 and 760°C, with a mean temperature of 538°C, for all the thermomechanical experiments. All TMF experiments (axial, torsional, and combined axial-torsional) were performed with cycle periods of 10 min/cycle under mechanical strain control; thermal strains were dynamically accounted for in the total strain command waveform. The strain-controlled isothermal experiments had cycle periods of 10 s. Therefore, the strain rates in the isothermal experiments were 60 times higher than the TMF experiments.

Figure 1 illustrates the relative phasing of the axial strain, torsional (or shear) strain, and temperature command inputs. In addition, Fig. 1 displays the implementation of the initial shift in phase among the three waveforms. Four acronyms are used to refer to each of the four AT-TMF experiments: MIPTIP (Mechanically In-Phase, Thermally In-Phase), MIPTOP (Mechanically In-Phase, Thermally Out-of-Phase), MOPTIP

(Mechanically Out-of-Phase, Thermally In-Phase), and MOPTOP (Mechanically Out-of-Phase, Thermally Out-of-Phase). Additional details on the techniques used to perform the AT-TMF experiments are available in Ref. 5. Table 1 shows the nominal conditions for the experiments analyzed in this paper.

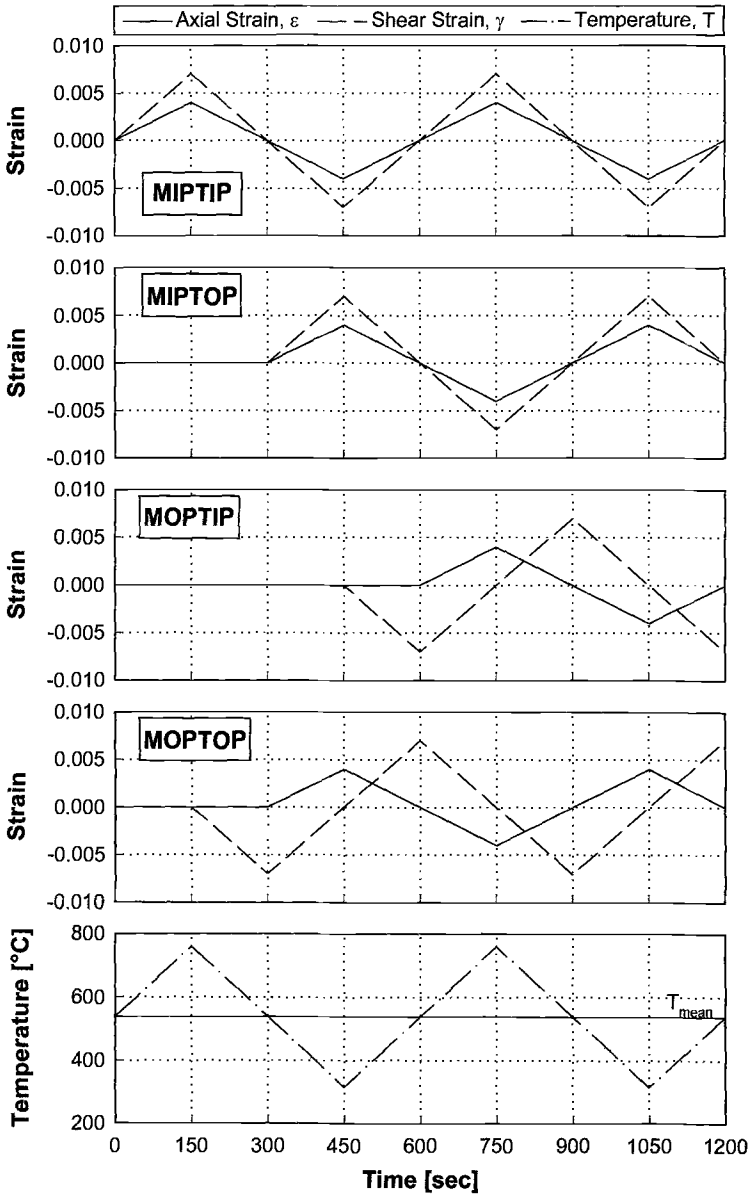


FIG. 1—Schematic of axial and torsional strain and temperature command waveforms for each of the AT-TMF experiments.

TABLE 1—*Fatigue test data analyzed in this investigation.*

Test Type	Axial Strain Range $\Delta\varepsilon$ [%]	Shear Strain Range $\Delta\gamma$ [%]	Mechanical Phase Shift ϕ [°]	Thermal Phase Shift θ [°]
316°C MIP	0.8	1.4	0	...
760°C MIP	0.8	1.4	0	...
316°C MOP	0.8	1.4	90	...
760°C MOP	0.8	1.4	90	...
MIPTIP	0.8	1.4	0	0
MIPTOP	0.8	1.4	0	180
MOPTIP	0.8	1.4	90	0
MOPTOP	0.8	1.4	90	180

NOTE: Strain ranges and phase shifts are nominal values.

Observed Deformation Behavior

Hysteresis Loops

Plots of the observed stress-strain behavior of Haynes 188 are presented in conventional hysteresis loops. The experimental data for the combined axial-torsional experiments are presented in separate axial and torsional hysteresis loops. The point where the maximum temperature occurred in each of the thermomechanical experiments is indicated in these plots. To further illustrate the phasing of the control inputs and material's response, axial strain versus shear strain and axial stress versus shear stress plots are also presented.

Mechanically In-Phase

Figures 2 and 3 show representative (50th cycle) axial and torsional hysteresis loops (stress versus strain) for mechanically in-phase AT-TMF experiments (MIPTIP and MIPTOP). For comparison, isothermal 760 and 316°C MIP experimental data are plotted. In both the axial and torsional plots the 760 and 316°C loops display similar stress-strain behavior. Some stress relaxation occurred, in both axial and torsional loops, in the AT-TMF experiments at the high temperature (760°C) end of the thermal cycle. There was essentially no relaxation in isothermal 760°C MIP experiments due to the substantially higher strain rates. One can also see the expected asymmetry in the stress response in the TMF experiments; e.g., higher stress magnitudes required to reach the strain peaks at the low temperature (316°C) end of the thermal cycles.

Figure 4 shows the axial strain versus the shear strain for the mechanically in-phase isothermal 316 and 760°C experiments and the MIPTIP and MIPTOP experiments. This figure illustrates that all four experiments had essentially no phase lag between the axial and shear strain control inputs. Figure 5 shows the axial stress versus the shear stress recorded for same experiments. There is some hysteresis in this plot because the material tends to have different flow behavior under axial and torsional loading. Although it is not

particularly clear in Fig. 5, one can see the expected asymmetry in the stress peaks in the TMF experiments.

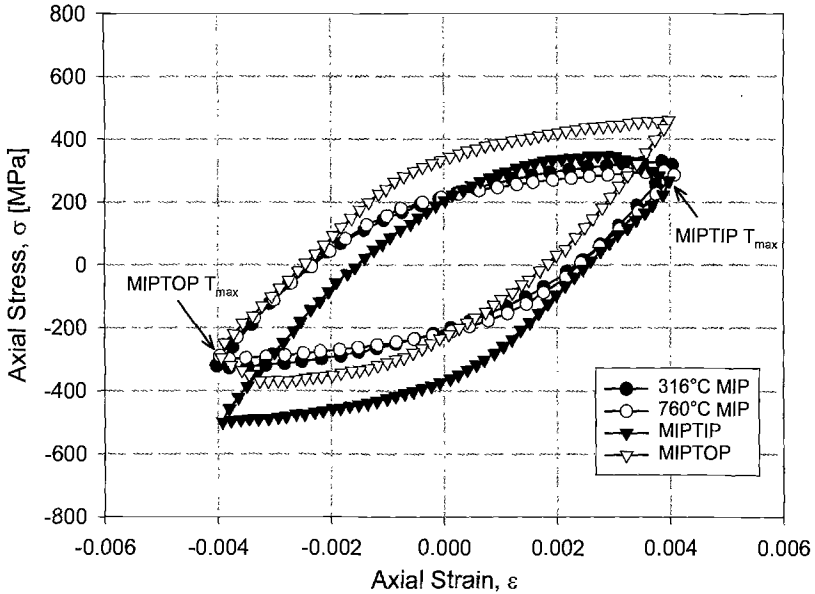


FIG. 2—Axial hysteresis loops for mechanically in-phase experiments.

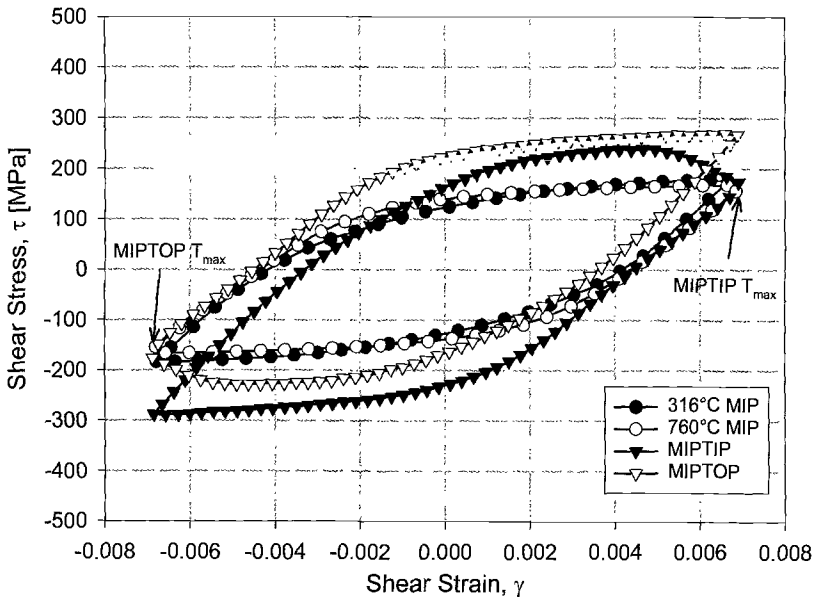


FIG. 3—Torsional hysteresis loops for mechanically in-phase experiments.

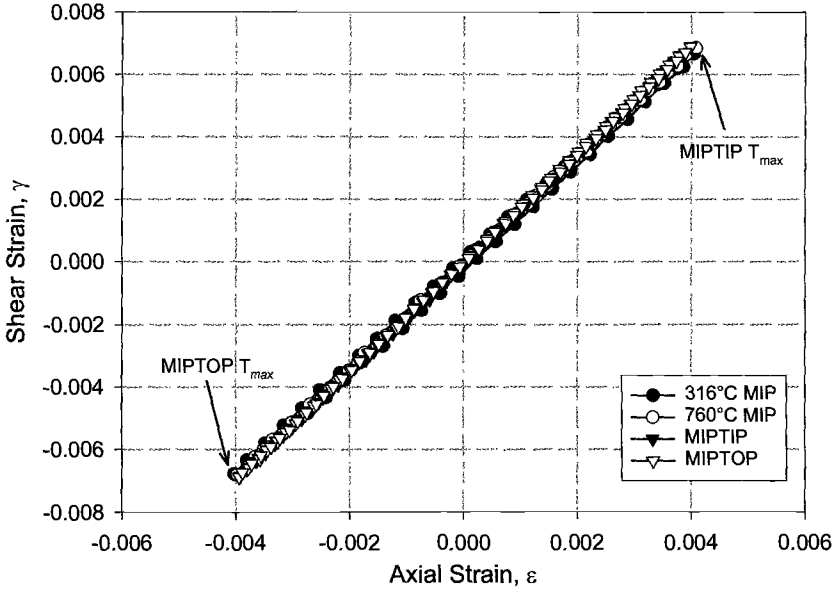


FIG. 4—Axial strain vs. shear strain for mechanically in-phase experiments.

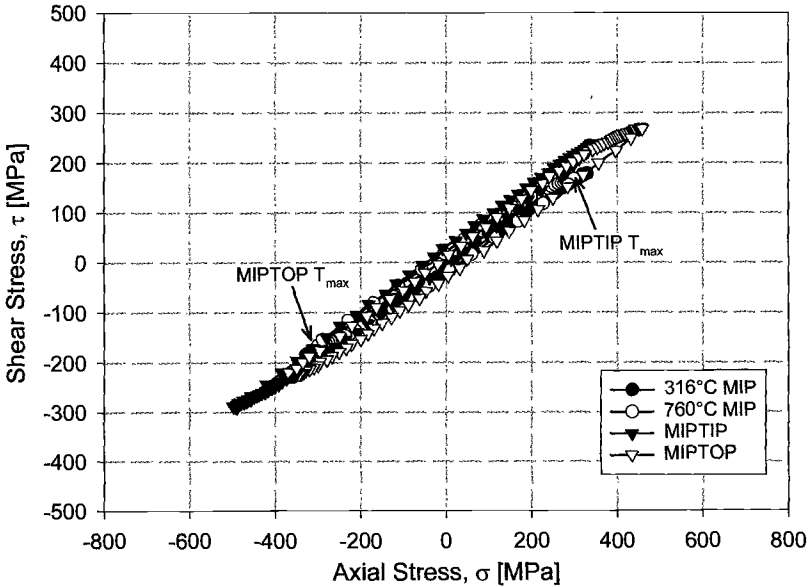


FIG. 5—Axial stress versus shear stress for mechanically in-phase experiments.

Mechanically Out-of-Phase

Figures 6 and 7 show representative (50th cycle) axial and torsional hysteresis loops for mechanically out-of-phase AT-TMF experiments (MOPTIP and MOPTOP). Again, the isothermal 316 and 760°C isothermal MOP data are also presented. In contrast to the mechanically in-phase experiments, the isothermal 760°C MOP response is markedly different from the isothermal 316°C MOP response. At the 50th cycle, the 760°C isothermal specimen requires significantly lower stresses to reach the same strains as the 316°C isothermal experiment. In the AT-TMF tests, the axial hysteresis loops again show the expected asymmetry in stress at the hot and cold ends of the thermal cycle in addition to the stress relaxation at the maximum temperature. In the mechanically out-of-phase TMF experiments the asymmetry between the shear stress maxima and minima are less pronounced because the shear strain peaks occur at the same temperature, 538°C, due to a 90° phase shift from both the axial strain and temperature waveforms. All loops show the characteristic inflection in the stress that occurs when the other imposed strain reaches an extremum and changes loading direction.

Again these loops are somewhat distorted due to the hardening in the axial direction at the 316°C end of the cycle and the stress relaxation in the axial direction at the 760°C end of the thermal cycle.

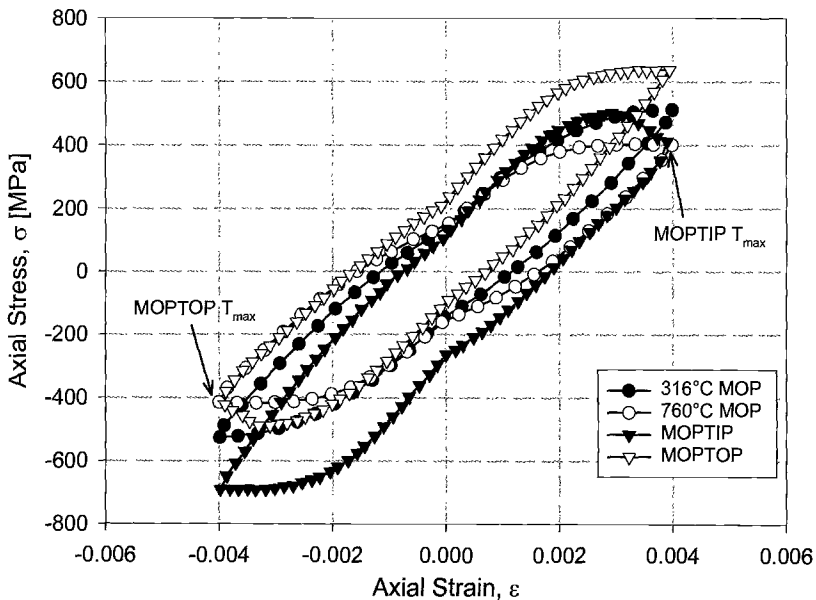


FIG. 6—Axial hysteresis loops for mechanically out-of-phase experiments.

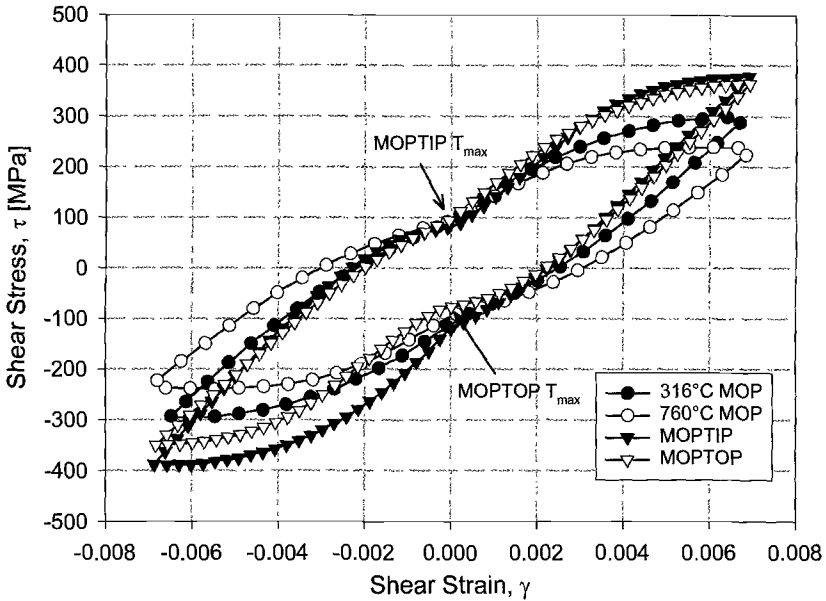


FIG. 7—Torsional hysteresis loops for mechanically out-of-phase experiments.

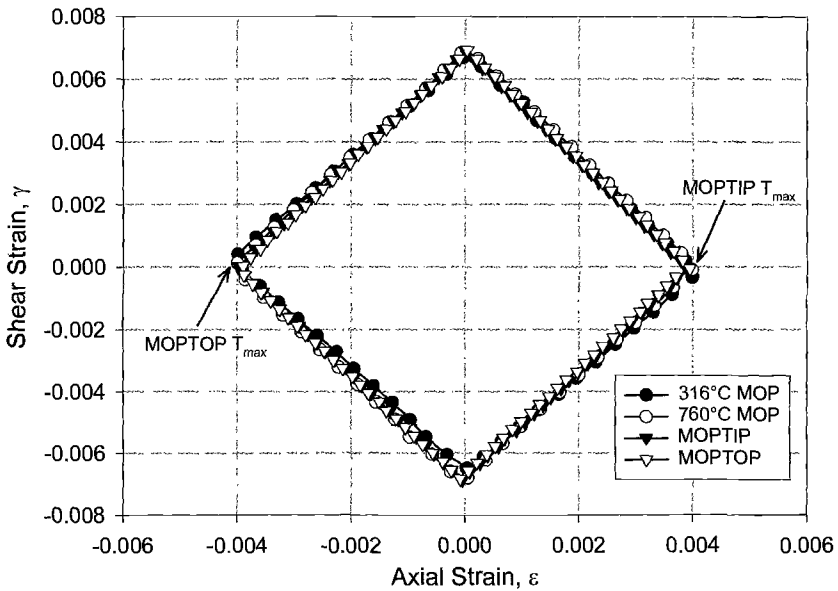


FIG. 8—Axial strain versus shear strain for mechanically out-of-phase experiments.

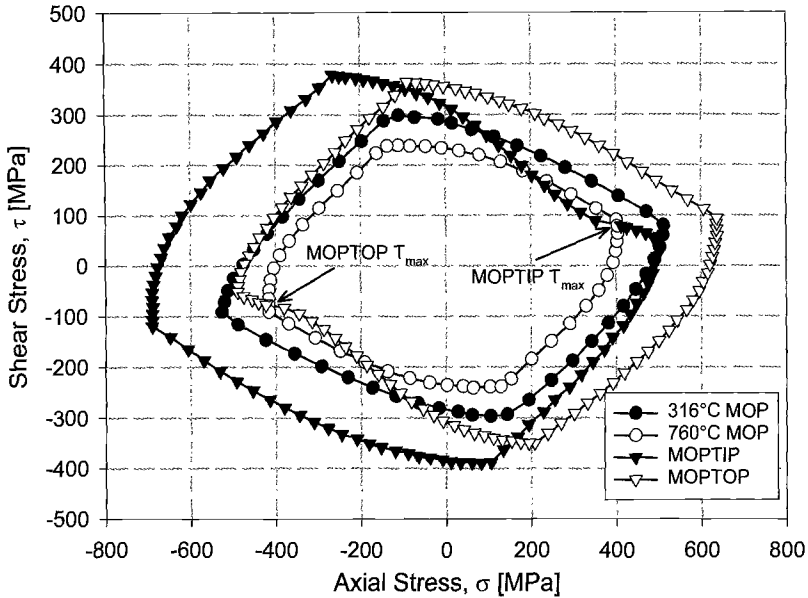


FIG. 9—Axial stress vs. shear stress for mechanically out-of-phase experiments.

Cyclic Stress Evolution

In Figs. 10–13 the maximum and minimum axial and shear stresses are plotted as a function of cycle number.

Mechanically In-Phase

Figures 10 and 11 clearly show the asymmetry in the stress extremes in the TMF experiments. As indicated earlier, at the 760°C end of the TMF cycle the material yields at a lower stress than the 316°C end of the cycle. The TMF experiments exhibit significantly more cyclic hardening than the isothermal experiments with a significant portion of this extra hardening occurring at the lower temperature end of the TMF cycle. This is particularly apparent in the axial plot (Fig. 10) where the 760°C end of the cycle (maximum stress in the thermally in-phase and minimum stress in the thermally out-of-phase) nearly parallels the isothermal experiments. This might be explained by the stress relaxation that is observed in the TMF experiments at the high temperature end of the cycle. Both the isothermal and TMF mechanically in-phase experiments seemed to have noticeable change in the rates of cyclic hardening after a few hundred cycles.

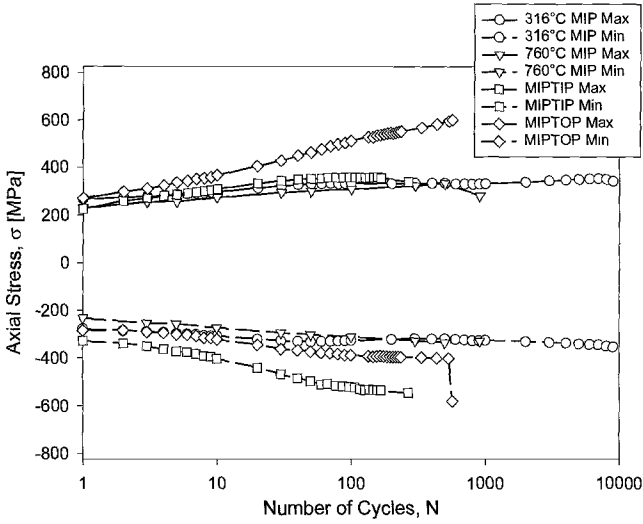


FIG. 10—Maximum and minimum axial stress evolution for mechanically in-phase experiments.

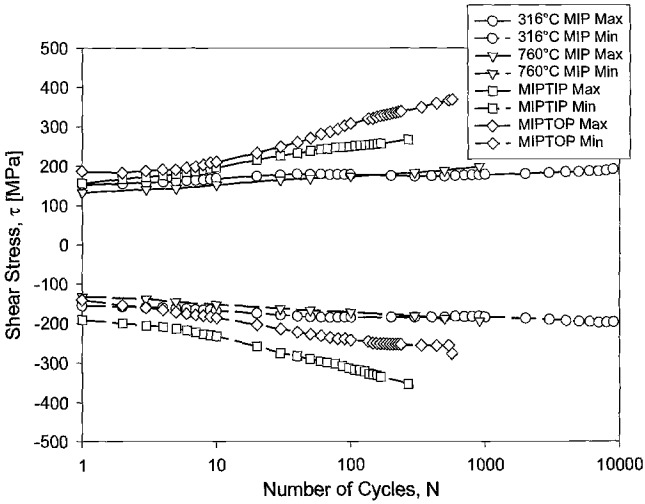


FIG. 11—Maximum and minimum shear stress evolution for mechanically in-phase experiments.

Mechanically Out-of-Phase

Figures 12 and 13 again show the increase in cyclic hardening under thermomechanical loading over isothermal loading at 316 and 760°C. As in the mechanically in-phase experiments, the axial data (Fig. 12) show that much of the additional hardening in the axial direction seems to occur at the lower temperature end of the TMF cycle. Since the peak shear strains in the mechanically out-of-phase experiments occur at mean temperature of the thermal cycle (538°C), the shear data from these experiments do not show the same asymmetry as axial data (Fig. 13).

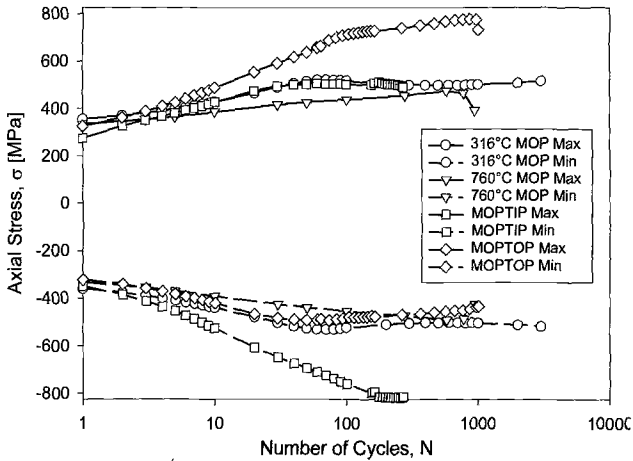


FIG. 12—Maximum and minimum axial stress evolution for mechanically out-of-phase experiments.

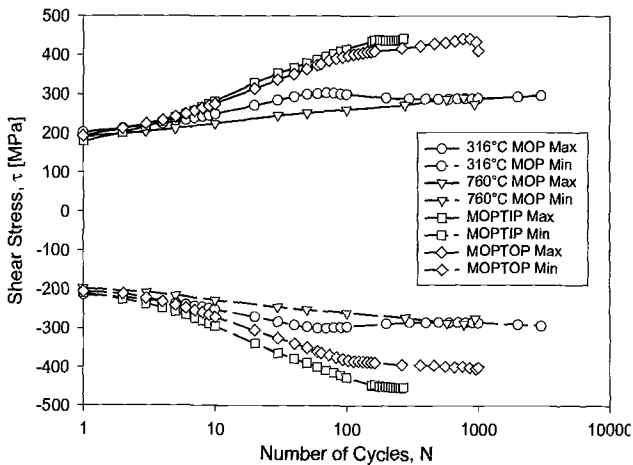


FIG. 13—Maximum and minimum shear stress evolution for mechanically out-of-phase experiments.

Stress Relaxation Under AT-TMF Loading

In the hysteresis loops, the dependence of stress on temperature is apparent. In these strain-controlled experiments, as the temperature approaches the maximum in the cycle (760°C), the stress reaches a maximum (or minimum) well before the strain peak. The magnitude of the stress relaxation is dependent on both the type of cycle performed and on the number of cycles accumulated. All the AT-TMF experiments show some stress relaxation at the 760°C end of the cycle where a strain peak corresponds with the maximum temperature. This includes both axial and torsional loops in the mechanically in-phase experiments and the axial loops in the mechanically out-of-phase experiments. As can be seen in Figs. 14 and 15, the magnitude of the stress relaxation evolves with cycling. Figure 14 shows the evolution in the axial stress relaxation for the four AT-TMF tests. Figure 15 shows the shear stress relaxation in the MIPTIP and MIPTOP experiments. Because the shear strain peaks occur at the mean temperature (538°C) in the mechanically out-of-phase tests, the torsional hysteresis loops do not show any measurable stress relaxation. In all cases, the magnitude of the stress relaxation increases in approximately the first hundred cycles and then either remains relatively constant or begins to decrease. This corresponds with the change in hardening rate seen in the cyclic stress plots (Figs. 10–13). There is some asymmetry between the amounts of relaxation in tension and compression. The amount of relaxation in the thermally in-phase experiments is larger than the thermally out-of-phase, suggesting that relaxation occurs more readily in tension than in compression. The magnitude of this relaxation seems to be dependent on the amount of cyclic hardening accumulated.

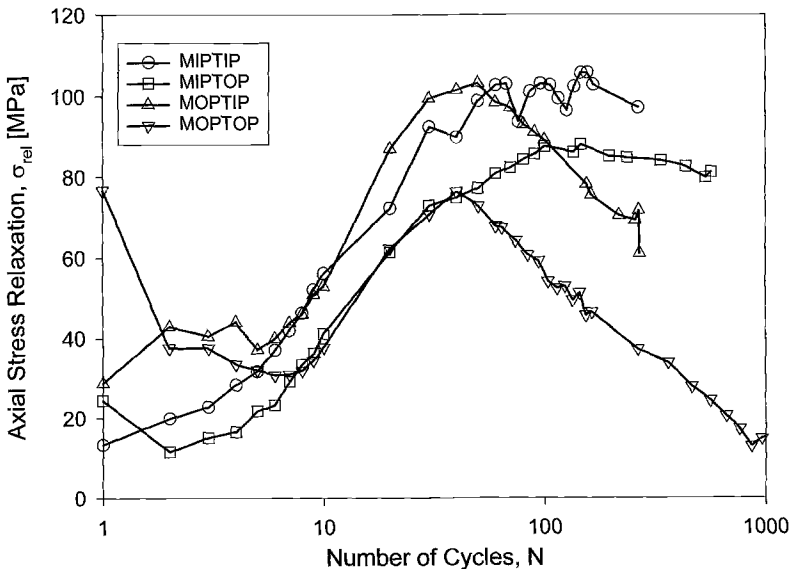


FIG. 14—Magnitude of axial stress relaxation as a function of cycles in AT-TMF experiments.

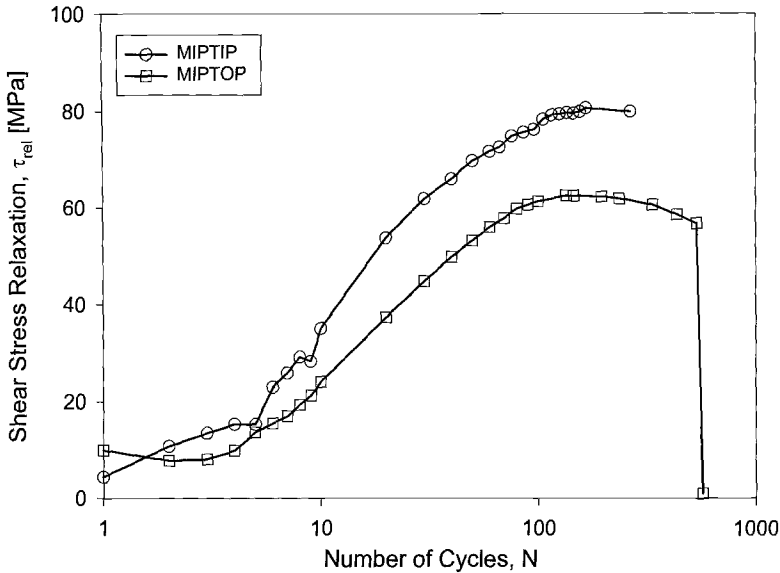


FIG. 15—Magnitude of shear stress relaxation as a function of cycles in mechanically in-phase AT-TMF experiments.

Discussion

In the isothermal mechanically in-phase tests (Figs. 10 and 11), there is only a small difference in the initial stress extrema between the 760 and 316°C in-phase experiments. This difference nearly vanishes as, at 760°C, Haynes 188 hardens to failure and at 316°C, the material cyclically softens somewhat after several hundred cycles before a slight increase in hardening to failure. The “hump” in the hardening in the 316°C isothermal experiments is more pronounced in the mechanically out-of-phase experiment (Figs. 12 and 13). The isothermal experiments were performed with a cycle period of 10 s. This was 60 times faster than the TMF experiments (10 min cycle). Direct comparisons between the isothermal and TMF experiments should take into account the additional time available for stress relaxation to occur at the hot end of the TMF experiments. Given the permutations performed in the fatigue tests, the effect of thermal cycling between 316 and 760°C on the stress response of Haynes 188 can be obtained by comparing the AT-TMF experiments with the isothermal experiments. Table 2 contains the near half-life stress ranges and mean stresses of the isothermal experiments and the AT-TMF experiments.

One can measure the additional hardening caused by mechanically out-of-phase loading by comparing the measured axial and shear stress ranges with those of a mechanically in-phase experiment, given that all are performed with the same imposed axial and shear strain ranges. The difference determines the magnitude of the additional hardening. The result of these comparisons is shown in Table 3. The 316 and 760°C columns refer to the isothermal experiment used as the baseline for the additional

hardening calculation. It should be noted, in the mechanically out-of-phase experiments, that at any of the strain peaks the absolute value of a combination of the two imposed strain components must always be less than that of an in-phase experiment (shear strain is zero when the axial strain reaches an extreme and vice versa). Even though the combined axial and shear strains at the peaks are lower in the out-of-phase experiments, the axial and shear stress ranges always exceed the corresponding values observed in the in-phase experiments.

TABLE 2—*Stress response at approximately half-life.*

Test Type	Axial Stress		Mean Shear Stress		N _f
	Range $\Delta\sigma$ [MPa]	Stress σ_0 [MPa]	Range $\Delta\tau$ [MPa]	Stress τ_0 [MPa]	
316°C MIP	690	5	382	-5	9448
760°C MIP	668	-2	377	0	910
316°C MOP	1018	-1	584	2	3410
760°C MOP	910	-10	544	0	1088
MIPTIP	892	-90	576	-34	282
MIPTOP	949	77	593	42	569
MOPTIP	1297	-149	883	-6	270
MOPTOP	1217	149	824	16	1004

TABLE 3—*Stress range comparisons.*

		Axial		Torsion	
		$\Delta\sigma_1 - \Delta\sigma_2$ [MPa]		$\Delta\tau_1 - \Delta\tau_2$ [MPa]	
Test 1	Test 2	316°C	760°C	316°C	760°C
Additional Hardening from Out-of-Phase Mechanical Cycling					
Isothermal MOP	Isothermal MIP	328	242	202	167
Additional Hardening from Thermal Cycling					
MIPTIP	Isothermal MIP	202	224	194	199
MIPTOP	Isothermal MIP	259	281	211	216
MOPTIP	Isothermal MOP	279	387	299	339
MOPTOP	Isothermal MOP	199	307	240	280
Additional Hardening from Combined Out-of-Phase Mechanical and Thermal Cycling					
MOPTIP	Isothermal MIP	607	629	501	506
MOPTOP	Isothermal MIP	527	549	442	447

The effect of in- and out-of-phase thermal cycling on cyclic hardening behavior can also be determined by similarly subtracting the isothermal mechanically in- and out-of-phase stress ranges from the mechanically identical AT-TMF experiments. The results of these calculations are also shown in Table 3. In spite of the stress relaxation that occurs in the 10-min cycle, AT-TMF experiments, the stress ranges are still higher, under TMF, than the 10-s cycle, isothermal experiments. Given the greater stress relaxation when the maximum temperature occurs at the maximum axial strain (Fig. 14), it is not surprising that the MIPTIP experiments show less additional hardening than the MIPTOP.

To determine if the additional hardening encountered in both out-of-phase mechanical loading and thermomechanical loading are additive, one can compare the MOPTIP and MOPTOP experiments with the isothermal mechanically in-phase experiments. This should give some measure of the combined effect of both out-of-phase mechanical loading and thermomechanical loading. Again, this result is shown in Table 3.

The individually measured effects of out-of-phase mechanical loading (calculated by comparing isothermal mechanically in- and out-of-phase experiments) and thermomechanical loading (comparing isothermal and thermomechanical tests with the same mechanical loading) can then be summed to see how they compare with observed combined effect. Figure 16 graphically shows the measured effect of combined thermal cycling and out-of-phase mechanical loading compared with the individually measured effects. The calculated additional hardening for Fig. 16 used 760°C isothermal MIP experiment as the baseline. It is clear that the mechanisms that contribute to the mechanical and thermal cyclic hardening interact synergistically.

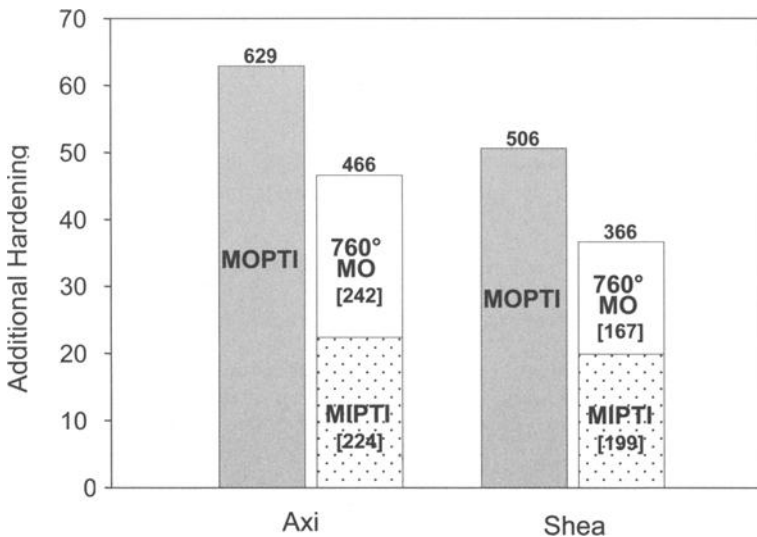


FIG. 16—Comparison of additional hardening due to combined out-of-phase mechanical loading and thermal cycling with the individually measured effects (760°C MIP experiment used as baseline).

Summary

Cyclic deformation behavior of a wrought cobalt-base superalloy, Haynes 188, tested under isothermal and thermomechanical axial-torsional loading conditions was examined. The following are the main findings of this study:

1. Haynes 188 exhibits a varied stress response under the different combinations of axial-torsional, mechanical, and thermal cycling considered in this study.
2. Cyclic hardening induced by out-of-phase mechanical and thermomechanical loading indicates that multiple deformation mechanisms actively contribute to the hardening process.
3. The deformation mechanisms that lead to additional hardening under out-of-phase mechanical loading and thermomechanical cycling appear to interact synergistically.

References

- [1] Castelli, M. G. and Rao, K. B. S., "Cyclic Deformation of Haynes 188 Superalloy Under Isothermal and Thermomechanical Loadings," *Superalloys 1996*, R. D. Kissinger, D. J. Deye, D. L. Anton, A. D. Cetel, M. V. Nathal, T. M. Pollack, and D. A. Woodford, Eds., *The Minerals, Metals, and Materials Society*, 1996, pp. 375–382.
- [2] Kalluri, S. and Bonacuse, P., "Estimation of Fatigue Life under Axial-Torsional Loading," *Material Durability/Life Prediction Modeling: Materials for the 21st Century*, PVP-Vol. 290, S. Y. Zamrik and G. R. Halford, Eds., American Society of Mechanical Engineers, 1994, pp. 17–33.
- [3] Bonacuse, P. J. and Kalluri, S., "Elevated Temperature Axial and Torsional Fatigue Behavior of Haynes 188," *Journal of Engineering Materials and Technology*, Vol. 117, 1995, pp. 191–199.
- [4] Kalluri, S. and Bonacuse, P. J., "In-Phase and Out-of-Phase Axial-Torsional Fatigue Behavior of Haynes 188 at 760°C," *Advances in Multiaxial Fatigue*, *ASTM STP 1191*, D. L. McDowell and R. Ellis, Eds., ASTM International, West Conshohocken, PA, 1993, pp. 133–150.
- [5] Kalluri, S. and Bonacuse, P. J., "An Axial-Torsional Thermomechanical Fatigue Testing Technique," *Multiaxial Fatigue and Deformation Testing Techniques*, *ASTM STP 1280*, S. Kalluri and P. J. Bonacuse, Eds., ASTM International, West Conshohocken, PA, 1997, pp. 184–207.
- [6] Bonacuse, P. J. and Kalluri, S., "Axial-Torsional, Thermomechanical Fatigue Behavior of Haynes 188 Superalloy," *Thermal Mechanical Fatigue of Aircraft Engine Materials*, *AGARD Conference Proceedings*, No. 569, 1996, pp. 15-1 to 15-10.
- [7] Bonacuse, P. J. and Kalluri, S., "Cyclic Axial-Torsional Deformation Behavior of a Cobalt-Base Superalloy," *Cyclic Deformation, Fracture, and Nondestructive Evaluation of Advanced Materials: Second Volume*, *ASTM STP 1184*, M. R. Mitchell and O. Buck, Eds., ASTM International, West Conshohocken, PA, 1994, pp. 204–229.
- [8] Ellis, J. R. and Bartolotta, P. A., "Adjustable Work Coil Fixture Facilitating the Use of Induction Heating in Mechanical Testing," *Multiaxial Fatigue and Deformation Testing Techniques*, *ASTM STP 1280*, S. Kalluri and P. J. Bonacuse, Eds., ASTM International, West Conshohocken, PA, 1997, pp. 43–62.

Damage Mechanisms Under Thermomechanical Fatigue

E. Tzimas,¹ P. Hähner,¹ P. Moretto,¹ S. D. Peteves,¹ and J. Bressers²

Damage and Failure Mechanisms of Thermal Barrier Coatings under Thermomechanical Fatigue Loadings

REFERENCE: Tzimas, E., Hähner, P., Moretto, P., Peteves, S. D., and Bressers, J., “**Damage and Failure Mechanisms of Thermal Barrier Coatings Under Thermomechanical Fatigue Loadings,**” *Thermomechanical Fatigue Behavior of Materials: 4th Volume, ASTM STP 1428*, M. A. McGaw, S. Kalluri, J. Bressers, and S. D. Peteves, Eds., ASTM International, West Conshohocken, PA, Online, Available: www.astm.org/STP/1428/1428_10594, 3 Feb. 2003.

ABSTRACT: The mechanical behavior of thermal barrier coated (TBC) systems under the influence of combined thermal and mechanical cyclic loading has been studied using a prototype experimental configuration that simulates realistically the operational conditions within a gas turbine. This study has demonstrated that the failure mechanisms of TBC systems under thermomechanical fatigue (TMF) conditions depend on the range of applied mechanical strain and on the phase angle between thermal and mechanical loading. The results highlight the importance of proper design of TMF experiments so that the failure mechanisms activated and studied during the experiments are the mechanisms responsible for the failure of TBC systems under service conditions.

KEYWORDS: thermomechanical fatigue (TMF), thermal barrier coatings (TBC), fracture, platinum aluminides, overlay coatings, MAR-M 509, CMSX-4

Introduction

Developments in gas turbines for electricity generation and aircraft propulsion follow the trend for increased thermal efficiency that may result in a reduction of the specific fuel consumption with direct environmental and economic benefits. The increase in the operational temperature of a turbine, called turbine inlet temperature, is the simplest and most efficient way to increase thermal efficiency. However, this increase in turbine inlet temperature is limited by the capability of materials used in the first stages of the turbine to retain their mechanical properties and their reliability in a very demanding corrosive environment at high temperatures. The increase in turbine inlet temperature was initially achieved by microstructural modifications of the alloys used (introduction of directionally solidified and single crystal alloys) and with the implementation of advanced cooling systems. More recently, thermal barrier coatings (TBCs) are used successfully to likely permit a further increase in the operational temperature of gas turbines [1–4].

A TBC system (or simply TBC) consists of: (i) the ceramic topcoat that provides

¹ Scientific officer, European Commission, DG-JRC, Institute for Energy, 1755 ZG Petten, The Netherlands.

² Retired scientific officer, European Commission, DG-JRC, Institute for Energy, The Netherlands.

thermal insulation; (ii) the metallic substrate, typically a superalloy; (iii) a bond coat that prevents high temperature oxidation and hot corrosion of the substrate and enhances the bonding between the topcoat and the substrate; and (iv) a thermally grown oxide (TGO), a few microns thick, typically Al_2O_3 , that forms between the bond coat and the topcoat. Two different families of bond coats are used: diffusion-type coatings, with a general composition $\beta\text{-NiAl}$, and overlay coatings with composition MCrAlY ($\text{M} = \text{Ni}, \text{Co}, \text{Ni} + \text{Co}$). The ceramic topcoat is made of ZrO_2 that contains 6–8% Y_2O_3 as a stabilizer for the crystal structure of the coating. The ceramic topcoat can be deposited either by plasma spray (PS) or by electron beam-physical vapor deposition (EB-PVD). Typical microstructures are shown in Fig. 1.

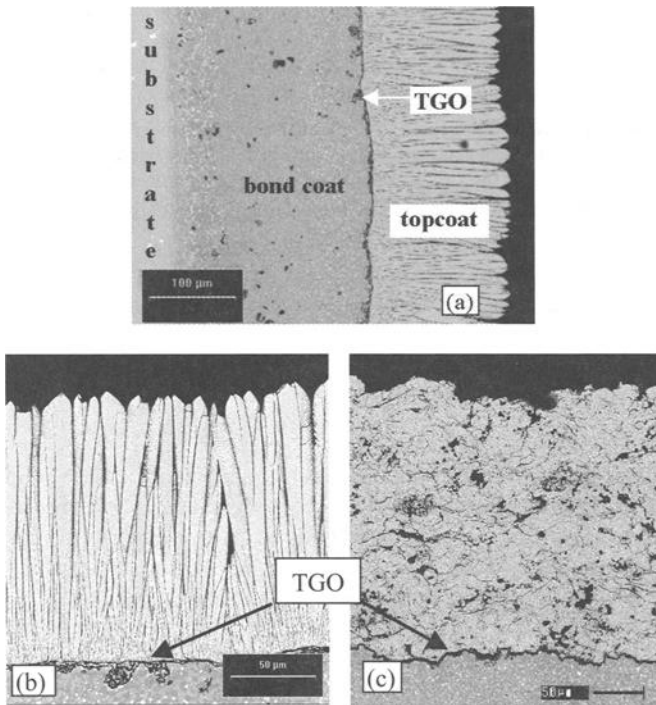


FIG. 1—Typical microstructures of: (a) a TBC system; (b) topcoats deposited by EB-PVD; and (c) PS.

During the operation of a gas turbine, the blades and vanes of the first stages of the turbine are subjected to cyclic thermal and mechanical loads. As a result, their reliability is limited by thermomechanical fatigue (TMF). TBCs are utilized nowadays primarily to increase the durability of the protected components by decreasing their operating temperature. However, TBCs operating at the “prime reliant” mode (that keeps the bulk temperature of the component unchanged, permitting the increase of the combustion temperature and thus the efficiency of the gas turbine) have not yet been designed

successfully. This demanding operating mode requires a comprehensive understanding of the TMF behavior of the coated systems since TBC performance is essential for the integrity of the coated component. TBC failure can be manifested, but not always, by spallation of the topcoat, being the result of several damaging mechanisms. Failure has been shown to be predominantly initiated at the bond coat - topcoat interface region. For PS TBC coated systems, investigators have demonstrated that failure initiates either in the TGO [5,6], or in the topcoat, but at close distance to the interface with the TGO [7–9]. These initiation cracks coalesce and propagate within the topcoat parallel to the interface, causing spallation after the application of compressive loads on the coated system. On the other hand, EB-PVD coatings fail by cracking either along the TGO - bond coat or the TGO - topcoat interface [8,10–12]. This subtle difference in failure mechanisms is primarily attributed to the dissimilarities in the microstructure of the topcoat: PS coatings are porous due to processing with a relatively uniform distribution of microcracks that weaken their fracture toughness ($\approx 0.5 \text{ MPa}\sqrt{\text{m}}$) [13]. EB-PVD coatings consist of loosely interconnected columnar grains, usually oriented normal to the coating-substrate interface. As a result, the EB-PVD coating is more strain-tolerant in directions perpendicular to the columns and thus more resistant to crack growth compared with the PS coatings. Another significant difference between the two systems is the morphology of the bond coat - topcoat interface: in PS systems, adhesion is mechanical, ensured by means of a rough interface that promotes layer interlocking but also amplifies the magnitude of stresses in the coating [14], while in EB-PVD coatings, interfacial adhesion is chemical and interfaces are relatively smooth.

The wealth of underlying mechanisms, the variability of the coatings' quality, the difficulties in characterizing TBC systems and the lack of testing protocols for TBCs have limited the success towards a mechanism-based lifing methodology. Thus, testing under near-service conditions is needed to assess durability and enable damage observations that can distinguish among potential failure mechanisms. Despite the importance of this issue, to our knowledge, only a few independent investigations have been published, reflecting most likely the difficulties in performing such experiments [15–19]. For example, very high cooling and heating rates are required ($\sim 100\text{K}/\text{min}$) as well as the establishment of a realistic temperature profile across the cross section of the sample, where the ceramic topcoat is at a higher temperature than the metallic substrate during heating.

This work presents an experimental approach adopted for assessing the TBC behavior and life under TMF testing. A specially designed TMF rig that allows for a realistic thermal gradient across the TBC system, enabling the simulation of a near-service thermomechanical-loading environment, has been developed and validated. Using this setup, TMF tests have been conducted on a number of TBC systems with commercially applied coatings, deposited by PS or by EB-PVD. The observed damage mechanisms are discussed based on the imposed TMF cycles and on the interaction between the coating and the substrate, obtaining valuable information for further improvements of the design of TMF experiments.

Experimental Setup

Cylindrical hollow specimens (inner diameter 6 mm, outer diameter 10 mm, straight section 18 mm) were machined from a polycrystalline MAR-M 509 Co-based superalloy

and from two different single crystal Ni-based superalloys (CMSX-4 and a second generation superalloy, referred to as A in the following discussion) that were used as substrates, see Fig. 2. The external surfaces of the substrates were industrially coated either with a Pt-modified diffusion coating (55 μm thick) or with a NiCoCrAlY overlay bond coat (200 μm) and finally with a topcoat deposited either by PS or EB-PVD. The corresponding thicknesses for the topcoats were 100 μm and 300 μm for the EB-PVD and for the PS coatings respectively.

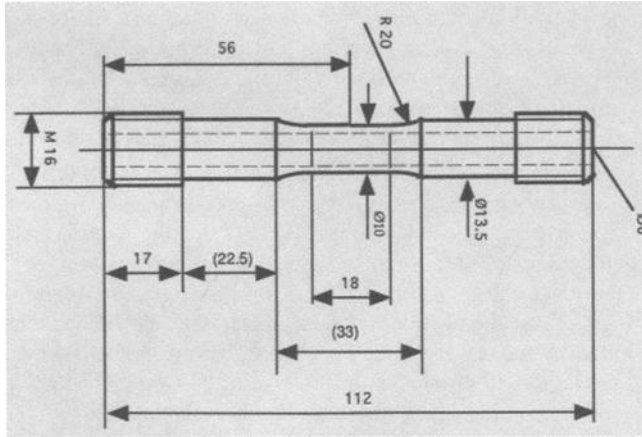


FIG. 2.—Specimen drawing (all dimensions are in mm).

Tests were performed in a servo-hydraulic universal testing machine. The temperature was controlled by means of a thermocouple located at the inner surface of the sample, at its mid-length. Strain was measured by means of a longitudinal extensometer, with its rods spanning a gauge length of 9 mm. The load was measured with a 100 kN load cell. For simplicity, the stress was calculated using the sample cross section including the bond coat and topcoat. The testing machine and the high frequency generator used for induction heating were both controlled by a computer. Elongation, load, temperature and cycle time were digitally recorded at a rate of 1 Hz.

Various cycles were used where the mechanical strain was either in phase with the thermal strain or with a phase difference of 180° with period times from 1200–3000 s. Where deemed necessary, more complex cycles were used, as discussed below. Tests were performed within a range of mechanical strain ranges of 0.3–1.0 % and with minimum and maximum temperatures of 120°C and 1050°C , respectively.

Prior to each TMF test, the apparent elastic modulus of the TBC system was determined for each sample as a function of temperature by subjecting the sample within its elastic regime to a load-controlled triangular cycle (± 3 kN, 0.05 Hz). From the stress–strain response, the elastic modulus was determined at different substrate temperatures within the temperature range of the imposed cycle. Subsequently, the thermal strain, ϵ_{therm} , was determined for each sample as a function of time within temperature cycles under zero mechanical load. The mechanical control parameter for the TMF test was the mechanical strain, ϵ_{mech} , calculated by subtracting the time-dependent thermal strain from

the measured total strain, ε_{tot} :

$$\varepsilon_{mech} = \varepsilon_{tot} - \varepsilon_{therm}$$

In order to reduce the expected lifetime of the samples to an acceptable testing time of less than one month, the mechanical strain range is generally enhanced compared with the in-service load during TMF testing. The mechanical strain ranges applied in our tests were up to 5-fold of typical in-service loads.

Fractographic analysis was performed in the tested samples in order to identify the crack initiation sites and the crack propagation paths across the TBC system. Polished cross sections of selected samples, cut parallel to the loading direction, were also observed under scanning electron microscope and analyzed by means of X-ray microanalysis. The metallographic specimen preparation followed a procedure, which has been developed to ensure that artifacts from preparation are avoided. This method includes embedding the specimen in an epoxy before cutting, and reproducible mechanical cutting and polishing procedures. The microstructure of the as-received material was also investigated by the same procedure.

Heating Methodology

To identify the optimum heating method that could generate a realistic temperature profile across the sample, various methods were investigated without success, including resistance heating, lamp heating and induction heating. Resistance furnace heating, using SiC heating elements, proved to yield very low heating and cooling rates. Lamp furnaces were evaluated due to their cleanliness and their documented potential for rapid heating. However, given the low absorption of zirconia, it is often customary to apply Fe_2O_3 -based paints on the ceramic surface to enable their heating by medium powered lamps. Not knowing whether these paints react chemically with the TBC at high temperatures, their use was excluded from this study. Despite the non-use of paint, it was possible to heat the TBC system and achieve the desired temperature profiles with specially designed lamp furnaces. However, the fast cycling between very high and relatively low temperatures required for the TMF tests create very harsh operating conditions for the lamp bulbs; for two different lamp furnace systems tested and employing the aforementioned specimen design and geometry, the average lifetime of the bulbs proved to be far below the expected lifetime of the samples.

These problems were overcome by induction heating, which proved to have the capacity for reliable, long-term temperature cycling with sufficient heating and cooling rates. However, as shown in Fig. 3, using conventional direct induction heating, the temperature at the topcoat surface is considerably lower than the temperature of the substrate, since the electromagnetic flux from the induction coil interacts with the metallic substrate and not with the topcoat. Following this approach, the topcoat is heated by the substrate via conduction, resulting in a temperature profile that is inverse to that experienced in-service by components coated with TBCs, and therefore is not appropriate. This shortcoming was overcome by placing a cylindrical metallic susceptor, made of a commercial Fe-Cr-Al alloy, concentrically around the sample (Fig. 4). In this set-up, the susceptor is heated by the induction coil. Eventually, the sample is heated via radiation and convection from the susceptor. Being next to the susceptor, the temperature at the topcoat surface is higher than that of the substrate (Fig. 3), thus yielding the desired temperature gradient.

Unfortunately, the indirect heating with a susceptor has drawbacks, as heating and cooling rates are smaller compared to direct heating. The maximum controlled heating rate obtained was about 5 K/s. Fastest cooling was achieved by switching off the induction heating where the substrate temperature drops from 950°C down to 130°C within 10 min. No attempts were made to use forced air-cooling in the tests. Furthermore, the indirect heating usually results in small temperature undulations during heating, about $\pm 5\text{--}15^\circ\text{C}$ depending on the target temperature, but always less than 3%. In combination with the slow cooling at temperatures below 300°C this causes a deviation of the experimental result of the mechanical strain/temperature curve from the target curve as was observed in these experiments.

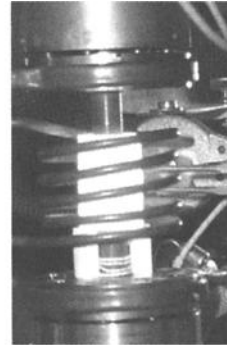
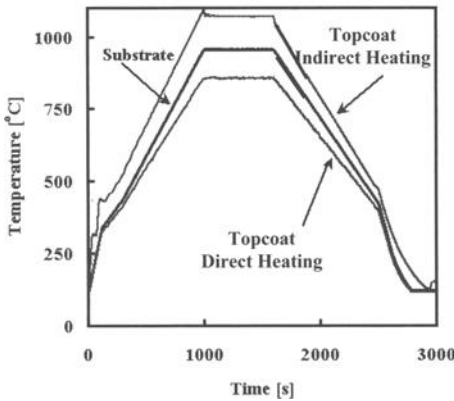


FIG. 3—Comparison of the substrate temperature during a temperature cycle with the temperature at the topcoat surface, applying direct and indirect induction heating.

FIG. 4—Image of the heating set-up, where the sample is heated indirectly by the induction coil via the susceptor.

Results

Influence of the Range of the Applied Mechanical Strain

A characteristic downfall of TMF tests is their long duration. A typical approach for TBC manufacturers, when testing the reliability of TBC coatings, is to subject the coated specimens to an enhanced mechanical or thermal strain range, typically several times the nominally experienced in-service range, in order to minimize the duration of each test.

In a series of experiments, coated specimens were subjected to thermomechanical cycle loading (see Fig. 5). In order to identify any possible influence of the applied mechanical strain range on the mechanisms that lead TBC systems to failure, tests were performed at two different levels of mechanical strain range, five times and three times the nominal strain range. Samples were machined from the Ni-based single crystal superalloy referred to as A, and were industrially coated with the overlay coating. The ceramic topcoat was applied by PS or by EB-PVD [19].

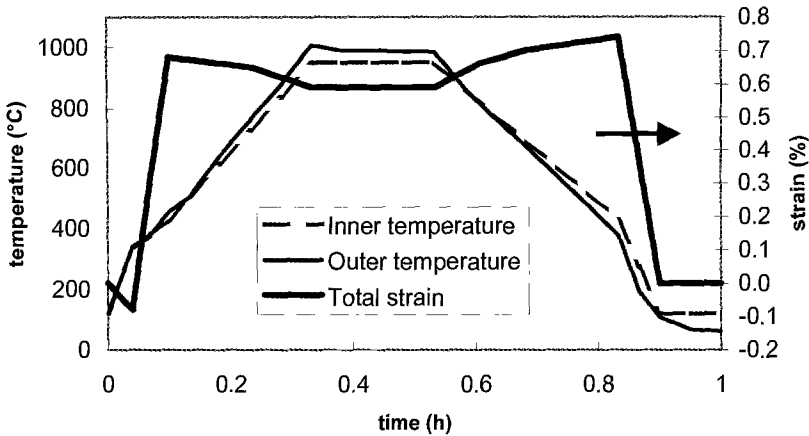


FIG. 5—Loading conditions: Profiles of (i) the inner (inside surface of the metal substrate) and (ii) outer (surface of ceramic topcoat) specimen temperatures during the TMF cycle, and (iii) the total strain imposed on the samples.

No significant differences in the number of cycles to failure (~400) and in failure mode were found for the two different systems (PS and EB-PVD) after testing under the highest applied mechanical strain. In PS coated specimens, a number of cracks developed perpendicular to the loading direction starting at the topcoat - bond coat interface and growing into the bond coat (Fig. 6a). It should be noted that these cracks almost always started at asperities arising from the interface roughness, namely at the concave parts of the interface. Crack flanks were oxidized, indicating that crack growth started early during TMF testing and continued throughout the test. These cracks eventually penetrated into the substrate and led the TMF specimens to failure. Delamination and/or spallation were not observed in tested samples. The TMF tests of specimens coated by EB-PVD, when tested with the higher mechanical strain, showed very similar failure behavior. Although the interface between the topcoat and the bond coat was noticeably smoother than for PS coated samples, cracks started growing from the topcoat-bond coat interface towards and into the substrate (Fig. 6b). Under this type of loading, crack initiation seems to be connected to inhomogeneities at the bond coat - topcoat interface. These inhomogeneities contain Al and Cr rich oxides, probably also in the form of spinels. Thus, the failure of both specimens has to be attributed to the cracking of the bond coat under thermomechanical loading, initiated at the bond coat - topcoat interface whereas delamination and spallation of the coating were absent. The TMF testing of EB-PVD coated specimens with reduced mechanical strain showed no cracking in the bond coat after 1200 cycles but a delamination of the topcoat, located at the TGO / bond coat interface over an extended area (Fig. 7).

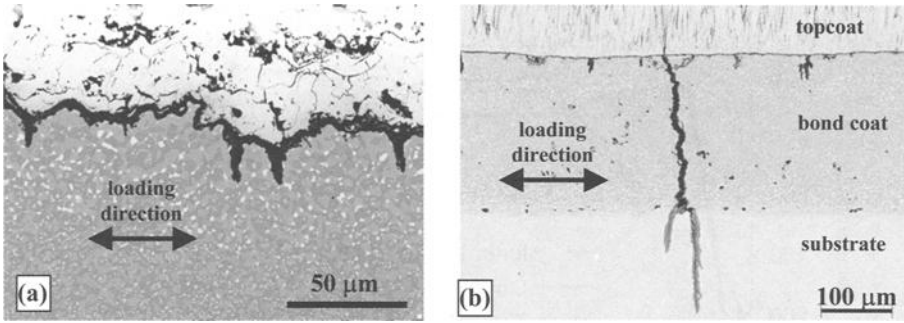


FIG. 6—Cracking of TBC systems tested with high mechanical strain: (a) topcoat - bond coat interface in a PS coated specimen. Several cracks started at the valleys of the interface and grew into the bond coat (b) Cracking through the bond coat in an EB-PVD coated specimen, showing that crack initiation is linked to inhomogeneities at the interface.

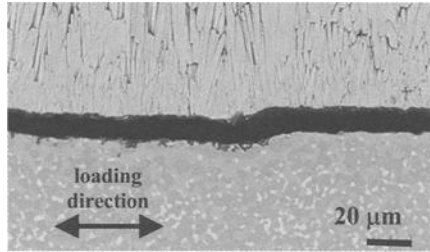


FIG. 7—Center of delamination of the topcoat from the bond coat in the EB-PVD coated specimen tested with low mechanical strain.

The results of the few TMF tests may point out that two different failure mechanisms can be active depending on the magnitude of the applied mechanical strain for the given thermomechanical cycle and TBC system. For the higher strain, life is limited by bond coat cracking. Cracks initiate at the bond coat - topcoat interface and propagate perpendicular to the loading direction driven by tensile axial stresses in the bond coat. Finite element analysis has shown that although the magnitude of axial stress in the bond coat does not vary significantly along the rough interface, the axial stresses developing in the TGO can vary in magnitude, but more importantly in sign, so that, while axial stresses in the TGO are compressive at convex regions of the interface due to residual stresses, at the concave they become tensile [14]. Since it has been shown that the TGO has a weak layered microstructure that contains several microcracks [6] it may be assumed that the TGO is weak in tension and therefore fails with the application of tensile loads. Therefore, based on these arguments, it can be concluded that the cracks observed in the bond coat have initiated within the TGO. This conclusion is verified by the observation that such cracks initiate at concave surfaces, the only locations where axial tensile stresses develop in the TGO [14]. In the EB-PVD coated samples, the density of the cracks observed in the bond coat is significantly reduced, compared with that in the PS specimens. Nevertheless, the life of these two specimens was statistically identical indicating that life to failure was not controlled by crack initiation but by

propagation of a single major crack. The difference in crack population between PS and EB-PVD coatings justifies the previous statement that cracks initiate in the TGO by tensile axial stresses. High tensile axial stresses develop in every concave surface of a rough interface in PS TBC systems that lead to the initiation of multiple cracks. These stresses have a much smaller magnitude during cycling when the interface is smooth in EB-PVD coated systems, however, combined with a local interfacial defect they can lead to the initiation of sparse cracks.

Reducing the applied mechanical strain, the peak tensile stresses in the TGO and bond coat become smaller, apparently below the failure stress of these materials, suppressing cracking in the bond coat. Eliminating cracking in the bond coat as failure mode, delamination occurs at higher cycle numbers as a result of degradation of the interface by enhanced oxidation and growth of the TGO, as observed upon sectioning the specimens tested with the lower mechanical loading.

Phase Angle Effects

To study the phase angle effects on the failure mechanisms, linear in-phase (IP) and out-of-phase (OOP) TMF cycles between mechanical strains, ϵ_{mech} , of 0 % and -0.5 % and between substrate temperatures of 400°C and 1050°C were applied. The period of the TMF cycle was 20 min with heating and cooling rates of 110 K/min and a dwell at maximum temperature for 10 min at constant mechanical strain [20].

The mechanical response of CMSX-4 samples coated with a Pt-modified diffusion aluminide coating and an EB-PVD TBC coating is shown in Fig. 8. During IP TMF cycling, the maximum compressive stress developed at the lowest temperature while the stress was negligible at the highest temperature of the cycle. Therefore, no significant inelastic deformation was expected in this type of TMF cycle. Only elastic deformation was observed with a stress response remaining unchanged for all cycles. The IP TMF test was stopped after 2000 cycles (~28 days). No obvious damage on the TBC surface was macroscopically observed. OOP testing with maximum compressive mechanical loading at maximum temperature led to severe inelastic deformation during the first cycle, see Fig. 8. For higher cycle numbers, less inelastic deformation occurred. However, as shown in Fig. 8, the curves of the stress response were shifted upwards with cycle number, reflecting the cyclic accumulation of inelastic compressive deformation. It is reminded that tests were performed under strain control.

Microstructural examination of the cross section of IP samples revealed considerable microstructural damage along the topcoat-TGO-bond coat interfaces, Fig. 9. The TGO thickness had grown from 0.5–1.0 μm prior to testing to 3–3.5 μm and appeared to be severely cracked: separations, primarily at the topcoat-TGO interface, with lengths up to 1 mm were observed. In addition, voids were formed in the bond coat at the interface with the TGO, the walls of which were also covered with TGO. Notably, there were sites where small-scale delamination at the TGO - bond coat interface was observed, whereas often delamination cracks at the topcoat-TGO interface had left the interface and entered into the topcoat.

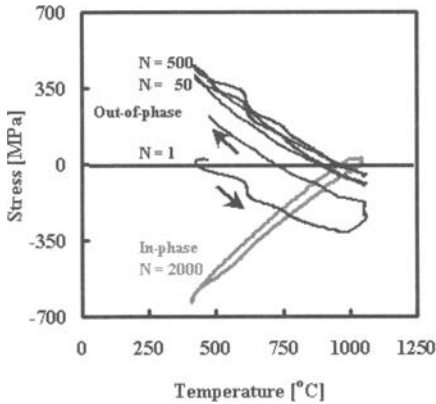


FIG. 8—Stress response during IP and OOP TMF cycling for a given cycle number.

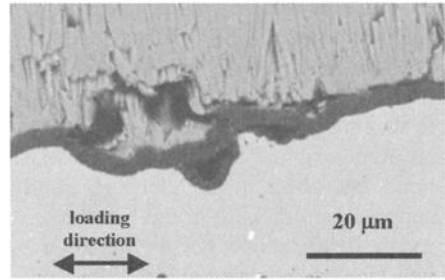


FIG. 9—Cross sectional view of the IP-tested specimen after 2000 cycles. Oxidized pores formed at the topcoat- bond coat interface.

Failure of OOP tested specimens was manifested either by detachment of the topcoat, by a significant drop of the maximum tensile stress, or by fracture. In all samples tested, fatigue cracks were observed, initiated at both surfaces of the specimen. The cracks that were visible from the coated surface of the samples nucleated at defects within the bond coat, at pores located next to the inter-diffusion zone. As a result of the high density of these defects, the bond coat was heavily fragmented. Under the action of the stress applied, these cracks propagated into the topcoat that ultimately led to the local detachment of the topcoat from the bond coat, probably during the ultimate fracture of the specimen (Fig. 10). In Fig. 10 it is also shown that such cracks may also propagate into the substrate.

While the density of the cracks from the inner unprotected surface of the substrate was significantly lower than that of the coated surface, the former cracks were life determining. Although delamination cracks were observed in all samples, in the IP tested sample, the topcoat did not spall. In contrast, in the OOP-tested samples, the TBC was found detached from the bond coat. This detachment was induced either by the plastic deformation ahead of a fatigue crack approaching the coated surface from the internal bored surface of the specimen (Fig. 11) or from the severe fragmentation of the bond coat that caused the segmentation of the topcoat in conjunction with the bending moments or the shock loading during the ultimate failure of the sample, as shown in Fig. 10.

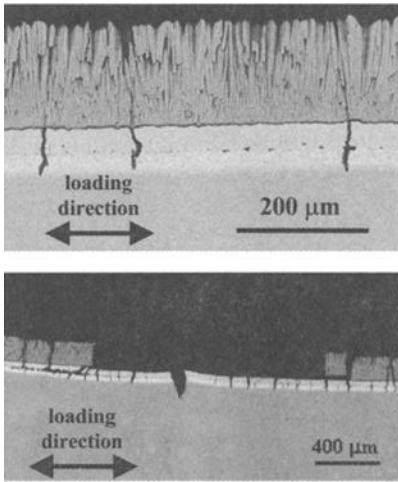


FIG. 10—Fragmentation of the topcoat by cracks initiated within the bond coat after OOP testing (top) that may lead to detachment of the topcoat (bottom).

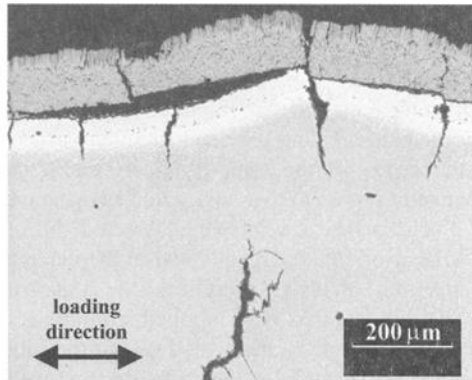


FIG. 11—Detachment of the coating induced by a propagating substrate crack during OOP testing.

In conclusion, it can be stated that in OOP tests, life was determined by a fatal fatigue crack emanating from the uncoated internal surface of the specimen, while cracks developed in the bond coat as well as delamination associated with the TGO were not lifetime controlling. Nevertheless, if fatigue cracking of the substrate could be inhibited, then failure would be induced by cracks emanating from the defects in the bond coat, highlighting the importance of the coating deposition methodology. Concerning the less severe loading conditions of the IP-TMF test, which was interrupted prior to failure after 2000 cycles, significant microstructural degradation of the TGO and of the bond coat owing to buckling and delamination at low temperature and void growth and oxide scale formation at high temperature was observed. By this thermal fatigue process, considerable damage accumulates, which is presumed to ultimately induce failure of the TBC system by spallation.

Influence of Substrate Microstructure

During the validation of the experimental setup, TMF tests were also performed in samples of MAR-M 509 substrate, with an overlay coating and a PS topcoat [21]. The TMF cycle applied in that study had a period of 3000 s. During the cycle the controlled substrate temperature was increased within 1100 s from 120 to 950°C, held at that temperature for 600 s and decreased within 1000 s down to 120°C (Fig. 12). At the end of each cycle a dwell time of 300 s at 120°C was applied. The TMF tests were carried out in three different mechanical strain ranges, $\Delta\varepsilon_{\text{mech}} = \varepsilon_{\text{max}} - \varepsilon_{\text{min}}$, namely 0.50 %, 0.85 %, and 1.00 %. Irrespective of the applied mechanical strain range during testing, failure analysis showed similar results for all samples. The samples failed within the gauge length, with the fracture surface oriented perpendicular to the loading axis. The fracture surfaces of the substrate revealed the presence of semi-elliptical features located at the inner

(uncoated) surface of the samples. These features are the oxidized crack flanks, which according to their size must have developed over a long period of time (several cycles) of the TMF test. The flanks of these cracks were smooth (marked as A in Fig. 13), indicating transgranular fracture, while the fracture surface outside the oxidized flanks was rough, revealing the dendritic microstructure of the substrate (B in Fig. 13). Finally, at the center of the semi-elliptical cracks, microstructural inhomogeneities were very frequently observed that have acted as the crack nucleation sites (see inset of Fig. 13).

Such surface cracks were detected throughout the inner surface of the substrate, invariably oriented perpendicular to the loading axis, although the density of these cracks decreased at distances away from the center of the gauge length, i.e., at locations where lower temperatures were applied during testing. While the examination revealed the presence of cracks at the coated side of the substrate, similar to the cracks observed at the uncoated inner surface, the crack density at the protected outer surface of the substrate was lower than the crack density at the inner surface. Furthermore, examination of polished cross sections in a sample tested at the same mechanical strain but subjected to only 90 cycles, revealed the presence of cracks only at the uncoated inner surface of the substrate (up to 350 μm in length). This indicates that the cracks at the inner surface form first, while the cracks at the protected surface develop at a later stage of testing.

The initiation of these surface cracks in the substrate is related with the presence of secondary phases, more specifically to MC-type carbides. For MAR-M 509 it is well established that the crack nucleation sites and preferred propagation paths are MC-type carbides [22]. The cracks propagate through the carbides, or along the carbide-matrix interface. It is interesting to note that carbides were fragmented even at locations ahead of the crack tip while the orientation of such carbide microcracks is not always perpendicular to the loading axis. These observations suggest brittle carbide fracture under the influence of the stress field ahead of the propagating crack (Fig. 14). Therefore, a crack grows by coalescence of microcracks developed in the carbides.

Finally, our analysis showed that the topcoat is rather damage tolerant, because transverse cracks were only rarely detected within the topcoat, despite tensile straining of the TBC system during cycling. It is interesting to note that these cracks did not penetrate into the bond coat but either stopped or were deflected upon reaching the topcoat-bond coat interface.

Based on these observations, the following failure mechanism is put forward. During loading at high temperatures, carbides at the free surface of the substrate in the inner part of the specimens oxidize and fragment under the influence of the applied tensile mechanical strain. These fragmented carbides act as crack initiation sites. Oxygen penetrates the cracks promoting further oxidation ahead of the crack tip. It is important to note that all of the crack initiation sites are located at the exposed surface of the substrate. The presence of the coating delays crack initiation and/or decelerates crack growth at the protected surface of the substrate, demonstrating the efficiency of the coating. In conclusion, the failure of the specimens is due to oxidation, crack nucleation and growth at the carbides at the inner, unprotected surface of the specimens.

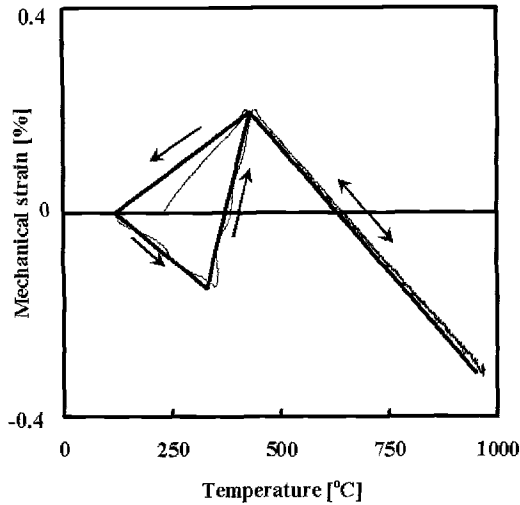


FIG. 12—Dependence of the mechanical strain on temperature during the TMF cycle. The thick line represents the target cycle and the thin line an experimental result for $\Delta\varepsilon_{mech} = 0.50\%$. (Arrows indicate the direction of the cycle.)

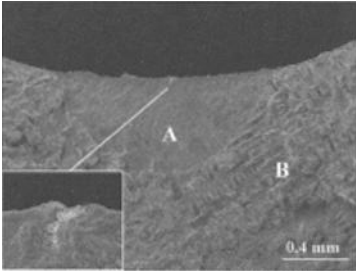


FIG. 13—Fracture surface at the inner surface of a sample tested until failure with $\Delta\varepsilon_{mech} = 0.50\%$, exhibiting an oxidized semi-elliptical crack flank. The detail inset shows that the fracture has started at an inhomogeneity (brighter contrast). The transgranular fracture surface is indicated by A and the interdendritic fracture surface by B.

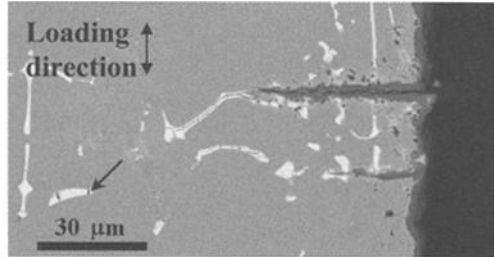


FIG. 14—Longitudinal section of a sample TMF tested for 90 cycles with $\Delta\varepsilon_{mech} = 0.85\%$. The oxidized cracks, perpendicular to the mechanical loading direction and to the inner sample surface, are following the morphology of MC carbides. Small cracks also develop inside the MC carbides, even ahead of the main crack tip, a possible result of the stress field ahead of the crack tip (arrow).

Closure

This investigation has demonstrated that there is a plethora of damage mechanisms that can be activated during TMF testing of TBC systems, highlighting the importance of selecting the proper testing conditions in order to activate and study those mechanisms that are responsible for the failure of TBCs in service. Furthermore, it has been demonstrated that it is difficult to simulate loading conditions that lead exclusively to spallation. The importance of the applied mechanical strain range and the phase angle has been highlighted for the investigated systems. A high mechanical strain range and out-of-phase loading are the least likely conditions to promote failure by delamination. Although there is strong evidence that spallation can result from in-phase loading when a small mechanical strain range is applied, the duration of such tests is too long to be practical. It must also be noted that, the substrate's performance, although usually neglected in related studies, may also play an important role as it can be the weakest component in a TBC system, as was demonstrated in our study using the MAR-M509 alloy as substrate.

Acknowledgments

Part of this work has been carried out within the Commission Research and Development program. The authors would like to acknowledge the discussions with H. Müllejans and B. Baufeld and the technical assistance of F. de Haan.

References

- [1] Stringer, J., "The Role of the Coating and Superalloy System in Enabling Advanced Land-Based Combustion Turbine Development," *Gas Turbine Materials Technology, Conference Proceedings from Materials Solutions '98*, Rosemont, IL, Oct. 1998, pp. 3–12.
- [2] Miller, R. A., "Current Status of Thermal Barrier Coatings—An Overview," *Surface and Coatings Technology*, Vol. 30, 1987, pp. 1–11.
- [3] Goward, G. W., "Progress in Coatings for Gas Turbine Airfoils," *Surface and Coatings Technology*, Vol. 108-109, 1998, pp. 73–79.
- [4] Tzimas, E. and Peteves, S. D., "Protective Coatings: A Contribution Towards Sustainable Energy," *13th International Symposium for Ultra High Temperature Materials*, Tajimi, Japan, 6–7 Sept. 2001, pp. 92–106.
- [5] Bartlett, A. and Dal Maschio, R., "Failure Mechanisms of Zirconia-8% Ytria Thermal Barrier Coating," *Journal of the American Ceramic Society*, Vol. 78, No. 4, 1995, pp. 1018–1024.
- [6] Haynes, J. A., Ferber M. K., Porter W. D., and Rigney E. D., "Characterization of Alumina Scales Formed during Isothermal and Cyclic Oxidation of Plasma Sprayed TBC Systems at 1150°C," *Oxidation of Metals*, Vol. 52, No. 1/2, 1999, pp. 31–76.
- [7] DeMasi-Marcin, J. T., Sheffler, K. D., and Bose, S., "Mechanisms of Degradation and Failure in a Plasma-Deposited Thermal Barrier Coating," *Journal of Engineering for Gas Turbines and Power*, Vol. 112, 1990, pp. 521–526.
- [8] Nissley, D. M., "Thermal Barrier Coating Life Modeling in Aircraft Gas Turbine Engines," *Journal of Thermal Spray Technology*, Vol. 6, No. 1, 1997, pp. 91–98.
- [9] Qian, G., Nakamura, T., Berndt, C. C., and Leigh, S. H., "Tensile Toughness Test

- and High Temperature Fracture Analysis of Thermal Barrier Coatings,” *Acta Materialia*, Vol. 45, No. 4, 1997, pp. 1767–1784.
- [10] Newaz, G. M., Nusier, S. Q. and Chaudhury, Z. A., “Damage Accumulation Mechanisms of Thermal Barrier Coatings,” *Journal of Engineering Materials and Technology*, Vol. 120, 1998, pp. 149–153.
- [11] Cheng, J., Jordan, E. H., Barber, B., and Gell, M., “Thermal/Residual Stress in an Electron Beam Physical Vapor Deposited Thermal Barrier Coating System,” *Acta Materialia*, Vol. 46, No. 16, 1998, pp. 5839–5850.
- [12] Sergo, V. and Clarke, D. R., “Observation of Subcritical Spall Propagation of a Thermal Barrier Coating,” *Journal of the American Ceramic Society*, Vol. 81, No. 12, 1998, pp. 3237–3242.
- [13] DeMasi-Marcin, J. T., Sheffler, K. D., and Ortiz, M., “Thermal Barrier Coating Life Prediction Model Development, Phase I,” Final Report, NASA CR-182230, 1989.
- [14] Tzimas, E., “Lifing Aspects and Mechanical Reliability of Thermal Barrier Coatings,” Final Report, European Commission, DG-JRC, Institute for Advanced Materials, Petten, The Netherlands, June 2000.
- [15] Wright P. K., “Influence of Cyclic Strain on Life of a PVD TBC,” *Materials Science and Engineering A*, Vol. 245, 1998, pp. 191–200.
- [16] Annigeri, R., DiMascio, P. S., Orenstein, R. M., Zuiker, J. R., Thompson, A. M., Lorraine P. W., et al., “Life Assessment of Thermal Barrier Coatings for Gas Turbine Applications,” *ASME Turbo Expo 2000*, Munich, Germany, 8–11 May 2000, 2000-GT-580.
- [17] Bartsch, M., Marci, G., Mull, K., Sick, C., “Fatigue Testing of Ceramic Thermal Barrier Coatings for Gas Turbine Blades,” *Advanced Engineering Materials*, Vol. 1, 1999, pp. 127–129.
- [18] Zhang, Y. H., Withers, P. J., Fox, M. D., and Knowles, D. M., “Damage Mechanisms of Coated Systems under Thermomechanical Fatigue,” *Materials Science and Technology*, Vol. 15, 1999, pp. 1031–1036.
- [19] Tzimas, E., Müllejans, H., Peteves, S. D., Bressers, J., and Stamm, W., “Failure of Thermal Barrier Coating Systems under Cyclic Thermomechanical Loading,” *Acta Materialia*, Vol. 48, 2000, pp. 4699–4707.
- [20] Baufeld, B., Tzimas, E., Hähner, P., Müllejans, H., Peteves, S. D., and Moretto, P., “Phase - Angle Effects on Damage Mechanisms of Thermal Barrier Coatings under Thermomechanical Fatigue,” *Scripta Materialia*, Vol. 45, No. 7, 2001, pp. 859–865.
- [21] Baufeld, B., Tzimas, E., Müllejans, H., Peteves, S. D., Bressers, J., and Stamm, W., “Thermal-Mechanical Fatigue of MAR-M 509 with a Thermal Barrier Coating,” *Materials Science and Engineering A*, Vol. 315, No. 1-2, 2001, pp. 231–239.
- [22] Reuchet, J. and Remy, L., “Fatigue Oxidation Interaction in a Superalloy—Application to Life Prediction in High Temperature Low Cycle Fatigue,” *Metallurgical Transactions*, Vol. 14 A, 1983, pp. 141–149.

Thermo-mechanical Creep-Fatigue of Coated Systems

REFERENCE: Rémy, L., Alam, A. M., and Bickard, A., “**Thermo-mechanical Creep-Fatigue of Coated Systems**” *Thermomechanical Fatigue Behavior of Materials: 4th Volume, ASTM STP 1428*, M. A. McGaw, S. Kalluri, J. Bressers, and S. D. Peteves, Eds., ASTM International, West Conshohocken, PA, Online, Available: www.astm.org/STP/1428/1428_10593, 16 Dec. 2002.

ABSTRACT: This paper presents an investigation of the damage mechanisms in protective coatings deposited on a single crystal superalloy, under TMF (thermo-mechanical fatigue) loading conditions. This includes an aluminide coating called C1A and a Thermal Barrier Coating (TBC). Different TMF cycles are used to assess the coating resistance in both cases and respective damage mechanisms are reported. TMF cycles derived from real service conditions prove to be better testing methods for coating resistance as compared to standard cyclic oxidation tests without mechanical loading. Implications for lifing procedures are tentatively discussed from the results of this investigation.

KEYWORDS: aluminide coatings, thermal barrier coatings, thermo-mechanical fatigue

Introduction

Blades and vanes in aeroengines as in land-based gas turbines are usually protected against oxidation and corrosion using aluminide coatings deposited by CVD technique or overlay MCrAlY coatings deposited by plasma – spray [1]. The presence of these coatings is often ignored in component design. Thermal barrier coatings (TBC) are used in advanced turbines to increase the turbine entry temperature when the temperature capability of the alloy comes to a limit. In this case coating integrity is a key issue in the life of component: coating spallation results in a large temperature increase in alloy substrate, which is detrimental for the overall component integrity.

Coating resistance is usually assessed using oxidation or cyclic oxidation tests on different kinds of specimens. Under service conditions however, coatings are experiencing cyclic oxidation under stress (due to centrifugal load) as well as thermal transients. Thermo-mechanical creep – fatigue using hold times under load is especially appropriate to assess damage of coated systems under realistic conditions. The present paper reports such an investigation using a single crystal superalloy AM1 used by SNECMA [2]. Two types of coatings were studied under different loading conditions: first, an aluminide coating, which is part of an-going work and second, a TBC, which was investigated in a thesis work completed three years ago [3].

¹ Director of Research, CNRS. Centre des Matériaux, P. M. Fourt, UMR CNRS 7633, ENSMP (École Nationale Supérieure des Mines de Paris), P.O Box 87, 91003 Évry Cédex France.

² Now with ALSTOM (Power), Brown Boveri Strasse 7, CH-5401 Baden AG Switzerland.

³ Presently with CRYOSTAR France ZI - BP 48, 68220 Hesingue, France.

Materials and Experimental Procedure

Material and Coatings

AM1 is a single crystal superalloy used for HPT (High Pressure Turbine) blades of SNECMA aircraft engines. Its chemical composition is given in Table 1.

Table 1—*Chemical composition (in Wt. %) of AM1.*

	Ni	Co	Cr	Mo	W	Ta	Al	Ti	C	Fe	S
Min	bal.	6	7	1,8	5	7,5	5,1	1			3ppm
Max	bal.	7	8	2,2	6	8,5	5,5	1,4	0,01	0,2	

At first, the C1A coating is elaborated by a chromium deposition and then a Nickel Aluminide (NiAl) deposition on the substrate's surface, through Chemical Vapour Deposition (CVD) process. After going through suitable heat treatments, the coating in its final state is composed of two distinct layers, as shown in Fig. 1.

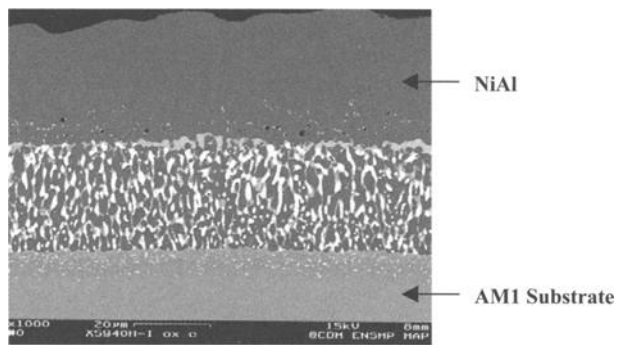


FIG. 1—SEM image using Back Scattered Electrons, of a polished section of C1A coating on AM1 substrate.

The external layer is of Nickel Aluminide (NiAl) in the form of (dark gray) β phase of fcc (face centered cubic) structure; whereas the internal layer contains precipitates rich in chromium, cobalt, molybdenum, titanium and tungsten.

The Thermal Barrier Coating is manufactured by electron beam physical vapor deposition (EBPVD) of yttria partly stabilized zirconia on a platinum modified nickel aluminide bondcoat. The chemical composition of the bondcoat is fairly similar to that of the C1A coating except for the presence of platinum [4]. The external layer near zirconia is β (NiAl) phase and the internal layer near substrate is a mixture of β (NiAl) phase and precipitates, which are enriched in heavy elements coming from the substrate. Platinum-modified aluminide coatings have an enhanced resistance to oxidation and corrosion, but the presence of platinum-rich precipitates lowers their ductility. EBPVD confers a well-known columnar structure to the partly stabilized zirconia that improves its resistance to transverse cracking. A small layer of alumina is present from the initial condition at the interface between partly stabilized zirconia and bondcoat.

Thermomechanical Fatigue Testing

A thermomechanical fatigue facility developed in our laboratory has been used, and a more complete description can be found in previous references [5,6]. Test control and monitoring is made using a homemade program written under Labview [6]. Hollow cylindrical specimens were machined from <001> cast single crystal cylinders 20 mm in diameter: specimen geometry is the same as for previous work on superalloys with an 11 mm outer diameter and a 1 mm wall thickness. The temperature is constant within 5°C on the extensometer gage length (of 10 mm). A four bulb lamp furnace is used for heating and forced air cooling enables a minimum temperature of 100°C. A constant temperature rate of 5°C/s was used for transients and temperature holds of 5 min were used. Temperature control can be quite a problem for TBC and a metal temperature is used to define the thermal cycle. An internal spot welded thermocouple was used to define the temperature input of the microcomputer to the temperature controller. A maximum metal temperature of 1050°C was used for CIA coated specimens; it was 1100°C for specimens with TBC. A longitudinal extensometer is used to impose mechanical strain in creep-fatigue tests on TBC specimens or to monitor strain in stress-controlled tests on CIA specimens.

CIA coated specimens were coated both on external and internal surfaces. TBC specimens were coated on the outer surface but the internal surface was aluminized to prevent excessive oxidation, as in previous investigations under thermal-mechanical fatigue without hold times [7,8]. Damage in the substrate was monitored using potential drop measurements. Damage in the coatings was mostly studied in a destructive manner using observations on outer surfaces and specimen sections, mostly longitudinal ones. These observations were carried on tests conducted to failure or on tests interrupted after a chosen fraction of expected number of cycles to failure or to spallation of coating. Failure was defined when a crack, nucleating mostly from external surface grew throughout specimen wall thickness (CIA coated specimens), as can be detected by potential drop measurements. Tests on TBC coated specimens were stopped at coating spallation, and checked by optical inspection after test interruption (macroscopic spall a few mm in mean diameter). A high resolution scanning electron microscope with a field emission gun (FEG) was used in this investigation and proved to be effective, especially for observing interface defects on TBC.

CIA Coated AM1 Superalloy*Cyclic Oxidation Tests*

A standard practice normally used in the industry for assessing the coating resistance is either static or cyclic oxidation tests. Figure 2 presents one of these cycles used at SNECMA.

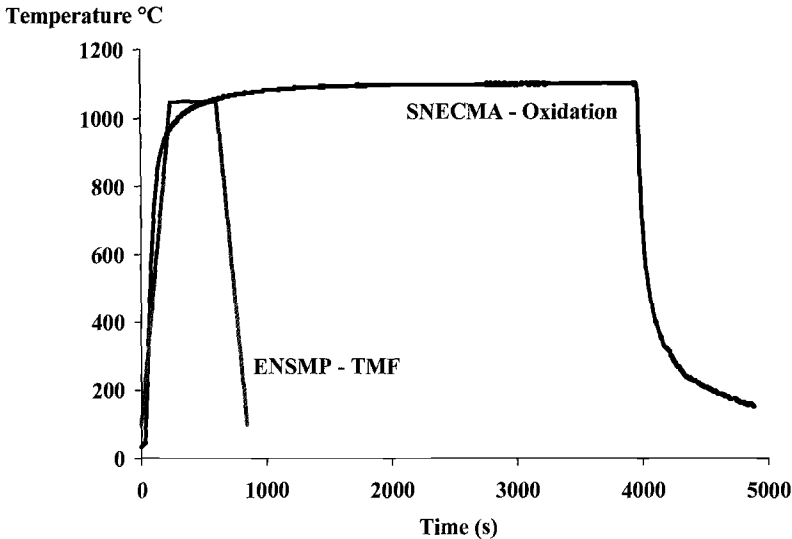


FIG. 2—Thermal cycles, the one used at SNECMA for coating resistance testing and the other one corresponding to the TMF tests at the ENSMP.

The thermal cycle used at SNECMA ranges between 100 and 1050°C and the hold time at 1050°C is 1 h. Insertion and removal of the test specimen from the furnace does the heating and cooling, respectively. For comparison with this cycle, we can note a thermal cycle used at the ENSMP as a part of the TMF cycles. This cycle has constant heating and cooling rates of 5°C/s and a hold time of 5 min at 1050°. The latter is derived from real loading conditions as experienced by a HPT blade at around 30% of its span. We can thereby notice that even the thermal part of real TMF cycles is much different from the cyclic oxidation cycles used for the assessment of coating resistance. The coating damage resulting from these cycles is quite different as well. Figure 3 shows the examples of coating damages after testing under these two cycles. Figure 3a presents an SEM image of the coating after 600 conventional oxidation cycles. Figure 3b presents another SEM image of the coating after 2000 TMF like cycles of ENSMP. We can observe that in the case of TMF like thermal cycle, a considerable part of the coating (dark gray) β NiAl phase has been transformed to (light gray) γ' Ni₃Al phase. This transformation occurs due to aluminum consumption through oxidation and diffusion. In the case of Fig. 3a however, only a little presence of the γ' phase can be noticed at the grain boundaries although the time of exposure at the highest temperature is much greater in this test. We can say that the TMF like thermal cycle is more harmful to the C1A coating as compared to the conventional oxidation cycle.

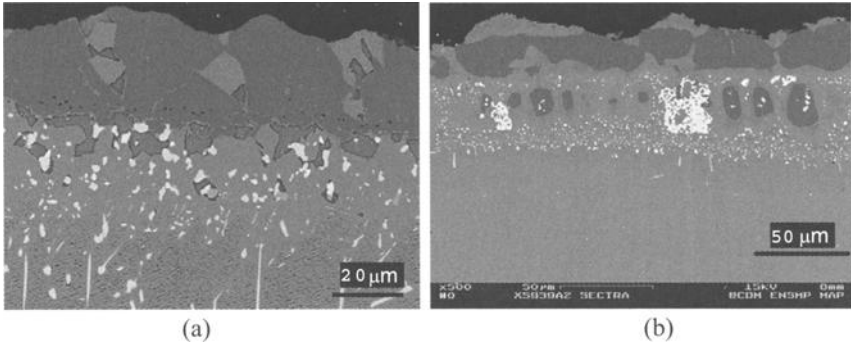


FIG. 3—CIA coating damage after cyclic oxidation tests. (a) SNECMA cycle 60 min hold time, 600 h at 1050°C, 600 cycles; (b) ENSMP, TMF like cycle 5 min hold time, 167 h at 1050°C, 2000 cycles.

Thermo-Mechanical Creep-Fatigue Tests

In real service, however, turbine blades are exposed to severe mechanical stress variations due to centrifugal forces, in time with strong temperature transients. Figure 4 represents an experimental TMF cycle derived from real service conditions at 30% height of an HPT blade. The so-called "Butterfly" cycle also contains a dwell time of 5 min at the highest temperature 1050°C and under 100 MPa stress. The temperature cycle alone is also drawn for comparison.

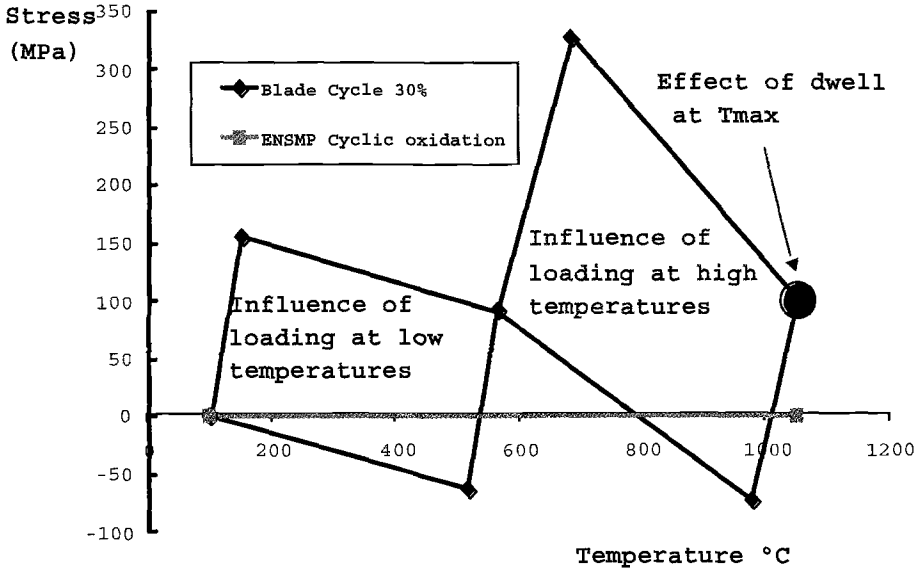


FIG. 4—Representation on a Stress-Temperature graph of an experimental TMF cycle (Butterfly cycle) and of the TMF like oxidation cycle used at ENSMP.

Different variants of the Butterfly cycle can be imagined in order to investigate the influence of various segments of a cycle on the damage of the coating. Figure 5 presents typical surface and subsurface damages of the coating after a TMF test using Butterfly cycle.

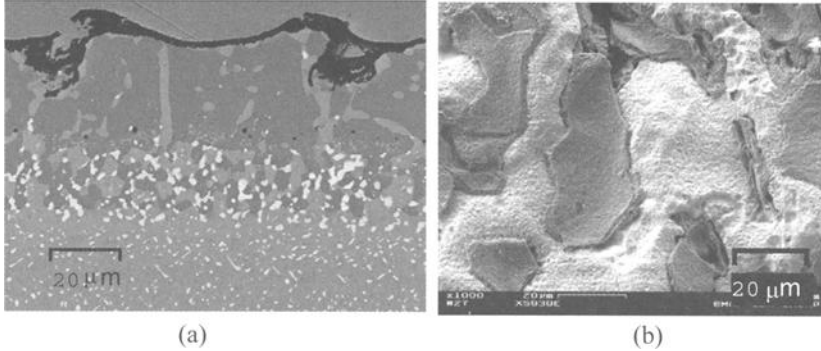


FIG. 5—Typical coating damage after TMF testing. (a) subsurface damage; (b) surface damage.

Figure 5b presents an SEM image of the surface of a test specimen after a Butterfly type TMF test (near 850 cycles). We can notice spalled (dark gray) aluminum oxide layer and underneath it, a white coating layer containing βNiAl , but also some Chromium, Cobalt, and Titanium diffused from the substrate. Figure 5a shows the image of a polished section of the same test specimen. We can observe many damage processes here, such as $\beta\text{-}\gamma'$ phase transformation, intergranular diffusion, increase of surface roughness and of course, aluminum consumption as a result of all these phenomena. Analyzing Figs. 3 and 5, we can see that the mechanisms of coating damage change with respect to the loading cycles. TMF cycles usually enforce more intergranular oxidation and phase transformations. They result also in rapid increase of the surface roughness. A few interesting questions arise from the experimental results we've just seen. How do different cycle segments damage the coating system? What is the role of loading at high or at low temperatures, and how does the dwell period affect the coating resistance? In these tests, the objective was to determine the degradation kinetics of the coating under different loading cycles, therefore tests were not run to the failure of specimens. No fatigue cracks from internal surfaces were observed.

TMF Cycles enhancing Alumina Scale Spallation in Aluminate Coating

We understand that the damage process in our case is a slow and steady process. The aluminum oxide (Al_2O_3) layer formed at high temperature tends to spall off locally when the compressive stresses increase at cooling due to difference of thermal expansion coefficients in the βNiAl and Al_2O_3 . This accelerates the oxidation process, which in turn uses the aluminum of the external layer, thereby pumping the aluminum out of the βNiAl reservoir. Now in order to understand the role of different cycle segments, we can imagine TMF cycles that accelerate the alumina scale spallation, and hence, quicken the damage process of the coating. Figure 6 presents two such cycles.

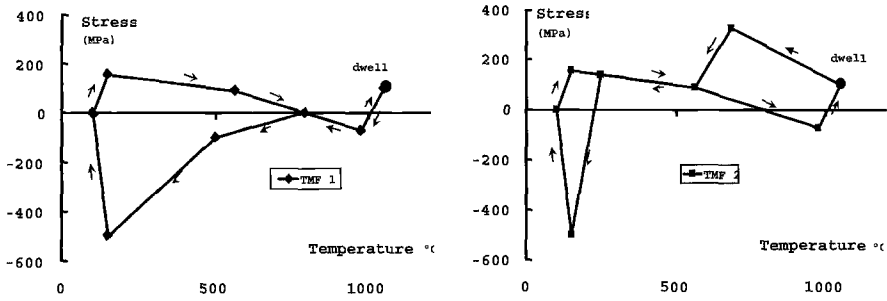


FIG. 6—Two special TMF cycles, forcing alumina scale spallation.

Both the TMF cycles presented in Fig. 6 have a part in common with the Butterfly cycle, i.e., the mechanical loading path while heating and during dwell period. At cooling however, the TMF1 cycle differs from the TMF2 in that it does not go towards high tensile stress and instead comes down towards compression. It then continues to follow the compressive stress direction reaching ultimately -500 MPa at around 170°C. Unlike TMF1 cycle, the TMF2 cycle evolves towards high tensile stresses after the dwell period and then reaches the -500 MPa compressive stress at nearly 170°C. The two TMF tests using TMF1 and TMF2 cycles were continued to approximately 825 cycles. Figure 7 presents two micrographs of coatings, corresponding to the two tested specimens.

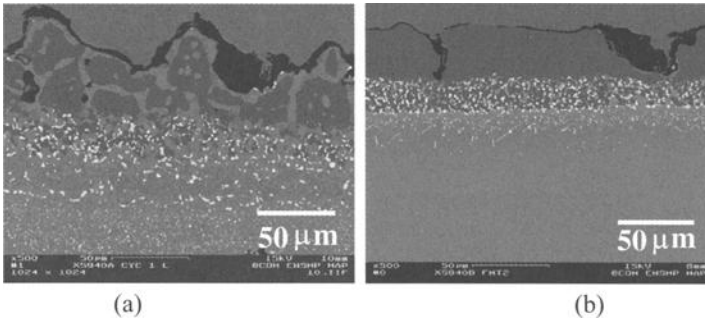


FIG. 7—SEM images of the coatings after 825 TMF cycles. (a) TMF1; (b) TMF2.

Figure 7a presents an SEM image of the coating after a test using TMF1 cycle. Observe that the coating is heavily damaged. There is severe phase transformation at the grain boundaries, but also inside the grains. The diffusion process seems to go deep down into the substrate as we can see those white precipitates covering all the lower part of the micrograph. The surface roughness has tremendously increased due to formation of crests and troughs. In case of the test with TMF 2 cycle, however, the damage process is much different. Here there is no heavy phase transformation and no deep diffusion zone into the substrate. The surface roughness has increased to some extent due to intergranular oxidation, but it remains quite localized.

This comparison shows that small differences in the shapes of thermo-mechanical cycles can lead to significant variations in the extents of coating damage. In the present case, this variation can be explained: loading path of the cycle at high temperature is particularly important, especially while cooling. When we cool down from the highest temperature, it results in

compressive stresses on the alumina scale due to the differences in thermal expansion coefficients. In the case of the TMF1 cycle, we compress the specimen after the dwell period, thereby adding to the compressive stresses. In the case of the TMF2 cycle, on the contrary, we increase the tensile stress on the specimen after the dwell period, which counter balances the thermally generated compressive stresses.

Quantifying Coating Damage

In a bid to formulate a model of engineering interest in taking care of coating damage for the lifetime evaluation of turbine blade material, we need to quantify this damage and determine its kinetics. Two prominent characteristics of this damage that can be evaluated easily are modification of the surface topography and reduction of the aluminum content in the external-coating layer.

Surface Roughness

In order to determine the kinetics of surface roughness modification, we need to perform interrupted tests at predetermined cycle intervals, and measure surface roughness. Moreover, we need to differentiate this kinetics between cyclic oxidation tests without mechanical stresses and TMF cycles. For this purpose, we chose to carry out interrupted tests with TMF1 cycle on one hand and TMF like cyclic oxidation cycle on the other. The values of surface roughness R_a (μm), the arithmetical mean of the surface unevenness, are calculated on the SEM micrographs of polished sections. Each value is averaged over 10 different micrographs of every specimen. These results are presented in Fig. 8. The surface roughness of as-coated specimens was not measured because of the scarcity of the material, but as indicated by the trend curves, untested specimens have a very low surface roughness of the order of $R_a = 2 \mu\text{m}$. Trend curves are drawn by fitting power functions to the data points using commercial software.

Figure 8 presents two curves of R_a vs Number of test cycles. It can be noticed that the TMF 1 curves exhibit a steep rise in the beginning and continues to progress even after at a rate higher than that in cyclic oxidation curve.

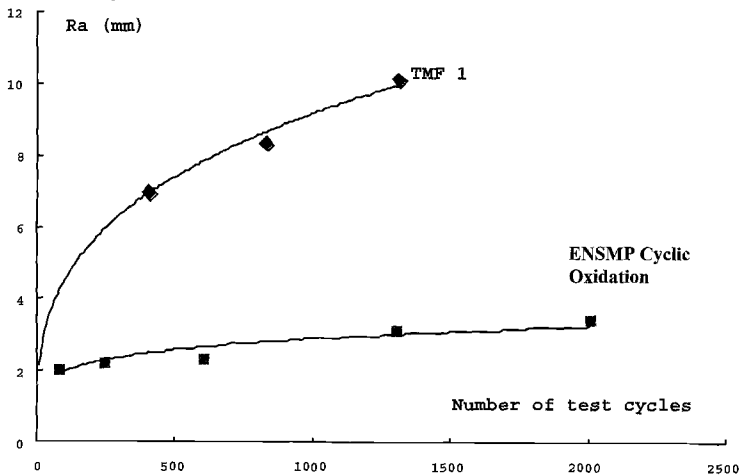


FIG. 8—Evolution of surface roughness as a function of number of cycles in case of TMF 1 test and TMF like cyclic oxidation test.

This abrupt rise of the surface roughness can be explained on the basis of microscopic observations. Figure 9 presents an SEM micrograph captured with the help of secondary electrons and which shows the presence of unstable oxides in case of TMF1 tests.

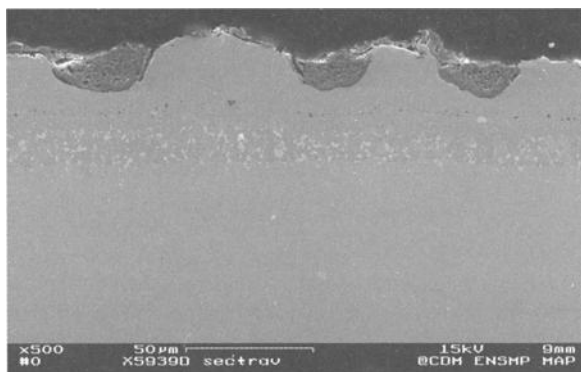


FIG. 9—Secondary electrons micrograph of a polished section of a specimen having undergone a TMF test.

As we can observe in Fig. 9, relatively huge amounts of unstable oxides have formed just after 200 cycles of the test. These oxides are porous in nature and can easily be ejected with the application of stresses. The origin of this rapid growth of oxides is not known perfectly, but this seems to be the major cause of surface roughness increase in the TMF case. In case of cyclic oxidation however, this is not observed; the slight increase of roughness is mainly due to local uneven oxidation, etc. The formation of oxides is more superficial and homogenous.

Aluminum Consumption

Another important parameter devised for the evaluation of coating damage is aluminum consumption. As we know, the external-coating layer constitutes a significant reservoir of aluminum that can form stable Al_2O_3 oxides and slow down further oxidation through passivation. But if the aluminum content decreases through a steady damage process, then the protective quality of the coating shall be diminished.

In order to evaluate the aluminum consumption, we measure the surface fraction of different material phases present in the external layer (β , γ , voids and other diffused elements, etc). Then, knowing the atomic percentage of aluminum in every phase, we can easily determine the atomic percentage of aluminum in the reservoir. Finally, by comparing this percentage with an untested specimen, we can estimate the percentage of the consumed aluminum content. The same is presented in Fig. 10 for a TMF 1 case and a TMF like cyclic oxidation case as a function of number of cycles.

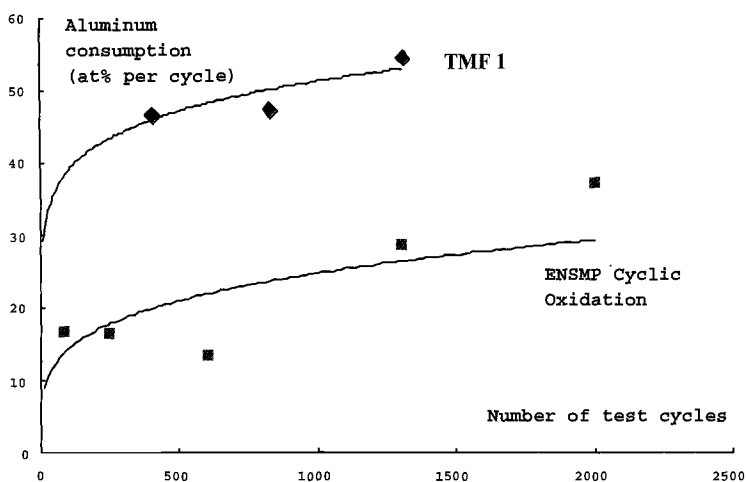


FIG. 10—Evolution of the aluminum consumption, as a function of number of cycles.

Once again it is clear that the initial aluminum consumption rate in TMF1 is much higher than that in the cyclic oxidation case. Past this initial rise, the rate of aluminum consumption in both tests is quite similar.

TB Coated AM1 Superalloy

Thermo-Mechanical Creep-Fatigue Test

The various investigations of life to spalling of the Thermal Barrier Coating have been conducted under isothermal oxidation or under cyclic oxidation tests, which are felt to be more representative of service loading. These spalling mechanisms are dependent on the nature of TBC. Plasma spray deposited zirconia failed internally even near the interface with bondcoat, due to the presence of numerous defects in the ceramics. EBPVD failed mostly at the interface with bondcoat due to the growth of alumina, since the columnar and defect structure of the ceramics allows easy transport of oxygen at the bondcoat interface. This thermally grown oxide (TGO) is considered as the major cause for spalling of TBC under service. The system AM1- EBPVD partly stabilized zirconia has been reported to delaminate along the alumina-bondcoat interface when tested after isothermal oxidation. A few results have been reported previously concerning the low-cycle fatigue behavior at 1100°C, using either triangular wave-shape or strain hold cycles [4].

A TMF cycle has been defined to simulate approximately the behavior of a critical area of a blade, at the leading edge. This cycle is depicted Fig. 11. The same hold time was used for 300 s as for the CIA aluminide coating, for a metal temperature of 1100°C. A V shape was used for the mechanical strain versus metal temperature cycle: the high temperature segment is in-phase while the low temperature segment is out-of phase.

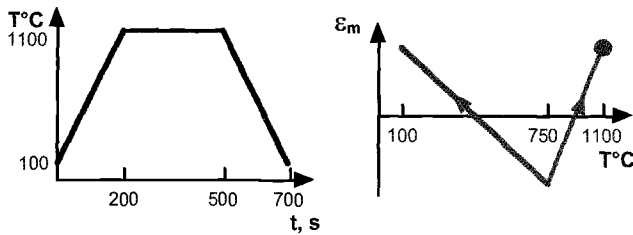


FIG. 11—Representation of Strain-Temperature and Temperature-Time graph of the experimental TMF cycle used for TBC testing.

After completion of this study, the authors discovered that Wright [9] investigated the behavior of a TBC on Rene N5 using a fairly similar thermal cycle but under pure cyclic compression strain cycles in phase or out of phase with temperature.

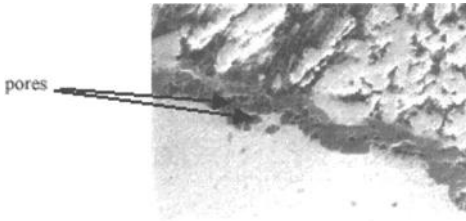


FIG. 12—Nucleation of pores in the alumina scale formed at bondcoat/zirconia interface after 10% of expected life to spallation.

Damage Evolution in Thermo-Mechanical Creep-Fatigue Tests

Such tests were conducted for a given mechanical strain amplitude for different number of cycles. Different specimens were conducted to spalling of the TBC and to different fractions of lifetime to spalling say about 10, 20, 40, and 50 %. Observations were made on longitudinal sections to investigate damage near the TGO between the nickel aluminide layer and the zirconia. After 10 % of expected life to spalling, only cavities are nucleated inside the alumina layer (Fig. 12).

For a longer duration, there is a large variation in damage. For a number of cycles corresponding to 20 % of expected life to TBC spallation, transverse cracks are observed in the bondcoat, which seem to initiate from the TGO-bondcoat interface and which are heavily oxidized. Some of them are arrested at the interface between substrate and interdiffusion layer and show branches in this layer (Fig. 13). The defects in the TGO grow substantially to small delaminated areas in the middle of the alumina layer mostly, but near the columnar grains of zirconia too. Some areas show decohesion at the interface between bondcoat and alumina, but much less frequently.

When the test is conducted to spalling, there is no significant modification in damage mechanisms. Variations are only quantitative. Cavities grow larger in the TGO and the oxidized transverse cracks are much more numerous in the bondcoat. Delaminated areas in the TGO are larger too. Figure 14 shows the edge of the spalled

area on a longitudinal section. Spalling has presumably occurred after buckling and the ceramic topcoat which remains adherent at the macroscopic level to the substrate shows de-lamination at a significant distance of the spalled area. This behavior is consistent with usual schemes proposed for spalling [10].

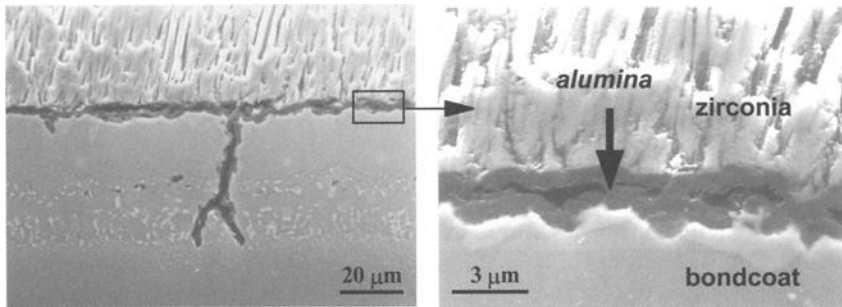


FIG. 13—Transverse crack in the bondcoat and internal pores and defects in the alumina scale formed at bondcoat /zirconia interface after 20% of life to spallation.

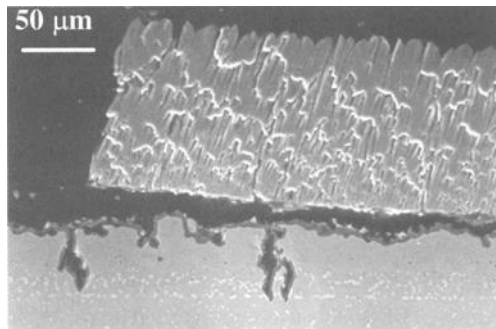


FIG. 14—Section at the edge of the spalled TBC zone in a test conducted to spallation. Transverse oxidized cracks are more numerous and delamination occurs preferentially within the alumina scale.

These observations show that spalling mechanisms for such a thermo-mechanical loading path are strongly different from those in isothermal oxidation [3], or even cyclic oxidation. For this TBC system on AM1, the bondcoat-TGO interface was the weakest interface after oxidation without superimposed load. Thermo-mechanical creep-fatigue favors damage inside the thermally grown oxide, as well as transverse cracking in the nickel aluminide layer. Transverse cracking is obviously associated with the tensile peak strain, which occurs at low temperature since nickel aluminide coatings are known to exhibit a very low ductility below 600-700 °C, depending upon composition [1,11-13]. On the higher temperature part of the TMF cycle, the bondcoat oxidizes and exhibits extensive visco-plasticity. The stress concentrations at the interface are relaxed during exposure at high temperature. This nucleation of transverse cracks due to the low ductility of the bondcoat favor energy dissipation and may explain the fact that

delamination at the TGO-bondcoat interface is much less favored under thermo-mechanical creep fatigue than under oxidation tests.

It is worth emphasizing that the same observations were made on components that have been exposed to service conditions for the same TBC system on AM1 superalloy. This shows that if actual service loading can be properly estimated, laboratory tests with a representative TMF cycle can be used to simulate actual damage and mechanisms occurring in components.

Conclusions

Thorough experimental work has been conducted using thermal-mechanical creep-fatigue tests to understand basic physical mechanisms taking part in the damage of protective coating on AM1 single crystal superalloy turbine blades.

Stress-controlled TMF tests were used for AM1 single crystals coated with C1A aluminide. Critical segments of thermo-mechanical fatigue cycles responsible for severe coating damage have been identified. They are during transients, compressive loading during the initial cooling from maximum temperature, in the high temperature loading part, compressive loading at low temperature, and tensile loading during dwell periods at high temperature.

Thermal-mechanical fatigue like cyclic oxidation tests prove to be very economical and effective when investigating high cycle operations. They cannot completely substitute to thermal-mechanical fatigue due to the absence of superimposed load but they are much more appropriate than conventional cyclic oxidation tests.

Interrupted tests have been carried out to determine the damage evolution with an increasing number of cycles. For the C1A aluminide coating, surface roughness and aluminium loss have been quantified. For the Thermal Barrier Coating deposited by EBPVD, defects were found to nucleate and grow under thermal-mechanical creep fatigue. The evolution of defects influences the occurrence of spalling.

Thermal-mechanical fatigue can be used to simulate the laboratory actual damage and damage mechanisms occurring in components, provided fairly good estimation of service cycles are available. Detailed observations of damage in such tests can provide the basis for the development of engineering models for the destruction of the aluminum tank, as for C1A coating, or spallation of thermal barrier coatings.

Acknowledgments

The authors are grateful to SNECMA Moteurs for financial support of this work, and for the supply of coated single crystal specimens. Discussions with engineers from the Materials and Process Department as well as from the Mechanical Engineering Department have been very instrumental in this study.

References

- [1] Duret-Thual, C., Morbioli, R., and Steinmetz, P., "A Guide to the Control of High Temperature Corrosion and Protection of Gas Turbine Materials," Report EUR 10682 EN CEC, Luxembourg, 1986.
- [2] Guédou, J.-Y. and Honnorat, Y., "Thermomechanical Fatigue of Turbo-Engine Blade Superalloys," *Thermomechanical Fatigue Behavior of Materials*, ASTM STP 1186,

- H. Sehitoglu, Ed., ASTM International, West Conshohocken, PA, 1993, pp. 157-175.
- [3] Bickard, A., Ph. D. Thesis, Ecole des Mines de Paris, 1998.
- [4] Bickard, A. and Rémy, L., "High Temperature Fatigue Behavior of a Thermal Barrier Coating on a Single Crystal Superalloy," Conference at Edinburgh, 23-25 Sept. 1997, *Proceedings of the 6th International Conference on High Temperature Surface Engineering*, J. R. Nicholls, D. S. Rickerby, and D. Allen, Eds., The Institute of Materials, London, 2000, pp. 183-198.
- [5] Malpertu, J. L. and Rémy, L., "Influence of Test Parameters on the Thermal-Mechanical Fatigue Behavior of a Superalloy," *Metallurgical Transactions A*, Vol. 21A, 1990, pp. 389-399.
- [6] Koster, A., Fleury, E., Vasseur, E., and Rémy, L., "Thermal-Mechanical Fatigue Testing," *Automation in Fatigue and Fracture: Testing and Analysis, ASTM STP 1231*, C. Amzallag, Ed., ASTM International, West Conshohocken, PA, 1994, pp. 563-580.
- [7] Bernard, H. and Rémy, L., "Advanced Materials and Process," *EUROMAT 89*, H. E. Exner and V. Schumacher, Eds., DGM, Oberursel, Vol. 1, 1990, pp. 529-534.
- [8] Chataigner, E. and Rémy, L., "Thermomechanical Fatigue Behavior of Coated and Bare Nickel-Based Superalloy Single Crystals," *Thermo-mechanical Fatigue Behavior of Materials: 2nd Volume, ASTM STP 1263*, M. J. Verrilli and M. G. Castelli, Eds., ASTM International, West Conshohocken, PA, 1996, pp. 3-23.
- [9] Wright, P. K., *Materials Science and Engineering*. Vol. 16, 1975, pp. 5-43.
- [10] Evans, A. G. and Hutchinson, J. W., *International Journal of Solids and Structures*, Vol. 20, 1984, pp. 455-466.
- [11] H. Bernard, L. Rémy, "Ductile-Brittle Transition of an Aluminide Coating on IN100 Superalloy," High Temperature Materials for Power Engineering 1990 Conference, Liege, 24-27 September 1990, *Proceedings*, E. Bachelet, R. Brunetaud, D. Coutouradis, et al., Eds., Kluwer Academic Publishers, Dordrecht, The Netherlands, Part II, pp. 1185-1194.
- [12] Bressers, J., Timm, J., Williams, S., Bennett, A., and Affeldt, E., "Effects of Cycle Type and Coating on the TMF Lives of a Single Crystal Nickel Based Gas Turbine Blade Alloy," *Thermo-mechanical Fatigue Behavior of Materials: 2nd Volume, ASTM STP 1263*, M. J. Verrilli and M. G. Castelli, Eds., ASTM International, West Conshohocken, PA, 1996, pp. 56-67.
- [13] Rémy, L., Koster, A., Chataigner, E., and Bickard, A., "Thermal-Mechanical Fatigue and the Modelling of Materials Behaviour Under Thermal Transients," *Thermo-mechanical Fatigue Behavior of Materials: Third Volume, ASTM STP 1371*, H. Sehitoglu and H. J. Maier Eds., ASTM International, West Conshohocken, PA, 1999, pp. 223-238.

Enhancement of Thermomechanical Fatigue Resistance of a Monocrystalline Nickel-base Superalloy by Pre-rafting

REFERENCE: Neuner, F. C., Tetzlaff, U., and Mughrabi, H., "Enhancement of Thermo-Mechanical Fatigue Resistance of a Monocrystalline Nickel-Base Superalloy by Pre-Rafting," *Thermomechanical Fatigue Behavior of Materials: 4th Volume, ASTM STP 1428*, M. A. McGaw, S. Kalluri, J. Bressers, and S. D. Peteves, Eds., ASTM International, West Conshohocken, PA, Online, Available: www.astm.org/STP/1428/1428_10599, 3 Sept. 2002.

ABSTRACT: In γ' -hardened monocrystalline nickel-base superalloys having a negative γ/γ' lattice misfit, the prior introduction of so-called γ/γ' rafts aligned parallel to the stress axis (by a small creep pre-deformation in compression) has been shown to enhance both the high-temperature isothermal fatigue strength and the tensile creep resistance. It was hence of interest to perform a systematic study of the thermo-mechanical fatigue (TMF) behavior of specimens of a monocrystalline nickel-base superalloy with the main aim to test whether an initial γ/γ' raft microstructure can also enhance the TMF resistance. The experiments were performed on [001]-orientated monocrystalline specimens of the superalloy SRR 99 which contained either the initial γ/γ' -microstructure with cuboidal γ' precipitates or a γ/γ' raft microstructure aligned roughly parallel to the stress axis. The latter was introduced by a small compressive creep deformation of less than 0.4% at a temperature of 1050°C and a stress of 120 MPa. Different strain-controlled TMF cycle forms were employed. However, in most tests a counter-clockwise-diamond (CCD) cycle (temperature interval $\Delta T = 600^\circ\text{C}$ -1100°C) was used with a total strain rate of $6.67 \cdot 10^{-5} \text{ s}^{-1}$. This CCD cycle is considered to be close to service conditions. The mechanical strain range $\Delta \epsilon_m$ was varied in the range of $\Delta \epsilon_{\text{mech}} = 1\%$, leading to fatigue lives in the order of some 1000 cycles. It could be shown that pre-rafting in compression enhances the TMF fatigue life significantly for all cases of CCD-cycles investigated.

KEYWORDS: pre-rafting, thermo-mechanical fatigue, nickel-base superalloy, single crystal, γ/γ' -microstructure, fatigue life, coarsening

Introduction

Monocrystalline nickel-base superalloys, precipitation-hardened with a high volume fraction of cuboidal γ' precipitates and orientated in good approximation in a $\langle 001 \rangle$ direction, fulfil the requirements for turbine-blade materials in the hot first stages of gas turbines and power engines. During service up to temperatures of 1100°C, turbine-blade materials must meet a number of specific requirements such as high creep and fatigue strength, high thermomechanical fatigue strength, and last but not least good resistance against hot corrosion and oxidation. In former investigations by the authors' group it could be shown that the prior introduction of rafts aligned parallel to the stress

¹ Research Associate and Professor, respectively, Institut für Werkstoffwissenschaften, Lehrstuhl I, Universität Erlangen-Nürnberg, Martensstrasse 5, D-91058 Erlangen, Federal Republic of Germany.

² Former Research Associate, now at AUDI AG, D-85045 Ingolstadt, Federal Republic of Germany.

axis in monocrystalline nickel-base superalloys of negative γ/γ' lattice misfit δ enhances the high-temperature tensile creep resistance as well as the isothermal fatigue strength [1].

Improvement of the Tensile Creep Strength by Pre-Rafting in Compression

At high temperatures and low stresses, the glide-climb motion of the dislocations, as proposed by Carry and Strudel [2], is the rate-determining process. The glide-climb motion along vertical γ/γ' interfaces in tensile or compressive deformation is always slower than along horizontal γ/γ' interfaces [3]. This leads to the suggestion that pre-raftering in compression, whereby extended rafts parallel to the stress axis are introduced for $\delta < 0$, should reduce the creep rate. Tensile creep tests performed by Tetzlaff et al. [4] come to the conclusion that this is indeed the case. This is shown in Fig.1, showing, as an example, two tensile creep curves, measured on two monocrystalline nickel-base superalloy SRR 99 specimens, one with the as-aged cuboidal γ' structure and the other with a γ/γ' raft structure lying parallel to the stress axis as the starting microstructures.

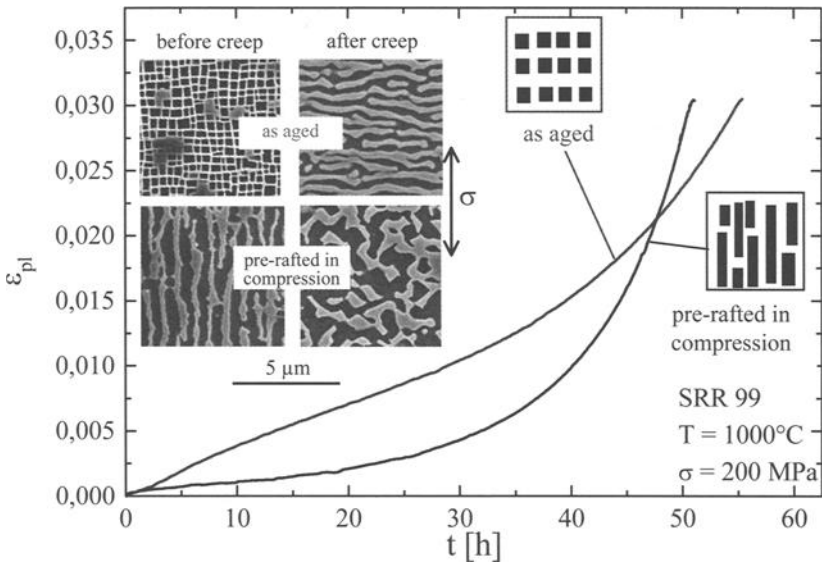


FIG. 1— Tensile creep curves ($T = 1000\text{ }^{\circ}\text{C}$, $\sigma = 200\text{ MPa}$) up to 3% plastic strain for two monocrystalline SRR 99 specimens with initial microstructures in the as-aged and pre-raftered (compression) condition (T : temperature, σ : axial stress, ϵ_{pl} : axial plastic strain, t : time), as indicated schematically. Inserts show scanning electron micrographs of the corresponding microstructural changes in $\{010\}$ sections parallel to the stress axis. After [4].

Up to a tensile creep strain ϵ_{pl} of about 2% the pre-raftered structure has better creep resistance than the cuboidal γ' structure. At larger strains, the γ/γ' raft structure, introduced by prior compressive creep deformation, becomes unstable, because the tensile stresses would normally produce a raft structure perpendicular to the stress axis.

Better LCF-Fatigue Resistance by Pre-Rafting in Compression

The isothermal high-temperature fatigue life is also enhanced by the introduction of a pre-raftered γ/γ' -microstructure lying parallel to the stress axis by prior compressive creep deformation [1,5]. Figure 2 shows some typical results in the form of cyclic deformation curves (stress amplitude $\Delta\sigma/2$ vs. number of cycles, N) obtained on monocrystalline specimens of the nickel-base superalloy CMSX-6, fatigued at 950 °C at a total strain range $\Delta\epsilon_t = 0.9\%$ and at a cyclic total strain rate of $9 \cdot 10^{-3} \text{ s}^{-1}$. The prior introduction of a raft structure parallel to the stress axis leads to higher number of cycles to failure, while rafts lying perpendicular to the stress axis reduce the fatigue life, compared to specimens with the as-aged cuboidal γ/γ' -microstructure.

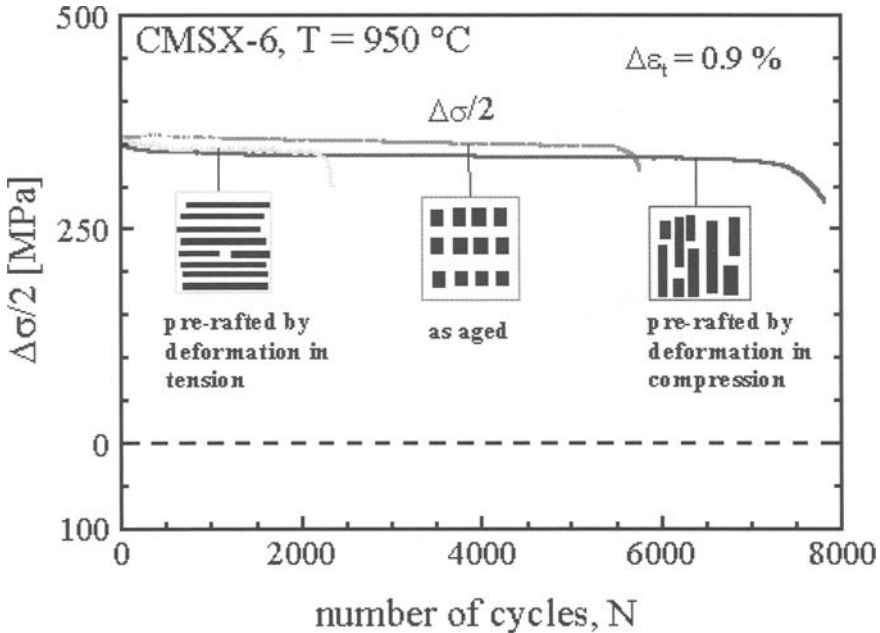


FIG. 2— *Cyclic deformation curves of three monocrystalline nickel-base CMSX-6 specimens with different initial microstructures (as-aged, pre-raftered in tension and in compression). $T = 950^\circ\text{C}$, $\Delta\epsilon_t = 0.9\%$, $\Delta\sigma/2$: stress amplitude. The different microstructures are indicated schematically. After [5].*

The γ/γ' raft structure parallel to the stress axis hinders the crack propagation perpendicular to the stress axis (and to the rafts) and forces the cracks to deviate, which is the reason for the longer fatigue life of the specimen pre-raftered in compression. On the other hand, rafts lying perpendicular to the stress axis facilitate the crack propagation and therefore lead to the shortest fatigue life.

As a next step, it is interesting to explore whether similar measures can also be applied successfully in order to improve the thermomechanical fatigue life by introducing a pre-raftered structure by prior compressive creep deformation. An improvement of the thermomechanical fatigue resistance, which is of major concern in the case of turbine blades would be most desirable. In the following, the results of such a study are reported.

Experimental Procedure

Material

For the following investigations, rods of the two-step annealed γ' -hardened monocrystalline nickel-base superalloy SRR 99 with orientations close to [001] were used. The composition of the alloy is given in Table 1:

TABLE 1— *Composition of SRR 99.*

Element	C	Si	Mn	Cr	Mo	Ni	Co	Ti	Al
Wt. %	0.017	0.040	<0.03	8.55	0.08	Rest	5.01	2.2	5.51
Element	Fe	V	W	Cu	Zr	Ta	B	P	S
Wt.%	0.05	0.03	9.37	<0.03	<0.003	2.82	0.0013	<0.005	0.01

After machining and electropolishing of the surface, the specimen had a gauge length of 12 mm and a diameter of 9 mm. The initial γ/γ' -microstructure consisted of fairly regularly aligned cuboidal γ' particles with a γ' edge length of 0.44 μm and a volume fraction of 72%.

Testing Method and Testing Parameters

The thermomechanical fatigue tests were performed on a closed-loop servohydraulic testing system (MTS 880), which is equipped with a 200 kHz induction furnace. The total strain, ϵ_t (mechanical strain ϵ_{mech} + thermal strain ϵ_{th}), was measured with a high-temperature axial extensometer with ceramic rods, and the temperature was measured and controlled in a contact-free manner with a 4-channel pyrometer. The mechanical strain ϵ_{mech} (elastic and plastic strain) is calculated afterwards by addition of the negative value of the thermal expansion $-\epsilon_{\text{th}}$ in an analog-digital (A/D) converter. The temperature signal is created simultaneously to control the induction heating which is necessary for rapid heating and cooling of the specimen. Figure 3 shows a schematic diagram of the material test rig for thermomechanical fatigue tests. More detailed information about the testing method and the material test rig can be found in [6].

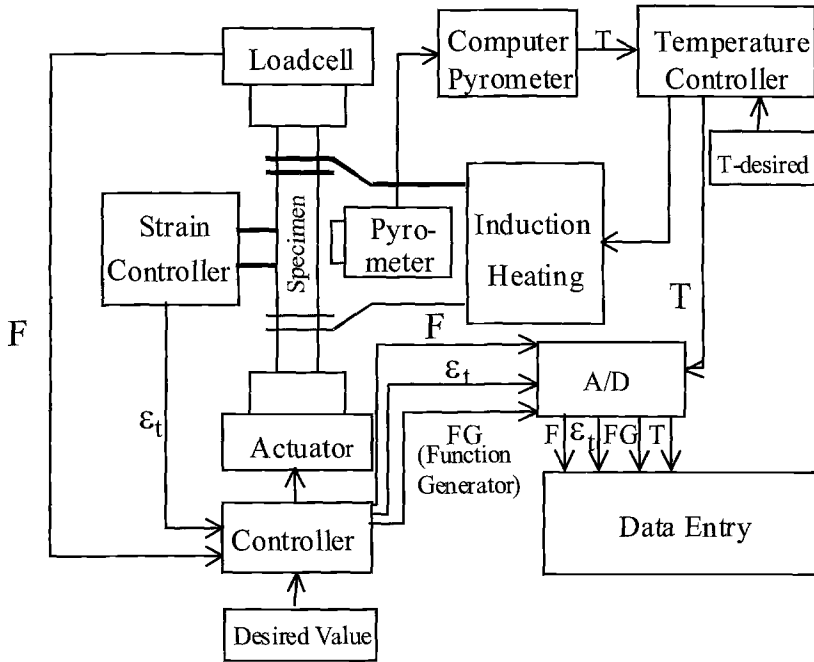


FIG. 3— Schematic diagram of the thermomechanical fatigue test rig (*F*: force).

All tests were conducted in air with mechanical strain ranges $\Delta\epsilon_{\text{mech}}$ of 8×10^{-3} and 1×10^{-2} , employing a triangular waveform with a constant cycle time of 300 s between 600 and 1100 °C. The TMF test cycle shape was selected so as to simulate approximately the conditions during start-up and shut-down operations of a turbine engine. Therefore a counter-clockwise-diamond (CCD) cycle shape (see Figure 4a) was used with the intermediate temperature (850 °C) being reached at largest tensile and compressive strains and the highest (1100 °C) and lowest (600 °C) temperatures at zero mechanical strain.

A limited number of TMF tests were performed with an out-of-phase (OP) cycle shape, characterized by the largest tensile and compressive stresses and strains at the lowest and highest temperatures, respectively. OP is considered to be the most severe loading in a component because of the very high tensile stress, which develops at the lowest temperature [7]. Figure 4 compares the CCD and OP cycle shapes in detail.

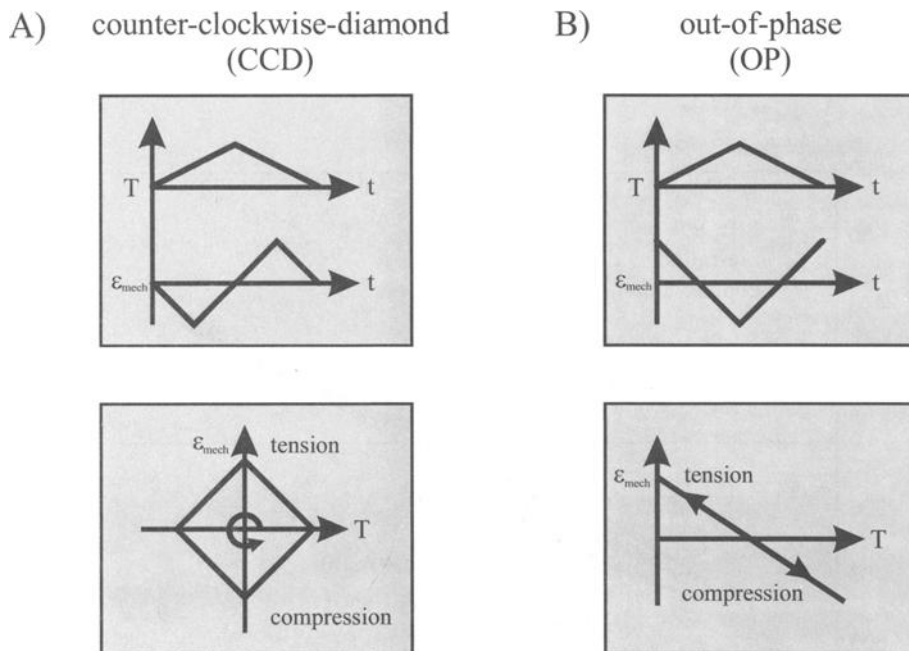


FIG. 4— Comparison between (A) counter-clockwise-diamond (CCD) and (B) out-of-phase (OP) cycle shape. Time is denoted by the symbol t .

For the TMF specimens with γ' -rafts parallel to the stress axis, the microstructure was produced by pre-deformation in compression at a stress σ of -120 MPa and a temperature T of 1050 °C. To avoid prior damaging, the plastic creep strains were kept small and were limited to less than 0.4 %. The deformed samples were investigated by scanning electron microscopy (SEM).

Experimental Results and Discussion

Mechanical Behavior

Hysteresis loop shapes— Figures 5 and 6 present examples of the shapes of the hysteresis loops (stress σ vs. mechanical strain $\varepsilon_{\text{mech}}$) in the CCD and OP TMF tests, respectively, for the different initial γ/γ' -microstructures. The specimens with the as-aged and pre-raftered microstructures show similar hysteresis loops in both cases. However, for the pre-raftered structure, the stress amplitudes in tension in the CCD test are about 100 MPa higher. The shapes of the hysteresis loops of the first cycles of the two testing conditions differ from the following cycle shapes with respect to the stress amplitudes in tension and compression and the extent of plastic yielding.

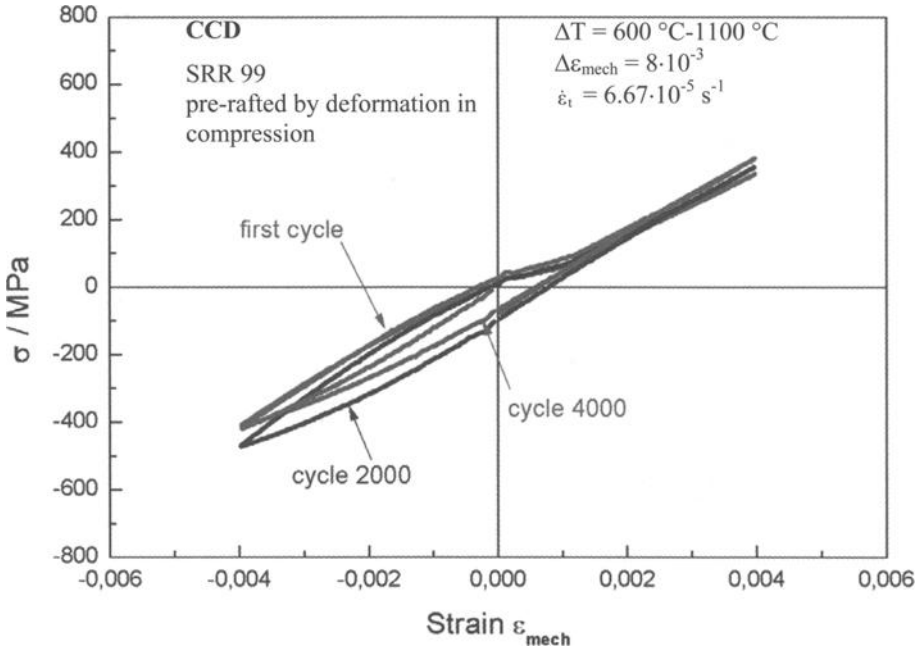


FIG. 5—Examples of different hysteresis loops for a counter-clockwise-diamond (CCD) TMF cycle on a specimen rafted in compression, $\Delta \epsilon_{mech} = 8 \cdot 10^{-3}$, $\Delta T = 600 \text{ }^\circ\text{C} - 1100 \text{ }^\circ\text{C}$ and $\dot{\epsilon}_t = 6.67 \cdot 10^{-5} \text{ s}^{-1}$.

For the CCD tests, intermediate and comparatively symmetric peak stresses, 300 MPa in tension and 500 MPa in compression, are found, because similar temperatures are reached at these points (850 °C). In contrast to these very similar peak stresses in tension and compression in the CCD tests, the OP tests exhibit dissimilar peak stresses in tension and compression. At the lowest temperature (600 °C), the OP tests show very high peak stresses up to 700 MPa in tension, at the highest temperature peak stresses of only 100 MPa are found in compression.

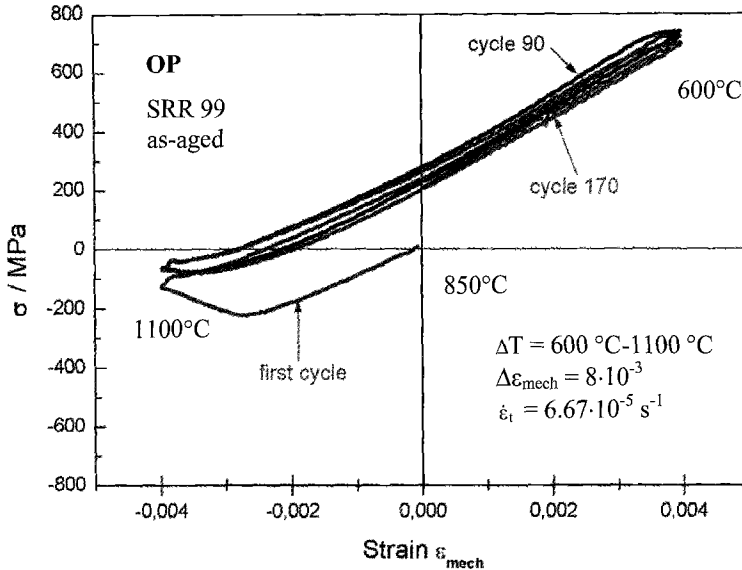


FIG. 6—Examples of different hysteresis loops for an out-of-phase (OP) TMF cycle on a specimen with the as-aged γ/γ' -microstructure $\Delta\epsilon_{\text{mech}} = 8 \cdot 10^{-3}$, $\Delta T = 600 \text{ }^\circ\text{C} - 1100 \text{ }^\circ\text{C}$ and $\dot{\epsilon}_t = 6.67 \cdot 10^{-5} \text{ s}^{-1}$.

Cyclic Stress Response Curves—Results of the TMF tests performed on specimens with different initial γ/γ' -microstructures (as-aged and pre-raftered in compression) and TMF cycle shapes (CCD with mechanical strain ranges $\Delta\epsilon_{\text{mech}}$ of 8×10^{-3} and 1×10^{-2} , respectively, and OP with $\Delta\epsilon_{\text{mech}}$ of 8×10^{-3}) are shown as cyclic stress (maximum/minimum stress) versus cycle number N response curves in Fig. 7.

The fatigue life of the material is found to be strongly dependent on the mechanical strain amplitude, cycle shape and γ/γ' -microstructure. In the TMF tests with CCD cycle, the pre-raftered specimens with a raft structure parallel to the stress axis have a significantly longer fatigue life than the specimens with the initial (as-aged) cuboidal γ' microstructure. At higher numbers of cycles, the stress amplitude decreases due to crack initiation and propagation. All OP tests show a very short fatigue life because of the severe loading. The maximum mechanical strain in tension is reached at the lowest temperature, therefore all samples fail by quasi-brittle rupture in tension. The fatigue life of the pre-raftered OP specimen is smaller than that obtained for the as-aged state. The microstructural features, which are thought to control fatigue life, will be discussed in the following.

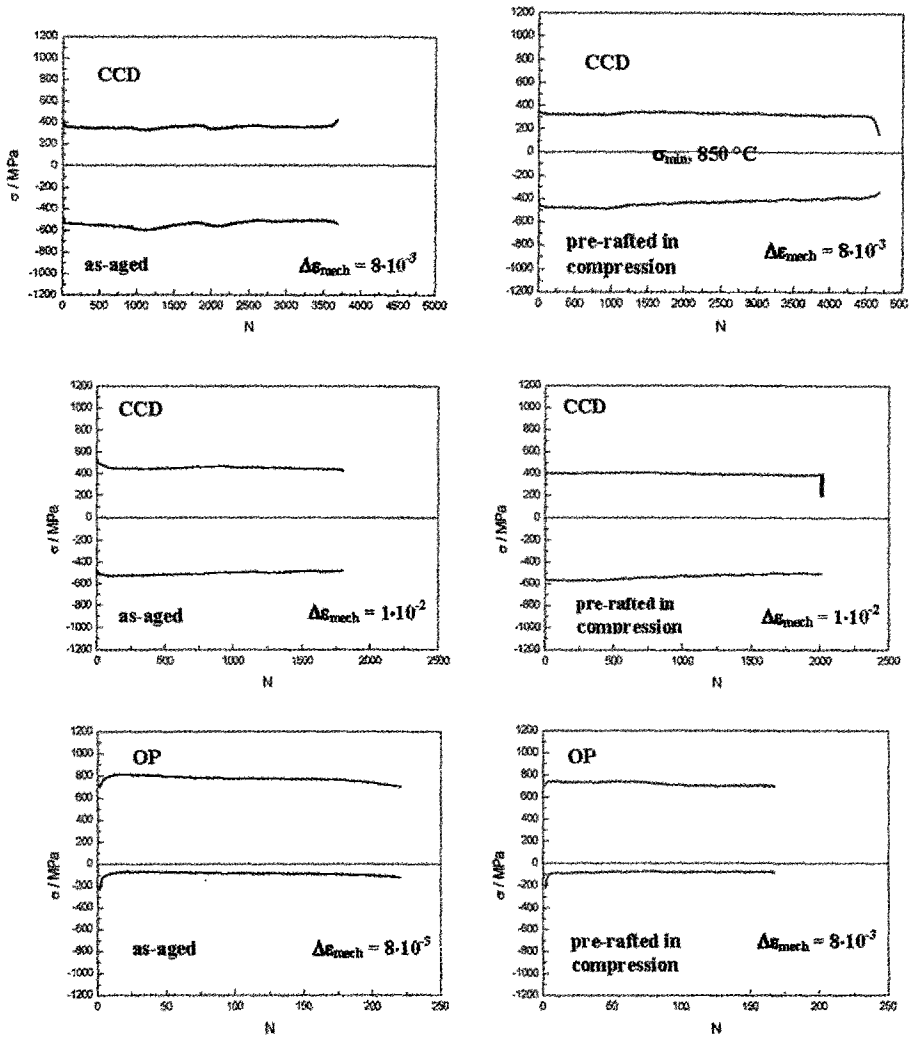


FIG. 7— Cyclic stress response curves of all TMF tests ($\Delta T = 600^\circ\text{C} - 1100^\circ\text{C}$ and $\dot{\epsilon}_t = 6.67 \cdot 10^{-5} \text{ s}^{-1}$, σ_{max} : maximum cyclic stress, σ_{min} : minimum cyclic stress). Directly corresponding TMF-tests for as-aged and pre-rafterd microstructures are shown next to each other.

Microstructural Changes During TMF Loading

CCD testing, as-aged specimens— During the CCD tests, the as-aged γ/γ' -microstructure develops into a coarse raft-like structure parallel to the stress axis. The example shown in Fig. 8 refers to SEM-micrographs taken from specimens fatigued at a mechanical strain range of $\Delta\varepsilon_{\text{mech}} 1 \times 10^{-2}$. The high upper temperature ($T_{\text{max}} = 1100 \text{ }^\circ\text{C}$) is held responsible for the strong coarsening. Similar changes in the microstructure have been found in former investigations on the alloy CMSX-6 [7].

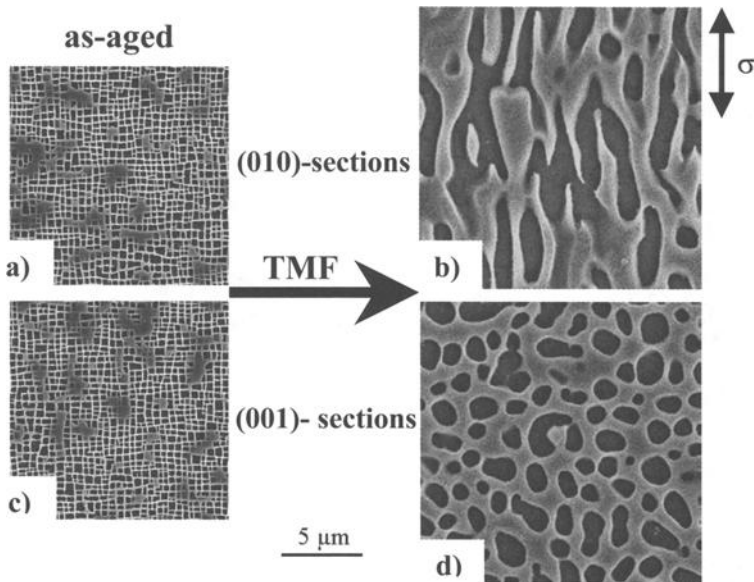


FIG. 8—SEM-micrographs of the microstructures in the initial as-aged state before and after thermomechanical CCD testing. The stress axis lies in the $[001]$ direction. a) and b): (010) -sections parallel to the stress axis before and after the CCD-testing. c) and d): (001) -sections perpendicular the stress axis before and after the CCD-testing.

The γ/γ' rafting is governed not only by the external stress but also by the internal stresses and by the built-up plastic tensile and compressive strains [8]. The internal stresses result from the superposition of the coherency stresses between γ and γ' and the internal stresses induced during deformation.

CCD Testing, Pre-Rafted Specimens—The microstructure of the specimens with the initial well-aligned raft structure parallel to the stress axis shows coarsening effects, but remains elongated parallel to the stress axis (Fig. 9). The reason for the longer fatigue life observed for the γ/γ' raft structure parallel to stress axis could be, as in the case of

isothermal fatigue studied earlier [1,5], that the rafts hinder the crack propagation perpendicular to the stress axis (and to the rafts) and cause the cracks to deviate. These results are similar to those of the isothermal high-temperature fatigue tests described in the introduction.

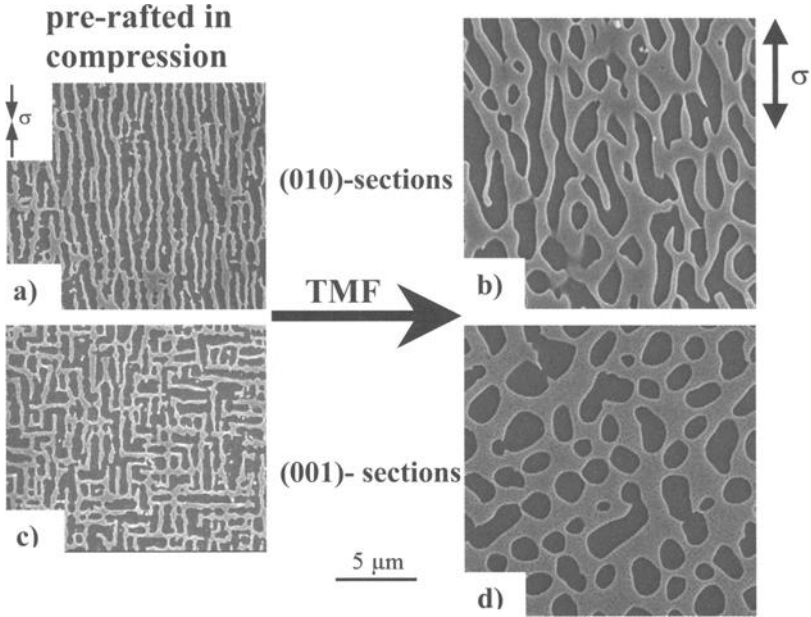


FIG. 9—SEM-micrographs of the microstructures in the initial state with a raft structure parallel to the stress axis before and after CCD testing. The raft structure after the CCD test is strongly coarsened. a) and b): (010)-sections parallel to the stress axis before and after the CCD-testing. c) and d): (001)-sections perpendicular the stress axis before and after the CCD-testing.

In Fig. 10, the main crack in a fatigued CCD-sample with a raft structure parallel to the stress axis can be seen. The crack starts at the surface of the specimen and propagates perpendicular to the stress axis. The crack propagation is hindered and crack branching occurs. The observation of the secondary crack tip (Figs. 10b and 10c) shows a dependence of the crack propagation mechanism on the state of the γ/γ' raft structure. If the crack runs parallel to the γ/γ' rafts, there is no cutting of the rafting structure. Cutting is only seen when the direction of crack propagation is not parallel to the rafting structure. Thus, the introduction of γ/γ' plates can induce crack branching and may hinder crack propagation. These results are broadly similar to findings made in former investigations on isothermal fatigue tests made by Ott [5] and in line with work of Lerch and Antolovich [9].

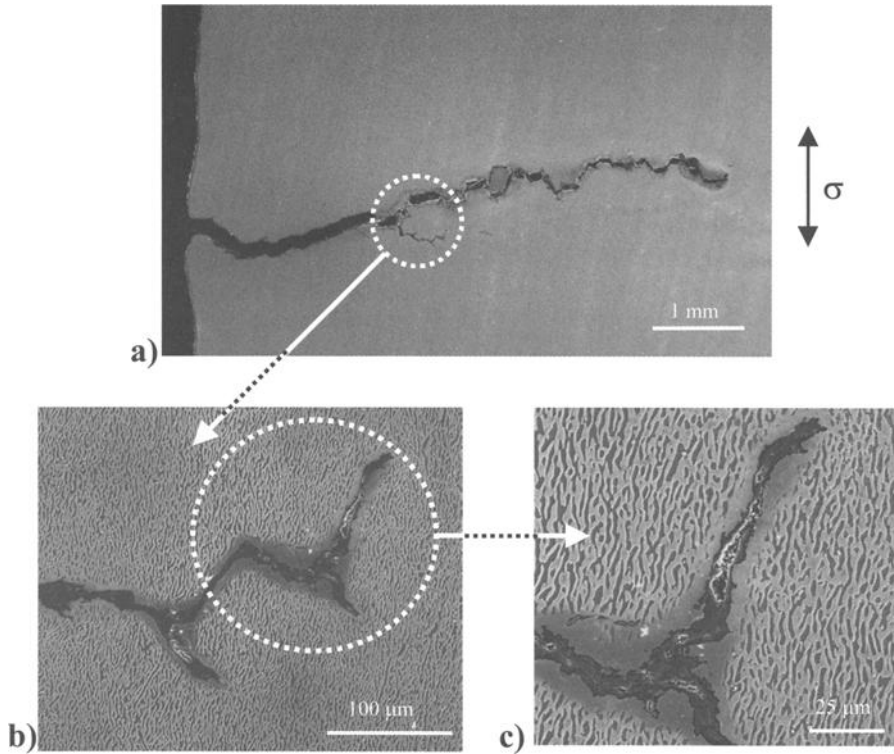


FIG. 10—Crack propagation after thermomechanical fatigue (CCD, $\Delta\epsilon_{mech} 1 \times 10^{-2}$) of the sample with a raft structure parallel to the stress axis (SEM); a) main crack starting from surface; b) and c) example of a secondary crack; (010)-section.

OP testing, as-aged specimens—The γ/γ' -microstructure of the as-aged specimens with cuboidal γ' precipitates is transformed into a coarse raft structure parallel to the stress axis (Fig. 11). Due to severe loading conditions (maximum mechanical strain in tension is reached at the lowest temperature), which produce high tensile stresses, the thermomechanical fatigue life is very short for all OP tests, independent of the microstructure. Compared to the CCD tests the effect of coarsening is less marked. This is presumably a consequence of the shorter fatigue lives and, thus, of the shorter time available for the diffusional mechanisms.

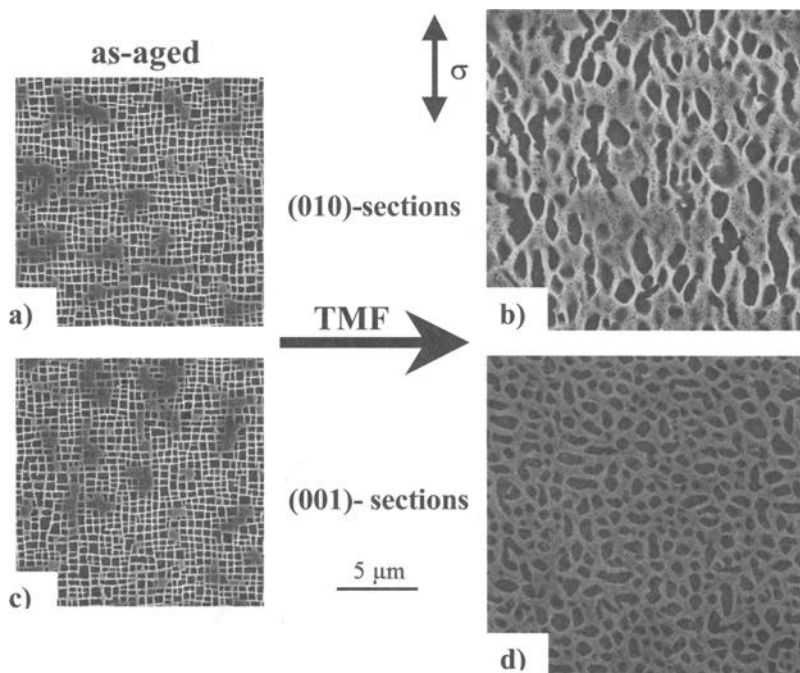


FIG. 11—SEM-micrographs of the microstructures in the initial as-aged state before and after OP testing. a) and b): (010)-sections parallel to the stress axis before and after the OP-testing. c) and d): (001)-sections perpendicular the stress axis before and after the OP-testing.

OP Testing, Pre-Rafted Specimens—The specimens with an initial rafted structure parallel to the stress axis change their microstructure towards a strongly coarsened irregular γ/γ' -structure. This irregular structure might be a reason for the shorter thermomechanical fatigue life compared to the sample with the as-aged microstructure. The microstructures in the initial state of the pre-raftered samples before and after OP testing, as observed by SEM, are shown in Fig. 12.

Origin of Strong Microstructural Coarsening—The very strong coarsening of the γ/γ' -structure in the cases discussed above is attributed to the rather high upper temperature of 1100 °C in all tests. In retrospect, this upper temperature is, in fact, considered to have been too high for the first generation alloy SRR 99. Presumably, coarsening would have been much less marked at a more appropriate upper temperature of ca. 1000 °C.

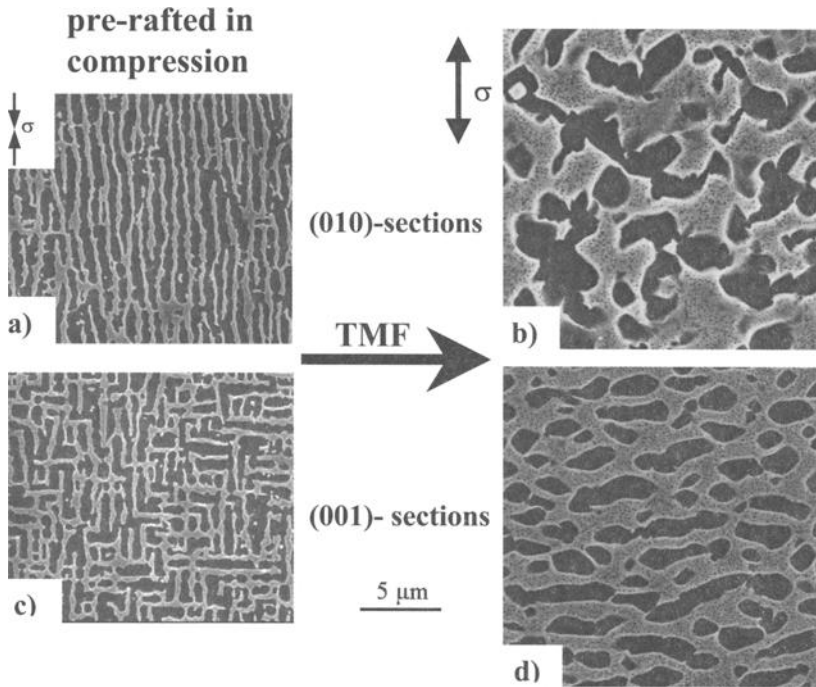


FIG. 12—SEM-micrographs of the microstructures in the initial state with a raft structure parallel to the stress axis before and after OP testing. a) and b): (010)-sections parallel to the stress axis before and after the OP-testing. c) and d): (001)-sections perpendicular the stress axis before and after the OP-testing.

Conclusions

In the present work on the monocrystalline superalloy SRR 99, it was shown exemplarily that pre-raftering in compression can be beneficial for thermomechanical high-temperature fatigue life with the CCD cycle. It is proposed that these results will apply also to other monocrystalline nickel-base-superalloys. The main results were as follows:

- Pre-raftering in compression is not only able to enhance the tensile creep strength and the isothermal fatigue life, as shown earlier, but also the thermomechanical high-temperature fatigue life for a CCD cycle, which simulates approximately service conditions.
- The investigation of the main crack of a fatigued CCD-sample with a raft structure parallel to the stress axis appears to show that the crack propagation is hindered by the rafts, and crack branching occurs. This is suggested to be the reason for the superior thermomechanical high-temperature fatigue resistance of material with a γ/γ' raft structure parallel to the applied stress axis.

- The TMF tests with OP cycle shape generally led to a very short fatigue life, which is shorter for the pre-rafted sample compared to a specimen with the as-aged structure. The reason may be the development of a very coarse irregular γ/γ' -microstructure.

References

- [1] Mughrabi, H. and Tetzlaff, U., "Microstructure and High-Temperature Strength of Monocrystalline Nickel-Base Superalloys," *Advanced Engineering Materials*, Vol. 2, 2000, pp. 319–326.
- [2] Carry, C. and Strudel, J.-L., "Apparent and Effective Creep Parameters in Single Crystals of a Nickel Base Superalloy – I. Incubation Period," *Acta Metallurgica*, Vol. 25, 1977, pp. 767–777.
- [3] Tetzlaff, U., Nicolas, M. and Mughrabi, H., "Can the High Temperature Tensile Strength of Nickel-Base Superalloys be Improved by Pre-rafting?" *Proceedings, EUROMAT '99*, Vol. 10, 2000, pp. 22–27.
- [4] Tetzlaff, U. and Mughrabi, H., "Enhancement of the High-Temperature Tensile Creep Strength of Monocrystalline Nickel-Base Superalloys by Pre-rafting in Compression," *Proceedings, SUPERALLOYS 2000*, T. M. Pollock, R. D. Kissinger, R. R. Bowman, K. A. Green, M. McLean, S. L. Olson and J. J. Schirra, Eds., TMS: The Minerals, Metals & Materials Society, 2000, pp. 273–282.
- [5] Ott, M. and Mughrabi, H., "Dependence of the Isothermal Fatigue Behaviour of a Monocrystalline Nickel-Base Superalloy on the γ/γ' -Morphology," *Proceedings, FATIGUE '96*, Vol. 2, 1996, pp. 789–794.
- [6] Christ, H.-J., Mughrabi, H., Kraft, S., Petry, F., Zauter, R. and Eckert, K., "The Use of Plastic Strain Control in Thermomechanical Fatigue Testing," *Fatigue Under Thermal and Mechanical Loading—Mechanisms, Mechanics and Modelling*, J. Bressers and L. Remy, Eds., Kluwer Academic Publishers, Dordrecht, 1996, pp. 1–14.
- [7] Kraft, S. and Mughrabi, H., "Thermo-Mechanical Fatigue of the Monocrystalline Nickel-Base Superalloy CMSX-6," *Thermomechanical Fatigue Behavior of Materials: Second Volume, ASTM STP 1263*, M.I. J. Verrilli and M. G. Castelli, Eds., ASTM International, 1996, pp. 27–40.
- [8] Kraft, S., Altenberger, I. and Mughrabi, H., "Directional $\gamma-\gamma'$ Coarsening in a Monocrystalline Nickel-Base Superalloy During Low-Cycle Thermomechanical Fatigue" *Scripta Metallurgica et Materialia*, Vol. 32, 1994, pp. 411–416 and *Scripta Metallurgica et Materialia*, Vol. 32, 1995, p. 1903 (Erratum).
- [9] Lerch, B. A. and Antolovich, S. D., "Fatigue Crack Propagation Behaviour of a Single Crystal Superalloy," *Metallic Transactions A.*, Vol. 21A, 1990, pp. 2169–2177.

Hans J. Maier,¹ Frank O. R. Fischer,² and Hans-Jürgen Christ²

Environmental Effects on the Isothermal and Thermo-mechanical Fatigue Behavior of a Near- γ Titanium Aluminide

REFERENCE: Maier, H. J., Fischer, F. O. R., and Christ, H.-J., "Environmental Effects on the Isothermal and Thermomechanical Fatigue Behavior of a Near- γ Titanium Aluminide," *Thermomechanical Fatigue Behavior of Materials: 4th Volume, ASTM STP 1428*, M. A. McGaw, S. Kalluri, J. Bressers, and S. D. Peteves, Eds., ASTM International, West Conshohocken, PA, 2002, Online, Available: www.astm.org/STP/1428/1428_10591, 24 June 2002.

ABSTRACT: High-temperature fatigue behavior of a near- γ titanium aluminide was studied over the temperature range from 500–750 °C under both isothermal and thermomechanical fatigue (TMF) conditions. Cyclic stress-strain (CSS) response was observed to change drastically with test temperature. In isothermal tests conducted below the ductile-to-brittle transition temperature (DBTT) initial cyclic hardening occurred. By contrast, in isothermal fatigue tests performed above the DBTT the material displayed pronounced cyclic saturation throughout the test. Still, modeling of CSS behavior under TMF conditions based solely on isothermal input data is feasible, as corresponding microstructures evolve in both types of tests. Environmental degradation plays a key role in this material, and the effects were assessed based on fatigue tests conducted in air and high-vacuum, respectively. Moreover, the material displays large mean stress effects below the DBTT, and thus, out-of-phase TMF tests were found to be most detrimental, when the temperature range encompassed the DBTT.

KEYWORDS: cyclic stress-strain behavior, environmental degradation, intermetallics, mean stress, microstructure, modeling, oxidation, thermomechanical fatigue, titanium aluminide

Introduction

Near- γ titanium aluminides have been developed mainly in response to the aerospace industries' need for new materials with higher strength to weight ratios at elevated temperatures. The design target set was to replace heavier alloys in the hottest section of the compressor in jet engines. At low temperatures TiAl alloys tend to display low ductility, with a ductile-to-brittle transition temperature (DBTT) of about 700 °C [1]. Thus, most of the earlier studies have focused on improving low-temperature ductility and fracture toughness of these alloys by varying chemical composition and heat treatment [2].

With the advent of more advanced near- γ titanium aluminides, reliability issues under high-temperature service conditions became most important. For high-temperature components such as turbine blades, complex loading conditions exist during service, and

¹ Professor, Lehrstuhl für Werkstoffkunde, Universität Paderborn, D-33095 Paderborn, Germany.

² Graduate Research Assistant and Professor, respectively, Institut für Werkstofftechnik, Universität Siegen, D-57068 Siegen, Germany.

life may be governed by creep, isothermal low-cycle fatigue (LCF) or thermomechanical fatigue (TMF). As a result of the relatively poor oxidation resistance, these alloys are also prone to environmental degradation effects, and thus, maximum service temperature should not exceed about 800 °C. For most technical applications temperatures in the range from 500–750 °C appear to be of most interest [3]. Much work has addressed creep of TiAl alloys in this temperature range, and the creep behavior of the material employed for the present study has been extensively characterized in related work [4,5]. By contrast, LCF and TMF tests on titanium aluminides are still rare [6].

The objective of the present paper was to shed light on the fatigue behavior of a 2nd generation titanium aluminide under conditions relevant to operation of compressor blades in advanced jet engines. The test conditions employed in the present study were chosen such as to closely resemble those thought to prevail at the notch root of a specific blade currently in the design stage. Given the complex loading situation present during service of such a component, a detailed understanding of cyclic stress-strain (CSS) response, mean stress effects, and environmental degradation is key in developing accurate life prediction methodologies.

The approach chosen here involved LCF and TMF tests performed at different strain ratios (R_ϵ), strain rates ($\dot{\epsilon}$), mechanical strain ranges ($\Delta\epsilon$), and temperatures (T) in high-vacuum and air, respectively. This allowed for an assessment of the effects of mean stress, environment, temperature, and strain-temperature phasing on fatigue life. Moreover, electron microscopy was employed to closely correlate the macroscopical material behavior to the relevant microstructural processes, and the ramifications of the results with respect to prediction of fatigue life under service conditions will be discussed in detail.

Experimental Procedure

Material

Near- γ titanium aluminide Ti-47Al-2Nb-2Mn (at.-%) + 0.8 vol.-% TiB₂ XDTM was employed for the present study. For actual composition including interstitial content see Ref. 4. The material³ had been investment cast, hot isostatically pressed at 1260 °C and 172 MPa to eliminate casting porosity, and then given a subsequent heat treatment at 1010 °C for 50 h. This resulted in a duplex microstructure consisting of equiaxed primary γ -TiAl grains and lamellar α_2 -Ti₃Al / γ -TiAl colonies. The volume fraction of the lamellar grains was between 15 and 20%, and the average grain size was determined to be 15 μ m and 30 μ m for the primary γ and the lamellar grains, respectively [4].

For fatigue testing, smooth cylindrical specimens with a gage length of 14 mm and a gage diameter of 8 mm were machined from the heat treated material. It has been reported that machining can affect fatigue properties of this type of material [7], and it is known that oxidation behavior also depends on surface preparation [8]. Thus, all fatigue samples used in the present study were electropolished in the gage section prior to testing. Electropolishing was accomplished using a solution of 600 ml methanol, 350 ml butanol, and 60 ml perchloric acid at a temperature of -30 °C and a voltage of 20 V until a surface layer of 0.1 mm was removed.

³ The fully-processed material was obtained from Howmet Corp., Whitehall, MI.

Mechanical Testing

All fatigue tests were conducted in a servohydraulic test system under closed-loop total strain control using a triangular wave shape. Specimen heating was accomplished by an induction heater, and the geometry of the induction coil was optimized until a temperature gradient of less than 5 °C was obtained within the gage length under isothermal test conditions. Part of the test parameters (R_ϵ , $\Delta\epsilon$, and T) employed were chosen, such as to simulate the loading conditions that might prevail at the root of certain turbine blades of advanced jet engines. In order to shed light on the deformation and damage mechanisms, additional tests were run, including fatigue tests conducted in an all stainless-steel vacuum chamber at $p < 10^{-5}$ hPa. The actual test parameters of the isothermal LCF tests employed in the present study are summarized in Table 1.

All TMF tests were conducted at a total mechanical strain range of 0.56% over a temperature range from 500–750 °C. In order to minimize the temperature gradients within the gage length, all TMF tests were performed at a rather low strain rate of 1.12×10^{-4} s⁻¹. In the out-of-phase (OP) and in-phase (IP) TMF tests maximum mechanical strain coincided with the minimum and maximum temperature, respectively. Again, tests were performed both in air and in high-vacuum. In addition, some more complex TMF tests were conducted, which will be described in detail later.

Microscopy

Scanning electron microscopy (SEM) was employed to study fracture surfaces and analyze the oxide scale formed during high-temperature exposure. In cases where oxidation obscured crack initiation mechanisms, longitudinal metallographic sections were prepared.

The microstructural details were studied by transmission electron microscopy (TEM). For TEM work, slices were cut normal to the loading axis of the fatigued specimens and ground carefully down to a thickness of about 150 μm . From the ground slices, electron transparent foils were prepared by conventional twin jet electropolishing at -30 °C and a voltage of 12 V using the previously described electrolyte.

TABLE 1—*Test parameters employed in the isothermal LCF tests. Test environments were air and high-vacuum of $p < 10^{-5}$ hPa, respectively.*

R_ϵ	$\dot{\epsilon}$, s ⁻¹	$\Delta\epsilon$, %	T, °C
-1,	1.12×10^{-4} ,	0.36,	500, 600,
0.1	3×10^{-3}	0.46,	650, ^a
		0.56	700,750

^aThe ductile-to-brittle transition temperature for the present alloy is about 650 °C.

Results

Cyclic Stress-Strain Response

Related work [6] has shown that CSS response is substantially different for test temperatures below and above the DBTT, respectively. In isothermal LCF tests conducted below the DBTT, which is about 650 °C for the material studied, rapid initial

cyclic hardening occurred. By contrast, an almost immediate stabilization of CSS response is observed in isothermal LCF tests performed at temperatures significantly exceeding the DBTT (Fig. 1). Consequently, for a given total strain range the plastic strain range at half life becomes larger with increasing temperature in total strain controlled LCF tests (Fig. 2). As seen in Fig. 2, stress range shows a weaker dependence on test temperature, and the effect of strain ratio on CSS response is only minor. However, it is appropriate to note here that strain ratio has a substantial effect on fatigue life as discussed later on.

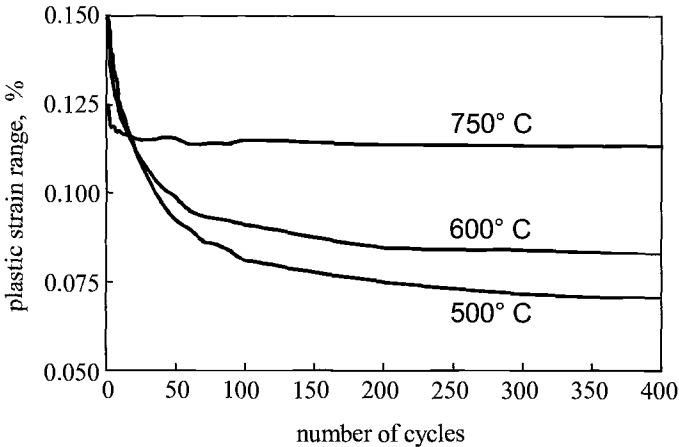


FIG. 1— Initial evolution of plastic strain range in isothermal LCF tests conducted below and above the DBTT, respectively. $R_e = -1$, $\Delta\epsilon = 0.56\%$ and $\dot{\epsilon} = 3 \times 10^{-3} s^{-1}$.

Given the profound effect of temperature on isothermal CSS behavior (Fig. 2) one might expect significantly different CSS response in isothermal LCF and TMF tests, if the temperature range of the latter include the DBTT. Nevertheless, TMF hysteresis loops could be modeled quite accurately on the basis of so-called pseudo-isothermal behavior. In this approach it is assumed that the microstructure at any given temperature within a TMF cycle corresponds exactly to the microstructure obtained in an isothermal LCF test conducted at that specific temperature [9].

As microstructural state determines mechanical response [10], modeling of CSS response is straightforward if the assumption of pseudo-isothermal behavior holds [9]. In order to test this concept, special fatigue tests were devised. Figure 3 is a series of cyclic stress-strain response curves recorded on a single specimen. The test was started as a conventional isothermal LCF test at 500 °C. Once CSS response had tended to stabilize, temperature was increased while strain cycling continued. In this fashion temperature was first increased in intervals to 750 °C, and then decreased again down to 500 °C. Finally, an IP TMF test was conducted between 500 and 750 °C.

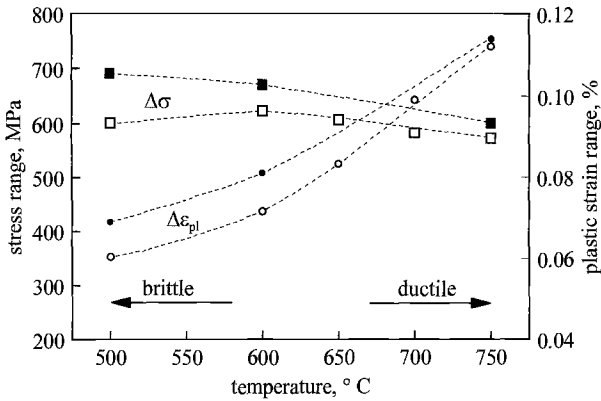


FIG. 2—Temperature dependence of plastic strain range and stress range at half life for isothermal LCF tests conducted in air at $\Delta\epsilon = 0.56\%$ and $\dot{\epsilon} = 3 \times 10^{-3} \text{ s}^{-1}$. Full symbols and open symbols denote tests with $R = -1$ and $R = 0.1$, respectively.

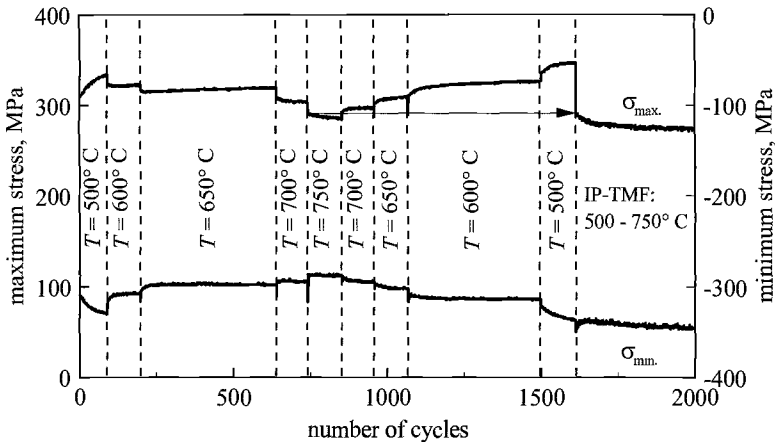


FIG. 3—Maximum and minimum stress vs number of cycles in a complex fatigue test designed to check for history effects on CSS response. The test was conducted in high-vacuum to allow for large number of cycles with fatigue damage still being negligible (the sample did not fail for another 10,000 cycles). $R_e = -1$, $\Delta\epsilon = 0.56\%$ and $\dot{\epsilon} = 1.12 \times 10^{-4} \text{ s}^{-1}$. See main text for details.

Despite the initial hardening observed at 500 °C, the minimum and maximum stresses recorded after the first increase in test temperature rapidly approached the one expected from a conventional LCF test conducted at 600 °C (Fig. 3). Obviously, no irreversible microstructural changes had taken place at 500 °C during the period of initial hardening. Likewise, stresses rapidly approached those expected from the conventional LCF tests after all of the following increases in test temperature. Moreover, the period of initial hardening re-occurred once the test temperatures were decreased again, (Fig. 3).

Obviously, neither the microstructural processes causing rapid cyclic hardening below the DBTT nor those resulting in stress relaxation above the DBTT are irreversible.

The notion that all microstructural processes are mainly reversible also explains the stress response observed in the IP TMF test that followed the last isothermal LCF test section conducted at 500 °C. In the high-temperature part of the TMF cycle all the previous hardening is rapidly relaxed, and thus, the maximum stress (σ_{\max}) obtained in the IP TMF test is equal to that observed in the isothermal LCF test conducted at 750 °C (marked with an arrow in Fig. 3).

From the data presented in Fig. 3 it is apparent that the *isothermal* LCF test did not cause irreversible microstructural changes. The complex fatigue test depicted in Fig. 4 was devised in order to see whether this holds true for TMF test conditions as well. This test was begun as a conventional IP TMF test, and then thermal cycling was stopped at the maximum temperature of TMF cycle while strain cycling continued, i.e., the test mode was changed to isothermal cycling at $T = 750$ °C. Maximum stress during this isothermal part is almost identical to that observed in the continuously run IP TMF test, and no effect on stress response is seen when the test mode was switched back to IP TMF. Moreover, the following isothermal test phase conducted at $T = 500$ °C produced significant cyclic hardening, but had no influence on the stress response once IP conditions were established again.

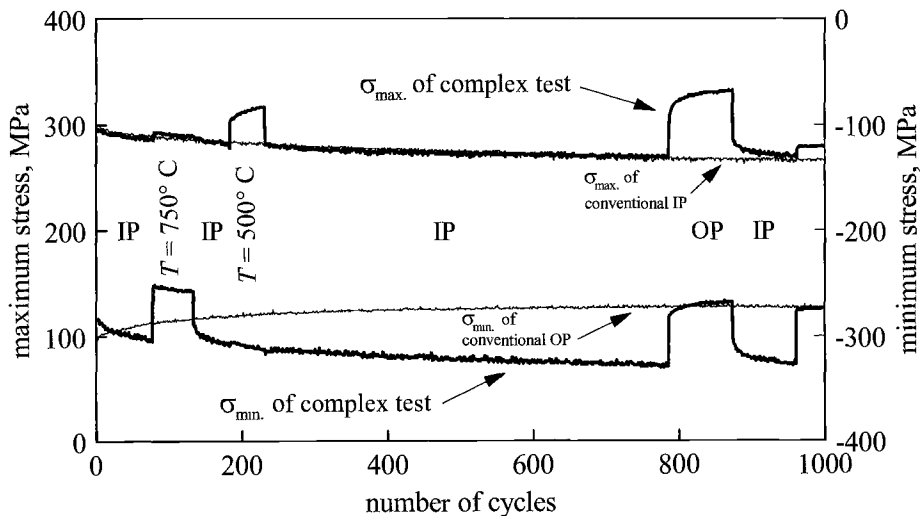


FIG. 4—Cyclic stress response in a TMF test with intermediate isothermal parts as compared to a conventional IP and OP test, respectively. For the sake of clarity only stresses corresponding to maximum temperature are given for the conventional TMF tests. $R_e = -1$, $\Delta\epsilon = 0.56\%$ and $\dot{\epsilon} = 1.12 \times 10^{-4} \text{ s}^{-1}$.

Following an extended period of IP TMF cycling, test conditions were changed to OP TMF. As expected, rapid cycling hardening occurs during the OP TMF part of this test at the minimum temperature, i.e., the maximum stress. The cyclic hardening observed is very similar to the one observed during the initial period of conventional OP TMF tests, and stresses in both tests soon approach each other. Clearly, all previous microstructural changes

are eliminated during the high-temperature part of the TMF cycle. Finally, when test conditions were changed back to IP, stress-strain response rapidly approaches that of the conventional IP TMF test. In summary, neither the intermediate isothermal LCF parts of the complex tests nor the changes in strain-temperature phasing had any significant influence on stress-strain response in the subsequent parts as all microstructural changes were reversible and the material displays almost no effect of prior load history. Consequently, the concept of pseudo-isothermal material appears to be valid, and thus, modeling of CSS response based on isothermal input data is straightforward.

Microstructure

TEM Observations—Titanium aluminides display a very complex microstructure, and the microstructural arrangement depends largely on the orientations of the γ and α_2 lamellae with respect to the external stress axis [11]. Figure 5 summarizes the main microstructural features observed in the cyclically deformed samples. The rapid initial cyclic hardening observed below the DBTT corresponds to a high dislocation density in both the primary γ phase and the γ phase in the lamellar grains (Fig. 5a and b). As expected, the γ/α_2 boundaries are effective obstacles to dislocation motion, and dislocation activity in the α_2 phase is only minor (Fig. 5a). Dislocation networks were observed frequently (Fig. 5b), and these are reported to be effective in increasing the ductility of titanium aluminides [12]. In favorably oriented primary γ -grains and lamellar γ -grains, deformation-induced twins could be observed. This is reported frequently as the material has low intrinsic stacking fault energy. As test temperature was increased, the number of deformation-induced twins increased as well, and above the DBTT the twins contribute significantly to overall deformation both in lamellar and in primary γ -grains (Fig. 5c).

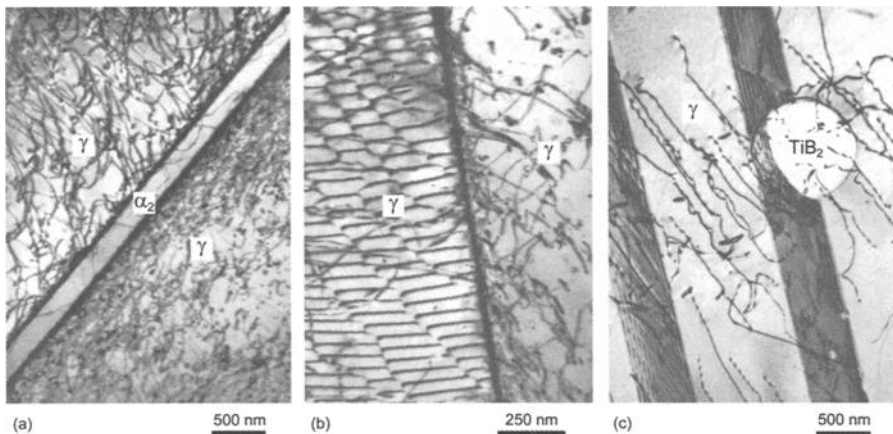


FIG. 5—TEM micrographs showing the various types of internal boundaries present in the samples after cyclic deformation. $R_e = 0.1$, $\Delta\epsilon = 0.56\%$ and $\dot{\epsilon} = 3 \times 10^{-3} \text{ s}^{-1}$. Test temperature was 500 °C for a) and b), and 700 °C for c).

It appeared that the TiB_2 particles present in the microstructure (Fig. 5c) had a negligible effect on overall deformation behavior. Also, degradation of the lamellae boundaries was observed to be insignificant in all the tests conducted. This was to be expected, as the microstructure of various Ti-47Al type alloys was reported to be stable during thermal exposure up to temperatures of 800 °C [13]. Finally, no distinct microstructural differences were observed between the samples cyclically deformed in isothermal LCF tests and in TMF tests. We also note that similar microstructures are reported for the present material to form during tensile tests [14] and in creep tests [4].

Fractography—Figure 6 displays the area where the fatal fatigue crack has initiated in a sample fatigued at 500 °C in high-vacuum. It is evident that most of the lamellae seen on the fracture surface are inclined with respect to the external stress, and that crack initiation has occurred at lamellae oriented about 45° to the external stress axis. This crack initiation mechanism was not immediately evident in samples fatigued in air environment as rapid oxidation initially hindered identification of the crack initiation mechanism. However, longitudinal metallographic sections clearly revealed that the fatigue cracks always had nucleated by the same mechanism irrespective of both the environment and the actual loading conditions.

Similarly, the appearance of the fracture surface was observed to be not affected substantially by test mode. This is to be expected as fatigue crack propagation is known to be very rapid in these materials. Thus, environmental effects on propagation of longer cracks should be negligible under the high stress conditions prevailing in LCF and in TMF tests.

By contrast, the surface crack density was found to be influenced significantly by the actual test conditions. In all fatigue tests conducted at $T < \text{DBTT}$, there were hardly any secondary cracks visible on the outer specimen surface (Fig. 6). As test temperature was increased, the number of secondary cracks increased, and above the DBTT small secondary cracks were abundant. This effect of test temperature on surface crack density was observed to exist for both high-vacuum and air environment.

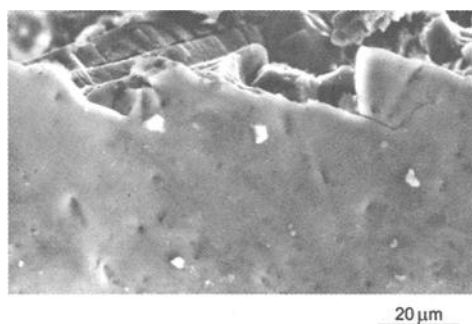


FIG. 6—SEM micrograph showing the crack initiation site at the outer surface and a small part of the fracture surface of a sample fatigued at 500 °C in high-vacuum. External stress axis is vertical. Crack nucleation at lamellae oriented at about 45° to the external stress axis is typical irrespective of actual test conditions.

Fatigue Life

In order to separate the different contributions to damage evolution, a variety of fatigue tests were conducted, and Figure 7 summarizes the effects of the actual test conditions on fatigue life in isothermal LCF tests.

Pure Fatigue—LCF tests in high-vacuum were employed in order to study pure fatigue, i.e., damage driven solely by cyclic plasticity. As seen in Fig. 7, fatigue life in high-vacuum is reduced as the temperature is increased. This is to be expected from Figs. 1 and 2, which demonstrate that plastic strain range, i.e., pure fatigue damage per cycle increases as temperature approaches and exceeds the DBTT.

Effect of Mean Stress—Additional isothermal LCF tests conducted at $R_e = 0.1$ in high-vacuum were used to characterize mean stress effects. The data presented in Fig. 7 demonstrate that mean stress effects are most pronounced at temperatures below the DBTT. Again, this is to be expected as mean stresses were observed to relax rapidly in all isothermal LCF conducted above the DBTT.

Asymmetric hysteresis loops resulting in mean stresses are also characteristic of TMF tests. Furthermore, isothermal LCF and TMF tests both have in common that rapid cycling hardening occurs whenever the temperature is significantly below the DBTT. Thus, TMF hysteresis loops are shifted during cycling, and in OP TMF tests the tensile mean stresses tended to increase with number of cycles (Fig. 8). Similarly, mean stresses became more negative in IP TMF tests as cycling proceeded, i.e., the initial IP part of the test shown in Fig. 4.

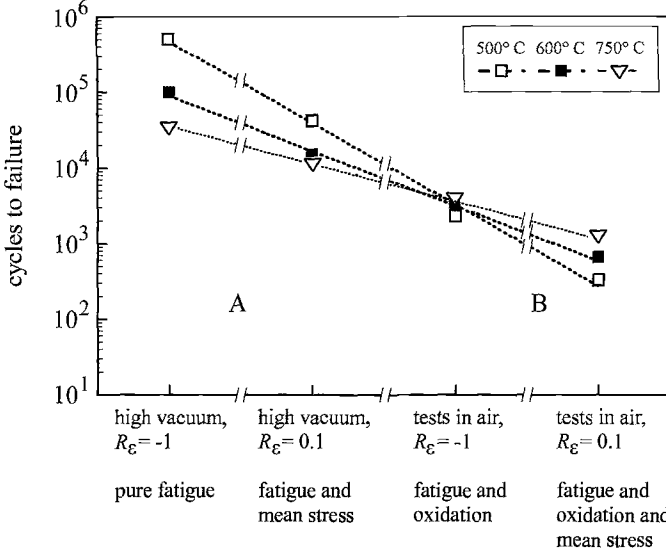


FIG. 7—Influence of test conditions on life in LCF tests conducted at $\Delta\epsilon = 0.56\%$ and $\dot{\epsilon} = 3 \times 10^{-3} \text{ s}^{-1}$. The number of mechanisms contributing to fatigue damage increases from left to right, but the x-axis is not truly linear. Note that depending on the actual test conditions fatigue life can decrease (“A”) or increase (“B”) with increasing temperature.

From the data presented in Fig. 7 it is evident that mean stress effects on fatigue life can be quite large (note the logarithmic scale). It is believed that this is the main reason for the drastic effect of strain-temperature phasing on fatigue life observed in the TMF tests. None of the OP TMF tests conducted with a mechanical strain range of 0.56% exceeded 5000 cycles to failure (Fig. 8). By contrast, none of IP TMF tests conducted at the same mechanical strain range failed within 20X the number of cycles to failure of the corresponding OP tests, and all IP TMF tests were interrupted at this stage.

Environmental Degradation—SEM studies revealed that a non-protective oxide layer forms during fatigue in air, and oxygen-uptake significantly embrittles the subsurface layer. As expected, the data presented in Fig. 7 demonstrate that fatigue life in air is substantially lower than in high-vacuum. In the symmetrical LCF tests ($R_\sigma = -1$) conducted in air, there is a slight tendency towards an increase in fatigue life with increasing temperature. If compared to the high-vacuum data, it is clear that environmental degradation is most pronounced below the DBTT. This is not observed in most other materials. This unusual inverse effect of temperature on fatigue life trend is even more pronounced whenever environmental degradation is combined with tensile mean stress effects, and fatigue lives became very low in such tests (Fig. 7). This holds true for both the isothermal LCF tests and the OP TMF tests (Fig. 8). Comparison of the high-vacuum data obtained at $R_\sigma = -1$ with the data obtained in air at $R_\sigma = 0.1$ reveals that fatigue life is reduced from about 10^5 to a few hundred cycles in the worst case (Fig. 7). Clearly, the material does have a high fatigue potential, but its properties are severely affected both by environment and superimposed mean stresses.

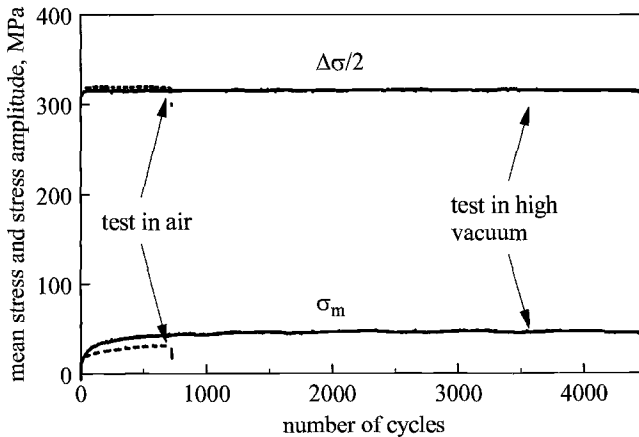


FIG. 8—Evolution of stress amplitude and mean stress in OP TMF tests conducted in air and high-vacuum, respectively. $R_\sigma = -1$, $\Delta\epsilon = 0.56\%$ and $\dot{\epsilon} = 1.12 \times 10^{-4} \text{ s}^{-1}$

Discussion

Cyclic Stress-Strain Response

With respect to modeling of CSS behavior, two microstructural observations made in the present study are paramount. Firstly, good thermal stability of the lamellae boundaries was observed. This eases extrapolation of stress-strain model predictions that are based on input data obtained in short term laboratory tests towards long-term service conditions. In fact, thermal aging experiments conducted by Ramanujan et al. [13] have demonstrated that aging produced little or no change in the lamellar structures up to temperatures of 800 °C.

Secondly, the TEM observations performed in the present study have revealed that there are no distinct differences between the dislocation arrangements established in isothermal LCF and TMF tests, respectively. This allows for modeling of CSS response under TMF conditions based solely on isothermal input data (Ref. 9). Similarly, the effects of prior load history are negligible (Figs. 3 and 4). Given this rather simple material behavior, it should be clear that the details of the actual stress-strain model used are of minor importance.

It is well established that dislocation rearrangements are rather slow, and thus, for most tests conditions, microstructure will not change drastically within an *individual* TMF cycle. Consequently, materials that develop significantly different microstructures in isothermal LCF tests at low and high temperatures, respectively, tend to form unique microstructures in TMF tests [15]. For such materials CSS response under TMF conditions is not directly predictable from isothermal LCF tests.

The isothermal stress-strain response, was found to be drastically different below and above the DBTT, (Fig. 1), and thus, dislocations arrangements formed are expected to vary substantially with test temperature. Hence, pseudo-isothermal behavior was not expected in TMF tests for the material studied, as the TMF cycle applied covered temperatures below and above the DBTT. Clearly, the rapid cyclic hardening observed in the LCF tests conducted at $T < \text{DBTT}$ does lead to dislocation configurations that are easily recovered in the high-temperature part of the TMF cycle ($T > \text{DBTT}$). In fact, TEM studies of fatigued polysynthetically twinned TiAl crystals [16] have shown that recovery can occur at temperatures as low as 400 °C.

Below the DBTT the motion of ordinary $\frac{1}{2}\langle 110 \rangle$ dislocation results in high dislocation density within the primary and the lamellar γ -grains. At low temperatures the internal boundaries present in the microstructure (Fig. 5) act as effective obstacles for dislocation motion [17] and eventually cause rapid cyclic hardening. Above the DBTT, the dislocations at the lamellae boundaries, which have pure screw character, annihilate easily [2,12]. It is also known that defects rapidly annihilate by diffusion of vacancies at $T > 700$ °C, and thus, contribute to recovery above the DBTT [17].

Furthermore, it is reported that deformation-induced twins (Fig. 5c) can also hinder dislocation motion in fatigue [11]. However, recent work [18] has indicated that twins are only weak obstacles, and thus, their effect on macroscopic deformation behavior is only minor unless their volume fraction becomes relatively high. In fact, unusual shapes of the hysteresis loops are commonly observed for this material [3,6], and this might be partly attributed to the formation of deformation-induced twins. For the scope of the present paper, however, it is sufficient to note that twins contribute significantly to deformation

only above the DBTT. Thus, their overall effect on CSS response is rather small as their volume fraction is either low ($T < \text{DBTT}$), or rapid recovery ($T > \text{DBTT}$) compensates for any hardening effect.

Modeling Environmental Degradation and Fatigue Life

As demonstrated in the following, fatigue behavior of the titanium aluminide studied is similar to that of high-temperature titanium alloys in many respects, and thus, it was tempting to try to adapt a TMF life model developed earlier for a titanium alloy [19].

First of all, OP TMF testing is most detrimental for both alloys as a result of environmental degradation. This largely results from the fact that neither material forms a truly protective oxide scale, despite the much higher aluminum content of the titanium aluminide [20]. At temperatures exceeding about 550 °C oxygen diffusion starts to become significant, and an oxygen embrittled subsurface layer is formed. In fact, measurements showed that microhardness in the subsurface layer of the titanium aluminide was increased by about 100 HV 0.0025 in samples fatigued in air as compared to samples tested in high-vacuum.

Conventional titanium alloys show a strong coupling between cyclic plasticity and oxidation [19]. In fatigue tests on the more brittle TiAl alloys, however, plastic strain ranges have to be much smaller. Thus, this effect should be negligible, and the thickness of the embrittled subsurface layer may be computed essentially based on diffusion data. It should be noted that the formation of a mixed $\text{TiO}_2/\text{Al}_2\text{O}_3$ oxide layer was observed in the present study, and oxidation does not demonstrate simple parabolic growth. Our thermogravimetric studies have shown that oxidation is better described by a bi-linear model. Modeling is complicated a bit more by the fact that partial pressures of both oxygen and water vapor affect the oxidation kinetics [21,22]. Consequently, details of the environmental conditions have to be known if the growth of the embrittled subscale is to be modeled accurately. However, the structure of the oxide scale is reported to be unaffected by temperature in the range from 600–1000 °C [23], and thus, it appears that modeling of oxidation is still possible with reasonable effort.

Environmental effects are most pronounced at temperatures below the DBTT, resulting in the unusual inverse effect of temperature on fatigue life for tests conducted in air environment (Fig. 7). Such an anomalous behavior was also observed in fatigue crack growth tests on pure TiAl and a TiNb particulate-reinforced alloy, where properties were reported to be worse at 600 °C than at 800 °C [24]. This is clearly different from the behavior observed in conventional high-temperature titanium alloys [19]. There are many studies indicating that hydrogen embrittlement contributes to damage evolution in titanium alloys at intermediate temperatures (~ 300 to 500 °C). Hydrogen embrittlement is thought to result from the interaction of water vapor with material freshly exposed at the crack tip during cyclic plastic deformation [25]. It is reported that this is also a viable mechanism for titanium aluminides [26], and below the DBTT the material should be much more susceptible to environmental degradation than above the DBTT. This does explain the unusual inverse effect of temperature on fatigue life seen in tests conducted in air (Fig. 7).

The fact that mean stress affects fatigue life most below the DBTT is easily rationalized by the observation that mean stresses rapidly relax in *isothermal* LCF conducted at higher test temperatures. By contrast, mean stresses do not relax in TMF

tests (Fig. 8). Hence OP TMF tests are much more detrimental than IP TMF tests, i.e., the pronounced effect of mean stress on fatigue life seen in the isothermal tests (Fig. 7) fully transfers to TMF loading.

With respect to modeling of fatigue life, crack initiation has to be addressed next. For the high-temperature titanium alloy it was shown that (i) crack initiation can be assumed to occur within the first few cycles, and (ii) initial crack size does correlate well with microstructural features. Both statements hold true for the TiAl alloy studied. As shown in Fig. 6, the fatal crack initiated at lamellae interfaces oriented approximately 45° with respect to the external stress axis. Thus, one can safely assume that a crack corresponding to the size of the lamellae ($\sim 30 \mu\text{m}$) rapidly forms within the first few cycles. In fact, when initial crack size was calculated from the number of cycles to failure observed for tests conducted in high-vacuum, values in the range from 17 to $56 \mu\text{m}$ were obtained. For these calculations, crack propagation was described using the cyclic ΔJ integral, for details see Ref. 19. All that is required in this approach is the initial crack size, CSS response of the material, and crack propagation constants. Initial crack size is known from microstructure, and CSS response can be modeled much easier than for most other materials. Unfortunately, crack growth curves tend to be very steep in the case of titanium aluminides, and below the DBTT, crack growth exponents easily reach values as high as 45 [27]. Consequently, minor inaccuracies in calculation of stress range finally lead to drastically inaccurate estimation of fatigue crack growth rate, and thus, fatigue life could not be predicted satisfactorily for any of the tests conducted in air environment. In this respect titanium aluminides are quite different from conventional high-temperature titanium alloys.

At present, a conservative approach to modeling fatigue life under TMF conditions could be using data obtained from isothermal LCF tests conducted at the *minimum* temperatures of the corresponding TMF cycle. Furthermore, the mean stress that builds up under TMF loading conditions has to be accounted for. Note that mean stresses and fatigue lives in the LCF tests conducted in air at $R_\sigma = 0.1$ and $T = 500^\circ\text{C}$ are very similar to those observed in the corresponding OP TMF test (Figs. 7 and 8).

Clearly, modeling of fatigue life under TMF loading conditions is still far from being satisfactory. With respect to application, however, the tremendous potential of the material, which is evident from the fatigue tests conducted in high-vacuum (Figs. 7 and 8), appears to be very promising. Hence, appropriate surface modifications or coatings [28] are an important issue in this respect. In fact, a few preliminary LCF tests have already indicated that surface modifications such as Cl⁻ ion implantation can substantially increase fatigue life in this alloy.

Summary

Isothermal low-cycle (LCF) fatigue and thermomechanical fatigue (TMF) tests were performed on near- γ titanium aluminide in the temperature range from $500\text{--}750^\circ\text{C}$ both in high-vacuum and air environment. The results of this study can be summarized as follows:

1. The dominating microstructural processes are similar both in isothermal LCF and TMF tests. Thus, cyclic stress-strain (CSS) response under TMF conditions is easily predicted based on isothermal input data.

2. The lamellar microstructure was not degraded substantially during cyclic deformation up to temperatures of 750 °C, and predictions of CSS behavior under long-term loading conditions appear feasible based on short-term laboratory tests.
3. The material displays drastic effects of mean stress and environment on fatigue life. Moreover, the effects are more pronounced below the ductile-to-brittle transition temperature (DBTT), which is about 650 °C for the present material. This results in an unusual inverse dependence of fatigue life on test temperature.
4. Above the DBTT, environmental degradation is mainly due to the formation of an oxygen-embrittled subsurface layer. At the lower test temperatures employed, oxidation is negligible. However, below the DBTT, the brittle material becomes susceptible to hydrogen embrittlement, and hydrogen is assumed to be generated by the reaction of water vapor with material freshly exposed at the crack tip.
5. Out-of-phase TMF tests conducted in air are most detrimental as these combine (i) tensile mean stresses with (ii) high tensile stresses acting on the material in the brittle state, and (iii) environmental degradation.

Acknowledgment

Financial support of this study by MTU München GmbH is gratefully acknowledged.

References

- [1] Wang, Y., Lin, T. L., and Law, C. C., "Brittle-to-Ductile Transition Temperature and its Strain Rate Sensitivity in a Two-Phase Titanium Aluminide with Near Lamellar Microstructure," *Journal of Materials Science*, Vol. 34, 1999, pp. 3155–3159.
- [2] Koeppe, C., Bartels, A., Seeger, J., and Mecking, H., "General Aspects of the Thermomechanical Treatment of Two-Phase Intermetallic TiAl Compounds," *Metallurgical Transactions A*, Vol. 24, 1993, pp. 1795–1806.
- [3] Recina, V., "High Temperature Low Cycle Fatigue Properties of Two Cast Gamma Titanium Aluminide Alloys with Refined Microstructure," *Materials Science and Technology*, Vol. 16, 2000, pp. 333–340.
- [4] Skrotzki, B., "Creep Mechanisms in a Near-Gamma TiAl-Alloy with Duplex Microstructure," *Gamma Titanium Aluminides 1999*, Y.-W. Kim, D. M. Dimiduk, and M. H. Loretto, Eds., The Minerals, Metals & Materials Soc., Warrendale, PA, 1999, pp. 619–626.
- [5] Skrotzki, B., Rudolf, Th., and Eggeler, G., "Creep Behavior and Microstructural Evolution of a Near- γ -TiAl Alloy with Duplex Microstructure," *Zeitschrift für Metallkunde*, Vol. 90, 1999, pp. 393–402.
- [6] Christ, H.-J., Fischer, F. O. R., and Maier, H. J., "High-Temperature Fatigue Behavior of a Near- γ Titanium Aluminide Alloy under Isothermal and Thermo-Mechanical Conditions," *Materials Science and Engineering*, Vol. A319-321, 2001, pp. 625–630.
- [7] Bentley, S. A., Mantle, A. L., and Aspinwall, D. K., "The Effect of Machining on the Fatigue Strength of a Gamma Titanium Aluminide Intermetallic Alloy," *Intermetallics*, Vol. 7, 1999, pp. 967–969.
- [8] Rakowski, J. M., Meier, G. H., Petit, F. S., Dettenwanger, F., Schumann, E., and Rühle, M., "The Effect of Surface Preparation on the Oxidation Behavior of Gamma TiAl-Base Intermetallic Alloys," *Scripta Materialia*, Vol. 35, 1996, pp. 1417–1422.
- [9] Maier, H. J. and Christ, H.-J., "Modeling of Cyclic Stress-Strain Behavior and Damage Mechanisms under Thermomechanical Fatigue Conditions," *International Journal of Fatigue*, Vol. 19, Supp. 1, 1997, pp. 267–274.
- [10] Asaro, R. J., "Elastic-Plastic Memory and Kinematic-Type Hardening," *Acta Metallurgica*, Vol. 23, 1975, pp. 1255–1265.

- [11] Nakano, T., Yasuda, H.Y., Higashitanaka, N., and Umakoshi, Y., "Anomalous Behaviour of Cyclic Deformation and Fatigue Properties of TiAl PST Crystals under Constant Applied Stress," *Acta Materialia*, Vol. 45, 1997, pp. 4807–4821.
- [12] Wunderlich, W., Kremser, T., and Frommeyer, G., "Mobile Dislocations at the α_2/γ Phase Boundaries in Intermetallic TiAl/Ti₃Al-Alloys," *Acta Metallurgica et Materialia*, Vol. 41, 1993, pp. 1791–1799.
- [13] Ramanujan, R. V., Maziasz, P. J., and Liu, C. T., "The Thermal Stability of the Microstructure of γ -based Titanium Aluminides," *Acta Materialia*, Vol. 44, 1996, pp. 2611–2642.
- [14] Morris, M. A., "Dislocation Mobility, Ductility and Anomalous Strengthening of Two-Phase TiAl Alloys: Effects of Oxygen and Composition," *Intermetallics*, Vol. 4, 1996, pp. 417–426.
- [15] Zauter, R., Petry, F., Christ, H.-J., and Mughrabi, H., "Thermomechanical Fatigue of the Austenitic Stainless Steel AISI 304 L," *Thermomechanical Fatigue Behavior of Materials*, ASTM, STP 1186, H. Sehitoglu, Ed., ASTM International, West Conshohocken, PA, 1993, pp. 70–90.
- [16] Yasuda, H. Y., Nakano, T., and Umakoshi, Y., "Thermal Stability of Deformation Substructure of Cyclically Deformed TiAl PST Crystals," *Intermetallics*, Vol. 4, 1996, pp. 289–298.
- [17] Appel, F., Beaven, P. A., and Wagner, R., "Deformation Processes Related to Interfacial Boundaries in Two-Phase γ -Titanium Aluminides," *Acta Metallurgica et Materialia*, Vol. 41, 1993, pp. 1721–1732.
- [18] Skrotzki, B., "Crystallographic Aspects of Deformation Twinning and Consequences for Plastic Deformation Processes in γ -TiAl," *Acta Materialia*, Vol. 48, 2000, pp. 851–862.
- [19] Maier, H. J., Teteruk, R. G., and Christ, H.-J., "Modeling Thermomechanical Fatigue Life of High-Temperature Titanium Alloy IMI 834," *Metallurgical and Materials Transactions A*, Vol. 31A, 2000, pp. 431–444.
- [20] Meier, G. H., Pettit, F. S., and Hu, S., "Oxidation Behavior of Titanium Aluminides," *Journal de Physique IV*, Vol. 3, Colloq. 9, 1993, pp. 395–402.
- [21] Zheng, N., Quadackers, W. J., Gil, A., and Nickel, H., "Studies Concerning the Effect of Nitrogen on the Oxidation Behaviour of TiAl-Based Intermetallics at 900 °C," *Oxidation of Metals*, Vol. 44, 1995, pp. 477–499.
- [22] Taniguchi, S., Hongawara, N., Shibata, T., "Influence of Water Vapour on the Isothermal Oxidation Behaviour of TiAl at High Temperatures," *Materials Science and Engineering*, Vol. A307, 2001, pp. 107–112.
- [23] Jang, J. H., and Lee, D. C., "Oxidation Behaviour of Intermetallic Compound TiAl at High Temperatures," *Journal of the Korean Inst. Met. Mat.*, Vol. 30, 1992, pp. 554–560.
- [24] Rao, K. T. V. and Ritchie, R. O., "High-Temperature Fracture and Fatigue Resistance of a Ductile β -TiNb Reinforced γ -TiAl Intermetallic," *Acta Materialia*, Vol. 46, 1998, pp. 4167–4180.
- [25] Gregory, J. K., "Fatigue Crack Propagation in Titanium Alloys," *Handbook of Fatigue Crack Propagation in Metallic Structures*, A. Carpinteri, Ed., Vol. 1, Elsevier, Amsterdam, 1994, pp. 281–322.
- [26] Mabru, C., Hénaff, G., and Petit, J., "Environmental Influence on Fatigue Crack Propagation in TiAl Alloys," *Intermetallics*, Vol. 5, 1997, pp. 355–360
- [27] Zhu, S. J., Peng, L. M., Moriya, T., and Mutoh, Y., "Effect of Stress Ratio on Fatigue Crack Growth in TiAl Intermetallics at Room and Elevated Temperature," *Materials Science and Engineering*, Vol. A290, 2000, pp. 198–206.
- [28] Niewolak, L., Shemet, V., Gil, A., Singheiser, L., and Quadackers, J. W., "Alumina-Forming Coatings for Titanium and Titanium Aluminides," *Advanced Engineering Materials*, Vol. 3, 2001, pp. 496–500.

Thermomechanical Fatigue Behavior and Cyclic Life Prediction

Using Fracture Mechanics Concepts for a Mechanism-Based Prediction of Thermomechanical Fatigue Life

REFERENCE: Christ, H.-J., Teteruk, R., Jung, A., and Maier, H. J., "Using Fracture Mechanics Concepts for a Mechanism-Based Prediction of Thermomechanical Fatigue Life," *Thermomechanical Fatigue Behavior of Materials: 4th Volume, ASTM STP 1428*, M. A. McGaw, S. Kalluri, J. Bressers, and S. D. Peteves, Eds., ASTM International, West Conshohocken, PA, 2002, Online, Available: www.astm.org/STP/1428/1428_10584, 27 May 2002.

ABSTRACT: An extensive database on the isothermal and thermomechanical fatigue behavior of high-temperature titanium alloy IMI 834 and dispersoid-strengthened aluminum alloy X8019 in SiC particle-reinforced as well as non-reinforced condition was used to evaluate both the adaptability of fracture mechanics approaches to TMF and the resulting predictive capabilities of determining material life by crack propagation consideration. Emphasis was put on the selection of the correct microstructural concepts, then adjusting them using data from independent experiments in order to avoid any sort of fitting. It is shown that the cyclic J-integral (ΔJ_{eff} concept) is suitable to predict the cyclic lifetime for conditions where the total crack propagation rate is approximately identical to plain fatigue crack growth velocity. In the case that crack propagation is strongly affected by creep, the creep-fatigue damage parameter D_{CF} introduced by Riedel can successfully be applied. If environmental effects are very pronounced the accelerating influence of corrosion on fatigue crack propagation can no longer implicitly be taken into account in the fatigue crack growth law. Instead, a linear combination of the crack growth rate contributions from plain fatigue (determined in vacuum) and from environmental attack was assumed and found to yield a satisfactory prediction, if the relevant corrosion process is taken into account.

KEYWORDS: High-temperature titanium alloy, IMI 834, high-temperature aluminum alloy, X8019, metal matrix composite, fracture mechanics, fatigue crack propagation, cyclic life, environmental damage, thermomechanical fatigue, life prediction

Introduction

Cyclic loading of metallic engineering materials at high temperature is known to cause a complex evolution of damage, which cannot be described in a unique and straightforward way. This is particularly true in the case of components subjected to thermomechanical fatigue (TMF) loading conditions. TMF loading occurs in service from a combination of thermal transients during startup and shutdown and mechanical strain cycling. This complex cycling may also lead to damage contributions from environmental degradation (usually termed *oxidation*), *fatigue*, and *creep*. The individual extent of these damage constituents and their mutual interactions depend strongly on the specific material considered and the loading conditions applied.

¹ Professor and Graduate Research Assistant, respectively, Institut für Werkstofftechnik, Universität Siegen, D-57068 Siegen, Germany.

² Professor, Lehrstuhl für Werkstoffkunde, Universität Paderborn, Pohlweg 47-49, D-33098 Paderborn, Germany.

Driven by the need for an accurate concept to predict life of metallic engineering materials subjected to complex loading conditions, as this is a prerequisite for improving reliability and economy of the use of such materials, a variety of life prediction models have been proposed for TMF (e.g., [1–17]). In order to account for the complex interaction of fatigue, creep, and oxidation, very different concepts have been proposed. These models can be subdivided into four classes: (i) empirical, (ii) damage mechanics, (iii) fracture mechanics, and (iv) physical models [6]. Currently, the maturity of physical models for TMF life prediction is rather low. This can mainly be attributed to the problem of modeling the interaction of damage mechanisms where sound physical concepts are lacking. The importance of the physical approach lies primarily in providing the physical background for empirical and damage mechanics models, e.g., by explaining the conditions that promote the formation of cavities. While the concept of damage mechanics is rarely applied to complex loading (e.g., [7]), phenomenological (empirical) approaches are often used [4,8–12] and preferred in practical applications [13]. However, despite the fact that often reasonable agreement between experimentally observed TMF life and predictions by empirical models is reported, the lack of a physical basis seems to be not only unsatisfactory but also dangerous for predictions made outside the range of loading conditions and temperatures collected.

Fracture mechanics concepts describe the growth of a fatal crack from its initial size to its size at failure. These methods are especially useful if a material contains microstructurally large initial flaws or if cracks are initiated early in cyclic life. The local conditions close to or at the crack tip are considered to be responsible for crack propagation and hence parameters such as K , J , and C^* and their cyclic counterparts are applied, since they can be determined on a macroscopic level. The striking advantage of fracture mechanics methods is that crack length represents a simple and physically reasonable measure of damage. Furthermore, the implications of microstructural changes can directly be taken into account in modeling. Hence, from the point of view of transferability and predictive capability, these models seem to be the most versatile for complex loading situations such as TMF. This benefit seems to be important, as laboratory tests are usually run under more severe conditions than those encountered by an actual high-temperature component. Consequently, fracture mechanics has been applied to TMF loading in several studies (e.g., [1,3,14–17]).

The objective of this paper is to provide a compact survey of fracture mechanics based life prediction methods applied to a series of isothermal and thermomechanical fatigue studies performed in the laboratory of the authors [18–20]. Two areas are emphasized in this paper. The first area is the selection and adaptation of models according to the relevant material-specific damage mechanisms as identified by means of thorough microstructural analysis. The second area is the expansion of these models with respect to TMF loading conditions. For the sake of clarity the paper is restricted to fracture mechanics concepts, while the results obtained by application of selected damage mechanics and empirical methods are reported separately [21].

Details on the Materials and Experimental Procedures

Materials Considered

The investigation was performed on three metallic materials, which basically fulfill the requirement of a short crack initiation stage. The first alloy was high-temperature titanium alloy IMI 834, which is a near- α Ti alloy of nominal composition Ti-5.8Al-4.0Sn-3.5Zr-0.7Nb-0.5Mo-0.35Si-0.06C (in wt pct). All data used in this study were obtained on the bimodal microstructure, which is designed to yield an optimum compromise between creep and fatigue performance [22]. Figure 1 shows an optical micrograph of this microstructure, which was established by solution annealing for 2 h in vacuum at 1020 °C, i.e., within the $\alpha+\beta$ phase field, followed by a rapid oil quench. During quenching the β phase transforms into lamellar α (transformed β), which surround the primary α grains. The average grain size and the volume fraction of the primary α grains were found to be 14 μm and 15 vol. percent, whereas the transformed β grains show a grain size of about 25 μm . Before mechanical testing, the material was aged for 2 h at 700 °C and air cooled. This improves the mechanical properties due to the precipitation of fine silicide particles and ordered Ti_3Al .

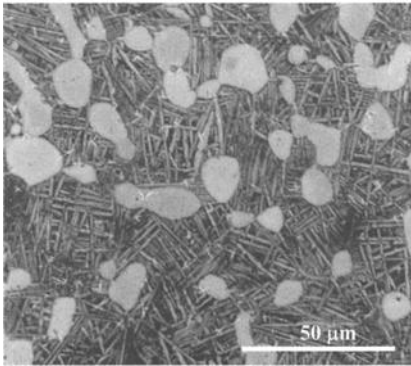


FIG. 1—Optical micrograph of the bi-modal microstructure of IMI 834.

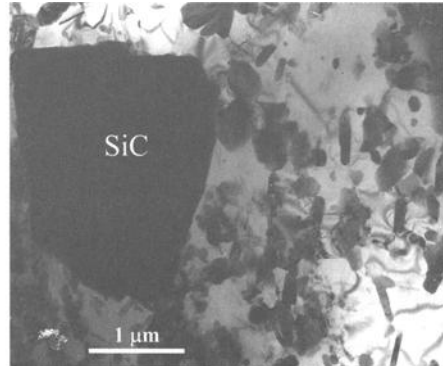


FIG. 2—TEM micrograph of X8019/12.5_p showing a SiC particle and dispersoids.

The second and third alloy used in this study were the high-temperature aluminum alloy X8019/12.5_p (nominal composition Al-8Fe-4Ce in wt pct), which is reinforced with 12.5 vol. pct SiC particles and the unreinforced (i.e., SiC-free) reference alloy. Both alloys are dispersion-strengthened and have excellent microstructural stability at elevated temperatures [23]. Dispersion strengthening is obtained by rapid solidification of the gas-atomized powder as part of the powder-metallurgy production process leading to a high volume fraction of fine intermetallic phases formed by iron, cerium, and aluminum. Transmission electron microscopy (TEM) indicated that the microstructure of both alloys is identical with regards to volume fraction, morphology of these dispersoids, and grain size (about 1 μm). Figure 2 shows a TEM image of the particle-reinforced variant. The

SiC particles present in this material were found to have an average diameter of about 3 μm and seem to have no effect on the dispersoid distribution. Metallographic inspection showed an excellent bonding at the SiC/matrix interface and a homogeneous distribution of both the dispersoids and the SiC reinforcement.

Experimental Procedure

The fatigue tests were performed in servohydraulic testing machines (MTS) equipped with induction heating systems using specimens with a cylindrical gage section, which were either mechanically (X8019 and X8019/12.5_p) or electrochemically (IMI 834) polished before testing. All TMF experiments and the isothermal fatigue tests were performed under fully reversed, push-pull, closed-loop, plastic strain control using a triangular function generator signal. This technique ensures that the specimens were always deformed at a constant (absolute value of) plastic strain rate easing the comparison of the behavior under TMF and isothermal test conditions [24]. In the TMF experiments, the temperature was varied linearly with time and synchronously in-phase (IP) and out-of-phase (OP) with the plastic strain. The tests were always started at the mean temperature and at zero plastic strain with the strain increasing. The fatigue tests were mainly run in laboratory air, however additional experiments were performed in high vacuum to characterize the significance of environmental effects on fatigue life.

In order to determine all the necessary data for the application of selected fracture mechanics life prediction models, creep tests were performed in conventional creep machines, which were modified such that the stress could be kept constant in each test. Furthermore, fatigue crack growth was studied using single edge notch specimens loaded in 4-point bending.

Microstructural changes were characterized applying TEM on samples that were thinned either using conventional twin-jet electropolishing (IMI 834) or ion milling (X8019 and X8019/12.5_p). Scanning electron microscopy (SEM) was used to determine the relevant damage mechanisms. Microhardness profiles were measured on samples of IMI 834, since this alloy forms an oxygen-enriched brittle subsurface layer (α -case) during high-temperature exposure to air. As will be shown below, this oxygen embrittlement is enhanced by cyclic plastic deformation and contributes significantly to fatigue crack propagation. Since hardness within this layer is approximately proportional to the square root of the oxygen concentration [25], microhardness profiles provide a simple means to quantify the depth of this zone.

The main results of the isothermal fatigue tests and the TMF experiments have been published in detail in refs. [26–30]. The description of the fatigue behavior is confined in this paper to those aspects that are relevant to the fracture mechanics life prediction methods used. Results reported in the literature [31–33] were employed where model parameters could not be determined from the experiments performed.

Selected Fracture Mechanics Concepts and Their Application

Cyclic J Integral

Theoretical Background—In the case of Ni-base superalloys, fatigue crack propagation can be described by means of linear-elastic fracture mechanics even at high temperatures. The ductile and less creep-resistant alloys dealt with in this study require a

consideration of the effect of non-elastic deformation on crack growth. According to the concept proposed by Dowling [34], the cyclic J integral can be applied for conditions where a solely cycle-dependent behavior is observed. Following Heitmann et al. [35] an analytically deduced approximation for semicircular cracks under plain strain conditions was used to calculate the effective cyclic J integral as

$$\Delta J_{\text{eff}} = (2.9W_{\text{el,eff}} + 2.5W_{\text{p}}) a = Z_{\text{D}} a \quad (1)$$

$W_{\text{el,eff}}$ and W_{p} are the effective elastic and the plastic deformation strain energy densities, respectively. An a denotes the crack length. Both energy densities can directly be determined from the stress-strain response of cyclic deformation. W_{p} is represented as the area under the ascending branch of the hysteresis loop in a plot of stress σ vs plastic strain ε_{pl} . Crack closure effects are accounted for in $W_{\text{el,eff}}$ using

$$W_{\text{el,eff}} = \frac{(\Delta\sigma_{\text{eff}})^2}{2E} \quad (2)$$

where E is the Young's modulus. The effective stress range $\Delta\sigma_{\text{eff}}$ can be calculated in a first approximation from the stress range $\Delta\sigma$ and the load ratio R using [35]

$$\Delta\sigma_{\text{eff}} = 3.72\Delta\sigma(3-R)^{-1.74} \quad (3)$$

The crack propagation rate (da/dN) is assumed to follow expression (4) so that the number of cycles to failure N_{f} results from an integration of this equation from the initial crack length a_0 at N_0 (which is 1 according to the concept) to the final crack length a_{f} .

$$\frac{da}{dN} = C(\Delta J_{\text{eff}})^m = C(Z_{\text{D}})^m a^m \quad (4)$$

$$N_{\text{f}} = \frac{(a_{\text{f}})^{1-m} - (a_0)^{1-m}}{(1-m)C(Z_{\text{D}})^m} + N_0 \quad (5)$$

An advantage of this concept is that the crack propagation constants C and m in equations (4) and (5) can be derived directly from the Paris regime of fatigue crack growth under loading conditions where linear elastic fracture mechanics applies. Under plane strain condition ΔJ_{eff} and the effective stress intensity range ΔK_{eff} are related via

$$\Delta J_{\text{eff}} = (\Delta K_{\text{eff}})^2 (1-\nu^2) / E \quad (6)$$

where ν is Poisson's ratio ($\nu \approx 0.3$).

Application of cyclic J integral to X8019 and X8019/12.5_p—The results of fatigue life prediction according to equation (5) depend heavily on the value assumed for a_0 . SEM study showed that in particle-reinforced material the fatigue crack always starts from cracked or debonded large SiC particles located at or close to the surface. Hence, irrespective of temperature an initial crack length of 15 μm , determined metallographically, corresponded reasonably well with the diameter of the largest SiC particles. In the SiC-free material, cracks are also formed very early in life starting from the surface in areas which appear brittle. However, metallographic inspection indicated that the initial crack size increases with temperature from a value of 8 μm at room temperature to 15 μm at 300°C. In both materials, fatigue crack propagation seems to govern cyclic life up to temperatures of 250°C where creep deformation can no longer be neglected.

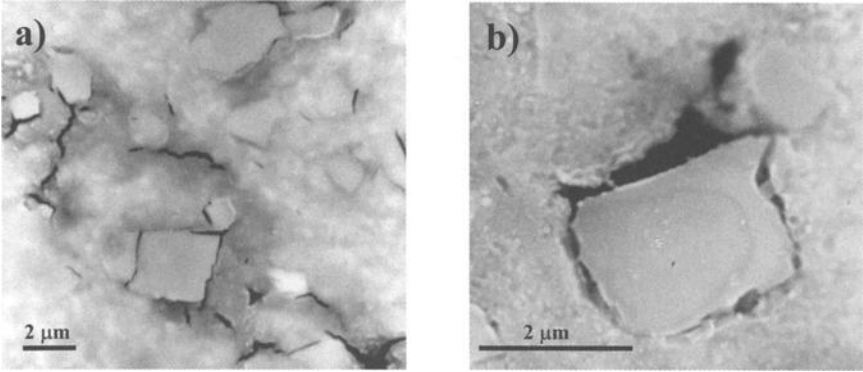


FIG. 3—SEM micrographs of longitudinal sections of specimens cyclically loaded at a plastic strain amplitude of 0.4% at (a) room temperature and (b) 300 °C (stress axis is vertical).

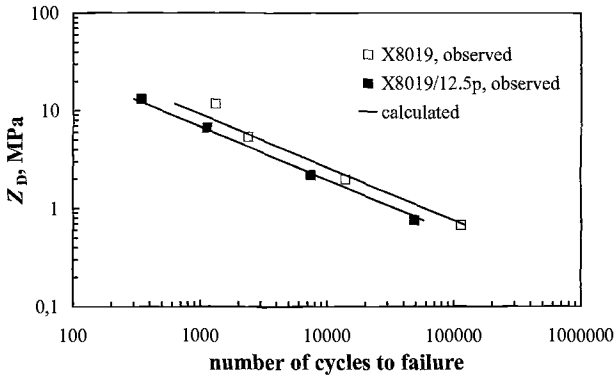


FIG. 4—Comparison of experimentally obtained and calculated lives at room temperature for X8019 and X8019/SiC_p as a function of Z_p .

In the case of the reinforced alloy, a change in damage mechanism both with increasing temperature under isothermal conditions and with strain-temperature phasing in TMF was observed. In isothermal tests at room temperature as well as in TMF OP tests, crack propagation takes place mainly within the matrix. Cracked SiC particles were only found on the fracture surface, i.e., cracking occurs in the stress field of the propagating crack without strong effect on crack growth rate. In the bulk (remote from the main crack) particles debond from the matrix (Fig. 3a) without cracking. At elevated temperature and under TMF IP conditions, voids are formed at the SiC/matrix interface (Fig. 3b) as a bulk phenomenon, and cracking in front of the growing crack seems to lose importance. Thus under these conditions fatigue cracks first extend preferentially within the matrix and later propagate by link-up with the SiC/matrix interface voids.

Because neither creep deformation nor void formation is modeled by the ΔJ concept, its application is only justified at low temperatures ($<250^\circ\text{C}$). The lines in Fig. 4 represent the result of the calculation according to Eq 5 performed for room temperature on the basis of a final crack size of 1 mm and values of C and m from long fatigue crack growth tests (4-point bending). The symbols depict the experimentally determined fatigue lives. Reasonable agreement between calculation and experiment is obtained.

Application of Cyclic J Integral to IMI 834—As has been stated above, the ΔJ concept is very sensitive to a_0 while it is rather insensitive to a_f . This fact was used to indirectly determine the initial crack size as a function of temperature for IMI 834 by adapting a_0 in equation 5 in such a way that it yields the values of N_f of fatigue tests performed in high vacuum. Since environmental effects can be excluded in vacuum and creep deformation was found to be negligible under the test conditions applied, this procedure seems to be justified. Moreover, it provides the basis to estimate the contribution of pure fatigue damage under complex loading conditions as will be shown later. The resulting values of a_0 are plotted versus temperature in Fig. 5.

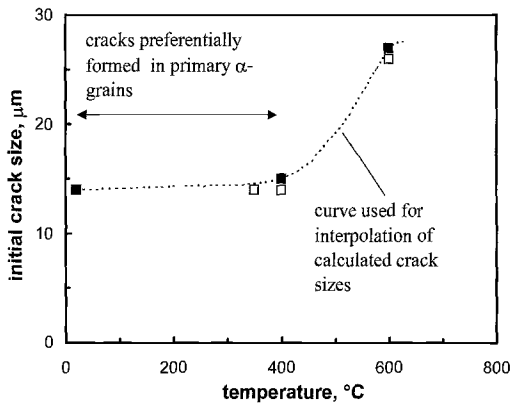


FIG. 5—Initial crack size in IMI 834 as a function of temperature in isothermal tests at a plastic strain amplitude of $2 \cdot 10^{-2}$; ■ calculated from fatigue life obtained in vacuum tests, □ observed by means of metallographic inspection.

In order to check whether the calculated increase of the initial crack size with temperature represents the real behavior, SEM was employed. Figure 6a and 6b show typical examples for crack initiation sites as observed after cyclic deformation at low and high temperature respectively. Up to a testing temperature of about 400°C , most cracks are formed within the primary α grains (Figure 6a). At higher magnification, it becomes apparent that cracks initiate along planar slip bands. Consequently, a_0 should be identical to the primary α grain size ($14 \mu\text{m}$). Hence, the values seen in Fig. 5 in the low temperature plateau are in excellent agreement with those metallographically determined. The increase of a_0 is also reflected in the SEM study. The few fatigue cracks that were found in the primary α grains at $T = 600^\circ\text{C}$ seem to become non-propagating as soon as they reach the grain boundary. The cracks formed in the transformed α grains (the prior β

grains) and seem to grow unhindered (Fig. 6*b*). Therefore, the prior β grain size, which is about 25 μm , provides a reasonable value for a_0 at high temperature in accordance to Fig. 5. A possible explanation for this change in the crack initiation mechanism is given in Ref. 36. The effect is mainly attributed to a transition in slip mode from planar to wavy, which occurs around 600 °C.

It should be noted that all tests dealt with in this study were performed under large scale yielding conditions. Therefore, threshold type behavior at the crack starting sizes observed can be excluded.

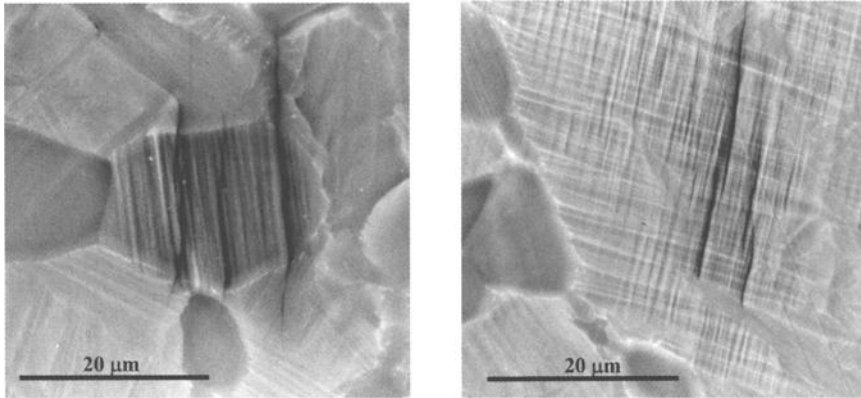


FIG. 6—SEM micrographs showing typical crack initiation sites for tests run at (a) $T = 400$ °C and (b) at $T = 600$ °C (stress axis is horizontal).

Creep-Fatigue Damage Parameter D_{CF}

In contrast to the behavior of IMI 834, creep was found to contribute significantly to cyclic plastic deformation during fatigue testing of X8019 and X8019/12.5_p at temperatures above 250 °C. As already shown above (Figure 3*b*), fractography showed that there was significant void formation at the SiC particles in the reinforced material. However, this creep damage mechanism seems to occur independent of fatigue damage, which continues to be governed by crack growth within the dispersion-strengthened matrix.

Riedel [37] proposed an expansion of the ΔJ approach for situations where void formation and crack propagation are not coupled. Then the crack growth rate depends on the creep-fatigue damage parameter D_{CF} as

$$\frac{da}{dN} = C(D_{CF})^m a^m. \quad (7)$$

Using some simplifying approximations, which are described in detail in [37], D_{CF} can be expressed as

$$D_{CF} = 2.9 \frac{\Delta\sigma_{\text{eff}}^2}{2E} + 2.4(1+3/n)^{-1/2} \Delta\sigma \Delta\varepsilon_{\text{pl}} \left[1 + \left(\frac{\Delta\varepsilon_{\text{cr}}}{\Delta\varepsilon_{\text{pl}}} \right)^{1+n'} \right] \quad (8)$$

where n denotes the Norton exponent determined from constant-stress creep experiments, and n' is the fatigue hardening exponent calculated from the slope of the cyclic stress-strain curve. The separation of plastic strain range $\Delta\varepsilon_{pl}$ and creep strain range $\Delta\varepsilon_{cr}$ for isothermal push-pull loading was performed with reasonable accuracy by means of fatigue tests that employed instantaneous changes in strain rate [38]. All the other parameters were treated exactly as described above in the context of the application of ΔJ so that no fitting was required.

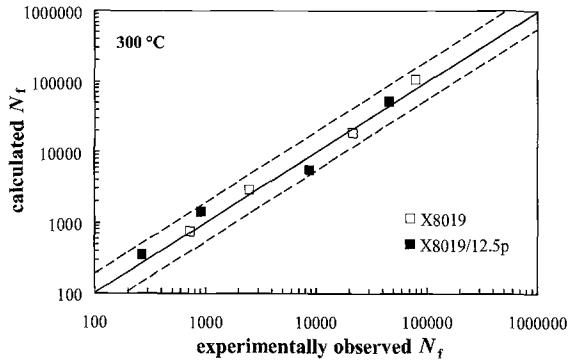


FIG. 7—Comparison of experimentally obtained and calculated lives at 300 °C for X8019 and X8019/SiC_p at a plastic strain rate of 10^{-3} s^{-1} .

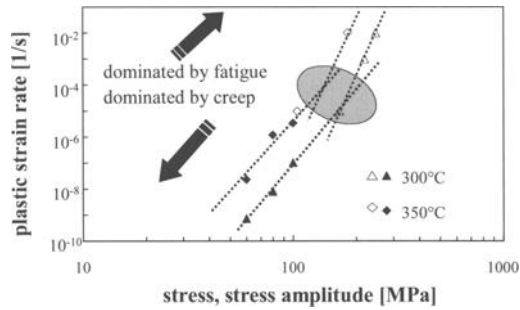


FIG. 8—Strain rate as a function of stress or stress amplitude for X8019/12.5_p; full symbols represent creep tests, open symbols show results from fatigue tests.

Figure 7 compares the experimentally determined number of cycles to fracture with the prediction results for both the reinforced and the SiC-free material at 300 °C and a plastic strain rate of 10^{-3} s^{-1} . It must be emphasized that reasonable agreement can only be expected if the loading conditions applied fulfill the requirements for application of D_{CF} . In particular, if the temperature is too high or the plastic strain rate too low, a strong interaction between creep cavity formation and crack growth may occur, or lifetime may be dependent on creep damage evolution. The regime where creep dominates and corresponding parameters such as C^* apply can be defined where the peak stress required in a fatigue experiment approaches that of a creep test when the inelastic strain rates are also

similar. Figure 8 represents fatigue data as open symbols, while creep data are plotted as full symbols. The change in slope from the fatigue line to the creep line indicates that below a critical plastic strain rate, which increases with temperature, creep dominates the behavior.

Considering Environmental Effects on Isothermal Fatigue and TMF Life of IMI 834

Basic Concept—Environmental effects are known to play an important role in high-temperature fatigue of titanium alloys. Because the dominant mechanism of the interaction of IMI 834 with laboratory air changes with temperature and this change takes place in each TMF cycle, a suitable life prediction model should treat the environmental effects separately instead of considering them implicitly in the fatigue crack growth law. On the other hand, systematic investigations applying various types of load cycles, including those incorporating dwell periods [28, 31], documented that creep damage is negligible in the temperature range where these alloys are currently used. Even in creep tests, large plastic strains must be accumulated to cause significant void formation. Hence, for modeling it is assumed that the overall crack growth rate contains two contributions, which account for pure fatigue and environmental effects. For the sake of simplicity a linear superposition law was applied:

$$\frac{da}{dN} = \left. \frac{da}{dN} \right|_{\text{fat}} + \left. \frac{da}{dN} \right|_{\text{env}} \quad (9)$$

The term in Eq 9 that corresponds to pure fatigue was expressed by means of the ΔJ concept (Eq 4) as described above. Since the crack propagation behavior of titanium alloys in high vacuum is almost independent of temperature, data observed at room temperature on long fatigue cracks were used [31].

Environmental Effect at High Temperature—Microhardness profiles obtained on cyclically deformed samples documented that oxygen uptake seems to be plasticity-enhanced. At temperatures above 600 °C fatigue crack propagation is strongly affected by the existence of an oxygen-embrittled subsurface zone. Following the suggestion of Reuchet and Rémy [39] the thickness of this zone e_m can be described by

$$e_m = \alpha_m \sqrt{t} = \alpha_m^0(T) \left(1 + K_m \frac{\Delta \varepsilon_{\text{pl}}}{2} \right) \sqrt{t} \quad (10)$$

where K_m is a constant and α_m^0 denotes the oxidation constant without cyclic loading, i.e., at zero plastic strain amplitude $\Delta \varepsilon_{\text{pl}}/2$. As the number of cycles N increases, the crack propagates faster, and the environmental contribution to fatigue crack rate decreases. In contrast with [39], where $da/dN|_{\text{env}}$ was assumed to be independent of N , the total crack advance due to the environment was assessed to be equal to the α -case layer thickness at the smooth surface determined metallographically, i.e.

$$\left. \frac{da}{dN} \right|_{\text{env}} = \left. \frac{da}{dN} \right|_{\text{Oxygen}} = \frac{de_m(t)}{dN} = \frac{d(\alpha_m \sqrt{\tau N})}{dN} = \frac{\alpha_m}{2} \left(\frac{\tau}{N} \right)^{1/2} \quad (11)$$

where τ is the cycle time. Inserting equations (11) and (4) into (9) results in an equation that cannot be integrated in closed form. Therefore, the number of cycles to failure was calculated using the Euler-Cauchy iteration method.

Environmental Effect at Intermediate Temperature—Oxygen uptake in high-temperature titanium alloys becomes negligible for temperatures below about 500 °C. As shown by comparative studies on the fatigue crack propagation in nitrogen and humidified air [32,33] the main environmental degradation can be attributed to hydrogen, which results from the reaction of water vapor with the freshly exposed crack tip. Unfortunately, this type of environmental effect on fatigue crack growth cannot be proved directly by metallographic studies. Hence published data on long fatigue crack growth was used to quantitatively describe the detrimental environmental effect in the intermediate temperature range. The expression

$$\left. \frac{da}{dN} \right|_{\text{env}} = \left. \frac{da}{dN} \right|_{\text{Hydrogen}} = H_1 H_2 \left. \frac{da}{dN} \right|_{\text{fat}} \quad (12)$$

was applied where H_1 was derived from the increase in fatigue crack growth rate observed in humidified argon as compared to high vacuum [33]. The parameter H_2 takes the effect of frequency into account and was deduced from test results observed at 0.5 and 35 Hz [32]. Since the effect of temperature and stress intensity factor range on H_1 and H_2 has been shown to be very small, constant values were assumed.

Application to Isothermal Fatigue and TMF—So far the concept presented is applicable to isothermal conditions only. In this case the environmental degradation is mostly dominated by one damage mechanism, which is determined by temperature. In order to describe the behavior over the temperature range of a TMF cycle, it is assumed that the modeled environmental effects are decoupled and therefore oxygen and hydrogen effects can be combined by means of linear superposition.

$$\left. \frac{da}{dN} \right|_{\text{env}} = \left. \frac{da}{dN} \right|_{\text{Oxygen}} + \left. \frac{da}{dN} \right|_{\text{Hydrogen}} \quad (13)$$

Figure 9 represents the maximum stress values observed in fatigue tests in vacuum and ambient air at various temperatures as a function of the number of cycles to failure. The fatigue lives in vacuum are reasonably well predicted with the assumption of pure fatigue (Eq 5). The curves labeled A and B in Fig. 9 represent the calculated results for dry air (Eqs 4, 9, and 11) and humid argon environment (Eqs 4, 9, and 12), respectively. The linear combination of both environmental damage contributions according to equation (13) yields satisfactory results over the whole temperature range (curve C).

Previous work [40] has shown that TMF hysteresis loops can be modeled for many materials based on isothermal data only. Hence, TMF fatigue life in *inert* environment can be predicted in a straightforward manner from isothermal data using the cyclic J integral concept introduced above. However, the question of the initial crack size needs to be addressed. SEM investigation showed that the change in a_0 with temperature observed under isothermal conditions (Fig. 5) does not occur in TMF. Crack nucleation was always observed in the lamellar transformed β matrix. In other words, initial crack size was assumed to be governed by the maximum temperature of the TMF cycle.

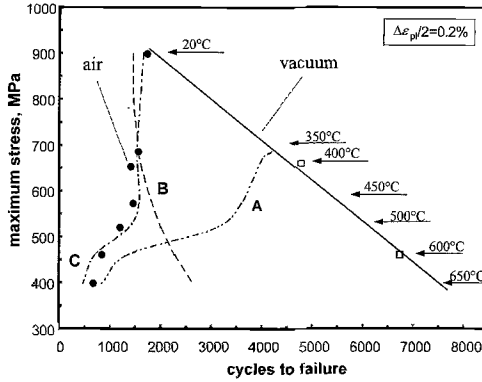


FIG. 9—Comparison of the values of N_f observed in vacuum (\square) and air (\bullet) with prediction results obtained on the basis of different assumptions (see text for details).

The consideration of environmental effects on fatigue life in TMF is more complicated and demands additional assumptions. Hydrogen embrittlement was assumed to be negligible in the case of IP TMF as stresses are mostly compressive in the low-temperature part of the cycle. Consequently, oxidation was the only environmental effect considered for IP TMF. By contrast, both environmental degradation mechanisms were accounted for to predict N_f of OP TMF tests. Oxygen uptake was assumed to be not affected by the sign of the stress and therefore should be rather independent of plastic strain-temperature phasing. Since high tensile stresses coincide with low temperature in OP TMF, hydrogen embrittlement must be expected due to the reaction of the alloy with water vapor.

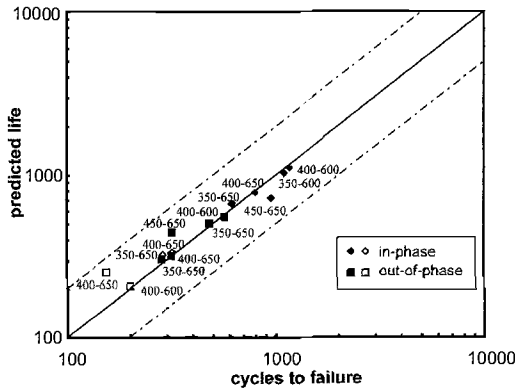


FIG. 10—Comparison of experimentally obtained and calculated lives for IMI 834 under TMF conditions at plastic strain amplitudes of 0.2% (full symbols) and 0.5 (open symbols). Temperature range of test is given next to symbol.

Figure 10 compares the experimentally observed TMF lives of IP and OP tests at two values of the plastic strain amplitude with the results of the prediction calculation. As can be seen, all data points lie within a ± 2 scatter band.

TMF Life Prediction for X8019 and X8019/12.5_p

In contrast to most of the isothermal tests performed on both aluminum alloys, TMF tests were performed applying a low plastic strain rate of 10^{-5} s^{-1} . This fact and the periodically changing temperature in TMF again demands a separate treatment of the oxidation damage contribution. Moreover, no solution is yet known for the D_{CF} parameter under non-isothermal conditions. Hence, a combined consideration of creep and fatigue contribution to damage evolution by means of D_{CF} is not possible for TMF. Therefore, the following basic equation was used assuming that there is no coupling between the individual damage mechanisms.

$$\frac{da}{dN} = \left. \frac{da}{dN} \right|_{\text{fat}} + \left. \frac{da}{dN} \right|_{\text{Creep}} + \left. \frac{da}{dN} \right|_{\text{Oxygen}} \quad (14)$$

Fatigue crack growth rate under pure fatigue conditions can be calculated directly applying equation (4). As crack propagation was found to occur within the matrix during most of the fatigue life, the time-dependent effects should not be contained in the fatigue term of equation (14). Therefore crack growth data obtained for the unreinforced material at room temperature and high frequency was used. The actual value of ΔJ_{eff} can either be taken from a measured TMF hysteresis loop or calculated from isothermal data, which can be justified by the stability of the microstructure [40].

Miller et al. [3] proposed a method to assess the *creep* damage from creep rates observed in monotonic creep tests. $da/dN|_{\text{Creep}}$ was calculated in this way, however it turned out that the creep damage under TMF cycling over the range of temperatures explored was negligible. This is simply a consequence of the strong temperature dependence of the creep rate such that creep deformation takes place only close to the maximum temperature of each TMF cycle.

Oxidation damage was treated analogously to the model of Miller et al. [3] according to

$$\left. \frac{da}{dN} \right|_{\text{Oxygen}} = C_{\text{Ox}} (\Delta J_{\text{eff}})^{m_{\text{Ox}}} \tau^{\psi} = C_{\text{Ox}}^* \exp\left(\frac{-Q_{\text{Ox}}}{RT_{\text{eff}}}\right) (\Delta J_{\text{eff}})^{m_{\text{Ox}}} \tau^{\psi} \quad (15)$$

where m_{Ox} and ψ are material constants and τ is the cycle time. The coefficient C_{Ox} accounts for the temperature dependence of oxidation and obeys an Arrhenius-type equation. In the original model, the apparent activation energy Q_{Ox} is a function of the stress at the minimum temperature of the TMF cycle in order to take mean stress effects on cyclic life into account. As the cyclic life of the materials studied was found to be a weak function of phasing (OP and IP), this extension was ignored ($Q_{\text{Ox}} = \text{const.}$). The oxide formation on aluminum alloys occurs quite rapidly on exposure of the material to air and leads to a thin layer of approximately constant thickness. The oxidation rate, and hence the relevant oxide thickness in TMF, is governed by the maximum temperature, T_{max} , in the cycle. Therefore, the effective temperature, T_{eff} , in Eq 15 was replaced by T_{max} . All the other oxidation parameters of equation (15) were obtained by non-linear least squares regression to *isothermal* fatigue life data from tests performed on *unreinforced* material.

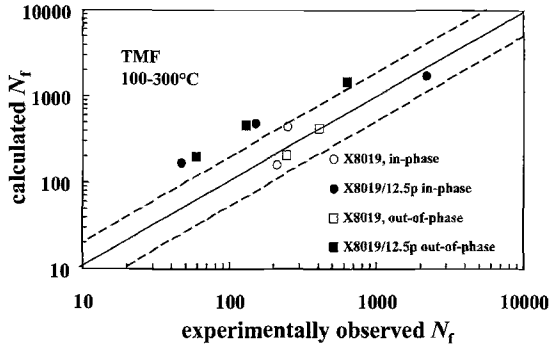


FIG. 11—Comparison of experimentally obtained and calculated TMF lives of X8019 and X8019/12.5_p at a plastic strain rate of 10^{-5} s^{-1} .

Figure 11 shows a comparison of the calculated values for TMF life and the experimental observations. As discussed in detail in ref. 29, a non-conservative prediction results for the particle-reinforced material that can be attributed to the apparent coupling of the damage mechanisms, which is not accounted for by the model.

Concluding Remarks

In principle, the concepts described throughout this paper and the predictions obtained show that fracture mechanics methods are a suitable means of describing fatigue life both for isothermal and thermomechanical conditions. However, the description given here indicates that the concepts must be selected carefully such that they relate closely to relevant damage mechanisms and microstructural processes. Hence, no fracture mechanics damage parameter is *a priori* qualified. Rather extensive testing in combination with detailed microstructural and fractographic studies must be performed, before an appropriate concept can be selected. This approach is illustrated for the alloy X8019/12.5_p in Figs. 12 and 13. In Figure 12, a map is presented, which shows the regimes of plastic strain amplitude (ordinate) and temperature or plastic strain rate (abscissa) where damage can be attributed to fatigue, creep, oxidation, or combinations of these damage types. On the basis of such a map, which resulted from metallographic inspection of correspondingly tested samples, a suitable damage parameter can be chosen and applied to the respective loading parameter regime (Fig. 13). In the case of TMF, adaptation of these concepts to non-isothermal conditions requires even more consideration in order to deduce simplifications, which enable the adaptation but are also reasonable from a mechanistic point of view.

A fundamental disadvantage that arises from the strong connection of the relevant damage processes with the suitable fracture mechanics parameter is the very restricted transferability of corresponding models to new loading conditions. This might be an important reason why empirical life prediction methods are still preferred in practical applications. Despite the lack of physical reasoning, empirical approaches provide similar predictive accuracy (compare [21]) and are simpler to apply. However, the acceptable range of applicability and the transferability are better defined for fracture mechanics methods, if a sound knowledge on the active damage mechanisms exists. Furthermore, in research

the application of fracture mechanics can help to identify those mechanisms that control damage evolution and to quantify these processes.

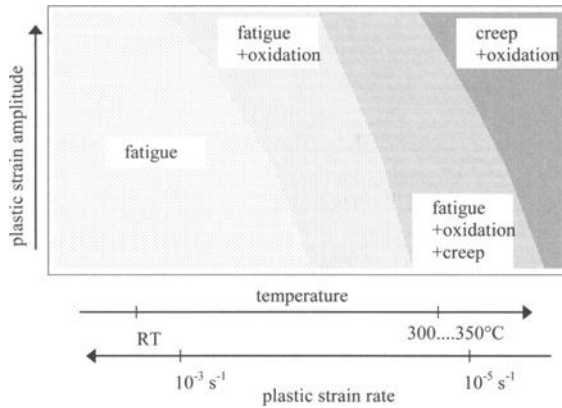


FIG. 12—Schematic map representing the regimes of the relevant main origins for damage as a function of testing parameters for X8019/12.5_p.

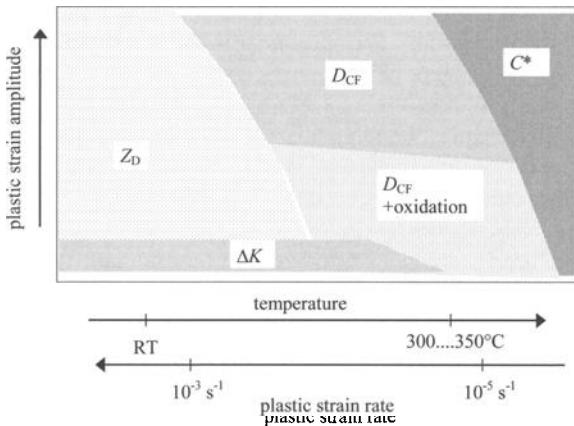


FIG. 13—Schematic map representing the regimes of the respective life prediction concepts deduced from Figure 12 for X8019/12.5_p.

One major limitation of *simple* fracture mechanics concepts has been shown by the poor accuracy of the calculated TMF life of X8019/12.5_p (Fig. 11). Because linear combination of the damage contribution has been used in the model applied, the unsatisfactory prediction result is not surprising, but simply a consequence of coupling of damage mechanisms as confirmed by metallographic observations. There are some models proposed in the literature that try to take these interactions into account. At present however, it appears that the understanding of the physical nature of these coupling effects and the development of a mathematical description of the relevant processes are much too incomplete to provide an appropriate basis for model development.

Acknowledgment

The authors are grateful to Deutsche Forschungsgemeinschaft for financially supporting this study.

References

- [1] Dai, J., Marchand, N. J., and Hongoh, M., "Thermal Mechanical Fatigue Crack Growth in Titanium Alloys: Experiments and Modelling," *Thermomechanical Fatigue Behavior of Materials: Second Volume, ASTM STP 1263*, M. J. Verrilli and M. G. Castelli, Eds., ASTM International, West Conshohocken, PA, 1996, pp. 187–209.
- [2] Neu, R. W. and Sehitoglu, H., "Thermo-Mechanical Fatigue, Oxidation and Creep: Part II – Life Prediction," *Metallurgical Transactions*, Vol. 20A, 1989, pp. 1769–1767.
- [3] Miller, M. P., McDowell, D. L., Oehmke, R. L. T., and Antolovich, S. D., "A Life Prediction Model for Thermomechanical Fatigue Based on Microcrack Propagation," *Thermomechanical Fatigue Behavior of Materials, ASTM STP 1186*, H. Sehitoglu, Ed., ASTM International, West Conshohocken, PA, 1993, pp. 35–49.
- [4] Ellison, E. G. and Al-Zamily, A., "Fracture and Life Prediction under Thermal-Mechanical Strain Cycling," *Fatigue and Fracture of Engineering Materials and Structures*, Vol. 17, 1994, pp. 53–57.
- [5] Rémy, L., Bernard, H., Malpertu, J. L., and Rezai-Aria, F., "Fatigue Life Prediction under Thermal-Mechanical Loading in a Nickel-Base Superalloy," *Thermomechanical Fatigue Behavior of Materials, ASTM STP 1186*, H. Sehitoglu, Ed., ASTM International, West Conshohocken, PA, 1993, pp. 3–16.
- [6] Danzer, R., *Lebensdauerprognose hochfester metallischer Werkstoffe im Bereich hoher Temperaturen*, Gebrüder Bornträger, Berlin-Stuttgart, 1988.
- [7] Chaboche, J. L. and Lesne, P. M., "A Non-linear Continuous Fatigue Damage Model," *Fatigue and Fracture of Engineering Materials and Structures*, Vol. 11, 1988, pp. 1–17.
- [8] Woodford, D. A. and Mowbray, D. F., "Effect of Materials Characteristics and Test Variables on Thermal Fatigue of Cast Superalloys," *Materials Science and Engineering*, Vol. 16, 1974, pp. 5–43.
- [9] Bernstein, H. L., Grant, T. S., McClung, R. C., and Allen, J. M., "Prediction of Thermal-Mechanical Fatigue Life for Gas Turbine Blades in Electric Power Generation," *Thermomechanical Fatigue Behavior of Materials, ASTM STP 1186*, H. Sehitoglu, Ed., ASTM International, West Conshohocken, PA, 1993, pp. 212–238.
- [10] Zamrik, S. Y. and Renauld, M. L., "Thermo-Mechanical Out-Of-Phase Fatigue Life of Overlay Coated IN-738LC Gas Turbine Materials," *Thermomechanical Fatigue Behavior of Materials: Third Volume, ASTM STP 1371*, H. Sehitoglu and H. J. Maier, Eds., ASTM International, West Conshohocken, PA, 2000, pp. 119–137.
- [11] Halford, G. R. and Manson S. S., "Life Prediction of Thermal-Mechanical Fatigue Using Strain Range Partitioning," *Thermal Fatigue of Materials and Components, ASTM STP 612*, D. A. Spera and D. F. Mowbray, Eds., ASTM International, West Conshohocken, PA, 1976, pp. 239–254.

- [12] Halford, G. R., Lerch, B. A., and Arya, V. K., "Thermal Strain Fatigue Modeling of a Matrix Alloy for a Metal Matrix Composite," H. Sehitoglu and H. J. Maier, Eds., ASTM International, West Conshohocken, PA, 2000, pp. 186–203.
- [13] ASME Boiler and Pressure Vessel Code, Section 3, "Rules for Construction of Nuclear Power Plant Components," ASME, New York, 1994.
- [14] Kadioglu, Y. and Sehitoglu, H., "Thermomechanical and Isothermal Fatigue Behavior of Bar and Coated Superalloys," *Journal of Engineering Materials and Technology*, Vol. 118, 1996, pp. 94–102.
- [15] Skelton, R. P., "Crack Initiation and Growth in Simple Metal Components during Thermal Cycling," *Fatigue at High Temperature*, R. P. Skelton, Ed., Applied Science Publishers, London, 1983, pp. 1–63.
- [16] Jordan, E. H. and Meyers, G. J., "Fracture Mechanics Applied to Nonisothermal Fatigue Crack Growth," *Engineering Fracture Mechanics*, Vol. 23, 1986, pp. 345–358.
- [17] Okazaki, M. and Koizumi, T., "Crack Propagation during Low Cycle Thermal-Mechanical and Isothermal Fatigue at Elevated Temperatures," *Metallurgical Transactions A*, Vol. 14A, 1983, pp. 1641–1648.
- [18] Pototzky, P., "Thermomechanischer Ermüdungsverhalten der Hochtemperaturtitanlegierung IMI 834," Doctorate Thesis, Universität Siegen, 1999.
- [19] Jung, A., "Einfluss einer Partikelverstärkung auf das Hochtemperaturermüdungsverhalten einer dispersionsgehärteten Aluminiumlegierung," Doctorate Thesis, Universität Siegen, 2000.
- [20] Teteruk, R., "Modellierung der Lebensdauer bei thermomechanischer Ermüdungsbeanspruchung unter Berücksichtigung der relevanten Schädigungsmechanismen," Doctorate Thesis, Universität Siegen, 2001.
- [21] Maier, H. J., Teteruk, R., and Christ, H.-J., "Modelling Thermomechanical Fatigue Life," *Materials at High Temperatures*, submitted.
- [22] Neal, D.F., "Optimization of Creep and Fatigue Resistance in High Temperature Titanium Alloys IMI 829 and IMI 834," *Titanium Science and Technology*, G. Lütjering, U. Zwicker, and W. Bunk, Eds., Deutsche Gesellschaft für Metallkunde e. V., Oberursel, Germany, 1985, pp. 2419–2424.
- [23] Angers, L., Fine, M. E., and Weertman, J. R., "Effect of Plastic Deformation on the Coarsening of Dispersoids in a Rapidly Solidified Al-Fe-Ce Alloy," *Metallurgical Transactions A*, Vol. 18A, 1987, pp. 555–562.
- [24] Christ, H.-J., Mughrabi, H., Kraft, S., Petry, F., Zauter, R., and Eckert, K., "The Use of Plastic Strain Control in Thermomechanical Fatigue Testing," *Fatigue Under Thermal and Mechanical Loading—Mechanisms, Mechanics and Modelling*, J. Bressers and L. Rémy, Eds., Kluwer Academic Publishers, Dordrecht, The Netherlands, 1996, pp. 1–14.
- [25] Liu, Z., and Welsch, G., "Effects of Oxygen and Heat Treatment on the Mechanical Properties of Alpha and Beta Titanium Alloys," *Metallurgical Transactions A*, Vol. 19A, 1988, pp. 527–542.
- [26] Pototzky, P., Maier, H. J., and Christ, H.-J., "Thermomechanical Fatigue Behaviour of the High-Temperature Titanium Alloy IMI 834," *Metallurgical and Materials*

- Transactions A*, Vol. 29A, 1998, pp. 2995–3004.
- [27] Pototzky, P., Maier, H. J., and Christ, H.-J., “Behavior of the High-Temperature Titanium Alloy IMI 834 under Thermomechanical and Isothermal Fatigue Conditions,” *Thermomechanical Fatigue Behavior of Materials: Third Volume, ASTM STP 1371*, H. Sehitoglu and H. J. Maier, Eds., ASTM International, West Conshohocken, PA, 2000, pp. 18–35.
- [28] Hardt, S., Maier, H. J., and Christ, H.-J., “High-Temperature Fatigue Damage Mechanisms in Near- α Titanium Alloy IMI 834,” *International Journal of Fatigue*, Vol. 21, 1999, pp. 779–789.
- [29] Jung, A., Maier, H. J., and Christ, H.-J., “Effect of SiC-Reinforcement on Thermomechanical Fatigue of a Dispersion-Strengthened High-Temperature Aluminum Alloy,” *Thermomechanical Fatigue Behavior of Materials: Third Volume, ASTM STP 1371*, H. Sehitoglu and H. J. Maier, Eds., ASTM International, West Conshohocken, PA, 2000, pp. 167–185.
- [30] Jung, A., Maier, H. J., and Christ, H.-J., “High-Temperature Fatigue Behaviour and Microstructure of a Dispersoid-Strengthened and SiC-Reinforced Aluminium Alloy,” *Microstructure and Mechanical Properties of Metallic High-Temperature Materials*, H. Mughrabi, G. Gottstein, H. Mecking, H. Riedel, and J. Tobolski, Eds., Wiley-VCH-Verlag, Weinheim, Germany, 1998, pp. 34–49.
- [31] Nowack, H. and Kordisch, T., “Kriech-Ermüdungsverhalten der Titanlegierung IMI 834 bei 600 °C,” *Materialwissenschaft und Werkstofftechnik*, Vol. 29, 1998, pp. 215–228.
- [32] Sarrazin-Baudoux, C., Lesterin S., and Petit, J., “Atmospheric Influence on Fatigue Crack Propagation in TiAl6V Alloy up to 300 °C,” *Titanium '95: Science and Technology*, P. A. Blenkinsop, W. J. Evans, and H. M. Flower, The Institute of Materials, London, 1996, pp. 1895–1902.
- [33] Lesterin S., Sarrazin-Baudoux, C., and Petit, J., “Temperature-Environment Interactions on Fatigue Behaviour in Ti6246 Alloy,” *Titanium '95: Science and Technology*, P. A. Blenkinsop, W. J. Evans, and H. M. Flower, The Institute of Materials, London, 1996, pp. 1211–1218.
- [34] Dowling, N. E., “Crack Growth during Low-Cycle Fatigue of Smooth Axial Specimens,” *Cyclic Stress-Strain and Plastic Deformation, ASTM STP 637*, L. F. Impellizzeri, Ed., ASTM International, West Conshohocken, PA, 1977, pp. 97–121.
- [35] Heitmann, H. H., Vehoff, H., and Neumann, P., “Life Prediction for Random Load Fatigue Based on the Growth Behavior of Microcracks,” *Advance in Fracture Research (ICF6)*, S. R. Valluri, D. M. R. Tuplin, P. R. Rao, J. F. Knott, and R. Dublex, Eds., Pergamon Press, Oxford, England, 1984, pp. 3566–3606.
- [36] Maier, H. J., Teteruk, R. G., and Christ, H.-J., “Modeling Thermomechanical Fatigue Life of High-Temperature Titanium Alloy IMI 834,” *Metallurgical and Materials Transactions A*, Vol. 31A, 2000, pp. 431–444.
- [37] Riedel, H., *Fracture at High Temperatures*, B. Ilschner and N. J. Grant, Springer, Berlin, 1987.
- [38] Jung, A., Maier, H. J., and Christ, H.-J., “Low-Cycle Fatigue Behaviour and Lifetime Prediction of a SiC-Particulate Reinforced Aluminium Alloy at Elevated

- Temperatures," *Proceedings, 12th Conference On Fracture (ECF12)*, M. W. Brown, E. R. de los Rios, and K. J. Miller, Eds., EMAS Ltd, UK, 1998, pp. 303–308.
- [39] Reuchet, J. and Rémy, L., "Fatigue Oxidation Interaction in a Superalloy—Application to Life Prediction in High Temperature Low Cycle Fatigue," *Metallurgical Transactions A*, Vol. 14A, 1983, pp. 141–149.
- [40] Maier, H. J. and Christ, H.-J., "Modeling of Cyclic Stress-Strain Behavior and Damage Mechanisms under Thermomechanical Fatigue Conditions," *International Journal of Fatigue*, Vol. 19, Suppl. 1, 1997, pp. 267–274.

Friederike Grube,¹ Ernst E. Affeldt,² and Haël Mughrabi¹

Thermomechanical Fatigue Behavior of an Aluminide-Coated Monocrystalline Ni-Base Superalloy

REFERENCE: Grube, F., Affeldt, E. E., and Mughrabi, H., "Thermomechanical Fatigue Behavior of an Aluminide-Coated Monocrystalline Ni-Base Superalloy," *Thermomechanical Fatigue Behavior of Materials: 4th Volume, ASTM STP 1428*, M. A. McGaw, S. Kalluri, J. Bressers, and S. D. Peteves, Eds., ASTM International, West Conshohocken, PA, Online, Available: www.astm.org/STP/1428/1428_10592, 24 June 2002.

ABSTRACT: This study is part of a project concerned with the effect of diffusional aluminide coatings on the stress response and life of a coated monocrystalline nickel-base superalloy (CMSX-6) during thermomechanical fatigue (TMF) testing.

In this project, the effects of different platinum-modified aluminide coatings are studied. To separate the effects induced by the coatings from other effects with respect to the TMF life, uncoated specimens are investigated as reference specimens.

In this paper, TMF studies on specimens coated with a two-phase platinum-modified aluminide coating are reported. The TMF tests were performed with a particular type of asymmetric counterclockwise diamond cycle (lower and upper temperatures: 400 °C and 1100 °C, respectively) representing typical loads experienced by turbine blades under conditions of service during start-up and shut-down operation. The life of the specimen is determined by crack initiation and propagation. Crack initiation is observed to occur early during TMF life at the surface of the coating as a consequence of its brittleness at low temperatures. Thus, the coating shortens the life of the substrate-coating system. In this context, the characteristics of the two-phase platinum-aluminide coating studied here and its influence on the mechanisms of crack initiation and propagation during TMF are of special interest.

KEYWORDS: thermomechanical fatigue, coating, platinum-aluminide, nickel-base superalloy, single crystal, crack initiation

Introduction

The components in today's aero engines experience several types of loads: mechanical and thermal loads and oxidative and corrosive attack. In the course of operating time, these loads can lead to failure of the material. Thermomechanical fatigue (TMF) failures, caused by simultaneous severe changes of temperature and stress, are of particular concern. In the aero engine, the blades in the high-pressure part of the turbine are exposed to the highest temperatures and mechanical loads. Therefore, these components are made of monocrystalline nickel-based superalloys. These alloys have sufficient mechanical strength at high temperatures but insufficient resistance against oxidation and corrosion and, as a consequence, are degraded by the hot gas stream, if they are not protected by an oxidation-resistant coating. A detailed overview of different

¹ Research Associate and Professor, respectively, University of Erlangen-Nürnberg, Institut für Werkstoffwissenschaften, Lehrstuhl 1, Martensstr. 5, D-91058 Erlangen, Germany.

² MTU Aero Engines, Dept. TWWZ, Dachauer Str. 665, D-80995 Munich, Germany.

types of coatings, their characteristics, applications, and failure mechanisms is given in Ref. 1.

In this context, the coatings of interest are several variants of diffusional aluminide coatings: either pure nickel aluminides or platinum-modified aluminides, which can be two-phase (β -NiAl + PtAl₂) or single-phase (β -NiAl). Simple aluminide coatings are widely used as protective coatings for high-temperature applications because of their excellent oxidation resistance. The platinum modification of the aluminide coatings has been developed because of the significantly increased resistance against hot corrosion compared to the conventional aluminide coatings [2,3]. Furthermore, an improved adherence of platinum-modified coatings is reported, especially for the combination of thermal barrier coatings on underlying metallic bond coats [4,5]. Finally, the oxidation resistance also tends to be increased by the platinum modification: the degradation of the coating is characterized by the transformation of the β -NiAl phase, the main phase of the coating, to the γ '-Ni₃Al phase because of the loss of aluminium. This is due to the spalling and the reforming of the surface oxide layer as well as to diffusion into the substrate. By the addition of platinum, the β -NiAl phase is stabilized, which is the reservoir for the replacement of aluminium atoms being lost during the coating life [6–8].

The above-mentioned coating materials show a good oxidation resistance, but are generally extremely brittle at low temperatures. This is due to the fact that the main constituents of these coatings are intermetallic alloys, namely the β -NiAl phase or β -NiAl in combination with the PtAl₂ phase. Ordered alloys are known to be brittle at low temperatures and to exhibit a brittle-to-ductile transition at a higher temperature. For the pure β -NiAl phase, the transition temperature is between 300 °C and 500 °C, and it increases with the content of alloying elements and with deviations from the stoichiometry [9]. The ductility of nickel aluminide as a coating material is reported to be a function of the aluminium content [10]. The brittle-to-ductile transition temperature of different coatings with and without platinum modification, investigated under tensile conditions, lies between 600 °C and 850 °C in both cases [11,12].

As a consequence, aluminide coatings can affect the TMF life drastically: the brittle nature of the coatings leads to crack initiation very early in TMF life, especially if the coating is loaded by tensile stresses during the low temperature part of the TMF cycle. As a consequence, oxidation and crack propagation into the substrate can start immediately after the cracking of the coating. As a result, the TMF life of the coated material is shortened in comparison to the TMF life of the uncoated material [13–15].

In comparison to isothermal fatigue tests, all the types of TMF cycles developed in recent times have the goal to simulate the real service conditions of the material as realistically as possible. In general, the temperature and the strain are used as command signals with triangular waveform. Depending on the phase shift between the two signals, different types of TMF cycles can be defined.

In this paper, we shall report the results of our investigations on the effect of a two-phase platinum-modified aluminide coating on the TMF life. The substrate material is the monocrystalline nickel-based superalloy CMSX-6. The TMF tests were performed with an asymmetric so-called counterclockwise diamond-shaped cycle, which is considered representative for the loads occurring in the component during start-up and shut-down operation of the turbine.

Experimental

In the laboratory, the real service conditions are simulated by the thermomechanical fatigue (TMF) test. The asymmetric cycle with a phase shift of -135° and a strain ratio $R_\epsilon = -1$ is considered to be one of the most typical cycle types with respect to the operating conditions in the turbine blade of the aero engine. This type of TMF cycle was the one performed in this study. The shape of this cycle type is shown schematically in Fig. 1. Minimum and maximum temperatures for all tests performed were 400°C and 1100°C , respectively. The heating and cooling rates were 10 K/s . Thus, the duration of one cycle was 140 s . The mechanical strain range was varied between 0.5% and 1.0% . Comparable TMF cycle types had been used in earlier work concerned with high-temperature applications of aluminide coatings on nickel-based superalloys [14,16–19].

The differences between the types of strain that are dealt with throughout this study have to be emphasized. As the *total* strain ϵ_{tot} we define the sum of the *thermal* strain ϵ_{th} and the *mechanical* strain ϵ_{mech} as shown in Eq 1, the mechanical strain being the sum of elastic and plastic strain.

$$\epsilon_{\text{tot}} = \epsilon_{\text{th}} + \epsilon_{\text{mech}} \quad (1)$$

During the TMF test, the mechanical strain, which is the command signal, is calculated from the measured total strain and the thermal strain. The latter is calculated as a function of the measured temperature at any instant of time during the test. As a consequence, the thermal strain as a function of the temperature has to be determined before each test under load-free conditions.

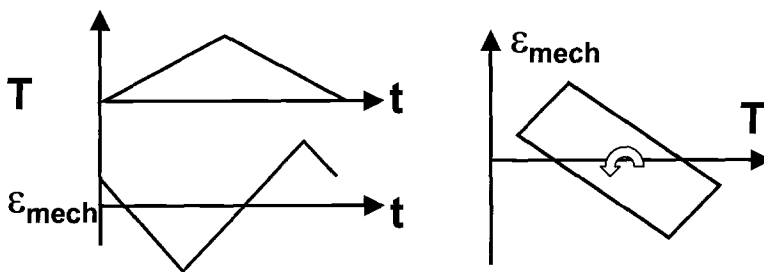


FIG. 1—Definition of the TMF cycle type performed in this study.

The experiments were carried out on a uniaxial servohydraulic testing system of the type MTS 810 with maximum loads of $\pm 50\text{ kN}$ and a digital controller, which was connected to a PC for the purpose of defining the command signals and for the data acquisition. The total strain was measured by means of a high-temperature extensometer with 12 mm gauge length. A detailed view of the central part of the TMF testing system with the specimen is shown in Fig. 2. The heating of the specimen was done by a high-frequency generator (200 kHz , max. 5 kW) and an induction coil whose shape was optimized with respect to the sample geometry in order to obtain a homogeneous

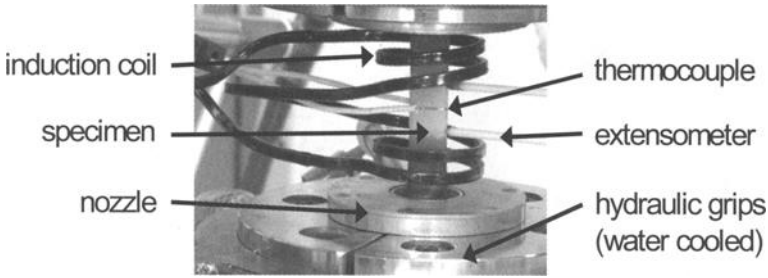


FIG. 2—View of the central part of the TMF testing system.

temperature profile over the gauge length of the sample. Special thermocouples were used for temperature measurements. Instead of spot welding, another technique of fixing the thermocouple to the specimen was preferred in order to avoid any influence on crack initiation. First the welded point of a thermocouple was pressed to a flat tape of about $100\ \mu\text{m}$ in thickness. Then, this thin tape was fixed to the surface of the specimen in the middle of the gauge length by a spring (which is not visible in Fig. 2).

Although a flat sample geometry was chosen for reasons of high natural cooling rates, forced air cooling had to be applied to reach the cooling rate of $10\ \text{K/s}$. To obtain a good reproducibility of the airflow, two nozzles with a ring-shaped geometry were built and placed at the top and the bottom of the specimen, respectively, so that the air was conducted homogeneously onto the specimen. With this set-up, the temperature along the gauge length, measured on the specimen surface, was always constant within $\pm 10\ ^\circ\text{C}$.

The longitudinal axis of the specimen is coincident within a few degrees ($< 10^\circ$) with the crystallographic $[001]$ direction, which at the same time is the growth direction of the monocrystalline material (Fig. 3).

To avoid crack initiation outside the range of the extensometer, the coated area was restricted to the gauge length of the specimen. Figure 4 shows the as-coated micro-

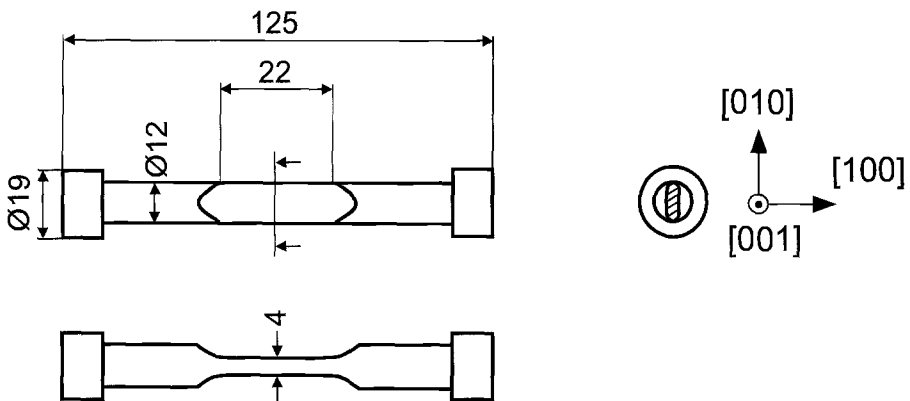


FIG. 3—The specimen geometry (all dimensions in mm) and the relationship of sample geometry and crystallography.

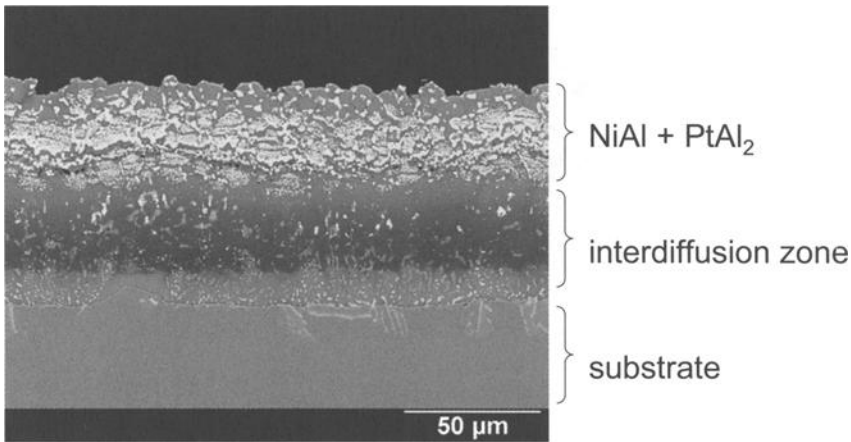


FIG. 4—Scanning electron micrograph (backscattered electron contrast, BSE) of the as-coated microstructure of the two-phase Pt-modified aluminide coating.

structure of the two-phase aluminide coating. The coating is produced by a special type of CVD (chemical vapour deposition) process, called pack cementation process. The coating thickness is about 50–70 μm .

The fine-grained main coating consists of the intermetallic phases β -NiAl (dark phase) and PtAl₂ (bright phase). The diffusion zone is mainly β -NiAl, containing a number of various precipitates (intermetallics, carbides). The monocrystalline substrate material is observed to exhibit the well-known γ/γ' -structure typical of all Ni-base superalloys.

Results and Discussion

Thermal Strain

The values of the thermal strain are used to calculate the command signal (which is the mechanical strain). It is important to determine the thermal strain as a function of the measured temperature as precisely as possible, because any difference between the calculated thermal strain and the actual thermal strain of the specimen will result in mechanical stresses which, ideally, should be equal to zero but are not exactly zero in the actual test. In Ref. 20, the requirements for high precision TMF test control under the conditions of high heating and cooling rates are discussed in detail.

The reason for the difference between calculated and actual thermal strain is the difference between the measured temperature, which in fact is the temperature of the surface of the specimen, and the average temperature of the bulk material. For this reason, a slight hysteresis of the measured thermal strain versus the temperature can be observed during the heating and cooling parts of the cycle, which reflects the difference between the bulk temperature and the surface temperature.

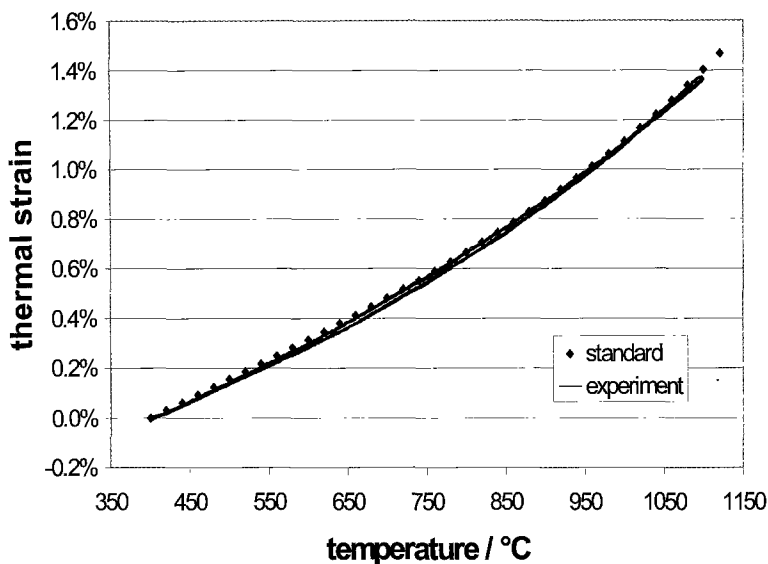


FIG. 5—Comparison of measured and standard values³ of the thermal strain of CMSX-6.

Optimizing the system with respect to the temperature control means minimizing the hysteresis of the thermal strain as a function of the temperature, as shown in Fig. 5. A reasonably narrow hysteresis curve is observed as well as a good agreement of the absolute values of the measured thermal strain with the standard values of CMSX-6.

TMF Life and Stress Response

A limited number of TMF tests with different mechanical strain ranges were performed for coated and for uncoated specimens. The parameters of each test and the TMF lives (number of cycles to failure, N_f) of the samples are listed in Table 1. The TMF life of the coated specimens is clearly reduced in comparison to the uncoated specimens. There is not much scatter within each series of tests. The results are summarized in the diagram in Fig. 6, where the mechanical strain range is plotted versus the number of cycles to failure N_f for each test. The failure criterion is either a 30% drop of the maximum stress or the catastrophic failure of the specimen.

In Ref. 19, a conventional coating without platinum-modification on a monocrystalline nickel-base alloy is investigated under identical cyclic conditions. The observed effect on the TMF life is basically the same as the one detected in this study. There is no evidence for a principal difference in the TMF behavior of the conventional and the two-phase platinum-modified coatings on monocrystalline superalloy substrates. This is also confirmed by the comparison of results presented in [13,14,17].

³ Internal standard, E. E. Affeldt, MTU Aero Engines, Personal communication.

TABLE 1—Mechanical strain ranges and TMF lives of all specimens investigated.

sample N°	$\Delta\epsilon_{\text{mech}}$	N_f
uncoated 1	0.9 %	3029
uncoated 2	0.8 %	5554
uncoated 3	0.7 %	9306
coated 1	0.8 %	921
coated 2	0.7 %	2296
coated 3	0.6 %	3001
coated 4	0.5 %	7119
coated 5	initial state	

There is no principal difference in the mechanical stress response of coated and uncoated specimens, which is expected because the coating thickness is only about 50 μm . For this reason, the contribution of the coating to the load-bearing cross section can be neglected. The interpretation of the results is based on the same assumption in Ref. 21. Figure 7 shows a typical example of a TMF cyclic deformation curve. Whereas the stress range $\Delta\sigma$ remains constant during the whole life of the sample except for the last cycles, the maximum and minimum stresses (σ_{max} , σ_{min}) shift (relax) towards more positive values within the first cycles of each test. Afterwards, saturation of the stress can be observed. At the end of the TMF life, when a crack is propagating through the material, reducing the load-bearing cross section, the maximum stress drops fast until the specimen fails. A similar evolution of the stresses as in the present study is observed in [19]. The deformation behavior and stress response under TMF loading can also be simulated by numerical methods, compare [22].

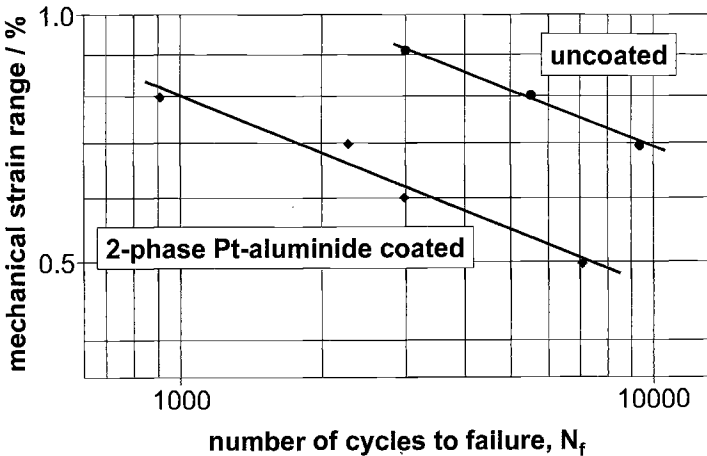


FIG. 6—Overview of tests performed in a plot of the mechanical strain range versus the TMF life.

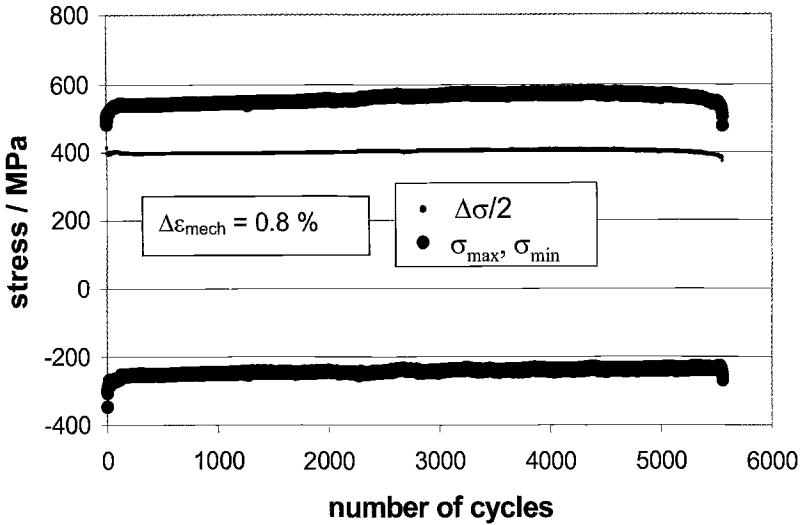


FIG. 7—Maximum and minimum stress values (σ_{max} , σ_{min}) and one half of the stress range ($\Delta\sigma/2$) versus the number of cycles N , uncoated specimen, $\Delta\varepsilon_{mech} = 0.8\%$.

The TMF behavior of the material can also be visualized by inspection of the hysteresis loops of the stress versus the mechanical strain which is shown in Figure 8. Once the material has relaxed completely, the stress response remains constant over a large portion of the TMF life until the onset of failure of the specimen. In other words, the hysteresis loops indicate that most of the plastic deformation of the material takes

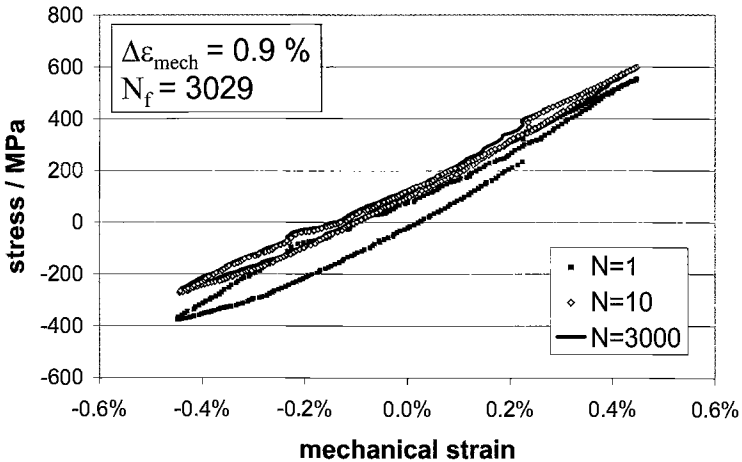


FIG. 8—Evolution of hysteresis loops of the stress versus the mechanical strain.

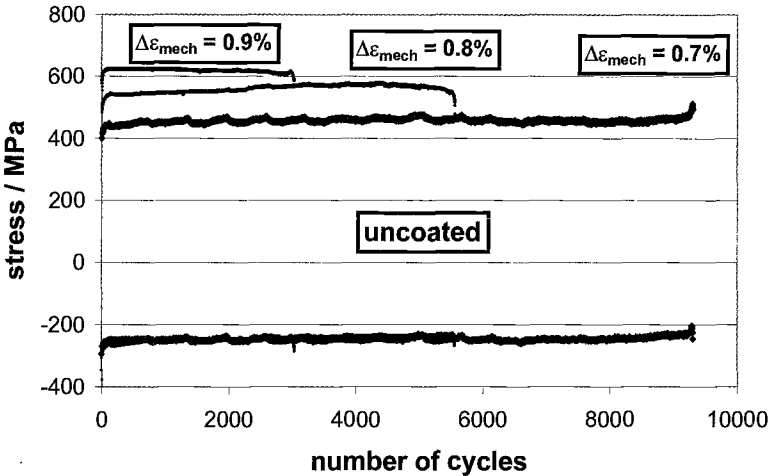


FIG. 9—Cyclic deformation curves: evolution of maximum and minimum stresses under TMF loading for uncoated specimens.

place in the first cycles, as had been reported earlier [15,18,19], whereas for the rest of the TMF life, deformation is predominantly elastic. The shape of the hysteresis loop of the first cycle ($N = 1$) is relatively broad, especially in the compressive part of the cycle, where the high temperature facilitates the plastic deformation. During the first few cycles, a shift towards more positive values of the stress is observed.

Afterwards, the stresses stay constant, and the hysteresis loops remain narrow over the whole range of the TMF life except for the very last cycles. This behavior is reflected in the almost perfect coincidence of the hysteresis loops observed after $N = 10$ and $N = 3000$ cycles (number of cycles to failure, $N_f = 3029$), as shown in Fig. 8.

The comparison of the results obtained for the uncoated specimens at different strain ranges shows a decrease of the TMF life with increasing strain range (Fig. 9). This is not surprising, as the maximum tensile stresses are higher the larger the strain range is. In contrast to the tensile stresses, the maximum compressive stresses coincide for all three strain ranges. This is supposed to be a consequence of the high temperature and the larger plastic deformation during the compressive part of the TMF cycle. Since the temperature of the specimen is lower in the tensile part of the cycle, there is little plastic deformation, and the different stresses observed are approximately proportional to the applied strain ranges. Finally, it is pointed out with reference to Fig. 9 that, in one case ($\Delta\varepsilon_{\text{mech}} = 0.7\%$), the tensile peak stress is found to increase in the final stage of fatigue life (a similar behavior is seen in Fig. 11). This is always the case, when the fatal crack develops outside the extensometer gauge range.

In the case of the coated samples, it is also observed, for similar reasons as in the case of the uncoated samples, that the compressive peak stresses are rather similar for the different strain ranges, whereas the tensile peak stresses differ markedly (Fig. 10).

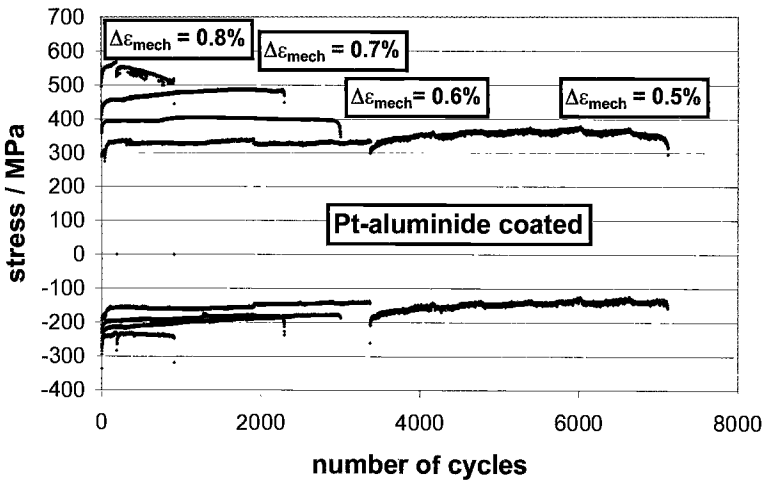


FIG. 10—Cyclic deformation curves: evolution of maximum and minimum stresses under TMF loading for coated specimens. The discontinuities in some of the curves stem from interruptions of the test for technical reasons.

For the coated specimen loaded at the mechanical strain range of 0.8%, a strong cyclic softening is observed, which was not the case for all other samples. This is possibly due to the fact that this test had to be restarted in order to replace the thermocouple. This restarting procedure could have damaged the specimen, leading to an acceleration of the crack initiation or propagation at least in the case of the high strain range applied.

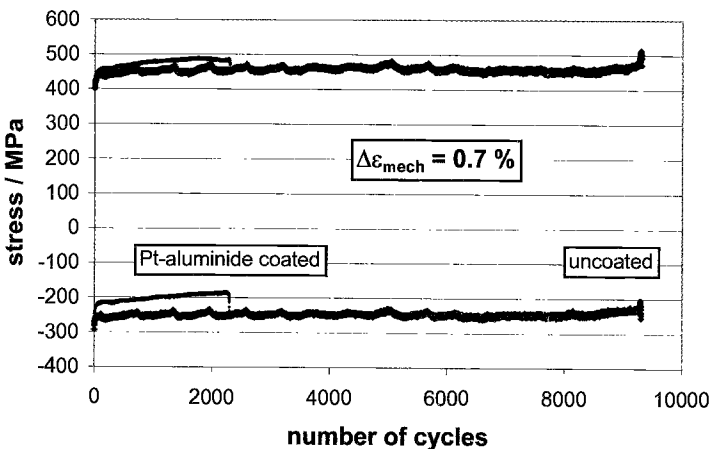


FIG. 11—Comparison of cyclic deformation behaviors of coated and uncoated samples under TMF loading ($\Delta\epsilon_{\text{mech}} = 0.7\%$). The small stress oscillations were caused by small temperature fluctuations (day/night, summer time).

The effect of the coating on the TMF life is clearly demonstrated by a direct comparison of the cyclic deformation behavior of a coated and an uncoated specimen loaded at the same strain range. As the results are similar for all comparable TMF tests performed, only one typical example is presented in Fig. 11. The TMF life of the coated specimen is reduced by a factor of 4 to 5 in comparison to the uncoated specimen.

Crack Initiation and TMF Life

The reason for the drastic effect of the coatings on the TMF life is a change in the mechanism of crack initiation. In Fig. 12, the macroscopic views of the surfaces of a coated and an uncoated specimen are compared. On the left, the gauge length of an uncoated specimen can be seen, which is broken into two pieces at the end of its TMF life. On the right, only one part of a coated specimen after catastrophic failure is shown, namely the upper part of the former gauge length (bottom) and some of the adjacent uncoated substrate material (top). To avoid the initiation and propagation of cracks outside the gauge length, the region to be covered with the coating was limited to the gauge length for all the coated specimens investigated.

During TMF cycling, many short cracks are initiated all over the surface of the uncoated specimen. The sites of crack initiation are oxide spikes forming during the high-temperature part of the TMF cycle (point initiation mode), as shown in scanning electron microscopy (SEM) micrographs in Fig. 13, using secondary electron (SE) and backscattered electron (BSE) contrast. The crack growth during the TMF life is accelerated by the oxidation and the cracking of the brittle oxides formed inside the crack during cycling.

For the coated specimens, brittle cracking of the coating occurs very early in TMF life. The cracks are long and macroscopically straight (line initiation mode). Only few cracks are observed, all of which are perpendicular to the load axis of the specimen and approximately equidistant (Fig. 14). Additionally, the length of the brittle cracks is not limited as the cracks propagate completely around the circumference of the specimen from the moment of their initiation. The terms "point" and "line" initiation have been used earlier in the literature, e.g. [21,23–25].

Figure 13 shows details of the crack initiation and propagation at oxide hillocks at the surface of an uncoated specimen, which corresponds to the mode of crack initiation

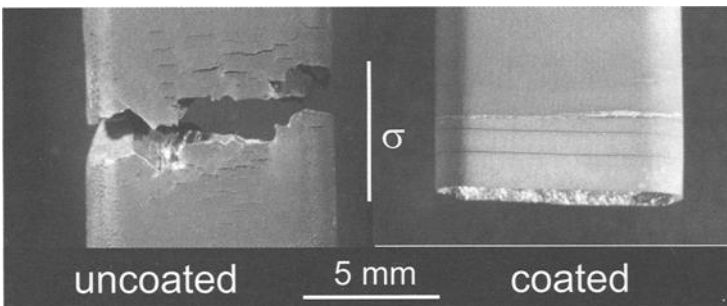


FIG. 12—Comparison of the two modes of crack initiation under TMF loading in an uncoated (left) and in a coated (right) specimen.

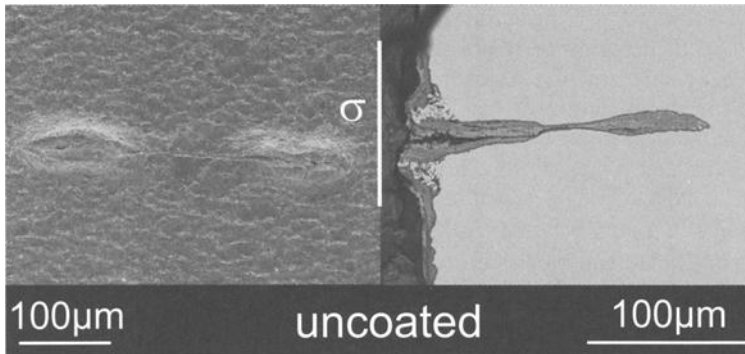


FIG. 13—Cracks form at oxide hillocks (point initiation mode) at the surface of an uncoated specimen after TMF loading, SEM micrographs, surface (left, SE contrast) and longitudinal cross section (right, BSE contrast).

described in references [19,21,23–25]. The micrograph on the left is a view of the surface of the as-tested specimen whereas, on the right, the polished cross section of the same location of the specimen is shown.

Details of the crack initiation at the surface of a coated specimen are apparent in Fig. 14, in the view of the surface of the coated specimen on the left (SE contrast) and the polished cross section of the sample on the right (BSE contrast). After propagating through the coating, the crack is observed to stop in the interdiffusion zone between the coating and the substrate. Once the substrate is reached, severe oxidation begins, followed by crack initiation and propagation.

The behavior of cracks that are initiated at the surface of the coating and stop at the diffusion zone or at the coating-substrate interface has been reported earlier. Observations of this kind are not restricted to conventional nickel-aluminide coatings [19,26–28] but are also valid for platinum-modified aluminide coatings [17].

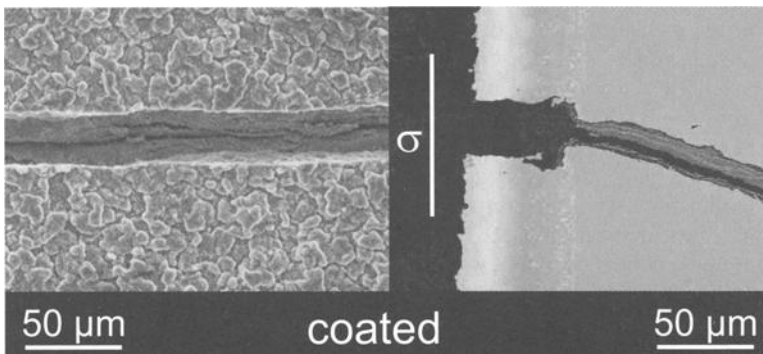


FIG. 14—Brittle cracks form at the surface of a coated specimen after TMF loading (line initiation mode), SEM micrographs, surface (left, SE contrast) and longitudinal cross section (right, BSE contrast).

In the literature, a critical fracture strain of aluminide coatings is observed below which no brittle cracking corresponding to the line initiation mode is found. Therefore, the protective function of the coating is fulfilled, and TMF lives similar to those of uncoated specimens can be reached [25,29–34]. Depending on the type of coating and the type of thermomechanical cycle, the critical value of the strain is reported to lie between $\Delta\varepsilon_{\text{mech}} = 0.6\%$ and $\Delta\varepsilon_{\text{mech}} = 0.8\%$. In the present study, no critical value of the fracture strain of the coating was detected, as the brittle cracking of the coating occurred at all mechanical strain ranges tested ($\Delta\varepsilon_{\text{mech}} = 0.5\%$ to $\Delta\varepsilon_{\text{mech}} = 0.9\%$). If a critical value for the two-phase platinum-modified coating exists, it must be below $\Delta\varepsilon_{\text{mech}} = 0.5\%$ and, therefore, is very small. This is in line with the extreme brittleness of the intermetallic PtAl₂ phase. As single-phase material, it can be more brittle than the β -NiAl phase, depending on the parameters of the modified aluminizing procedure [35].

As the brittleness of the coatings is considered to be the factor that limits the TMF life of aluminide-coated nickel-base superalloys, further investigations must concentrate on the understanding of the properties of the coatings. Thus, the interest should focus on the aluminium and platinum content, the distribution and the stability of the phases of the coating, the crystallographic relationship of coating and substrate, etc., and their effect on the TMF behavior. At present, a new, more ductile single-phase platinum-modified coating is under investigation under identical conditions of TMF as in the present study with the aim to compare the results with these obtained for the coating used in the present study. First preliminary results show an appreciable improvement of the TMF resistance.

Conclusions and Outlook

In this study, the TMF behavior of coated and uncoated CMSX-6 specimens was investigated. The coating was a two-phase platinum-modified diffusional aluminide coating. Thermomechanical fatigue tests with an asymmetric counterclockwise diamond cycle shape were performed. In the case of coated specimens, the TMF life of the specimens was reduced by a factor of 4 to 5, compared to the uncoated specimens. The major cause lies in the brittleness of the coating at low temperatures, which consists mainly of intermetallic phases. Thus, the coating is observed to crack during the first TMF cycles, when the tensile stresses reached exceed a critical value.

The brittle cracks of the coating generally stopped at the coating-substrate interface and then acted as sites of fatigue crack initiation in the substrate material. Crack initiation is accelerated by the influence of oxidation setting in, once the protective coating is penetrated by the cracks.

Platinum-modified coatings, compared to conventional aluminide coatings, also tend to be very brittle, while they offer an increased oxidation resistance and – as shown in the literature – an improved hot corrosion resistance. Both features are important for the high-temperature application in aero engines.

Therefore, as a next step, a new, single-phase platinum-modified coating is currently being tested. Since this coating exhibits an increased ductility, in particular at low temperatures, it was hoped that the negative effect of the coating on the TMF life by early crack initiation caused by brittle cracking would be less pronounced. Preliminary results look very promising, revealing a significant enhancement of the fatigue lives compared with the results obtained on the coated specimens in this work.

Acknowledgment

Funding of this work by MTU Aero Engines, Munich, is greatly appreciated.

References

- [1] Bressers, J., Peteves, S., and Steen, M., "Coatings for Hot Section Gas Turbine Components," *Fracture Mechanics: Applications and Challenges*, M. Fuentes, M. Elices, A. Martín-Meizoso, and J. M. Martínez-Esnaola, Eds., Elsevier, NY, 2000, pp. 115–134.
- [2] Bauer, R., Schneider, K., and Grünling, H. W., "Experience with Platinum Aluminide Coatings in Land-Based Turbines," *High Temperature Technology*, Vol. 3, 1985, pp. 59–64.
- [3] Mévrel, R., Duret, C., and Pichoir, R., "Pack Cementation Processes," *Materials Science and Technology*, Vol. 2, 1986, pp. 201–206
- [4] Haynes, J. A., "Potential Influences Of Bond Coat Impurities and Void Growth on Premature Failure of EB-PVD TBCs", *Scripta Materialia*, Vol. 44, 2001, pp. 1147–1152.
- [5] Pint, B. A., Haynes, J. A., More, K. L., Wright, I. G., and Leyens, C., "Compositional Effects on Aluminide Oxidation Performance: Objectives for Improved Bond Coats," *Superalloys 2000*, T. M. Pollock, R. D. Kissinger, R. R. Bowman, K. A. Green, M. McLean, S. Olson, and J. J. Schirra, Eds., The Minerals, Metals and Materials Society TMS, 2000, pp. 629–638
- [6] Cheruvu, N. S., Chan, K. S., and Leverant, G. R., "Cyclic Oxidation Behavior of Aluminide, Platinum Modified Aluminide, and McRaly Coatings on GTD-111," preprint of paper in *International Gas Turbine and Aero Engine Congress and Exhibition*, Stockholm, Sweden, 2–5 June, 1998, ASME # 98-GT-468, pp. 1–6
- [7] Dahotre, N. D., "Functional Coatings and Their Applications: A Web Perspective," *Journal of Materials*, Vol. 52, 2000, p. 14.
- [8] Peichl, L. and Johner, J., "High Temperature Behavior of Different Coatings in High-Performance Gas Turbines and in Laboratory Tests," *Journal of Vacuum Science and Technology*, Vol. 6, 1986, pp. 2583–2592.
- [9] Miracle, D. B., "The Physical and Mechanical Properties of NiAl," *Acta Metallurgica et Materialia*, Vol. 41, 1993, pp. 649–684.
- [10] Affeldt, E. E., "Ductility of an Aluminide Coating on a Single-Crystal Nickel-Based Alloy," *Advanced Engineering Materials*, Vol. 2, 2000, pp. 811–813
- [11] Arana Antelo, M., Johnson, P. K., Ostolaza, K. M., and Bressers, J., "Analysis of the Fracture Behavior Of An Aluminide Coating On A Single-Crystal Superalloy Under Tensile Conditions," *Materials Science and Engineering*, Vol. A247, 1998, pp. 40–50
- [12] Boudot, A., Crabos, F., Fournier, D., and Monceau, D., "Thermomechanical Characterizations of Coatings for HP Turbines," preprint of paper in *International Gas Turbine and Aero Engine Congress and Exhibition*, Stockholm, Sweden, 2–5 June, 1998, ASME # 98-GT-324, pp. 1–6.
- [13] Bressers, J., Ostolaza, K., and Arana, M., "Coating Induced Life Reductions of Single Crystal Superalloy Gas Turbine Blade Materials," *Elevated Temperature Coatings: Science and Technology II*, N. B. Dahotre and J. M. Hampikian, Eds., The Minerals, Metals and Materials Society, 1996, pp. 275–285.
- [14] Bicego, V., Bontempi, P., and Taylor, N., "Low Cycle Fatigue and Thermomechanical Fatigue Behavior of Coated and Uncoated in 738 Superalloy," *Low Cycle Fatigue and Elasto-Plastic Behavior of Materials*, K.-T. Rie and P. D. Portella, Eds., Elsevier Science, NY, 1998, pp. 137–140.
- [15] Kowalewski, R. and Mughrabi, H., "Thermomechanical and Isothermal Fatigue of a Coated Columnar Grained Directionally Solidified Nickel-Base Superalloy," *Thermomechanical Fatigue Behavior of Materials: 3rd Volume, ASTM STP 1371*,

- H. Sehitoglu and H. J. Maier, Eds., ASTM International, West Conshohocken, PA, 2000, pp. 3–17.
- [16] Ostolaza, K. M., Johnson, P. K., Arana, M., and Bressers, J., "Effect of Cycle Type on the Damage of a Diffusion Aluminide Coating on a Ni-Based Monocrystalline Superalloy Tested Under TMF Conditions," *Anales de la Mecánica de la Fractura*, Vol. 13, M. Elices, M. Fuentes, and J. Llorca, Eds., Spanish Group of Fracture, 1996, pp. 272–298.
- [17] Moretto, P., Bressers, J., and Arrell, D. J., "Evolution of a PtAl₂ Coating On The Nickel-Base Alloy Cmsx-6 Subjected To Thermomechanical Fatigue," *Materials Science and Engineering A272*, 1999, pp. 310–320.
- [18] Arrell, D. J., Bressers, J., and Timm, J., "Effect of Cycle History on Thermomechanical Fatigue Response of Nickel-Base Superalloys," *Proceedings of ASME-IMCE 99 Symposium on "High Temperature Applications," International Mechanical Engineering Congress and Exhibition*, American Society of Mechanical Engineers ASME, NY, 1999, pp. 1–6.
- [19] Affeldt, E. E., "Influence of an Aluminide Coating on the TMF Life of a Single Crystal Nickel-Base Superalloy," *Transactions of the ASME, Journal of Engineering for Gas Turbines and Power*, Vol. 121, pp. 687–690.
- [20] Esslinger, J. and Affeldt, E. E., "Thermomechanical Fatigue (TMF) in Turbine Airfoils: Typical Loading, 3D-effects, and Adjusted Testing," *Low Cycle Fatigue and Elasto-Plastic Behavior of Materials*, K.-T. Rie and P. D. Portella, Eds., Elsevier, NY, 1998, pp. 131–136.
- [21] Peteves, S. D., De Haan, F., Timm, J., Bressers, J., Hughes, P. M., Moss, S. J., et al., "Effect of Coating on the TMF Lives of Single Crystal and Columnar Grained Cm 186 Blade Alloy," *Superalloys 2000*, T. M. Pollock, R. D. Kissinger, R. R. Bowman, K. A. Green, M. McLean, S. Olson, J. J. Schirra, Eds., The Minerals, Metals & Materials Society, 2000, pp. 655–663.
- [22] Affeldt, E. E., Hammer, J., and Cerdan, L., "Modelling of Deformation under TMF Loading," *Thermomechanical Fatigue Behavior of Materials: 4th Volume, ASTM STP 1428*, M. A. McGaw, S. Kalluri, J. Bressers, and S. D. Peteves, Eds., ASTM International, West Conshohocken, PA, 2002, in press.
- [23] Lindé, L. and Henderson, P. J., "Thermomechanical and Low Cycle Fatigue Behavior of a Coated Nickel-Base Superalloy," *Materials for Advanced Power Engineering*, Part II, D. Coutsouradis, Ed., Kluwer Academic Publishers, NY, 1994, pp. 1367–1376.
- [24] Martinez-Esnaola, J. M., Arana, M., Bressers, J., Timm, J., Martin-Meizoso, A., Bennett, A., and Affeldt, E. E., "Crack Initiation in an Aluminide Coated Single Crystal During Thermomechanical Fatigue," *Thermomechanical Fatigue Behavior of Materials: 2nd Vol., ASTM STP 1263*, M. J. Verrilli and M. G. Castelli, Eds., ASTM International, West Conshohocken, PA, 1996, pp. 68–81.
- [25] Bressers, J., Timm, J., Williams, S., Bennett, A., and Affeldt, E., "Effects of Cycle Type and Coating on the Tmf Lives of a Single Crystal Nickel-Based Gas Turbine Alloy," *Thermomechanical Fatigue Behavior of Materials: 2nd Vol., ASTM STP 1263*, M. J. Verrilli and M. G. Castelli, Eds., ASTM International, West Conshohocken, PA, 1996, pp. 56–67.
- [26] Lindé, L. and Henderson, P. J., "High Temperature Fatigue Behavior of Coated IN738 LC," *Low Cycle Fatigue and Elasto-Plastic Behavior of Materials*, K.-T. Rie and P. D. Portella, Eds., Elsevier, NY, 1998, pp. 143–148.
- [27] Johnson, P. K., Arana, M., Ostolaza, K. M., and Bressers, J., "Crack Initiation in a Coated and an Uncoated Nickel-Base Superalloy Under TMF Conditions," preprint of paper in *International Gas Turbine & Aeroengine Congress and Exhibition*, Orlando, FL, 2–5 June, 1997, ASME # 97-GT-236, American Society of Mechanical Engineers, NY, pp. 1–6.

- [28] Bernhard, H. and Rémy, L., "Thermal-Mechanical Fatigue Damage of an Aluminide Coated Nickel-Base Superalloy," *Advanced Materials and Processes*, EUROMAT 1989, H. Exner and V. Schumacher, Eds., Vol. 1, D. Driver, and H. Mughrabi, Eds., Deutsche Gesellschaft für Materialkunde (DGM) e.V., 1990, pp. 529–534.
- [29] Bressers, J., Timm, J., Affeldt, E., and Bennett, A., "Effects of Cycle Type and Coating on the TMF Lives of CMSX6," 81st Meeting of the *AGARD (Advisory Group for Aerospace Research and Development) SMP Panel on "Thermal Mechanical Fatigue of Aircraft Engine Materials,"* Conference Proceeding CP-569, Banff, Canada, 2–4 Oct. 1995, pp. 9/1–9/10.
- [30] Moretto, P. and Bressers, J., "Thermomechanical Fatigue Degradation of a Nickelaluminide Coating on a Single Crystal Nickel-Based Alloy," *Journal of Materials Science*, Vol. 31, 1996, pp. 4817–4829.
- [31] Bain, K. R., "The Effects of Coatings on the Thermomechanical Fatigue Life of a Single Crystal Turbine Blade Material," *AIAA/ SAE/ ASME/ ASEE 21st Joint Propulsion Conference*, Monterey, CA, 1985, paper # AIAA-85-1366, American Institute for Aeronautics and Astronautics, Reston, VA, 1985, pp. 1–6.
- [32] Zhang, Y. H., Withers, P. J., Fox, M. D., and Knowles, D. M., "Damage Mechanisms of Coated Systems under Thermomechanical Fatigue," *Materials Science and Technology*, Vol. 15, 1999, pp. 1031–1036.
- [33] Zhang, Y. H., Knowles, D. M., and Withers, P. J., "Micromechanics of Failure Of Aluminide Coated Single Crystal Ni Superalloy Under Thermomechanical Fatigue," *Scripta Materialia*, Vol. 37, 1997, pp. 815–820.
- [34] Zhang, Y. H., Knowles, D. M., and Withers, P. J., "Microstructural Development in Pt-Aluminide Coating on CMSX-4 Superalloy During TMF," *Surface and Coatings Technology*, Vol. 107, 1998, pp. 76–83.
- [35] Vogel, D., Newman, L., Deb, P., and Boone, D. H., "Ductile-to-Brittle Transition Temperature Behavior of Platinum-Modified Coatings," *Materials Science and Engineering*, Vol. 88, 1987, pp. 227–231.

Masakazu Okazaki,¹ Koji Take,² Koji Kakehi,³ Yasuhiro Yamazaki,⁴ Masao Sakane,⁵
Masayuki Arai,⁶ Shigeo Sakurai,⁷ Hideaki Kaneko,⁸ Yoshio Harada,⁹ Akihiro Itoh,¹⁰
Takanari Okuda,¹¹ Isamu Nonaka,¹² Kazunari Fujiyama,¹³ and Kouichi Nanba¹⁴

Collaborative Research on Thermo-Mechanical and Isothermal Low-Cycle Fatigue Strength of Ni-Base Superalloys and Protective Coatings at Elevated Temperatures in The Society of Materials Science, Japan (JSMS)

REFERENCE: Okazaki, M., Take, K., Kakehi, K., Yamazaki, Y., Sakane, M., Arai, M., Sakurai, S., Kaneko, H., Harada, Y., Sugita, Y., Okuda, T., Nonaka, I., Fujiyama, K., and Nanba, K., "Collaborative Research on Thermo-Mechanical and Isothermal Low-Cycle Fatigue Strength of Ni-Base Superalloys and Protective Coatings at Elevated Temperatures in The Society of Materials Science, Japan (JSMS)," *Thermomechanical Fatigue Behavior of Materials: 4th Volume, ASTM STP 1428*, M. A. McGaw, S. Kalluri, J. Bressers, and S. D. Peteves, Eds., ASTM International, West Conshohocken, PA, 2002. Online, Available: www.astm.org/STP/1428/1428_10596, 9 Sept. 2002.

ABSTRACT: Results of collaborative research by "Subcommittee on Superalloys and Coatings" in The Society of Materials Science, Japan (JSMS), are presented, which cover the thermo-mechanical fatigue (TMF) and high temperature isothermal low-cycle fatigue (ILCF) strengths of Ni-Base superalloy, substrate alloys and the protective coatings. Three kinds of Ni-base superalloys were selected as the substrate: a single crystal alloy, CMSX-4; a directionally solidified alloy, CM247LC; and a polycrystalline alloy, IN738LC. On these substrate specimens the CoNiCrAlY alloy was coated by 250 μm in thickness by low pressure plasma spraying, and then aluminized. This process was managed and undertaken by one of member companies of the Subcommittee. The round robin TMF and ILCF tests were carried out under a strain ratio of -1 at temperature ranged between 400 and 900°C. In the former the tests were performed under the out-of-phase and diamond phase conditions in which the phase difference between strain and temperature were 180° and 90°, respectively. It is shown by the round-robin tests that the TMF lives, as well as the ILCF, were strongly dependent on the substrate alloys. Many important, or

¹ Professor, The University of Tokyo, Hongo 7-3-1, Bunkyo-ku, Japan.

² Chief Researcher, Kawasaki Heavy Ind, Kawasaki-tyo 1-1, Akashi, Japan.

³ Associate Professor, Tokyo Metropolitan University, Minamioosawa 1-1, Hachioji, Japan.

⁴ Research Associate, Niigata Institute of Technology, Fujihashi 1719, Kashiwazaki, Japan.

⁵ Professor, Ritsumeikan University, Norohigashi 1-1-1, Kusatu, Japan.

⁶ Chief Researcher, Cent. Research Inst. of Electric Power Ind., Iwatokita 2-11-1, Komae, Japan.

⁷ Senior Researcher, Hitachi Ltd., saiwai-tyo 3-1-1, Hitachi, Japan.

⁸ Chief Researcher, Mitsubishi Heavy Ind., Ltd., Arai-machi 2-1-1, Takasago, Japan.

⁹ General Manager, TOCALO Co., Higashinada-ku 4-13-4, Kobe, Japan.

¹⁰ Chief Researcher, Chubu Electric Power Co., Inc., Midori-ku 20-1, Nagoya, Japan.

¹¹ Chief Researcher, Kobe Steel Co., Nishi-ku 1-5-5, Kobe, Japan.

¹² Chief Researcher, Ishikawajima Heavy Ind., Toyosu 3-1-15, Koto-ku, Japan.

¹³ Chief Researcher, Toshiba Co., Turumi-ku 1-9, Yokohama, Japan.

¹⁴ Chief Researcher, Mitsui Eng. & Shipbuilding Co, Ltd., Tama 3-1-1, Tamano, Japan.

noteworthy results were also found: e.g., the TMF fracture behavior of the coated specimens revealed some unique characteristics that were hardly deduced from that of the bare specimens. The effect of coating on the ILCF life was strongly dependent on the temperature. It was not reasonable, or difficult to try to estimate the TMF life of the coatings from the ILCF test results. Based on the observations on the crack initiation, propagation and the fracture surface, the effects of the substrate alloy and the coating on the TMF and ILCF lives were discussed.

KEYWORDS: Ni-base superalloys, protective coatings, CoNiCrAlY, thermo-mechanical fatigue, isothermal low-cycle fatigue, crack density, dislocation structure

Introduction

Industrial gas turbines are used as electrical generators by both utilities and private industrial companies [1–6]. Nowadays so called 1500°C level combined cycle gas turbines have been developed, which can provide thermal efficiencies greater than 55% [3]. The durability of a gas turbine is principally limited by those components operating at high temperatures in the turbine sections. The gas path components experience a complex thermal and mechanical history during a typical cycle of operation, consisting of start-up, steady state operation, shut-down, and emergency shut-down [1]. Ni-base superalloys; most reliable materials for these components, have to endure several kinds of damage: fatigue, creep, oxidation and so on. In the case of utility gas turbines, in which long life-time durability and cost reductions using cheaper fuel are required, protective coatings and thermal barrier coatings, which shield the underlying substrate materials from oxidation and corrosion attacks and reduce the temperature, respectively, are essential requirements for the hot section components. These coatings induce additional thermal stress due to the mismatch of thermal expansion coefficient between the substrate and the coating, which impel the Ni-base superalloys to be exposed to more severe conditions. Thus, thermo-mechanical fatigue strength is one of critical issue to determine the life. Many efforts have been made to estimate the TMF lives [1,2,6,8]. One of interesting and historical approaches is a trial to predict them from simple isothermal low cycle fatigue (ILCF) tests. Regarding this article, a group of the High Temperature Committee (chaired by Prof. Taira) in the Society of Materials Science, Japan, has conducted pioneer research for twenty years [8]. According to their results, the TMF life of monolithic materials under the out-of-phase condition, for an example, was successfully estimated from the LCF life conducted at the intermediate temperature of the TMF tests. Nowadays this aspect has been one of guides. However, there is little information on TMF failure of Ni-base superalloys and the coatings all over the world. Thus, questions are: Are these findings applicable to the Ni-base superalloy coatings? What are special phenomena in the failure of coatings to which special attention should be paid?

From these backgrounds, collaborative research has been conducted by the Subcommittee on Superalloys and Coatings, The High Temperature Committee of Materials, JSMS, in order to get basic information on the above articles. This project covers strength in thermo-mechanical fatigue (TMF) and isothermal low-cycle fatigue (ILCF) of Ni-Base superalloys and the protective coatings at elevated temperatures. Based on the observations of the crack initiation, the fracture surface and the dislocation structures, the effects of the substrate alloy and the coating on the TMF and ILCF lives are presented in this paper. The correlation between the TMF and ILCF are also discussed.

Collaborative Research by "Subcommittee on Superalloys and Coatings," JSMS*Objectives*

Subcommittee, "Superalloys and Coatings" (chaired by Prof. M. Okazaki, The Univ. Tokyo, Japan), was established by the Committee of High Temperature Strength of Materials, The Society of Material Science, Japan (JSMS) in 1998. The members of the Subcommittee are listed in Table 1.

This subcommittee is engaged in collaborative research on the high temperature strengths of superalloys and coatings, with special attention being paid to the interaction between the substrate and the coatings. The main objectives of the subcommittee are: (i) to quantitatively make clear the mechanics and mechanisms of failure by TMF, in comparison with those by ILCF; (ii) to make clear the effect of coating on TMF and ILCF lives; (iii) to quantify the effect of substrate alloy on the TMF and ILCF lives; and (iv) to develop life prediction method(s), summarizing the items (i)-(iii).

TABLE 1—*The members of the subcommittee.*

Affiliation	Chief Member	Working Member
The University of Tokyo (Formerly Nagaoka University of Technology)	Masakazu Okazaki (Chairman)	
Kawasaki Heavy Ind.	Koji Take (Secretary)	Mitsuhiro Kaku
Tokyo Metropolitan University	Koji Takehi (Secretary)	
Kyoto University	Takayuki Kitamura	
Okayama University (Formerly Kyoto University)	Naoya Tada	
Ritsumeikan University	Masao Sakane	
Niigata Institute of Technology	Yasuhiro Yamazaki	
Japan Defense Agency	Toyoichi Satoh	
VOLVO Aero Co.	Thomas Hansson	
Central Research Inst. of Electric Power Ind.	Akito Nitta	Masayuki Arai
Hitachi Ltd.	Shigeo Sakurai	
Mitsubishi Heavy Ind.	Hideaki Kaneko	Hiroshi Ishikawa
TOCALO Co..	Yoshio Harada	Tatsuo Suizu
Chubu Electric Power Co., Inc.	Akihiro Itoh	
Kobelco Research Institute, Inc.	Toshinori Yokomaku	Takanari Okuda
Ishikawajima Heavy Ind..	Isamu Nonaka	Takuya Itoh
Toshiba Co..	Kazunari Fujiyama	Keisuke Takagi
Mitsui Eng. & Shipbuilding Co., Ltd.	Kouichi Namba	

Research Procedure and Program

Three typical types of Ni-base superalloys were selected as the substrate: a polycrystalline alloy, IN738LC; a directionally solidified alloy, CM247LC; and a single crystal alloy, CMSX-4. The chemical compositions and the conditions of heat treatments

are summarized in Table 2. The size of γ' precipitates and the volume fractions are given in Table 3. From these substrates the cylindrical specimens were machined for the TMF and ILCF tests. The geometry of the specimens were different a little, depending on the research institute where the tests were carried out, however, the gauge section dimensions were around 6 mm in diameter and 20 mm in length, respectively.

The coated specimens were also prepared according to the following procedures: after the machining of the specimen with same geometry as the substrate specimen, the surface was shot-blasted by #60 alumina powders, followed by sputtering to clean up. Then the CoNiCrAlY alloy was overlay coated by about 250 μm in thickness by low pressure plasma spraying (LPPS), followed by the aluminizing treatment of the surface layer of CoNiCrAlY coating by 20 μm in thickness by a pack diffusion method. These operations were managed and performed by TOCALO Co. (Kobe, Japan), a member of the Subcommittee. The chemical compositions of the CoNiCrAlY alloy powder are: 20.3 Cr, 8.2 Al, 0.51 Y, 31.3 Ni, and bal. Co, in wt.%. During the plasma spraying the substrate temperature was not strictly controlled, but it was about 750°C. Finally the diffusion and ageing treatments were applied at 1120°C for 2 h and at 850°C for 24 h in air, respectively.

TABLE 2—Chemical compositions and the conditions of heat treatments of Ni-base superalloys.

Chemical Compositions

	C	Si	Cr	Co	Mo	W	Ta	Re
CMSX-4	-	-	6.40	9.60	6.4	-	6.5	2.9
CM247LC	0.07	-	8.04	9.31	9.38	-	3.27	-
IN738LC	0.09	0.04	16.0	8.14	8.14	1.65	1.72	-
					Al	Ti	Hf	Ni
					5.7	1.0	-	bal.
					5.63	0.72	1.56	bal.
					3.57	-	-	bal.

Heat Treatments

CMSX-4:

Solution heat treatments (1277°C × 2 h....1296°C × 3 h....1304°C × 3 h...1313°C × 3 h 1316°C × 3h°C...1321°C × 2 h.... in Ar.) → ageing treatments(1080°C × 4 h ... 880°C × 20 h in Ar.).

CM247LC:

Solution heat treatments (1232°C × 2 h....1252°C × 3 h....1265°C × 3 h.....in Ar.) → ageing treatments (1080°C × 4 h...880 °C × 20 h.....in Ar.).

IN738LC:

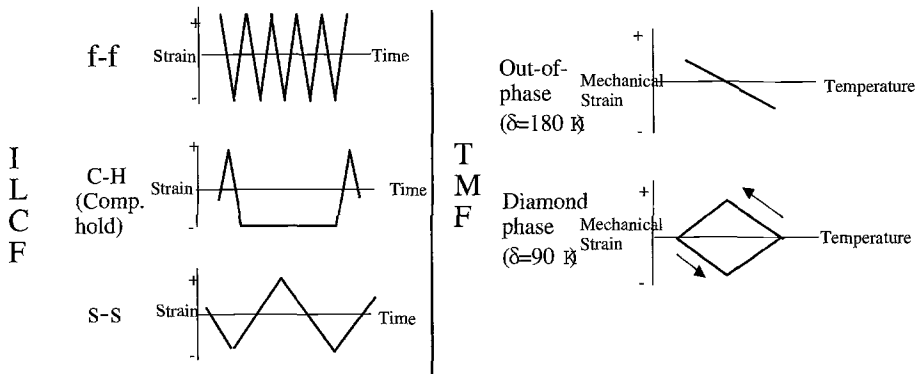
Solution heat treatments (1120°C × 2 h....in Ar.) → ageing treatments (845 °C × 24 h.) → HIP (1200°C × 1100 atg × 4 h. in Ar.) → ageing treatment (1080 °C × 4 h... in Ar.)

TABLE 3—The size of γ' precipitates and the volume fractions of the substrate alloys.

Specimen	Average size of γ' (μm)	Volume fraction of γ' (%)
CMSX-4	≈ 0.43	66
CM247LC	≈ 0.48	58
IN738LC	≈ 0.8	46

TABLE 4— Summary of test program.

Specimen	Test type	Strain waveform	Frequency (Hz)	Hold time (sec.)	Temp. strain phase difference $\delta(^{\circ})$	Max. Temp. ($^{\circ}\text{C}$)	Min. Temp. ($^{\circ}\text{C}$)
Bare & Coated	ILCF	f-f	1/20	0	-	900 & 400	900 & 400
		s-s	1/480	0			
		Comp. Hold	1/620	600			
	TMF	Out-of-phase	1/480	0	180	900	400
		Diamond phase	1/480	0	90		



Round robin tests, which consisted of ILCF and TMF tests, were carried out according to the test program summarized in Table 4. All of these tests were performed under strain-controlled condition, utilizing servo-electro hydraulic test machines. In the ILCF tests three strain wave shapes were applied: fast-fast wave (denoted by f-f) in which the tension- and compression-going strain rates were high; compression-hold (denoted by C-H) wave in which a dwell time for 10 min was introduced into the f-f

wave at maximum compression strain; and slow-slow wave (denoted by s-s) in which the tension- and compression-going strain rates were low compared with those in the f-f wave, respectively (see the illustration in Table 4). The test temperatures were 400 and 900°C. In the TMF test, on the other hand, mechanical strain was applied so that it was superimposed on thermal free expansion strain in a synchronized manner with thermal cycling under the following two phase angle conditions: one is the out-of-phase condition and the other is diamond-phase condition, in which the phase differences between strain and temperature cycling are 180° and 90°, respectively (see the illustration in Table 4). All the TMF tests were carried out at temperatures ranged between 400 and 900°C. The ILCF and TMF lives were defined by the number of cycles at which a 25% drop in tensile load was attained.

Results and Discussions

TMF and ILCF Lives of Substrates and Coatings

The results of the TMF and ILCF lives of the substrates and the coatings are summarized in Figs. 1 and 2, where some best-fit curves are drawn for representative data set in Fig. 1 and they are reproduced in Fig. 2. Note that the vertical axis of these figures for the TMF tests is mechanical strain range: i.e., net strain range applied to the specimen in which thermal free expansion strain is subtracted from apparent total strain. This kind of expression enables us to directly compare the TMF life with the ILCF one. On the other hand, according to the traditional results which dealt with the correlation between TMF and ILCF life [8], it has been semi-empirically deduced that the TMF lives under in-phase and out-of-phase conditions may be almost comparable to the ILCF lives which is measured at the maximum and at the intermediate temperatures of the TMF tests, respectively. Taking the above semi-empirical understandings into consideration, the following characteristics should also be pointed out in these figures:

(1) Regarding the substrate specimens (See Figs. 1 (a) through 1(c)):

(i) The ILCF lives of the substrate specimens are strongly influenced by the strain waveshape: the lives under the S-S and the C-H waves (see Table 4) are noticeably lower than those under the f-f wave. This effect can be clearly seen in IN738 alloy substrates. These trends are familiar to those in conventional materials [8].

(ii) The TMF life under the out-of-phase condition is shorter than that under the diamond phase condition. This trend is pronounced in CMSX-4 and CM247LC.

(iii) The lives of the CMSX-4 were the longest of all the substrates specimens, not only in ILCF but also in TMF tests (Compare between Figs. 1 (a) through 1 (c)).

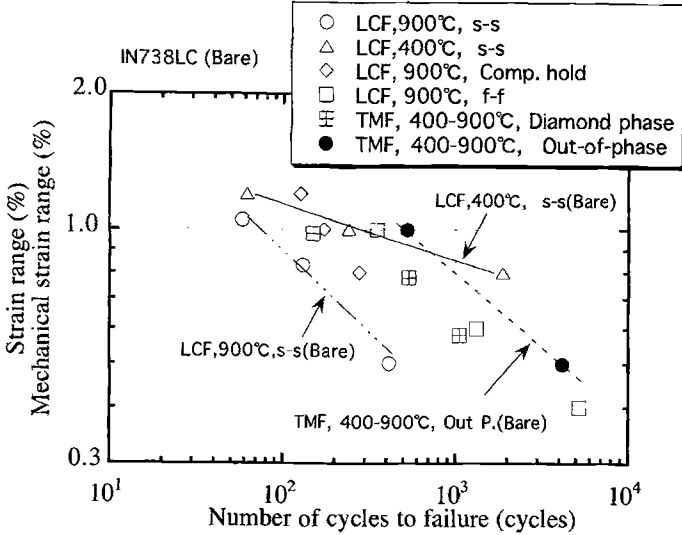
(2) Regarding the coated specimens (see Figs. 2 (a) through 2(c)):

(iv) The TMF lives of the coated specimens are the shortest under the out-of-phase condition, and they are near to the ILCF lives conducted at the minimum temperature of the TMF test (400°C), rather than those conducted at the maximum temperature (900°C).

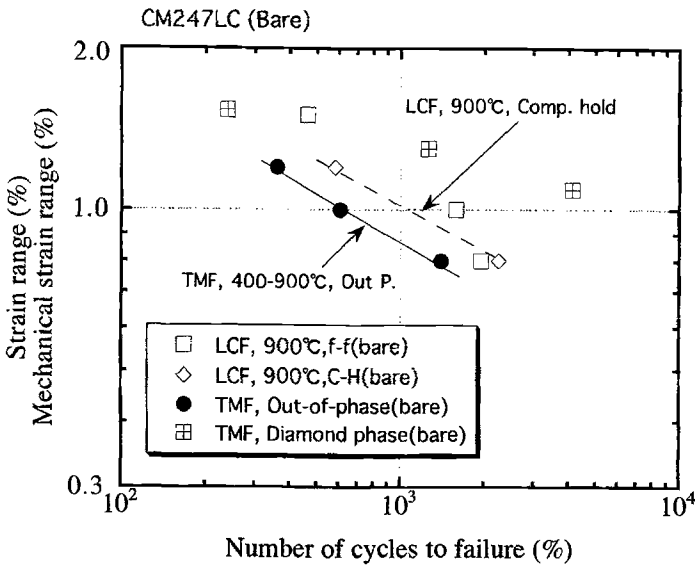
(v) The TMF lives of the coated specimens were significantly reduced, compared with those of the bare specimens. On the contrary, the ILCF lives at 900°C were rather improved by coating.

(vi) The features (iv) and (v), can be seen in common independently of the substrate alloy.

(vii) The TMF and ILCF lives of the CMSX-4 were the longest of all the coated specimens.



(a)



(b)

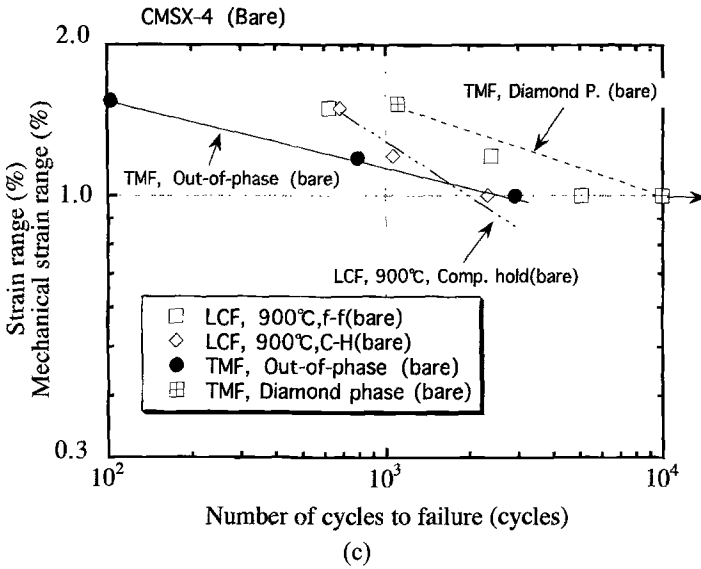
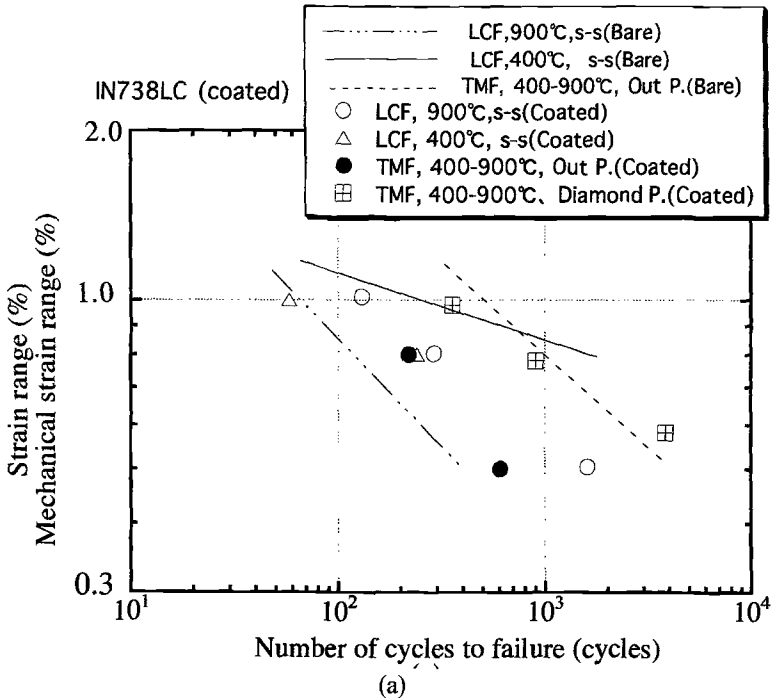


FIG. 1— Summary of TMF and ILCF lives of the substrate alloys. (a) IN738LC, (b) CM247LC, (c) CMSX-4.



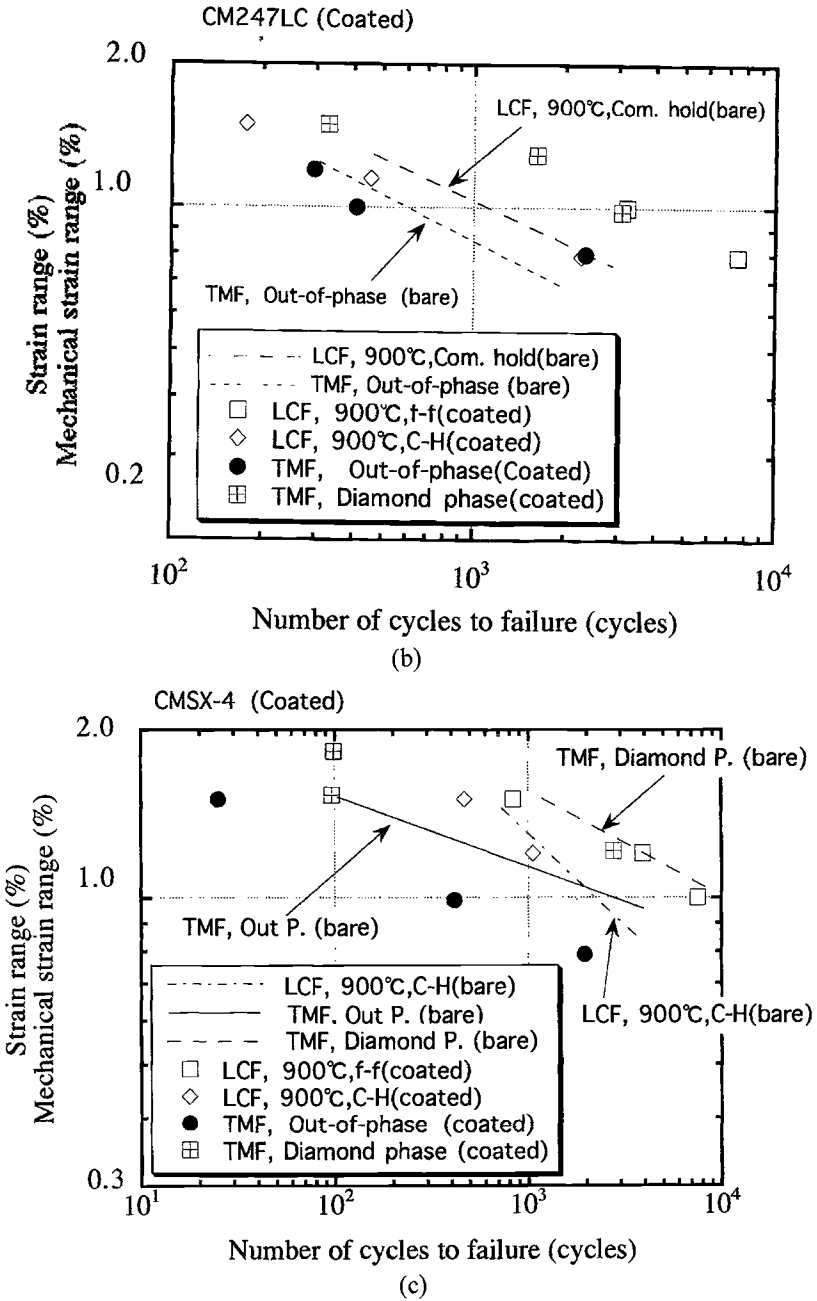


FIG. 2— FIG. 2—Summary of TMF and ILCF lives of the coated alloys. (a) IN 738 LC, (b) CM247LC, (c) CMSX-4.

The above characteristics (iv)–(vi) clearly demonstrate that the ILCF test can provide only limited or inadequate information for the TMF failure of the Ni-base superalloy coatings. From the feature (ii) this aspect seems to be the case not only in the coatings but also in the substrate. In the other words, the traditional understanding may not be always applicable to the Ni-base superalloy substrates and the coatings, which will be discussed again later based on the observation of dislocation structures. Furthermore, it is also important to emphasize from the above characteristics that the TMF life of the coatings can be hardly estimated only from that of the substrate, without any consideration on interaction between the substrate and the coating. The comparison of the cyclic stress- (mechanical) strain relation between the out-of-phase and the diamond phase TMF tests indicated that the mean stress in the former was significantly higher than that in the latter. This difference must be responsible for the characteristics (ii).

Cracks in Coated Specimens

As shown in the previous section, the TMF life of the coatings can be hardly estimated from that of the substrate alone. In order to study the unique fracture behavior of the coatings, crack density was measured in the longitudinal cross section through the coated specimen after the failure. The cracks were classified into the following three types in this project (Fig. 3): one is crack of which the tip was in the aluminized region (Type I), the second is the crack in the CoNiCrAlY alloy coating (Type II), and the third is the crack penetrating into the substrate (Type III). The cracks, which were arrested at the CoNiCrAlY alloy coating/substrate interface, were included into the Type II crack. The degree of the cracking was represented by the line density (i.e., number of cracks/unit length on the longitudinal cross section along the specimen gage length).

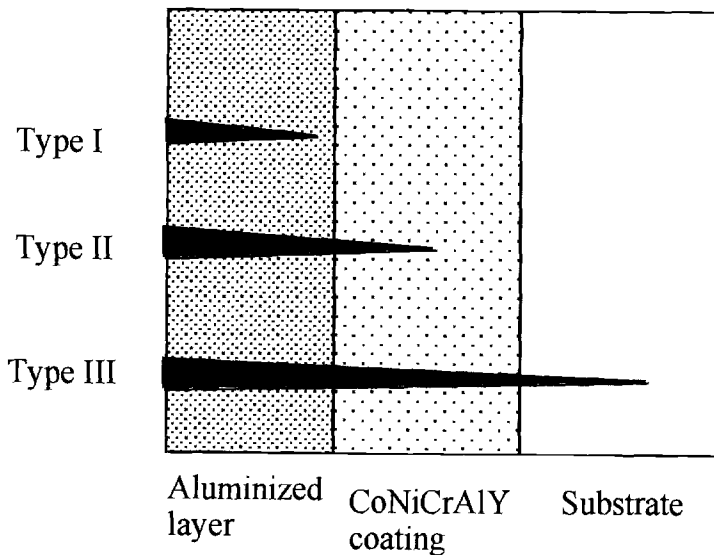


FIG. 3—Classification of cracks.

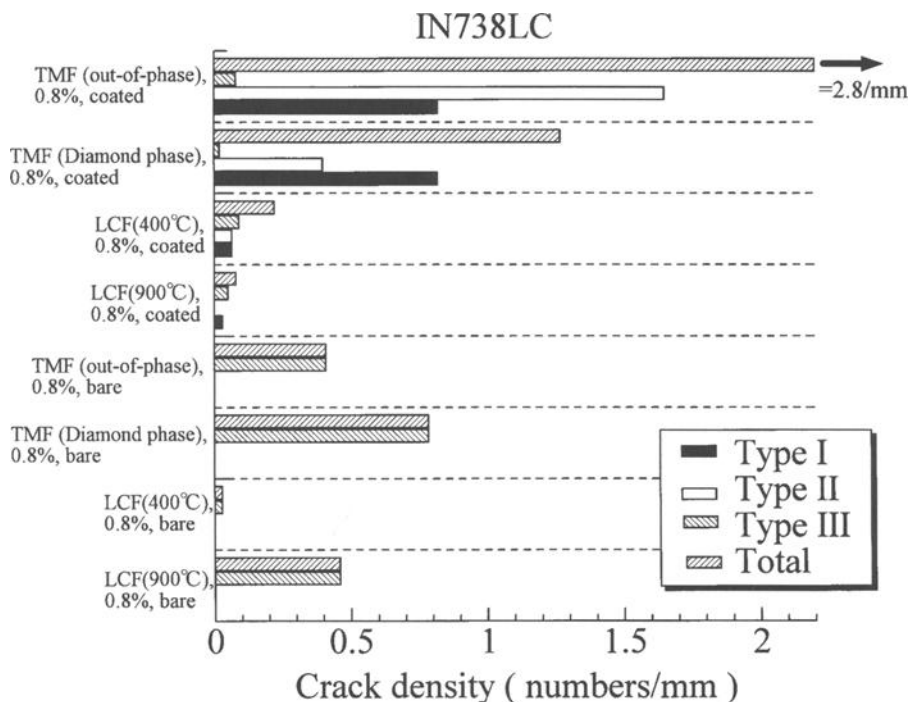


FIG. 4—Comparison of crack densities between TMF and ILCF tests.

The crack density in the TMF tests of the IN738LC coated specimens is shown in Fig. 4 in comparison with that in the ILCF tests. It is found that the crack density in the TMF tests under the out-of-phase condition is extremely higher than any other test conditions. The majority of the cracks were classed as Type I and II. More or less, similar features were also seen in the coated specimens subjected to the ILCF at 400°C. This means that the crack initiation is promoted by the coating under these test conditions. Note that the maximum tensile strain was reached at 400°C in the both tests. On the contrary, the crack density in the coated specimen subjected to ILCF at 900°C was significantly lower than that in the substrate specimen. Especially the Type III crack density was remarkably reduced, indicating that the CoNiCrAlY coating inhibited the crack initiation. Thus, the TMF failure, especially under out-of-phase condition, was not well reproduced by the ILCF lives at 900°C, concerning the crackings. Cracking behavior must be related to the mechanical properties of the coating: that is, ductile-brittle transition temperature (DBTT) of the CoNiCrAlY coating has been measured to be about 700°C [7]. Therefore, it is essential for the TMF life prediction of Ni-base superalloy coatings to get mechanical properties not only of the substrate but also of the coating film.

Dislocation Structure of Superalloys during TMF tests

As shown in the previous section, the traditionally established semi-empirical law regarding as the correlation between TMF and ILCF [8] was not always applicable to the Ni-base superalloy substrates. In order to discuss this result, the thin films were extracted from the bare specimens after the failure to observe the dislocation by transmission electron microscope (TEM). The thin foils were extracted from the [001] plane in the specimen gauge section region that was far apart enough from the finally ruptured position under the respective test conditions.

The dislocation structures of the CMSX-4 substrate specimens exposed to the out-of-phase and diamond phase TMF cyclings are given in Figs. 5 and 6. It is found in Fig. 5 that almost all the dislocations exist in the narrow γ channels with the same Burgers vector, and few dislocations inside the γ' precipitates. Some stacking faults which extend across the precipitates are also seen on multiple $\{111\}$ planes, indicating that the $\{111\}\langle 112\rangle$ slip system was activated under this condition, associated with widespread cutting of γ' precipitates [9]. The similar characteristics are also seen in Fig. 6. A few dislocation loops, which appear to have taken 90° change in direction during the process of traveling through the matrix were also observed in Fig. 5 (see the left-hand side of the photograph). This must have resulted from the cross sliding of the leading screw dislocation segments from one (111) plane to another (111) plane. It has been clarified that the cross glide is necessary for the systematic spreading of the dislocations into the narrow γ channels [10]. The features were more or less similar in the CM247LC specimen that failed by the out-of-phase TMF cycling. From these observations the deformation and damage in the out-of-phase TMF test might chiefly evolve by bowing the dislocations through the matrix channels on $\{111\}$ planes. Further investigation is necessary with respect to the similarity and dissimilarity between the out-of-phase and diamond phase TMF cyclings.

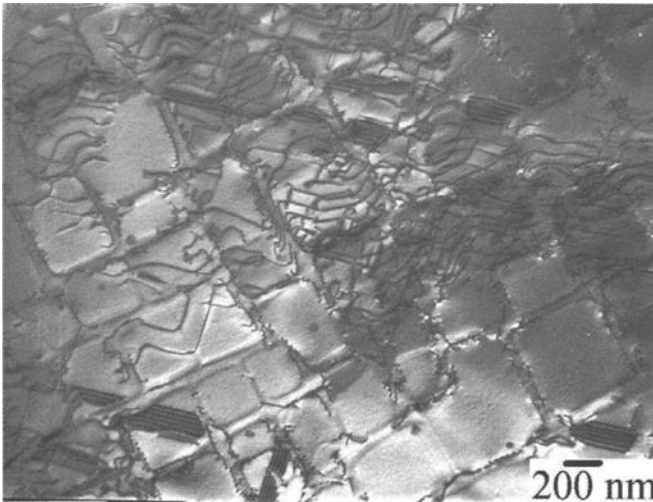


FIG. 5—Dislocation structures of CMSX-4 subjected to out-of-phase TMF cycling (400-900 °C, $\Delta\varepsilon = 1.55\%$). The foil normal is [001]. $g = 002$.

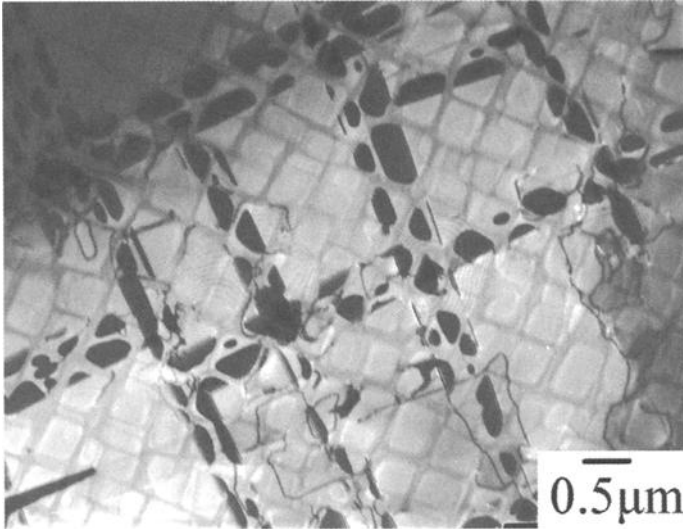


FIG. 6— Dislocation structures of CMSX-4 subjected to diamond-phase TMF cycling (400-900°C, $\Delta\varepsilon = 1.53\%$). The foil normal is [001]. $g=002$.

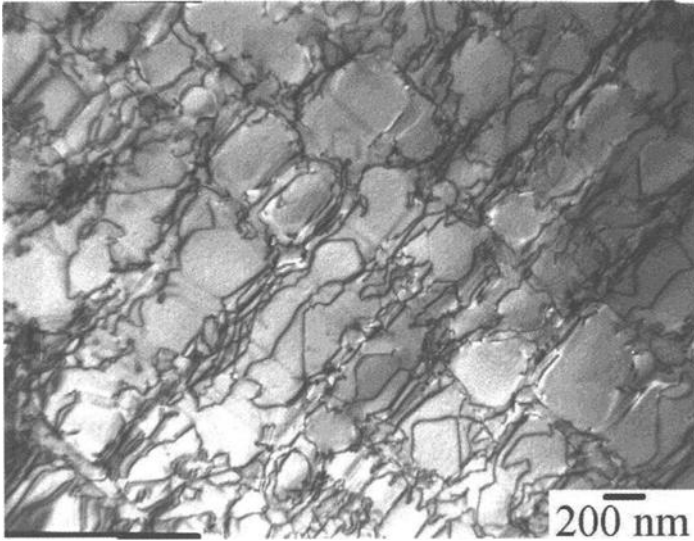


FIG. 7— Dislocation structures of CMSX-4 subjected to ILCF cycling under *f-f* waveshape (900 °C, $\Delta\varepsilon = 1.53\%$). The foil normal is [001]. $g=002$.

The dislocation structure in the ILCF test under the *f-f* strain waveshape (see Table 4) at 900°C is given in Fig. 7. It is found that a significant fraction of the dislocations form a cage around the γ' precipitates. The two-plane analysis showed that most of dislocations were not always on, or escaped from the {111} planes. In the other

words, edge dislocations were climbing in the $\gamma - \gamma'$ interfaces. It is worth noting a significant difference of the Burgers vector and that of dislocation network between Figs. 5–7. In addition, superlattice-stacking faults were not observed under this condition, dissimilarly to Fig. 5. These features indicate that diffusion might be a major mechanism to dominate the deformation and damage during the ILCF test at 900°C.

The comparison between Figs. 5–7 demonstrates that the deformation mechanism under the TMF tests was essentially different from that under the ILCF test at 900°C. It is important to point out again that the dislocation structure given in Figs. 5–7, or the deformation and damage mechanism, is closely related to the γ / γ' composite microstructure in the Ni-base superalloys; a unique microstructure that is different from that in other monolithic materials. Thus, it is natural rather than surprising, that the traditionally established semi-empirical law between TMF and ILCF was not applicable to the TMF failure of the Ni-base superalloy substrates.

Summary and Future Work

The outline of collaborative research by "Subcommittee on Superalloys and Coatings" in The Society of Material Science, Japan (JSMS), which cover the thermo-mechanical fatigue (TMF) and high temperature isothermal low-Cycle fatigue (ILCF) strengths of Ni-Base superalloys and the protective coatings, was presented.

The results obtained by the collaborative research are summarized as follows:

1. The TMF life, as well as the ILCF, was strongly dependent on the substrate alloys. The single crystal and directionally solidified alloys and their coatings generally exhibited the most excellent properties, compared with those of the traditional polycrystalline alloy.
2. The observation of dislocation structures indicated that the controlling and deformation mechanisms were intrinsically different between the TMF under the diamond and out-of-phase conditions and ILCF at 900°C in the Ni-base superalloys. Accordingly, it must be unreasonable in principle to reproduce and to estimate the TMF failure of the Ni-base superalloys by the ILCF tests.
3. Remarkable reductions in the TMF life of the Ni-base superalloy coatings under the out-of-phase condition was found to occur, compared with that of the bare materials. Meanwhile, the TMF lives of the coated specimens under the diamond phase condition were almost comparable to those of the substrates. It was shown by the investigation of crack density that the above behavior was closely related to the ductility of the coating film at the temperatures at which the maximum tensile strain was reached in the TMF tests. Hence, it is essential for the TMF life prediction of Ni-base superalloy coatings to get an understanding of the mechanical properties of coating films at elevated temperatures, as well as those of substrate alloys.
4. Regarding the relation between TMF and ILCF life of the coatings, attention should be paid to that ILCF tests may sometimes provide us with somewhat misleading information for TMF failure: e.g., the TMF life under the out-of-phase condition was significantly reduced by the coating, although the ILCF life at 900°C was improved.

From these results a project has just begun to explore the following articles, focusing on "interface":

- I. TMF life prediction method of the coatings,
- II. Evaluation method of adhesion strength,
- III. Optimization and control of interfaces for an improved TMF life, and
- IV. Establishment of recoating, repair and refurbishment technology.

Acknowledgments

The authors wish to express their gratitude to the members of the Committee of High Temperature Strength of Materials, JSMS, for their encouragement for this project.

This work is supported by the Ministry of Education, Japan, as Grant-in-Aid for Scientific Research (No: 10555027 & 12650072).

References

- [1] Bernstein, H. L., Grant, T. S., McClung, R. C., and Allen, J. M., "Prediction of Thermal-Mechanical Fatigue Life for Gas Turbine Blades in Electric Power Generation," *ASTM STP1186*, H. Sehitoglu, Ed., ASTM International, West Conshohocken, PA, 1993, pp. 212–238.
- [2] National Research Council, *Coatings for High Temperature Structural Materials—Trends and Opportunities*, National Academy Press, Washington, D.C., 1996.
- [3] Seth, B.B., "Superalloys: The Utility Gas Turbine Perspective," *Superalloy 2000*, TMS, Warrendale, PA, 2000, pp. 3–16.
- [4] Okazaki, M., "High Temperature Strength of Ni-Base Superalloy Coatings," *Science and Technology of Advanced Materials*, Vol. 2, 2001, pp. 357–366.
- [5] Schneider, K. and Grunling, H. W., "Mechanical Aspects of High Temperature Coatings," *Thin Solid Films*, Vol. 107, 1983, pp. 395–416.
- [6] Hocking, M. G., Vasantathan, V., and Sidky, P. S., *Metallic and Ceramic Coatings*, Longsman Scientific & Technical Publishers, London, 1989.
- [7] Itoh, Y., "Protective Coatings for Gas Turbine," *Kikai-No-Kenkyu*, Vol. 44, 1992, pp. 257–263, 369–376 (in Japanese).
- [8] Taira, S., Fujino, M., and Ohtani, R., "Collaborative Research on Thermo-Mechanical Fatigue Lives of Heat Resisting Alloys in Japan," *Fatigue of Engineering Materials and Structures*, Vol. 1, 1979, pp. 495–501.
- [9] Courbon, J., Louchet, F., Iganat, M., and Debrenne, P., "Analysis of in Situ Shearing Mechanism of γ' precipitates in a Ni-Base Superalloy," *Phil. Mag. Letters*, Vol. 63, 1991, pp.73–78.
- [10] Pollock, T. M. and Argon, A. S., "Creep Resistance of CMSX-3 Nickel Base Superalloy Single Crystals," *Acta Metallurgica Mater.*, Vol. 40, 1992, pp.1–30.

The Fatigue Behavior of NiCr22Co12Mo9 Under Low-Frequency Thermal-Mechanical Loading and Superimposed Higher-Frequency Mechanical Loading

REFERENCE: Moalla, M., Lang, K.-H., and Löhé, D., “The Fatigue Behavior of NiCr22Co12Mo9 Under Low-Frequency Thermal-Mechanical Loading and Superimposed High-Frequency Mechanical Loading,” *Thermomechanical Fatigue Behavior of Materials: 4th Volume, ASTM STP 1428*, M. A. McGaw, S. Kalluri, J. Bressers, and S. D. Peteves, Eds., ASTM International, West Conshohocken, PA, 2003, Online, Available: www.astm.org/STP/1428/1428_10598, 31 March 2003.

ABSTRACT: The repeated start-ups and shut-downs experienced by gas turbines cause complex thermal-mechanical loading, which may result in the low-cycle fatigue failure of components such as the walls of the combustion chambers. In addition, a higher frequency high cycle fatigue loading (HCF) is often superimposed due to mechanical vibrations and unsteady combustion processes. It is known that such a superimposed HCF loading may not only change the cyclic deformation behavior, but also reduce the lifetime considerably. In the present study, the cyclic response of a combustion chamber material, NiCr22Co12Mo9 (Inconel 617), was investigated under combined TMF/HCF loading in total strain controlled out-of-phase (OP) and in-phase (IP) TMF tests with and without superimposed HCF loading. The minimum temperature of the TMF tests was 200 °C, and the maximum temperature was varied from 750 to 1200 °C. For each maximum temperature condition, the superimposed HCF amplitude was varied between 0 and 0.2%. Cyclic hardening was observed, but it became less pronounced the higher the maximum temperature, and at the highest T_{max} the material was cyclically neutral. With increasing superimposed HCF amplitude the cyclic deformation behavior was more and more determined by the HCF. Further, as a result of the superimposed HCF loading the TMF lifetimes decreased significantly. In general, the lifetimes decreased with increase in HCF amplitude and approached only 10% of the fatigue lifetime obtained in the pure TMF experiments. The relation between the applied total strain amplitude, $\epsilon_{a,t}^{mc}$, and the number of cycles to failure, N_f , could be expressed as $\epsilon_{a,t}^{mc} = A \cdot N_f^{-b}$ for each T_{max} and type of TMF-test. With the use of this empirically determined relationship it was possible to estimate the lifetime reduction caused by a superposition of a higher frequency HCF loading on the OP- as well as IP-TMF loading.

KEYWORDS: nickel-base superalloy, thermomechanical fatigue, superimposed loading, cyclic deformation behavior, lifetime behavior

In many technical applications, the cyclic loading of a component involves a low frequency basic loading cycle and a superimposed higher frequency loading cycle. The basic loading can be induced either mechanically, as for example in the case of a submarine hull, or thermally as in the case of the disk of an aircraft turbine engine. These

¹ Dr.-Ing., formerly with Institut für Werkstoffkunde I; Universität Karlsruhe (TH), now with Robert Bosch GmbH, D-70442 Stuttgart, Germany.

² Dr.-Ing., Institut für Werkstoffkunde I, Universität Karlsruhe (TH), D-76128, Germany.

³ Prof. Dr.-Ing., Institut für Werkstoffkunde I, Universität Karlsruhe (TH), D-76128 Karlsruhe, Germany.

basic loading cycles frequently lie in the low cycle fatigue (LCF) range. In addition, a superimposed higher-frequency loading is often present, for example, due to the variation of gas pressure in a combustion engine or because of resonant vibrations. These higher-frequency loading components generally lie in the high cycle fatigue (HCF) range. Despite the fact that this type of combined loading occurs in many technical applications, only a very few systematic investigations in this field are to be found in the literature.

With respect to the complex loading of submarines, experiments have shown that a superimposed higher-frequency mechanical loading reduced the lifetime considerably [1–3]. Similar results have been obtained in experiments with cast iron for internal combustion engines [4,5], and a Ni-base superalloy for gas turbines [6]. In addition, experiments that simulated the loading of titanium alloy components of combustion engines or compressor disks showed that the growth of fatigue cracks was considerably accelerated by a higher frequency superimposed loading [7,8]. Nonetheless, although there are but a few references, it is clear that the problems associated with superimposed low frequency and higher frequency loading of components are very important in many technical applications.

It is also clear that the development of suitable experimental facilities to carry out such combined experiments is not a simple matter [9]. In fact, although in many technical applications the superimposed high frequency loading occurs at different temperatures in an operating cycle, the experimental studies to date, with one exception, have all been performed at a constant temperature. In this one exception, Ref. 10, tests involving the superposition of a high frequency mechanical loading cycle on a low frequency thermal-mechanical loading cycle were carried out for the first time [10]. In that study, a cobalt base alloy was tested with the thermal expansion and mechanical loading inputs being out-of-phase (OP). The present contribution is a further step in the development of this research program in which a nickel base alloy was tested under both in-phase (IP) and out-of-phase conditions.

Material

The material investigated was the solid solution and carbide precipitation hardened Nickel base superalloy NiCr22Co12Mo9 (Nicrofer 5520 Co, Inconel alloy 617). The chemical composition of this alloy is 22.25 Cr, 11.45 Co, 8.88 Mo, 1.28 Al, 0.56 Fe, 0.40 Ti, 0.11 Si, 0.06 C, balance Ni (all quantities in wt. %). It was supplied as 19 mm diameter rods after annealing at 1 200 °C and water quenching at Krupp VDM, Germany. Cylindrical specimens with gauge length of 10 mm and a diameter of 7 mm within the gauge length were machined from the rods. The microstructure of the alloy consisted of grains whose mean diameter was 180 μ , which contained a high density of twin boundaries and a relatively high number of homogeneously distributed primary M_6C carbides and Ti(C,N) carbonitrides.

Experimental Details

The experiments were performed on a servohydraulic fatigue-testing machine, which had a maximum loading capacity of 100 kN. For the strain measurements, a high temperature capacitive extensometer was used. The temperature of a specimen was determined by means of a Ni-CrNi thermocouple, which was spot-welded close to the gauge length, the actual temperature in the gauge length being established by a calibration procedure. During the thermal-mechanical fatigue (TMF) tests, the specimens

were heated up in an inductive furnace, which was equipped with a closed loop control. The specimens were cooled by thermal conduction to the water cooled grips and additionally, if necessary, by blowing with proportionally controlled air jet on the surface of the specimen.

All experiments were performed under total strain control with $T_{\min} = 200^{\circ}\text{C}$. T_{\max} was set at a value of 750, 850, 1000, or 1200°C . The heating and cooling rate was 14 K/s, resulting in cyclic periods of 79, 93, 114, or 143s, respectively.

At the beginning of a TMF test, each specimen was first heated up to a pre-selected mean temperature, T_m , and then subjected to three triangle-shaped temperature cycles between T_{\max} and 200°C while under stress control with the stress maintained at zero. The purpose of this initial testing was to establish the magnitude of the thermal strains. It is noted that because of differences in the thermal gradients on heating and cooling, the thermal expansion of the specimens above and below the mean temperature were not exactly equal. After determining the magnitude of the thermal strains, the testing machine was switched to total strain control and the TMF loading was started. In the thermal mechanical tests the total thermal strain was obtained by subtracting the total mechanical strain.

In-phase (IP) and out-of-phase (OP) thermal mechanical fatigue tests were performed with and without a superimposed higher frequency mechanical (HF) loading. During the OP experiments without the superimposed HCF loading the total strain ϵ_t , which is the sum of the total mechanical strain ϵ_t^{me} and the thermal strain ϵ^{th} , was kept constant ($\epsilon_t = \epsilon_t^{\text{me}} + \epsilon^{\text{th}} = \epsilon_t^{\text{TMF}} + \epsilon^{\text{th}}$) throughout each test. To do so, a mechanical strain amplitude $\epsilon_{a,t}^{\text{me}} = \epsilon_{a,t}^{\text{TMF}}$, which was equal to the thermal strain amplitude ϵ_a^{th} , was induced. In OP TMF tests the phase shift between the temperature and the mechanical strain was 180° . Thus, tensile stresses acted at low temperatures and compressive stresses at high temperatures. In the IP TMF tests the phase shift between the thermal and the mechanical strain was 0° . Thus, tensile stresses acted at high temperatures and compressive stresses at low temperatures. The test program input to the servohydraulic controller came from two computers, which individually determined the set points for the low frequency TMF cycle and the higher frequency (5Hz) loading. During TMF tests with superimposed HCF loading, a sinusoidal HCF loading with a frequency of 5 Hz and an amplitude $\epsilon_{a,t}^{\text{HCF}}$ between 0.05 and 0.2% was superimposed upon the OP or IP cycle described above. In this case $\epsilon_{a,t}^{\text{me}} = \epsilon_{a,t}^{\text{TMF}} + \epsilon_{a,t}^{\text{HCF}}$. The superposition of the HCF loading therefore led to an increase in the total strain amplitude, which ranged from 0.05–0.20%.

Results

Cyclic Deformation Behavior

The hysteresis loops formed in the first few cycles of both pure IP and OP loading exhibited serrations in the tensile portion of the loops, an indication that dynamic strain aging was taking place. With further cycling these serrations generally disappeared. Figure 1 is an example of the nominal stress—mechanical total strain hysteresis loops for $T_{\max} = 850^{\circ}\text{C}$ at half of the lifetime for experiments under OP conditions, without and with a superimposed HCF loading $\epsilon_{a,t}^{\text{HCF}}$ of 0.05, 0.1, or 0.2%. Distinctive dynamic strain aging effects, which appeared only within the first cycles pure OP loading, were observed predominantly in the tensile phase of the loading cycle. Under superimposed OP/HCF loading, evidence of dynamic strain aging was observed even at the half-lifetime under

both tensile and compressive stresses. From the width of the hysteresis loops at mean stress it is seen that the plastic strain amplitude at $N_f/2$ increases with increasing $\epsilon_{a,t}^{HCF}$. On the other hand, the stress amplitude decreases slightly with increasing $\epsilon_{a,t}^{HCF}$. The hysteresis loops show that under OP test conditions dynamic relaxation processes occurred during compressive loading at high temperatures. This relaxation resulted in an asymmetrical form of the hysteresis loops, which resulted in a shift of the loops in the tensile stress direction and therefore to the development of tensile mean stresses.

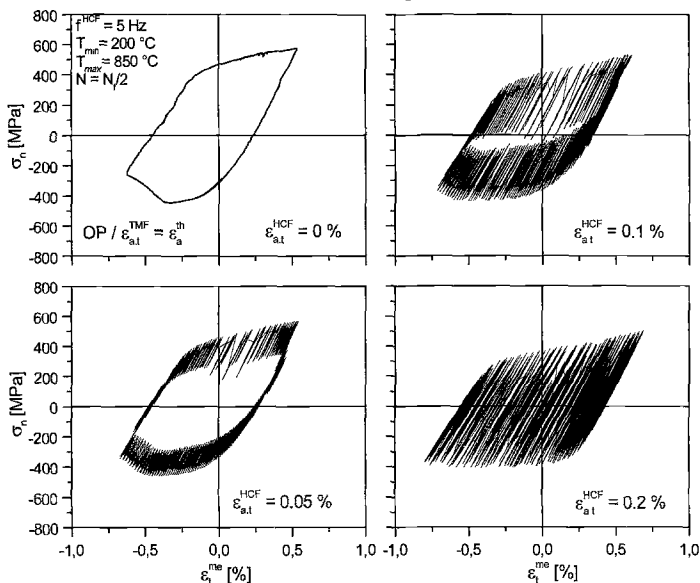


FIG. 1—Stress-total mechanical strain hysteresis loops at out-of-phase thermal-mechanical fatigue tests at $T_{max} = 850^{\circ}\text{C}$ without and with superimposed higher frequency mechanical loading at $N_f/2$.

Figure 2 gives examples of the hysteresis loops obtained under IP conditions at $N_f/2$ for $\epsilon_{a,t}^{HCF}$ of 0, 0.05, 0.1, and 0.2% for $T_{max} = 850^{\circ}\text{C}$. Since the phase shift between temperature and mechanical total strain is zero, tensile stresses are induced at higher temperatures and compressive stresses at lower temperatures. The cyclic plastic deformation is essentially determined by thermally activated dislocation glide processes in the low temperature range and by diffusion controlled creep processes in the high temperature range. Furthermore, the cyclic plastic deformation behavior is influenced by dynamic strain aging processes, which appear under superimposed IP/HCF loading mainly during the compressive deformation phase at high $\epsilon_{a,t}^{HCF}$ during a large portion of the lifetime. At the 50% lifetime the width of the hysteresis loops, and with that $\epsilon_{a,p}^{me}$, increases with increasing $\epsilon_{a,t}^{HCF}$, as in the case of OP testing. The cyclic stresses rose as the $\epsilon_{a,t}^{HCF}$ increased from 0–0.05%. However, at higher values of $\epsilon_{a,t}^{HCF}$ any further change in the cyclic stress amplitude, σ_a , was quite small. In each case dynamic relaxation of the tensile stress occurred as T approached T_{max} . As a consequence, the tensile stresses decreased and the mean stress was shifted in the compressive direction in all IP experiments.

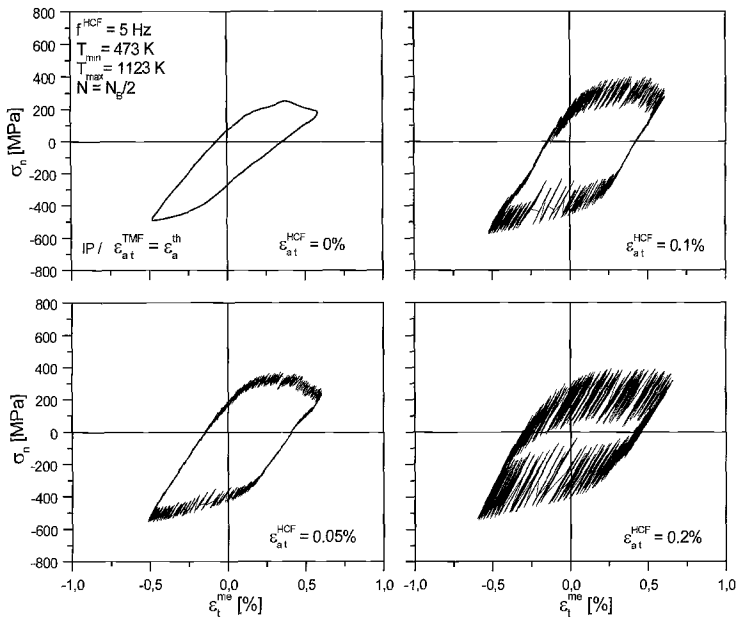


FIG. 2—Stress-total mechanical strain hysteresis loops at in-phase thermal-mechanical fatigue tests at $T_{max} = 850^{\circ}\text{C}$ without and with superimposed higher frequency mechanical loading at $N_f/2$.

For all T_{max} values below 1000°C the influence of the superimposed HCF loading on the cyclic deformation behavior was comparable. Figure 3 shows the cyclic deformation curves for a T_{max} value of 850°C . In this figure the stress amplitude is plotted as a function of the plastic strain range, which was taken to be the half-width of the hysteresis loop at the mean stress level. Results from OP-TMF experiments are presented on the left side of the figure and those from IP experiments on the right side of the figure. The upper part of the figure shows the variation of the plastic strain amplitude with number of cycles, and the lower part shows variation of the stress amplitude and the mean stress as a function of the number of cycles. Cyclic hardening behavior was observed under all test conditions, which meant that since the total mechanical strain range was held constant, the elastic component increased as the plastic component decreased. For all OP loading conditions a marked increase in σ_a in the first 20 cycles was observed, and for those tests lasting more than 20 cycles only a slight additional increment in cyclic hardening occurred up to the point of macroscopic crack initiation. Under IP conditions a similar effect of the superimposed HCF loading on the cyclic deformation behavior was observed. For all of the IP $\epsilon_{a,t}^{HCF}$ values investigated, cyclic hardening developed, which was considerably more pronounced as compared to IP-TMF loading without the superimposed HCF loading. The stress amplitudes at saturation in the case of superimposed loading reached values that were about 120 MPa higher than for $\epsilon_{a,t}^{HCF} = 0\%$.

In OP loading, with increase in $\epsilon_{a,t}^{HCF}$ the values of $\epsilon_{a,p}^{me}$ and σ_a increased. It is interesting to note that at the lower HCF total strain amplitudes a change in $\epsilon_{a,t}^{HCF}$ resulted in a relatively strong change in $\epsilon_{a,p}^{me}$ and only a relatively weak change in σ_a . However, in the range of higher $\epsilon_{a,t}^{HCF}$ values, the opposite trend occurred as the influence of the superimposed HCF loading on the cyclic deformation behavior increased with increase in $\epsilon_{a,t}^{HCF}$ and T_{max} . At higher values of $\epsilon_{a,t}^{HCF}$ cyclic hardening was promoted by HCF-induced dynamic strain aging. Therefore, a further increase of $\epsilon_{a,t}^{HCF}$ was almost fully elastic, which resulted in a corresponding increase in σ_a , but a nearly negligible influence on $\epsilon_{a,p}^{me}$. This behavior also occurred under IP loading, but was less pronounced.

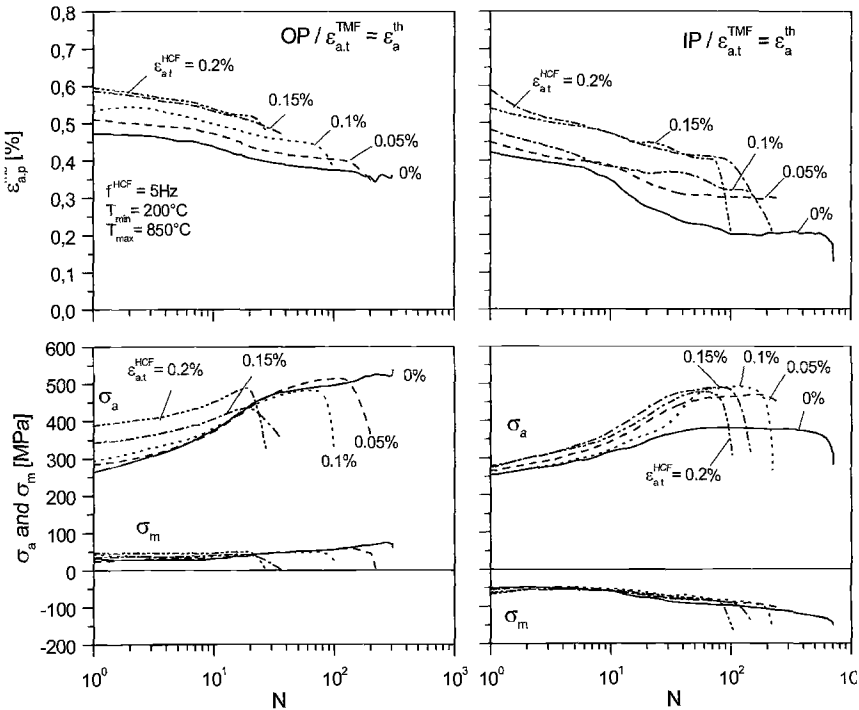


FIG. 3—Cyclic deformation curves for OP- (left) and IP- (right) TMF loading at $T_{max} = 850^\circ\text{C}$ without and with superimposed higher frequency mechanical loading.

As in the case of the TMF experiments without superimposed loading, the development of mean stresses under HCF loading was due to dynamic relaxation at high temperatures because of different material resistances at high and low temperatures. Under OP/HCF loading at $T_{max} = 850^\circ\text{C}$ the tensile mean stress rose in the first TMF cycle. The mean stress remained approximately constant up to the 10th cycle and then increased continuously with further cycling. Under IP/HCF loading a compressive mean stress of about -50 MPa was produced in the first cycle at all maximum temperatures. After minor changes within the 10 first cycles, the absolute values of the mean stress

increased continuously as the result of the pronounced cyclic hardening. At a T_{max} of 1200°C the material behaved under OP/HCF as well as under IP/HCF loading in a cyclically neutral manner. The plastic strain amplitude, the stress amplitude, and the mean stress remained approximately at the level, which developed in the initial cycles up to the point of macroscopic crack initiation.

Lifetime Behavior

TABLE 1—Coffin-Manson type parameters α and ϵ_f for superimposed OP/HCF and IP/HCF loading.

T_{max} [°]	OP/HCF		IP/HCF	
	α	$\epsilon_f 10^{-3}$	α	$\epsilon_f 10^{-3}$
750	-0.37	18.7	-0.62	70
850	-0.15	8.7	-0.37	24
1000	-0.08	9.3	-0.27	20.7
1200	-0.08	12	-0.106	13.6

In Fig. 4, the values of the log of $\epsilon_{a,p}^{me}$ at $N_f/2$ are plotted versus the log of the number of cycles to failure for superimposed OP/HCF loading (top) and IP/HCF loading (bottom). For each T_{max} the experimental data can be described by a straight line, thus establishing that a type of Coffin-Manson relationship is valid for superimposed TMF/HCF loadings. Note, however, that the reduction in fatigue life under combined TMF and HCF cycling is not simply due to an expansion of the plastic strain range. The HCF cycling process must also be playing a role. Since the deformation processes are temperature dependent, and the total mechanical strain due to the TMF loading increases with increasing T_{max} , the relation between plastic deformation and number of cycles to failure yields separate lines for every maximum temperature. Relatively low values of the

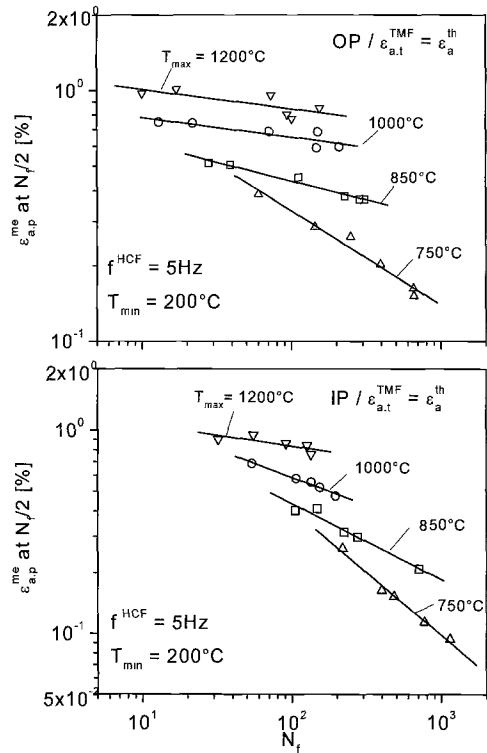


FIG. 4—Plastic strain amplitude at $N_f/2$ versus the number of cycles to failure N_f for superimposed OP/HCF loading (top) and IP/HCF loading (bottom).

slope α were determined, and these values decreased with increase in T_{max} . The estimated values of the Coffin-Manson type parameters α and ϵ_f are listed in Table 1.

The ratio of the fatigue lifetime under HCF cycling to that without HCF cycling is given as a percentage in Fig. 5 as a function of the % total strain amplitude in HCF (OP/HCF, top, IP/HCF, bottom). Under OP/HCF loading, a given $\epsilon_{a,t}^{HCF}$ resulted in approximately the same lifetime reduction independent of the maximum temperature. For example, the superposition of $\epsilon_{a,t}^{HCF} = 0.1\%$ in OP loading reduces the number of cycles to failure by about 60% as compared to the lifetime under pure OP conditions. On the other hand, under IP/HCF, the relative lifetime reduction at a given $\epsilon_{a,t}^{HCF}$ does depend on the maximum temperature because the tensile stresses, which primarily determined the lifetime, were developed at high temperatures. It is noted that the highest lifetime reductions due to a super-imposed HCF loading occurred at T_{max} values of 750°C and 850°C due to a

combination of high tensile stresses and oxidation damage. This temperature dependence was most pronounced at low and medium $\epsilon_{a,t}^{HCF}$ values. It also seems clear that the damaging effects of the HCF loading cannot be accounted for on the basis of a straightforward linear damage summation. For example, if all of the HCF cycles were assumed to be applied at the highest temperature (850°C), presumably the worst case for IP HCF, then the isothermal lifetime at total strain amplitude of 0.2% at 850°C and a frequency of 5 Hz for this alloy would be about 1.2×10^4 cycles [11]. The IP/TMF lifetime at 850°C is 700 cycles. The experimentally determined TMF/HCP damage fraction is 0.14 ($N_f = 100$ cycles). In 100 TMF cycles, the number of HCF cycles would be $100 \text{ cycles} \times 5 \text{ Hz} \times 93 \text{ s/cycle} = 46\,500$ cycles, a number in excess of the fatigue lifetime at 850°C. Most of these cycles, however, would have been applied at temperature levels below the maximum value of 850°C where the fatigue lifetimes would have been larger than at 850°C. In addition, much of the IP/TMF cycle is in compression where

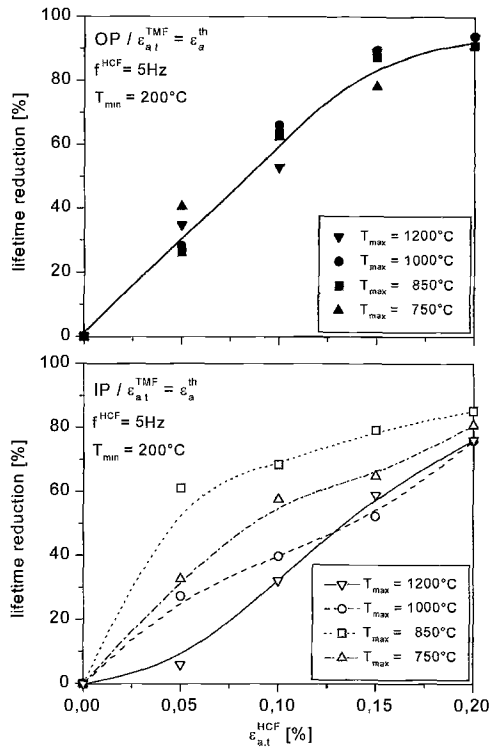


FIG. 5—Lifetime reduction under super-imposed HCF loading as a percentage of the pure TMF loading as a function of $\epsilon_{a,t}^{HCF}$ for super-imposed OP/HCF loading (top) and IP/HCF loading (bottom).

little damage due to the HCF is expected. It would be a challenging task, but if the damaging effect of the HCF cycles could be properly accounted for, perhaps in terms of their influence on fatigue crack growth, a damage summation closer to unity might be obtained, with the effective number of cycles under HCF being 54 000, i.e., 46 500/54 000 = 0.86.

In Fig. 6 the total mechanical strain amplitude $\epsilon_{a,t}^{me}$, i.e., the sum of the total mechanical strain amplitude $\epsilon_{a,t}^{TMF}$ of the pure TMF loading and the amplitude of the superimposed HCF loading $\epsilon_{a,t}^{HCF}$, ($\epsilon_{a,t}^{me} = \epsilon_{a,t}^{TMF} + \epsilon_{a,t}^{HCF}$) is plotted double logarithmically as a function of the number of cycles to failure (open symbols). In addition, the $\epsilon_{a,t}^{me}$ versus N_f Wöhler curves (full symbols), which were determined under pure TMF loading at $T_{min} = 200^\circ\text{C}$ and T_{max} values between 750 and 1200°C are included (OP/HCF top, IP/HCF bottom). As with Fig. 4, both the OP and the IP loading conditions show a distinct decrease of the lifetime with increasing amplitude of the super-imposed HCF loading for all T_{max} values investigated.

It is noted that t_{hfe} lifetime data from the superimposed TMF/HCF experiments can be described for each maximum temperature by a straight line, which is given by a power function,

$$\epsilon_{a,t}^{me} = AN_f^{-b} \tag{1}$$

where A is a constant, which can be determined from the TMF experiments without superimposed loading. The exponent b, which is defined by the slope of the straight line, decreases with increasing T_{max} for all loading conditions and seems to be dependent on the material properties at the respective maximum temperature. This is suggested by the linear relation between the exponent b and the tensile strength at the maximum temperature, which has been found for a Co-base superalloy [10]. (This type of relationship could not be checked in the present case because the tensile properties were not determined.) By means of the empirical relation (1) and the given test conditions, it is possible to make an estimate of the lifetime reduction due to a superimposed HCF loading.

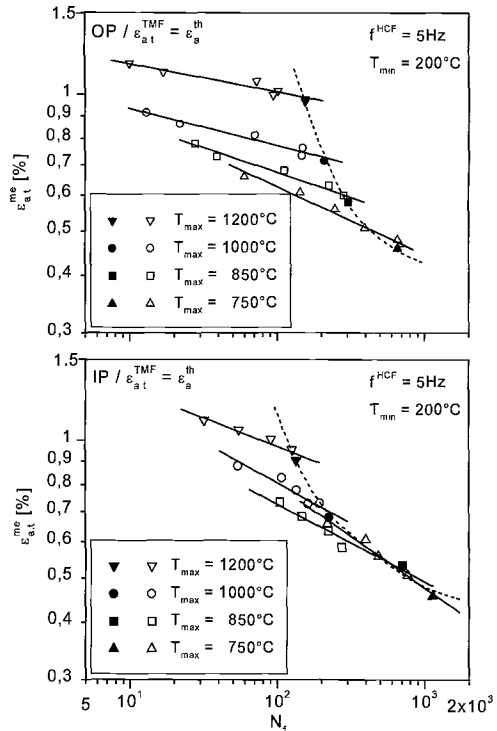


FIG. 6—Total mechanical strain amplitude, $\epsilon_{a,t}^{me}$, versus number of cycles to failure, N_f , for superimposed OP/HCF loading (top) and IP/HCF loading (bottom).

Discussion

The cyclic deformation behavior of the alloy investigated under superimposed OP/HCF and IP/HCF loading was dominated by thermally activated dislocation slip at the lower cycle temperatures, by dynamic strain aging processes at intermediate temperatures and by diffusion controlled time-dependent creep processes at higher temperatures. The latter manifested itself clearly by a decrease of the applied stresses due to dynamic relaxation processes. These stresses occurred under OP (IP) loading at compressive (tensile) loading before the minimum (maximum) mechanical total strain at the maximum temperature was reached (see hysteresis loops in Figs. 1 and 2). Dynamic strain aging effects occurred predominantly during the reverse deformation during cooling down to T_{\min} as a result of interactions between gliding dislocations and diffusing alloying atoms. At still lower cycle temperatures, the decreasing thermal activation of dislocation slip resulted in relatively high tensile (OP) or compressive (IP) stresses, as the temperature approached T_{\min} . Under OP loading the plastic strain amplitude at $N_f/2$ increased with increasing $\epsilon_{a,t}^{\text{HCF}}$, whereas the stress amplitude at $N_f/2$ decreased slightly because the cyclic hardening was incomplete due to a decreasing number of cycles to failure. Under IP-conditions at $T_{\max} = 750$ and 850°C where saturation was reached at all $\epsilon_{a,t}^{\text{HCF}}$, generally an increase of the σ_a values was observed at half of the lifetime. This was more pronounced for an increase of $\epsilon_{a,t}^{\text{HCF}}$ from 0–0.05% (Fig. 2) and was caused by an increasing cyclic hardening due to an increase in the dislocation density.

Under OP as well as at IP conditions at $T_{\max} < 1000^\circ\text{C}$ cyclic hardening was less pronounced than higher T_{\max} because, with increasing temperature, diffusion controlled recovery processes became more and more important. This was reflected after OP loading by a microstructure that consisted of subgrains, which showed evidence of carbide dissolution and coarsening [12]. At $T_{\max} = 1200^\circ\text{C}$, an equilibrium between hardening and recovery processes developed. Hence, either cyclic hardening nor cyclic softening i.e., neutral cyclic deformation behavior, was observed for all $\epsilon_{a,t}^{\text{HCF}}$ values investigated.

Generally, with an increase in $\epsilon_{a,t}^{\text{HCF}}$ a shift in the level of $\epsilon_{a,p}^{\text{mc}}$ and σ_a to higher values was observed because of the increasing mechanical loading (Fig. 3). The cyclic deformation behavior was the more affected by the HCF loading the smaller T_{\max} and the higher the value of $\epsilon_{a,t}^{\text{HCF}}$. For OP/HCF loading with $T_{\max} = 850^\circ\text{C}$ the growing influence of HCF can be readily recognized in Fig. 7, where $\epsilon_{a,t}^{\text{HCF}}$ values of 0.05 and 0.1% did not cause any substantial change

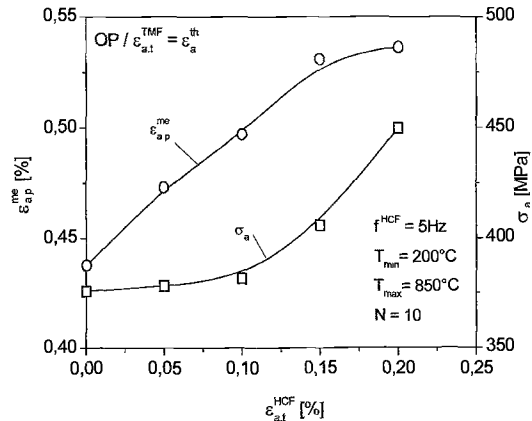


FIG. 7—Plastic strain amplitude and stress amplitude at $N_f/2$ versus HCF- total mechanical strain amplitude under superimposed OP/HCF.

in the material's resistance to cyclic plastic deformation. Therefore, the HCF loading was taken up in almost a purely plastic manner. This led to a corresponding rise of $\varepsilon_{a,p}^{me}$ and a negligible change of the stress amplitude. HCF loading with an amplitude of 0.15 and 0.2% resulted in a considerable rise of the material resistance to cyclic plastic deformation. Therefore, the $\varepsilon_{a,t}^{HCF}$ strain was taken up in a mainly elastic manner. As a result the stress amplitude increased and the plastic strain amplitude changed only slightly. Under IP/HCF superposition the relationships are less clear. At $T_{max} = 850^{\circ}C$, similar $\varepsilon_{a,p}^{me}$ values as in the case of OP/HCF superposition were obtained. However, at high $\varepsilon_{a,t}^{HCF}$ values, a considerable increase of the stress did not occur. This is compatible with the corresponding development of damage. Since $\varepsilon_{a,t}^{me}$ increased with $\varepsilon_{a,t}^{HCF}$, whereas $\varepsilon_{a,p}^{me}$ hardly changed at all, the compliance of the specimen had to increase. This increase in the compliance was caused by the initiation and propagation of microcracks.

The complex relationship between the superimposed TMF/HCF loading and the number of cycles to failure can be described for every T_{max} by the extent of the plastic deformation at $N_f/2$ by means of the Coffin-Manson relationship. The values of the Coffin-Manson exponent α (see Table 1) showed a considerable decrease with increasing T_{max} . This again reflects the complex interactions between TMF and HCF loading in the development of stress and plastic strain amplitudes. For such cases it seems reasonable check on the applicability of a damage parameter such as the Smith-Watson-Topper parameter, P_{SWT} , or the Ostergren parameter, P_{Ost} , for the assessment of the lifetime behavior. These parameters take the total strain amplitude or the plastic strain amplitude as well as the maximum stresses developed into account. These parameters were evaluated in Fig. 8. The upper half of this figure shows the fatigue lifetime a function of P_{SWT} for both OP/HCF and IP/HCF loading. The lower part of the figure shows similar plots in terms of P_{Ost} . The P_{SWT} parameter provides only a weak basis for assessing the fatigue lifetime due to the low slope of the data points under OP/HCF loading and the strong scattering of the data points under IP/HCF loading. The P_{Ost} parameter provides a somewhat better basis for lifetime predictions, but is also characterized by a high degree of scatter. A more detailed analysis [12] shows that for a particular T_{max} different relationships exist. However, no improvement in lifetime prediction is obtained over that obtainable through the use of Figs. 5 and 6.

The lifetime reduction under superimposed TMF/HCF loading with respect to the lifetime under pure TMF loading increased considerably with increase in $\varepsilon_{a,t}^{HCF}$ (Fig. 5). For example the superposition of a $\varepsilon_{a,t}^{HCF}$ of 0.2% led to a lifetime reduction of approximately 95% under OP loading and approximately 80% under IP loading. Under OP loading the lifetime reduction was largely independent of T_{max} because the HCF loading influenced mainly the initiation and propagation of microcracks. This damage developed predominantly under the action of tensile stresses in the range of the minimum temperature, which was the same for all experiments. On the other hand, under IP loading, the lifetime reduction depended on the maximum temperature (Fig. 5) because in this case, the tensile stresses that determined the lifetime developed in the range of T_{max} . The highest lifetime reduction occurred at T_{max} values of 750 and 850°C. This was due to the high tensile stresses developed at these temperatures because of pronounced cyclic hardening, which was associated with a microstructure that contained high densities of dislocations and carbides [12].

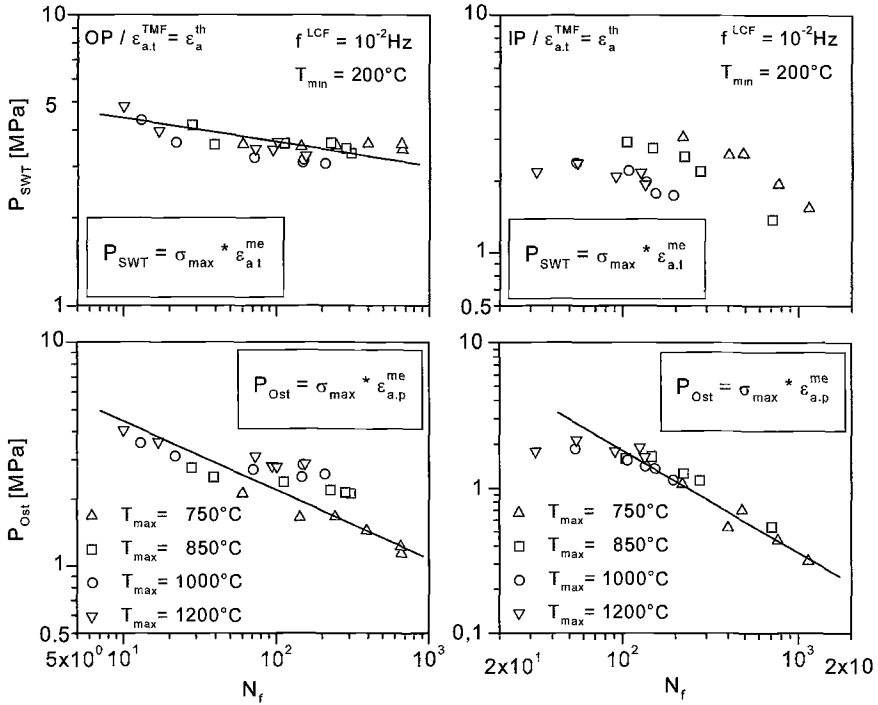


FIG. 8—The Smith-Watson-Topper damage parameter (top) and the Ostergren damage parameter (bottom) versus N_f for superimposed OP/HCF loading (left) and IP/HCF loading (right).

A comparison of N_f under pure and superimposed TMF loadings on the basis of the total mechanical strain amplitude $\epsilon_{a,t}^{me} = \epsilon_{a,t}^{TMF} + \epsilon_{a,t}^{HCF}$ shows a considerable lifetime reduction under OP loading for $\epsilon_{a,t}^{me} > 0.5\%$ and under IP-loading with $\epsilon_{a,t}^{me} > 0.57\%$. This lifetime reduction increased with increasing $\epsilon_{a,t}^{me}$ (Fig. 6). It was mainly caused by the accelerated growth under HCF loading of cracks, which are created by low frequency LCF loading [6]. In addition, the change of the microstructure at high $\epsilon_{a,t}^{HCF}$ and T_{max} values from a subgrain structure to a diffuse planar dislocation arrangement with a high dislocation density resulted in a reduction of the mobility of dislocations as compared with pure TMF loading. This strongly localized dislocation movement favored the development of microscopic damage [12].

As shown in Fig. 4, for every T_{max} temperature the relation between $\epsilon_{a,t}^{me}$ as the sum of $\epsilon_{a,t}^{TMF}$ and $\epsilon_{a,t}^{HCF}$ and the resulting lifetime under superimposed TMF loading with different $\epsilon_{a,t}^{HCF}$ can be described by a simple power law (Eq 1). The exponent b of these equations decreased with increasing T_{max} or $\epsilon_{a,t}^{TMF}$, and seemed to be dependent on the material properties at the different maximum temperatures. In order to verify this relationship, additional OP/HCF experiments at $T_{max} = 850^\circ\text{C}$ were carried out with $\epsilon_{a,t}^{TMF} = 0.5 \epsilon_a^{th}$. The results of these tests are indicated by solid symbols in Fig. 9. These results indicate that the slope of a straight line through the data points has a higher slope as compared to the corresponding line in Fig. 4 (0.23 versus 0.15). If the exponent b is plotted on a logarithmic scale as a function of the log of the total mechanical total strain

amplitude from pure TMF experiments, the data points of the OP experiments can be described by a straight line (Fig. 10). The results of IP tests are also shown in Fig. 10, and it is seen that the values of b are higher for IP/HCF than for OP/HCF loading. This comes about because under IP/HCF conditions at the same T_{max} (same $\epsilon_{a,t}^{TMF}$) the induced tensile stresses are lower. Therefore, under IP/HCF loading the effect of the HCF loading on the lifetime is lower as compared to OP/HCF superposition. Again, the dependence of the exponent b of $\epsilon_{a,t}^{TMF}$ may be explained by the fact that the initiation of microcracks is mainly affected by the magnitude of the pure thermal mechanical loading, and only the propagation of these microcracks is influenced by the superimposed higher frequency HCF loading.

In Fig. 11, the mechanical total strain Wöhler curves from pure TMF (a) and superimposed OP/HCF and IP/HCF experiments at $\epsilon_{a,t}^{HCF} = 0.1\%$ (b) and 0.2% (c) is shown. Under pure TMF loading the Wöhler curves of OP and IP loading cross. Under OP loading $\epsilon_{a,t}^{me} > 0.7\%$ ($T_{max} > 1100^\circ\text{C}$) resulted is a higher lifetime. For lower values of $\epsilon_{a,t}^{me}$ (T_{max}) the opposite is the case. This behavior is caused by the development of damage. At lower $\epsilon_{a,t}^{me}$ (T_{max}) the tensile mean stresses which are produced under OP loading accelerate microcrack initiation and propagation. Therefore, under this loading condition the lifetime at OP is lower than under IP loading. At high $\epsilon_{a,t}^{me}$ (T_{max}) values tensile stresses in the range of T_{max} produce creep damage under IP loading which reduces the lifetime in comparison with OP loading despite of the compressive mean stresses which develop under IP loading. Under superimposed TMF/HCF loading the Wöhler curves did not cross. This was a consequence of the growing influence of the superimposed loading mainly on the increasing tensile stresses that controlled microcrack propagation. Under OP conditions, microcrack initiation at the surface was accelerated by the high tensile

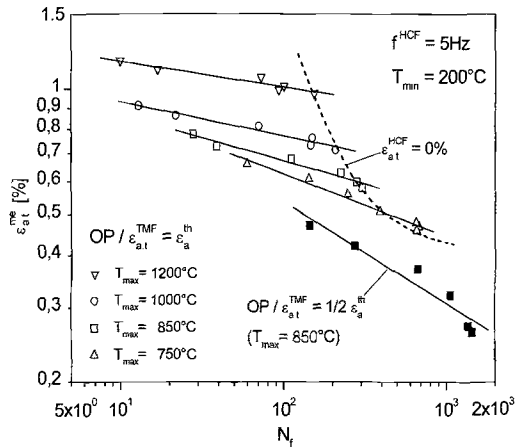


FIG. 9—Total mechanical strain amplitude versus number of cycles to failure for superimposed OP/HCF loading for different TMF constraints

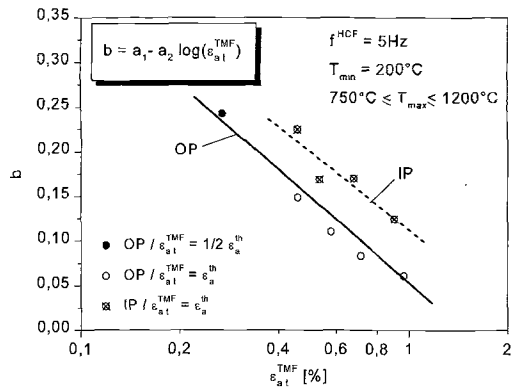


FIG. 10—Exponent b versus TMF total mechanical strain amplitude for pure and superimposed HCF loading for OP- and IP loading with different TMF constraints.

stresses developed at low temperatures. Therefore, during OP/HCF loading the faster microcrack propagation due to the superimposed HCF loading resulted in earlier failure than under IP/HCF loading. As can be seen from Fig. 11, under an $\epsilon_{a,t}^{HCF}$ loading of 0.2%, a much larger influence of the phase shift existed than for an $\epsilon_{a,t}^{HCF}$ loading of 0.1%.

Summary

From the results obtained in this study, the following conclusions can be drawn:

- A superimposed HCF loading decreased the TMF lifetime significantly. The lifetime reduction increased with increase in $\epsilon_{a,t}^{HCF}$ and approached 90% of the lifetime obtained in pure TMF experiments. The dependence between the applied total strain amplitude $\epsilon_{a,t}^{me}$ and the number of cycles to failure N_f can be described as $\epsilon_{a,t}^{me} = A N_f^{-b}$ for each T_{max} and type of TMF-test.
- Under OP/HCF loading the lifetime reduction at a given $\epsilon_{a,t}^{HCF}$ did not depend on the maximum temperature because tensile stresses, which determine the lifetime, developed when the temperature approached the minimum temperature of the thermal cycle and T_{min} was the same at all OP tests. In contrast, for IP/HCF superposition the lifetime reduction did depend on the maximum temperature because tensile stresses developed when the temperature approached T_{max} .
- With increasing $\epsilon_{a,t}^{me}$ the lifetime decreased under OP/HCF conditions more so than under IP/HCF conditions because the lifetime reduction depended mainly on the developing tensile stresses, which controlled microcrack initiation and propagation. At a given T_{max} , faster microcrack initiation and propagation during OP/HCF loading due to HCF resulted in an earlier failure than for IP/HCF loading. With increasing $\epsilon_{a,t}^{me}$, the differences increased.

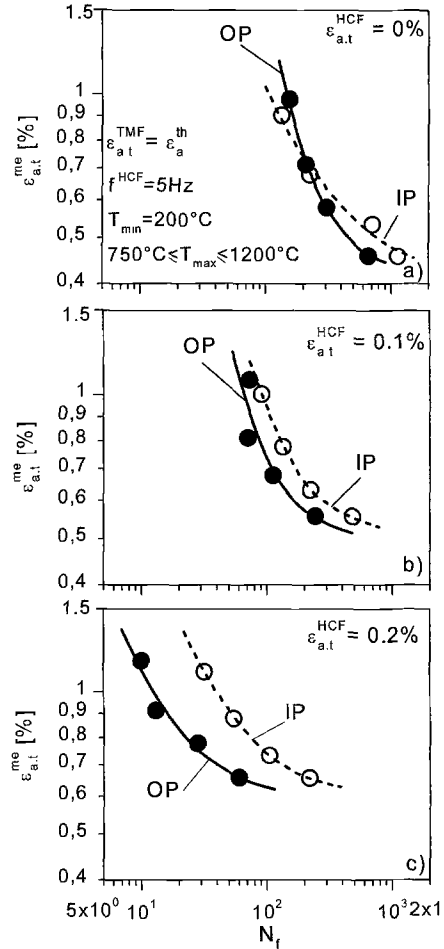


FIG. 11—Mechanical total strain Wöhler curve for (a) pure TMF loading, and (b) superimposed OP/HCF and IP/HCF loading for $\epsilon_{a,t}^{HCF} = 0.1$ and (c) 0.2%.

Acknowledgment

The financial support of this investigation by the “Deutsche Forschungsgemeinschaft (DFG)” within the “Sonderforschungsbereich 167: Hochbelastete Brennräume – Stationäre Gleichdruckverbrennung” is gratefully acknowledged.

References

- [1] Shah Khan, M. Z. and Burch, I. A., “Effect of Superimposed High Frequency Flutter on the Fatigue Life of a Submarine Hull Steel,” *International Journal of Fracture*, Vol. 44, 1990, pp. R35–R38.
- [2] Shah Khan, M. Z. and Burch, I. A., “Effect of Cyclic Waveforms with Superimposed High Frequency Flutter on the Corrosion Fatigue Behaviour of a Submarine Hull Steel,” *International Journal of Fracture*, Vol. 52, 1991, pp. R57–R60.
- [3] Shah Khan, M. Z., “Influence of Loading Profile and Superimposed Flutter Load Frequency on the Fracture Behaviour of a Submarine Hull Steel in Seawater,” *International Journal of Fatigue*, Vol. 15, No. 3, 1993, pp. 199–203.
- [4] Lang, K.-H., Eifler, D., and Macherauch, E., “Detection, Development and Propagation of Fatigue Cracks in High Temperature Loaded Cast Irons (in German),” *FVV-Forschungsberichte*, Heft 372, FVV, Frankfurt, Germany, (1986).
- [5] Lang, K.-H., “Influence of Near Service Loadings on the Lifetime of the Cylinder Head Materials GG-30 and GGV-30 (in German),” *Werkstoffkunde, Beiträge zu den Grundlagen und zur interdisziplinären Anwendung*, P. Mayr, , O. Vöhringer, H. Wohlfahrt, Eds., DGM-Verlag, Oberursel, (1991).
- [6] Moalla, M., Lang, K.-H., Löhe, D., and Macherauch, E., “Isothermal High Temperature Fatigue Behaviour of NiCr22Co12Mo9 under Superimposed LCF and HCF Loading,” *Proceedings, 4th International Conference on Low Cycle Fatigue and Elasto-Plastic Behaviour of Materials*, K. T. Rie, P. D. Portella, Eds., Elsevier Science, Oxford, UK, 1998, pp. 27–32.
- [7] Powell, B. E., Duggan, T. V., and Jeal, R., “The Influence of Minor Cycles on Low Cycle Fatigue Crack Propagation,” *International Journal of Fatigue*, Vol. 4, No. 1, 1982, pp. 4–14.
- [8] Powell, B. E. and Duggan, T. V., “Crack Growth in Ti-6Al-4V Under the Conjoint Action of High and Low Cycle Fatigue,” *International Journal of Fatigue*, Vol. 9, No. 4, 1987, pp. 195–202.
- [9] Stoten, D. P. and Smith, D. J., “The Design of a Control System for a Superimposed Frequency Fatigue Test Machine,” *Journal of Testing and Evaluation*, Vol. 21, No. 3, 1993, pp. 154–159.
- [10] Moalla, M., Lang, K.-H., and Löhe, D., “Effect of Superimposed High Cycle Fatigue Loading on the Out-Of-Phase Thermal-Mechanical Fatigue Behaviour of CoCr22Ni22W14,” *Material Science and Engineering A*, Vol. 319-321, 2001, pp. 647–651.
- [11] Mündel, A., “One- and Two-Step Fatigue Experiments and Crack Growth Investigations on CoCr22Ni22W14 and NiCr22Co12Mo9 in Selected Temperature Ranges (in German),” *VDI-Fortschrittsberichte*, Reihe 18, Nr. 218, VDI-Verlag, Düsseldorf, Germany, 1997.
- [12] Moalla, M., “Isothermal and Thermal-Mechanical Fatigue Behavior Under Superimposed LCF/HCF Loadings and Isothermal Fatigue Crack Propagation of NiCr22Co12Mo9 and CoCr22Ni22W14 (in German),” publication series *Werkstoffwissenschaft und Werkstofftechnik*, Nr. 2001.9, Shaker Verlag, Aachen, Germany, 2001.

C. N. Kong,¹ C. K. Bullough,² and D. J. Smith¹

Thermomechanical Response of Single Crystal Nickel-base Superalloy CM186 SX

REFERENCE: Kong, C. N., Bullough, C. K., and Smith, D. J., "Thermomechanical Response of Single Crystal Nickel-base Superalloy CM186 SX," *Thermomechanical Fatigue Behavior of Materials: 4th Volume, ASTM STP 1428*, M. A. McGaw, S. Kalluri, J. Bressers, and S. D. Peteves, Eds., ASTM International, West Conshohocken, PA, Online, Available: www.astm.org/STP/1428/1428_10589, 23 June 2003.

ABSTRACT: CM186 SX is a second generation Rhenium (Re) containing single crystal nickel-base superalloy, which exhibits improved creep and oxidation performance compared with its first generation counterparts. In this paper, the thermomechanical (TMF) response of coated and uncoated <001> single crystal nickel-base superalloy, CM186 SX is presented. In-phase (IP) and Out-of-Phase (OP) cycles were examined using coated and uncoated hollow dumbbell test pieces. Linear heating and cooling with a temperature rate of 6°C/s between 350 and 950°C was applied. The tests were mechanical strain controlled with strain ranges between 0.5 to 1.0%. Detailed examination of the experimental results revealed that variations in wall thickness of the hollow test pieces played a significant role in the set-up of the experiments and interpretation of the results. Finite element analysis was also performed to investigate the influence of the variation in wall thickness and its relevance to the experimental results. Overall, the results showed that the coating reduced the TMF life, particularly for OP cycles. Brittle cracking of the coating, especially at low temperatures, occurred at low strains. For the IP cycle the coating appeared to have less of an influence on life than for OP cycles. The results are compared with those from an earlier program using solid rectangular test pieces.

KEYWORDS: thermomechanical fatigue, single crystal, nickel-base superalloy, aluminide coating, Sermalloy 1515 and CM186 SX

Introduction

The development of nickel-base superalloys has been driven primarily by the gas turbine and aero-engine industry. Over the past few decades, more advanced casting processes have allowed the introduction of more sophisticated and stronger nickel-base superalloys, such as the directionally solidified (DS) and single crystal (SC) forms. CM186LC, a second generation DS superalloy, is used as blade material in small industrial gas turbines [1]. It is an attractive superalloy due to its low production cost as it has good castability and does not require a solution heat treatment. Further cost reduction is possible by using foundry revert material from other superalloys such as CMSX4[®], due to their chemistry resemblance. The successful implementation of CM186LC[®] as blade material in industry has promoted interest in the possibilities of further improvement in engine performance by using the single crystal form of this material, CM186 SX. This

¹ Research Student and Professor, respectively, Department of Mechanical Engineering, University of Bristol, Queen's Building, University Walk, Bristol, BS8 1TR, United Kingdom.

² Deputy Head of Materials, ALSTOM Power Technology Centre, Cambridge Road, Whetstone, Leicester, LE8 6LH, United Kingdom.

necessitates more characterization of mechanical properties of this material, such as high temperature creep, fatigue, oxidation resistance and most importantly, thermomechanical (TMF) behavior.

Despite their superiority in high temperature creep and fatigue resistance compared with the first generation superalloys, the improved strength of the newer generation superalloys is often accompanied by lower surface oxidation and corrosion resistance, due to lower content of chromium (Cr). Hence, various types of surface coatings are often used to improve their surface oxidation and corrosion resistance. Although it is generally accepted that coatings have minimal influence on the structural integrity of the component, it is important to optimize the performance of the coated component through a better understanding of its mechanical behavior.

Gas turbine blades experience transient thermal and mechanical loading during service, especially during start-up and shutdown of the engine. Thermal induced strain, combined with mechanical strain, has a detrimental effect on the blade's service life. Different damage mechanisms are expected to occur in coated turbine blades during a thermal cycle as the coating has a ductile-brittle transition temperature (DBTT) at an intermediate temperature in the cycle. It is therefore essential to study the material response of the newer superalloys during thermal and mechanical fatigue.

Different methods are often used when conducting TMF tests and there is no standard procedure. Thin wall test pieces are generally used in TMF tests to reduce thermal mass and help minimize thermal gradients. The thin wall test piece is also intended to resemble a volume of material in the thin section of a turbine blade. In the work presented in this paper, the influence of nonuniform wall thickness of the test piece was examined.

Turbine blades in service experience various TMF cycles. The Diamond type cycle with 135° phase shift is particularly popular among many researchers [2-4,8]. In this work, simple In-phase (IP) and Out-of-phase (OP) cycles were used to study coated and uncoated CM186 SX test pieces. The effect of the coating on the TMF lives of the same coating-substrate system was studied by Peteves et al [5] under OP and $R = -\infty$ condition. The results from their work are compared with the results presented later in this paper.

Material and Experiments

Material and Test Piece Geometry

CM186 SX is a highly alloyed cast superalloy with 3% Re and 70% volume fraction of the coherent γ' precipitate strengthening phase. The nominal chemical composition of the alloy is shown in Table 1.

TABLE 1—Nominal chemical composition of CM186 Superalloy (in wt. %).

Co	W	Al	Cr	Ta	Re	Hf	Ti	C	Mo	Ni
9.25	8.5	5.7	6	3.4	3	1.4	0.7	0.07	0.5	Bal

The material was cast to the shape of the test piece, with the longitudinal axis intended to be the [001] crystallographic orientation. A two-stage aging heat treatment process was applied. In the first stage, the cast test piece was vacuum heated at 1080°C for 4 h. The second stage was 20 h at 870°C. In both stages, rapid gas fan quenching in high purity argon followed heating. The external surface of the cast test piece was then machined and polished. The inner wall of the test piece was honed. This was to avoid crack initiation at machining scratches and casting defects at the bore surface. Button-end hollow test pieces with gauge length of 15 mm and nominal wall thickness of 0.75 mm were used. The dimensions are shown in Fig. 1. After testing, it was found that the wall thickness was non-uniform, and the steps taken to understand and ameliorate this effect are described later in this paper.

Coated and uncoated test pieces were used in this work. The coating used was a modified aluminide coating, Sermalloy 1515[®]. The Al/Si coating was applied as sprayed slurry on the gauge section of the test piece, followed by a diffusion process at about 870°C. The process (spraying and heat treatment) was repeated three times, resulting in three layers of coating with an approximate total thickness of 80 μm . No coating was applied to the bore surface or other areas of the test piece. The crystallographic orientation of the test pieces was within 6.5° deviation from the nominal [001] direction.

Experimental Equipment

TMF tests were performed using an Instron 100kN closed loop electromechanical testing machine at DERA, Farnborough. Strain was measured using a high temperature side-contacting axial extensometer with gauge length of 12.5 mm. A 10 kW solid-state high frequency induction heater provided heating. Cooling of the test piece was achieved by passing compressed air through the middle of the test piece and also by conduction through water-cooled hydraulic grips at both ends. A single color pyrometer with spot size of 0.35 mm diameter and temperature range between 200°C and 1200°C was used to control the temperature. The pyrometer was connected to a Eurotherm 900EPC controller, which received command signals from the test machine controller. A 2-color pyrometer with a spot size of 7 mm diameter and temperature range between 600°C and 1600°C, was used to monitor the temperature of the test piece and was independent from the control system. An R-type thermocouple was spot-welded outside the gauge section for over-temperature monitoring purposes.

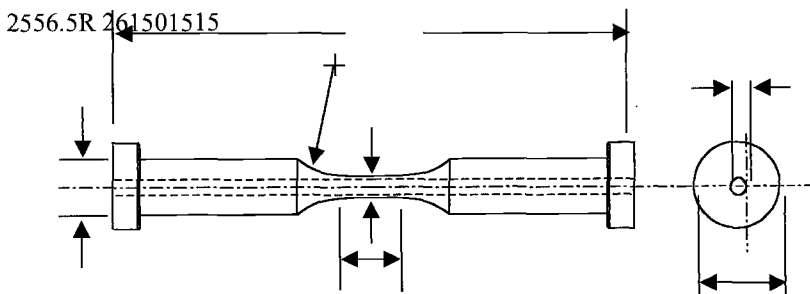


FIG. 1—TMF Test Piece Geometry (All dimensions in mm).

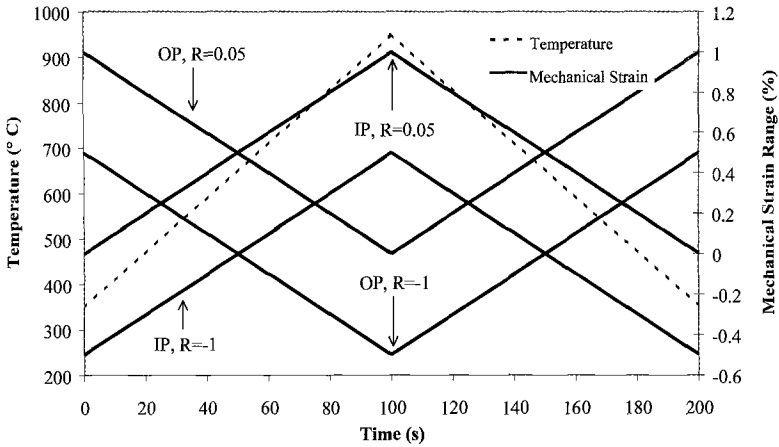


FIG. 2—Applied variations of temperature and mechanical strain with time.

TMF Cycle

Basic In-phase (IP) and Out-of-phase (OP) TMF cycles were used in this work. The same temperature cycle was used in all IP and OP cycle tests. Linear heating and cooling rates of $6^{\circ}\text{C}/\text{s}$ were applied between 350 to 950°C , which gave rise to a cycle period of 200 s. Triangular strain cycles were applied with R-ratio (mechanical strain ratio) of -1 and 0.05 . Total mechanical strain ranges applied were 0.5 , 0.6 , 0.8 , and 1.0% . Different TMF conditions are illustrated in Fig. 2 for a mechanical strain range of 1.0% as an example.

Experimental Procedure

Before the start of this series of tests, an alignment check was carried out on the test machine using a strain-gauged test piece and any misalignment of the load train was corrected. Then, at room temperature, each test piece was cycled between $\pm 0.5\text{kN}$ and the axial strain measured at different locations around the test piece. The value of “local” axial strain at any location was recorded directly and the recorded value of load was divided by the average cross section area of the test piece to obtain “average” stress. The “local stiffness” was obtained from the values of “average stress” and “local” strain measured.

Since the accuracy of measurement from the pyrometer was affected by the stability and condition of the test piece's surface (both coated and uncoated), the test piece was preoxidized at 950°C before the actual test, to allow a layer of stabilized oxide to build up on the surface. Initial investigations revealed that there was a spatial variation of the surface temperature of the test pieces. As part of the procedures to account for temperature variation around the test piece due to nonuniform wall thickness, the temperature around the test piece at the gauge section was recorded. This was examined in more detail by heating the test piece to 950°C , and then the temperature measured at 30° intervals around the test piece. Typically, a sinusoidal variation was obtained, which was later found to be correlating with the wall thickness. The maximum variation in

temperature depends on the variation of the wall thickness. It was decided to control the temperature at an "average" location. This was defined as the location where the mean value $\left(\frac{T_{\max} + T_{\min}}{2}\right)$ of the temperature variation was measured, where T_{\max} and T_{\min} were the measured maximum and minimum temperatures, respectively, around the test piece. For the strain measurements, the extensometer was set up to measure "average" local axial strain. By adopting this method, the temperature and strain was set to be controlled and measured at a location having an intermediate wall thickness, with the results intended to represent the "average" response of the material.

For the test program each test piece was cycled first with the desired temperature cycle under zero load control. The thermal strain was recorded and the TMF software was used to transfer the thermal strain recorded into a set of polynomial parameters. The parameters were then transferred to the computer's memory. During the TMF test, the total strain was measured and the instantaneous thermal strain calculated and subtracted by the computer. Consequently, the correct mechanical strain was applied to each test piece. Each test piece was also cycled thermally under zero strain for six cycles followed by the actual TMF loading. This was to allow thermal equilibrium to be reached before the mechanical loading was applied.

Tests were stopped when there was a stress drop from a stabilized value of 50% or sometimes when the test piece fractured. Tests that completed 3000 cycles with no sign of failing were also stopped. Test conditions for all the TMF tests conducted are shown in Table 2. Also shown in Table 2 are the number of cycles to crack initiation (N_i) and number of cycles to failure (N_f). N_i and N_f were defined as the number of cycles when there was a 2% and 50% stress change from the stabilized maximum stress, respectively.

TABLE 2—*Test Matrix of CMI 86SX<001> TMF tests.*

Test No.	Mis-Orientation, θ , °	TMF Cycle	$\Delta\varepsilon_{\text{mech}}$, %	R	Coating	N_i ($0.98\sigma_{\max}$)	N_f ($0.5\sigma_{\max}$)
1	4.2	OP	0.5	-1	Yes	3000*	3000*
2	6.5	OP	0.6	-1	Yes	2238	2516
3	4.8	OP	0.8	-1	Yes	423	508
4	6.5	OP	0.6	0.05	Yes	423	441
5	1.7	OP	0.8	0.05	Yes	282	282
6	3.0	OP	0.8	-1	No	1374	1469
7	2.1	IP	0.8	0.05	Yes	3000*	3000*
8	1.6	IP	0.8	-1	Yes	895	895
9	0.8	IP	1.0	-1	Yes	278	567

*Unfailed tests

Metallographic Examination

Fracture surfaces of the failed test pieces were analyzed using a scanning electron microscope (SEM). Transverse sections of the samples were obtained from the failed test pieces and mounted using cold-setting epoxy resin. Samples were polished down to 1 μm and then examined using an optical microscope.

Experimental Results

Variation in Wall Thickness, Temperature, and Stiffness

During the experimental set-up, it was found that the stiffness and temperature varied as a function of angular position around the test piece. Examples of the variation of temperature and local stiffness with wall thickness are shown in Fig. 3a and b, respectively. Post test examination of test pieces' cross sections revealed that the wall thickness within the gauge length was not uniform. The design specification required a wall thickness of 0.75 mm. The average coating thickness for coated test pieces was about 80 μm . However, the average results of all the test pieces showed that the variation in wall thickness was from 0.59–1 mm for coated test pieces and 0.5–0.96 mm for the uncoated test piece. This represented a variation from the design value of 0.75 mm of about -21% and +33% for coated test pieces and -33% and +28% for the uncoated test piece.

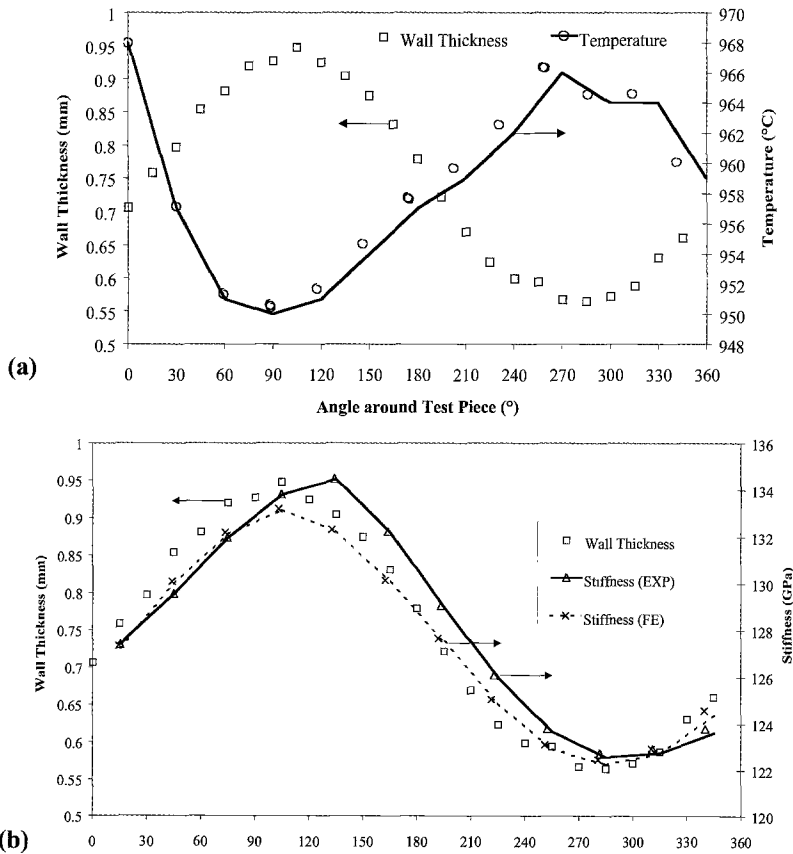


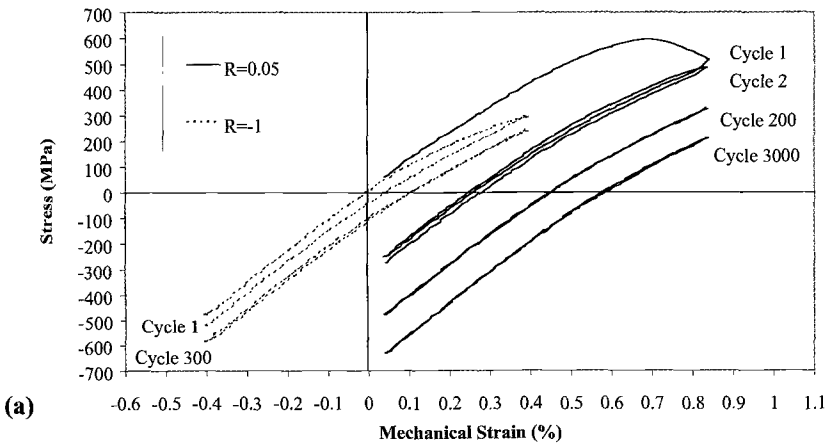
FIG. 3—*a) Variation of temperature with wall thickness; b) Variation of stiffness with wall thickness.*

Figure 3 shows the variation in wall thickness for one test piece where the minimum and maximum wall thickness were 0.56 and 0.95 mm, respectively. It can be seen in Fig. 3a that the minimum temperature coincides with the maximum wall thickness. Conversely, the maximum temperature occurred at the minimum wall thickness. The variation in the measured local stiffness shown in Fig. 3b corresponds also to the change in wall thickness. Investigation on all the test pieces revealed that highest variation for local stiffness at room temperature and temperature (controlled at 950°C) was 26GPa and 30°C, respectively.

Experimental TMF Stress-strain Response

Typical hysteresis loops from coated test pieces subjected to IP and OP cycles are shown in Fig. 4a and b, respectively. It is shown that in both cases, most of the inelastic strain was accumulated in the first cycle. Apart from the first cycle, very narrow loops were obtained in the following cycles. This is one of the main thermomechanical characteristics of this material. Different shapes of loops were found in IP and OP tests, mainly caused by changes in stiffness with temperature. Similar loops were found for coated and uncoated test pieces tested in identical conditions. This indicates that the coating had only a small effect on the load bearing capacity of the test pieces. However, generally higher stiffness was found for coated test pieces compared to uncoated test pieces.

The evolution of maximum and minimum stresses during TMF tests was influenced by the loading condition at the high temperature part of the cycle. Typical results are shown in Fig. 5. In IP cycles, relaxation of the maximum and minimum stress occurred at high temperatures due to creep deformation and caused the mean stress to become more negative. In OP cycles, these effects were less evident with very little relaxation of the peak and mean stress prior to crack initiation.



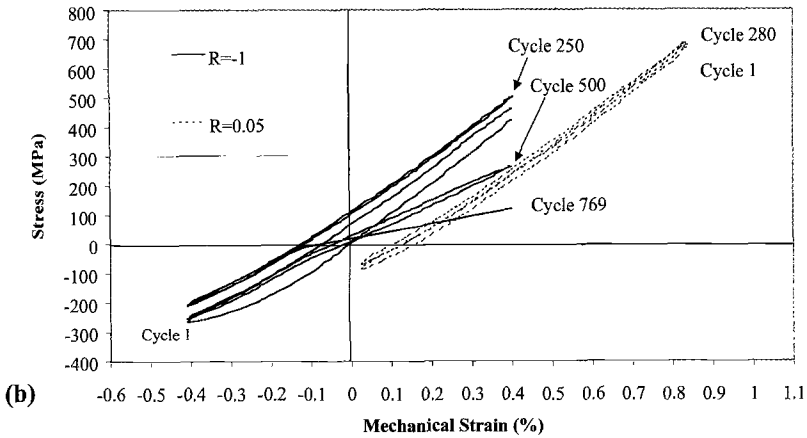


FIG. 4—*a)* Experimental hysteresis loops for IP tests, coated and $\Delta\epsilon_{mech} = 0.80\%$; *b)* Experimental hysteresis loops for OP tests, coated and $\Delta\epsilon_{mech} = 0.80\%$.

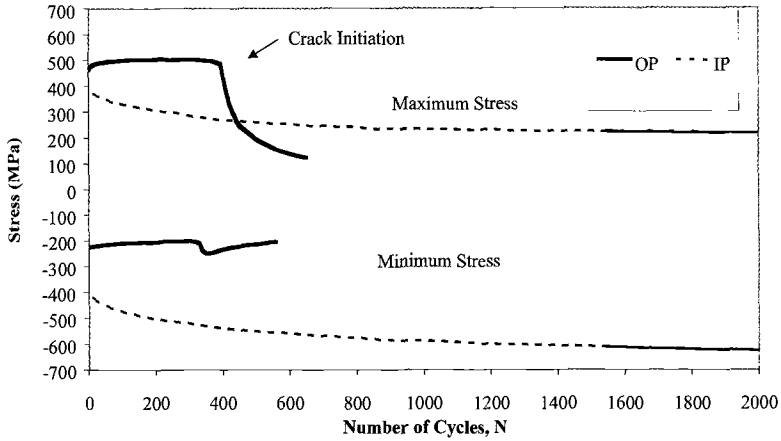


FIG. 5—Evolution of maximum and minimum stress for coated test pieces under OP ($R = -1$) and IP cycles ($R = 0.05$), $\Delta\epsilon_{mech} = 0.8\%$.

TMF Lives

The TMF lives for different tests are summarized in Fig. 6. The results show that the OP cycle was more damaging than the IP cycle for both R-ratios (0.05 and -1). R = 0.05 was found to be more damaging than R = -1 in OP tests. This was the reverse for IP tests. In OP tests, a reduction of the mechanical strain range from 0.80% to 0.60% in an R

= 0.05 test resulted in an increase of life of about 50%, while an increase of five times was achieved in the case of $R = -1$ tests for the same reduction in strain range. In IP conditions, $R = -1$ tests were found to be more damaging than $R = 0.05$. For an applied strain range of 0.80%, the $R = 0.05$ test was found to last at least three times longer than $R = -1$ test. The presence of the coating appeared to reduce the TMF life by about three times when compared with a similar uncoated test piece tested in the OP condition, $R = -1$ and with a mechanical strain range of 0.80%.

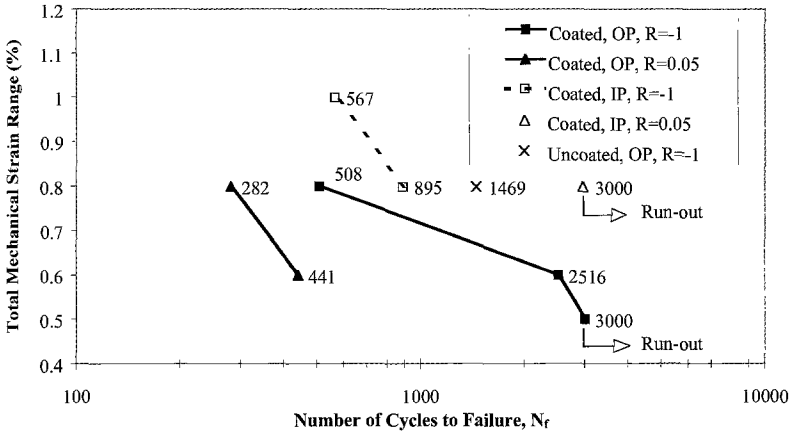


FIG. 6—Experimental TMF lives for CM186SX<001>.

Metallographic Observations

SEM fractography and optical metallography were performed on specimens prepared from tested TMF test pieces. SEM analyses of the fracture surfaces revealed multiple crack initiation sites on all samples. Different crack initiation mechanisms were identified, generally regarded as “line initiation” for the coated material and “point initiation” for the uncoated material [2]. Crack initiation from sub-surface pores was also observed.

For the uncoated test piece, multiple crack initiation sites were observed and were invariably associated with “point initiation” from broken oxide hillocks on heavily oxidized surfaces, especially on the bore surface. These features are shown in Fig. 7a. Crack initiation occurred also from subsurface casting pores near both the inner and outer surfaces of the uncoated test piece. However, it is not clear which of these mechanisms led to final failure of the uncoated test piece. The presence of a casting pore on a fracture surface is shown in Fig. 7b. In coated test pieces, parallel transverse cracks perpendicular to the loading axis were observed on the outer surface of the test piece. This is regarded as “line initiation.” The coating cracked at low strain in a brittle manner at temperatures below its DBTT, which is thought to be around 600°C [6].

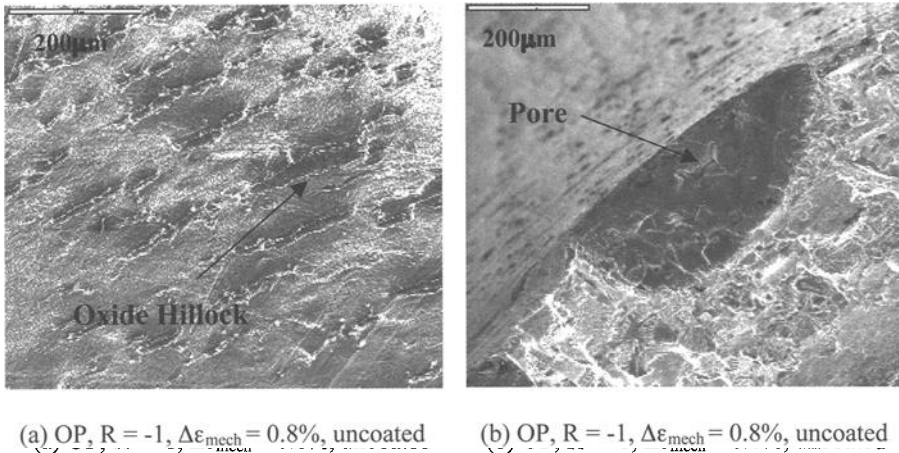


FIG. 7—*a) SEM micrograph showing oxide hillocks on heavily oxidised bore surface of uncoated test piece; b) SEM micrograph showing crack initiation site at subsurface casting pore of uncoated test piece.*

Finite Element Simulations

Finite element (FE) analyses on 3-dimensional (3-D) models of the hollow TMF test piece were performed to investigate the effects caused by the nonuniform wall thickness. Hollow test piece models were created using the dimensions of several experimental test pieces described earlier. The external dimensions of the piece were the same as shown in Fig. 1. The objective was to create a 3-D model with the same wall thickness variation as observed in the experiments. A typical wall thickness variation is shown in Fig. 3*b*.

To create the model, a 3-D geometric model was created using AutoCAD 2000. The model was then imported into ABAQUS/CAE, where mesh creation was performed. 3-D solid elements, of type C3D20R were used throughout the model. Elements with reduced integration were used to reduce computational times. Fifteen elements were created along the gauge section and 24 elements around the test piece in the gauge section, with two layers of elements through the cross section. A total of 10296 nodes and 1824 elements were used in the complete model. In addition to the 3-D model of the test-piece, an analysis using a 3-D single element was also carried out.

The material model in the FE analysis included anisotropic elasticity together with a single crystal creep model in a UMAT subroutine. The details of the material models are described elsewhere [9,10]. No details of the coating were included in the analysis. Also, no effect of crystallographic mis-orientation was included in the FE analysis.

Boundary and Loading Conditions

For the 3-D test piece model a local cylindrical coordinate system was defined for all the nodes on the base of one end of the test piece. All these nodes were constrained in the hoop and axial directions. To apply loading on the test piece, uniform displacement was applied to all the nodes on the surface of the other end of the test piece in the uniaxial direction Z .

As the average stress on the test piece was required for direct comparison with experimental results, a cross section was defined at the middle of the gauge section. The total area and force on the section were used to compute the average stress acting on the test piece. To obtain the local strain, two nodes along the gauge were identified. The original distance between the two nodes was 12.5 mm and equal to the gauge length used in the experiments. The strains at different angular positions on the model were determined by using nodes at the corresponding positions.

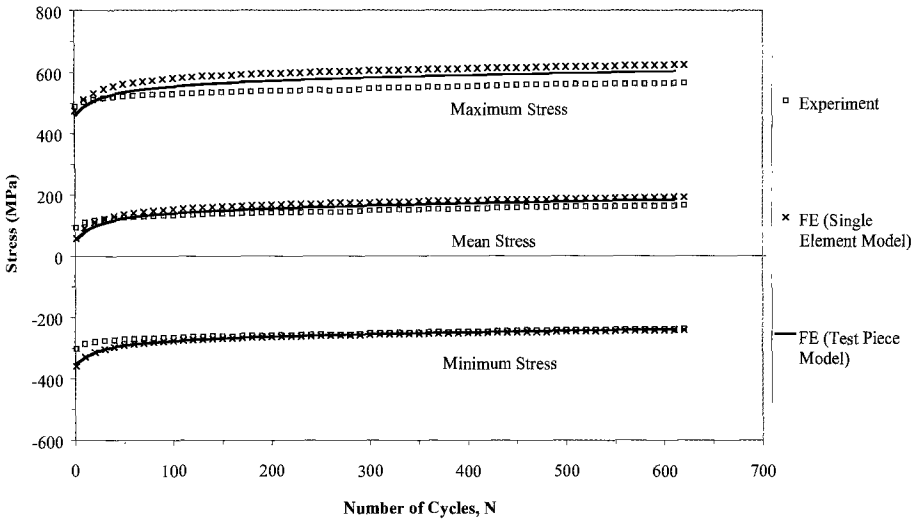
To simulate the thermal cycle for TMF conditions on the 3-D model the temperature at all nodes was set to 350 C in the first step and then 950 C in the next step. The total time for each step was 100 s. In the first cycle, remote displacement values were determined by trial and error so that the local strain, equivalent to that controlled in the experiments, was equal to experimental values. For subsequent cycles the remote displacements were adjusted to match the required local strain control.

To investigate the effect of nonuniform thickness on the TMF results, the same analysis was repeated by controlling the strain at other locations with different wall thickness.

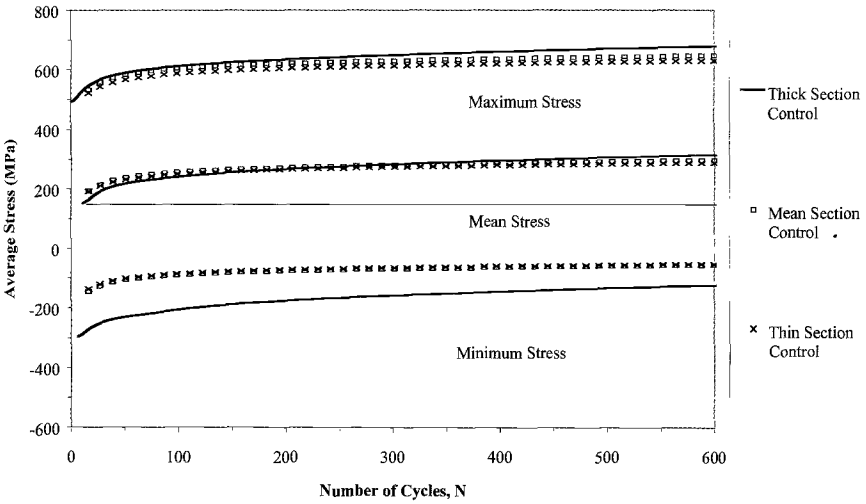
Results

Results of 3-D FE analysis of the test piece model were obtained in such a way to allow direct comparison with experimental data [9] and FE results of the single element model represents pure material response predicted by the material model. Figure 3*b* shows the variation of the local elastic stiffness with angular position around the test piece, together with the variation of wall thickness. The results show that the specimen experienced greater stiffness at positions when the wall thickness was largest, and the results agree very well with the experiments.

Typical results from the TMF simulations are shown in Fig. 8. Figure 8*a* shows the experimental and FE results of the variation of stresses with number of cycles. Here, the local strain was controlled at the position of the mean wall thickness. The results show good agreement between FE and experimental data, especially at high temperatures. Good agreement between FE results from the single element model and the test piece model suggests that the mechanical response measured in the experiments were representative of the material response or at least within the practical experimental scatter or prediction uncertainty.



(a)



(b)

FIG. 8—*a*) FE and experimental variation of stresses with number of cycles (OP, $R = -1$, $\Delta\epsilon_{mech} = 0.8\%$); *b*) FE and experimental variation of stresses with number of cycles (OP, $R = -1$, $\Delta\epsilon_{mech} = 0.8\%$).

Figure 8b shows the FE results from three separate analyses on the same test piece model. Each analysis was performed by simulating the TMF test with strain controlled at different locations around the test piece. The locations corresponded to the mean (as in the case of the experiment) smallest and largest wall thickness. The thickness at each location was 0.78, 0.49, and 0.96 mm, respectively. Both experimental and FE results in Fig. 3b show that a stiffer mechanical response was obtained at a location with the largest wall thickness. The same is observed in Fig. 8b, where a higher stress response was obtained when the strain was controlled at the location of greatest thickness. However, the results show that there is very little difference between the three sets of simulations for minimum stress and the difference is more significant for maximum stress.

Discussion

Influence of Coating, R-ratio, and Cycle Type on TMF Lives

It was thought the the reduction in TMF lives in coated test pieces when compared to uncoated test pieces was caused by the premature cracking of the coating. This induced cracking would then cause crack initiation into the substrate in the early part of the TMF lives. The results showed that for both R-ratios investigated, the effect was more significant in the case of OP tests compared with IP tests. As the coating has a very low fracture strain at low temperatures, premature brittle cracking of the coating was expected in OP tests, since the material was subjected to maximum tension at low temperatures. A smaller effect was expected in IP tests.

The premature cracking of the coating during the early part of the test not only exposed the substrate to the environment and allowed oxidation, it also acted as a crack initiation site for cyclic crack propagation. Affeldt [3] reported that this occurred in the first cycle for high strain tests. However, it was observed in the present tests that the cracks did not extend into the substrate in the first cycle, since the fracture surface revealed heavily oxidized coating-substrate interfaces, which is illustrated in Fig. 8a. This suggests there was long exposure of the interface to the environment, indicating that the coating cracked very early during the test and only extended to the substrate after a considerable amount of time [7]. Figure 9a also shows regions indicating a feature of classical fatigue crack growth, which propagates to the substrate from the coating-substrate interface.

The overall picture is that the coating cracks at the early part of the test, but usually stops at the coating-substrate interface and allows oxidation to take place. After a considerable amount of oxidation, cracks start to extend into the substrate through “line” crack fronts via classical cyclic crack propagation. The early part of the TMF life is therefore strongly influenced by oxidation, followed by the TMF induced crack propagation at a later stage.

Irrespective of the dominant mechanism leading to failure, crack initiation also occurred from the uncoated bore surface in all tests. This mechanism was more evident in tests subjected to small strain ranges and hence longer lives. This is because the material was exposed to the environment for longer periods, allowing more severe surface oxidation on the uncoated inside surface to take place. In the case of all tensile cyclic tests ($R = 0.05$), it was observed that the crack initiation from sub-surface pores became more evident.

Casting of the hollow test pieces produced nonuniform wall thickness. As illustrated in Fig. 3, this feature influenced the local temperature and stiffness of the test pieces. The variation in wall thickness caused nonuniform deformation (and hence stresses) across the section. As might be expected initiation of failure occurred at the thinnest section of the wall in all test pieces. An example is shown in Fig. 9b. Final failure usually occurred in the thicker section of the wall thickness. Consequently, although the test pieces had nonuniform wall thickness, this variation is not expected to have a significant influence on the test variability. This is because failure initiated at the thinnest section and strain was controlled at a location corresponding to the mean wall thickness. Nevertheless, further work using finite element analysis is being undertaken to assess the implications of the nonuniform wall thickness on TMF failure.

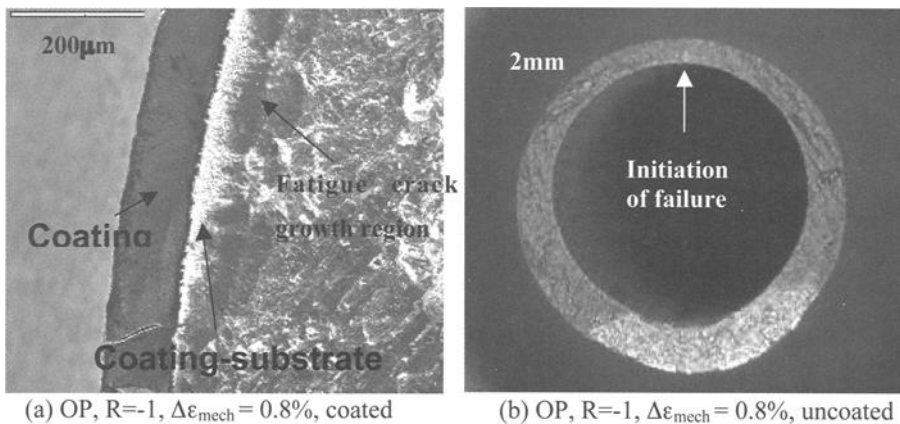


FIG. 9—*a) SEM micrograph showing the coating, heavily oxidised coating-substrate interface and flat region of fatigue propagation area; b) Photography showing cross section of failed TMF test piece.*

Variation of Wall Thickness

The FE results have demonstrated that, despite the significant variation observed in measured elastic stiffness at locations with different wall thickness, the experimental material data obtained with the special experimental procedures employed was within acceptable experimental scatter. The good agreement between FE and experimental results suggests that the mechanical response measured in the experiments were representative of the material response. The FE results also demonstrated that the special experimental procedures employed were able to measure acceptable data despite the variations observed in the measured elastic stiffness.

In industry, the difficulty in casting hollow components with precise wall thickness is already well known. The benefit of using cast hollow test pieces compared to machined hollow samples is that the inner wall of the hollow cast specimen better represents the surface conditions of actual engine components. Using as-cast samples provides more realistic material data. Furthermore, the FE results form a basis for

determining suitable tolerances for variations in wall thickness for this type of test piece. This is because it is economically impractical to manufacture and reproduce cast components with a precise wall thickness.

Comparison with Other Data

The results for the thin wall test pieces subjected to TMF were compared with earlier test results from the Joint Research Centre (JRC) in Petten, Netherland [5] on the same coating-substrate system, but using different test piece geometry. The test piece used by JRC was a solid rectangular cross section of 12 mm \times 3 mm. The TMF lives from the JRC study for OP, R = $-\infty$ test are compared with OP, R = -1 hollow cylinder tests in Fig. 10. The results suggested that R = $-\infty$ tests was the least damaging among all R-ratios (0.05, -1, $-\infty$) investigated. However, there may also be an influence of test piece geometry. JRC also recorded the early crack initiation life of the test pieces. This corresponded to surface crack lengths of 30 μ m. In contrast, initiation of failure in the thin wall test pieces corresponded to a stress reduction of 2%. Although different R-ratios were used, the results show that initiation occurs early on in life for OP loading irrespective of geometry and R-ratio. Subsequent crack growth in the hollow test pieces was then dependent on the local stress and strain state. This arises because the wall thickness was nonuniform. Nevertheless, it was reasonable to expect the failure lives of the tests at DERA to be shorter than that of the tests from JRC because of the complicated stress state.

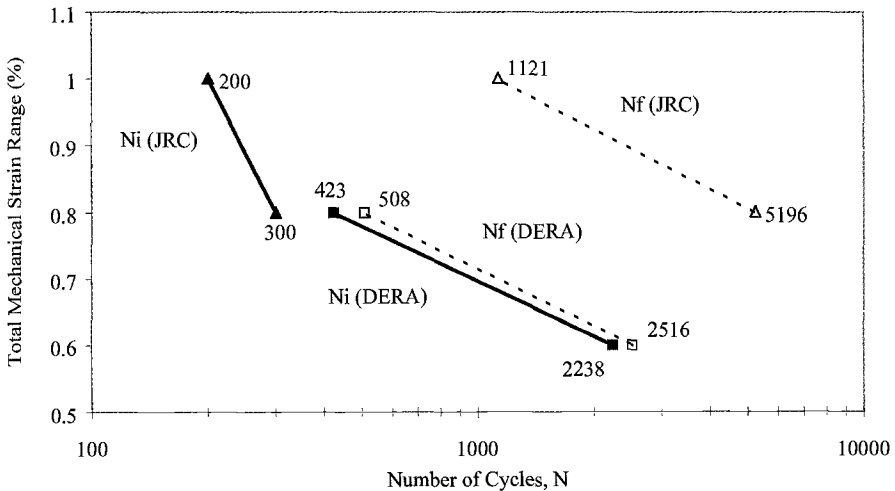


FIG. 10—TMF lives for coated CM186SX<001> tested with OP cycles.

Conclusion

Strain-controlled TMF tests have been performed on single crystal nickel-base superalloy, CM186 SX <001> in coated and uncoated conditions. IP and OP cycles with $R = -1$ and $R = 0.05$ were applied at different mechanical strain ranges. A procedure was developed to detect and ameliorate the effect of nonuniform wall thickness on the temperature and local stiffness of the test pieces. The beneficial effect of this procedure was later confirmed by good comparison between the experimental data and FE analysis results. Brittle cracking of the coating at low temperatures occurred very early during the tests and was found to be detrimental to the TMF lives for OP cycles. Different deformation mechanisms occurred when different TMF conditions were applied due to the changes in ductility of the coating with temperatures. Comparison with earlier work on the same material also demonstrated the effect of test piece geometry on the TMF lives.

Acknowledgment

The authors would like to acknowledge the Defence and Evaluation Research Agency (DERA), now Qinetiq, Farnborough, UK for providing the TMF facilities, and in particular Dr. Peter Johnson for his help and guidance on conducting the TMF tests. Dr Kong expresses his thanks to ALSTOM Power for financial support during his Ph.D. studies.

References

- [1] McColvin, G. M., Sutton, J., Whitehurst, M., Fleck, D. G., Van Vranken, T. A., Harris, K., Erickson, G. L., and Wahl, J. B., "Application of the Second Generation DS Superalloy CM186LC to First Stage Turbine Blading in EGT Industrial Gas Turbines," *IOM 4th International Charles Parsons Turbine Conference Proceedings*, Newcastle Upon Tyne, UK, November 4–6, 1997.
- [2] Martinez-Esnaola, J. M., Arana, M., Bressers, J., Timm, J., Martin-Meizoso, A., Bennett, A., and Affeldt, E. E., "Crack Initiation in an Aluminide Coated Single Crystal During Thermomechanical Fatigue," *Thermomechanical Fatigue Behavior of Materials: Second Volume, ASTM STP1263*, Michael J. Verrilli and Micheal G. Castelli, Eds., ASTM International, West Conshohocken, PA, 1996, pp. 68–81.
- [3] Affeldt, E. E., "Influence of an Aluminide Coating on the TMF Life of a Single Crystal Nickel-base Superalloy," presented at the International Gas Turbine and Aeroengine Congress and Exhibition, Stockholm, Sweden, 2–5 June, 1998.
- [4] Bressers, J., Timm, J., Williams, S., Bennett, A., and Affeldt, E., "Effects of Cycle Type and Coating on the TMF Lives of a Single Crystal Nickel Based Gas Turbine Blade Alloy," *Thermomechanical Fatigue Behavior of Materials: Second Volume, ASTM STP 1263*, Michael J. Verrilli and Michael G. Castelli, Eds., ASTM International, West Conshohocken, PA, 1996, pp. 56–67.
- [5] Peteves, S. D., De Haan, F., Timm, J., Bressers, J., Hughes, P. M., Moss, S. J., Johnson, P., and Henderson, M., "Effect of Coating on the TMF Lives of Single Crystal and Columnar Grained CM186 Blade Alloy," *Superalloys 2000*, Pollock, T. M., Kissinger, R. D., Bowman, R. R., Green, K. A., McLean, M., Olson, S. and Schirra, J. J., 2000, pp. 665–663.
- [6] Zhang, D., "Effect of Ductile-Brittle Transition Temperature of Al-Si Coating on Fatigue Properties of Ni-Base Superalloys," *ACTA METALLURGICA SINICA*

- (*ENGLISH EDITION*) Series A, Vol. 3, No. 6, Nov. 1990, pp. 435–438.
- [7] Zhang, Y. H., Knowles, D. M., and Withers, P. J., "Micromechanics of Failure of Aluminide Coated Single Crystal Ni Superalloy under Thermomechanical Fatigue," *Scripta Materialia*, Vol. 37, No. 6, 1997, pp. 815–820.
- [8] Zhang, Y. H., Withers, P. J., Fox, M. D., and Knowles D. M., "Damage Mechanisms of Coated Systems under Thermomechanical Fatigue," *Materials Science and Technology*, Vol. 15, September 1999, pp. 1031–1036.
- [9] Kong, C. N., "High Temperature Mechanical Behaviour of Single Crystal Nickel-Base Superalloys," *Ph.D. Thesis*, University of Bristol, United Kingdom, September 2002.
- [10] White, P. S. and Kong, C. N., "Modelling of High Temperature TMF Tests of Single Crystals by a Pure Creep Law," *Materials for Advanced Power Engineering*, Proceedings of the 7th Liège Conference, 30th Sept-2nd Oct 2002, Liège, Belgium.

Thermomechanical Fatigue Behavior of Stainless Steel Grades for Automotive Exhaust Manifold Applications

REFERENCE: Santacreu, P. O., Simon, C., and Coleman, A., "Thermomechanical Fatigue Behavior of Stainless Steel Grades for Automotive Exhaust Manifold Applications," *Thermomechanical Fatigue Behavior of Materials: 4th Volume, ASTM STP 1428*, M. A. McGaw, S. Kalluri, J. Bressers, and S. D. Peteves, Eds., ASTM International, West Conshohocken, PA, 2002, Online, Available: www.astm.org/S/STP/1428/1428_10585, 16 Dec. 2002.

ABSTRACT: This paper describes a study performed on the thermomechanical fatigue behavior of stainless steel grades for exhaust systems, especially for exhaust manifolds. A testing rig has been developed to characterize the thermomechanical fatigue resistance of bent stainless steel sheets. In particular, the behaviors of ferritic and austenitic stainless steels are compared. After the identification of the elasto-viscoplastic constitutive law of the materials, the numerical simulation of the test is performed, enabling the computation of the viscoplastic strain accumulated during each cycle. Examination of the failed specimens indicated that cracks could be mainly attributed to out-of-phase thermomechanical fatigue in the case of ferritic grades and to in-phase thermomechanical fatigue in the case of austenitic grades. A Taira type damage criterion is proposed, which correlates the amplitude of the viscoplastic strain and the number of cycles to failure. But due to a coupling with oxidation and creep during in-phase thermomechanical fatigue, the phasing between the thermal and the mechanical loads has to be taken into account in the criteria. The hydrostatic pressure at maximum temperature is proposed as such a phasing factor.

KEYWORDS: thermomechanical fatigue, stainless steel, exhaust, damage, life prediction

Nomenclature

T	Temperature
$\underline{\sigma}$	Stress tensor
$\underline{\varepsilon}$	Strain tensor, e , th and vp subscripts for elastic, thermal, viscoplastic
f, k	Yield function and yield limit
α, X	Kinematic hardening variables
C, D	Kinematic hardening parameters (Chaboche law)
n, K	Viscoplastic parameters (Norton law)
N_f	Number of cycles to failure
ε^{vp}	Equivalent viscoplastic strain
$\Delta\varepsilon^{vp}$	Equivalent viscoplastic strain amplitude during a stabilized cycle

¹ Research Engineers, Automotive Steel Solutions Design Center, Usinor Research and Development, Ugine&Alz, BP15-62330 Isbergues, France.

² Automotive Development Engineer, J&L Specialty Steel, Inc, 18915 West 12 Mile Road, Lathrup Village, MI 48076.

Introduction

Stainless steel grades are now widely used for exhaust applications like muffler, catalytic converters, pipes, or manifolds. This evolution is driven by the need to increase the durability of the exhaust parts, which are subjected to more severe conditions as a consequence of the effort to decrease automotive pollutant emissions. In this framework, high temperature stainless steel grades were developed to provide high temperature mechanical properties and better oxidation resistance especially for the hot end of the exhaust system. Today, exhaust suppliers test manifolds on engine dynamometers under severe thermal cyclic loads at high temperatures. The exhaust gas temperature can be as high as 950°C and in the future it will probably reach around 1050°C, especially for the gasoline engine. The test conditions are generally specified by the automakers, so different cycles can be observed including short to long dwell time at high temperature. The cycle duration is around 10 min. with dwell time of around 5 min. Different types of cooling processes are also used: natural convection, pulsed air or water-cooling. An exhaust manifold has to pass approximately 1500 cycles to be considered validated for production. Figure 1 shows an example of a ferritic stainless steel exhaust manifold.

In an effort to reduce cost and development time, simulation tools have to be proposed for the fatigue design of such a component including a mechanical behavior model and a damage model under non-isothermal mechanical loads. The general procedure for the lifetime prediction of an exhaust manifold under thermomechanical fatigue is summarized on Fig. 2. Finally, the main improvements of the approach are now:

- Meshing rules for singular area (weld seam, small curvature area)
- Take account of the forming process inducing thinning or residual stresses
- An accurate temperature distribution by a 3D flow-thermal simulation
- Provide models and data for both behavior and damage analysis
- Validation of the approach by comparing experimental and FEA results.

The present paper is focused on the behavior and damage models, and the simulation of the thermomechanical fatigue process of the stainless steels.

Thermal Fatigue Test

Tested Materials

The materials studied are stainless steel grades commonly used for exhaust manifold application in the form of bent and hydroformed tubes or deep-drawn sheets. The considered thickness for exhaust applications is often below 2 mm. Standard designation and chemical compositions of the tested materials are listed in Table 1.



FIG. 1 — A 4-cylinders ferritic stainless steel exhaust manifold (Courtesy of Benteler).

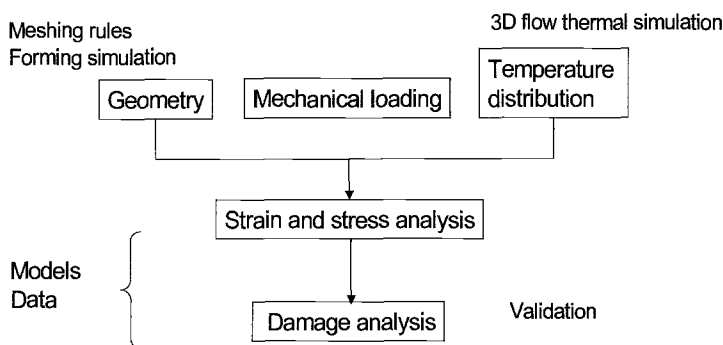


FIG. 2—General procedure for lifetime prediction on an exhaust manifold under thermomechanical fatigue.

TABLE 1 — Typical chemical composition of the tested materials in weight percent.

Grades	Cr	Ni	Si	Mn	C	Others
Ferritic Grades						
AISI409	11.5		0.5	0.3	0.02	Ti
AISI441	17.8		0.5	0.5	0.02	Ti+Nb
Austenitic Grades						
AISI304	18.2	8.7	0.5	1.5	0.04	
AISI321	17.5	9.2	0.5	1.3	0.03	Ti
Austenitic Refractory Grades						
AISI308S	19.8	12.7	2.0	1.7	0.04	

Ferritic grades have low ultimate tensile strength at temperatures above 800°C but good cyclic oxidation properties and a low thermal expansion coefficient compared to those of austenitic grades. So stresses induced by a thermal cycle in ferritic grades are of a lower level than those induced in austenitic grades. Antoni et al. presented in [1] a comparison between the cyclic oxidation properties of stainless steels and observed an important scaling of the austenitic grades like AISI 304 and 321. Also, it is well known that the creep properties of ferritic grades can be improved significantly by adding niobium as in the AISI441 grade. In the austenitic refractory grades, the sigma-phase precipitation in this temperature range can lead to an embrittlement of the metal at room temperature.

Experimental Procedure

A special test has been developed to determine the thermomechanical fatigue (TMF) resistance of steel sheet specimens. The testing rig and the experimental procedure are described in [2] and [3]. This test permits the imposition of a thermal cycle on a clamped V-shaped specimen by alternate resistance heating and air-cooling (Fig. 3). It has also been adapted to the case of welded specimen [4]. Specimens are constrained at each end, which causes strain-stress response. Specimens are taken from sheets of thickness between 1 and 2 mm. Constraining force at cold temperature, temperature, and the number of cycles are recorded during the test.

The TMF life of a specimen is expressed as the number of cycles to failure determined conventionally as the time after which a 50% decrease of the constraining

force has occurred. For a given grade, the fatigue life depends on the maximum and minimum temperature of the cycle, dwell time at the maximum temperature and the specimen thickness. The fatigue life is the mean value of three tests and standard deviation is below 10% (duration of one test is around 3 weeks). The advantage of this test is that it is both simple for classifying the TMF resistance of the stainless steel grades and representative of the TMF process occurring in exhaust manifolds, while focusing on a study of the damage mechanisms.

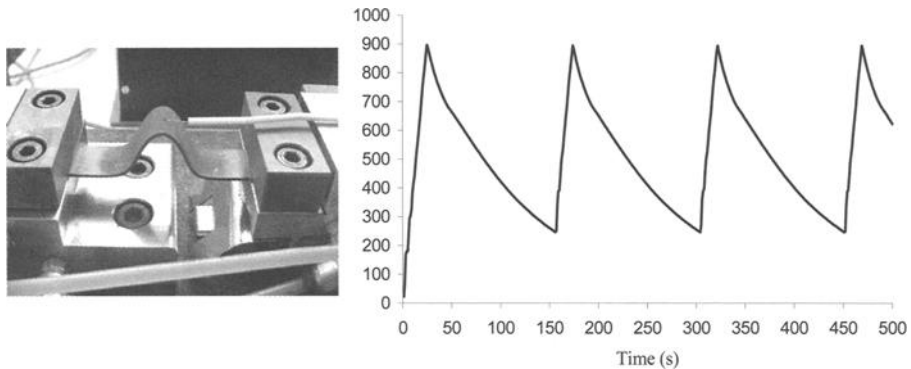


FIG. 3—Principle of the TMF fatigue test developed and typical thermal cycles imposed on thin sheet specimens.

Experimental Results

Figure 4 presents results in the case of 2 mm thick specimen loaded from 250°C to 900°C and for different dwell times from 0–180 s at the maximum temperature. Classical austenitic grades (AISI 304 or 321) exhibit poor thermomechanical fatigue resistance compared to the ferritic grades (AISI 409 or 441) or high-chromium refractory grades (AISI 308S). In fact, the AISI 441 ferritic grade offers the best thermomechanical fatigue resistance, even compared to the AISI 308S refractory grade, which can be more sensitive to the detrimental effect of the dwell time at the maximum temperature (Fig. 4). Oku et al. investigated in [5] the TMF resistance of ferritic stainless steels and found the same difference between ferritic and austenitic grades. In fact, microstructural observations performed on our specimens showed that the fatigue crack propagation occurs at intrados of the specimen (concave side) in the case of ferritic grades and at extrados of the specimen (convex side) in the case of austenitic grades.

The difference between the thermal expansion coefficients of ferritic grade and those of austenitic grades is not sufficient to explain the difference between the TMF lives and crack locations. The coupling with creep and oxidation seems to be the main factor for the damage process especially at extrados where a tensile state of stresses occurs at higher temperature. Finally, it has to be noticed that these TMF results differ significantly from results obtained in isothermal conditions—low-cycle or high-cycle fatigue—where resistances generally follow high temperature tensile strength.

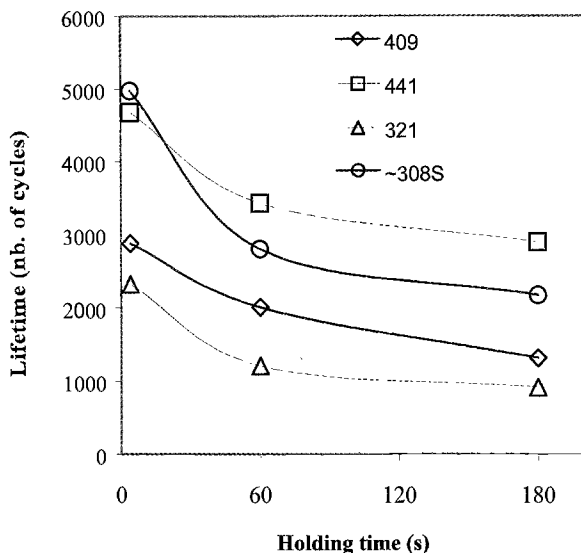


FIG. 4—TMF results on 409, 441, 321 and 308S stainless steel grades for 250°C–900°C – 2-mm thick specimens for different dwell times.

Numerical Simulation of the Thermomechanical Fatigue Process

Constitutive Law for Material and Identification Procedure

In order to simulate numerically the TMF process occurring in the test, constitutive laws for materials behavior have to be identified. Because of the temperatures involved, an elasto viscoplastic behavior description is to be preferred to a solely elastoplastic one. In fact, the viscoplastic behavior of a metal subjected to cyclic loading at high temperature is well described using a non-linear kinematic hardening model coupled with a Norton law. We chose the unified model proposed by J. L. Chaboche [6]. In our procedure, the coupling between the mechanical behavior and the damage is not considered.

Following Chaboche, the deformation behavior is defined by the following constitutive equations in the two domains:

Elasticity:

$$\underline{\underline{\sigma}} = E \cdot \underline{\underline{\varepsilon}} \quad (1)$$

where E represents the matrix of elasticity, a function of the Young modulus and Poisson ratio.

Viscoplasticity: Yield function, viscoplastic strain and kinematic hardening rule are defined as follows

$$f = J(\underline{\underline{\sigma}} - \underline{\underline{X}}) - k \quad (2)$$

$$\underline{\underline{\dot{\varepsilon}}}^{vp} = \dot{p} \left(\frac{\partial f}{\partial \underline{\underline{\sigma}}} \right) \quad (3)$$

$$\dot{p} = \left\langle \frac{f}{K} \right\rangle^n \quad (4)$$

$$\underline{\underline{\dot{\alpha}}} = \dot{p} \left(n - \frac{3D}{2C} X \right) \text{ and } \underline{\underline{X}} = \frac{2}{3} C \underline{\underline{\alpha}} \quad (5)$$

where J is the von Mises invariant. The strain accumulation rule is given by

$$\underline{\underline{\varepsilon}} = \underline{\underline{\varepsilon}}^e + \underline{\underline{\varepsilon}}^{vp} + \underline{\underline{\varepsilon}}^{ih} \quad (6)$$

All the material parameters of the model (E , C , D , n , ...) were assumed to depend only on temperature and are identified using the stress-strain curves derived from low-cycle fatigue tests performed in isothermal conditions — from room temperature to 950°C — and for different strain amplitudes and strain rates: from 0.05–0.8%, and from 10^{-4} to 10^{-2} per second.

In our identification procedure no relaxation tests were performed; so our set of parameters did not allow for a simulation of a long period creep process (strain rate below 10^{-4} s^{-1}). Because the stabilized strain-stress loop was chosen for the parameter identification, we assumed that the material reached a saturated cyclic hardening state. The parameters of the model are optimized to make the model fit the experimental curves. In Ref. 7 Watanabe et al. preferred the first half cycle, which appears to describe more closely a softened material especially when a recovery process occurs during a long period at high temperature. The difference is mainly significant at low temperature. It is clear that a complete coupled metallurgical behavior to take account of the softening (no phase transformations occur in the studied temperature range) will be a significant improvement for the model but identification and implementation in finite element code are substantially more complex.

Application to the Thermomechanical Fatigue Specimen

ABAQUS™ finite element code [8] was used to solve both the thermal and mechanical analysis of the different experiments where thickness, maximum, and minimum temperatures and holding time were varied. Only a $\frac{1}{4}$ of the specimen was meshed using 8-nodes 3D finite elements (Fig. 5). First, the thermal analysis was done to fit precisely the experimental measurements by thermocouples: only the four first cycles were simulated.

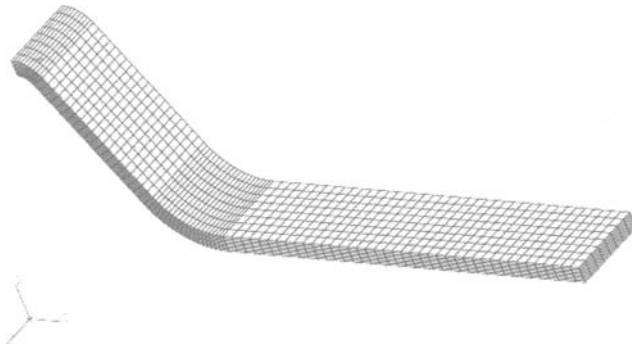


FIG. 5—3D meshing of a $\frac{1}{4}$ of the thermal fatigue specimen.

A specific subroutine was necessary to perform the non-linear thermomechanical analysis using the elasto-viscoplastic Chaboche model with ABAQUS. In that aim, we used the Z-ABA™ software [9]. Different experimental conditions were simulated to determine the effect of the maximum temperature (T_{\max}), minimum temperature (T_{\min}) and temperature range (ΔT). Figure 6 shows a comparison between the experimental and calculated clamping force, which is considered as a satisfactory result regarding our assumptions. Also, Fig. 6 evidences an accommodation process just after the first half cycle and thereafter the clamping force reaches a stable loop. The interest in modeling a few thermal cycles rather than modeling only one heating and to use a kinematic hardening law rather than isotropic was also demonstrated.

Figure 7 shows two typical features of the TMF process of our component:

- An in-phase mode at extrados of the specimen implying viscoplastic strain at the maximum temperature under tension;
- An out-of-phase mode at intrados of the specimen implying viscoplastic strain at the maximum temperature under compression.

These two modes would determine the main damage mechanisms involved in a stainless steel part under TMF.

Damage Mechanisms and Lifetime Prediction Methods

Thermomechanical Fatigue Damage Process

Failures of exhaust parts are often attributed to an out-of-phase (OP) TMF process [7]. Many of these examinations are performed on ferritic stainless steel grades but such a conclusion cannot be generally applied to austenitic grades where an in-phase (IP) thermal fatigue process appears more detrimental. On the other hand, some thermal fatigue conditions probably exist, which lead to failure in IP for ferritic grade and OP process for austenitic. By microscopic observations of failed austenitic specimens, we conclude that the two main damage mechanisms are: mechanical damage by fatigue-

creep process and oxidation damage at high temperature under tensile stress. Whereas OP-TMF is due to mechanical damage, the IP-TMF implies both mechanical and oxidation mechanisms. Figure 8 shows that the ferritic and austenitic grades failure is caused by out-of phase and in phase TMF respectively: thus, cracks due to mechanical damage propagate at intrados in the case of ferritic grades and cracks with a tip oxidation propagate at extrados in the case of austenitic grades. In the case of austenitic grades, intergranular cavitation is often observed due to creep damage.

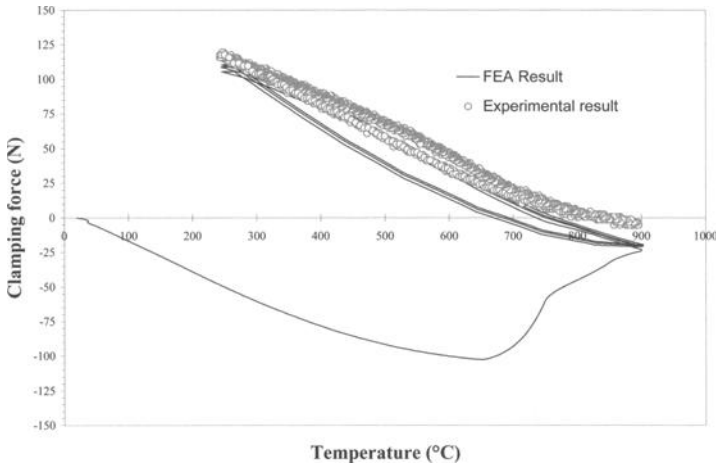


FIG. 6 — Comparison between experimental and calculated constraining force for AISI 441 250°C ↔ 900°C no dwell time.

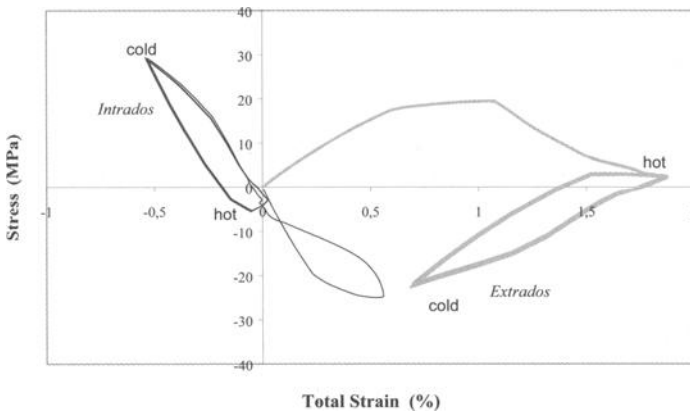
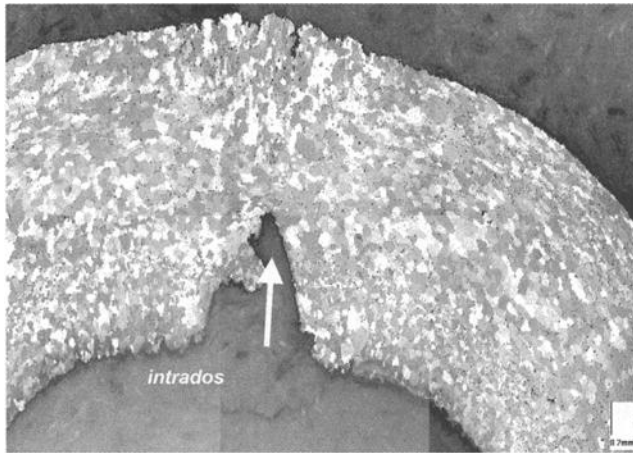
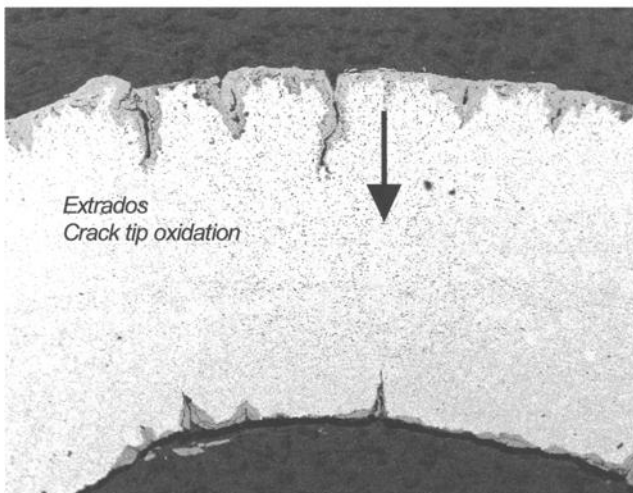


FIG. 7—Stress-strain curves at intrados and extrados of the specimen, showing an in-phase and an out-of-phase process.



(a)



(b)

FIG. 8—SEM observations of a failed ferritic specimen (a) and austenitic specimen (b): EN1.4509/AISI441 and EN1.4541/AISI 321 for $250^{\circ}\text{C} \leftrightarrow 950^{\circ}\text{C}$ cycle.

Thermomechanical Fatigue Criterion

Taira, in Ref. 10, formulated a non-isothermal Manson-Coffin criterion, which relates the equivalent viscoplastic strain amplitude $\Delta\varepsilon^{vp}$ accumulated during each cycle to the number of cycles to failure N_f in the form,

$$\Delta \varepsilon^{vp} = \lambda \cdot (Nf)^n \quad \text{where} \quad \Delta \varepsilon^{vp} = \int_{\text{cycle}} \left[\frac{2}{3} \dot{\varepsilon}^{vp} : \dot{\varepsilon}^{vp} \right]^{1/2} dt \quad (7)$$

where the constants λ and n may depend on an effective temperature for a given grade. The proposed version of the model depends implicitly on two other parameters:

- The dwell time, which plays both on the strain value and on parameter λ ;
- A phasing factor describing IP or OP process defined afterwards.

A mean value of $\Delta \varepsilon^{vp}$ is computed for cycles 2–4. Evolution of ε^{vp} as a function of time is shown in Fig. 9 where the increment $\Delta \varepsilon^{vp}$ at the intrados is greater than at the extrados. The failure is naturally related to this local quantity. The model has been fitted successfully on AISI441 ferritic grade for different maximum and minimum temperature: T_{\max} varies from 850–950°C and T_{\min} from 100–250°C. In the analysis, the maximum temperature was chosen as the effective temperature. Results are displayed in Fig. 10 and the scattering of the results obtained on AISI441 is only the consequence of a more important effect of the maximal temperature on fatigue lives in the studied range.

Particular Case of Austenitic Grades

In the case of the test described earlier, the model cannot predict alone the thermal fatigue failure of austenitic specimens because, whatever the grade, the viscoplastic strain amplitude is always greater in intrados than in extrados. The conclusion would be the same using other criteria based on the strain, the stress or the dissipated energy (like Skelton model).

TABLE 2 — *Parameters of the damage model (6) for maximal temperature in range 850–950 °C.*

	n	λ	Mode
AISI 441	-0.85	572.9	Out-of-Phase
AISI 308S	-0.32	10.7	In-phase

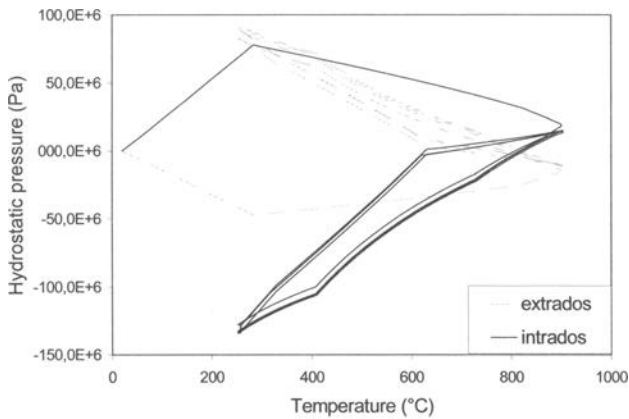
Thus a phasing factor able to distinguish in-phase or out-of phase mode appears necessary to establish a more general TMF law. It was shown that a tensile state of stress at high temperature leads to the opening of the cracks and therefore the oxidation penetration. Cracks propagate more rapidly in the in-phase mode in the case of austenitic grade because of their poor cyclic oxidation resistance. So the relation (7) for the 308S was identified using viscoplastic strain amplitudes computed at extrados in IP mode. The parameters of the Taira criterion are given in Table 2.

To apply the procedure on a real component, the phasing between thermal cycle and the mechanical cycle has to be computed first. The hydrostatic pressure at the maximum temperature is a good local quantity to describe this phasing,

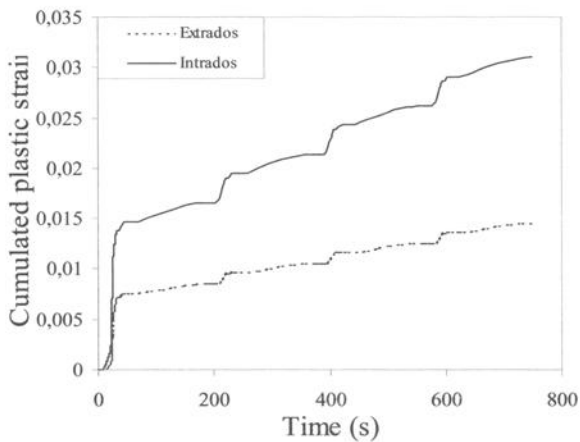
$$p(T_{\max}) = 1/3 \cdot \text{tr}(\underline{\underline{\sigma}}) \quad \text{at maximal temperature} \quad (8)$$

where tr designated the trace of the tensor.

Thus, $p(T_{max})$ is positive in in-phase process and negative in out-of-phase process and consecutively determines the choice of the damage curve on the diagram of Fig. 10, relating the number of cycles to failure, the equivalent viscoplastic strain amplitude and the fatigue mode (in-phase or out-of-phase). These curves are used during the post-processing of finite element modeling on real exhaust manifolds in order to evaluate critical fatigue zones and fatigue life of the components.



(a)



(b)

FIG. 9—(a) hydrostatic pressure versus temperature (b) Cumulated viscoplastic strain versus time at intrados and extrados – EN 1.4509 (AISI 441) 250°C↔ 900°C no dwell time.

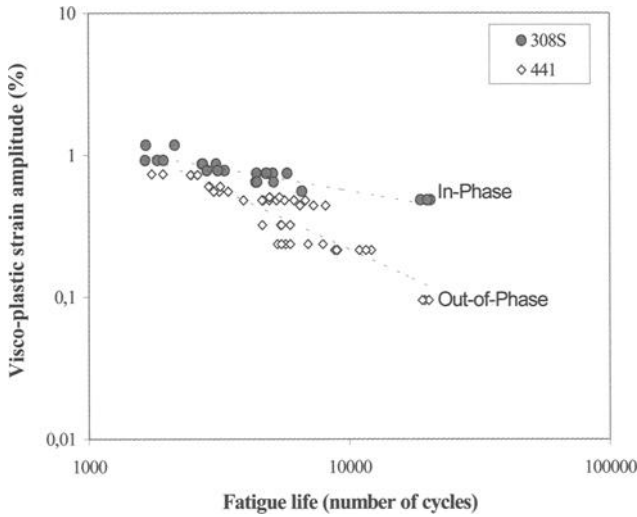


FIG. 10—Damage curves for 441 ferritic grade (in out-of-phase mode) and 308S refractory grade (in in-phase mode).

Conclusions and Perspectives

The thermomechanical fatigue resistance of different stainless steel grades was studied by means of a specific test. Further, the developed test appears as a useful means to study the damage process and to identify or validate damage criteria. So, two typical features of the thermomechanical fatigue are simulated in our test:

- An in-phase mode implying viscoplastic strain at the maximum temperature under tension, which appears to be the most detrimental damage mode for austenitic grades;
- An out-of phase mode implying viscoplastic strain at the maximum temperature under compression, which appears to be the most detrimental damage mode for ferritic grades.
- Results evidenced that the ferritic AISI441 grade offers the best resistance compared to the austenitic grades, which are more sensitive to the detrimental effect of holding time at high temperature due to a creep and oxidation coupling with fatigue. In the out-of-phase damage mode of ferritic grades, the viscoplastic strain amplitude was used as the crack initiation criterion using a non-isothermal Manson-Coffin law.

Concerning the in-phase damage mode of austenitic grades, the phasing between the thermal load and the mechanical load has to be taken into account in the criteria. The

hydrostatic pressure at the maximum temperature is proposed as such a phasing factor. Finally, our study evidences that a damage model for such a structural part submitted to thermomechanical fatigue loads needs to include both crack initiation and propagation processes description.

Acknowledgment

The authors wish to acknowledge the valuable inputs of O. Cleizergues and thank I. Evenepoel, H. Sassoulas, B. Proutt, and F. Moser, from Research centers of Ugine and Isbergues (Usinor Group) for the performing of the finite elements analysis and the experiments.

References

- [1] Antoni, L., Herbelin, J.-M., *EFC Working Party Report on Cyclic Oxydation of High temperature Materials: Mechanisms, Testing Methods, Characterisation and Lifetime Estimation*, M.Schütze, W. J. Quadackers Eds, Publication No. 27 in European Federation of Corrosion Series, Institute of Materials, 1999, p. 187.
- [2] Sassoulas, H., Santacreu, P.-O., "18^{ème} Journée de Printemps, Commission de Fatigue des Matériaux- Dimensionnement en Fatigue des Structures: Démarches et Outils," Société Française de Métallurgie et de Matériaux SF2M, Paris, 2–3 Juin, 1999, p. 161.
- [3] Santacreu, P.-O. et al., "Third International Congress on Thermal Stresses," *Thermal Stress '99*, Cracow, Poland, 13–17 June 1999, J. J. Skrzypek and R. B. Hetnarski, Eds., p. 245.
- [4] Renaudot, N., et al., SAE Technical paper series N° 2000-01-0314, SAE 2000 World Congress Detroit Michigan, 6–9 March, 2000.
- [5] Oku, M. et al., *Nisshin Steel Technical Report*, 66, 1992, p. 37.
- [6] Lemaitre, J., Chaboche, J.-L., "Mécanique des Matériaux Solides," Bordas, Paris, 1988.
- [7] Watanabe, Y., et al., SAE Technical paper series 980841, SAE Int. Congress, Detroit Michigan, 23–26 February 1998.
- [8] Abaqus, Hibitt, Karlsson and Sorensen, Inc., 1998.
- [9] Northwest Numerics and Modeling Inc. and Ecole des Mines de Paris, Z-Set /Z-Aba, Version 8 Manual, 1999.
- [10] Taira, S., *Fatigue at Elevated Temperatures*, ASTM STP 520, ASTM International, West Conshohocken, 1973, pp. 80–101.

Xuming Su,¹ Michael Zubeck,¹ John Lasecki,¹ Huseyin Sehitoglu,²
Carlos C. Engler-Pinto, Jr.,¹ Chung-Yao Tang,³ and John E. Allison¹

Thermomechanical Fatigue Analysis of Cast Aluminum Engine Components

REFERENCE: Su, X.M., Zubeck, M., Lasecki, J., Sehitoglu, H., Engler-Pinto Jr., C. C., Tang, C.-Y., and Allison, J. E., "Thermomechanical Fatigue Analysis of Cast Aluminum Engine Components," *Thermomechanical Fatigue Behavior of Materials: 4th Volume, ASTM STP 1428*, M. A. McGaw, S. Kalluri, J. Bressers, and S. D. Peteves, Eds., ASTM International, West Conshohocken, PA, 2002, Online, Available www.astm.org/STP/1428/1428_10587, 22 July 2002.

ABSTRACT: Cast aluminum engine components are increasingly being used in the automobile industry. Due to high engine operating temperature, thermal fatigue during start-stop cycles is a very important design consideration. In this paper we will describe the application of newly developed analysis methods to analyze these complex problems. A user material subroutine for viscoplasticity stress analysis using the commercial FEA code ABAQUS has been developed. Stress and strain of engine heads during thermal cycle are thus analyzed and this code verified. The thermomechanical fatigue model developed by Neu and Sehitoglu, a damage accumulation model including fatigue, oxidation and fatigue damage, has been extended to three-dimensional state of stress by using the concept of critical planes. The enhanced damage model has been implemented in a FEA postprocessor for engine component life analysis. The predictions of thermal strains and fatigue life based on 3D FEA analysis are compared with measurements of engine component tests. Three different thermal loading cycles are considered. The thermal fatigue life predictions are within 30% error of actual component test data.

KEYWORDS: thermal fatigue, thermomechanical fatigue, viscoplasticity, engine components, aluminum castings, fatigue prediction, finite element analysis

Introduction

The automotive industry has been facing the challenge to increase the engine efficiency and overall performance and at the same time deliver a vehicle that meets increased customer expectation for safety, fuel economy and price. The use of cast aluminum alloys has provided a significant reduction in weight, notably in the cylinder heads and blocks. Shifting the material for engine components from iron to aluminum, however, also brings about new challenges. To increase efficiency the maximum operation temperature of these components has also increased from below 170°C in earlier engines to peak temperatures well above 200°C in recent engines [1]. For the cast aluminum cylinder head, an important challenge is its resistance to thermal fatigue. For diesel engines, the operating temperatures can be even higher. In this case, the visco-

¹ Technical specialists, research engineers and senior staff technical specialist, respectively, Scientific Research Laboratories, Ford Motor Company, MD 3182, Dearborn, MI 48124.

² Professor, Department of Mechanical Engineering, University of Illinois, Urbana, IL 61801.

³ Technical specialist, Powertrain Operations, Ford Motor Company, MD 65, Dearborn, MI 48121.

plastic behavior, such as strain rate effect, of the material has to be taken into consideration to accurately predict the thermomechanical fatigue response.

The principal thermomechanical cycle of concern in engine head analysis is the start-stop cycle. Consider an engine starting up during cold winter, where the ambient temperature can be lower than -30°C , and warming up to over 230°C . The non-uniform thermal expansion and contraction of different parts of an engine head during such a thermal cycle introduce large thermomechanical loads to the structure of the engine head. These thermomechanical loads, together with the firing load of an operating engine can cause an engine head to fail in low cycle fatigue if not properly accounted for.

In this paper, we describe extension of the unified viscoplasticity relation and thermal mechanical damage model developed by Neu and Sehitoglu et al. [2,3] to 3D simulations and the implementation of this model to the analysis of engine cylinder head thermal fatigue.

Thermomechanical Fatigue Theory

The thermomechanical fatigue (TMF) life prediction model, originally developed by Neu and Sehitoglu for steels [2,3], is used in the present investigation. The total fatigue damage per cycle is obtained by summing the damage due to mechanical fatigue, creep and oxidation, respectively, as

$$D^{total} = D^{fat} + D^{ox} + D^{creep} \quad (1)$$

or, in terms of fatigue cycles,

$$\frac{1}{N_f^{total}} = \frac{1}{N_f^{fat}} + \frac{1}{N_f^{ox}} + \frac{1}{N_f^{creep}} \quad (2)$$

where D^{total} , D^{fat} , D^{ox} and D^{creep} are total damage, mechanical fatigue damage, oxidation and creep damage, respectively. And N_f^{total} , N_f^{fat} , N_f^{ox} and N_f^{creep} are total cycles to failure, cycles to failure due to mechanical fatigue, oxidation and creep damage, respectively.

The mechanical fatigue damage is calculated using the well-known strain-life equation, which is obtained by adding the Manson-Coffin and Basquin equations [4]:

$$\frac{\Delta \varepsilon_{mech}}{2} = \frac{\sigma_f'}{E} (2N_f^{fat})^b + \varepsilon_f' (2N_f^{fat}) \quad (3)$$

where σ_f' is the fatigue strength coefficient, E is Young's modulus, b is the fatigue strength exponent, ε_f' is the fatigue ductility coefficient, and c is the fatigue ductility exponent. The constants E , σ_f' , b , ε_f' , and c are determined from isothermal room-temperature fatigue tests.

The oxidation damage is due to repeated formation of an oxidation layer at the crack tip and its rupture,

$$\frac{1}{N_f^{\alpha}} = \left[\frac{h_{cr} \delta_o}{B \Phi^{\alpha} K_p^{eff}} \right]^{-1/\beta} \frac{2(\Delta \epsilon_{mech})^{(2/\beta)+1}}{\dot{\epsilon}_{mech}^{1-(\alpha/\beta)}} \quad (4)$$

where h_{cr} , δ_o , α , β , and B are material parameters. $\dot{\epsilon}_{mech}$ is mechanical strain rate and K_p^{eff} is the effective oxidation constant,

$$K_p^{eff} = \frac{1}{t_c} \int_0^{t_c} D_0 \exp\left(\frac{-Q}{RT(t)}\right) dt \quad (5)$$

where D_0 is a constant, Q is activation energy for oxidation and R the universal gas constant. The Oxidation Phasing Factor

$$\Phi^{\alpha} = \frac{1}{t_c} \int_0^{t_c} \exp\left[-\frac{1}{2} \left(\frac{\dot{\epsilon}_{th} / \dot{\epsilon}_{mech} + 1}{\xi^{\alpha}}\right)^2\right] dt \quad (6)$$

where ξ^{α} measures the relative amount of damage associated with different phasing. $\dot{\epsilon}_{th}$ is thermal strain rate. The damage is higher for out-phase thermomechanical cycling than in-phase thermomechanical cycling.

The creep damage is related to mechanisms such as void growth and intergranular cracking and assessed by using

$$\frac{1}{N_f^{creep}} = \Phi^{creep} \int_0^{t_c} A e^{(-\Delta H / RT)} \left(\frac{\alpha_1 \bar{\sigma} + \alpha_2 \sigma_H}{K} \right)^m dt \quad (7)$$

where $\bar{\sigma}$ is equivalent stress, σ_H the hydrostatic stress and K the drag stress. These terms are to be defined later when constitutive relations for the materials are discussed. α_1 and α_2 are scaling factors, which present the relative amount of the damage occurring in tension and compression, Φ^{creep} is the Creep Phasing Factor

$$\Phi^{creep} = \frac{1}{t_c} \int_0^{t_c} \exp\left[-\frac{1}{2} \left(\frac{\frac{\dot{\epsilon}_{th}}{\dot{\epsilon}_{mech}} - 1}{\xi^{creep}}\right)^2\right] dt \quad (8)$$

where ξ^{creep} defines the sensitivity of the phasing to the creep damage. Creep damage is at its worst when the thermomechanical deformation is in-phase.

A comprehensive testing matrix, involving more than 100 samples has been employed to define all the parameters in the above formulation for the 319 cast aluminum alloy in a T7 heat treatment condition. All isothermal and thermo-mechanical fatigue experiments were conducted on uniaxial cylindrical specimens under total strain control

and constant strain rate. The isothermal fatigue experiments were performed at temperatures ranging from 20°C to 300°C with three different strain rates: $\sim 2 \times 10^{-1} \text{ s}^{-1}$ (40 Hz), $\sim 2 \times 10^{-3} \text{ s}^{-1}$ (0.5 Hz) and $5 \times 10^{-5} \text{ s}^{-1}$. A wide range of mechanical strain ranges ($\Delta \varepsilon_m$) was considered (0.2–2.0%).

The thermo-mechanical fatigue tests were conducted at the University of Illinois at Urbana-Champaign using a servo-hydraulic Instron testing machine in conjunction with a 15 kW Lepel induction heater. The temperature was measured using a Raytek non-contact infrared pyrometer. The strain and temperature waveforms followed a triangular wave-shape. TMF experiments were conducted at a mechanical strain rate of approximately $5 \times 10^{-5} \text{ s}^{-1}$ and over a temperature range of 100–300°C.

The original TMF theory of Neu and Sehitoglu [2,3] as formulated above is one-dimensional. Since engine components are normally subjected to three-dimensional loadings, a three-dimensional TMF model is needed. This is achieved by extending the one-dimensional Neu and Sehitoglu theory to a three-dimensional state of stress by using the critical planes concept [5,6]. Since the state of stress at the critical area of a cylinder head is close to pure shear, it is assumed that the plane of maximum mechanical shear strain range is the critical plane and that the 319 cast aluminum alloy fatigues by alternating shear deformation.

The cycles to failure due to three-dimensional mechanical fatigue damage is calculated, corresponding to Eq 3

$$\frac{\Delta \gamma_{mech}}{2} = \frac{(1 + \nu_e) \sigma_f}{2E} (2N_f^{fat})^b + \frac{(1 + \nu_p)}{2} \varepsilon_f' (2N_f^{fat})^c \quad (9)$$

where $\Delta \gamma_{mech}$ is the maximum mechanical shear strain range on the critical shear plane, E is Young's modulus, ν_e and ν_p is Poisson's ratio for elastic and plastic deformation, respectively. ν_e is chosen to be 0.25 and ν_p is 0.5.

Oxidation damage occurs by repeated formation and rupture of an oxidation layer, mostly a mode I tensile phenomenon. The normal strain range on the critical plane and its rate are used in Eq 4 for three-dimensional calculation of oxidation damage.

$$\frac{1}{N_f^{ox}} = \left[\frac{h_{cr} \delta_o}{B \Phi^{ox} K_p^{eff}} \right]^{-1/\beta} \frac{2 \left(\frac{\Delta \varepsilon_{nm}}{1 - \nu_e} \right)^{(2/\beta)+1}}{\left(\frac{2 \dot{\varepsilon}_{nm}}{1 - \nu_e} \right)^{1-(\alpha/\beta)}} \quad (10)$$

where ε_{nm} is the normal strain and $\dot{\varepsilon}_{nm}$ the normal strain rate on the critical plane. Using the normal strain in oxidation damage is also consistent with the idea of phasing, as the idea of phasing loses its significance when pure shear is considered. Using the normal strain rate on critical plane, the Oxidation Phasing Factor is modified to

$$\Phi^{ox} = \frac{1}{t_c} \int_0^{t_c} \exp \left[-\frac{1}{2} \left(\frac{\frac{(1-\nu_e)\dot{\epsilon}_{th}}{2\dot{\epsilon}_{m}} + 1}{\xi^{ox}} \right)^2 \right] dt \quad (11)$$

Since creep damage in Eq 7 is based on stress invariants, Eq 7 is three-dimensional. However, the Creep Phasing Factor is now calculated using normal strain and normal strain rate on the critical plane

$$\Phi^{creep} = \frac{1}{t_c} \int_0^{t_c} \exp \left[-\frac{1}{2} \left(\frac{\frac{(1-\nu_e)\dot{\epsilon}_{th} - 1}{2\dot{\epsilon}_{mech}}}{\xi^{creep}} \right)^2 \right] dt \quad (12)$$

Without new testing data, all parameters in Eqs 9–12 are those from one-dimensional formulations, i.e., Eqs 3–9.

The three-dimensional fatigue formulation has been programmed in a postprocessor for ABAQUS, called HotLife, to process finite element analysis results.

Material Constitutive Relation

In many cases, sections of cylinder heads can experience temperatures as high as over 230°C. The material stress-strain relations are drastically different when they are tested at 230°C compared with those at room temperatures. Figure 1 provides such an example. The stress at 0.5% strain when tested at room temperature is 100 MPa higher than that tested at 250°C. Strain rate effects are also important. Figure 2 shows stress-strain relations at different strain rates at 250°C. The stresses at 0.5% strain for samples tested with strain rate of $5 \times 10^{-6} \text{ s}^{-1}$ is only about half of that when tested with rate $5 \times 10^{-3} \text{ s}^{-1}$. These strain rates are within the range of strain rates an engine cylinder head could experience.

To accurately predict thermomechanical fatigue, a reliable constitutive relation is needed. The constitutive model proposed by Slavik and Sehitoglu is used in this study [7,8] with modifications for cast aluminum [1,9]. This model is a comprehensive unified viscoplasticity model using 26 temperature dependent parameters. Two state variables, a drag stress, K , and a tensor back stress, S_y^c , are used to describe the microstructural changes of the material at different temperatures and strains. As a detailed discussion of the model with all formulations has already been published [1,9], only the major equations are listed here.

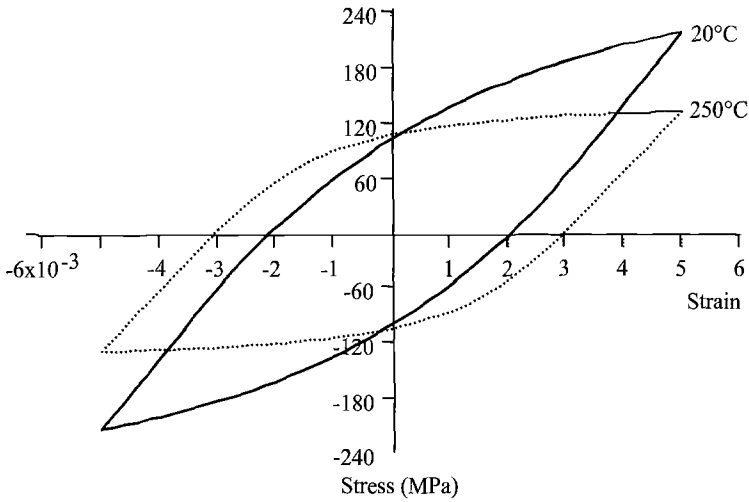


FIG. 1—Comparison of stress-strain relations at 20°C and 250°C, 319-T7.

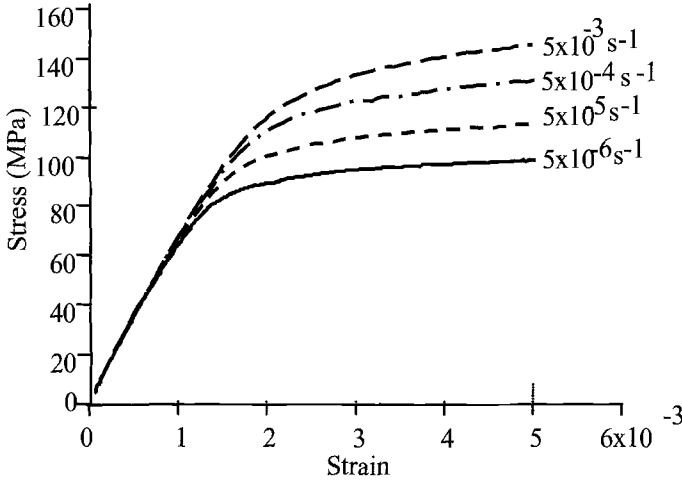


FIG. 2—Stress-strain relations at different strain rates tested at 250°C, 319-T7.

The total strain rate $\dot{\epsilon}_{ij}$ is divided into elastic part $\dot{\epsilon}_{ij}^e$ and inelastic part $\dot{\epsilon}_{ij}^{in}$, respectively, as

$$\dot{\epsilon}_{ij} = \dot{\epsilon}_{ij}^e + \dot{\epsilon}_{ij}^{in} \tag{13}$$

where inelastic strain rate is

$$\dot{\epsilon}_{ij}^{in} = \frac{2}{3} Af(\bar{\sigma} / K) \frac{S_{ij} - S_{ij}^c}{\bar{\sigma}} \tag{14}$$

S_{ij} in the above equation is the deviatoric stress $S_{ij} = \sigma_{ij} - \frac{1}{3}\sigma_{kk}$. $\bar{\sigma}$ is equivalent stress defined by $\bar{\sigma}^2 = \frac{3}{2}(S_{ij} - S_{ij}^c)(S_{ij} - S_{ij}^c)$. A is a material parameter. The strain rate function f is defined as

$$\begin{aligned} f\left(\frac{\bar{\sigma}}{K}\right) &= \left(\frac{\bar{\sigma}}{K}\right)^{n_1} && \text{when } \left(\frac{\bar{\sigma}}{K}\right) < 1.0 \\ f\left(\frac{\bar{\sigma}}{K}\right) &= \exp\left[\left(\frac{\bar{\sigma}}{K}\right)^{n_2} - 1\right] && \text{when } \left(\frac{\bar{\sigma}}{K}\right) \geq 1.0 \end{aligned} \tag{15}$$

where n_1 and n_2 are material parameters. The evolution of back stress S_{ij}^c is governed by equations

$$S_{ij}^c = \frac{2}{3}h_\alpha \dot{\epsilon}_{ij}^{in} - [r_\alpha^D \dot{\epsilon}^{in} + r_\alpha^S] S_{ij}^c \tag{16}$$

where h_α describes hardening, r_α^D and r_α^S are dynamic and static recovery term, which are also functions of back-stress and inelastic strain rate.

The evolution of drag-stress is formulated as

$$\dot{K} = B(K_{sat} - K)\dot{\epsilon}^{in} - B_3(K - K_{rec}) + \theta \dot{T} \tag{17}$$

where B and B_3 are parameters and K_{sat} and K_{rec} are saturation and recovery drag-stress.

The above constitutive relation has been programmed into a user material subroutine, HotStress, for stress analysis using the finite element code ABAQUS. Since the unified constitutive relation is strongly nonlinear, with both strain rate equation and back stress evolution governed by nonlinear differential equations with terms of stacked exponential and power function, writing a user material subroutine is quite a challenge, especially, in getting analytical formulation of the Jacobian of the material relation. Improvements of the material subroutine have been achieved since we first reported our work in [10].

Thermal Fatigue Test and Its Numerical Simulation

The thermomechanical cycles considered are the start and stop cycles. To test a new design for thermal fatigue, accelerated tests are frequently used. Figure 3 shows such an accelerated test for thermal fatigue of an engine cylinder head. It will be referred as TFT, or Thermal Fatigue Test.

As shown in Fig. 3, the engine head is bolted to a plate. The plate has open circular windows so that the combustion chamber areas of the cylinder head are exposed. Thermocouples and strain gauges are mounted side by side to record temperatures and strains. The test starts by directing gas flames to the combustion areas through the open windows to rapidly raise the temperatures on the surfaces of combustion chambers of the cylinder head to some designated value. The maximum temperature achieved at the valve bridge area, where a thermocouple is placed, controls the severity of the tests. The

maximum temperature of engine head during a TFT cycle can be controlled by changing the gas flames and their duration. The plate covering the engine head helps in insulating the flames from direct contact with other parts of the engine head. A water jet is then applied to cool down the head to the room temperature, simulating the engine stop cycle. The test is regularly interrupted for inspection by ultrasonic and dye penetrant methods; if a crack is detected, the test stops and the number of cycles to failure is recorded.

The TFT described above has been simulated using the thermomechanical fatigue life model and constitutive relation introduced in previous sections. The simulation of TFT includes three sequential analyses, i.e., thermal analysis, stress analysis and fatigue analysis. Stress analysis was performed by using finite element code ABAQUS with HotStress, the user material subroutine introduced in the section of material constitutive relation. The finite element mesh is shown in Fig. 4. The model includes 94 000 cubic elements and 83 000 nodes. Pre-tension was used for the bolt load and contact surface for contact between the plate and engine head. For convenience of interfacing thermal and stress analysis, ABAQUS is also used for the thermal analysis. The thermal transfer between the plate and the engine head is modeled by gap conductance. Fatigue analysis is achieved by postprocessing the results of stress analysis using HotLife, as mentioned previously. For thermal and stress analysis, both the cylinder head and the plate are modeled as shown in Fig. 4.

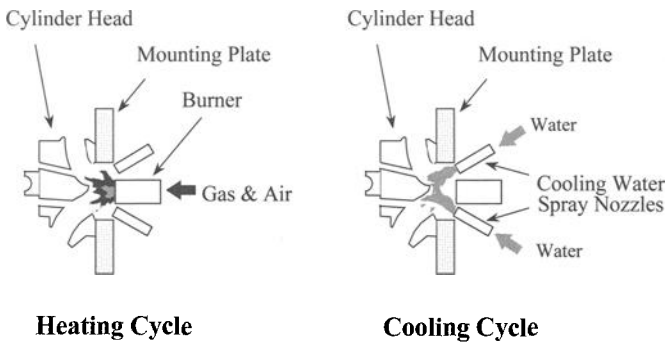


FIG. 3—Sketches showing the thermal fatigue test (TFT).

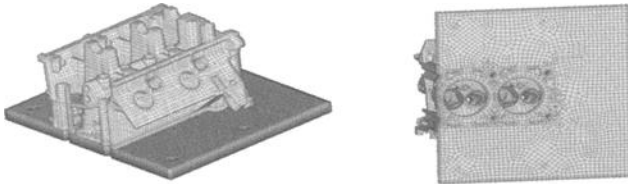


FIG. 4—Finite element model for the thermal fatigue test.

Heat flux is used as the boundary condition for thermal analysis. The only non-zero heat flux is assumed to be on the combustion surface and is obtained by an optimal inverse modeling technique, as described below. In this effort, one of the cylinder heads tested is instrumented with 13 thermocouples in different locations. The center of the gas flame is assumed to be located at the center of the combustion chamber and the heat flux

is a one-dimensional decreasing function of the distance from the flame center. An initial function of the heat flux is assumed and temperature calculated based on the heat flux assumption. The temperature distribution obtained is then compared with the temperature measurements at the 13 points where thermocouple data are available. If the simulation and the experimental results do not match, the boundary conditions are adjusted until a satisfactory simulation is obtained. Figure 5 shows the optimized results of such an analysis for one of the thermocouples.

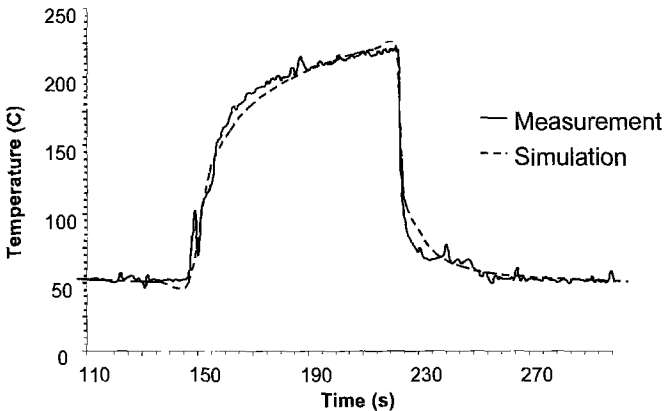


FIG. 5—Comparison of predicted and measured temperature during a TFT cycle.

The temperature field obtained is directly input as loading for stress analysis. For comparison, finite element stress analysis with elastic material relation has also been carried out. The dependency of Young's modulus on temperature is achieved by using a look-up table in ABAQUS input file. Figure 6 shows the comparison of predictions and measurements. The solid curve in Fig. 6 is the measurement from a strain gage in the combustion chamber near the critical region (where crack initiation is detected). The points connected by dotted line are finite element results from viscoplasticity analysis. Since the results from ABAQUS analysis take up a large disc space, only limited intermediate results are stored. The same is true for elastic analysis, whose results are points connected by using dashed line.

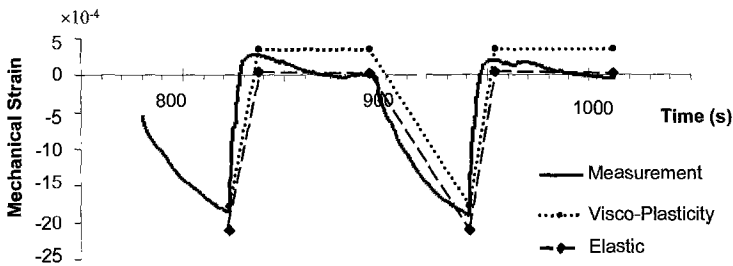


FIG. 6—Comparison of predicted and measured strain.

By the results from Fig. 6, one sees that the viscoplasticity theory used in the present study can capture stress and strain behavior quite accurately. The elastic analysis, on the other hand, introduces sizable error; especially it underestimates the tensile strain when the engine cools down.

Plots in Fig. 7 show the contours of cycles to failure due to fatigue, oxidation, creep and total damage, respectively. Only the first cycle is simulated in order to predict the thermal fatigue life. These results are the output of HotLife, the TMF postprocessor. Apparently, the most critical damage is from mechanical fatigue as is obvious by comparing cycles to failure recorded in Fig. 7a–7c. It is also interesting to note that the most critical oxidation damage and most critical creep damage do not always occur at the same place. From Fig. 7c, the critical area for creep damage is close to the valve bridge area while for oxidation, as shown in Fig. 7b, the most critical area is the corner between the exhaust valve and outer edge of the combustion area, which happens to be also the most critical area for mechanical fatigue, Fig. 7a. This is quite reasonable if one realizes that deformation is more tensile in the bridge area and more compressive in the exhaust corner. At the exhaust corner, deformation is clearly out of phase while in the bridge area it is more mixed.

Table 1 compares the predictions of the numerical simulation with the measured life from three different test conditions. A total of seven samples were tested at each maximum temperature and the average thermal fatigue life observed is presented in Table 1. The difference in the predictions and measurements is generally less than 30%. Predictions for all three cases were conservative.

TABLE 1—*Predicted and measured life for the TFT methodology.*

Maximum Temperature	Measured Life	Predicted Life
210 °C	3000	2312
230 °C	1700	1415
250 °C	560	447

In the three dimensional formulation of the thermomechanical fatigue theory, shear strain ranges are calculated on the most critical plane, i.e., the plane that has the maximum shear range during thermomechanical cycles. The mechanical fatigue damage is assumed to be a result of alternating shear deformation, as in Eq 9. However, since normal strains and all stress components are used in the calculations of oxidation damage and creep damage as shown in Eqs 10–12, the total life is not decided only by alternating shear strain. By results from engine head analysis, shown in Fig. 7(a)–7(d), creep damage and oxidation damage contribute sizably to total damage. Further exploration is needed to fully understand the physical meaning of the accumulated damage theories in three-dimensional cases.

In engineering thermomechanical fatigue analysis, the so-called “Strain Invariance Principle” [11] is sometime used. This practice assumes that strain calculated based on elastic analysis is very good approximation for a viscoplasticity analysis. The strain ranges from elastic analysis are thus used in fatigue analysis directly. Creep damage is assessed by using stresses recalculated by using a viscoplasticity relation often attached to a fatigue processor with strain from elastic analysis as input. This should be used with caution, as even for constrained plastic deformation results from an elastic analysis and a viscoplasticity analysis can be very different, as shown in Fig. 6.

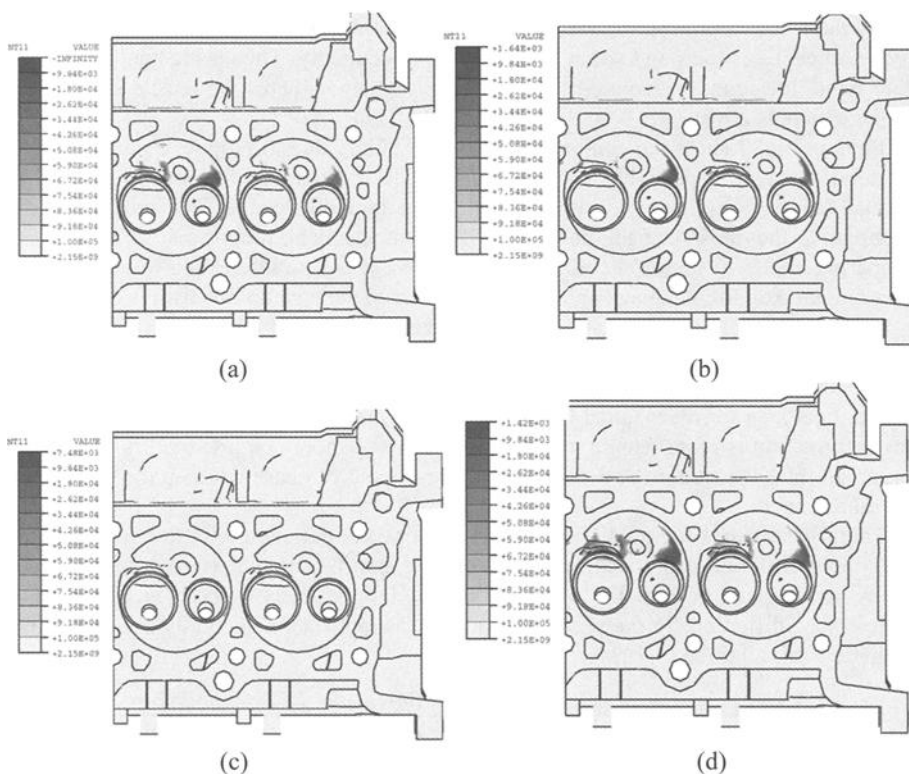


FIG. 7—Predicted cycles to failure of an engine cylinder head undergoing TFT (maximum temperature of 230 °C, Table 1): (a) contour of mechanical fatigue life; (b) contour of oxidation life; (c) contour of creep life; and (d) contour of total life.

Summary

A thermomechanical fatigue model based on the concept of damage accumulation has been presented. The damage considered includes fatigue, oxidation and creep damage. The model is extended to three dimensional formulation based on the concept of critical plane. Based on experimental observation and finite element analysis, thermomechanical fatigue for cylinder head with cast 319 T7 is judged to be a shear failure. The plane of maximum mechanical shear range is assumed to be critical plane. The three-dimensional thermomechanical model has been programmed into a postprocessor, HotLife, for thermomechanical analysis.

A comprehensive constitutive material relation has been applied to cast aluminum for stress analysis. The unified viscoplasticity theory takes both temperature and strain rate effects into consideration. The evolution of microstructure of the material during thermomechanical deformation is described by using two state variables, a drag stress and a back stress tensor. The material relation has been written into a user material subroutine, HotStress, for finite element analysis using commercial code ABAQUS.

The accuracy of this approach was evaluated by comparing FEA results with measurements from an accelerated component test. The tests were simulated by using finite element method. Comparison of the analysis results with strain measurements is quite encouraging. Predicted fatigue lives are within 30% of measurements. Predictions for all three cases are conservative.

Acknowledgments

Team members of Ford Motor Company's TFT team, especially, Mark Griffith, Craig, Putnam, Edward Akpan and John Loncke are acknowledged.

References

- [1] Smith, T. J., Maier, H. J., Sehitoglu, S., Fleury, E., and Allison, J., "Modeling High-Temperature Stress-Strain Behavior of Cast Aluminum Alloys," *Metallurgical and Materials Transactions A*, January 1999, Vol. 30A, pp. 133–146.
- [2] Neu, R. W. and Sehitoglu, H., "Thermomechanical Fatigue, Oxidation, and Creep: Part I – Damage Mechanisms," *Metallurgical Transaction*, 1989, 20A, 1755–1767.
- [3] Neu, R. W. and Sehitoglu, H., "Thermomechanical Fatigue, Oxidation, and Creep: Part II – Life Predictions," *Metallurgical Transaction*, 1989, 20A, 1769–1781.
- [4] Suresh, S., "Fatigue of Materials," *Cambridge Solid State Science Series*, Cambridge University Press, 1st edition, 1992.
- [5] Brown, M. W. and Miller, K. J. "A Theory for Fatigue Under Multiaxial Stress-Strain Conditions," *Proceedings of Institute of Mechanical Engineers*, Vol. 187, 1973, pp. 745–756. Critical Plane Reference.
- [6] Socie, D. F. and Marquis, G. B., "Multiaxial Fatigue," SAE International, Warrendale, PA, 2000.
- [7] Slavik, D., and Sehitoglu, H., "Constitutive Models Suitable for Thermal Loading," *Journal Engineering Material and Technology*, 1986, Vol. 108, pp. 303–312.
- [8] Sehitoglu, H., Qing, X., Smith, T., Maier H., and Allison, J., "Stress-Strain Response of a Cast A319-T6 Aluminum under Thermomechanical Loading," *Metallurgical and Materials Transactions*, 2000, Vol. 31A, pp. 139–146.
- [9] Engler-Pinto, C.C., Jr., Sehitoglu, H., and Maier, H. J., "Cyclic Behavior of Al319-T7B Under Isothermal and Non-Isothermal Conditions," *Thermomechanical Fatigue Behavior of Materials: 4th Volume, ASTM STP 1428*, M. A. McGaw, S. Kalluri, J. Bressers, and S. D. Peteves, Eds., ASTM International, West Conshohocken, PA, 2002.
- [10] Su, X. M. and Mgbokwere, C., "Numerical Implementation of a Viscoplasticity Model for Automobile Engine Cylinder Head Analysis," *Fourth International Conference on Constitutive Laws for Engineering Materials*, R. C. Picu and E. Krempl, Ed., Rensselaer Polytechnic Institute, Troy, New York, 1999.
- [11] Manson, S. S., "Thermal Stress and Low-Cycle Fatigue," McGraw-Hill Book Company, New York, 1966.

Experimental Techniques for Thermomechanical Testing

Yannis Vougiouklakis,¹ Peter Hähner,¹ Frits de Haan,¹ Vassilis Stamos,¹ and Stathis D. Peteves¹

Acoustic Emission Analysis of Damage Accumulation During Thermal and Mechanical Loading of Coated Ni-Base Superalloys

REFERENCE: Vougiouklakis, Y., Hähner, P., de Haan, F., Stamos V., and Peteves, S. D., "Acoustic Emission Analysis of Damage Accumulation During Thermal and Mechanical Loading of Coated Ni-Base Superalloys," *Thermomechanical Fatigue Behavior of Materials: 4th Volume, ASTM STP 1428*, M. A. McGaw, S. Kalluri, J. Bressers, and S. D. Peteves, Eds., ASTM International, West Conshohocken, PA, 2002, Online, Available: www.astm.org/STP/1428/1428_10597, 20 May 2002.

ABSTRACT: Acoustic emission (AE) allows for the in-situ monitoring of damage during the thermal and mechanical solicitation of a material and can be used to identify various damage mechanisms and interpret the way they interact, in particular, in multi-material systems. In the present work AE activity was monitored during the step-wise tensile testing and during the thermomechanical fatigue (TMF) of Ni-base superalloys (in single-crystalline and directionally solidified form), coated with oxidation protection coatings. The classification analysis of the AE signals revealed that AE monitoring provides complementary and specific information about the surface-, subsurface-, and bulk damage processes. In combination with the mechanical response and the surface damage analysis by video imaging, it represents a powerful means for non-destructive damage assessment and it offers possibilities for the lifing of coated material systems.

KEYWORDS: Nickel-base superalloys, thermomechanical fatigue, acoustic emission, damage mechanisms, CMSX4, CM186

Introduction

The research and development efforts for enhanced performance of high-temperature materials for gas turbines is driven by the need to meet the demands for increased lifetimes and higher efficiencies at lower costs and reduced environmental impact. These ambitious goals can only be achieved through a combined approach comprising the development of new material systems and the use of advanced materials testing methods, in order to improve the understanding of the materials behavior and to allow for less conservative designs. While the trend in the development of hot-section gas turbine materials goes from monolithic metallic materials towards composite material systems

¹ Grantholder, Scientific Officer, Technical Officer, and Scientific Officer, respectively, European Commission, DG-Joint Research Centre, Institute for Energy, NL-1755 ZG Petten, The Netherlands.

(coated superalloys, bimetallic joints, metal matrix, and ceramic matrix composites), more reliable material property data are obtained by close-to-service testing procedures and advanced damage analyses.

In the present work, Ni-base superalloys are investigated, which are used for high-pressure gas turbine blades, as they retain high mechanical strengths up to about 80% of their melting temperature. Due to their limited high-temperature oxidation resistance, however, protective measures must be taken to slow down reactions of the superalloy with the aggressive environment. Indeed, to improve the performance of the turbine blades under specific service conditions, coatings are used for the oxidation and corrosion protection of the components. The damage processes of these coated material systems are rather complex, including oxidation, corrosion, plasticity, precipitate cracking, erosion, and microstructural degradation caused by the interdiffusion between the substrate and the coating [1–4]. The actual failure mode, however, is predominantly controlled by thermomechanical fatigue (TMF) due to mechanically applied and thermally induced alternating stresses, resulting from the thermal strains generated by the strong temperature gradients experienced during start-up and shut-down. Owing to the complex damage and failure behavior, the coating's performance cannot be extrapolated from simpler isothermal low cycle fatigue tests in the temperature spectrum of operation, but should be assessed through close-to-service TMF testing backed-up by appropriate damage analysis.

In that respect, acoustic emission (AE) represents a valuable tool, as it allows in situ monitoring of the damage evolution, provided that the damage mechanisms of the material system can be identified and correlated with specific signals by a proper analysis of the AE data. In a first step of this study, such an AE data analysis was applied to simple isothermal tensile tests, where AE activity turned out to be associated with only two damage mechanisms. The tensile tests were performed on two different MCrAlY coatings applied on the same single-crystalline Ni-base bulk material (CMSX4) and tested at various temperatures. In a second step, TMF tests on single crystalline and directional solidified CM186 blade alloys in the uncoated and Sermalloy 1515-coated conditions are reported. Here more complex degradation mechanisms are revealed through specific AE activity, distributed over several stages of TMF life and reflecting various interdependent damage mechanisms.

The objectives of this study were first to establish the validity of the AE monitoring as a means to assess the material response under thermal and mechanical loading conditions and, second, to correlate classes of AE signals with specific damage processes.

Experimental

As already mentioned, two different test series were conducted on two types of material systems, in order to investigate the performance of AE analysis as a tool for the identification of damage processes in those materials. In both material systems, the front surfaces of the test specimens were monitored via an automated video imaging system, which was synchronized with the mechanical loading [5].

The first material system tested was the single crystal Ni-base superalloy CMSX4 with two different types of plasma sprayed MCrAlY overlay coatings, referred to as Type I and Type II, having about the same thickness of 220 μm . Tensile specimens having a

rectangular cross section of $7 \times 3 \text{ mm}^2$ and a parallel length of 18 mm were machined with the tensile axis along the crystallographic [001] direction. Isothermal tensile tests were performed for both types of coated systems at four different temperatures (300°C, 500°C, 700°C, and 900°C), which are representative of the temperature range covered during start-up and shut down of gas turbines. Strains were applied in steps of 0.1% at a strain rate of 10^{-4} s^{-1} with intermediate dwell times of 30s, in order to allow images of the gauge length to be taken for optical surface crack analysis. Provided that failure had not intervened, the tests were interrupted at 5% total strain for microstructural analysis.

The second type of material system consisted of specimens prepared from single crystal (SC) and columnar grained (CG) (directionally solidified) Ni-based superalloy CM186 bars with [001] orientation of the tensile axis. Threaded end TMF specimens with a solid rectangular cross section of $12 \times 3 \text{ mm}^2$ and a parallel length of 9 mm were machined. Some of the SC and CG samples were coated with a modified aluminide coating, Sermalloy 1515, via an Al/Si slurry diffusion process, with an approximate thickness of 80 μm . In this second series of tests, asymmetrical triangular out-of-phase TMF cycles with mechanical strain ranges $\Delta\varepsilon_m$ of 0.8% and 1.0%, respectively, and a temperature range $\Delta T = 600^\circ\text{C}$ with temperature cycled between 350°C and 950°C were applied (minimum to maximum mechanical strain ratio $R = -\infty$, cycle period $\Delta t = 200 \text{ s}$). Thus, temperature and mechanical strain both varied linearly with time, but with a phase shift of 180°. This cycle imposes maximum mechanical strain (tension) at minimum temperature and minimum strain (compression) at maximum temperature. The tests were started at the minimum temperature and zero mechanical strain, and conducted until failure, or stopped when the cyclic load had dropped below 50% of the previously stabilized value. TMF life is then defined as the corresponding cycle number.

In both series of tests, AE monitoring was achieved by two broadband piezoelectric sensors, which were attached at the rims of the grips just outside the two cooling plates placed to protect the gripping system and to stabilize the temperature control. The signals of the sensors were pre-amplified and fed into a two-channel acoustic emission digital signal processor. AE data processing was done by means of the commercial software MISTRAS 2001 [6]. The software parameters for the AE monitoring were optimized with respect to the external noise sources (ambient or from the induction heating system), the mechanical set-up, the geometry, and the gauge length of the specimens to be monitored. The final AE set-up was optimized and validated by measuring the difference in the arrival time of artificially AE signals generated within and outside the gauge length. The same software parameter settings have been used for all the tests within a series, in order to ensure comparability among the AE data sets.

The monitored AE signals were in time order and seven different AE features were registered for each signal (rise time, counts, energy, duration, amplitude, average frequency, and counts to peak). Besides these AE parameters, the mechanical stress, temperature, and time were also registered as external parameters, every time that an AE signal was received.

Cluster Analysis of the AE Data

The main objective of this study consists of correlating the AE signals with specific damage mechanisms for both material systems and analyzing their characteristic

evolution. For this purpose, the recorded AE data have to be evaluated, in order to group them into classes (clusters) of damage events.

Initially the AE data were filtered in order to eliminate signals induced by the electromagnetic field of the induction heating system as well as other noise sources emanating from the experimental configuration. This was achieved by pre-recording the specific AE signature of the electromagnetic field and by excluding similar signals in the final post processing of the received AE data. Furthermore, the signals obtained from the two different channels (sensors) were compared with respect to the values of all the AE parameters and their times of detection, to ensure that only those AE data, which originated from events inside the specimen gauge length, were taken into account (in particular, signals with zero value of energy were disregarded). For the subsequent cluster analysis, only the AE signals registered by one of the sensors (the same in all the cases) were processed.

Since the AE activity of the studied material systems had not been analyzed previously, an unsupervised cluster analysis was followed. The NOESIS software [6] was used to manage the unsupervised cluster analysis of the AE data in terms of the recorded AE parameters and the external parameters of the AE events. These parameter sets form an extended dimensional parameter space, within which neighborhood relationships have to be established for the identification of clusters. To this end, all the values of the aforementioned parameters were initially normalized to lie between zero and one and their Euclidean distances were computed.

The choice of an appropriate subset of parameters that could serve as descriptors for the classification of the data was made with respect to their degree of independence [7]. First, the AE data series of all tests were subjected to a trial and error procedure, in order to determine those parameters, which were most appropriate for a global classification of all the AE data series. Since the comparability of the classified results among the different tests was a prerequisite, identical descriptor sets were used for all the tests within a series. The FORGY© routine [6], a k-means based algorithm, was selected as the most suitable to perform the classification of the AE data. The results from this analysis showed that the behavior of the clusters in the descriptor space is robust and comparable among all the tests.

Tensile Tests

Mechanical and Video Imaging Data

The isothermal tensile tests were performed at four different temperatures; within the investigated temperature range, the two types of coatings exhibit different characteristics as far as their surface cracking behavior (Fig.1) and their final strain values are concerned (Table 1).

At 300°C the specimen of coating type I develops only one single crack (the fatal one), at 500°C a single crack spanning the whole specimen width grows out from an array of short cracks confined to one of the edges of the specimen, and at 700°C and higher no surface cracks were observed at all. As opposed to this, the specimens of coating type II support the development of many specimen-wide cracks perpendicular to the loading axis at 500°C and below, while at 700°C no surface cracks besides the fatal one are observed.

TABLE 1—Test matrix of the tensile tests (unless otherwise indicated the final strain refers to failure of the sample).

Temperature (°C)	Specimen	Coating	Final Strain (%)
300	A1	Type I	1.1
	A2	Type II	5 (interrupted)
500	A3	Type I	4.9
	A4	Type II	3.9
700	A5	Type I	5 (interrupted)
	A6	Type II	4.4
900	A7	Type I	5 (interrupted)
	A8	Type II	5 (interrupted)

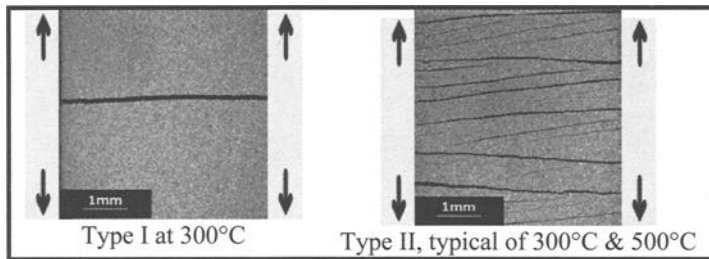


FIG. 1—Illustration of the surface crack behavior of coating types II and I. Arrows indicate tensile loading direction.

So a major difference exists with respect to the cracking behavior at 500°C and below: Type I exhibit single crack mode, whereas Type II is referred to as multiple crack mode. Note that for both types of coatings the tensile tests at 900°C did not produce any surface cracks within the 5% strain range.

Fractographic Analysis

After testing, cross sections of selected samples have been metallographically prepared for SEM investigation and analyzed by means of EDS. The micrographs in Fig. 2 are representative of the evolution of the cracks from the coating-substrate interface towards the surface (Fig. 2a) and within precipitates located at the coating/substrate interface region (Fig. 2b). The initiation of the coating cracks relates to the cracking of these precipitates, which consist of alumina oxides (as suggested by EDS), and which are randomly distributed at the interface in the interdiffusion zone of the coating. Frequently, cracks are observed to bridge cracked precipitates before propagating towards the surface (Fig. 2a).

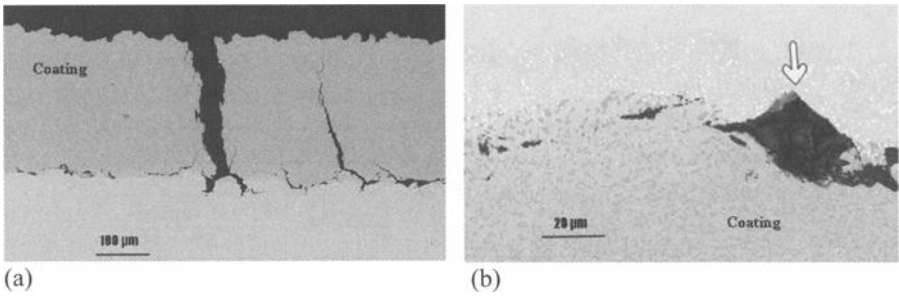


FIG. 2—Scanning electron micrographs, as prepared from Specimen A2 [Type II, 300°C, micrograph (a)] and Specimen A5 [Type I, 700°C, micrograph (b)].

AE Analysis

By following the cluster analysis procedure outlined above and utilizing amplitude, rise time, duration, and counts as descriptors three distinct groups of signals (clusters) resulted (Fig. 3).

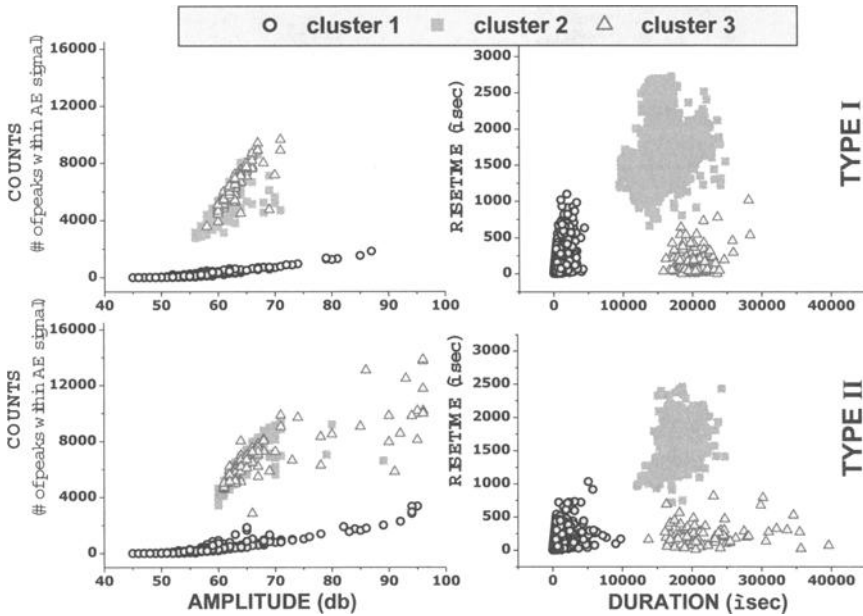


FIG. 3—Clustering of AE signals in the descriptor domain at 500°C.

From the location of each cluster in the descriptor domain and its individual activity in the time domain it becomes apparent that Cluster 3 results from a superposition of simultaneously recorded events of the types that form Clusters 1 and 2. However, the available AE information is not sufficient for a direct deconvolution of Cluster 3 into

signals corresponding to the two generic clusters. Therefore, an indirect method was required to analyze the information provided by Cluster 3. Given the premise that Cluster 3 is constituted by pairs of simultaneously recorded events, which are actually characteristic of Clusters 1 and 2, the question arises whether these are randomly superimposed pairs of events originating from different locations in the specimen (uncorrelated events), or whether one event is inducing the other one in its immediate vicinity (correlated events).

To address this question, one may estimate the probability that a Cluster 2 event happens to be initiated during the time window defined by the duration of a Cluster 1 event, and vice versa. The number of the expected uncorrelated Cluster 3 events can then be calculated and compared with the actually observed number of events in Cluster 3. If more Cluster 3 events are observed than expected from uncorrelated superposition, one concludes that the underlying micromechanisms are interrelated, rather than superimposed independently.

The ratio q between the number of actually observed events in Cluster 3 and the number of events expected if Cluster 3 originated from uncorrelated superposition of independent pairs of events pertaining to Clusters 1 and 2 is given by

$$q = \frac{n_{3,obs}}{n_{3,uncor}} \quad (1)$$

with

$$n_{3,uncor} = \frac{n_{1,eff}n_{2,eff}}{\Delta t_{tot}} \langle \Delta t_1 \rangle + \frac{n_{2,eff}n_{1,eff}}{\Delta t_{tot}} \langle \Delta t_2 \rangle \quad (2)$$

where $n_{1,2,eff} = n_{1,2,obs} + n_{3,obs}$ is the effective number of events in Clusters 1 and 2, Δt_{tot} is the duration of the AE active part of the test, and $\langle \Delta t_{1,2} \rangle$ are the average durations of signals of Cluster 1 and 2, respectively.

The ratio q shows a strong increase with temperature, as summarized in Table 2. This leads to the conclusion that at the lower temperatures (300°C and 500°C), Cluster 3 results from uncorrelated pairs of events, whereas the significantly higher q values at the highest temperature (700°C) must be attributed to an interaction of the damage processes underlying Clusters 1 and 2. The observed dependence of q on temperature also reflects the ductile-to-brittle transitions (DBT) of the overlay coatings (Type I and II), which occur around 500°C.

TABLE 2—*Values of correlation factor q .*

Temperature	Type I	Type II
300°	4	2.5
500°	0.68	6.3
700°	115	23

Discussion

The cluster analysis revealed that all AE activity could be traced back to two concurring damage mechanisms, as characterized by Clusters 1 and 2. It is characteristic of AE events belonging to Cluster 1 that certain AE features, such as amplitude, energy,

rise time and counts to peak, are decreasing with increasing test temperature. This temperature dependence of Cluster 1 was observed irrespectively of the type of coating. The fact that the temperature dependence of the AE parameters goes along with the change from brittle to ductile behavior of the coatings (DBT temperatures are around 500°C), suggests that the ductility of the coating plays a significant role in the signature of Cluster 1 in the descriptor domain. The majority of AE events belonging to Cluster 1 are registered during the straining periods of the stepwise tensile tests, while its activity sets in only after a minimum stress, ca. 500 MPa, is exceeded. Furthermore, combining the information provided by the video imaging system with that from the AE monitoring, it is revealed that those AE events from Cluster 1 (as well as those AE events from Cluster 3), which exhibit the highest values of amplitude (>90db), coincide with the appearance of surface cracks. Thus, Cluster 1 can be attributed to crack growth in the coating, either towards the surface or along the interdiffusion zone between coating and substrate.

As opposed to that, Cluster 2 comprises AE events whose parameter values are fairly constant up to 700°C, while the events cease to appear at 900°C. Signals of Cluster 2 are registered continuously during the whole test (during straining and dwell intervals) and its activity starts already at stress values as low as about 200 MPa. It is important to note that Cluster 2 precedes Cluster 1 in time, i.e., the activation of Cluster 2 appears to be a prerequisite for the subsequent activation of Cluster 1. Consequently, Cluster 2 is associated with the precipitate cracking in the interdiffusion zone that has been clearly evidenced by the microstructural investigations. The absence of Cluster 2 at 900°C is attributed to the extreme ductility of the coating. At that high temperature the MCrAlY matrix relaxes the applied stress almost completely so that the critical stress for precipitate cracking is not reached within the coating [8].

Below 500°C, Cluster 3 results from the superposition of independent events stemming from different locations, whereas in the ductile regime at 700°C the Cluster 3 activity is induced by pairs of events from the same location. Therefore, as Cluster 2 relates to the fracture of Al-O rich precipitates and Cluster 1 to crack growth inside the coating, the prevailing damage processes can be separated in two stages. In the low-temperature stage (< 500°C), precipitate cracking on the one hand and crack growth on the other hand represent two independent processes, which are occurring in parallel and which are associated with Clusters 2 and 1, respectively. In this low-temperature stage, Cluster 3 mainly results from a random superposition of independent events from the other two clusters.

At 700°C, the two above-mentioned damage processes still combine to form Cluster 3 events. However, these events now relate to crack growth, which is strongly related to the fracture of precipitates. The corresponding damage mode can be envisaged in terms of precipitate cracking and bridging of cracked precipitates. As the precipitates are located in the interdiffusion zone of the coating/substrate interface, this damage mode is confined to the interface, which is in accordance with the fact that no surface cracks have been observed at 700°C. At the transition temperature around 500°C, the high-temperature and low-temperature damage modes seem to be co-existing, and the damage processes include (i) precipitate cracking, (ii) crack growth, and (iii) bridging of cracked precipitates.

TMF Tests

The TMF results and post mortem fractographic and microstructural analyses of the samples have been reported and discussed elsewhere [9]. As such, a few relevant results will be presented only here, namely the pronounced cyclic creep during the first cycles caused by the accumulation of compressive inelastic deformation due to plastic flow at high temperature (Fig. 4), and the cracking mode (Mode I) of the coating based on the microstructural investigation, which revealed that cracks are initiated in the coating at the coating/substrate interface, grow towards the surface, and finally propagate also into the substrate by Mode I extension, producing a crack front almost parallel to the specimen surface and a crack path perpendicular to the loading direction. This is obvious from Fig. 5, which also shows the triple-layer structure of the coating.

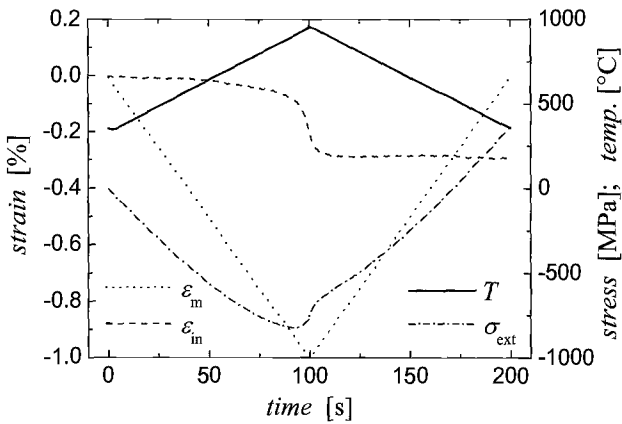


FIG. 4—Thermomechanical behavior of uncoated CG CM186 sample during the first cycle (ϵ_m : mechanical strain, ϵ_{in} : inelastic strain, T : temperature, σ_{ext} : external tensile stress).

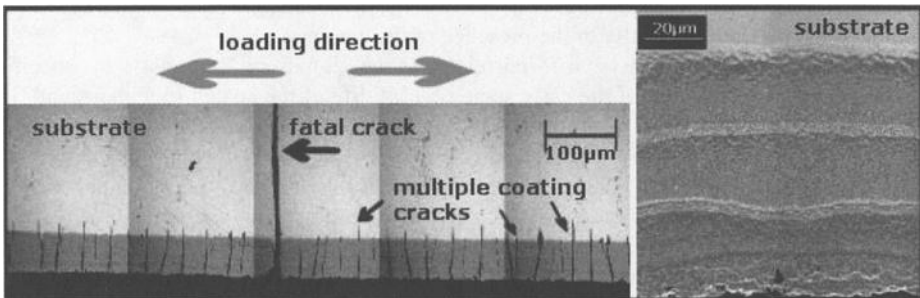


FIG. 5—Post-mortem scanning electron micrographs from a coated CM186 sample.

AE Analysis

For the analysis, the AE signals were separated according to the mechanical load state of the system when they were received: compressive or tensile signals. Table 3 presents the above information for each test. A first conclusion resulting from Table 3 is that more AE signals were received from the coated specimens. Where this is mainly due to the AE activity during tension, some increase of AE events between coated and uncoated specimens was also observed during the compressive part of the TMF cycle.

When the overall AE activity during the test is considered, two distinct regimes of AE activity are revealed, Regions I and II in Fig. 6, which are sometimes (but not necessarily, cf. Fig. 8*b*) separated by an inactive period. In the case of the coated samples, both regimes are present, whereas in the case of the uncoated samples only Region II is active during the last 20% of the TMF life (Fig. 6).

TABLE 3—*Experimental conditions and AE activity in terms of number of AE events.*

Specimen	TM1	TM2	TM3	TM5	TM7	TM9
Material	SC	SC	SC, coated	SC, coated	CG	CG, coated
Mechanical strain range	1%	0.8%	1%	0.8%	1%	1%
TMF lives (# cycles)	1941	9165	1121	5300	1412	2404
AE events in tension	749	1309	2393	7022	742	14693
AE events in compression	2491	4238	4813	5918	850	2629
AE events in Region I						
in tension	1675	6484	...	6453
in compression	1475	1640	...	1892
End of Reg. I (cycle #)	335	2508	...	933
(% of TMF life)			(30%)	(47%)		(39%)
First crack at cycle #	600	1000	200	300	400	200

This observation provides a clear distinction between signals originating exclusively from the coating (Region I) and those involving also the substrate (Region II). Therefore, signals from Region I relate to damage processes in, or induced by the presence of the coating, while signals from Region II reflect the mechanical response of the whole material system independently of the presence of the coating.

Thus, the objective has been to correlate (i) the signals of Region I with specific damage micromechanisms at the early stage of TMF life of the coated specimens and (ii) the signals of Region II with the final damage evolution leading to failure. This information is caught from a cluster analysis of the AE activity inside both regions, in conjunction with the video imaging observations. For this purpose, the AE data from the coated samples have been divided into two data sets. Initially only the AE data belonging to Region I, as presented in Table 3, are taken into account. Table 3 includes also the number of cycles after which surface cracks became visible, as made available by the in situ video imaging system.

The number of signals of Region I received during the compressive parts of the cycles is comparable for the three coated tests (Table 3) while their activity fades away well before the end of Region I. Hence, the AE activity during compression does not seem to have a direct effect on TMF life.

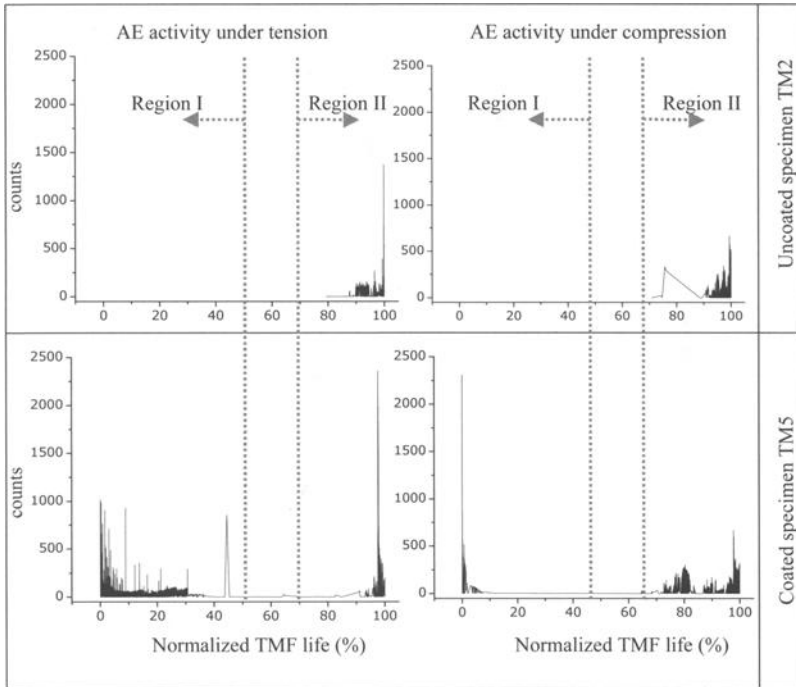


FIG. 6—AE activity for a coated and an uncoated specimen throughout the test.

However, this AE activity in the compressive part of the early cycles reflects the excess inelastic compression of the coating at high temperatures that induces tensile internal stress in excess to the substrate during the low temperature part of the cycles. The tensile stresses in turn, are expected to have a detrimental effect on TMF lives, as they induce cracking of the coating. What is clearly distinct among the three tests, yet, is the AE activity during the tensile parts of the cycles, as seen in Table 3. As such, it was decided to use these AE data for the pattern recognition analysis.

Classification of the AE data

For a cluster analysis of the AE signals from Region I, the AE parameters (i) counts, (ii) amplitude, (iii) duration, and (iv) counts to peak were chosen as the appropriate descriptors for the classification, while the temperature and the cycle number were used as additional external descriptors to establish the correlation with the mechanical behavior. A typical classification result obtained by the cluster method is presented in Fig. 7, which reveals the trend of specific clusters to form “branches.”

The cluster analysis revealed that for each TMF test at least one cluster (actually two clusters in the case of TM3) emerged already during the first TMF cycles close to the maximum stresses, i.e., minimum temperature, imposed in the cycles (cf. Cluster 5 in Fig. 7). These clusters correspond to AE signals with high values of all AE features, in particular, amplitude, duration, and energy. As far as the time domain with respect to the

video imaging observations is concerned, the clusters refer to AE events, which occurred prior to the detection of any surface cracks, continued to be present after the appearance of surface cracks, while their activity was decreasing and finally vanished well before the end of Region I was reached. For reasons explained below, the damage mechanism underlying these clusters is referred to as an *athermal process*.

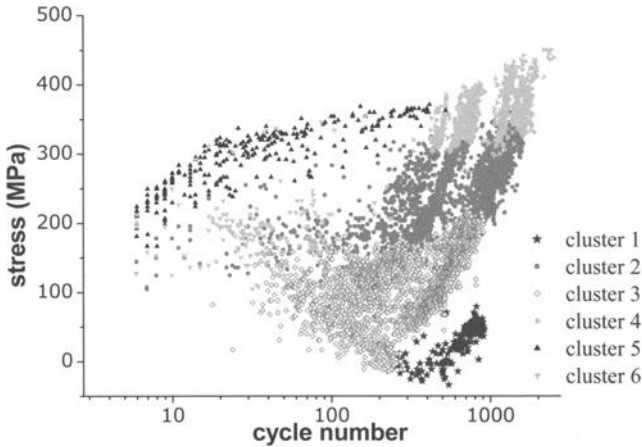


FIG. 7—Cluster analysis result for specimen TM5.

A second distinct group of clusters is the one that exhibits the aforementioned branching behavior (Clusters 2, 3, and 4 for TM5, cf. Fig. 7). The initiation of these clusters is closely related to the appearance of surface cracks. The behavior in the AE parameter domain was found to change gradually during the cyclic evolution of the branches. While the values of duration and amplitude were almost constant, the values of counts to peak and energy started from medium values at the beginning of each branch underwent a minimum and finally reached the highest values at the end of the branches. The evolution of the characteristic stresses (Fig. 7) points to a *thermally activated process* as the underlying damage mechanism that gives rise to these AE branches.

Discussion

For an interpretation of those AE clusters in terms of damage processes, it is necessary to consider (i) the characteristic stresses at which AE activity is observed and (ii) whether or not the AE activity is exhausted at a certain stage of TMF life. While the first criterion reflects a possible contribution of thermal activation in the damage process, the second criterion gives information on the possibly limited number of sources that may cause the AE events.

In view of these criteria, the first type of AE clusters can be associated with an athermal damage process, since the corresponding AE activity peaks at the highest tensile stresses available in the TMF cycles, without showing any characteristic temperature dependence. Furthermore, the gradual decrease in activity with increasing cycle number indicates that, given the stress range, only a limited number of 'sites' is available to contribute to this type of AE activity. Together with the observation that the AE activity

commences already in the tensile part of the first cycle and, hence, precedes any other kind of activity in tension, this damage process can be attributed to brittle crack nucleation. Presumably this is associated to precipitate (silicide) cracking at the interface, which commences with the largest precipitates and subsequently involves smaller ones as the maximum tensile stresses increase with increasing cycle number. The exhaustion of the corresponding AE activity can then be explained by assuming that eventually the available stress does not suffice for further cracking of small precipitates/precipitate fragments.

As opposed to that athermal process, the second type of AE clusters, which exhibit the branching behavior, is characterized by narrow stress intervals of occurrence that carry over to characteristic temperatures if the cyclic evolution of internal stresses is also taken into account. Given the athermal crack nucleation at the interface, which precedes those branches, it is natural to associate the branches with the growth of cracks inside the coating, perpendicular to the loading direction and parallel to the surface.

The fact that the characteristic stresses of those branches first decrease with cycle number, pass through a minimum, and finally increase again (Fig. 7), relates to the cyclic evolution of internal stresses. The initial downward branching is supposed to be associated with the plastic compression at high temperature of the ductile coating, in excess to the substrate. In the low and intermediate temperature regimes of the cycles, this excess plastic compression gives rise to excess tensile stresses, which assist the thermally activated crack growth. Consequently, as these tensile internal stresses gradually build up, AE activity is occurring at decreasing applied stress levels. At some point, however, a counteracting relief of tensile stresses due to multiple cracking of the coating balances the downward branching. As the post-mortem fractographic analyses have revealed (Fig. 5), dense arrays of coating cracks develop due to the lateral growth of these cracks along the surface (average crack spacing $\approx 60\mu\text{m}$, which is to be compared to the average crack depth $\approx 80\mu\text{m}$ corresponding roughly to the thickness of the coating). This will tend to shield a considerable part of the applied tensile stress and the internal tensile stresses developed by excess plastic deformation. This kind of crack interaction is the reason why the branch is turned upward and continues until the characteristic stress exceeds the maximum stress reached in the TMF cycle (and governed by the bulk mechanical behavior). Then the stress level available is no longer sufficient to maintain the thermally activated surface cracking.

It should be noted that the discussion given so far refers to a single branch, whereas in Figs. 7 and 8 several of them can be discerned which evolve almost parallel to each other in the $\sigma_{\text{ext}}-N$ plane. It is natural to assume that this multiple branching relates to different crack growth configurations, which are associated with the triple-layer structure of the coating, Fig. 5, and which involve slightly different internal stresses assisting/obstructing the propagation of the crack configurations.

Future AE Analysis in TMF Tests

As a next step, the AE data recorded during the late stages of the TMF tests, i.e., events from the aforementioned Region II are considered. This stage is also important as it may reveal precursory events before the immanent failure due to the fatal fatigue crack growth becomes obvious from the mechanical response of the specimens.

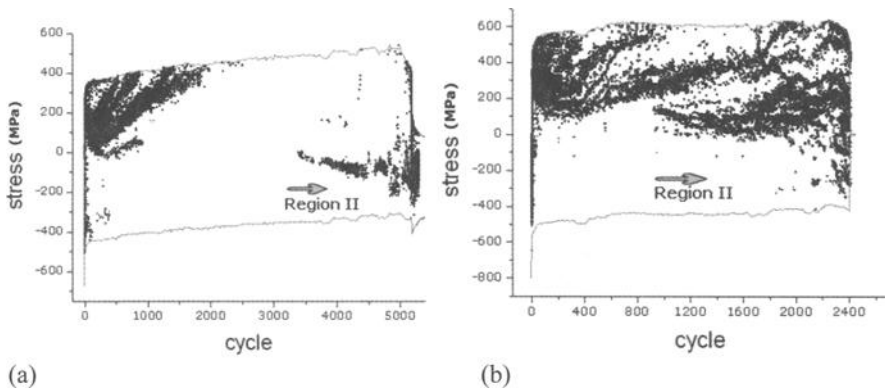


FIG. 8—AE events (symbols) and cyclic maximum and minimum stress envelopes (solid lines) during TMF tests for SC (a) and CG (b) coated samples.

Figure 8 shows two examples of the overall AE activity. For the SC sample, Region II is well separated from Region I by an inactive period, which is missing in the case of the CG sample. In both cases, AE activity in Region II starts at an intermediate stress level (close to zero stress or slight compressive stresses), and it spreads with respect to its stress range of occurrence, while its rate of activity increases as TMF cycling continues. At a certain point of TMF life (80–90%) another type of AE activity emerges, which relates to the maximum stresses (min. temp.) available within the TMF cycles. This AE activity accompanies the ultimate fatigue crack propagation (Fig. 9).

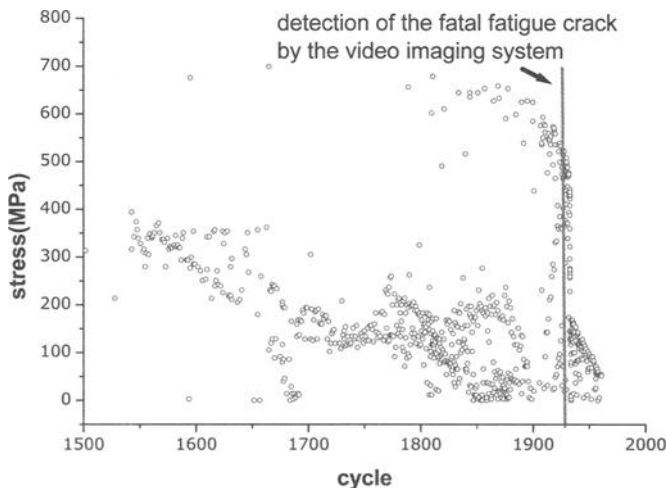


FIG. 9—Last stage (Region II) of AE data under tension for an uncoated sample (TM1).

Figures 6 and 8 show that Region II may start as early as approximately 40% of the ultimate TMF life; thus, providing important information about damage mechanisms

preceding the propagation of the fatal crack. Further analysis of this last part of the AE data is needed to consolidate the observed trend for these samples; by studying the signature of Region II in the AE parameter domain it may be possible to relate the Region II AE activity to specific damage mechanisms.

Conclusions

The analysis of the AE data generated during the previously described experiments revealed valuable information about the validity of AE as a method to monitor and identify damage processes. Utilizing these methodically and judiciously analyzed AE data and combining it with information provided by mechanical, video and post mortem observations, the damage evolution was monitored and damage assessment could be performed. Furthermore, by classifying the AE data into clusters, groups of signals in various cases were correlated with pre-identified damage mechanisms. Future analysis is expected to reveal common trends of these material systems concerning the signature of the AE data prior to the activation of surface damage processes. This opens up possibilities for life prediction methodologies for coated material systems during thermal and mechanical loading.

References

- [1] Affeldt E. E., "Influence of an Aluminide Coating on the TMF Life of a Single Crystal Nickel-Base Superalloy," *Journal of Engineering for Gas Turbines and Power*, Vol. 121, 1999, p. 687.
- [2] Martinez-Esnaola J. M., Arana M., Bressers J., Timm J., Martin-Meisoza, A., Bennett, A., et al., "Crack Initiation in an Aluminide Coated Single Crystal During Thermo-Mechanical Fatigue," *Thermo-mechanical Fatigue Behavior of Materials, 2nd Vol., ASTM STP 1263*, M. J. Verrilli and M. G. Castelli, Eds., ASTM International, West Conshohocken, PA, 1995, p. 68.
- [3] Wood M. I., "The Mechanical Properties of Coatings and Coated Systems," *Materials Science and Engineering A*, Vol. A121, 1989, pp. 633–643.
- [4] Burgel, R., "Coating Service Experience with Industrial Gas Turbines," *Materials Science and Technology*, Vol. 2, 1986, pp. 302–308.
- [5] Arrell, D. J. and Wieneke, B., "An in-situ Optical Technique for Surface Strain Evolution Measurement," *Nontraditional Methods of Sensing Stress, Strain and Damage in Materials and Structures, 2nd Vol., ASTM STP 1323*, G. F. Lucas, P. C. McKeighan, and J. S. Ransom, Eds., ASTM International, West Conshohocken, PA, 2000.
- [6] Physical Acoustics Corporation, Princeton, NJ.
- [7] Pappas, Y. Z, Markopoulos, Y. P., Kostopoulos, V., Paipetis, S. A., "Failure Mechanism Analysis of Ceramic Matrix Composites on the Pattern Recognition Approach of Acoustic Emission," *1st Hellenic Conference on Composite Materials and Structures*, Ksanthi 1997, pp. 192–206.
- [8] Kowalewski R. and Mughrabi H., "Thermo-Mechanical and Isothermal Fatigue of a Coated Columnar-Grained Directionally Solidified Nickel-Base Superalloy," *Thermo-mechanical Fatigue Behavior of Materials, 3rd Vol., ASTM STP 1371*, H. Sehitoglu and H. J. Maier, Eds., ASTM International, West Conshohocken, PA, 2000, p.3.
- [9] Peteves S. D., De Haan F., Timm J., Bressers J, Hughes P. M., Moss S. J., et al., "Effect of Coating on the TMF Lives of Single Crystal and Columnar Grained Cm186 Blade Alloy," *Proceedings of the 9th International Symposium on Superalloys, Superalloys 2000*, 17–21 Sept., 2000, pp. 655–665.

B. Roebuck,¹ M. G. Gee,¹ A. Gant,¹ and M. S. Loveday¹

Miniature Thermomechanical Ramping Tests for Accelerated Material Discrimination

REFERENCE: Roebuck, B., Gee, M. G., Grant, A., and Loveday, M. S., "Miniature Thermomechanical Ramping Tests for Accelerated Material Discrimination," *Thermomechanical Fatigue Behavior of Materials: 4th Volume, ASTM STP 1428*, M. A. McGaw, S. Kalluri, J. Bressers, and S. D. Peteves, Eds., ASTM International, West Conshohocken, PA, Online, Available: www.astm.org/STP/1428/1428_10600, 3 March 2003.

ABSTRACT: Conventional thermomechanical fatigue tests are usually performed under conditions of close control of strain amplitude, temperature cycle, loading rates, and frequency—mainly for the purposes of developing data for design. However, in some cases, it is helpful to have a rapid assessment of the likely response to specific thermomechanical environments of those materials, particularly when new materials are being developed, or when material is in short supply, or when material production processes have been changed.

For this purpose a miniature test system, developed at the National Physical Laboratory, has been evaluated for its ability to discriminate between different materials under these general circumstances, but with conditions of ramping load or temperature to accelerate material response and failure characteristics.

The miniature test system uses D-C current to heat test pieces to appropriate temperatures, up to 1300°C in under a minute if necessary, using small cross-sectional (2×1 mm) rectangular samples. Strain was measured using changes in electrical resistance of the central 2–3 mm of the gage length (16–20-mm grip separation), where temperature was known to be acceptably uniform.

Several material types were studied, including a powder metallurgy high speed steel, cemented carbides, a refractory metal, Ta, and a Ni-base superalloy. Tests were performed under combinations of either ramping load or temperature ramping. The system was shown to discriminate well between the different materials under various conditions of the thermomechanical environment with respect to the effects of accumulated strain.

KEYWORDS: thermomechanical, miniature, ramping tests, high temperature properties

Introduction

Reliable thermomechanical fatigue (TMF) data are required for predicting the life of a number of safety critical components and for the design of such components to ensure their efficient operation over longer periods of time, or at higher temperatures, particularly in the power generation, transport (road, rail, and air), and process industry sectors. In the transport sector, improved design can lead to reduced weight, resulting in improved fuel economy with the consequent beneficial impact on the environment by reducing emissions.

The purpose of TMF studies is twofold: first and foremost, to obtain engineering relationships and mathematical models for macroscopic material behavior, allowing the design, evaluation, and validation of engineering components; second, to gain deeper understanding of deformation behavior and damage initiation and growth as influenced

¹Materials Centre, National Physical Laboratory, Queens Road, Teddington, Middlesex, TW11 0LW, UK.

by microstructure. Materials and mechanics scientists conducting basic research are interested in the second goal, while the first goal is pursued by engineers and designers who are integrating this basic information and the experimental data to develop structural models for application in component design, as well as for the validation of the design. The reliability of the test results, therefore, has implications with respect to safety in, for example, aero-engines, as well as with regard to economy of operation. An example of the latter is the cost associated with critical component failure in a power plant.

Conventional TMF testing is aimed at simulating the thermomechanical loading history of critical volume elements in components in a laboratory test setup. This is achieved by exposing the test specimen synchronously to a temperature cycle and to a mechanical strain cycle, applied at predefined rates between given temperature and strain limits. The phase angle between the temperature and strain cycles is chosen to represent the condition in a given volume element of the component. Spatial uniformity of the temperature and mechanical strain (that both change with time) over the volume of the test specimen's gage length is critical and must be maintained at all times. Continuous measurement of the corresponding stress provides the unique relationship between stress, strain, and temperature that controls the behavior of the material in the selected volume element of the component.

There are several reasons for using miniature tests. For example, test pieces can be taken from in-service components and tested to assess material degradation without, in principle, affecting performance. Often advanced materials are in short supply, and thus, the use of small test pieces can accelerate the production of useful data. However, strain measurement becomes more difficult as the test piece size diminishes. Extensometers are typically used on gage lengths of 10–25 mm, but smaller test pieces present some problems in the use of conventional extensometers. An innovative method of strain measurement based on resistance changes was developed in the current work to circumvent the extensometer problem.

Conventional thermomechanical tests usually apply a well defined strain-temperature cycle to the test piece and measure various parameters as a function of number of deformation cycles, such as the drop in load that occurs as damage develops [1,2]. This procedure generates information vital for lifing components. However, there is another aspect to thermomechanical testing—that of assessing the relative abilities of new materials to resist thermomechanical deformation and that of characterizing the effects of changes in microstructure that occur during service life. In the current work, this aspect of thermomechanical deformation has been evaluated using a new miniature system employing various forms of parameter ramping. This approach was chosen to accelerate the acquisition of data. There are many possibilities:

- [1] Temperature and stress ramping monotonically;
- [2] Either temperature or stress ramping with the other constant;
- [3] Temperature and stress cycling, but with increasing amplitude (ramping);
- [4] Either temperature or stress cycling with one constant amplitude and the other with a ramping amplitude.

Aspects of this testing envelope were assessed in the current project on a number of materials in a new thermomechanical test system (the ETMT), where the use of miniature

test pieces allows more rapid heating and cooling rates than are possible in conventional systems. The test method involved the use of a miniature electro-mechanical test system in which direct current is used to heat the test piece.

The primary objective of this work was to evaluate the versatility of the ETMT for performing accelerated ramping tests to assess the thermomechanical deformation resistance of materials for elevated temperature service performance.

Test System

The miniature electro-thermomechanical test system (the ETMT) has been developed at NPL [3–5] to obtain multiproperty data over a range of temperatures. The system uses D-C electric current to heat rectangular cross section test pieces. Strain is measured using changes in electrical resistance. Both thermal and mechanical loads can be cycled.

The ETMT can perform experiments that can be categorized into three types:

- [1] Measurement of physical properties, such as thermal expansion and conductivity;
- [2] Measurement of mechanical properties, such as creep, fatigue, and strength;
- [3] Measurement of microstructural stability under thermal exposure, such as recrystallization and phase transformation.

The ETMT consists of an environmental chamber ($500 \times 250 \times 120$ mm) with electrical leadthroughs, water cooled grips, and inert gas supply for prevention of test piece oxidation. A computer-controlled d-c heating power supply (200 A) is used to heat the specimen, with an integral test piece resistance and thermocouple measurement facility. Test piece geometries are determined by test piece resistance. Metallic test pieces are typically 2×1 mm cross section along the full length of the test piece (40 mm). The gripped ends are typically 10–15-mm long leaving a freely suspended central portion of 10–20 mm, Fig 1. Heating rates up to 200°C s^{-1} are possible, dependent on the thermal characteristics of the test piece. Cooling rates are determined by the thermal diffusivity of the test piece and loss of heat to grips. This can typically be between 100°C s^{-1} or 10°C s^{-1} for good and poor conductors, respectively. The test piece grips are held at a fixed temperature (room temperature) to provide a constant reference point. This results in a parabolic temperature distribution for test pieces smaller than about 20 mm in length with a central temperature up to 800°C . Temperature distributions in test pieces heated to much higher temperatures are more uniform in the central 2–4 mm of the test piece, typically less than $\pm 5^\circ\text{C}$ at a central temperature of 1250°C . The system uses a mechanical loading assembly (± 4 kN maximum), with an in-line drive and a versatile gripping system, a load cell (0.5 N resolution) and capacitance displacement transducers (0.4- μm resolution). A computer-controlled motor is included for null, mean, ramping, or fatigue load capability (in- or out-of-phase d-c current cycle), or constant displacement tests for stress relaxation or thermal shock experiments. The motor response is set to about 1000 N s^{-1} for nominally square wave fatigue experiments, while maintaining less than about 0.5 % overshoot of maximum load. Uniaxial tests can have variable (step loading) rates, typically 0.1–20 N s^{-1} . Full thermomechanical control is possible in load or displacement control modes with options for sinusoidal, triangular, trapezoidal, or arbitrary waveforms for both load and temperature, together with any

degree of phase lag. Full strain control is not yet possible, due to the difficulty of strain measurement on such small test pieces. The system uses customized LabView[®] software to monitor and control tests and temperature cycles by appropriate feedback control.

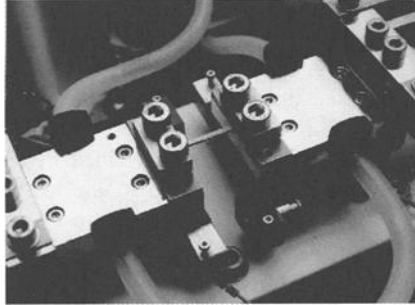


FIG.1—Close-up photograph of test piece and grips.

Temperature Measurement and Distribution

Because the test piece is held in water-cooled grips, a nonuniform temperature distribution develops along the test piece. Measurements and analysis [1–3] have shown that the steady state temperature profile along the test piece is parabolic at temperatures up to about 800°C. The indicated temperature of the central 3 mm of the test piece is approximately within the range:

$$\begin{array}{ll} \pm 1^{\circ}\text{C up to } 200^{\circ}\text{C} & \pm 2^{\circ}\text{C at } 200\text{--}400^{\circ}\text{C} \\ \pm 3^{\circ}\text{C at } 400\text{--}1000^{\circ}\text{C} & \pm 5^{\circ}\text{C at } 1000\text{--}1500^{\circ}\text{C} \end{array}$$

The program software maintains control of temperature even if the test piece changes in cross section, providing the strain rate is not greater than about 0.01 s^{-1} . For uniaxial tests, the loading rate can be set between 0.05 and 1000 N s^{-1} . During the test, changes in length are monitored by the capacitance transducers mounted on the grips, and results are plotted as load against displacement. However, it must be noted that the displacement contains an element due to the compliance of the rig, which is about $0.05 \mu\text{m N}^{-1}$.

A further issue is the accuracy of temperature measurement, since thermocouples are made at NPL individually for each test, using 0.1-mm diameter wires of Pt and Pt-13 % Rh that are fusion welded to form a small bead. The bead is then spot welded to the test piece. Furthermore, the voltage is processed by a standard LabView[®] software routine to give a direct reading in degrees centigrade. A sample of pure Ti was used in order to check the combined ETMT software and thermocouple. Ti has a well-defined transformation temperature. Repeat measurements were made and the indicated temperature of the transformation was within 2°C of the handbook value for pure Ti. The resistance of the test piece was measured over a 3-mm length in the center, where it is known that the temperature is reasonably uniform. A two-color pyrometer has also been recently installed and can be used in the range 400–1200°C in situations where it is difficult to spot weld a conventional thermocouple.

Samples typically fracture and deform in the central region, which acts rather like a reduced cross section in a conventional test because the material is softer in this part of the test piece.

Strain Measurement

Because of the difficulties of deconvoluting the load/displacement data from rig compliance and with a temperature distribution, an alternative strain measurement procedure was developed based on the use of resistance measurements. Resistance is measured over the central 2–3 mm of the test piece, where the temperature distribution is reasonably constant, using thin, 0.1 mm, spot welded Pt-13 % Rh wires as potential contacts. The resistance in the central 2–3 mm of the test piece changes significantly during a deformation test, due to a change in the cross-sectional area. The resistance increases in tension and decreases in compression. The following analysis was developed to allow true stress/strain data to be obtained from these changes. The resistances before and during deformation, R_s and R_t , are given by

$$R_s = rL_s/w_s h_s \text{ and } R_t = rL_t/w_t h_t \quad (1)$$

where r is the resistivity, L is the length between the contact points for measuring resistance, and w and h are the width and height of the test piece. Assuming that the volume, V , remains constant, and neglecting elastic changes

$$V_s = V_t = L_s w_s h_s = L_t w_t h_t \quad (2)$$

Consequently,

$$R_s/R_t = L_s^2/L_t^2 \quad (3)$$

Thus, true strain, ϵ , is given by

$$\epsilon = \ln(L_t/L_s) = \ln\sqrt{(R_t/R_s)} \quad (4)$$

which is a single expression allowing strain to be calculated as a function of the measured change in resistance.

The formulae given in Eqs 2–5 allow an uncertainty in the measurement of strain to be calculated from changes in resistance using a simplified analysis, since

$$\epsilon = \ln\sqrt{R_t/R_s} = \ln\sqrt{M} \quad (5)$$

where R_t/R_s is defined as M .

Thus, the fractional error in strain, $d\epsilon/\epsilon$, is given by

$$\frac{d\epsilon}{\epsilon} = \frac{1}{2 \ln\sqrt{M}} \frac{dM}{M} = \frac{1}{2\epsilon} \frac{dM}{M} \quad (6)$$

The fractional error in strain, $d\epsilon/\epsilon$, thus varies with strain and fractional error in the resistance ratio. The error in measurement of the resistance ratio, M , is dependent on material, but was typically 0.2%. Thus, the error in strain measurement at 5% strain was

about 2% of this value, i.e., $(5 \pm 0.1)\%$. The uncertainty is, however, larger at lower values of strain [6].

Materials, Test Pieces, and Tests

Ni Base Superalloy

The Ni base superalloy was Nimonic 901 obtained from Inco International Ltd, Hereford, UK, with a nominal wt % composition of 12.6 Cr; 5.8 Mo; 3.0 Ti; 0.2 Al; 0.25 Co; 0.1 Si; 0.1 Cu; 0.16 Mn; 0.04 C; balance Ni. Cast bars were extruded and homogenized at 1090°C for 3 h and air cooled.

Powder Metallurgy, High Speed Steel (PM HSS)

Three variants of M42 were tested. Two with different aging treatments (austenitized at 1150°C followed by triple tempers to either peak-age at 540°C or over-age at 575°C) and one with sulphide additions for improved high temperature tribological properties (also peak-aged). The materials were obtained from Federal Mogul Ltd, Coventry, UK. The nominal composition of the M42 HSS was 3–6% Cr; 6–11% Mo; 5–10% Co; 0.0–3% C; 0.3–2% Si; 0.5–3% V; 0.1–3% W; balance Fe.

Tantalum and WC Hardmetals (Cemented Carbides)

The pure tantalum samples were obtained from Plansee AG, Reutte, Austria, and tested in the as-received condition. Three hardmetals (cemented carbides) were tested in the as-received condition. Each was based on WC as the hard phase. Each cemented carbide contained an alloy binder phase that was different from the Co that is conventionally present. The nominal wt % composition and hardnesses of the three hardmetals were:

1300 HV30: 92 WC/8 Ni
 1950 HV30: 95 WC/5 Co/Ni
 1250 HV30: 80 WC/20 Fe/Ni/Co

The hardmetals were provided by the research group of the British Hardmetal Association.

Test pieces were wire electrodischarge machined (EDM) from larger blocks of material. The final sizes were rectangular, $1 \times 2 \times 40$ mm. The surfaces were lightly ground using fine SiC paper to clean off EDM residues. The following test types were examined:

Superalloy	Cyclic temperature, step ramp fatigue load
PM HSS	Constant temperature, step ramp fatigue load
	Constant load, temperature ramp
	Constant load, ramp fatigue temperature
Tantalum	Constant temperature, ramp fatigue load
Hardmetals	Constant temperature, step ramp load

The primary objective for all the different ramping tests was to generate information on the dependence of thermomechanical strain rate on stress and temperature in ramping

tests. The usual convention in high temperature deformation studies of plotting log strain rate against stress or inverse temperature was followed.

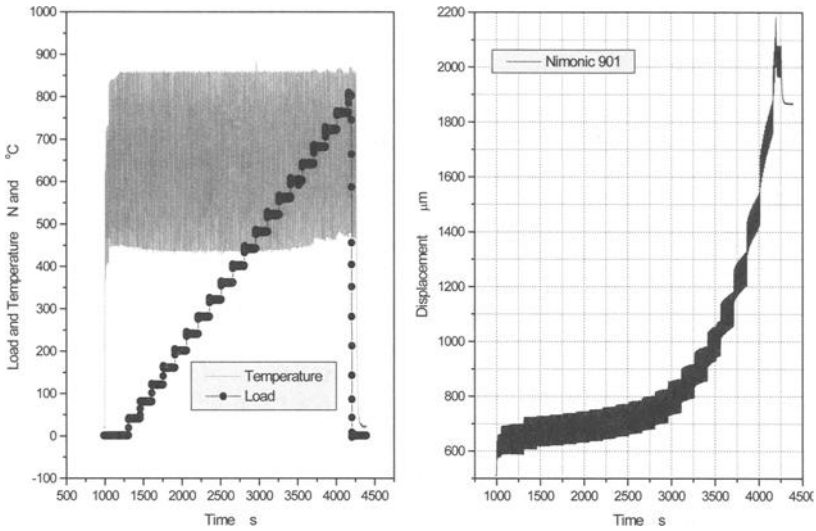


FIG. 2—Representative ramping test on Nimonic 901 superalloy.

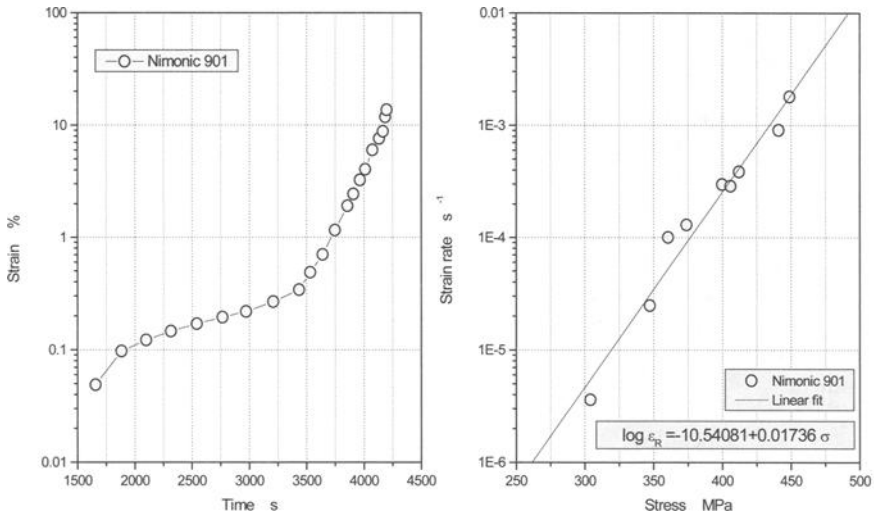


FIG. 3—Analysis of ramping test on Nimonic 901 superalloy.

Results and Discussion

Superalloy

The superalloy was used to illustrate a typical ramping test in which temperature was cycled (triangular, with a frequency of about 0.1 Hz) between 450 and 850°C, while the load was step ramped from 0 N in 50 N steps (equivalent to 25 MPa) about every 200 s until significant deformation had occurred (Fig. 2)—as indicated by the displacement/time plot. The resistance method was used to calculate strain, and this is shown as a strain/time plot in Fig. 3 from which the dependence of strain rate on stress was calculated (Fig. 3).

PM HSS

Two ramping procedures were evaluated in the tests on the three M42 PM HSS. Significant differences in thermomechanical behavior were sought that could be correlated with their different microstructures. In the first type of test, the load was held constant at 800 N (approximately 400 MPa) while the temperature was ramped at 2°C s^{-1} . In the second type of test, the temperature was held constant at 650°C, while the load was step ramped in a square wave fatigue mode with a frequency of 0.3 Hz and $R = 0$. The initial P_{max} was 500 N and was incremented by 100 N every 100 min. Typical outputs of displacement/time are shown in Fig. 4 for these two test types. Both tests show a clear discrimination between the different structures, with the peak-aged M42 being the most resistant to thermomechanical deformation.

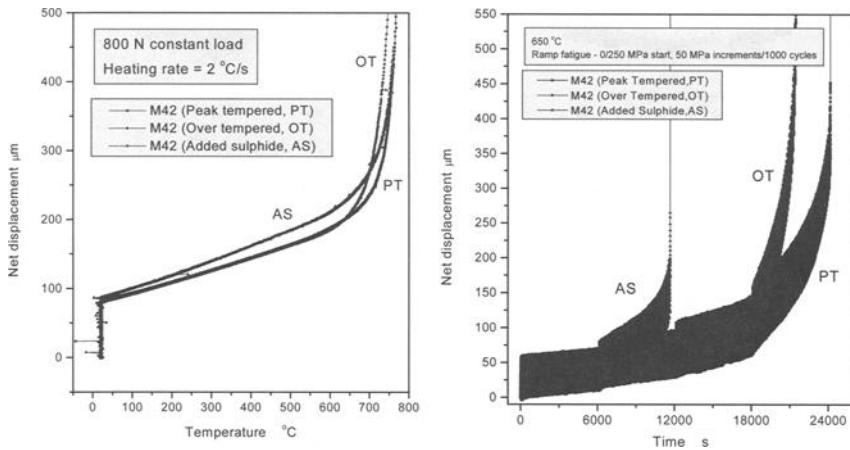


FIG. 4—Displacement/time plots for two different types of ramping test on PM HSS.

A plot of resistance/time is shown in Fig. 5 for the fatigue load, step ramp test. It can be seen that after an initial period the resistance rapidly increases, corresponding to significant deformation, and this increase was used to calculate the strain/time plot, also shown in Fig. 5. However, it can also be seen that, initially, for the two peak-aged M42 HSS, that the resistance decreases slightly. This corresponds to aging of the material, as the microstructure is not stable at 650°C. This is an illustration of the additional benefit of using resistance measurements, since they can be used to monitor the kinetics of phase changes as well as the strain that occurs during deformation. Clearly, to measure strain, the data have to be first corrected for any microstructural change. This is performed by conducting isothermal or isochronal tests with constant zero load.

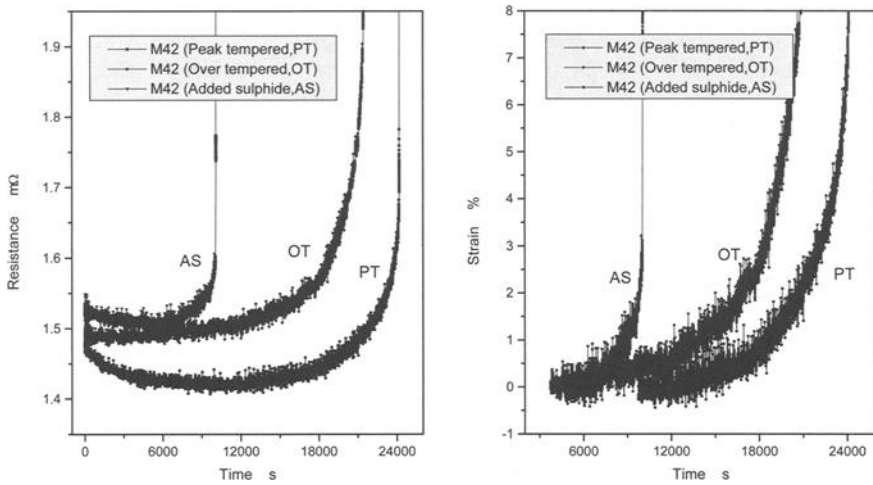


FIG. 5—Strain and resistance data at 650 °C from PM HSS tests.

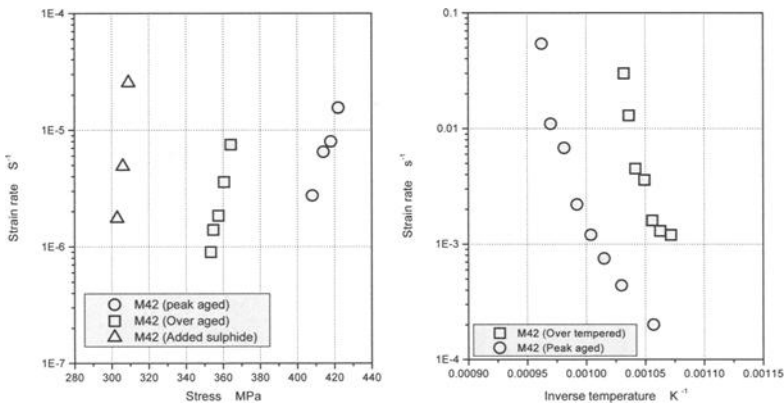


FIG. 6—Analysis of ramping test data on PM HSS.

The strain/time data from the two different ramping procedures were then converted to either strain rate/stress or strain rate/inverse temperature plots (Fig. 6), where it can be seen that the analysis discriminates well between the different metallurgical conditions.

Tantalum

For the tantalum samples, the ramping test comprised a constant temperature at 1100°C, together with a fatigue ramp load. In this case, a ramp was imposed in which P_{\max} was increased linearly with time while P_{\min} was held constant at 0 N (Fig. 7). There was some oxidation of the sample, even though the test was carried out in flowing argon. Consequently, as for the HSS tests, the resistance/time data had to be corrected for the effects of a loss in cross section due to oxidation. Clearly, the kinetics of oxidation could also be studied with the apparatus if needed—making it a true multiproperty test rig. A strain rate/stress diagram was then constructed (Fig. 7) that again showed characteristic linear log strain rate/stress thermomechanical behavior.

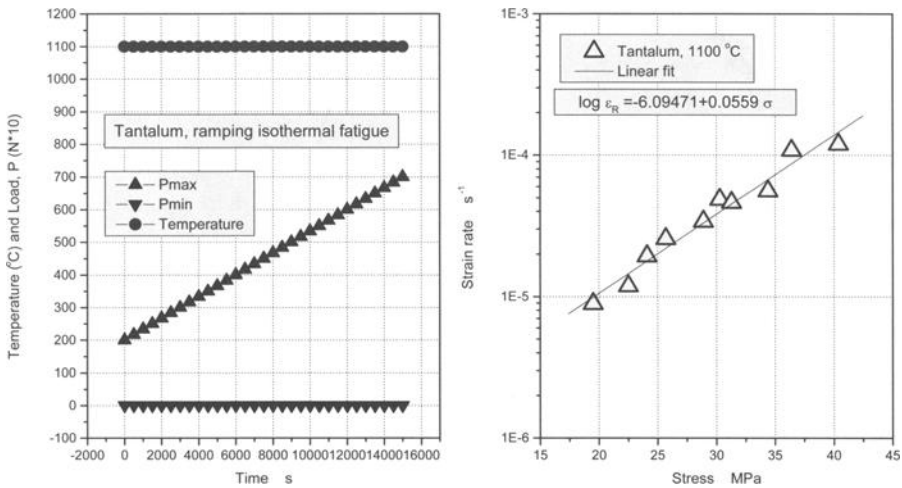


FIG. 7—Temperature constant/fatigue load ramp tests on tantalum.

Hardmetals

The ramp test on the hardmetals consisted of a step load ramp at a constant temperature of 850°C. These materials sometimes contain significant residual stresses. So, before each test, the sample was heated to about 1000°C and then cooled slowly (about 5°C s⁻¹). During this cycle data are captured relevant to thermal expansion and resistivity. Typical plots are shown in Fig. 8 where the phase transformation associated with the Fe/Co/Ni material can be seen at about 600°C in both the expansion and resistivity plots.

Figure 9 shows load/displacement plots for each material demonstrating good discrimination. The ramping test for the Ni and Co/Ni hardmetals was commenced at 400 N (200 MPa), and there was little deformation before what was essentially brittle fracture. The Fe/Co/Ni material was considerably more ductile, and so the test in this

case was started at 100 N (50 MPa). As in the tests on the other materials, this enabled log strain rate/stress plots to be calculated (Fig. 9) showing the typical linear correlation that is observed in high temperature deformation studies.

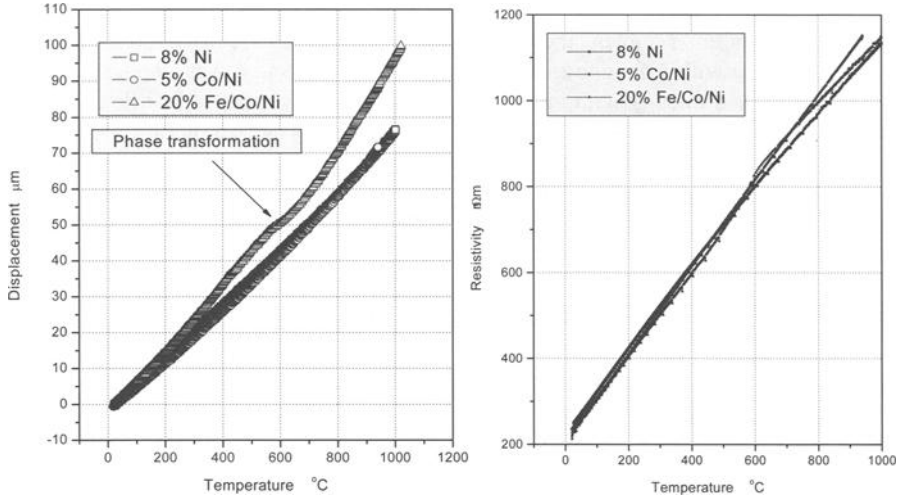


FIG. 8—Temperature dependence of expansion and resistivity for hardmetals.

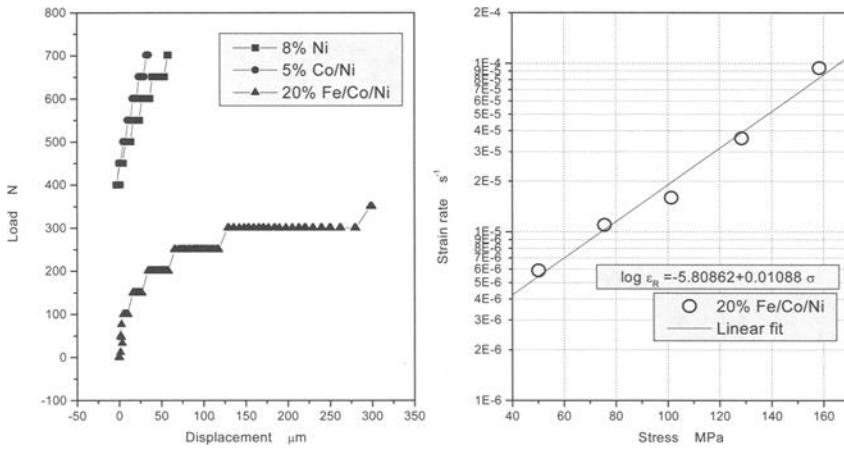


FIG. 9—Thermomechanical ramping data for hardmetals at 850°C.

Summary

A new test system for miniaturized thermomechanical tests has been evaluated for its ability to discriminate between materials in ramping experiments. Tests on a range of materials, including a refractory metal, two tool materials (cemented carbide and high speed steel), and an Ni base superalloy have demonstrated its versatility. A number of different ramping experiments were explored with the objective of measuring the dependence of deformation strain rate on applied stress. This was successfully achieved for all the materials evaluated. However, it was necessary to use an unconventional method for monitoring strain, using the change in electrical resistance as the test pieces experienced significant plastic deformation. The ramping tests were shown to discriminate particularly well between high speed steel materials in different states of heat treatment.

Acknowledgments

This work was performed with the support of the UK Department of Trade and Industry Measurement Programme on Characterisation and Performance of Materials (CPM). The authors would like to thank colleague M. Brooks for assistance with developing the Labview program. Also, thanks are due to Dr. P. Maulik, Federal Mogul Sintered Products, for supply of the HSS, the British Hardmetal Association for supply of the cemented carbides, and Plansee AG for supply of the tantalum.

References

- [1] Fleury, E. and Ha, J. S., "Thermomechanical Fatigue Behaviour of Ni Base Superalloy IN738LC Part 2—Lifetime Prediction," *Material Science and Technology*, Vol. 17, September 2001, pp. 1087–1092.
- [2] Jiang, Q. C., Fang, J. R., and Guan, Q. F., "Thermomechanical Fatigue Behaviour of Cr-Ni-Mo Cast Hot Work Die Steel," *Scripta Materialia*, Vol. 45, 2001, pp. 199–204.
- [3] Roebuck, B., Gee, M. G., Lord, J. D., and McCartney, L. N., "Miniature Thermal Cycling Tests on Aluminium Alloy Metal Matrix Composites," *International Conference on MMC VI*, Institute of Materials, London, November 1997; *Material Science and Technology*, September–October 1998, Vol. 14, pp. 1001–1008.
- [4] Dary, F.-C., Roebuck, B., and Gee, M. G., "Effects of Microstructure on the Thermo-mechanical Fatigue Response of Hardmetals using a New Miniaturised Testing Rig," *Sixth International Conference on the Science of Hard Materials*, Lanzarote, March 1998; *International Journal of Refractory Metals and Hard Materials*, Vol. 17, 1999, pp. 45–53.
- [5] Roebuck, B., Gee, M. G., Brooks, M., Cox, D., and Reed, R., "Miniature Multiproperty Tests at Elevated Temperatures," *COMPASS 99 Component Optimisation from Materials Properties and Simulation Software*, W. J. Evans, R. W. Evans, and M. R. Bache, Eds., University of Wales, Swansea, UK, March 29–April 1, 1999, pp. 233–240.
- [6] Roebuck, B., Lord, J. D., and Orkney, L. P., "Validation of a Miniature Tensile Strength Measurement System," *ASTM International Fourth Symposium on Small Specimen Test Techniques*, Reno, NV, January 23–25, 2001.

T. Brendel,¹ M. Naderhirn,¹ L. del Re,² and C. Schwaminger¹

Improving the Reproducibility and Control Accuracy of TMF Experiments with High Temperature Transients

REFERENCE: Brendel, T., Naderhirn, M., del Re, L., and Schwaminger, C., “Improving the Reproducibility and Control Accuracy of TMF Experiments with High Temperature Transients,” *Thermomechanical Fatigue Behavior of Materials: 4th Volume, ASTM STP 1428*, M. A. McGaw, S. Kalluri, J. Bressers, and S. D. Peteves, Eds., ASTM International, West Conshohocken, PA, Online, Available: www.astm.org/STP/1428/1428_10601, 3 Sept. 2002.

ABSTRACT: Three different approaches to minimize control deviations in the case of TMF experiments with high temperature transients (10K/s and higher) will be presented. In the first approach, an empirically derived algorithm is used to calculate a modified temperature command function based on the recorded control deviations. In a second approach, a two-zone model of the plant (specimen, grips, heating and cooling device) is used for control design. The model is first used to design a “soft” PI controller for generating a robust starting output profile. This output profile is then used as a basic reference input profile. The remaining error is minimized by a “fast” PI controller. A third controller approach is characterized by the determination of an inverse model that is used to define an “ideal” profile of the command variable. This “ideal” profile is then used as a reference input profile.

KEYWORDS: thermomechanical fatigue, temperature control, control design, inverse control, TMF

Motivation

In the design and construction of thermomechanically stressed components, such as those found in modern aircraft engines, stationary gas turbines, rocket engines and combustion engines, material data generated from TMF experiments are required for component lifetime predictions.

In order to gain reliable material data, it is necessary to achieve reproducible testing conditions and to keep the defined temperature-mechanical-strain cycle as exact as possible in the experiment. In order to realize a mechanical strain-control, during a non-isothermal cycle, it is necessary to record the thermal strain function by means of a suitable procedure. Then the total strain is calculated by adding the mechanical strain function to the measured thermal strain.

With constant environmental conditions, such as the ambient temperature, the temperature of the grips, the contact of the thermocouple to the specimen etc., an accuracy of +/-0.01% for the mechanical strain control is attainable with a stable, tuned temperature control loop. This causes a relative control deviation of 1% corresponding to a TMF test with 1% mechanical strain range.

¹ MTU Aero Engines GmbH, Dachauer Straße 665, D-80995 München, Germany.

² Institute of Automatic Control and Electrical Machines of the Johannes Kepler University, A-4040 Linz, Austria.

By controlling the temperature of the specimen with a customary PID-controller, a higher percentage control deviation occurs. This is due to the relatively slow processes of heat conduction and convection. In addition, the slow response times of heating and cooling devices causes a delayed response of the specimen temperature to the changing command variable.

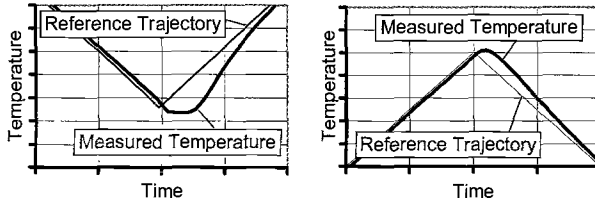


FIG. 1—Command and actual values at the turning points of the linear temperature command cycle. (Temperature and time units are arbitrarily chosen).

Figure 1 shows the control characteristics of the customary PID-controller with stable control parameters, into which an analog input of ideal triangle temperature cycles with transients is fed. At the turning points, in each case, overshoot and undershoot occurs. This corresponds to a deviation of approximately 5%, which is related to the total temperature range of a typical TMF cycle. The deviation in the linearity causes a distortion of the stress temperature loop, especially adjacent to the temperature turning points, and therefore influences the TMF-life. Furthermore the overshoot and undershoot characteristics are not reproducible and therefore contribute to the increase of the spread of data reducing the significance of each test. A larger number of tests are necessary for one statistically reliable test series. In the following, three methodologies are presented. These methodologies seek to minimize the described control deviations and thus increase the repeatability of each individual TMF test.

Approach 1: Empirical Algorithm for Input Profile Optimization

Experimental Background

Figure 2 shows the specimen during testing as well as the grips, the coil, the cooling air nozzles, the axial extensometer and the thermocouple. In order to keep the test conditions as constant as possible, the grips and the extensometer are water-cooled.

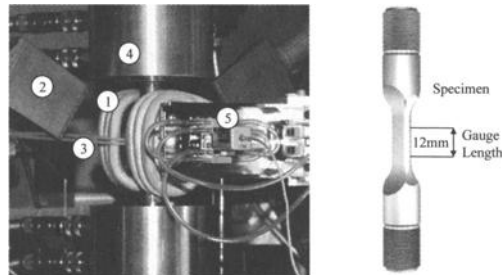


FIG. 2—Experimental set up with: induction coil (1), cooling air nozzle (2), thermocouple (3), water cooled grip (4), water cooled extensometer (5).

The coolant temperature for the extensometer is held constant by thermostat at $\pm 0.5\text{K}$ in order to minimize the influence of specimen and ambient temperature fluctuations on the extensometer.

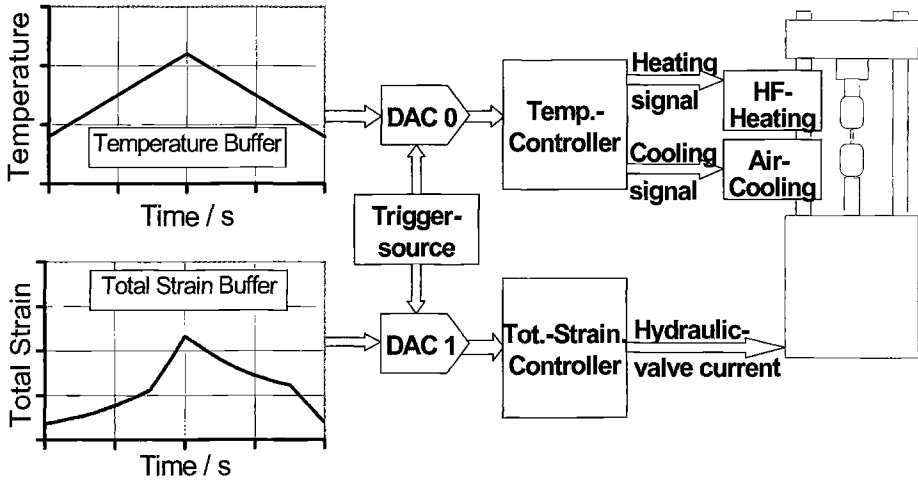


FIG. 3—Scheme of the TMF test set-up.

Figure 3 shows the scheme of the TMF experimental setup. The command variables of the temperature and the total strain are generated prior to testing as arrays saved in the computer. During testing, both command variable functions are fed into the temperature and strain control loops. The command variable functions are then converted into $\pm 10\text{V}$ -signals by two digital to analog converters, which are triggered synchronously by a common clock source. The customary PID temperature controller generates the heating signal for the induction heating and the cooling signal for the air valve.

Theoretical Background

Figure 4 shows the closed control loop consisting of the PID-controller and the controlled system (plant). Essentially, the plant contains the heating device, the cooling device, the specimen, the grips and the thermocouple.

In Fig. 4, the reference trajectory is fed into the control loop. The resulting temperature profile shows a typical deviation at the upper turning point (overshoot with asymptotic approximation to the command value). The control characteristics and the extent of the deviation depend on:

- Control parameters of the PID controller,
- Thermal conductivity of the specimen and the surface resistance between the specimen and the grips,
- Specimen geometry, heat radiation, coil geometry, natural and forced convection, and
- Response times of the heating and cooling device etc.

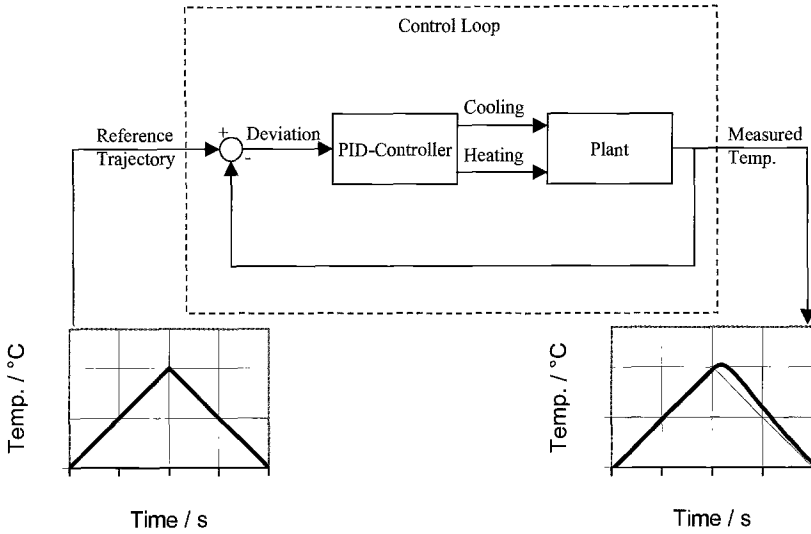


FIG. 4—Block diagram of the control loop including PID-controller and plant.

The properties of the closed control loop determine the transfer characteristics (transfer function) from the input profile to the output profile. With this transfer function, a temperature function for the specimen can be determined for each temperature input function. Therefore, by inverting this transfer function, it is possible to determine the corrected input profile, which is necessary to obtain an ideal output function with minimum deviations. A command variable function, which is not identical to the reference trajectory, is fed into the controller, in order to obtain the minimum deviations in the specimen temperature (Fig. 5).

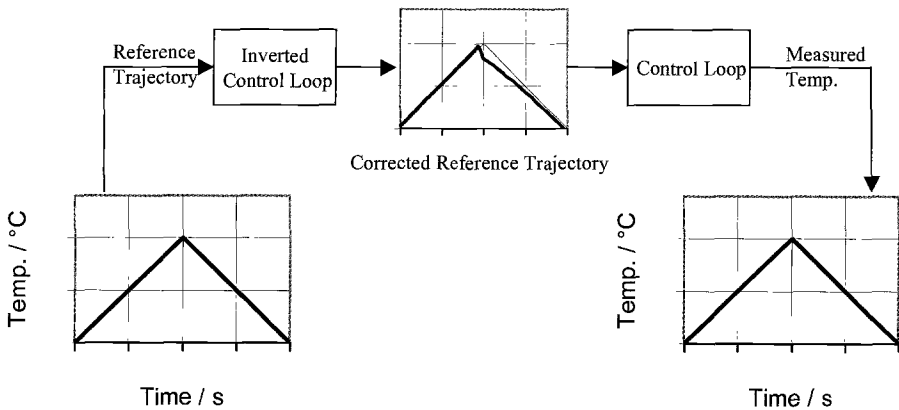


FIG. 5—Minimized control deviation at the maximum temperature turning point by conversion of the reference trajectory to the corrected trajectory.

Because this procedure contains the completely inverted control loop, consisting of controller and plant, the resulting corrected command value function can be applied without modifying the experimental set-up.

Algorithm for Input Profile Optimization

As already described, the characteristic of the control error depends on the transfer function of the control loop. It is therefore possible, based on the cyclically occurring control error, to deduce a corrected input profile, with which a minimization of the control error can be obtained. In this way, an inverse model of the control loop can be implemented without explicit knowledge of the transfer function.

The principal item of the correction algorithm used here is a function (1), which calculates a modified input profile of the temperature command variable. In addition to the error function and the error differential, a proportionality factor, a differential factor and a rate time of this function must be assigned (Fig. 6). The value of the parameters are optimized empirically, in such a way that over correcting of the command variable function does not occur, i.e., no control error in the opposite direction results from a correction step. Therefore it is possible to achieve by iterative application of this function, a gradual convergence of the control error on the maximum margins of error admissible in the test.

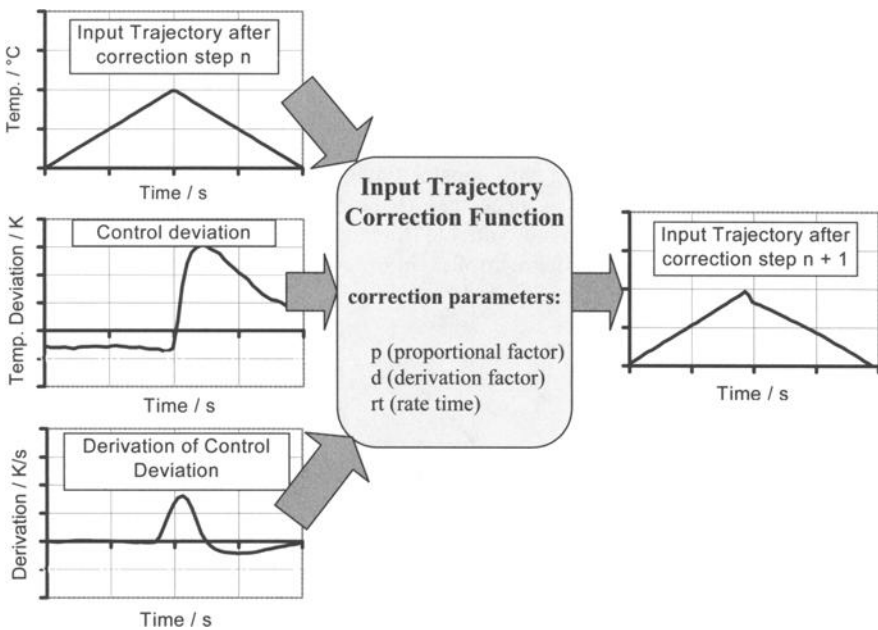


FIG. 6—The correction function of the input trajectory receives the input trajectory to be corrected, the control deviation, the derivation of the control deviation and the correction parameters p , d , rt .

On the basis of the control deviation E and the differential E' at the time $t+rt$, the modified command variable function $W_n(t)$ is calculated. The size of the correction is determined by the factors p and d , which are empirically derived.

$$W_n(t) = W_{n-1}(t) - (p \cdot E(t+rt) + d \cdot E'(t+rt)) \quad (1)$$

W_n	Input trajectory at t after correction step n
W_{n-1}	Input trajectory at t after correction step $n-1$
E	Control deviation referring to the reference (non corrected) input trajectory
p	proportional factor
d	differential factor

The correcting function is merged into an iteration loop, where an error function is calculated. Then a new, corrected input profile is created for each iteration until the error limit (e.g., $\pm 4\text{K}$) is no longer exceeded. In order to reduce the influence of sporadic control deviations on the input profile correction procedure, an appropriate correction step should be derived from an average cycle calculated over several cycles. (e.g., 5)

Results of Measurements

After the parameters of the correcting transfer function are empirically determined once, they may be left unchanged as long as no modifications of the controlled system are made. Therefore, the procedure described above has been integrated into a fully automated TMF experimental procedure, where first the temperature input profile is optimized and then the thermal strain is measured during simultaneous temperature cycling.

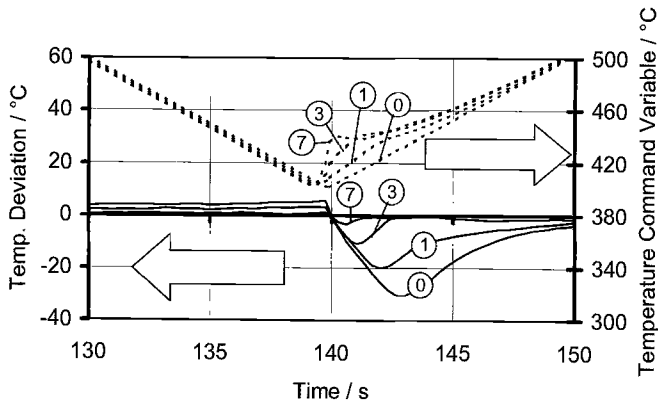


FIG. 7—Gradual reduction of the temperature deviation after correction step 0 to 7 at the lower turning point.

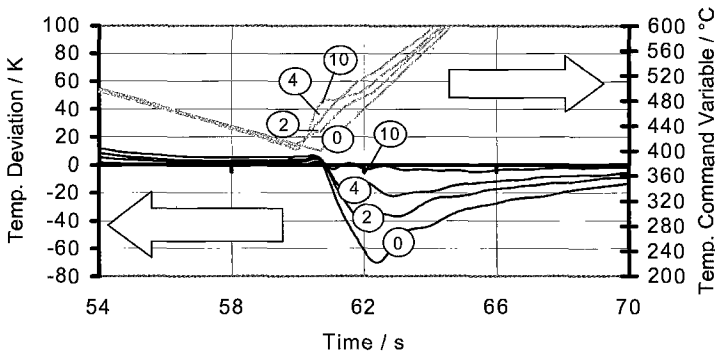


FIG. 8—Gradual reduction of the temperature deviation at the lower turning point (cooling ramp: 15K/s, heating ramp: 50K/s).

Figure 7 shows the reduction of the control deviation at the lower point of a temperature cycle with 10K/s. The linearity error is reduced from approximately 30K (correction step 0) to fewer than 4K after correction step 7. Tests carried out with higher temperature transients (up to 50K/s) also showed a reduction of the remaining control deviations to +/-4K (Fig. 8).

Control Design by Modeling and Simulation

Another approach for finding a solution to the control problem is through simulation. This method is typically used in the field of automation engineering. The first step is to find a model which describes the dynamics of the open loop circuit. This can be done either numerically, e.g., training a neural net or using black box identification, or using physical properties of the plant. Once the model has been validated, i.e., the results calculated with this model are consistent with measured data; the second step is to design a corresponding controller. The following section shows two different controllers, which were designed according to such procedures. One controller is a modified self tuning inverse online controller with a double integrator. The other one is based on an offline input profile correction method with recursive least square (RLS) identification.

Physical Background of Specimen Heating

Heat transfer occurs within the test piece as well as between the test piece and its surroundings due to conduction, radiation, natural convection and forced convection [1]. The principle equations used to calculate a power balance of the various heat flows such as conduction, radiation etc., are shown:

$$P_{heat} = B_m^2 l h \frac{\omega}{4\mu} k d^2 \frac{\sinh kd - \sin kd}{\cosh kd - \cos kd} \quad (2)$$

The heating power P_{heat} is calculated from (2) [2]. Where μ is the permeability of the specimen. B is the magnetic field. The variables l , h and d represent the length,

height, and thickness of the test piece respectively. The variable ω is the frequency of the electrical field and the symbol k represents the inverse penetration depth which is approximately in the range of 1mm. The influence of the heating output is proportional to B and therefore is nonlinear.

$$P_{cond} = \lambda \frac{A}{l} (T_1 - T_2) \quad (3)$$

Where $\lambda(T)$ is the heat conductivity (strongly non-linear), A is the cross-sectional area of transmission, l is the length of transmission, T_1 and T_2 are the corresponding temperatures.

$$P_{radiation} = \varepsilon_1 \sigma A_s (T_1^4 - T_{ambient}^4) \quad (4)$$

Where ε_1 is the emissivity (equal to 1 for blackbodies), σ is the Boltzmann constant, which equals $5.67 \times 10^{-8} \text{ Wm}^{-2} \text{ K}^{-4}$. Note: The power of the radiation is proportional to T^4 .

$$P_{natural} = \alpha A_s (T_1 - T_{ambient}) \quad (5)$$

Where A_s is the surface area of natural convection and the heat transfer coefficient α is determined from the Nusselt number.

$$P_{forced} = \alpha A_s (T_1 - T_{ambient}) \quad (6)$$

Where α is the heat transfer coefficient, which is a function of the Reynolds number and the velocity of the fluid.

Modeling

An exact description of the physical situation would lead to a complex PDE. In order to create an exact simulation finite element techniques requiring an intensive programming effort must be used. As an alternative a simplified mathematical model may be used to evaluate differential equations in one or more states [4]. The model is implemented in a numerical program (e.g., Matlab).

One-Zone Model

Considering only one representative temperature, in the middle of the test piece, leads to the use of only one temperature (one state) in the differential equation. To find the model, it is necessary to use a power balance such as:

$$mc\dot{T} = P_{in} - P_{out} \quad (7)$$

where m is the mass of the piece, c is the specific heat capacity, T is the temperature (state), P_{in} is the power input to the test piece, P_{out} is the heat (power) flow out of the piece.

Combining the above formulas, the first model is as follows:

$$\dot{T} = \frac{1}{mc} (P_{heat} - P_{natural} - P_{radiation} - P_{forced}) \quad (8)$$

The above formula was used as the basis of a numerical simulation of the plant response to the step input. The results of this simulation were compared to actual system response data given the same step input. It was found that the steady state value of the simulated response matched that of the actual response. However, there were significant discrepancies observed in the dynamic characteristics of the response. This result implies that the consideration of only one representative temperature on the whole specimen (gauge length + shaft) is not an accurate description of the plant. Therefore, in this case, it is not possible to use a one-zone-model for controller design purposes.

Two-Zone Model

In order to expand the model with one additional state, the test piece is split into two parts. The first part (index 1) is the gauge length and the second part (index 2) is the upper and lower shaft. The shaft enables the heat to flow from the gauge length to the water-cooled grip. The influence of the induction heating on both gauge length and shaft is described by introducing a weighting factor. The simulation showed that about 65% of the heating power is generated in the specimen gauge length and 35% in the shaft:

$$\begin{aligned} \dot{T}_1 &= \frac{1}{c_1 m_1} (0.65 P_{heat} - P_{1,natural} - P_{1,radiation} - P_{1,forced} - P_{trans}) \\ \dot{T}_2 &= \frac{1}{c_2 m_2} (0.35 P_{heat} - P_{2,natural} - P_{2,radiation} - P_{2,clamp} + P_{trans}) \end{aligned} \quad (9)$$

or rewritten

$$\begin{aligned} \dot{T}_1 &= f(T_1, T_1^4, T_2, u_1^2, u_2) \\ \dot{T}_2 &= f(T_2, T_2^4, T_1, u_1^2) \end{aligned} \quad (10)$$

where u_1 = heating signal, u_2 = cooling signal and P_{trans} is the power being transmitted from zone 1 to zone 2. It can be seen, that the model is strongly nonlinear. The specific heat capacities (c_1 and c_2) and the heat conductivity have non-linear characteristics. The cooling factor also has a nonlinear characteristic and a lag-time.

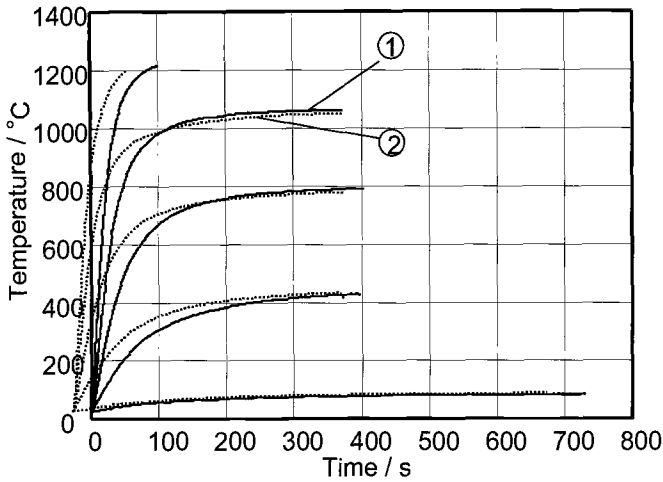


FIG. 9—Step response experiment (simulation (2) based on the two-zone-model and measured (1) temperature).

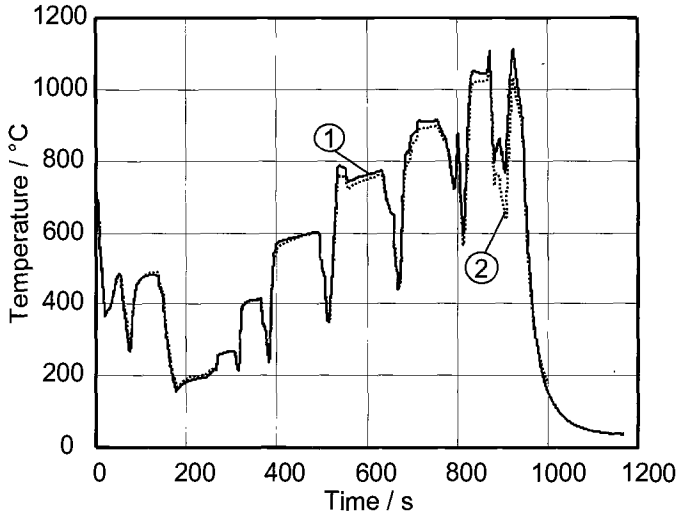


FIG. 10—Random cycle (simulated (2) and measured (1) temperature).

It can be seen in Figs. 9 and 10 that during both steady and transient states, the simulation corresponds very well to the measurement. Due to its accurate description of the plant, this model enables the design of a viable controller.

Controller Design 1: Modified Self Tuning Inverse Control

To control a circuit with a standard inverse controller, it is necessary to solve the differential equation to get the input profiles. In this case, a numerical method is used to solve the differential equation. This is why a process, which leads to a basic input profile for the induction heating, must be found. This is done as follows:

1. The process starts by carrying out five update cycles controlled by the double integrating controller. (For example, 1st cycle, see Fig. 12) The factors for P, I and I² are calculated by the frequency domain method [3]. The parameters are calculated in a way, such that the control algorithm shows a slow response characteristic. Subsequent to the update cycles an average basic input profile is calculated from the recorded heating signal (u) as follows:

$$u_i = \frac{1}{5} \sum_{k=1}^5 u_{k,i} \tag{11}$$

2. During testing the calculated basic input profile (11) of the heat signal and the input profile of the cooling signal is fed into the plant. In order to minimize the remaining error, the loop is closed by inputting the control deviation (error) into the PI2 controller, thus influencing the heat signal trajectory. The factors for P, I and I² for the controller are calculated in order to achieve a quick response. The input profile (11) can be interpreted as an inverse model of the process because the shape of the input profile depends on the properties (transfer function) of the plant.

In the realized test setup (Fig. 11), the input profile for the cooling factor has to be determined one time by the operator manually for each temperature reference trajectory.

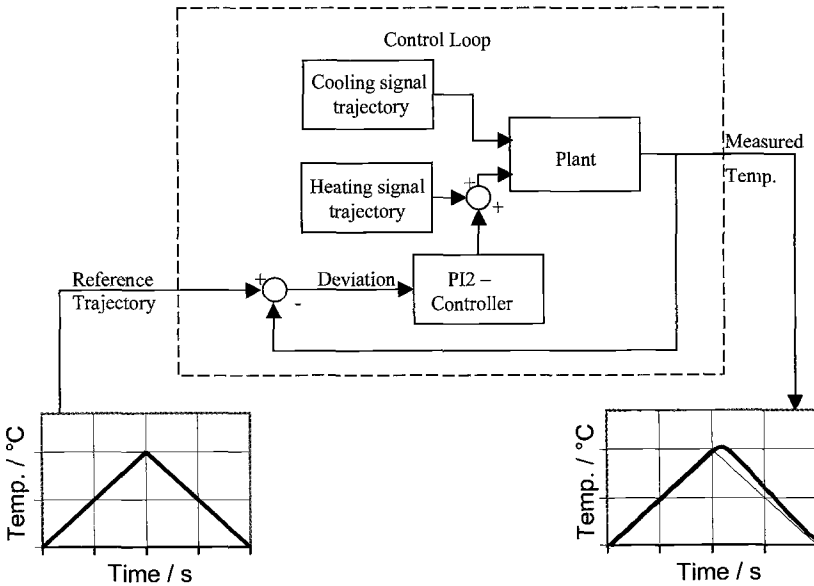


FIG. 11—Scheme of self-tuning inverse control.

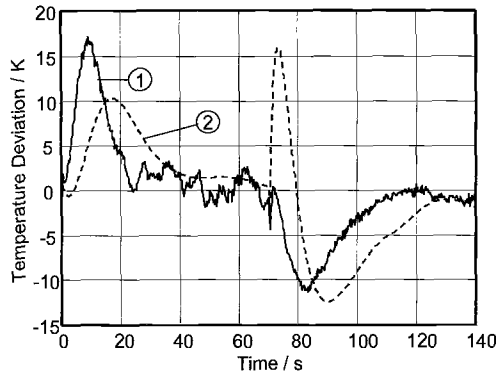


FIG. 12—Simulated (2) and measured temperature (1) deviation during update cycles.

Subsequent to the updated cycles, the remaining error is corrected and the remaining temperature deviation from the original input profile is less than $\pm 4^{\circ}\text{C}$ (not displayed).

Testing with a real-time card showed that the resulting error on the real circuit was reduced to $\pm 2^{\circ}\text{C}$ during the tracking period and to $\pm 4^{\circ}\text{C}$ at the turning points.

Controller Design 2: Correction of the Ideal Trajectory with Identification

If the reference trajectory fits better to the plant dynamics, a simpler controller can be used, for instance, a simple P-controller. To this end, the model of the plant can be linearized around a working point, yielding the following continuous transfer function:

$$G(s) = \frac{b_{1s} + b_{0s}}{s^2 + a_{1s} + a_{0s}} \quad (12)$$

Discretizing the transfer function for the open-loop system results:

$$G(z) = \frac{b_1 z + b_0}{z^2 + a_1 z + a_0} = \frac{y}{u} \quad (13)$$

$G(z)$ represents the plant, therefore, is a part of the transfer function (17). In order to invert the transfer function of the whole circuit, it is necessary to determine the time varying coefficients b_1 , b_0 , a_1 and a_0 . This is possible through dynamical identification [5] with a recursive least square (RLS) algorithm, on the basis of the input and the output data from the open-loop circuit. The identification is as follows:

$$V = \frac{1}{2} \sum_{k=1}^n (y_k - \varphi_k^T \theta_k)^2 \equiv \text{MIN} \quad (14)$$

where y_k is the measured temperature and $\varphi_k^T \theta_k$ is the predicted temperature. The difference between the measured and the predicted temperature is called the error. To find the minimum error, the derivative of (14) must be calculated. It follows a recursive

algorithm for θ_k which converges automatically to zero for the error. By transforming the discrete transfer function into a difference equation:

$$y_k = b_1 u_{k-1} + b_0 u_{k-2} - a_1 y_{k-1} - a_0 y_{k-2} = \varphi_{k-1}^T \theta_{k-1} \quad (15)$$

Now the recursive algorithm can be found for the discrete transfer function:

$$\varphi_{k-1}^T = (-y_{k-1} \quad -y_{k-2} \quad u_{k-1} \quad u_{k-2}) \text{ and } \theta_{-1} = (a_1 \quad a_0 \quad b_1 \quad b_0) \quad (16)$$

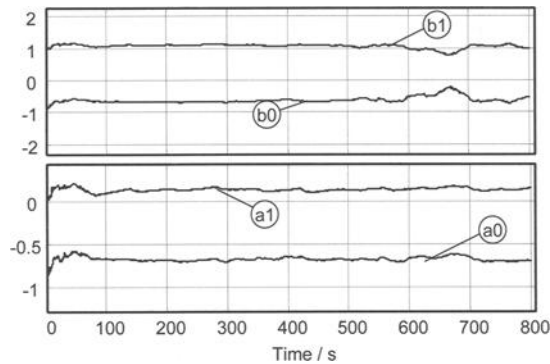


FIG. 13—Coefficients b_0, b_1, a_0, a_1 , during identification process.

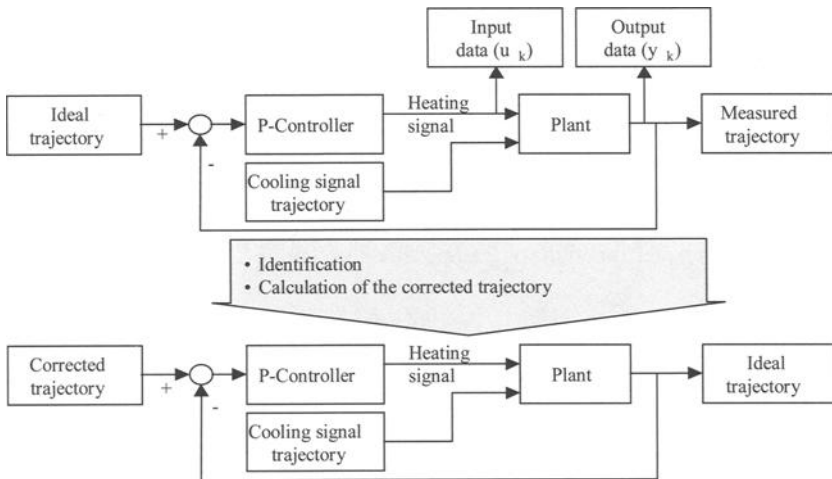


FIG. 14—Block diagram of the set-up during identification and during controlling.

Figure 13 shows the typical identification of the factors of the numerator and the denominator. If the closed-looped circuit with P-controller is introduced, the result of the transfer function is as follows:

$$T_{y,w} = \frac{PG(z)}{1+PG(z)} = \frac{Vb_1z + Vb_0}{z^2 + a_1z + a_0 + Vb_1z + Vb_0} \quad (17)$$

or rewritten

$$(z^2 + (a_1 + Vb_1)z + a_0 + Vb_0)y = (Vb_1z + Vb_0)w \quad (18)$$

Dividing this equation by z and solving for w_k it follows:

$$w_k = \frac{1}{Vb_1}(y_{k+1} + y_k(a_1 + Vb_1) + y_{k-1}(a_0 + Vb_0) - w_{k-1}Vb_0) \quad (19)$$

where V is the gain factor for the P-controller. With this equation, it is now possible to calculate a corrected ideal trajectory for the input. A conceptual understanding of this process may be realized by reviewing the block diagram of Fig. 14.

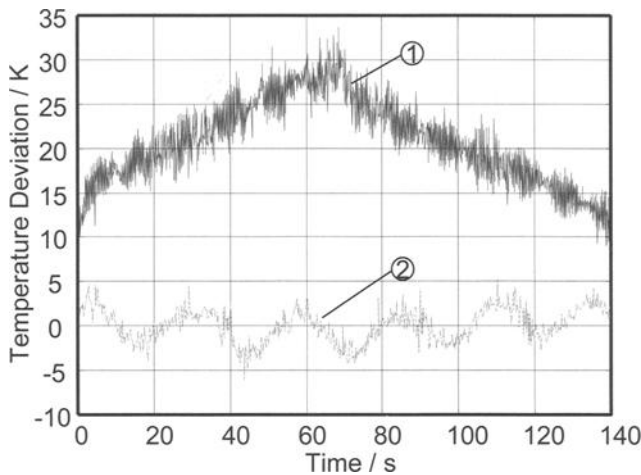


FIG. 15—Control deviation prior (1) and subsequently (2) to identification and calculation of an optimized input profile.

As it can be seen in Fig. 15 above that the error during the tracking period and in the turning points is $\pm 4^\circ\text{C}$.

Conclusions

Three approaches intended to reduce deviations in cyclic temperature input profiles were presented: 1) empirical algorithm for input profile optimization, 2) modified self-tuning inverse control, and 3) correction of the input profile with identification.

The resulting control accuracy, observed during experiments, is comparable among all procedures mentioned (approximately $\pm 4\text{K}$ for a triangle cycle with 10K/s). The deviation at the measuring location is small relative to the overall deviation on the

gauge length of the specimen due to inhomogenities in the longitudinal and transversal temperature distribution.

Considering the degree of automation of the TMF test start procedure, Approach 1 is most advantageous, since the cooling trajectory need not be determined manually. Also, the expense of hardware and programming for the implementation into a TMF testing process is smallest with Approach 1. It can be implemented with a AD/DA-converting board, with two D/A channels. For Approaches 2 and 3, a PC real-time system is most suitable, with at least 3 D/A channels. For the real time hardware, processes such as PI-controllers, analog output and analog input must be programmed.

When a TMF system is already equipped with real time hardware, Procedure 2 should be favored. Changing conditions of the system during a running test (e.g., ambient temperature or oxide coating growth) can be compensated by the principle of self-tuning inverse control, which would inevitably lead to a deviation in Approach 1. Due to the controller design by the frequency domain method, the stability of the control characteristic is also more reliable.

References

- [1] VDI – *Summary of Thermodynamic Physical Properties and Formulas 5th Edition*, Association of German Engineers, VDI Publishing Firm, Düsseldorf, 1988.
- [2] Philippow, E., “Theoretical Fundamentals of Electronics. Current Displacement,” *Electronic Handbook in 6 Volumes – Volume 1 Fundamentals*, E. Philippow, Ed., Carl Hanser Publishing Firm, München, 1976, pp. 171–176.
- [3] Schlacher, K., *Automation Technology I* (Transcript), Johannes Kepler University, Linz, 1995.
- [4] Naderhirn, M., “Optimization of Temperature Regulation by TMF Experiments,” Graduate thesis, MTU Aero Engines, 2001.
- [5] del Re, L., “Model Construction and Identification,” (Transcript), Johannes Kepler University, Linz, 2000, pp. 21–25, 34–35.

Two Specimen Complex Thermal-Mechanical Fatigue Tests on the Austenitic Stainless Steel AISI 316 L

REFERENCE: Rau, K., Beck, T., and Löhé, D., “Two Specimen Complex Thermal-Mechanical Fatigue Tests on the Austenitic Stainless Steel AISI 316 L,” *Thermomechanical Fatigue Behavior of Materials: 4th Volume, ASTM STP 1428*, M. A. McGaw, S. Kalluri, J. Bressers, and S. D. Peteves Eds., ASTM International, West Conshohocken, PA, 2002, Online, Available: www.astm.org/STP1428_10602, 26 August 2002.

ABSTRACT: Start-stop and load change processes of combustion engines result in inhomogenous and instationary temperature fields, which induce cyclic mechanical loadings, e.g., in solid and cooled turbine blades and vanes. The present study shows results of so-called complex thermal-mechanical fatigue“ (CTMF) tests carried out with a two specimen testing system in order to simulate the interaction of the “hot“ outer and the “cold“ inner side of a cooled turbine blade and the influence of superimposed mechanical loadings. The test pieces were made from the austenitic steel AISI 316 L. Specimen 1 represents the “hot“ and specimen 2 the “cold“ side of the component, respectively. Both specimens were loaded by individual thermal cycles. The mechanical interaction of the “hot“ and the “cold“ side is simulated firstly by keeping the total strains of both specimens at identical values. Secondly, in order to simulate external loadings such as centrifugal forces at turbine blades, the sum of the forces at both specimens is given as a function of time. The influence of dwell times at the maximum temperatures as well as of superimposed forces on the cyclic deformation and the cyclic creep behavior of the two specimen system is presented and discussed.

KEYWORDS: thermal fatigue, thermal-mechanical fatigue, austenitic steel, AISI 316 L, cyclic creep

Introduction

Start-Stop cycles and load changes in high-temperature parts of combustion engines, such as turbine blades, vanes, and discs, result in inhomogenous and instationary temperature fields, which induce complex cyclic mechanical loadings within these components [1,2]. For example, the hollow blades and vanes in the first stages of gas turbines are cooled at their inner side by air from the compressor. In Fig. 1, the temperature-time courses occurring during a start-stop cycle at the inner and the outer side of such a blade, as well as the respective mechanical loadings, are plotted schematically. At the outer side, larger temperatures and higher temperature rates arise during heating up and cooling down than at the inner side. The thermal strain at the “hot“ outer side that is represented by the volume element 1 in Fig. 1 is partially constrained by colder material elements within the blade. This results in mechanical loadings which are about 180° phase shifted against the temperature-time path. Accordingly, at the inner side

¹ Dipl.-Ing., Scientific Employee, Institut für Werkstoffkunde 1, Universität Karlsruhe, Germany.

² Dr.-Ing., Head of Laboratory for Near Service Loadings, Institut für Werkstoffkunde 1 Universität Karlsruhe, Germany.

³ Prof. Dr.-Ing, Head of the Institut für Werkstoffkunde 1, Universität Karlsruhe, Germany.

(volume element 2 in Fig. 1) mechanical loadings occur with nearly no phase shift to the temperature cycle. Additionally, centrifugal forces can cause a superimposed overall tensile loading F_s of the component which is drawn schematically in Fig. 1. Increasing F_s lead to increasing tensile stresses in the cold parts of the component and decreasing compressive stresses at the outer side at the same time.

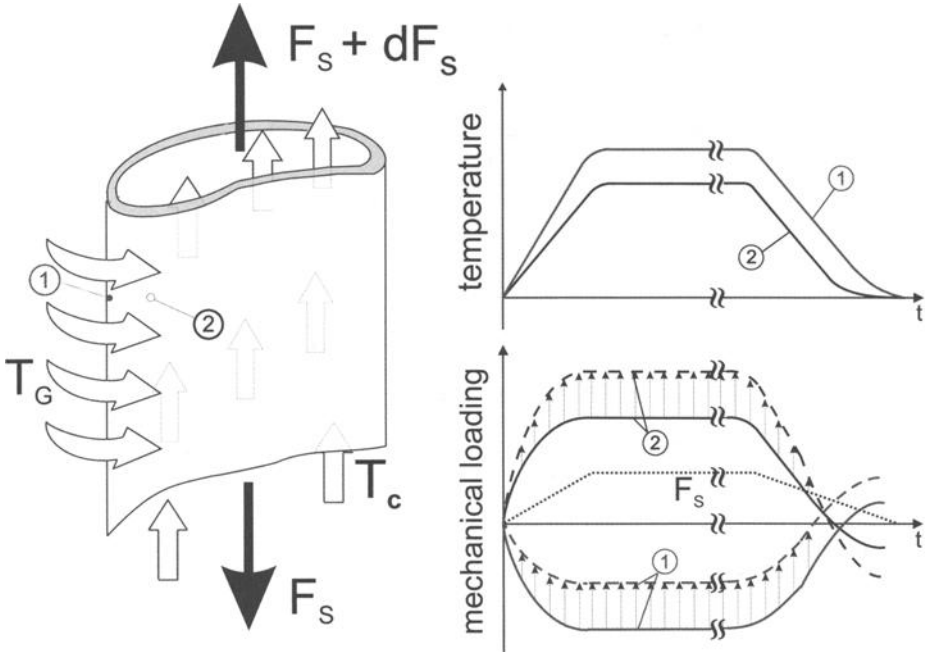


FIG. 1—Thermal and mechanical loading in cooled turbine blades with external force F_s .

Repeated start-stop cycles result in so-called thermal fatigue (TF), which is often responsible for the initiation of fatigue cracks in turbine blades, vanes, and discs. Assessing the lifetime of TF-loaded components using data from isothermal fatigue (IF) tests can give strongly non-conservative results, because other deformation- and damage mechanisms occur under TF- than under IF-loadings [3–5]. Due to that, thermal-mechanical fatigue (TMF) tests are carried out in total strain control, where the thermally induced loadings arising in critical volume elements of the components are simulated at specimens that are loaded uniaxially and homogeneously. This leads to more realistic results concerning the cyclic deformation, lifetime, and damage behavior than IF tests [3–5]. However, in such “conventional” TMF tests, the interaction between different volume elements on the “hot” and the “cold” side of a construction part with the respective re-distributions of stress and strain are not considered because a fixed total strain - time course is applied to the specimen. Furthermore, it is impossible to simulate external mechanical loadings such as centrifugal forces, which are acting at the complete component by one specimen TMF tests. So-called complex thermal-mechanical fatigue

(CTMF) tests using a two-specimen testing facility as described in detail in [6–8] are especially taking these effects into account: one specimen represents a hot and the other a cold volume element in a thermally loaded component, each with its individual temperature-time course. The interaction between both elements is firstly realized by keeping the total strains of both specimens at identical values all the time. Secondly, in order to simulate external loadings F_S (see Fig. 1), the sum of the forces is risen to a given value during the heating phase of the cycle, kept constant during the dwell time at maximum temperature and decreased to zero at minimum temperature. The results of such tests on the steel AISI 316 L are described in the present paper. The influence of dwell times at maximum temperature and of superimposed overall loadings F_S on the cyclic deformation, as well as on the cyclic creep behavior of the system consisting of both specimens, is discussed.

Test Material and Sample Geometry

The tests were carried out on the austenitic steel AISI 316 L (X 2 CrNiMoN 17 12) with a content of δ -ferrite below 1.0 vol.%. The material was supplied as plates with a thickness of 40 mm, which were solution annealed in vacuum at 1100°C. The austenite grains with a size of 50–250 μm (Class 4 according to the ASTM standard) have a relatively high twin density. The chemical composition of the material is given in Table 1. The nitrogen content has no influence on the corrosion behavior, but increases the yield strength at room temperature and decreases significantly the content of brittle χ - and σ -phases.

TABLE 1—Chemical composition of AISI 316L.

Fe	C	Cr	Ni	Mo	N	Mn	Si	Cu
Bal.	0.019	17.14	12.6	2.40	0.053	1.796	0.3	0.138

Figure 2 shows the geometry of the solid round test pieces as were used for the CTMF experiments. The temperature within the gage length and its homogeneity were determined by three type K (Ni-CrNi) thermocouples, which were spot welded at the positions as depicted in Fig. 2. The spot welding process was optimized in order to get a minimal influence on the microstructure and to avoid damage, which would lead to an accelerated crack initiation at the thermocouple locations. Furthermore, the thermocouple locations were chosen in such a way that the measured values were not affected by the air jets blowing radially on the surface in the cooling phase of the TMF cycle (see below).

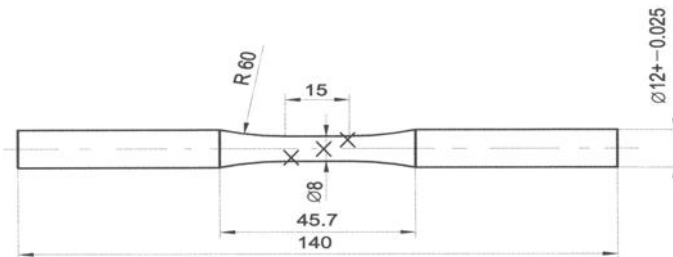


FIG. 2—Specimen geometry.

Experimental Details

All tests were carried out on a two-specimen testing facility mainly consisting of two servohydraulic load frames with a nominal force of 100 kN, a four-channel digital controller and two inductive furnaces [6–8]. Figure 3 shows a schematic sketch of the test equipment.

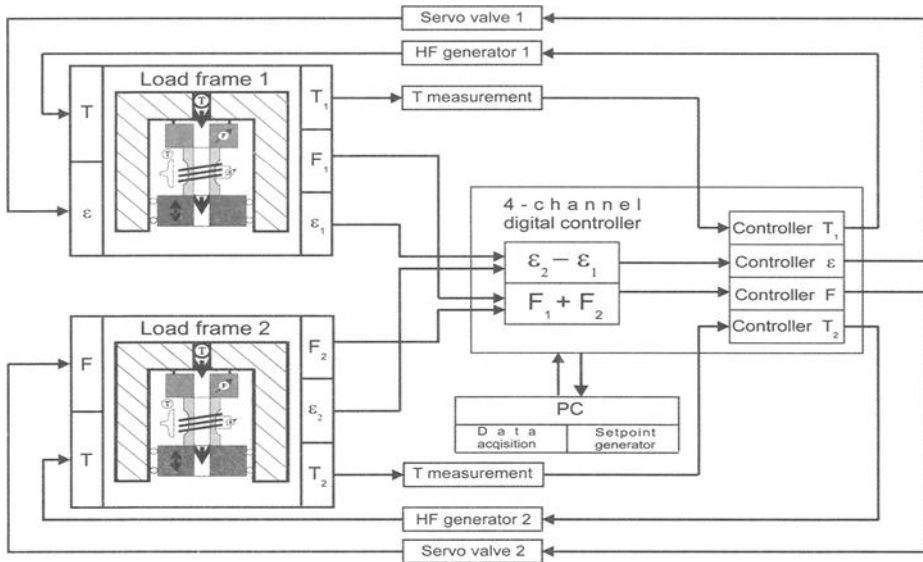


FIG. 3—Test equipment (schematical view).

The specimens are fixed in the load frames by water-cooled hydraulic grips. The strain is measured at each specimen by an air-cooled high temperature extensometer. The test pieces are heated by two 5 kW high frequency generators with induction coils that are adapted to the specimen geometry in such a way that the temperature difference within the gage length is kept below $\pm 5^\circ\text{C}$. The cooling of the specimens is achieved by the heat flux into the water cooled grips and, if necessary, by proportionally controlled air jets blowing radially upon the specimen surfaces. The thermal expansion behavior determined in reference temperature cycles at zero force with the same $T - t$ course as in the CTMF tests gave evidence that neither significant radial temperature gradients nor plastic deformations due to inhomogenous temperature distributions within the gage length occur. The complete system is controlled by a 4-channel MTS TestStar device. Separate control circuits are realized for the temperature of specimens 1 and 2. The third channel controls the sum of the forces and the fourth channel the difference between the total strains occurring on both specimens. This experimental setup results in a minimization of the phase angles between the single control loops with respect to the usage of separate control units for each channel [8]. According to the structure of the control circuits, the following setpoint values have to be given for each experiment:

- Separate temperature-time-courses for specimens 1 and 2
- The sum of the forces on both specimens as a function of time (e.g., in order to simulate centrifugal forces at turbine blades)
- Identical total strains at specimens 1 and 2 all the time (no thermally induced bending of the considered component)

These boundary conditions can be summarized as follows: $T_1 = f_1(T)$, $T_2 = f_2(T)$, $F_S = F_1 + F_2 = g(t)$, $\varepsilon_{1,t} = \varepsilon_{2,t}$. At given numbers of cycles, the forces, total strains, and temperatures of both specimens are stored as a function of time with a sample rate of 1/s. At the beginning of each test, the thermal strain ε^{th} was determined as a function of temperature for each specimen during five reference cycles without mechanical loading. The total strain ε_t is the sum of ε^{th} and the total mechanical strain ε_t^{me} :

$$\varepsilon_t(t) = \varepsilon_t^{me} + \varepsilon^{th}$$

According to this equation, the nominal stress σ_n is calculated and plotted as a function of the total mechanical strain. The resulting hystereses are evaluated in order to get cyclic deformation curves of the maximum and minimum stress σ_{max} and σ_{min} as well as the maximum and minimum strain $\varepsilon_{t,max}$ and $\varepsilon_{t,min}$ versus the number of cycles N . Additionally, the plastic strain ε_p is calculated for each cycle using the equation:

$$\varepsilon_t^{me} = \varepsilon_e + \varepsilon_p = \frac{\sigma_n}{E(T)} + \varepsilon_p$$

where ε_e is the elastic strain and $E(T)$ the Young's modulus as a function of the temperature, which was determined in separate tests and subsequently approximated by a polynomial of 3rd order. The resulting hystereses of σ_n versus ε_p are evaluated to get cyclic deformation curves of the plastic strain amplitude $\varepsilon_{a,p}$ versus the number of cycles for each specimen. All tests were carried out with trapezoidal temperature-time paths without any phase shift between specimens 1 and 2. The heating and cooling rate at specimen 1 was 10°C/s. The dwell time at maximum temperature of specimen 1 was varied between $t_D = 0$ s and 600 s. The maximum temperature of this specimen $T_{1,max}$ was generally 650°C. The respective minimum temperature was $T_{1,min} = 200$ °C. The temperature of specimen 2 T_2 was kept constant at a value of 200°C. The influence of the dwell time on the cyclic deformation behavior was investigated with an overall force on both specimens of $F_S = 0$. The impact of F_S on the CTMF behavior was considered at a dwell time of 40 s. Generally, the ultimate number of cycles was 10³.

Results and Discussion

Influence of Dwell Times on the CTMF Behavior at $F_S = 0$

In Fig. 4 the courses of the temperatures T_1 and T_2 , of the total strain $\varepsilon_{1/2,t}$, which is identical at both specimens, and of the nominal stresses σ_1 and σ_2 , all as a function of time, are plotted for the first cycle.

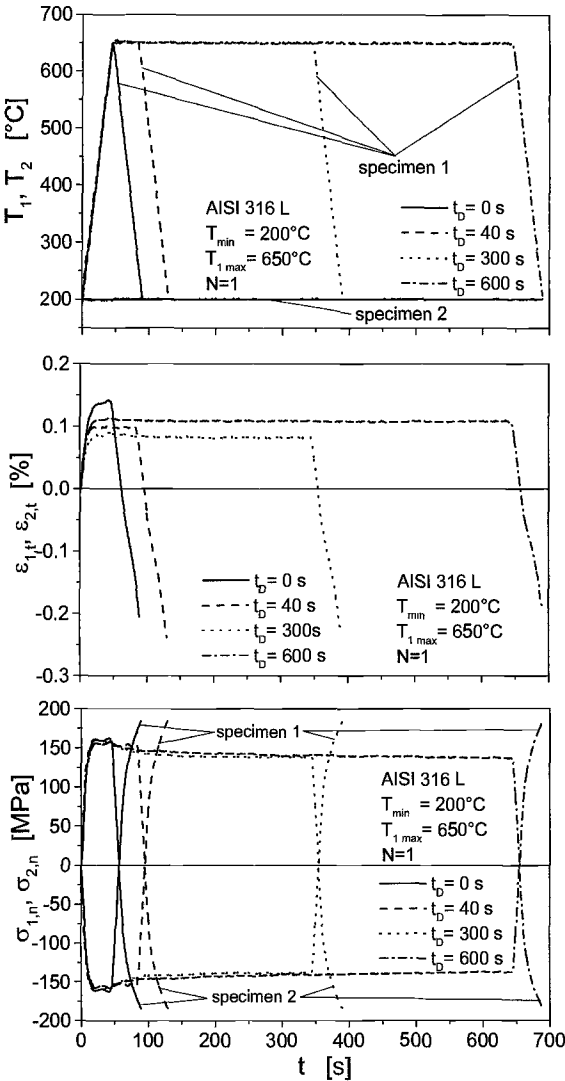


FIG. 4 – Temperatures, total strains, and stresses versus time in the first cycle ($F_S = 0$).

The interaction between two AISI 316 L specimens during a CTMF test without dwell time, $T_{1/2,min} = 200^\circ\text{C}$, $T_{1,max} = 650^\circ\text{C}$, $T_{2,max} = 200^\circ\text{C}$, and an overall force $F_S = 0$ has been presented and discussed in more detail in a previous study [9]. As also shown there, at the beginning of the first cycle, the total strains $\epsilon_{1/2,t}$ and the stress in specimen 2 σ_2 increase, whereas σ_1 decreases with increasing temperature. Before $T_{1,max}$ is reached, the flattening of the stress- and total strain-time courses indicate extensive plastic deformation. However, the peak stresses and strains are reached at $t = 45$ s when $T_1 = T_{1,max} = 650^\circ\text{C}$. After that, for a dwell time of zero, $\epsilon_{1/2,t}$ continuously decreases until

$T_{1,min}$ is reached, and, due to the plastic deformation during heating up, negative total strains remain after the first cycle. The absolute values of σ_1 and σ_2 decrease at the beginning of the cooling phase. Then the stresses change their sign at $T_1 \approx 400^\circ\text{C}$ and further increase continuously up to their peak value at the end of the first cycle. The large remaining tensile stresses in specimen 1 and compressive stresses in specimen 2 are again due to plastic deformation, mainly during heating up to $T_{1,max}$.

Dwell times at $T_{1,max}$ lead to a stress relaxation, especially in the “hot” specimen 1, and therefore, because of the condition $F_1 + F_2 = 0$, to a continuous decrease of the stress values in both specimens. Consequently, during cooling down to $T_{1,min}$, higher remaining total strains are developing. The largest part of the stress relaxation occurs within the first 40 s of the dwell time. If t_D is increased to a value of 300 s, a further slight decrease of the stress amounts until the beginning of the cooling phase is observed. A dwell time of 600 s does not lead to a significant further stress relaxation with respect to $t_D = 300$ s.

In Fig. 5, the hystereses of the nominal stresses σ_1 and σ_2 versus the total mechanical strains $\varepsilon_{1,t}^{me}$ and $\varepsilon_{2,t}^{me}$ are given for the first cycle. Fig. 6 shows the respective hystereses at $N = 1000$ cycles.

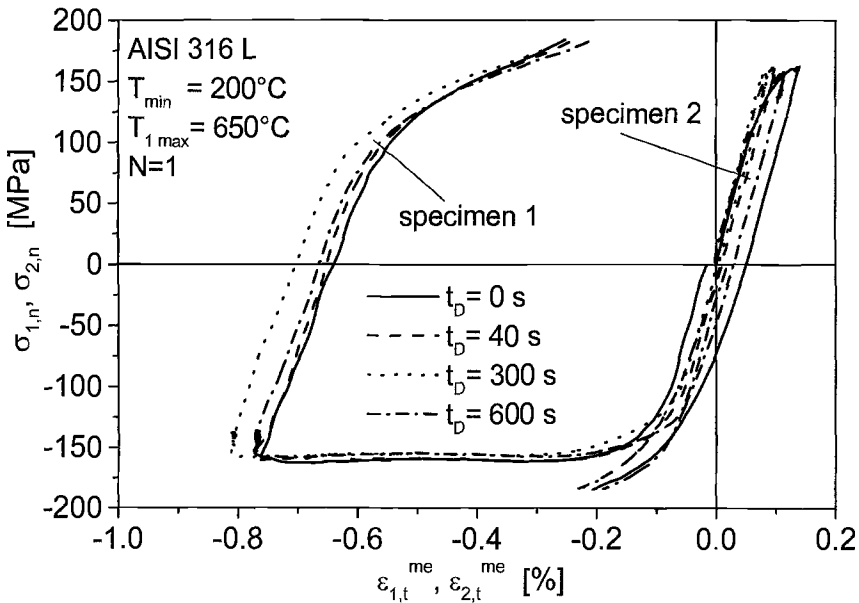


FIG. 5 – Stress-total mechanical strain hystereses at $N = 1$ ($F_S = 0$).

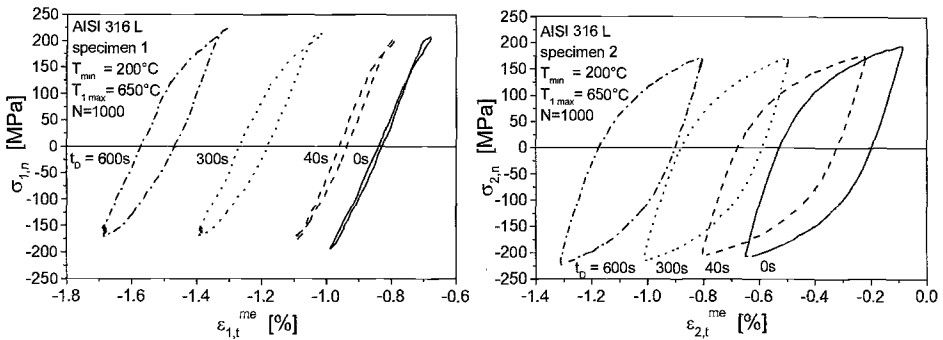


FIG. 6—Stress-total mechanical strain hystereses at $N = 1000$ ($F_S = 0$).

From Fig. 5 it becomes obvious that in the “hot” specimen 1 a large plastic deformation in compression occurs during heating up to $T_{1,max}$. At the same time, specimen 2, which is at the constant temperature of 200°C , undergoes an elastic-plastic deformation in tension. However, because of the lower temperature of this sample with respect to T_1 , this plastic strain is small. If no dwell time at $T_{1,max}$ is applied, the elastic-plastic reformation in tension (specimen 1) and in compression (specimen 2) begins immediately after $\sigma_{1,min}$ and $\sigma_{2,max}$ (as well as $\epsilon_{1,t,min}^{me}$ and $\epsilon_{2,t,max}^{me}$) are reached. Due to the fact that the compressive deformation of specimen 1 occurs at the same absolute stress value and at the same time as the tensile deformation of specimen 2 and due to the higher temperature of specimen 1, which results in a lower resistance of the material against plastic deformation, a compressive plastic deformation of the complete system consisting of both specimens is observed after the first cycle.

As mentioned in the discussion of Fig. 4, introducing a dwell time at $T_{1,max}$ leads to stress relaxation especially in specimen 1 at $\epsilon_{1,t,max}^{me}$, which also results in decreasing σ_2 during t_D because of the condition $F_S = F_1 + F_2 = 0$. Due to that, the elastic-plastic reformation during cooling down specimen 1 to $T_{1,min} = 200^{\circ}\text{C}$ starts at lower compressive (tensile) stresses in specimen 1 (specimen 2). However, the stress values in both samples, which are measured at the end of the first cycle, are nearly unaffected by the dwell times investigated because of the stress-strain course being relatively flat as soon as plastic deformation occurs.

If one compares the stress-strain behavior as given in Fig. 6 for $N = 1000$ with the hystereses for $N = 1$ in Fig. 5, the following observations are made: Firstly, and most surprising, at $N = 1000$ the plastic deformation of the “cold” specimen 2 is much larger than the respective strain for specimen 1, in spite of the fact that the specimen 1 is deformed at significantly higher temperatures. This means that, as discussed in a previous paper [9], the thermal-mechanical loading of specimen 1 leads to a cyclic hardening which is so pronounced that this sample gets a higher resistance against plastic deformation, even at $T_{1,max} = 650^{\circ}\text{C}$, than specimen 2 which is isothermally loaded at 200°C . Secondly, Fig. 6 shows that the plastic strain amplitude in specimen 1 increases and the stress range decreases with increasing dwell time. From this, it is concluded that the cyclic hardening of specimen 1, which is mainly due to dynamic strain aging processes [9], is superimposed by recovery during the dwell time and is, consequently,

diminished. The cyclic deformation behavior of specimen 2 is assumed to be unaffected by the dwell time. Therefore, the decrease of the plastic strain amplitude and of the stress range in specimen 2 with increasing t_D is attributed to the lower amount of loading that is induced by the thermal cycling of specimen 1, which becomes “softer” when t_D is risen, combined with the boundary conditions $\varepsilon_{1,t} = \varepsilon_{2,t}$ and $F_1 = -F_2$. The third point to be discussed concerning Figure 6 is the negative cyclic creep of the CTMF system which becomes obvious in the shift of the hystereses at $N = 1000$ towards compressive strains with respect to $N = 1$. This behavior is the more pronounced the higher t_D is. The reason is that the compressive deformation of specimen 1 occurs at higher temperatures and, therefore, results in larger plastic strain than the tensile reformation in the range of $T_{1,\min}$. The impact of this effect raises with increasing t_D , because the relaxation during t_D (see Fig. 4) always occurs in compression and, therefore, leads to a further shortening of specimen 1 that is not fully compensated by the deformation during cooling down to $T_{1,\min}$ which is, as shown above, not affected significantly by the dwell time.

Figure 7 gives an overview of the cyclic deformation behavior of the CTMF system. In Fig. 7a the peak strains $\varepsilon_{1/2,\max/\min}$ are plotted versus the number of cycles N . Fig 7b gives the respective courses of the plastic strain amplitudes in both specimens and Fig. 7c and d the peak stresses $\sigma_{1,\max/\min}$ and $\sigma_{2,\max/\min}$, respectively, all versus N .

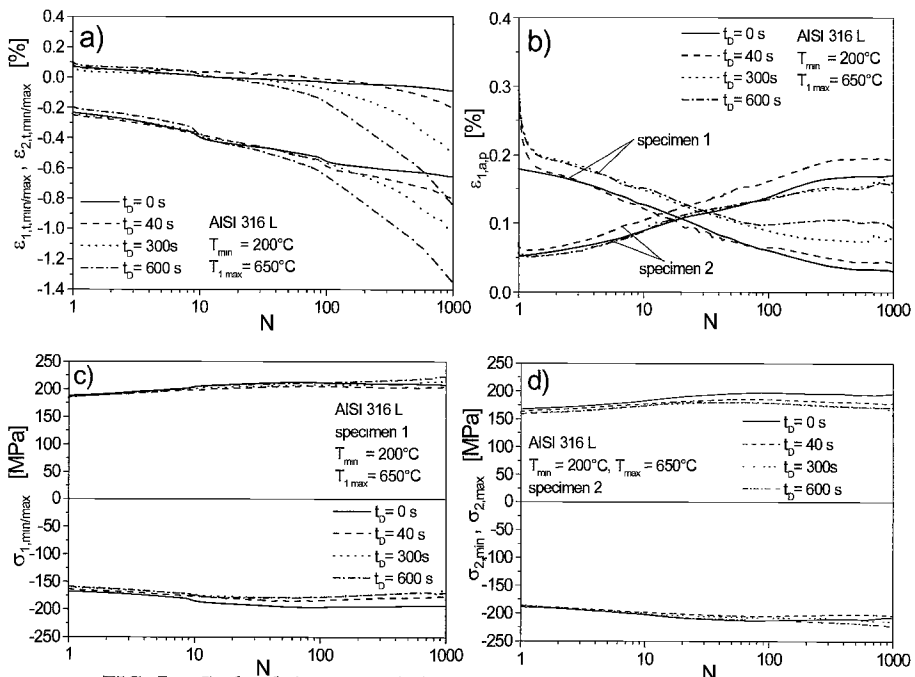


FIG. 7—Cyclic deformation behavior at different dwell times ($F_S = 0$).

The reasons for the negative cyclic creep, which becomes obvious in Fig. 7a and increases with the dwell time, have been discussed above. The courses of the plastic strain amplitude in specimen 1 (Fig. 7b) together with the nearly constant stress ranges

in this sample (Fig. 7c) give evidence of the cyclic hardening which could be seen by the comparison of the $\sigma_n - \varepsilon_t^{\text{me}}$ hystereses at $N = 1$ and $N = 1000$. Again, it becomes clear that, due to superimposed recovery, $\varepsilon_{1,\text{ap}}$ increases with increasing dwell time. The development of the $\varepsilon_{2,\text{ap}}$ seems at the first glance to indicate cyclic softening of the isothermally loaded specimen 2. But, if one considers additionally the course of the respective maximum and minimum stresses versus N (Fig. 7d), it becomes obvious that the material behavior under CTMF loading cannot be interpreted in the simple terms of cyclic softening or hardening because the redistribution of stresses and strains in both specimens as a consequence of the change of the cyclic stress strain behavior have a strong impact on the cyclic deformation curves in Fig. 7. Therefore, the cyclic deformation behavior has to be interpreted as a reaction of the complete system consisting of both specimens, which is, of course, strongly influenced by the properties of the material itself. Keeping this fact in mind, the following consistent interpretation can be made: The boundary condition $F_1 + F_2 = 0$, which is equivalent to $\sigma_1 + \sigma_2 = 0$, means that the absolute value of the nominal stresses occurring in both specimens has to be the same all the time. When specimen 1 is heated up for the first time ($N = 1$), the compressive stresses in this sample are acting at a higher temperature and, therefore, are working against a lower resistance of the material against plastic deformation than the tensile stresses with the same absolute value in specimen 2 which has a constant temperature of 200°C. This leads to a higher plastic strain amplitude in specimen 1. In the subsequent cycles, the resistance of specimen 1 against plastic deformation continuously increases due to the cyclic hardening [9]. This results in a decrease of $\varepsilon_{1,\text{ap}}$ and, more important, in a slight increase of the maximum and minimum stresses in specimen 1 and in specimen 2 (see Fig. 7c and d). Because cyclic hardening does not occur in specimen 2 and because AISI 316 L shows a relatively flat stress-strain path as soon as plastic deformation occurs, increasing peak stresses result in a strong increase of $\varepsilon_{2,\text{ap}}$, as shown in Fig. 7b. At the same time, the increase of σ_{max} and σ_{min} in the complete system is limited because of the condition $|\sigma_1| = |\sigma_2|$ that results from $\Sigma(F) = 0$. Due to that, σ_{max} and σ_{min} increase less pronounced and $\varepsilon_{1,\text{ap}}$ decreases steeper than it would be observed in a strain controlled one specimen TMF test with the same total strain - time course as observed in the first cycle of the considered CTMF experiment.

Whereas a clear influence of dwell times on the courses of $\varepsilon_{1,t}$ and $\varepsilon_{2,t}$ as well as on $\varepsilon_{1,\text{ap}}$ is observed, which is attributed to the relaxation and recovery processes occurring in specimen 1 during t_D combined with the boundary condition $|\sigma_1| = |\sigma_2|$, no systematic influence of t_D on the plastic strain amplitude of specimen 2 is observed in Fig. 7b. On the one hand, dwell times result in increasing plastic deformations and, therefore, in increasing total mechanical strain ranges in specimen 1 (see Fig. 6). Because the total strain is the sum of the thermal strain and the total mechanical strain and, due to the fact that the thermal strain $\varepsilon_1^{\text{th}}$ is about 180° phase shifted with respect to $\varepsilon_{1,t}^{\text{me}}$, the cyclic relaxation and recovery processes which increase the total mechanical strain amplitudes in specimen 1 lead to a decrease of the total strain amplitude $\varepsilon_{1,\text{at}}$. In specimen 2, the total- and the total-mechanical strain amplitudes are identical, because no thermal strain occurs in this sample. Therefore, the total mechanical strain range and, consequently, the stress range in specimen 2 should be reduced due to the dwell times (see Fig. 7a, c, and d). The other way round, time dependent plastic deformation in specimen 2 during the

dwell time which would lead to an increase of $\varepsilon_{2,ap}$ can't be excluded even at $T = 200^\circ\text{C}$. The superposition of both effects results in the plastic strain amplitudes $\varepsilon_{2,ap}$ as observed in Fig. 7b. The similar peak stresses occurring at all t_D investigated are again due to the relatively flat stress-strain path of AISI 316 L in the plastic deformation regime.

Influence of Superimposed Forces $F_S = F_1 + F_2$ on the CTMF Behavior with $t_D = 40$ s

In order to investigate the influence of superimposed overall forces F_S on the behavior of the CTMF system, tests with identical temperature and strain conditions as presented in the previous chapter for $t_D = 40$ s were carried out. Additionally, F_S was risen linearly up to a given value of 5 kN up to 15 kN during the first 45 s of the cycle when specimen 1 was heated up. During the dwell time, F_S was kept constant. While cooling down to $T_{1,min}$, F_S was linearly decreased to its initial value of zero. For these tests, Fig. 8 gives the courses of the total strain $\varepsilon_{1/2,t}$, which is identical at both specimens as well as of the nominal stresses σ_1 and σ_2 as a function of time for $N = 1$.

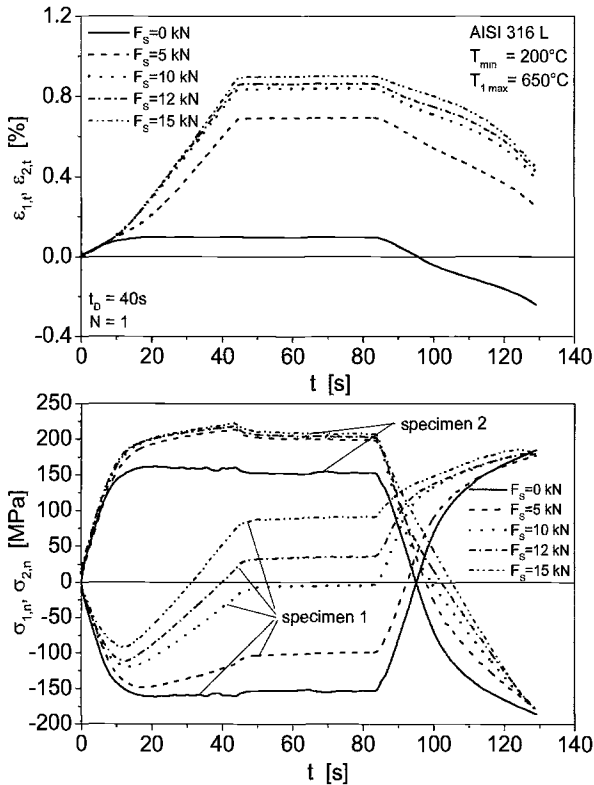


FIG. 8 – Total strains and stresses versus time in the first cycle ($F_S \geq 0$).

Increasing F_S significantly raises the total strains in both specimens throughout the first cycle. Consequently, the remaining strain after this cycle is positive for $F_S \geq 5$ kN, whereas a negative value of $\varepsilon_{1/2,t}$ at $t = 130$ s is observed for $F_S = 0$. The stresses in both

specimens are also shifted to higher values by increasing F_S . However, in specimen 2, which is loaded by tensile stresses during heating up of specimen 1 ($t < 45$ s) and the subsequent dwell time (45 s $< t < 85$ s), an increase of F_S beyond 5 kN does not result in further increasing stresses because the stress in this specimen is limited by the relatively flat stress-strain path of AISI 316 L as soon as plastic deformation occurs. Due to that, the main part of the overall force is compensated by a reduction of the compressive loading in specimen 1 and, for $F_S > 5$ kN, even by tensile loadings up to 100 Mpa in this sample during the dwell time. The elastic-plastic deformation occurring in both samples during the cooling phase of specimen 1 finally leads to similar remaining stresses after the first cycle as they were observed for $F_S = 0$.

Figure 9 shows the hystereses of the nominal stresses σ_1 and σ_2 versus the total mechanical strains $\epsilon_{1,t}^{me}$ and $\epsilon_{2,t}^{me}$ in the first cycle for all F_S investigated. In Fig. 10 the respective hystereses at $N = 1000$ cycles are given.

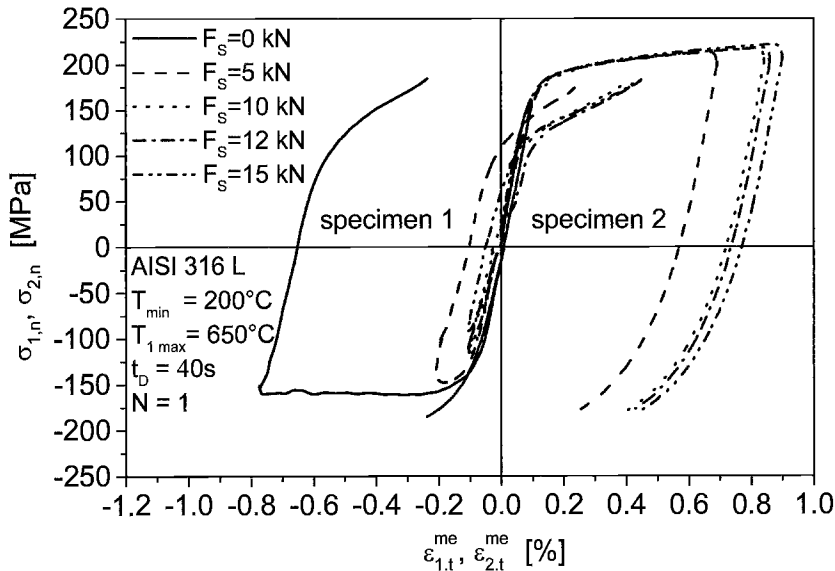


FIG. 9 – Stress-total mechanical strain hystereses at $N = 1$ ($F_S \geq 0$).

In the first cycle, increasing F_S led to a pronounced reduction of the compressive deformation of specimen 1 and, the other way round, to a strong increase of the tensile plastic deformation of specimen 2 during the first 45 s of the cycle where specimen 1 is heated up to 650°C and F_S is risen up to its maximum value at the same time. Whereas at $F_S = 0$ the compressive plastic deformation dominates the total strain in the system consisting of both specimens, which leads to negative remaining strains after the first cycle, for higher overall forces the plastic deformation of specimen 2 in tension more and more determines $\epsilon_{1/2,t}$.

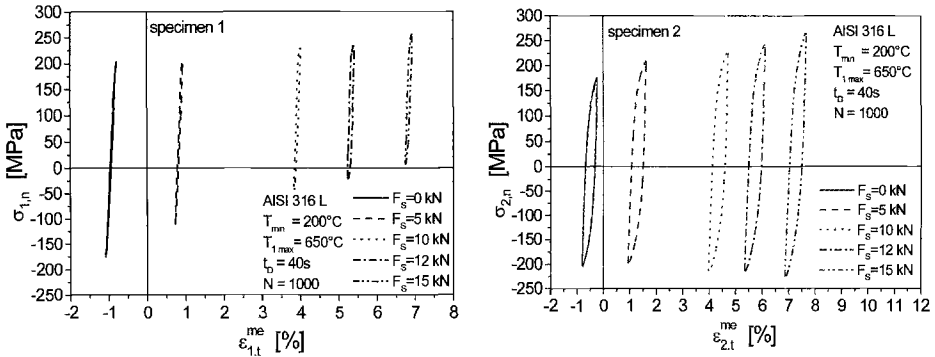


FIG. 10—Stress-total mechanical strain hysteresses at $N = 1000$ ($F_S \geq 0$).

After 1000 cycles the $\sigma_n - \varepsilon_t^{\text{me}}$ hysteresses of both samples are shifted to positive strains if overall forces up from 5 kN are applied. This effect is the more pronounced the higher F_S is, whereas $F_S = 0$ leads to negative cyclic creep as discussed above. It can further be seen from Fig. 10 that the stress amplitudes in specimen 1 decrease with increasing F_S and that lower $\sigma_{1,a}$ occur at $N = 1000$ compared with $N = 1$. Furthermore, the mean stress in this sample at $N = 1000$ increases with F_S . Contrarily, in specimen 2 only small tensile mean stresses occur even for the highest F_S investigated. The stress amplitude $\sigma_{2,a}$ is increasing with F_S , whereas the plastic strain amplitude is nearly independent from F_S . Comparing Fig. 10 with Fig. 9 reveals that the cyclic plastic deformation of specimen 2 leads to cyclic hardening, especially at high values of F_S .

The cyclic deformation behavior of the AISI 316 L specimens under CTMF loading with different F_S is shown in Fig. 11 in the representation of the peak strains $\varepsilon_{1/2,t,\text{max/min}}$ (Fig. 11a), the plastic strain amplitudes $\varepsilon_{1/2,ap}$ (Fig. 11b), and the peak stresses $\sigma_{1,\text{max/min}}$ (Fig. 11c), $\sigma_{2,\text{max/min}}$ (Fig. 11d), all versus the number of cycles N .

From Fig. 11c it becomes obvious, that, especially at overall forces of 10 kN and more, the maximum stress and the stress range in specimen 1 increase up to $N \approx 70$. For higher numbers of cycles a very slow decrease of the stress amplitude and of $\sigma_{1,\text{max}}$ and a small increase of $\sigma_{1,\text{min}}$ is observed. Furthermore, at $F_S \geq 10$ kN the absolute values of both, the maximum and the minimum stress in specimen 2 increase in the cycle range $N \leq 70$. This indicates cyclic hardening in this sample, because, as obvious from Fig. 11b, at $F_S \geq 10$ kN, the plastic strain amplitude of sample 2 decreases at the same time. However, F_S has no significant influence on the qualitative course of $\varepsilon_{1,ap}$ versus N . The development of tensile mean stresses in specimen 1 and the cyclic hardening of specimen 2 is clearly visible for high values of F_S , whereas at $F_S = 5$ kN these effects are less pronounced. The behavior of the CTMF system at $F_S = 0$ kN still has been discussed in the previous chapter. As mentioned above, the cyclic creep towards positive total strains is the more pronounced the higher F_S is. In Fig. 11a it can additionally be seen, that the cyclic creep rate is relatively high from the first cycle up to $N \approx 70$. From this, it is concluded that the cyclic hardening of specimen 2 combined with the stress redistribution within the system consisting of both samples which becomes obvious in the increase of the mean stress of specimen 1 up to $N \leq 70$ in Fig. 11a, diminishes the overall cyclic reep of the system. As soon as the peak stresses have saturated, the creep rate tends towards zero at $5 \text{ kN} \leq F_S \leq 12 \text{ kN}$. At $F_S = 15$ kN, a reduced creep rate occurs up from this point.

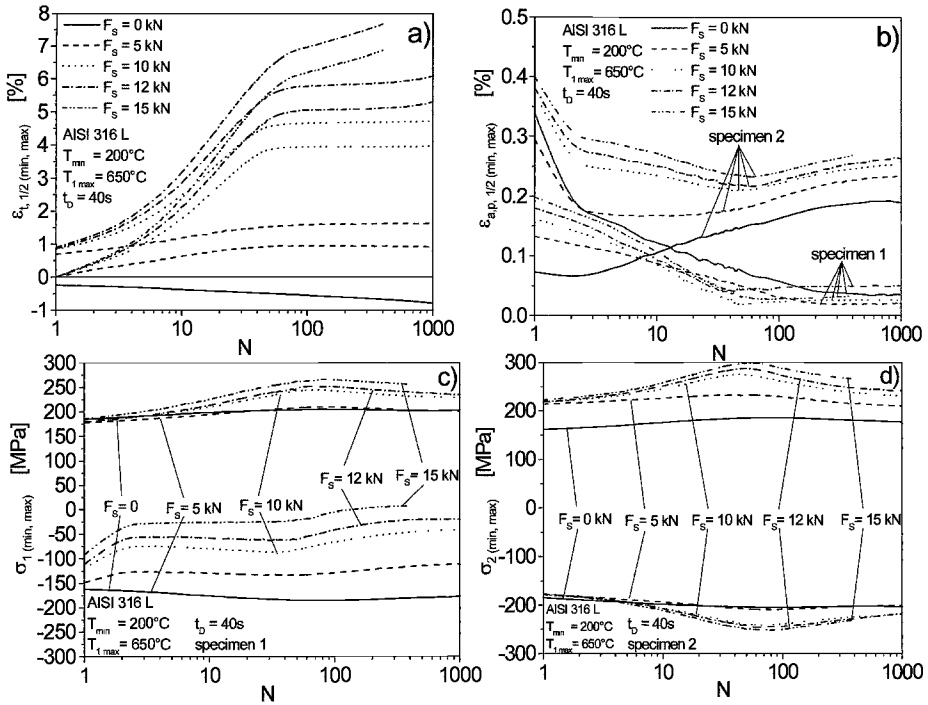


FIG. 11—Cyclic deformation behavior at different overall forces F_s .

Concluding Remarks

The two-specimen complex thermal fatigue (CTMF) testing system that was used for the present study provides a helpful means to experimentally simulate and to understand the complex interaction between the “hot” and “cold” regions in thermally loaded components such as turbine blades which additionally undergo external mechanical loadings. However, one should keep in mind that this two-specimen system makes some strong simplifications of the real service loadings in the considered components. But, in spite of neglecting the multiaxiality as well as the gradients occurring in real components and using strongly simplified temperature cycles, the study gives evidence of the complicated interactions between mechanically coupled volume elements in construction parts under service conditions that cause inhomogenous and instationary temperature fields. It has been shown that this interaction results in a cyclic deformation behavior, which cannot be simulated by classical strain controlled TMF tests. The other way round, at least in the near future, TMF tests will further be used as the best practise method for the determination of sufficiently reliable databases for materials used in high temperature components which are subjected to thermal fatigue. But it should be noted that the basic understanding of the processes occurring “inside” such components which is arising from CTMF tests is a helpful means for the determination of mechanical boundary conditions of TMF tests in such a way that the results from these experiments are as useful and as realistic as possible with respect to the

real service loadings. Furthermore, the CTMF tests, which were performed under well-defined boundary conditions, give good reference data for the assessment of the reliability of the modeling of the thermal mechanical fatigue behavior of components using advanced constitutive viscoplastic materials laws [10].

Acknowledgment

The financial support of the Deutsche Forschungsgemeinschaft (DFG) is gratefully acknowledged. The authors also give special thanks to the Forschungszentrum Karlsruhe for the supply of the test material.

References

- [1] Weronski, A. and Hejwowski, T., *Thermal Fatigue of Metals*, Marcel Dekker, New York, 1991.
- [2] Löhe, D., "Thermische Ermüdung," *Proceedings DVM*, "Rissbildung und Rissausbreitung unter Mehrachsiger Mechanischer und Thermischer Belastung," Berlin, 1993, pp. 33–48.
- [3] Lang, K.-H., Beck, T., Flaig, B., Hallstein, R., and Löhe, D., "Einfluß von Haltezeiten auf das Lebensdauerverhalten von Zylinderkopfwerkstoffen unter thermisch-mechanischer Ermüdungsbeanspruchung," VDI-Bericht 1472 zur Tagung "Werkstoff und Automobilantrieb," VDI-Verlag Düsseldorf, 1999, pp. 437–454.
- [4] Pitz, G., Beck, T., Lang, K.-H., and Löhe, D., "Thermisch-mechanisches und isothermes Ermüdungsverhalten der Nickelbasis-Superlegierung IN 792 CC," *Mat.-wiss. u. Werkstofftech.*, Vol. 28, 1997, pp. 142–148.
- [5] Beck, T., Pitz, G., Lang, K.-H., and Löhe, D., "Thermal-Mechanical and Isothermal Fatigue of IN 792 CC," *Mat. Sci. Engng.* A234-236, 1997, pp. 719–722.
- [6] Pitz, G., Lang, K.-H., and Löhe, D., "Konzeption und Realisierung eines Prüfsystems für komplexe thermisch-mechanische Belastung," *Vorträge der DVM-Tagung "Werkstoffprüfung"*, Bad Nauheim, 1995, pp. 69–78.
- [7] Pitz, G., "Ermüdungsverhalten metallischer Hochtemperaturwerkstoffe unter komplexer thermisch-mechanischer Beanspruchung," PhD-Thesis, Universität Karlsruhe, 1997.
- [8] Angarita, L., Pitz, G., Lang, K.-H., Löhe, D., "Realization of Complex Thermal-Mechanical Fatigue by a Two-Specimen Testing System," *Third Symposium on Thermo-Mechanical Fatigue Behavior of Materials, ASTM STP 1371*, ASTM International, West Conshohocken, PA, 1998, pp. 304–318.
- [9] Beck, T., Lang, K.-H., Vöhringer, O., and Löhe, D., "Experimental Analysis of the Interaction of "Hot" and "Cold" Volume Elements during Thermal Fatigue of a Cooled Component made from AISI 316 L Steel," *Z. Metallkunde* Vol. 92, No. 8, 2001, in print.
- [10] Kühner, R., Aktaa, J., Angarita, L., Lang, K.-H., "The Role of Temperature Rate Terms in Viscoplastic Modelling – Theory and Experiments," *Third Symposium on Thermo-Mechanical Fatigue Behavior of Materials, ASTM STP 1371*, ASTM International, West Conshohocken, PA, 1998, pp. 103–118.

Analysis of Thermal Gradients during Cyclic Thermal Loading under High Heating Rates

REFERENCE: Affeldt, E. E., Hammer, J., Huber, U., and Lundblad, H., "Analysis of Thermal Gradients during Cyclic Thermal Loading under High Heating Rates," *Thermomechanical Fatigue Behavior of Materials: 4th Volume, ASTM STP 1428*, M. A. McGaw, S. Kalluri, J. Bressers, and S. D. Peteves, Eds., ASTM International, West Conshohocken, PA, 2003, Online, Available: www.astm.org/STP/1428/1428_10603, 14 April 2003.

ABSTRACT: The magnitude of temperature gradients and their variation with temperature and time was investigated for a thermomechanical fatigue (TMF) cycle between 400°C and 1100°C under a heating rate of 10°C/s. The measurements of the temperature distribution in the gauge section of a flat rectangular specimen of the Nickel base superalloy CMSX-6 were carried out by means of thermocouples located at various positions on the surface and in the volume, respectively. As a reference the temperature distribution was calculated by finite element analysis based on the temperature signal of the control thermocouple. Additionally, the surface temperature distribution was studied by thermographic measurements.

The results reveal that thermal gradients establish in longitudinal and in transverse direction of the gauge section. Although the temperatures in the bulk material exceed the reference given by the control signal during the entire cycle, this effect is most pronounced (+40°C) during cooling by forced air. In comparison, the predictive results of the finite element calculation lead to slightly enhanced surface temperatures during heating (+8°C) and to reduced surface temperatures during cooling (-5°C). Therefore, it is concluded that heat transport in the bulk material is sufficiently fast to guarantee almost homogeneous temperature distribution. The significantly enhanced volume temperatures in the experiment were found to result from influences of the experimental set-up, and from superimposed effects due to forced air cooling and heat flow through the wires of the spot welded thermocouple.

KEYWORDS: thermo-mechanical fatigue testing, nickel-base superalloy, finite element modeling, temperature measurement, thermographic analysis

Introduction

Components and structures of industrial machinery are in many cases exposed to a complex superposition of mechanical and thermal loads changing with time, which in most cases results in a serious reduction in lifetime. This interaction between separately varying temperatures and loads is considered as thermal mechanical fatigue, TMF [1]. In particular, the influence of the changing temperature with time results in thermally induced stresses due to temperature gradients over the component, or even by a mismatch of the thermal expansion between different materials or geometries. Frequently, the mechanical loading of these components due to operation conditions is superimposed by these thermal stresses. The major cause of failure in single crystal nickel based turbine

¹ Dr. rer. nat., MTU Aero Engines GmbH, Dachauer Straße 665, 80995 Munich, Germany.

² Professor Dr.-Ing., University of Applied Sciences, Galgenbergstr. 30, 93053 Regensburg, Germany.

³ Dipl. phys. EADS Airbus GmbH, 28183 Bremen, Germany.

⁴ Dipl.-Ing., materials engineer, MTU Aero Engines GmbH, Dachauer Straße 665, 80995 Munich, Germany.

blades of advanced aero-gas turbines is due to these thermally induced stresses [2,3]. For a precise definition of the inspection intervals and for the calculation of the lifetime the material behavior under service loading conditions is of superior interest for design and operation purposes of these components. Therefore, data from laboratory testing are essential for an economic design of these parts. Isothermal mechanical testing cannot provide the information required for this task [3,5]. Therefore, TMF tests are carried out under specific laboratory conditions, mostly close to loading in operation. To simulate the service conditions by using laboratory testing parameters, aspects like temperature range, heating and cooling rates, strain limits and phase angle between mechanical and thermal load are of utmost importance [5].

In order to apply the testing results to critical components the laboratory simulation should perform precisely. Therefore, a highly reliable experimental set-up is essential. The simultaneous uniformity of the applied temperature and the mechanical strain over the volume of the test specimen's gauge length is critical and has to be maintained at all times while both are functions of time [6]. This is generally realized by continuously measuring and controlling both variable parameters. TMF tests are performed under control of the total strain ε_{tot} , which consists of thermal strain contributions ε_{th} due to thermal cycling and the superposition of a mechanical strain $\varepsilon_{\text{mech}}$, according to:

$$\varepsilon_{\text{tot}} = \varepsilon_{\text{th}} + \varepsilon_{\text{mech}} \quad (1)$$

Effects of variability in the temperature-strain signal, in particular, concerning issues such as thermal strain measurement and thermal strain compensation, result in a misleading calculation of the thermal strain and thus lead to a misinterpretation of the control variable $\varepsilon_{\text{mech}}$:

$$\varepsilon_{\text{mech}} = \varepsilon_{\text{tot}} - \varepsilon_{\text{th}} \quad (2)$$

While under heating rates not exceeding approximately 5°C/s [7] the heat flow from the induction heated surface into the volume can be considered as sufficiently fast to instantaneously guarantee homogenous temperatures in the volume of the gauge section; first investigations reveal that thermal cycling under 10°C/s results in thermal gradients along the gauge section and in the volume, respectively. The objective of the present study is to characterize these thermal gradients and their variations with temperature and time for high heating rates of 10°C/s. In addition, the experimental results of the temperature measurements will be supplemented by finite element calculations.

Experimental Details

Temperature Measurement

For the investigation of the thermal gradients during thermal cycling, a conventional servo hydraulic testing machine with a 150 kHz induction heating was used (Fig. 1). The coil was specifically designed for the heating of flat rectangular samples with semicircular corners. Thermal cycling was carried out in a temperature range between $T = 400^\circ\text{C}$ and $T = 1100^\circ\text{C}$ at a heating/cooling rate of 10°C/s. In the temperature regime from 1100–750°C natural cooling was sufficiently effective. For temperatures below

750°C additional cooling by forced air quench of the specimen surface was necessary to meet the defined cooling rate. The volume stream and the air pressure were calculated by the temperature controller and directed to the surface through two adopted nozzles. For the temperature measurement a platinum/platinum-rhodium (Pt/PtRh) thermocouple spot-welded onto the side face in the center of the gauge length was used. In addition, for investigating the thermal gradients along the surface and to minimize influences on temperature measurement due to induction [8,9], flattened thermocouples with 0.1 mm in thickness were additionally attached to various positions of the surface. All other thermocouples had wire diameters of 0.35 mm.

The temperature in the volume was also measured by a Pt/PtRh thermocouple that was attached into the volume of the gauge section (Fig. 2). The channel for this thermocouple was produced by spark erosion and additional over-spraying with matrix material after the fixation of the thermocouple.

To guarantee stable and reproducible thermal conditions and to minimize influences of transient effects, a minimum of five thermal cycles was performed prior to the temperature measurements. In addition, thermographic analysis of the temperature distribution was performed for representative temperatures under isothermal heating conditions in vertical and in horizontal direction, respectively. The camera resolution was better than 0.16 mm.

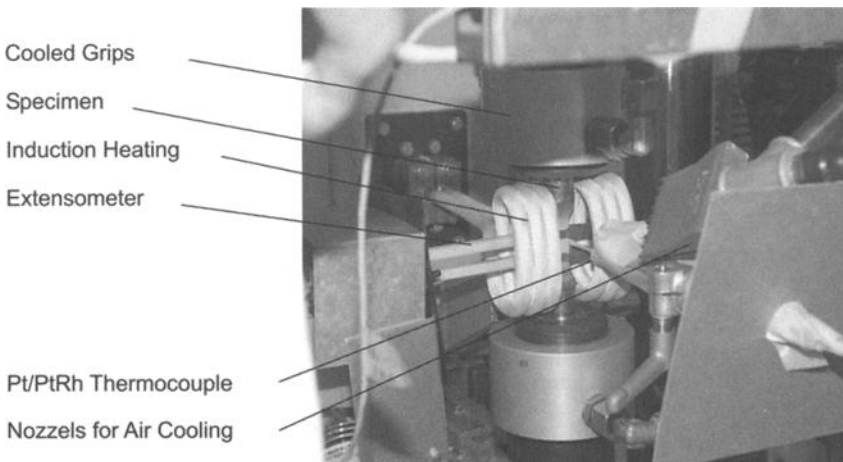


FIG. 1—*Experimental set-up with induction heating and fixtures for the test specimen.*

Finite Element Modeling

Heat Input—In the applied model [12] the distribution and the power density of the heat sources within the skin area of the gauge length were defined by the finite element program Qtran [13]. The current penetration depth δ was calculated according to Eq 3:

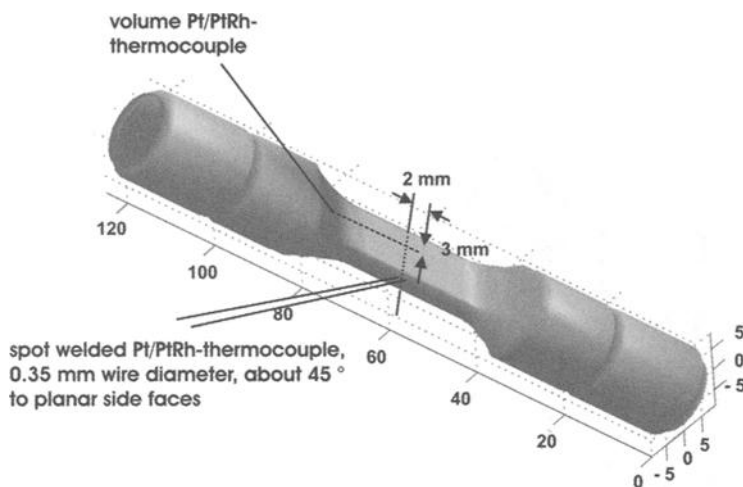


FIG. 2—Specimen geometry and positions of the thermocouples attached to the specimen surface and to the volume, respectively.

$$\delta = \sqrt{\frac{\rho}{\pi \mu_o \mu_r f}} \quad (3)$$

where ρ is the specific electric resistance, μ_o, r the permeability, and f the frequency.

For the specific experimental setup, δ is determined to 0.38 mm. The enhanced contribution to heating by thermal source elements located directly beneath the surface was taken into account by partitioning δ into two layers aligned parallel to the specimen surface [12]. Each single element had a cube length of 0.19 mm. 86% of the heat input were generated by the outer and 14% by the inner layer (Fig. 3a). Thermal sources were only defined within this area of the gauge section, which is covered by the induction coil. Due to their orientation to the magnetic field, in the model both semicircular corners of the specimen were not specifically considered to provide significant contributions to heat input.

All variables necessary for the modeling, like interactions between induction coil design and specimen geometry and material data are functions of time and cannot be measured directly from the experiment. During the entire cycle the power of the generator is controlled by the computer as well as the velocity and the volume stream of the forced air operating in the cooling branch at temperatures below 750°C. Therefore, no quantitative input data concerning the individual contributions of the heat sources during the thermal cycle are available. Furthermore, this implies undefined variations in the boundary conditions required for the modeling of the heat flux into the specimen volume. Instead of a numerical solution by modeling the time and temperature dependence of these variables, variations concerning the individual contribution of the thermal sources were defined between 0–100% by the definition of an appropriate scaling function in the

calculation program Qtran. In detail, for the defined position of the control thermocouple used in the experimental part (Fig. 2) the calculated temperature field is continuously adjusted to the experimentally measured temperatures until both temperature versus time functions exactly correspond.

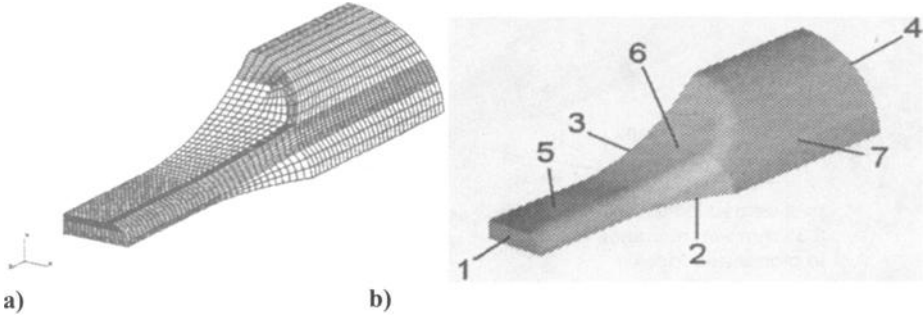


FIG. 3—*a) Finite element mesh for the modelling of the thermal sources; b) surfaces for which specific boundary conditions were defined in the model.*

Temperature Distribution and Boundary Conditions—The modeling of the temperature distribution was performed with the FEM program Abaqus [14]. For the calculation of non-steady heat transfer due to temperature fields varying with both time and specimen position, the general equation for heat transfer was applied with respect to the specific boundary conditions, Eq 4 [10]:

$$\lambda_x(\vartheta) \frac{\partial^2 \vartheta}{\partial x^2} + \lambda_y(\vartheta) \frac{\partial^2 \vartheta}{\partial y^2} + \lambda_z(\vartheta) \frac{\partial^2 \vartheta}{\partial z^2} + \dot{W}(\vartheta, \bar{x}, t) - \rho c(\vartheta) \frac{\partial \vartheta}{\partial t} = 0 \quad (4)$$

where $\lambda_{x,y,z}(\vartheta)$ is the thermal conductivity, ρ is the density of the material, $c(\vartheta)$ is the heat capacity, and \dot{W} represents the power density of the internal heat sources. For the solution of Eq 4 the following boundary conditions were considered:

Symmetry—Based on the symmetry, only one eighth of the test specimen was described by the finite element mesh, (Fig. 3). Therefore, the internal surfaces 1-3 were defined adiabatic (Fig. 3b).

Thermal Contact Between the Threads and the Cooled Grips—With respect to the complex problems concerning thermal transition at the threads this condition was not specifically considered and instead substituted by the assumption of pure heat flux through the planar front face (surface 4). The coefficient for contact resistance h_c was calculated to 2000 W/m²K according to the definition of a hypothetical length l for the fixed end of the sample required to achieve equal amounts of heat flow under conductive conditions as can be realized under convective boundary conditions.

Convection and Radiation at Faces 5-7: The convective boundary conditions were calculated according to Eq 5:

$$\Pi_c = \frac{1}{\gamma} \int_A h (T_w - T_v)^2 dA \quad (5)$$

Until the onset of the cooling by forced air at 750°C only free convection is acting. Due to the applied software the temperature dependence of the coefficient for heat transfer h could not be taken into account. Instead, a mean value for h was used, but individually balanced with respect to the actual length and inclination of the specific surfaces considered: face 5: $h = 5.0 \text{ W/m}^2\text{K}$, face 6: $h = 4.7 \text{ W/m}^2\text{K}$, face 7: $h = 4.5 \text{ W/m}^2\text{K}$. With the onset of the air cooling, forced convection has to be considered additionally. Due to the undefined conditions under turbulent air-flow this effect was also balanced individually as an increase in h by an appropriate function in the calculation program Qtran.

Radiation— Π_R considers the contribution by radiation including the coefficient for heat transfer resulting from radiation h_R Eq 6 [11]. The emissivity was measured thermographically to 0.57.

$$\Pi_R = \frac{1}{2} \int_A h_R (T_w - T_u)^4 dA \quad (6)$$

Conclusively, it can be summarized that during the entire cycle until the onset of the air-cooling at 750°C the calculation of the temperature versus time function is based on the variation of the power density for heat input. During the additional air-cooling between 750°C and 400°C only the coefficient for heat transfer is varied in order to obtain the identical temperature versus time function as that measured in the experiments for the defined position of the control thermocouple.

Results

Temperature Measurement

Surface Temperatures—Thermographic analysis of the specimen surface under isothermal heating at different temperatures indicates that temperature gradients are acting in horizontal and in vertical direction, respectively (Fig. 4a). In horizontal direction the deviation in temperature is more pronounced for higher temperatures, i.e., 900–1100°C (Fig. 4b). For this temperature range deviations of $\Delta T = -18^\circ\text{C}$ were measured for the position of the control thermocouple. On the opposite side only slightly enhanced temperatures with $\Delta T \approx 7^\circ\text{C}$ are registered. For lower temperatures (500°C to 900°C) the temperature profile appears more homogeneous, but also in this case the temperatures on the side of the thermocouple fixing position are below the signal temperature whereas on the other side slightly higher temperatures are measured. Irrespective of the heating or the cooling sequence of the thermal cycle the deviations in temperature at representative isothermal temperatures are in a comparable range. In vertical direction (z-axis) for a given temperature of $T = 500^\circ\text{C}$ the temperature profile appears sufficiently constant over almost the entire length, (Fig. 4c). For isothermal heating at temperatures exceeding 500°C the length where temperature deviations in the order of $\Delta T = 5^\circ\text{C}$ are acting is significantly reduced. Whereas for 700°C an almost stable temperature profile is observed over a distance of 8.5 mm, this section is continuously reduced for higher temperatures (7.7 mm at 1100°C). It should also be pointed out that the temperature profiles for all surface temperatures investigated appear to be asymmetric compared to the middle of the gauge section with a deviation which is more pronounced

for the lower part of the gauge length. For greater distances $\Delta z = \pm 5$ mm from the center position the temperature gradient rapidly increases up to -30°C .

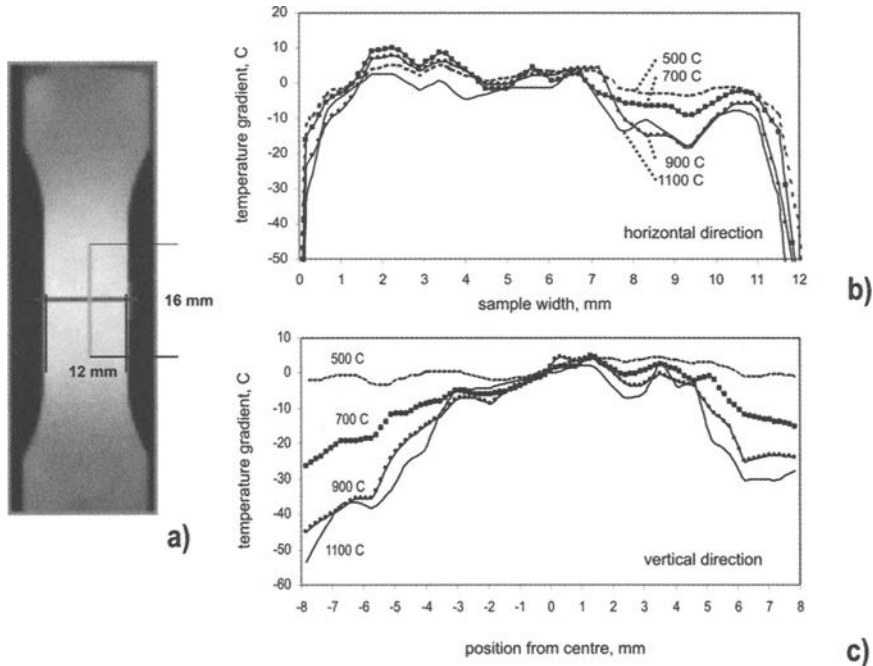


FIG. 4—Results of thermographic measurements on the specimen surface for four isothermal heating conditions: a) thermographic image of the specimen, showing the lines along which the measurements were done and corresponding temperature deviations with respect to the control thermocouple in horizontal (b) and in vertical direction (c).

Volume Temperatures—The results obtained from the volume thermocouple are shown with reference to the temperature signal and also to the surface temperature given by the spot welded thermocouple. It should be pointed out that four thermal cycles were performed prior to that reported (Fig. 5). During the entire cycle the volume is exposed to higher temperatures when compared to both references. Furthermore, it is evident that during most temperature regimes of the cycle, the temperature indicated by the control temperature is (slightly) delayed with respect to the temperature signal.

Heating Cycle—Directly at the onset of the heating phase the volume temperature is approximately 40°C above both, the signal temperature and the temperature measured by the spot welded thermocouple (Fig. 5).

With increasing signal temperature to 600°C (i.e., first 10 s of heating) this overshooting is reduced to $\Delta T \approx 25^\circ\text{C}$. This indicates a pronounced increase in the surface temperature compared to the volume. This higher volume temperatures increase with further heating according to the signal temperature up to values of $\Delta T = 32^\circ\text{C}$ for an intermediate temperature range from 650–850°C. In the high temperature regime from 850°C up to the maximum temperature of 1100°C a steady increase in the volume temperature is observed. This increase approaches a maximum deviation of $\Delta T = 45^\circ\text{C}$ at the peak temperature of the cycle. At this time the specimen volume is overheated to about 1140°C.

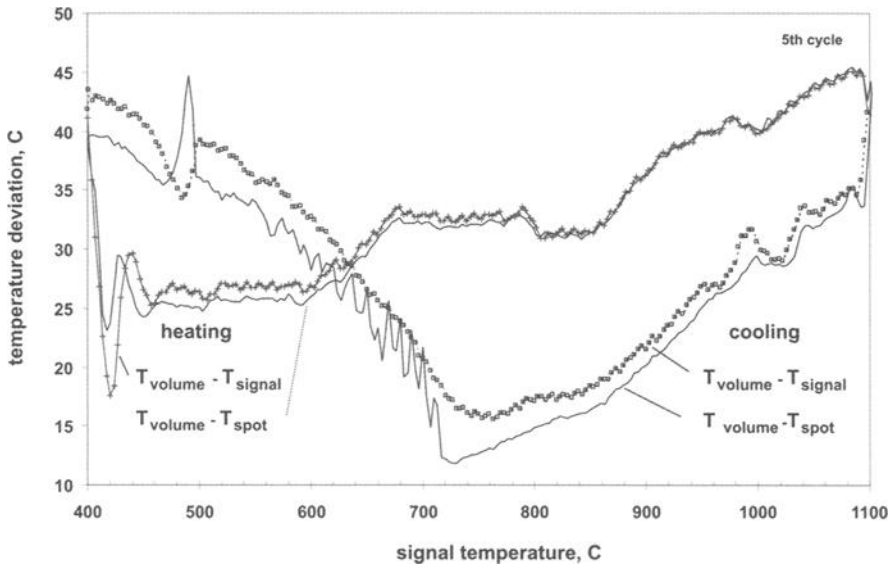


FIG. 5—Temperature deviations between volume and surface and between signal and volume for the heating and for the cooling phase as a function of the temperature signal.

Cooling Cycle—In the section of the cooling cycle between 1100°C and 850°C, both curves indicate that the higher volume temperature is continuously reduced from 45°C to approx. 17°C, (Fig. 5). In this sequence the deviations between the signal temperature and the spot welded thermocouple are in the order of $\Delta T = 3^\circ\text{C}$. With the onset of forced air cooling in the temperature interval from 750°C down to 400°C both curves change from a positive to a negative gradient, i.e. the volume temperature deviation continuously increases from $\Delta T = 15^\circ\text{C}$ (at 750°C) to $\Delta T = 40^\circ\text{C}$ (at 400°C). In this sequence, oscillations in the curve $T_{\text{volume}} - T_{\text{spot}}$ due to influences of the airflow on the spot welded control thermocouple are observed. The mean deviations between the signal temperature and the temperature of the spot welded thermocouple are again in the order of approximately 3°C.

Irrespective of the subsequent heating or cooling cycle in any case at the turn over the volume temperature is about $\Delta T = 40^\circ\text{C}$ above the signal temperature.

Finite Element Modeling

Figure 6 shows significant positions of the test specimen for which measured temperature data are available. For comparison, in the following the calculated temperatures during one thermal cycle will be presented for these representative positions (Fig. 7 and Fig. 8). All calculated temperature data refer to thermally stable conditions, which in the model are already obtained after the completion of the 3rd thermal cycle.

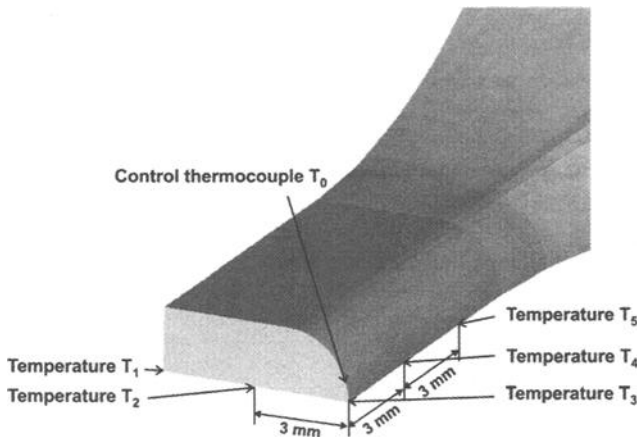


FIG. 6—Representative positions for the comparison of measured temperatures with the results obtained by finite element modeling.

The results obtained from the modeling of the surface temperatures in axial and in vertical direction are summarized in Fig. 7. Additionally, the calculated volume temperatures are plotted. With respect to the reference temperature, T_0 , given by the control thermocouple, the thermal gradients in horizontal direction of the cross section where the control thermocouple is spot-welded are negligible, T_3 . With increasing distance in vertical direction (6 mm) the surface temperature, T_5 , at the corner decreases with increasing temperature during the heating phase and reaches a maximum value of $\Delta T \approx 18^\circ\text{C}$ at the peak temperature of 1100°C . During the following cooling phase this deviation is again reduced with decreasing temperature.

In the heating sequence from 400°C to the peak temperature of 1100°C the specimen surface is exposed to slightly enhanced temperatures compared to the specimen volume. For the cooling phase the conditions are vice versa. This effect results from the reduced heat input into the surface layer during cooling where as the contributions of radiation and convection remain unchanged irrespective of the heating or the cooling phase for both effects are only affected by the surface temperature.

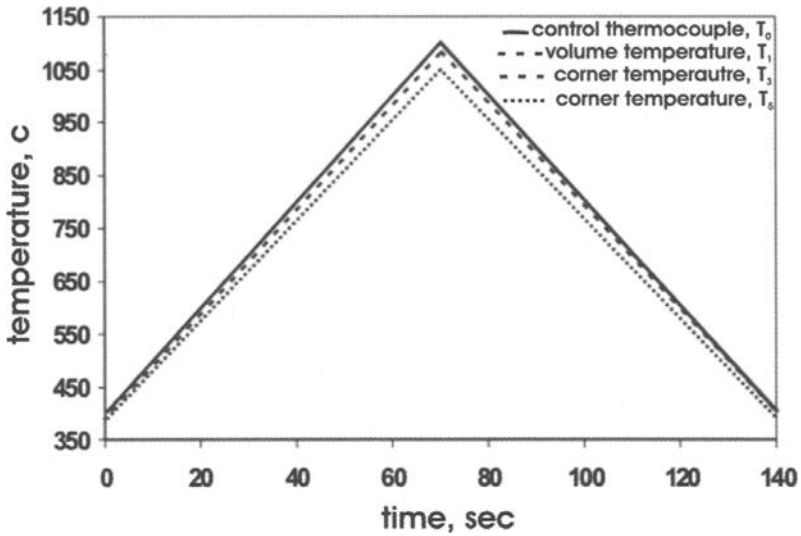


FIG. 7—Calculated cycle temperatures for various positions of the specimen.

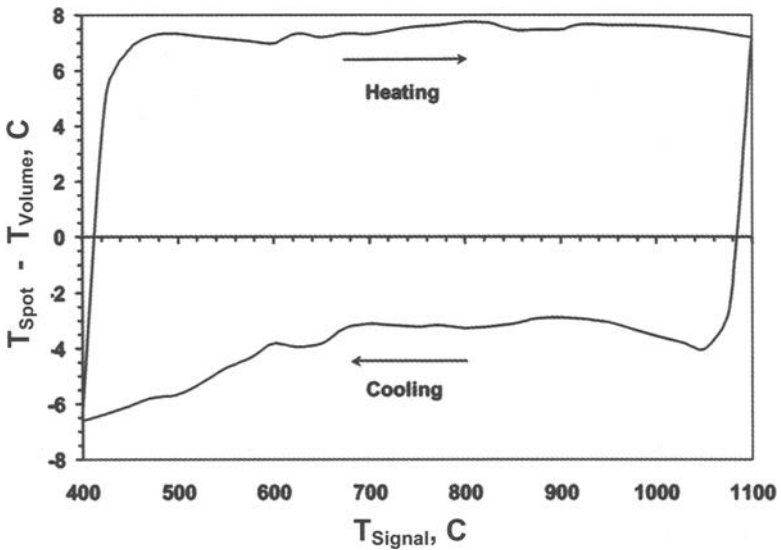


FIG. 8—Calculated thermal gradients between surface and volume within one thermal cycle for the heating and cooling phase.

Within the cross section in the center of the specimen volume the temperature deviations are approximately $\Delta T \approx 10^\circ\text{C}$ smaller compared to the measured temperature deviations between surface and volume (Fig. 8). This indicates that under the conditions as assumed in the model, the heat transfer into the volume appears to be sufficiently fast to guarantee almost stationary thermal conditions, which are required for TMF experiments. In axial direction of the gauge length deviations of up to 42°C are maintained by this calculation.

Discussion

Surface Temperatures

Already the analysis of the temperature profiles investigated under isothermal heating at specific temperatures, i.e., without any cooling by forced air, indicates that thermal gradients are acting on the surface in vertical and in horizontal direction, respectively. These surface gradients are more pronounced for higher temperature regimes, i.e., 900°C to 1100°C . In vertical direction the variations from the temperature signal are significantly increased for the lower half of the gauge section. This effect is mainly contributed to free convection for influences on the temperature profile due to non-steady surface radiation or heat flux through the cooled grips should be excluded due to the symmetry of the sample and the fixture system. Figure 4 has indicated that for this side where the control thermocouple is fixed only slight deviations from the signal temperature are detected, whereas for the opposite position a temperature increase of about 10°C is present. This indicates that heat flux through the wires of the thermocouple leads to locally reduced surface temperatures in the surrounded area of the spot weld position. Consequently, for the compensation of this deviation the thermal controller reacts with additional heating until the appropriate signal temperature is obtained. Due to this locally induced further heating the entire specimen is overheated.

The results of the analysis concerning the surface temperature distribution obtained from thermocouple measurements at various positions of the surface during thermal cycling also exhibit these reported variations in the actual surface temperature. For the temperature regime experimentally investigated, this side where the thermocouple is attached is clearly exposed to lower temperatures. In direct comparison, on the opposite side face slightly enhanced temperatures are registered. The temperature deviations in both horizontal and vertical direction are in good accordance with the results obtained by FEM calculations for defined positions (Fig. 6). This sensitivity of the temperature measurement concerning "external influences" is also confirmed by the oscillations in temperature, which are observed with the onset of the cooling by forced air. Although the wires of the control thermocouple are protected against convection by flexible glass fiber tubes, forced convection effects on the weld spots on the unprotected surface induce enhanced heat flux.

Volume Temperatures

During the entire cycle the volume temperatures are significantly enhanced compared to both the surface temperatures and the signal temperatures, respectively. Already with the onset of the fifth thermal cycle, i.e., after thermally stable conditions within the specimen volume should be obtained, this overheating of the volume is observed. Although the position of the volume thermocouple is slightly asymmetric (Fig. 2) to the

center axis of the sample, the results are considered to be representative also for the center position. These enhanced volume temperatures indicate that the reduction of the heat quantity stored in the volume cannot be reduced effectively by pure "natural cooling processes" (convection and radiation as well as heat flow through the cooled grips) to provide a temperature profile close to that defined by the thermal cycle. Nevertheless, the excess heat is reduced from $\Delta T = 45^{\circ}\text{C}$ to approx. $\Delta T = 15^{\circ}\text{C}$ during cooling from peak temperature to 750°C at the beginning of the air-cooling. At that sequence of the cycle the volume temperature again steadily increases until a maximum deviation of approx. 40°C is present at the beginning of the subsequent cycle. During this period the heat flux through the wires causes additional artificial cooling of the surrounding surface, which simulates reduced actual temperatures, but also the superimposed forced convection due to additional air-cooling. Consequently, the actual temperature signal appears as too low and is therefore adjusted by the thermal controller, which is combined with excessive heat input and consequently results in an overheated volume.

In contrast to the experimentally investigated deviations in temperature, the FEM results normalized by the experimentally measured surface temperatures indicate the opposite behavior. Under the limitation that all measured temperatures refer to the center area of the gauge section this comparison between the experimental and the calculated temperatures can be drawn.

The surface is exposed to slightly enhanced temperatures during heating and vice versa in the cooling sequence. The deviations from the temperature of the spot welded thermocouple are negligible. The results indicate that the heat transfer through the volume is not the time controlling step as could be concluded from the results of the experimentally recorded temperatures. The temperature difference between surface and volume provides an indication concerning the magnitude of the thermal gradients.

Finite Element Calculations

Due to the complex experimental set-up the boundary conditions required for the modeling cannot be accurately reproduced. All input variables are time dependent and experimentally not measurable. The major efforts in the FEM calculations were therefore aimed on a satisfactory modification of the temperatures calculated for those positions on the specimen surface for which also experimental data are available. Under the limitation that all measured temperatures refer to the center area of the gauge section this correlation between the experimental and the calculated temperatures can only be performed for this plane of the cross section, but it can be concluded that the model is sufficiently precise to also correctly predict the conditions in the surrounding area.

Conclusions

The detailed investigations concerning the temperature distribution in flat rectangular specimens of a Nickel base superalloy during thermal cycling indicate:

The accuracy of the temperature measurement is highly influenced by heat flux through the wires of the control thermocouple. This effect is observed under isothermal heating as well as under thermal cycling. Therefore, lower temperatures are registered and thus corrected by the thermal controller until for the control thermocouple the signal temperature is maintained. This leads to an overheating of the specimen volume.

Additional cooling by forced air as required to guarantee cooling rates in the order of 10°C/s affects the signal of the control thermocouple by forced convection effects.

Consequently, the measured actual temperature is reduced and thus the cooling does not provide sufficient reduction of the heat stored in the specimen volume.

According to the finite element modeling the heat flow within the volume is fast enough to provide stable and constant temperature distributions, even for heating rates in the order of 10°C/s .

Acknowledgments

The authors thank C. Schwamminger and J. Ross for their assistance and the performing of the experimental work and also M. Pieper for the analytical investigations.

References

- [1] Spera, D. A., *Thermal Fatigue of Materials and Components*, ASTM STP 612, D. A. Spera, Ed., ASTM International, West Conshohocken, PA, 1976, p. 3.
- [2] Miller, D. A. and Priest, R. H., "High Temperature Fatigue: Properties and Life Prediction," R. P. Skelton, Ed., Elsevier Applied Science, London/New York, 1987, p. 113.
- [3] Guédou, J.-Y. and Honnorat, Y., *Thermo-Mechanical Fatigue Behavior of Materials*, ASTM STP 1186, H. Sehitoglu, Ed., ASTM International, West Conshohocken, PA, 1993, p. 157.
- [4] Rémy, L., Bernard, H., Malpertu, J. L., and Rézai-Aria, F., *Thermo-Mechanical Fatigue Behavior of Materials*, ASTM STP 1186, H. Sehitoglu, Ed., ASTM International, West Conshohocken, PA, 1993, p. 3.
- [5] Marchionni, M., Bressers, J., Joos, R., Rémy, L., Timm, J., and Vasseur, E., *Materials for Advanced Power Engineering 1994, Part II*, D. Coutsouradis, J. H. Davidson, J. Ewald, P. Greenfield, T. Khan, M. Malik, D. B. Meadowcroft, V. Regis, R. B. Scarlin, F. Schubert, and D. V. Thornton, Eds., Kluwer Academic Publishers, Dordrecht, Boston, London, 1994, p. 989.
- [6] Bressers, J., Timm, J., Williams, S. J., Bennett, A., and Affeldt, E. E., *Thermo-mechanical Fatigue Behavior of Materials, 2nd Volume*, ASTM STP 1263, ASTM International, M. J. Verrilli and M. G. Castelli, Eds., ASTM International, West Conshohocken, PA, 1996, p. 56.
- [7] Stärk, K. F., personal communication, Darmstadt, Germany, February 2000.
- [8] Petry, F., Doctorate Thesis, Friedrich-Alexander-Universität Erlangen-Nürnberg, 1989.
- [9] Miller, D. A. and Priest, R. H., *High Temperature Fatigue: Properties and Prediction*, R. P. Skelton, Ed., Elsevier Applied Science, London/New York, 1987, p. 113.
- [10] Rao, S. S., *The Finite Element Method in Engineering*, Pergamon Press, 1989.
- [11] Pieper, M., Diploma Thesis, Fachhochschule University of Applied Sciences Münster, 2000.
- [12] Zienkiewicz, O. C. and Cheung, Y. K., "Transient Field Problems: Two-Dimensional Analysis by Isoparametric Finite Elements," *International Journal for Numerical Engineering*, Vol. 2, 1970, p. 61.
- [13] Qtran, "Internal Calculation Software," MTU Aero Engines GmbH, München, Germany, 1997.
- [14] Hibbitt, Karlsson & Sorensen Inc., *Abaqus Theory Manual*, Version 5.8, 1998.

Author Index

A

Affeldt, Ernst E., 15, 164, 312
 Alam, Adil M., 98
 Allison, John E., 240
 Andersson, H. C. M., 31
 Arai, Masayuki, 180
 Au, P., 3

B

Beck, T., 297
 Bickard, Anny, 98
 Bonacuse, Peter J., 65
 Brendel, T., 282
 Bressers, J., 83
 Bullough, C. K., 210

C

Cerdán de la Cruz, Lorena, 15
 Christ, Hans-Jürgen, 127, 145
 Coleman, Arthur, 227

D

de Haan, Frits, 255
 del Re, L., 282

E

Engler-Pinto, Carlos C., Jr., 45, 240

F

Fischer, Frank O. R., 127
 Fujiyama, Kazunari, 180

G

Gant, A., 270
 Gee, M. G., 270
 Grube, Friederike, 164

H

Hähner, Peter, 83, 255
 Hammer, Joachim, 15, 312
 Harada, Yoshio, 180
 Huber, U., 312

I

Immarigeon, J.-P., 3
 Itoh, Akihiro, 180

J

Jung, Arnd, 145

K

Takehi, Koji, 180
 Kalluri, Sreeramesh, 65

Kaneko, Hideaki, 180
 Kong, C. N., 210

L

Lang, Karl-Heinz, 195
 Lasecki, John, 240
 Løhe, Detlef, 195, 297
 Loveday, M. S., 270
 Lundblad, H., 312

M

Maier, Hans Jürgen, 45, 127, 145
 Moalla, Mourad, 195
 Moretto, P., 83
 Mughrabi, Haël, 112, 164

N

Naderhirn, M., 282
 Nanba, Kouichi, 180
 Neuner, Frank C., 112
 Nonaka, Isamu, 180

O

Okazaki, Masakazu, 180
 Okuda, Takanari, 180

P

Peteves, Stathis D., 83, 255

R

Rau, K., 297
 Rémy, Luc, 98
 Roebuck, B., 270

S

Sakane, Masao, 180
 Sakurai, Shigeo, 180
 Sandström, R., 31
 Santacreu, Pierre-Olivier, 227
 Schwaminger, C., 282
 Sehitoglu, Huseyin, 45, 240
 Simon, Christian, 227
 Smith, D. J., 210
 Stamos, Vassilis, 255
 Su, Xuming, 240

T

Take, Koji, 180
 Tang, Chung-Yao, 240
 Teteruk, Rostislav, 145
 Tetzlaff, Ulrich, 112
 Tzimas, E., 83

V

Vougiouklakis, Yannis, 255

W

Wu, X. J., 3

Y

Yamazaki, Yasuhiro, 180

Yandt, S., 3

Z

Zubeck, Michael, 240

Subject Index

A

ABAQUS, 240
 Accelerated material discrimination,
 270
 Acoustic emission, 255
 Activation energy, 3
 AISI 316 L, 297
 Aluminum alloy, 145
 Aluminide coatings, 98, 164, 210
 Aluminides, 83
 A1319-T7B, 45
 Austenitic stainless steel, 227, 297
 Automotive components, 45
 Axial-torsional, 65

B

Back stress, 45
 Brittle cracking, 210

C

Carbide strengthened alloy, 15
 Cast aluminum alloy, 45, 240
 CM186 SX, 210
 CM196, 255
 CM247LC, 180
 CMSX-4, 83, 180, 255
 CMSX-6, 164, 312
 Coarsening, 112
 Coatings, 98, 164, 180
 Cobalt-based superalloy, 65
 Computer simulations, 31
 CoNiCrAlY, 180
 Constitutive modeling, 45
 Control design, 282
 Counter-clockwise-diamond cycle, 112
 Crack density, 180
 Crack growth rate, 145
 Crack initiation, 164
 Crack propagation, 145
 Cracks, 227
 Creep, 31, 210
 Creep-fatigue damage parameter, 145
 Crystal, single, 112, 164, 210
 Cyclic behavior, 45
 Cyclic creep, 297
 Cyclic deformation, 3, 65, 195
 Cyclic hardening, 15, 65, 127
 Cyclic J-integral, 145
 Cyclic life, 145
 Cyclic stress-strain behavior, 127

D

Damage, 227
 mechanisms, 255
 Deformation behavior, 15
 Diamond phase, 180
 Dislocation structure, 180
 Drag stress, 45
 Ductile-to-brittle transition temperature, 127

E

Elastic deformation, 15, 31
 Elasto-viscoplastic constitutive law, 227
 Engine components, 240
 Environmental damage, 145
 Environmental degradation, 127
 Exhaust, 227

F

Fatigue crack propagation, 145
 Fatigue life, 112
 Fatigue prediction, 240
 Ferritic stainless steels, 227
 Finite element analysis, 210, 240
 Finite element modeling, 312
 Fracture, 83, 145, 180

G

γ/γ' -microstructure, 112

H

Haynes 188 superalloy, 65
 High cycle fatigue loading, super-imposed, 195
 High temperature, 45, 180
 properties, 270
 High-temperature aluminum alloy, 145
 High-temperature titanium alloy, 145
 High temperature transients, 282
 Hysteresis loop, 3, 15, 31

I

IMI 834, 145
 IN738LC, 180
 Inelastic deformation, 3
 In-phase cycling, 31, 65, 210, 227
 Intermetallics, 127
 Inverse control, 282
 Isothermal low-cycle fatigue, 180

L

Life prediction, 145, 180, 227
 Lifetime behavior, 195
 Low-cycle fatigue, 15

M

MAR-M 509, 83
 Metal matrix composite, 145
 Microstructure, 127
 Miniature test system, 270
 Modeling, 3, 15, 31, 127
 Multiaxial, 65

N

Nickel base alloy, 15
 Nickel-base superalloy, 164, 180,
 195, 210, 255, 312
 monocrystalline, 112
 NiCr22Co12Mo9, 195

O

Out-of-phase cycling, 31, 65, 127,
 180, 210, 227
 Overlay coatings, 83
 Oxidation, 127
 performance, 210
 protection coatings, 255

P

Phase angle, 83
 Plastic deformation, 31
 Platinum aluminides, 83, 164
 Pre-rafting, 112

R

Ramping tests, 270
 Relaxation, 15
 Reproducibility, 282
 Rhenium, 210

S

Sermalloy 1515, 210

Silicon carbide particle-reinforced, 145
 Simulation, 15
 Stainless steel alloys, 31, 227, 297
 Strain, 195, 240
 Stress, 240
 mean, 127
 Stress-strain curves, 3
 Stress-strain response, 45
 Superimposed loading, 195
 Surface damage analysis, 255

T

Taira type damage, 227
 Temperature, 195
 control, 282
 measurement, 312
 Thermal activation, 3
 Thermal barrier coatings, 83, 98
 Thermal fatigue, 240, 297
 Thermal gradients, 312
 Thermographic analysis, 312
 Thermomechanical fatigue, resistance, 112
 Thermomechanical loading, 65
 low-frequency, 195
 Titanium aluminide, 127

V

Video imaging, 255
 Viscoplasticity, 240

X

X8019, 145

Y

Yielding, 15